

PROGRESS IN RESEARCH

April 1, 2011 - March 31, 2012

CYCLOTRON INSTITUTE

Texas A&M University

College Station, Texas

PROGRESS IN RESEARCH

APRIL 1, 2011- MARCH 31, 2012

Prepared By

The Cyclotron Institute Staff

Texas A&M University

College Station, TX 77843-3366

Phone: (979) 845-1411

Fax: (979) 845-1899

Web: <http://cyclotron.tamu.edu>

August 2012

TABLE OF CONTENTS

Introduction	X
R.E. Tribble, Director	
SECTION I: NUCLEAR STRUCTURE, FUNDAMENTAL INTERACTIONS AND ASTROPHYSICS	
The isoscalar monopole resonance in the A~90 region	I-1
D.H. Youngblood, Y.-W. Lui, Krishichayan, J. Button, M.R. Anders, M.L. Gorelik, M.H. Urin, and S. Shlomo	
Superallowed beta deca	I-3
J.C. Hardy, I.S. Towner, V.E. Iacob, H.I. Park, L. Chen, V. Horvat, N. Nica, J Goodwin, M. Bencomo, L. Trache and R.E. Tribble	
Measurement of branching-ratios in the β decay of ^{38}Ca	I-7
H.I. Park, J.C. Hardy, V.E. Iacob, M. Bencomo, L. Chen, J.R. Goodwin, V. Horvat, N. Nica, B.T. Roeder, L. Trache and R.E. Tribble	
Weak beta branches in ^{32}Cl β decay	I-8
I.S. Towner, D. Melconian, and J.C. Hardy	
Tests of internal-conversion theory with precise γ- and x-ray spectroscopy: the case of $^{119}\text{Sn}^m$	I-10
N. Nica, J. Goodwin, J. C. Hardy, V. Horvat, V. E. Iacob, S. Miller, and M. B. Trzhaskovskaya	
United States nuclear data program and evaluated nuclear structure data file (ENSDF): data evaluation at Texas A&M	I-12
N. Nica and J. C. Hardy	
Calculation of isospin-mixing corrections for the isobaric analogue Fermi decay of ^{32}Cl	I-13
J.C. Hardy, V.E. Iacob, D. Melconian, N. Nica, H.I. Park, G. Tabacaru, I.S. Towner, L. Trache, R.E. Tribble, and Y. Zhai	
The absolute γ and β branches following the β^+ decay of ^{32}Cl	I-16
J.C. Hardy, V.E. Iacob, D. Melconian, N. Nica, H.I. Park, G. Tabacaru, I.S. Towner, L. Trache, R.E. Tribble, and Y. Zhai	

The ANC for $^{15}\text{C} \leftrightarrow ^{14}\text{C} + n$ and the astrophysical $^{14}\text{C}(n,\gamma)^{15}\text{C}$ rate	I-19
M. McCleskey, A.M. Mukhamedzhanov, L. Trache, R.E. Tribble, V. Goldberg, Y.-W. Lui, B. Roeder, E. Simmons, A. Spiridon, and F. Carstoiu	
Progress in the analysis of the beta delayed proton and gamma decay of ^{27}P for nuclear astrophysics.....	I-27
E. Simmons, L. Trache, A. Banu, A. Saastamoinen, M. McCleskey, B. Roeder, A. Spiridon, R.E. Tribble, T. Davinson, P. J. Woods, G. J. Lotay, J. Wallace, and D. Doherty	
Measurement of the $d(^{26}\text{mAl},p)^{27}\text{Al}$ reaction with TECSA	I-34
B.T. Roeder, M. McCleskey, L. Trache, S. Cherubini, V.Z. Goldberg, M. Gulino, V.E. Jacob, M. La Cognata, G. Lotay, R.G. Pizzone, G.G. Rapisarda, E. Simmons, R. Sparta, A. Spiridon, C. Spitaleri, and R.E. Tribble	
The $^{18}\text{F}(p,\alpha)^{15}\text{O}$ reaction studied via TECSA	I-38
R.G. Pizzone, B.T. Roeder, L. Trache, C. Spitaleri, V.Z. Goldberg, M. Gulino, M. Kurokawa, I. Indelicato, M. La Cognata, M. McCleskey, G.G. Rapisarda, E. Simmons, R. Sparta, A. Spiridon, and R.E. Tribble	
The two-proton decay of ^{12}O and its isobaric analog state in ^{12}N	I-42
M.F. Jager, R.J. Charity, J.M. Elson, J. Manfredi, H. Mohammad, and L.G. Sobotka, M. McCleskey, L. Trache, B.T. Roeder, A. Spiridon, E. Simmons, R.G. Pizzone and M. Kurokawa	
Preliminary results of the indirect study of the $^{12}\text{C}(^{12}\text{C},\alpha)^{20}\text{Ne}$ reaction via the THM applied to the $^{16}\text{O}(^{12}\text{C},\alpha)^{20}\text{Ne}$ reaction.....	I-46
G.G. Rapisarda, C. Spitaleri, C. Bordeanu, Z. Hons, G.G. Kiss, M. La Cognata, J. Mrazek, C. Nita, D. Pantelica, H. Petrascu, R.G. Pizzone, S. Romano, T. Szücs, L. Trache, A. Tumino, and G. Velisa	
Clustering in non-self-conjugate nuclei.....	I-51
V.Z. Goldberg, M. Avila, S. Cherubini, G.V. Rogachev, M. Gulino, E.D. Johnson, A.N. Kuchera, M. La Cognata, L. Lamia, S. Romano, L.E. Miller, R.G. Pizzone, G.G. Rapisarda, M.L. Sergi, C. Spitaleri, R.E. Tribble, W.H. Trzaska, A. Tumino	
Highly excited high spin states in ^{22}Ne	I-56
V.Z. Goldberg, S.Yu. Torilov, M. Brenner, K.A. Gridnev, S.V. Khlebnikov, M. Mutterer, B.G. Novatski, Yu.G. Sobolev, W.H. Trzaska, L.I. Vinogradov, V.I. Zhrebchevsky	
Resonance scattering to study exotic nuclei at the limits of stability.....	I-60
V.Z. Goldberg, B.T. Roeder, G.G. Chubarian, A.A. Alharbi, A. Banu, M. McCleskey, E. Simmons, G. Tabacaru, L. Trache, R.E. Tribble, G.V. Rogachev, E.D. Johnson, C. Fu, M.L. Avila, J.P. Mitchell	

Resonances in elastic alpha-particle scattering as evidence of clustering at high excitation in ^{34}S and ^{40}Ca	I-67
V.Z. Goldberg, M. Norrby, T. Lönnroth, G.V. Rogachev, M.S. Golovkov, K.-M. Källman, S.V. Perov, M. Lattuada, S. Romano, B.B. Skorodumov G.P. Tiourin, W.H. Trzaska, A. Tumino	

Spin physics with STAR at RHIC	I-70
Z. Chang, P. Djawotho, J.L. Drachenberg, C.A. Gagliardi, L. Huo, M.M. Mondal, R.E. Tribble, and the STAR Collaboration	

SECTION II: HEAVY ION REACTIONS

A search for super heavy elements using a catcher foil.....	II-1
M. Barbui, K. Schmidt, J.B. Natowitz, H. Zheng, K. Hagel, A. Bonasera and M. Barbino	

Probing clusterization in $^{40}\text{Ca} + ^{40}\text{Ca}$ reactions.....	II-7
K. Schmidt, M. Barbui, J. B. Natowitz, K. Hagel, A. Bonasera, G. Giuliani, M. Rodrigues, R. Wada, M. Huang, C. Botosso, G. Liu, G. Viesti, S. Moretto, G. Prete, S. Pesente, D. Fabris, Y. El Masri, T. Keutgen, S. Kowalski, and A. Kumar	

Yield of D-D and D-^3He fusion reactions produced by the interaction of intense ultrafast laser pulses with molecular clusters	II-10
M. Barbui, A. Bonasera, K. Hagel, J.B. Natowitz, K. Schmidt, W. Bang, G. Dyer, H. Quevedo, A. Bernstein, E. Gaul, T. Borger, A. Bernstein, M. Martinez, M. Donovan, T. Ditmire, F. Consoli, R. De Angelis, P. Andreoli	

Clusterization in low density nuclear matter	II-13
K. Hagel, R. Wada, L. Qin, J. B. Natowitz, S. Shlomo, A. Bonasera, G. Röpke, S. Typel, Z. Chen, M. Huang, J. Wang, H. Zheng, S. Kowalski, C. Botosso, M. Barbui, M.R. D. Rodrigues, K. Schmidt, D. Fabris, M. Lunardon, S. Moretto, G. Nebbia, S. Pesente, V. Rizzi, G. Viesti, M. Cinausero, G. Prete, T. Keutgen, Y. El Masri, and Z. Majka	

Temperature measurements in reactions at low excitation energies to probe a possible phase transition.....	II-15
A. Raphelt, B. Stern, P.J. Cammarata, L. Heilborn, J. Mabilia, L.W. May, A.B. McIntosh, A. Zarella, and S.J. Yennello	

Investigation of the nuclear phase transition using the Landau free energy approach	II-17
J. Mabilia, A. Bonasera, H. Zheng, A.B. McIntosh, L.W. May, P. Cammarata, Z. Kohley, K. Hagel, L. Heilborn, A. Zarella, A. Raphelt, and S.J. Yennello	

Signatures of the liquid-gas phase transition from fermionic quantum fluctuations	II-21
J. Mabilia, A. Bonasera, H. Zheng, A. B. McIntosh, L.W. May, P. Cammarata, Z. Kohley, K. Hagel, L. Heilborn, A. Zarrella, A. Raphelt, and S.J. Yennello	
Equation of state effects on Nucleon Transport.....	II-23
L.W. May, P. Cammarata, L. Heilborn, J. Mabilia, A. McIntosh, A. Raphelt, A. Zarrella, and S. J. Yennello	
Probing the symmetry energy at high energies with the ASY-EOS collaborations at GSI.....	II-26
Paul Cammarata, Lauren Heilborn, Larry May, Paola Marini, and S.J. Yennello for Asy-EOS Collaboration	
Using break-up mechanisms in heavy ion collisions at low energies to constrain the symmetry energy at low nuclear density	II-29
Paul Cammarata, Alan McIntosh, Lauren Heilborn, Larry May, Andrew Raphelt, Andrew Zarrella, and S.J. Yennello	
Temperature dependence of the nuclear caloric curve	II-33
A.B. McIntosh, A. Bonasera, Z. Kohley, S. Galanopoulos, K. Hagel, L.W. May, P. Marini, D.V. Shetty, W.B. Smith, S.N. Soisson, G.A. Souliotis, B.C. Stein, R. Tripathi, S. Wuenschel, and S.J. Yennello	
Correlation functions in constrained molecular dynamics (CoMD)	II-36
Lauren Heilborn, H. Zheng, Z. Kohley and SJY Group	
Proximity effect in multifragmentation events.....	II-39
Lauren Heilborn, G. Souliotis, S. Soisson, P. Cammarata, P. Marini, L.W. May, A. McIntosh, A. Raphelt, B. Stein, and S.J. Yennello	
Production of nuclides near the N = 126 shell in ⁴⁸Ca, ⁵⁰Ti, and ⁵⁴Cr induced reactions.....	II-42
D.A. Mayorov, T.A. Werke, M.C. Alfonso, M.E. Bennett, and C.M. Folden III	
Development of a gas stopper for heavy element chemistry	II-46
M. C. Alfonso and C. M. Folden III	
Improvements to the heavy elements program aimed toward reaching lower cross-sections at the Texas A&M University Cyclotron Institute	II-52
T.A. Werke, M.C Alfonso, M.E. Bennett, D.A. Mayorov, and C.M. Folden III	
Extraction chromatographic studies of Rf homologs with TEVA resin	II-56
Megan E. Bennett, Marisa C. Alfonso, and Charles M. Folden III	

Measurement of the $^{nat}\text{Lu}(p,x)^{175}\text{Hf}$ excitation functionII-71
Megan E. Bennett, Dmitriy A. Mayorov, Kyle D. Chapkin, Marisa C. Alfonso,
Tyler A. Werke, and Charles M. Folden III

Toward understanding relativistic heavy-ion collisions with the STAR detector at RHICII-79
M. Cervantes, M. Codrington, A. Hamed, S. Mioduszewski, Y. Mohammed, and
the STAR Collaboration

SECTION III: NUCLEAR THEORY

**High order corrections to density and temperature of fermions and bosons from quantum
fluctuations and the CoMD- α Model..... III-1**
Hua Zheng, Gianluca Giuliani, Matteo Barbarino, and Aldo Bonasera

New insight into deuteron stripping to bound states and resonances III-8
A.M. Mukhamedzhanov, I. Thompson, and J. Escher

Asymptotic normalization coefficients from the $^{14}\text{C}(d,p)^{15}\text{C}$ reaction..... III-10
A.M. Mukhamedzhanov, V. Burjan, M. Gulino, Z. Hons, V. Kroha, J. Mrazek,
J. Novak, S. Piskor, S. Romano, M.L. Sergi, C. Spitaleri, and R.E. Tribble

Electron - and photon - impact atomic ionization..... III-12
I. Bray, D.V. Fursa, A.S. Kadyrov, A.S. Kheifets, A.M. Mukhamedzhanov,
and A.T. Stelbovics

**Generalized Faddeev equations in the AGS form for deuteron stripping with explicit
inclusion of the Coulomb interactions..... III-13**
A.M. Mukhamedzhanov, V. Eremenko, and A. I. Sattarov

Reexamination of the astrophysical S factor for the $\alpha+d\rightarrow{}^6\text{Li}+\gamma$ reaction III-14
A.M. Mukhamedzhanov, L.D. Blokhintsev, and B. F. Irgaziev

Theory of deuteron stripping: From surface integrals to a generalized R-matrix approach III-15
A.M. Mukhamedzhanov

Skyrme-Hartree-Fock calculations of isospin-symmetry breaking..... III-16
I.S. Towner and J.C. Hardy

Approximate expressions for the beta-neutrino angular correlation coefficient III-20
I.S. Towner and J.C. Hardy

Isoscalar and isovector giant resonances in ^{40}Ca and ^{48}Ca.....	III-24
M.R. Anders, S. Shlomo, T. Sil, D.H. Youngblood, Y.-W. Lui, Krishichayan and J. Button	
Nuclear matter properties from energies of giant resonances	III-27
M.R. Anders and S. Shlomo	
Clusters in nuclei, nuclear matter, heavy ion collisions and astrophysics- report on the ECT* workshop, June 13-17, Trento, Italy	III-29
Gerd Roepke, David Blaschke, Thomas Klähn, Shalom Shlomo and Stephan Typel	
Deducing the neutron skin thickness in ^{208}Pb from the strength function distribution of the isovector giant dipole resonance	III-31
M.R. Anders and S. Shlomo	
Hadronic potential effects in elliptic flow in heavy ion collisions	III-33
J. Xu, L.W. Chen, C.M. Ko, and Z.W. Lin	
Charmonium production in relativistic heavy ion collisions.....	III-35
T. Song, K.C. Han, and C.M. Ko	
Nuclear symmetry energy and single-nucleon potential in asymmetric nuclear matter	III-37
C. Xu, B.A. Li, L.W. Chen, and C.M. Ko	
Bottomonium suppression in relativistic heavy ion collisions.....	III-38
T. Song, K.C. Han, and C.M. Ko	
Subthreshold cascade production in heavy ion collisions.....	III-40
L. Feng, L.W. Chen, C.M. Ko, and S.H. Lee	
Exotic hadrons in heavy ion collisions.....	III-42
S. Cho, T. Furumoto, T. Hyodo, D. Jido, C.M. Ko, S.H. Lee, M. Nielsen, A. Ohnishi, T. Sekihara, S. Yasui, and K. Yazak	
Higher-order flows and dihadron correlations in heavy ion collisions at LHC	III-44
J. Xu and C.M. Ko	
Triangular flow and dihadron correlations in heavy ion collisions at RHIC	III-45
J. Xu and C.M. Ko	
Dilepton production in relativistic heavy ion collisions	III-46
E.L. Bratkovskaya, W. Cassing, C.M. Ko, O. Lynnk, J. Manninen, and V. Ozvenchuk	

Energy release from hadron-quark phase-transition in neutron stars	III-48
W. Lin, B.A. Li, J. Xu, C.M. Ko, and D.H. Wen	
Thermal photons and collective flow at RHIC	III-49
H. van Hees, C. Gale, and R. Rapp	
Bottomonia in the quark-gluon plasma and their production at RHIC and LHC	III-51
A. Emerick, X. Zhao and R. Rapp	
Heavy-quark diffusion and hadronization in quark-gluon plasma.....	III-53
Min He, Rainer J. Fries, and Ralf Rapp	
Ideal hydrodynamics for bulk and multistrange hadrons in $\sqrt{s_{NN}} = 200$ A GeV Au-Au collisions	III-55
Min He, Rainer J. Fries, and Ralf Rapp	
Directed flow from color glass condensate	III-57
R.J. Fries and G. Chen	
Dileptons from the deconfinement phase transition	III-58
R.J. Fries and G. Chen	

SECTION IV: MISCELLANEOUS

Ernest Rutherford and the origins of nuclear physics.....	IV-1
J.C. Hardy	

SECTION V: SUPERCONDUCTING CYCLOTRON, INSTRUMENTATION AND RIB UPGRADE

K500 operations and development	V-1
D.P. May, G.J. Kim, H.L. Clark, and F.P. Abegglen	
Texas A&M cyclotron radiation effects facility April 1, 2011 – March 31, 2012.....	V-3
H.L. Clark, J. Brinkley, G. Chubarian, V. Horvat, B. Hyman, B. Roeder and G. Tabacaru	
Cyclotron computing	V-5
R. Burch and K. Hagel	

Cyclotron Institute upgrade project.....	V-6
H.L. Clark, F. Abegglen, G. Chubarian, G. Derrig, G. Kim, D. May, and G. Tabacaru	
The charge breeding ECR ion source at the Cyclotron Institute	V-16
G. Tabacaru and D.P. May	
Radiation monitor data logging	V-19
R. Burch, F. Abegglen, L. Gathings, and D. Menchaca	
Upgrade of equipment to measure precise β-decay branching ratios	V-21
V.E. Iacob, J.C. Hardy and H.I. Park	
Precision measurement of $^{26}\text{Al}^m$ half-life with digital β^+ counting method	V-24
L. Chen and J. C. Hardy	
Event analysis of β decay	V-28
V. Horvat, J.C. Hardy, and V.E. Iacob	
TAMUTRAP facility status report.....	V-33
R.S. Behling, B. Fenker, M. Mehlman, D. Melconian, and P.D. Shidling	
Upgrade of the ^{37}K asymmetry measurement experiment	V-37
R.S. Behling, B. Fenker, M. Mehlman, D. Melconian, and P.D. Shidling	
TAMUTRAP—Design of the cylindrical Penning trap system	V-40
R.S. Behling, B. Fenker, M. Mehlman, D. Melconian, and P.D. Shidling	
Source specific neutron detection efficiencies of the TAMU Neutron Ball.....	V-42
Andrew Zarrella, P. Marini, A.B. McIntosh, P. Cammarata, L. Heilborn, J. Mabilia, L.W. May, A. Raphelt, and S.J. Yennello	
SAMURAI TPC: detailed design and construction of a time projection chamber	V-45
A.B. McIntosh, J. Barney, J. Dunn, J. Estee, T. Isobe, M. Famiano, W.G. Lynch, T. Murakami, R. Olsen, R. Shane, A. Taketani, M.B. Tsang, and S.J. Yennello	
On-line transactinide homolog chemistry	V-47
Megan E. Bennett and Charles M. Folden III	
Heavy element targetry	V-49
Megan E. Bennett, Charles M. Folden III, and J.P. Greene	
AstroBox – a new type of low energy proton detector	V-52
L. Trache, E. Simmons, A. Spiridon, M. McCleskey, B.T. Roeder, R.E. Tribble, E. Pollacco, G. Pascovici, Marc Riallot, Jean Philippe Mols, and Mariam Kebbiri	

GEANT4 Simulations for the design of AstroBox2	V-55
B.T. Roeder, E. Pollacco, and L. Trache	
STAR LiTe.....	V-58
M. McCleskey, G. Kim, R.E. Tribble, J.T. Burke, R. Casperson, and STARS Collaboration	
Characterization of a front-end circuit for SAMURAI Si detection system	V-62
M. Kurokawa, M. McCleskey, B. Roeder, A. Saastamoinen, L. Trache, R.E. Tribble, L. Sobotka, and J. Elson	
Test of completed decay detector for ISGMR study.....	V-65
J. Button, Krishichayan, J. Shafer, Y.-W. Lui, and D.H. Youngblood	

SECTION VI: PUBLICATIONS

Papers published	VI-1
-------------------------------	-------------

SECTION VII: APPENDIX

Talks presented	VII-1
Research personnel and engineering staff	VII-10
Students.....	VII-11
Organizational chart.....	VII-12
Graduate degree students.....	VII-13
Institute colloquia and seminars	VII-14

Introduction

April 1, 2011 – March 31, 2012

Progress in research and operations at the Texas A&M Cyclotron Institute is summarized in this report for the period April, 1, 2011 through March 31, 2012. The format follows that of previous years. Sections I through IV contain reports from individual research projects. Operation and technical developments are given in Section V. Section VI lists the publications with Cyclotron Institute authors and the Appendix gives additional information including talks presented by members of the Institute during the past year. Once again, the full volume of this year's Progress in Research is available only on our web site (<http://cyclotron.tamu.edu>). *Since most of the contributions presented here are truly reports on progress in research, results and conclusions should not be quoted from the report without the consent of the authors.*

We have now completed 7 1/2 years of the Upgrade Project, which will give us accelerated radioactive beams at intermediate energies very soon. The K150 cyclotron is operational for both positive-ion and negative-ion beams and has been used in a number of experiments since late fall 2011. During the January, 2012 shutdown, we installed the switching magnet in the K500 axial injection line that allows us to inject beams from the ECR source or the ion-guide cave. All of the elements for the injection line from the ion-guide cave are in place and final work is being done to integrate them into the control system. We have observed charge-breeding in the ion-guide cave ECR source and work is now underway to optimize its efficiency. The high-power beam dump, which is the final element needed to begin production tests with the light-ion guide system, is being assembled in the machine shop and will be available before the end of August, 2012. A rebuild of the BigSol cryostat was completed in the spring of 2012. The new cryostat consumes liquid helium at a significantly lower rate than the previous one and shows no sign of a leak from the helium vessel into the surrounding vacuum region.

The search for faculty members to fill positions in the Nuclear Solutions Institute continued into 2012. We have active candidates for the two senior level radiochemistry positions and we hope to fill them very soon. We are still searching for a person to fill the senior-level position in the physics department and cyclotron institute.

Construction on a new floor of offices at the Institute began in March, 2012. A total of 13 months is scheduled to complete the construction. During the summer and fall of 2012, Institute faculty and staff have had to relocate offices to an adjacent building.

As in previous reports, I include here some highlights of work carried out over the past year.

- The gamma and beta branches following the decay of ^{32}Cl were measured, and led to the largest-ever observed isospin-symmetry-breaking effect seen in a superallowed transition. This result agrees with a shell-model calculation and serves as a new benchmark for other models of calculations of these corrections.

- A first experimental determination of in-medium binding energies for d , t , ${}^3\text{He}$ and ${}^4\text{He}$ clusters has been carried out for specific combinations of temperature and density in low density nuclear matter produced in collisions of 47A MeV ${}^{40}\text{Ar}$ and ${}^{64}\text{Zn}$ projectiles with ${}^{112}\text{Sn}$ and ${}^{124}\text{Sn}$ target nuclei. The experimentally derived values of the in-medium-modified binding energies confirm recent theoretical predictions based upon the implementation of Pauli blocking effects in a quantum statistical approach and extend the applicability of that method to the nuclear equation of state, which is of great interest in astrophysics.
- A new detector system based on GEM technology has been developed for proton-decay studies and used to measure beta-delayed protons in the decay of ${}^{23}\text{Al}$ and ${}^{27}\text{P}$. The new detector substantially reduces the electron energy loss signal allowing very low-energy protons to be observed, which are the protons from resonances that are most important in the inverse (p,γ) capture reactions in stars.
- The Heavy Elements Group continued its study of "warm fusion" reactions and completed fabrication of a specially-designed "gas stopper" that will allow for the chemical study of heavy elements.
- The giant monopole resonance energies in ${}^{92}\text{Zr}$ and ${}^{92}\text{Mo}$ lead to nucleus compressibilities 27 MeV (5σ) and 56 MeV (8σ) above HF-RPA predictions, suggesting significant nuclear structure effects, which could affect conclusions about the compressibility of nuclear matter.
- Determination of experimental temperatures and densities of the fragmenting system using the quantum fluctuation method for protons.
- We obtained the first experimental evidence for non-zero gluon polarization in the proton, through measurements of the longitudinal double-spin asymmetry for inclusive jet production in 200 GeV p+p collisions with STAR.
- New generalized Faddeev equations for deuteron stripping were obtained with explicit inclusion of the Coulomb interaction and target excitation. It represents the ultimate theory of low energy transfer reactions, which takes into account all coupled channel and target excitation effects.
- The theory of deuteron stripping to resonance states has been developed in the surface integral formalism leading to the R matrix approach allowing one to parameterize the cross sections in terms of the observable resonance partial widths. The theory is free of divergences, which has been the main obstacle to understand stripping to resonance states.
- Within the framework of a multiphase transport model, we have found that including mean-field potentials in the baryon-rich hadronic matter leads to a splitting of the elliptic flows of particles and their antiparticles, thus providing a plausible explanation of the experimental observations in the Beam Energy Scan program at the Relativistic Heavy-Ion Collider.
- A thermal rate-equation approach with in-medium bottomonium spectral properties has been used to predict Upsilon observables at RHIC and LHC; initial data seem to favor a strong-binding scenario.
- Calculations of thermal photon production at RHIC suggest that the large photon elliptic flow observed by PHENIX requires the dominant emission source to radiate from around the phase transition region, rather than from the early quark-gluon plasma phases.

- It was found that for all over 16 commonly employed Skyrme interactions, the calculated HF based RPA energy of the isoscalar giant monopole resonance of ^{48}Ca is lower than that of ^{40}Ca , in disagreement with recent experimental data.

Institute scientists remain active in a number of collaborative research efforts around the world. Major programs include: mass measurements using the Penning Traps at Argonne National Laboratory and the University of Jyväskylä; continued work with the STAR collaboration at RHIC; the measurement of neutron beta decay with the UCNA collaboration; and participation in the SAMURAI collaboration at RIBF in Tokyo, Japan.

Once again, I am indebted to Dr. Y.-W. Lui for assembling this report.

R.E. Tribble

August 8, 2012

SECTION I

NUCLEAR STRUCTURE, FUNDAMENTAL INTERACTIONS AND ASTROPHYSICS

The isoscalar monopole resonance in the A~90 region

D.H. Youngblood, Y.-W. Lui, Krishichayan,¹ J. Button, M.R. Anders, M.L. Gorelik,²
M.H. Urin,² and S. Shlomo

¹*Dept. of Pure and Applied Physics, Guru Ghasidas University Bilaspur-495009 C G India*

²*National Research Nuclear University "MEPhI", Moscow, 115409 Russia*

The isoscalar giant monopole resonances (ISGMR) in $^{90,92,94}\text{Zr}$ and $^{92,96,98,100}\text{Mo}$ have been studied with inelastic scattering of 240 MeV α particles at small angles including 0° . Strength corresponding to approximately 100% of the ISGMR (E0) energy-weighted sum rule was identified in each nucleus. In all cases the strength consisted of two components separated by 7-9 MeV. Except for the mass 92 nuclei, the upper component contained 14-22% of the E0 energy weighted sum rule (EWSR), however 38% and 65% of the E0 EWSR was located in the upper components in ^{92}Zr and ^{92}Mo respectively. The energies of the ISGMR for ^{92}Zr and ^{92}Mo are 1.22 MeV and 2.80 MeV higher, respectively, than for ^{90}Zr , suggesting a significant nuclear structure contribution to the energy of the ISGMR in these nuclei.

The energy of the isoscalar giant monopole resonance (ISGMR) is related to the compression modulus of the nucleus (K_A) [1,2] as follows:

$$E_{\text{GMR}} = (\hbar^2 K_A / m \langle r^2 \rangle)^{1/2} \quad (1)$$

where m is the nucleon mass and $\langle r^2 \rangle$ is the mean square nuclear radius. Using for E_{GMR} the experimental energies corresponding to the scaling model $\{(m_3/m_1)^{1/2}\}$ and radii obtained from Hartree-Fock calculations with the KDE0v1 interaction [4] having $K_{\text{NM}} = 227.5$ MeV, the experimental scaling model

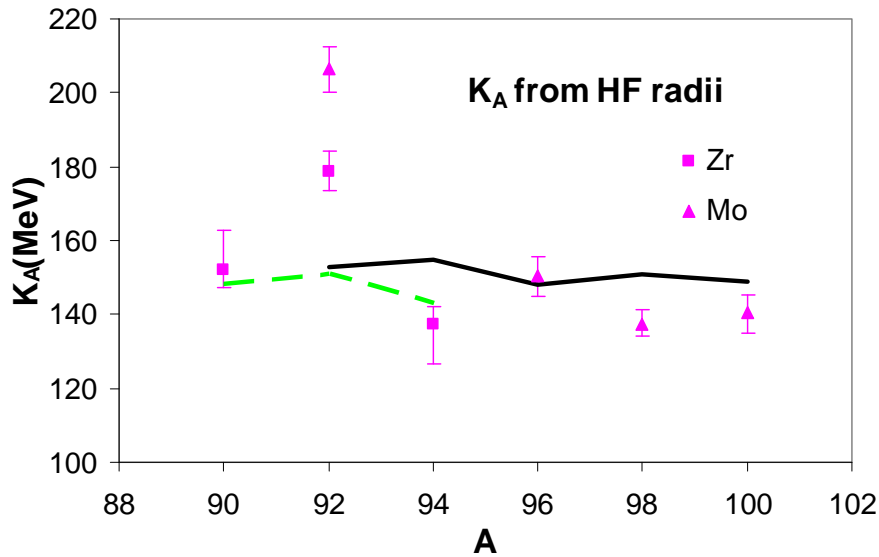


FIG. 1. The scaling model K_A values obtained from the measured scaling energies $(m_3/m_1)^{1/2}$ are shown for the Zr isotopes by squares and for the Mo isotopes by the triangles plotted versus A . The error bars reflect the uncertainties in $(m_3/m_1)^{1/2}$. Also shown are lines connecting the HF-based RPA values of K_A calculated within HF-RPA using the KDE0v1 interaction for the Zr (green-dashed) and Mo (black) isotopes.

values of K_A for the Zr and Mo isotopes were obtained from Eq. (1) and are plotted versus A in Fig. 1. For ^{92}Zr and ^{92}Mo , K_A values obtained from the experimental energies are 27 MeV (5σ) and 56 MeV (8σ) higher than the values predicted with HF-RPA.

[1] J.P. Blaizot, Phys. Rep. **64**, 171(1980).

[2] J. Treiner, H. Krivine and O. Bohigas, Nucl. Phys. **A371**, 253 (1981).

Superallowed beta decay

J.C. Hardy, I.S. Towner, V.E. Iacob, H.I. Park, L. Chen, V. Horvat, N. Nica,
J Goodwin, M. Bencomo, L. Trache and R.E. Tribble

Superallowed $0^+ \rightarrow 0^+$ beta decay between $T=1$ analogue states has been a subject of continuous and often intense study for five decades. The ft values of such transitions are nearly independent of nuclear-structure ambiguities and depend uniquely on the vector part of the weak interaction. Their measurement gives us access to clean tests of some of the fundamental precepts of weak-interaction theory, and, over the years, this strong motivation has led to very high precision being achieved in both the experiments and the theory used to interpret them. We have a major program at the Cyclotron Institute to study superallowed beta decay.

To obtain the ft value for any transition, three quantities must be measured: the half life of the parent, the Q_{EC} value for the transition of interest and the branching ratio for that transition. Our most recent complete survey of existing data on these superallowed decays, published in 2009 [1] provided a critical evaluation of all the experimental data and obtained final ft values from the averaged results, to which improved radiative and isospin-symmetry-breaking corrections [2] were applied in order to derive a final set of “corrected ft values”, denoted Ft . One of the new features added at that time was that we calculated the radial-overlap correction, δ_{C2} , with Hartree-Fock radial wave functions as well as the Saxon-Woods wave functions we have used before. The differences in the results from these two methods are used as a measure of the systematic uncertainty to be applied to the theoretical corrections. These differences also offer the possibility that measured ft values with the highest precision could actually distinguish between the two methods and thereby reduce the systematic uncertainty.

With the updated world data and improved corrections the Ft values were seen to be completely consistent with one another, thus demonstrating the constancy of G_V to 1.3 parts in 10^4 . Not only is this an important confirmation of the Conserved Vector Current (CVC) hypothesis but it sets the stage for using the average value of G_V to test a fundamental principle of the electroweak standard model: the unitarity of the Cabibbo-Kobayashi-Maskawa (CKM) matrix. The up-down quark mixing element of that matrix, V_{ud} , is given by $V_{ud} = G_V / G_F$, where G_F is the weak interaction constant for the purely leptonic muon decay. The value of V_{ud} is a key component of the most demanding test available for the unitarity of the CKM matrix, the sum of squares of its top-row elements [1]. As elaborated in our recent review article on the evaluation of V_{ud} [3], superallowed nuclear beta decays provide by far the most precise and reliable value for V_{ud} and, in fact, that element is also the most precisely known one in the CKM matrix – by an order of magnitude! Its current value [1,3] is 0.97425(22), a result that yields a CKM unitarity sum of 0.99990(60) [3], in full agreement with the standard-model expectation, and carrying the smallest uncertainty yet obtained.

This result is not only a significant verification of the standard model but the uncertainty quoted on the sum provides a tight limit on any possible new physics beyond the standard model, such as right-hand currents, extra Z bosons or supersymmetric models. In short, superallowed $0^+ \rightarrow 0^+$ beta decay

provides a high-profile application of nuclear-physics measurements to the study of fundamental symmetries, a subject of vital interest to both nuclear and particle physicists. Although much has already been achieved in this field by nuclear physicists, improvements are still possible. Reducing the uncertainty on the unitarity sum – and, with it, the scope for new physics – remains the primary goal of our research program.

Our approach follows from the observation [1,3] that the second largest contributor to the uncertainty in V_{ud} is the theoretical uncertainty in the nuclear-structure-dependent corrections, δ_{NS} and δ_C , used in the derivation of the Ft values. Though these corrections are only of order 1%, their effect is very significant: Fig. 1, which is taken from our 2009 survey [1], shows the result of applying δ_{NS} and δ_C (together with δ'_R , which is nearly independent of Z). Obviously they act very well to remove the considerable “scatter” in ft values apparent in the left panel, replacing it with the consistent set of corrected Ft values appearing in the right panel. Since these corrections were determined [2] completely independently of the superallowed decay data, this consistency in Ft values is already a powerful validation of these calculated corrections, but obviously the remaining uncertainty still influences the

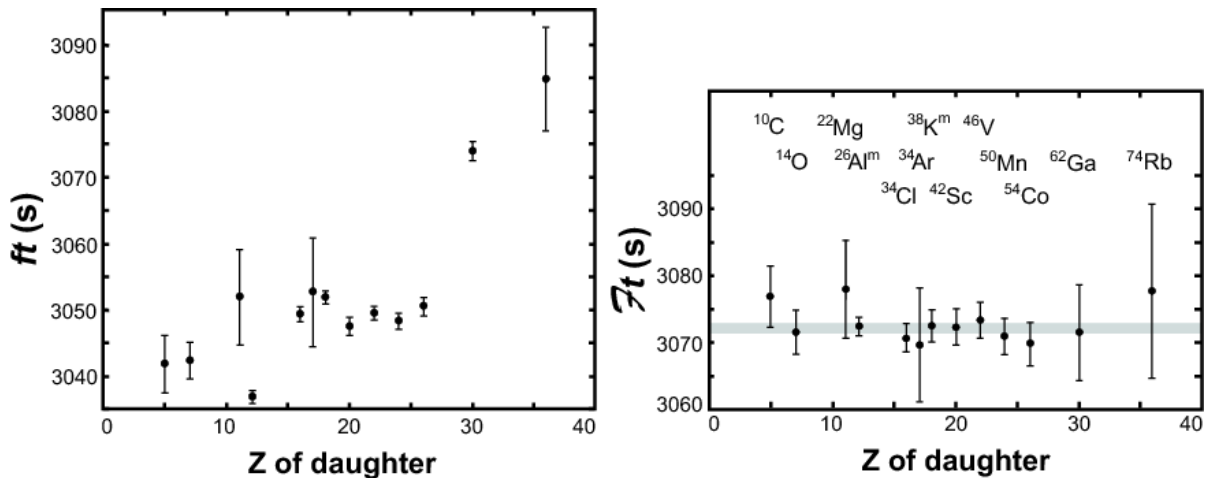


Figure 1. Results from the 2009 survey [1]. The uncorrected ft values for the thirteen best known superallowed decays (left) are compared with the same results after corrections have been applied (right). The grey band in the right-hand panel is the average Ft value, including its uncertainty.

final result for V_{ud} .

Even though the 2009 survey [1] included more than 145 individual measurements relating to 13 precisely known ft values, it is still possible for well selected experiments to make real improvements in the validation tests of the nuclear-structure-dependent correction terms. At TAMU we are currently focusing on adding to the ft -value list new superallowed transitions, selected from amongst those with *large* calculated corrections. If the ft values measured for cases with large calculated corrections also turn into corrected Ft values that are consistent with the others, then this must verify the calculations' reliability for the existing cases, which have smaller corrections. We are studying decays from $T_z = -1$ parent nuclei, which consistently have higher predicted structure-dependent correction terms than the well known $T_z = 0$

cases. In that context, during this past year we have published our half-life measurement for the decay of ^{38}Ca [4], which means that we have now published new precise half-lives for five such $T_z = -1$ superallowed emitters: ^{10}C , ^{22}Mg , ^{26}Si , ^{34}Ar and ^{38}Ca . We are also hard at work on improving the precision of our branching-ratio measurement capability, which (unlike for the $T_z = 0$ cases) is crucial to the characterization of $T_z = -1$ parent decays. To this end, we have made considerable improvements to our electronics and data-acquisition system [5] using off-line sources to generate β - γ coincidences. On-line measurements have so far focused on ^{38}Ca as a test case [6]. At the same time, we have continued to explore from a theoretical perspective [7] what else can be learned from a more exact experimental characterization of the nuclear-structure-dependent correction terms.

There are also compelling reasons to confirm and improve the ft values for the $T_z = 0$ cases as well. After all, these are the transitions that principally determine the value of V_{ud} . Since ^{46}V was a key transition that led to important improvements in the structure-dependent corrections when its Q_{EC} value was found to have been incorrectly measured by reaction studies in the past, we published a re-measurement of its Q_{EC} value last year [8] and this year published its half-life [9]. This confirmed that no errors were lurking in either place.

Each superallowed ft -value determination depends critically on the precision of the corresponding Q_{EC} -value measurement, which enters to the fifth power in the determination of f . In recent years we have made many such measurements with the JYFLTRAP Penning-trap mass spectrometer at the University of Jyväskylä cyclotron facility in Finland, where we collaborate with the team there. This facility is ideally suited to the measurement of Q_{EC} -values to sub-100-eV precision. By now we have measured the Q_{EC} -values for 10 superallowed emitters there: ^{10}C , $^{26}\text{Al}^m$, ^{34}Cl , ^{34}Ar , $^{38}\text{K}^m$, ^{38}Ca , ^{42}Sc , ^{46}V , ^{50}Mn and ^{54}Co . A review of this work and the steps we have taken to increase its precision has recently been published [10].

We are also endeavoring to improve our data acquisition techniques for half-life measurements by a variety of means, including a new TDC-based data-acquisition system [11] and a digital-pulse-analysis system for the signals from our 4π proportional gas counter [12]. We are working to eliminate spurious pulses and to reduce our system dead time. Since we limit our count rate to avoid too large a dead-time correction, any reduction in the dead time itself will translate directly into improved statistical uncertainties on our measurements.

Finally, this year in collaboration with D. Melconian and his group we addressed the question of isospin symmetry breaking in the $1^+ \rightarrow 1^+$ superallowed decay of ^{32}Cl to ^{32}S [13]. This is a particularly interesting case since the daughter 1^+ ($T = 1$) analog state in ^{32}S is at high excitation energy and is surrounded by numerous $T = 0$ states. Thus the opportunities for isospin mixing are much greater than they are in the $0^+ \rightarrow 0^+$ decays we use to test CKM unitarity. Consequently, the ^{32}Cl superallowed decay branch provides an excellent test of the calculations we use to evaluate isospin symmetry breaking. The calculated δ_C for this case was an unprecedentedly large 4.6(5)%, which turned out to be in fine agreement with the value we measured: 5.3(9)%. In obtaining this result we recognized another complication resulting from the high level density within the β -decay window in ^{32}S , which required our taking special care to account for the Pandemonium effect in the decay analysis [14].

[1] J.C. Hardy and I.S. Towner, Phys. Rev. C **79**, 055502 (2009).

- [2] I.S. Towner and J.C. Hardy, *Phys. Rev. C* **77**, 025501 (2008).
- [3] I.S. Towner and J.C. Hardy, *Rep. Prog. Phys.* **73**, 046301 (2010).
- [4] H.I. Park, J.C. Hardy, V.E. Jacob, A. Banu, L. Chen, V.V. Golovko, J. Goodwin, V. Horvat, N. Nica, E. Simmons, L. Trache and R.E. Tribble, *Phys. Rev. C* **84**, 065502 (2011).
- [5] V.E. Jacob, J.C. Hardy, and H.I. Park, *Progress in Research*, Cyclotron Institute, Texas A&M University (2011-2012), p. V-21.
- [6] H.I. Park, J.C. Hardy, V.E. Jacob, M. Bencomo, L. Chen, J.R. Goodwin, V. Horvat, N. Nica, B.T. Roeder, L. Trache and R.E. Tribble, *Progress in Research*, Cyclotron Institute, Texas A&M University (2011-2012), p. I-7.
- [7] I.S. Towner and J.C. Hardy, *Progress in Research*, Cyclotron Institute, Texas A&M University (2011-2012), p. III-16.
- [8] T. Eronen, D. Gorelov, J. Hakala, J.C. Hardy, A. Jokinen, A. Kankainen, V.S. Kolhinen, I.D. Moore, H. Penttila, M. Reponen, J. Rissanen, A. Saastamoinen and J. Aysto, *Phys. Rev. C* **83**, 055501 (2011).
- [9] H.I. Park, J.C. Hardy, V.E. Jacob, L. Chen, J. Goodwin, N. Nica, E. Simmons, L. Trache and R.E. Tribble, *Phys. Rev. C* **85**, 035501 (2012).
- [10] T. Eronen and J.C. Hardy, *Eur. Phys. J. A* **48**: 48 (2012).
- [11] V. Horvat, J.C. Hardy and V.E. Jacob, *Progress in Research*, Cyclotron Institute, Texas A&M University (2011-2012), p. V-28.
- [12] L. Chen and J.C. Hardy, *Progress in Research*, Cyclotron Institute, Texas A&M University (2011-2012), p. V-24.
- [13] D. Melconian, S. Triumbak, C. Bordeanu, A. Garcia, J.C. Hardy, V.E. Jacob, N. Nica, H.I. Park, G. Tabakaru, L. Trache, I.S. Towner, R.E. Tribble and Y. Zhai, *Phys. Rev. Lett.* **107**, 182301 (2011) and *Phys. Rev. C* **85**, 025501 (2012).
- [14] I.S. Towner, D. Melconian and J.C. Hardy, *Progress in Research*, Cyclotron Institute, Texas A&M University (2011-2012), p. I-8.

Measurement of branching-ratios in the β decay of ^{38}Ca

H.I. Park, J.C. Hardy, V.E. Iacob, M. Bencomo, L. Chen, J.R. Goodwin, V. Horvat,
N. Nica, B.T. Roeder, L. Trache, and R.E. Tribble

In the past year, we have continued to improve our data-acquisition electronics with the goal of achieving 0.1% precision in the branching-ratio measurement of superallowed β transitions. One of our major focuses was to ensure that all events causing a β - γ trigger have β and γ -ray energies that are in the range of our ADC's; and to independently measure dead-times by recording the number of β - γ coincidence triggers in the data stream on a cycle-by-cycle basis. These improvements were strongly motivated by our ^{38}Ca branching-ratio measurement in 2010 [1] in which approximately 20% of all events triggering β - γ coincidences in the ADC did not appear as complete events in the recorded data stream. The improvements we have made to the system are discussed in more detail in the instrumentation section of this report [2].

The improved system was used to measure the branching ratio for the superallowed transition of ^{38}Ca again in the fall of 2011. We produced ^{38}Ca via the reaction $^1\text{H} (^{39}\text{K}, 2n) ^{38}\text{Ca}$ at a primary beam energy of 30A MeV. As a collect-move-count cycle was repeated with our fast tape-transport system, the time-tagged β - γ coincidence events were measured with the 1-mm-thick plastic scintillator for β particles and our well-calibrated 70% HPGe detector for the γ rays. Approximately 5 million β - γ coincidence events were collected from over 200 million β singles in 29 separate runs. This experiment allowed us to test the behavior of the upgraded system. On the one hand, we succeeded in reducing the loss of all events triggering β - γ coincidences in the ADC from 20% to 3.5%. On the other, we observed that our system did not record any β - γ coincidence events for the first 45 ms of the 1.6-s count time, possibly because a high counting rate during and immediately after the accelerator beam was present effectively blocked the system. This problem is being investigated in off line tests. Currently, we are making off-line measurements of β - γ coincidences with a ^{22}Na source, using our normal on-line configuration. The branching ratio for ^{22}Na β^+ decay is precisely known and is essentially 100%. These measurements have told us more about the response of our system to positrons and high-energy γ rays comparable to those from ^{38}Ca . A number of improvements have been made, including the reduction of event losses relative to β - γ coincidence triggers to less than 1%.

- [1] H.I. Park *et al.*, *Progress in Research*, Cyclotron Institute, Texas A&M University (2010-2011), p. I-27.
- [2] V.E. Iacob, J.C. Hardy, and H.I. Park, *Progress in Research*, Cyclotron Institute, Texas A&M University (2011-2012), p. V-21.

Weak beta branches in ^{32}Cl β decay

I.S. Towner, D. Melconian, and J.C. Hardy

In the β^+ decay of ^{32}Cl , precisely-calibrated γ -ray yields have been measured and corresponding β branches determined [1, 2]. The nine lowest $(0, 1, 2)^+$ states previously observed by Détraz *et al.* [3] along with a 1% ground-state branch determined by Armini *et al.* [4] represent most of the γ -ray yield; however, little is known about states populated above 7.2 MeV of excitation energy. Since the Q-value is quite large, $Q_{\text{EC}} = 12.7$ MeV, there remains a further 5 MeV of Q-value window in which no β transitions have been identified. This suggests that there is no strong β feeding of any individual states in this energy region, but it does not rule out the possibility of a large number of weak β transitions. Each of these transitions may be too weak to be detected individually, but they could cumulatively contribute a total β strength of up to a few per cent. This “Pandemonium” effect, originally proposed in Ref. [5], was raised again recently [6] in the context of superallowed β decay in *pf*-shell nuclei. Following the approach advocated in these references, we have used a shell-model calculation to compute the weak β branches and include their predicted strengths in our analysis of the β -delayed γ -ray data. The model space used was the full *sd* shell with three different sets of effective interactions: the USD set of Wildenthal [7] and the two more recent updates USD-A and USD-B of Brown and Richter [8].

We include in our analysis of the branches and yields a total of 51 excited states in ^{32}S . Our shell-model calculation correctly predicts all of the nine lowest $(0, 1, 2)^+$ states with $E_x < 7.2$ MeV reported in Détraz *et al.* [3]. We find that the RMS deviations of the shell-model calculations from the known excitation energies are quite good: 120 keV (USD), 209 keV (USD-A), and 172 keV (USD-B). This is a gratifying indication that the shell model is performing well in this *sd*-shell nucleus. Even though selection rules prohibit β decays to the six lowest $(3,4)^+$ states, those states are included in the analysis when we are accounting for γ -ray de-excitations. The shell-model calculations identify approximately 40 β transitions to states whose excitation energies in ^{32}S lie between 7.2 and 12.2 MeV. Unfortunately, the high density of states in this energy region makes a state-by-state comparison with known states in ^{32}S difficult, especially for the 2^+ states. Nevertheless, based on the good correspondence of excitation energies and de-excitation branches, we are able to identify five of the shell-model 0^+ or 1^+ states in this region with ones in the ENSDF Data Tables [9]. None of the individual shell-model states with high excitation energy is fed by a β -transition with strength greater than 0.3%, but cumulatively the strengths sum to 0.50% in the USD, 0.69% in the USD-A, and 0.55% in the USD-B calculations. We include these weak β strengths and de-excitation rays predicted by the shell model in our overall analysis.

In the analysis, a β branch could be identified as long as there was at least one γ ray lying within the 7.35-MeV energy range of our HPGe detector. The ground-state branch and higher excitation-energy shell-model-state branches that were not observed in this experiment were included in the analysis as missing strength. For the ground state, we take the branch to be $(1.0_{-0.5}^{+0.2})\%$, as determined by Armini *et al.* [4], and the combination of all the unseen shell-model states at energies above 7.2 MeV was taken to be the average of the USD, USD-A, and USD-B calculations, with an uncertainty that spans the variation: $(0.60 \pm 0.10)\%$. The final results for excitation energies and β branches are published in Table I of Ref. [2].

- [1] D. Melconian, S. Triambak, C. Bordeanu, A. Garcia, J.C. Hardy, V.E. Jacob, N. Nica, H.I. Park, G. Tabacaru, L. Trache, I.S. Towner, R.E. Tribble and Y. Zhai, Phys. Rev. Lett. **107**, 182301 (2011).
- [2] D. Melconian, S. Triambak, C. Bordeanu, A. Garcia, J.C. Hardy, V.E. Jacob, N. Nica, H.I. Park, G. Tabacaru, L. Trache, I.S. Towner, R.E. Tribble and Y. Zhai, Phys. Rev. C **85**, 025501 (2012).
- [3] C. Détraz, C.S. Zaidins, D.J. Frantsvog, R.L. Wilson and A.R. Kunselman, Nucl. Phys. **A203**, 414 (1973).
- [4] A.J. Armini, J.W. Sunier and J.R. Richardson, Phys. Rev. **165**, 1194 (1968).
- [5] J.C. Hardy, L.C. Carraz, B. Jonson and P.G. Hansen, Phys. Lett. B **71**, 307 (1977).
- [6] J.C. Hardy and I.S. Towner, Phys. Rev. Lett. **88**, 252501 (2002).
- [7] B.H. Wildenthal, Prog. Part. Nucl. Phys. **11**, 5 (1984).
- [8] B.A. Brown and W.A. Richter, Phys. Rev. C **74**, 034315 (2006).
- [9] Evaluated Nuclear Structure Data File ENDSF, [www.nndc.bnl.gov].

**Tests of internal-conversion theory with precise γ - and x-ray spectroscopy:
the case of $^{119}\text{Sn}^m$**

N. Nica, J. Goodwin, J. C. Hardy, V. Horvat, V. E. Jacob, S. Miller, and M. B. Trzhaskovskaya¹
¹*Petersburg Nuclear Physics Institute, Gatchina RU-188300, Russia*

In the past year we continued the study of the internal conversion coefficient (ICC) of the 65.7-keV $M4$ transition in $^{119}\text{Sn}^m$, which we described in last year's annual report. This is the latest in a series of precision measurements of the ICCs of high-multipolarity transitions to establish the accuracy of calculated ICCs and, in particular, to discriminate between the theoretical prescriptions used to deal with the atomic vacancy left by the emitted electron. The $^{119}\text{Sn}^m$ case has a lower Z than any case we have examined so far. The transition originates from the 293.1-day isomeric state at 89.5 keV in $^{119}\text{Sn}^m$, which decays 100% by cascade via a 65.7-keV $M4$ and a 23.9-keV $M1/E2$ transition. Since the latter cannot convert in the K shell, the K x rays in the measured photon spectrum from this decay scheme are exclusively from the $M4$ transition. Consequently, the K conversion coefficient for the $M4$ transition can be determined from the equation

$$\alpha_K \omega_K = \frac{N_K}{N_\gamma} \cdot \frac{\varepsilon_\gamma}{\varepsilon_K} \quad (1)$$

where ω_K is the fluorescence yield; N_K and N_γ are the total numbers of observed K x rays and 65.7-keV γ rays, respectively; and ε_K and ε_γ are the corresponding detector efficiencies. This is our standard method for making such measurements and, although our detector efficiency in the 23-29 keV region of the tin K x-rays is not as well established as it is at higher energies, we still anticipate being able to measure the ICC to high enough precision to distinguish between the theory that ignores the atomic vacancy and the one that includes it. The two calculated ICC values differ from one another by about 5%.

The main difficulty of this measurement comes from the large value of the total ICC, ~ 5000 , which means that the γ -ray component of the 65.7-keV transition is extremely weak and difficult to detect. This difficulty is further increased by the small cross section for thermal-neutron capture on ^{118}Sn , ~ 10 mb, which we use to produce $^{119}\text{Sn}^m$. Also, as noted in last year's report, two impurity activities, ^{75}Se and ^{182}Ta , contribute quite strongly to the region of the 65.7-keV γ ray peak. In the case of ^{182}Ta , the subtraction of the impurity presents problems since the main ^{182}Ta γ -ray peak at 67.7 keV is unresolved from three tantalum K_β x-ray components, whose total strength relative to that of the γ ray depends critically on possibly unreliable published data.

To resolve this latter difficulty, we activated a thin foil of pure ^{181}Ta to produce a clean spectrum of ^{182}Ta decay. From the observed spectrum we planned to extract a template for the ^{182}Ta peak structure, which we could use to subtract the ^{182}Ta impurity from our primary $^{119}\text{Sn}^m$ spectrum. Unfortunately the spectrum of ^{182}Ta was affected by fluorescence K x rays from the tantalum, so the template itself required some correction. The template ratios extracted from both $^{119}\text{Sn}^m$ and ^{182}Ta spectra were in agreement and

we used their average value for the final correction. In the end we determined that impurities accounted for 40.3(10) % of the 65.7-keV γ ray – 26.6(8) % from ^{182}Ta and 13.7(6) % from ^{75}Se .

We also addressed the problem of precise efficiency calibration for the 23-29-keV interval, where the tin K x rays and the 23.9-keV $M1/E2$ γ ray from $^{119}\text{Sn}^m$ decay are located. We produced samples of 54-minute $^{116}\text{In}^m$ by activating samples of about 1-mg of 99%-enriched ^{115}In oxide (In_2O_3) as a thin powder layer between two thin Mylar foils. Two separate activations were made in the Triga reactor of Texas A&M University, one for 10 s and the other 40 s, at a flux of 7.5×10^{12} n/(cm²s). The nucleus $^{116}\text{In}^m$ β -decays to states in ^{116}Sn , which subsequently decay by γ -ray transitions that partially convert and thus produce tin x rays. Since the strong transitions are all of relatively high energy and low multipolarity their α_K values can be unambiguously calculated, so the intensity of the K x rays can be calculated relative to that of the γ rays in the observed spectrum. Applying Eq. (1) to this situation where we know α_K , we can deduce ε_K , the detection efficiency at 25.8-keV, which is the weighted average energy of Sn K x rays.

Although scattered photons have little effect on higher energy photo-peaks, at energies as low as 25 keV they make significant contributions to the peaks themselves. The amount depends strongly on the particular geometry of the experiment. For this reason, we measured the first ^{116}In source on our usual detector table, while for the second source there was a deep gap between the source and the detector. In both cases the distance between source and detector was 151 mm, the distance for which our detector is well calibrated (at higher energies). This distance was measured precisely and maintained by means of a laser-based device. The first of these two set-ups favored scattering, while the second one was essentially scattering-free. Indeed, there was a significant difference between the two results. Gratifyingly, the ε_K experimentally determined with the second scattering-free set-up was found to agree exactly with the Cyltran Monte-Carlo calculation for our detector.

Our analysis also revealed an unexpected impurity in the $^{116}\text{In}^m$ decay spectrum: namely indium K x rays coming from the (n,n') population of a 4.5-hour, 336-keV isomeric state in ^{115}In . While we have never before encountered any significant (n,n') population in our series of neutron-activation experiments at the Texas A&M Triga reactor, we convincingly identified this one by the energy and measured half-life of its 336-keV γ ray. We later confirmed that at the activation location in the reactor there is indeed an unavoidable fast neutron flux component that can account for population of the 336-keV ^{115}In isomeric state.

Finally by applying all corrections to the 65.7-keV transition from $^{119}\text{Sn}^m$, we get the preliminary result $\alpha_K(\text{exp}) = 1607(60)$. This can be compared to the calculated ‘no-hole’ value of $\alpha_K(\text{calc}) = 1544$ and ‘with-hole’ value of $\alpha_K(\text{calc}) = 1618$, which accounts for the hole using the “frozen orbital” method. Our previous α_K measurements on heavier nuclei have all favored the latter calculations. In this case, our preliminary result shows the same preference but the high uncertainty so far precludes a definitive statement. We plan next to consolidate our measured result and, if possible, reduce its uncertainty.

United States nuclear data program and evaluated nuclear structure data file (ENSDF): data evaluation at Texas A&M

N. Nica¹ and J. C. Hardy

¹under contract with Brookhaven National Laboratory

Since 2005 we have been an important participant in the nationwide United States Nuclear Data Program (USNDP). This is a national-interest activity financed by DOE, through which the relevant nuclear-science results in virtually all world publications are retrieved and put together in a large Evaluated Nuclear Structure Data File (ENSDF) database according to *general policies* [1], a set of rules that make possible a standard approach through which the data are uniformly evaluated. This activity is supported by a relatively small group of professionals organized as a national data network located mostly in national institutes but also hosted by a few universities. The nuclear data network is the nodal point for the wide dissemination of nuclear knowledge to many customers, from those in basic science to those engaged in commercial applications in American and international businesses.

The US network is the most consistent part of an international network similarly organized worldwide. The output is published in the Nuclear Data Sheets, an Elsevier publication, and also is disseminated by different on-line databases which can be retrieved at the NNDC site (<http://www.nndc.bnl.gov>), IAEA Vienna's site (<http://www-nds.iaea.org>) and several other locations.

During these years we have covered essentially all the regions of the periodic table. The superheavy $A=252$ mass chain, the very data-rich mid-mass chains, $A=147$ and $A=140$, and the relatively lighter chains, $A=97$ and $A=84$, have all been published previously in Nuclear Data Sheets. More recently, we have done the $A=34$, 36 , 37 and 77 chains in collaboration with B. Singh of McMaster University, Canada. Since nuclear-data evaluation depends critically on the experience of the evaluator, with a veteran evaluator typically completing only a couple of mass chains per year, coverage of such a wide range of A chains in such a short time is a considerable accomplishment. This once more testifies to Texas A&M's qualifications to be considered a national evaluation center.

During the past year we covered a relatively heavy mass chain, $A=148$, by considering all world publications since 2000, when the previous full evaluation of this mass chain was published. The chain includes Xe, Cs, Ba, La, Ce, Pr, Nd, Pm, Sm, Eu, Gd, Tb, Dy, Ho, Er, and Tm, a total of 16 nuclei about which approximately 300 papers have been published during this interval, an increase in the database file of about 22%. This work [2] is in the after-review stage and will be published in Nuclear Data Sheets by the end of this year.

This year we were also able to work with B. Singh on the review and preparation for publication of the four A chains we had evaluated together, $A=34$, 36 , 37 , and 77 ; one of these chains, $A=36$, has already appeared in print [3].

[1] Nucl. Data Sheets **111**, v (2010).

[2] N. Nica, Nuclear Data Sheets (accepted).

[3] N. Nica, J. Cameron, and B. Singh, Nucl. Data Sheets **113**, 1 (2012)

Calculation of isospin-mixing corrections for the isobaric analogue Fermi decay of ^{32}Cl

J.C. Hardy, V.E. Jacob, D. Melconian, N. Nica, H.I. Park, G. Tabacaru, I.S. Towner,
L. Trache, R.E. Tribble, and Y. Zhai

As mentioned in Ref. [1], the branching ratio of the $1^+, T = 1$ β decay of ^{32}Cl to the analogue $1^+, T = 1$ state in ^{32}S provides a sensitive test of nuclear-structure-dependent isospin-symmetry-breaking (ISB) effects in superallowed Fermi β decays. The correction, denoted by δ_C , is defined by the equation $|M_F|^2 = |M_0|^2(1 - \delta_C)$, where M_F is the Fermi matrix element for the transition and M_0 is its value in the limit of strict isospin symmetry, which is broken by Coulomb and charge-dependent nuclear forces. We use a shell-model calculation of ISB for this case and compare to our experimentally observed value $\delta_C = 5.3(9)\%$ (see Ref. [1])

The technique is to introduce Coulomb and other charge-dependent terms into the shell-model Hamiltonian. However, because the Coulomb force is long range, the shell-model space has to be very large indeed to include all the potential states that the Coulomb interaction might connect. Currently this is not a practical proposition. To proceed, Towner and Hardy divide δ_C into two parts: δ_{C1} and δ_{C2} , where δ_{C1} arises from configuration mixing between states of the same spin in a shell-model calculation using a restricted basis (in this case the full s, d shell), while δ_{C2} separately encompasses mixing beyond this model space. Starting with δ_{C1} , we perform a shell-model calculation in the truncated $0\hbar\omega$ model space of the s, d -shell orbitals. Charge-dependent terms are added to the charge-independent Hamiltonians of USD, USDA, and USDB. The strengths of these charge-dependent terms are adjusted to reproduce the b and c coefficients of the isobaric multiplet mass equation as applied to the $1^+, T = 1$ triplet of states in $A = 32$, the states involved in the β transition under study. The bulk of the isospin mixing in the 7001-keV IAS occurs with the nearby $1^+, T = 0$ state at 7190 keV. In the limit of two-state mixing, perturbation theory implies that $\delta_{C1} \propto 1/(\Delta E)^2$, where ΔE is the energy separation of the analogue and non-analogue 1^+ states. Experimentally, it is known to be 188.2 ± 1.2 keV (compared to the much larger 2–4 MeV of most $0^+ \rightarrow 0^+$ transitions). The shell model calculates this separation to be 184 keV with USD, 248 keV with USDA and 387 keV with USDB interactions. We avoid the large uncertainties this would impose on our calculation by following the Towner-Hardy recommendation [1] of scaling the calculated δ_{C1} value by a factor of $(\Delta E)_{\text{theo}}^2 / (\Delta E)_{\text{exp}}^2$, the ratio of the square of the energy separation of the 1^+ states in the model calculation to that known experimentally. Following this procedure, the δ_{C1} values obtained in the three shell-model calculations are reasonably consistent: $\delta_{C1} = 3.73\%$ for USD, $\delta_{C1} = 3.32\%$ for USDA and $\delta_{C1} = 4.19\%$ for USDB. We average these three results and assign an uncertainty equal to half the spread between them to arrive at $\delta_{C1} = 3.75(45)\%$. As Fig. 1 shows, this is over an order of magnitude larger than δ_{C1} calculated for any of the 13 $0^+ \rightarrow 0^+$ transitions used to determine V_{ud} .

For the calculation of δ_{C2} we consider mixing with states outside the $0\hbar\omega$ shell-model space. The principal mixing is with states that have one more radial node. Such mixing effectively changes the radial function of the proton involved in the β decay relative to that of the neutron. The practical calculation, therefore, involves computing radial-overlap integrals with modeled proton and neutron radial functions. Details of how this is done are given in Ref. [2]. The radial functions are taken to be eigenfunctions of a Saxon-Woods potential whose strength is adjusted so that the asymptotic form of the radial function has

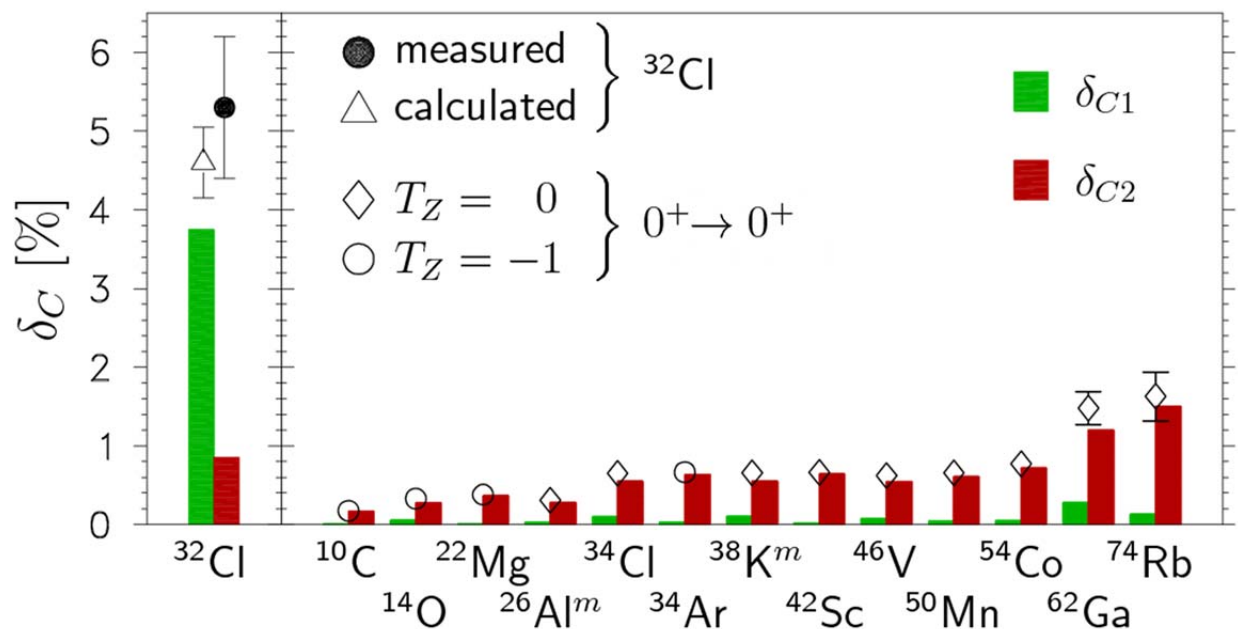


FIG. 1. Our determination of the isospin-breaking correction for ^{32}Cl (filled circle), and calculations for ^{32}Cl as well as other superallowed transitions (open points), with the δ_{C1} and δ_{C2} components shown separately. The measurement and prediction for ^{32}Cl , particularly the δ_{C1} component, is significantly larger than in any of the $0^+ \rightarrow 0^+$ transitions.

the correct dependence on the separation energy. The initial and final A -body states are expanded in a complete set of $(A - 1)$ -parent states. The separation energies are the energy differences between the A -body state and the $(A - 1)$ -body parent states. A shell-model calculation is required to give the spectrum of parent states and the spectroscopic amplitudes of the expansion. For the three USD interactions, we compute $\delta_{C2} = 0.827\%$ for USD and 0.865% for both USDA and USDB. Our adopted value is $\delta_{C2} = 0.85(3)\%$. The uncertainty, calculated in the same manner as described in Ref. [2], represents the range of results for the USD interactions, the different methodologies considered in adjusting the strength of the Saxon-Woods potential, and the uncertainty in the Saxon-Woods radius parameter as fitted to the experimental charge radius of ^{32}S .

Combining our adopted shell-model calculations, $\delta_{C1} = 3.75(45)\%$ and $\delta_{C2} = 0.85(3)\%$, we find $\delta_C^{\text{theor}} = 4.6(5)\%$, which agrees with the experimentally determined $5.3(9)\%$ of [1] within stated uncertainties. The agreement between theory and experiment in this case where δ_C is so large represents a very important validation of the theoretical procedures outlined here to calculate the ISB effects in nuclei. In particular, for (shell-model) calculations which separate configuration-mixing and radial-overlap components, this δ_{C1} -dominated result provides an especially sensitive benchmark for the approximations used when calculating configuration-mixing contributions to the total ISB effect in superallowed $0^+ \rightarrow 0^+$ decays.

This result has been recently published in Refs. [3, 4].

[1] J.C. Hardy, V.E. Jacob, D. Melconian, N. Nica, H.I. Park, G. Tabacaru, I.S. Towner, L. Trache, R.E. Tribble, and Y. Zhai, *Progress in Research*, Cyclotron Institute, Texas A&M University (2011-2012), p. I-16.

[2] I.S. Towner and J.C. Hardy, *Phys. Rev. C* **77**, 025501 (2008).

- [3] D. Melconian, S. Triambak, C. Bordeanu, A. Garcia, J. Hardy, V. Iacob, N. Nica, H. Park, G. Tabacaru, I. Towner, L. Trache, R. Tribble and Y. Zhai, Phys. Rev. Letts. **107**, 182301 (2011).
- [4] D. Melconian, S. Triambak, C. Bordeanu, A. Garcia, J. Hardy, V. Iacob, N. Nica, H. Park, G. Tabacaru, I. Towner, L. Trache, R. Tribble and Y. Zhai, Phy. Rev. C **85**, 025501 (2012).

The absolute γ and β branches following the β^+ decay of ^{32}Cl

J.C. Hardy, V.E. Jacob, D. Melconian, N. Nica, H.I. Park, G. Tabacaru, I.S. Towner,
L. Trache, R.E. Tribble, and Y. Zhai

The β and γ branches of the β^+ decay of 1^+ , $T = 1$ ^{32}Cl have been measured to provide a discriminating test of the isospin-mixing corrections, δ_C , applied to the 0^+ to 0^+ superallowed transitions used to determine V_{ud} . Up until now, there have been no nuclei studied where δ_C is larger than $\sim 2\%$. We focused on improving the branching ratio of the transition to the analogue 1^+ , $T = 1$ state in ^{32}S whose position in the spectrum at 7002-keV excitation is very close to a known 1^+ , $T = 0$ state at 7190 keV; this greatly enhances the size of the isospin-symmetry-breaking (ISB) correction. Our calculation of the ISB effect for this nucleus is $\delta_C = 4.6(5)\%$ [1], a value significantly larger than those found in any of the nuclei used to extract V_{ud} . In this way, ^{32}Cl provides a unique opportunity to test ISB calculations where the effect is relatively quite large. Furthermore, a precise knowledge of the absolute β and γ branches following the β decay of ^{32}Cl may be used as an *in situ* efficiency calibration for the β -delayed proton decay of ^{32}Ar which itself may be used to test isospin-mixing corrections (see Ref. [2]).

The ^{32}Cl was produced via the inverse-kinematic transfer reaction $^1\text{H}(^{32}\text{S}, n)^{32}\text{Cl}$ using a LN₂-cooled, H₂ gas target with a 400 nA ^{32}S primary beam at 24.8 MeV/nucleon. The reaction products were spatially separated by MARS, resulting in a 91% pure, 20 MeV/nucleon ^{32}Cl beam with an intensity of $\sim 2 \times 10^5$ ions/s. The beam was implanted and collected in an aluminized-Mylar tape for 0.8 s before a fast tape-transport system moved the activity to a shielded counting station 90 cm away. Data for β - γ coincident events, shown in Fig. 1, were acquired using a 1.5 inch-diameter, 1 mm-thick scintillator and a

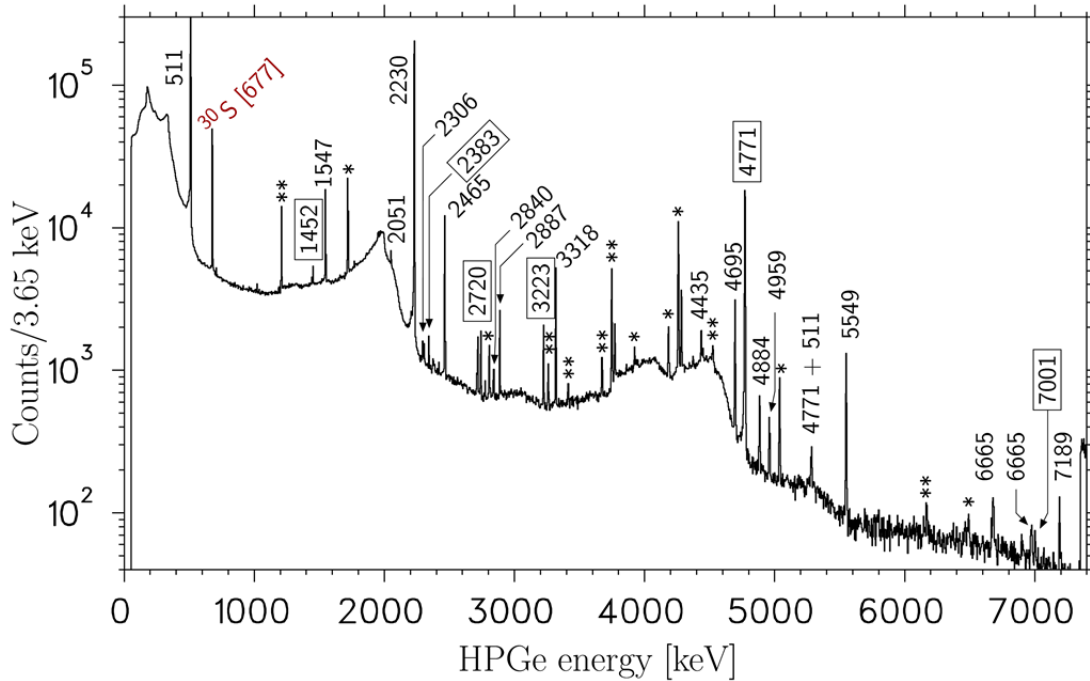


FIG. 1. γ spectrum observed by the HPGe in coincidence with a β . Full-energy peaks are labeled with their energy, and ones associated with the 7001-keV isobaric analogue state are highlighted with boxed values. The symbol * and the symbol ** refer to single- and double-escape peaks, respectively.

70% HPGe detector. Count times were for 1, 2, and 4 sec (83%, 11%, and 6% of the data, respectively). The scintillator was placed 0.5 cm from the activity, detecting >40 keV positrons with $\sim 32\%$ efficiency. On the opposite side of the tape the HPGe was placed a large distance away (15.1 cm) to reduce the effects of coincidence summing of the γ rays. The cycle of collecting, transporting and measuring the ^{32}Cl activity was repeated continuously throughout the experiment.

Once the peak areas were obtained, we used the precisely known efficiency of the HPGe detector to convert them into relative yields of γ rays. We then fit the β and γ branches to reproduce these yields. Our measurement has found 3 new β branches, 22 new γ lines, placed limits on 10 potential γ transitions, and improved the precision of the branches and yields reported previously [3, 4] by about an order of magnitude and is summarized in Fig. 2.

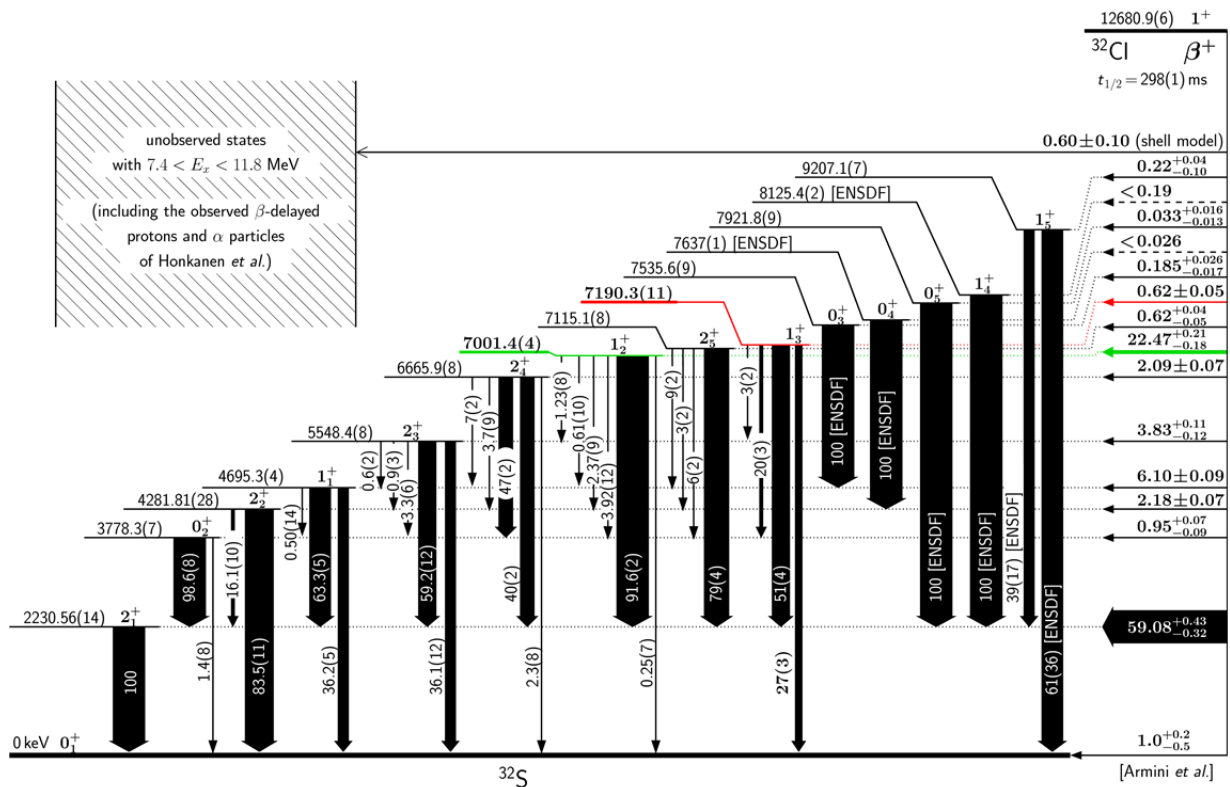


FIG. 2. Decay scheme for ^{32}Cl based on this work (with results taken from Armini *et al.* and ENSDF labeled). The 1^+ , $T = 1$ analogue state at 7001 keV mixes with the nearby 1^+ , $T = 0$ state, giving rise to the (relatively) large observed isospin-mixing correction.

With regard to ISB effects, we found the β branch to the isobaric-analogue state (IAS) at 7002 keV is $R = (22.47 \pm 0.13^{+0.16}_{-0.12})\%$. The first uncertainty is statistical and the second is dominated by two sources of systematic uncertainty: $^{+0.11}_{-0.12}\%$ is from the $(1.0^{+0.2}_{-0.5})\%$ ground state branch reported by Armini *et al.* [5], and $\pm 0.10\%$ from the photopeak efficiency of the HPGe detector. The partial half-life of the superallowed branch is given by $t = \frac{t_{1/2}}{R}(1 + P_{\text{EC}})$, where the ^{32}Cl half-life is $t_{1/2} = 298(1)$ ms, R is the superallowed branching ratio quoted above, and the small electron-capture fraction is calculated to be $P_{\text{EC}} = 0.071\%$. The statistical rate function is calculated to be $f = 2411.6 \pm 2.3 \pm 0.3$, where the first uncertainty

is from the Q_{EC} value and the second is from the shell-model calculation of the shape-correction factor. Combined, we find the experimental ft value for decay to the IAS is $ft = 3200(30)$ s, where the precision is dominated by the $\pm 0.9\%$ uncertainty in the branch to the IAS. This result can be interpreted in terms of an ISB effect via

$$\delta_C^{exp} = 1 + \delta_{NS} - \frac{2\langle Ft^{0^+ \rightarrow 0^+} \rangle}{ft(1 + \delta'_R)[B(F) + B(GT)]},$$

where δ_{NS} is a nuclear-structure-dependent radiative correction calculated to be $-0.15(2)\%$, $\langle Ft^{0^+ \rightarrow 0^+} \rangle = 3071.81(83)$ s is the average corrected ft value of the 13 most precisely measured pure Fermi superallowed transitions [6], $\delta'_R = 1.421(32)\%$ is another radiative correction, and $B(GT)$ is calculated to be $(1.8_{-1.7}^{+2.3}) \times 10^{-3}$ which is negligibly small compared to the dominant Fermi strength of $B(F) = 2$. Thus we arrive at an ISB effect of $\delta_C^{exp} = 5.3(9)\%$, the largest ever determined in a superallowed Fermi transition.

This result has been recently published in Refs. [7, 8].

- [1] J.C. Hardy, V.E. Jacob, D. Melconian, N. Nica, H.I. Park, G. Tabacaru, I.S. Towner, L. Trache, R.E. Tribble, and Y. Zhai, *Progress in Research*, Cyclotron Institute, Ttexas A&M University (2011-2012), p.I-13.
- [2] M. Bhattacharya, D. Melconian, A. Komives, S. Triambak, A. Garcia, E. Adelberger, B. Brown, M. Cooper, T. Glasmacher, V. Guimaraes and P. Mantica, *Phys. Rev. C* **77**, 065503 (2008).
- [3] C. Détraz, C. Zaidins, D. Frantsvog, R. Wilson and A. Kunselman, *Nucl. Phys.* **A203**, 414 (1973).
- [4] W. Anderson, L. Dillman and J. Kraushaar, *Nucl. Phys.* **77**, 401 (1966).
- [5] A. Armini, J. Sunier and J. Richardson, *Phys. Rev.* **165**, 1194 (1968).
- [6] J.C. Hardy and I.S. Towner, *Phys. Rev. C* **79**, 055502 (2009).
- [7] D. Melconian, S. Triambak, C. Bordeanu, A. Garcia, J. Hardy, V. Iacob, N. Nica, H. Park, G. Tabacaru, I. Towner, L. Trache, R. Tribble and Y. Zhai, *Phys. Rev. Letts.* **107**, 182301 (2011).
- [8] D. Melconian, S. Triambak, C. Bordeanu, A. Garcia, J. Hardy, V. Iacob, N. Nica, H. Park, G. Tabacaru, I. Towner, L. Trache, R. Tribble and Y. Zhai, *Phy. Rev. C* **85**, 025501 (2012).

The ANC for $^{15}\text{C} \leftrightarrow ^{14}\text{C}+n$ and the astrophysical $^{14}\text{C}(n,\gamma)^{15}\text{C}$ rate

M. McCleskey, A.M. Mukhamedzhanov, L. Trache, R.E. Tribble, V. Goldberg, Y.-W. Lui,
B. Roeder, E. Simmons, A. Spiridon, and F. Carstoiu¹
¹*IFIN-HH, Bucharest, Romania,*

The motivation for determining the asymptotic normalization coefficient (ANC) for $^{15}\text{C} \leftrightarrow ^{14}\text{C}+n$ is two fold. First, the ANC has been used to determine the astrophysically important $^{14}\text{C}(n,\gamma)^{15}\text{C}$ rate. Second, it was used in the evaluation of a method proposed to determine spectroscopic factors utilizing the ANC [1]. All of the experiments were conducted at Texas A&M Cyclotron Institute (TAMU-CI) and have been described in previous reports ([2,3]).

Determination of the ANC

The ANC is the normalization of the tail of the overlap function at large radii. This value is useful in the calculation of rates for peripheral reactions, where the largest contribution to the reaction cross section comes from these large distances. The ANC, C , is defined as

$$I_{Ax(nlj)}^B(r) \stackrel{r>R}{\approx} C_{Ax(nlj)}^B \frac{W_{\eta_B, l_B + 1/2}(2\kappa_B r)}{r} \quad (1)$$

for a reaction $A(a,b)B$ where $B=A+x$ and $b=a-x$. nlj are the quantum numbers describing the state to which nucleon n is transferred. I is the nuclear overlap function and W is a Whittaker function. This leads to a parameterization of the cross section of a peripheral reaction in terms of the ANCs [4],

$$\frac{d\sigma}{d\Omega} = \sum_{j_B l_B} (C_{Ax l_B j_B}^B)^2 (C_{bx l_a j_a}^a)^2 \frac{\sigma_{l_B j_B l_a j_a}^{DW}}{b_{Ax l_B j_B}^2 b_{bx l_a j_a}^2} \quad (2)$$

Here DW is the calculated DWBA cross section and l and j are orbital angular momentum and its projection respectively. To find the ANC for $^{15}\text{C} \leftrightarrow ^{14}\text{C}+n$ a peripheral reaction for which the other ANC of Eq. (2) is known is required. Two such reactions were utilized. First, (d,p) on ^{14}C in both forward and inverse kinematics (for the deuteron $C_{pn}^d = 0.88 \text{ fm}^{-1/2}$) and second, the heavy ion (HI) reaction $^{13}\text{C}(^{14}\text{C}, ^{15}\text{C})^{12}\text{C}$. For $^{13}\text{C}(^{14}\text{C}, ^{15}\text{C})^{12}\text{C}$, the ANC for $^{13}\text{C} \leftrightarrow ^{12}\text{C}+n$ is needed and the value of $C^2 = 2.31 \pm 0.08 \text{ fm}^{-1}$ was measured before [5].

a. HI transfer $^{13}\text{C}(^{14}\text{C}, ^{15}\text{C})^{12}\text{C}$

This reaction was performed with an incident ^{14}C energy of 12 MeV/nucleon and reaction products were measured using the MDM spectrometer and the Oxford detector. Elastic scattering was measured at the same time as the transfer and was used in the search for an acceptable optical model potential (OMP) to be used in the calculation of σ^{DW} . Two different approaches were employed, one using a grid search in real potential depth and the second based on a semi-microscopic double folding calculation [6]. For the grid search a potential with real and imaginary parts was assumed,

$$U_{OMP} = V + iW, \quad (3)$$

where V and W are of the Wood-Saxon (WS) form

$$V_{WS} = -\frac{V_0}{1 + \exp\left(\frac{r - R_0}{a_0}\right)} \quad (4)$$

For each value of V_0 , the real potential depth, the remaining five parameters were fit to reproduce the elastic scattering data. The potential was found to be continuously ambiguous, with a wide range of values of V_0 producing good fits. Because of this, five values were arbitrarily selected and the results of these are shown on the left in Fig. 1, and the values found are given in Table I. The transfer angular distributions calculated with these are shown on the right in Fig. 1 along with the measured distribution.

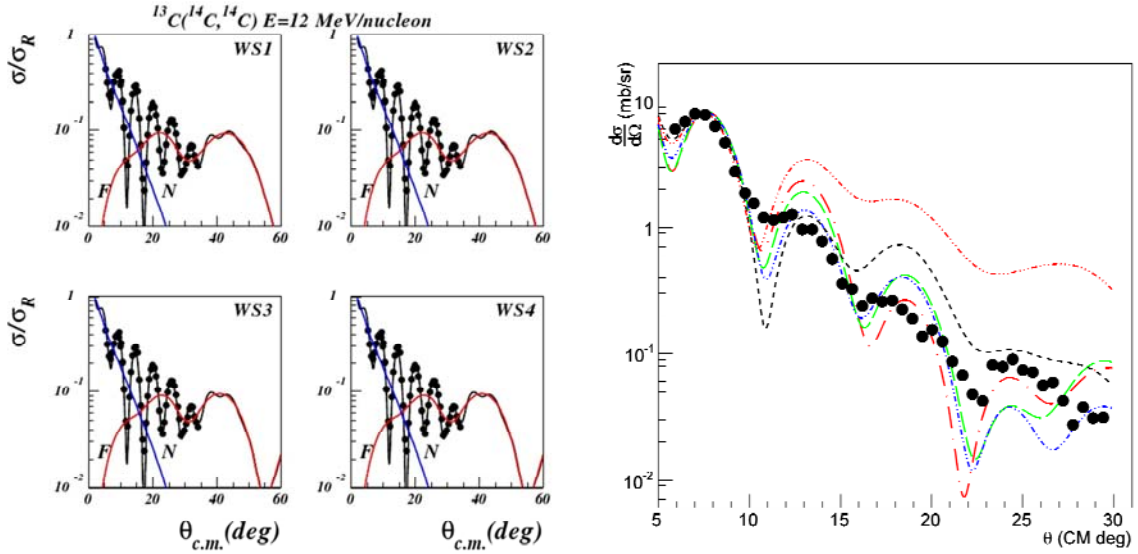


FIG. 1. On the left is the elastic scattering measurement (black dots) plotted with the results scattering calculation using the OMPs resulting from the grid search (black line). Red and Blue lines are the near/far decomposition. On the right is the DWBA calculation for the neutron transfer plotted along with the measured transfer distribution.

Table I. Optical model potential parameters for 12 MeV/nucleon ^{14}C elastic on ^{13}C .

	V (MeV)	W (MeV)	r_v (fm)	r_w (fm)	a_v (fm)	a_w (fm)	χ^2	J_v (MeV fm^3)	R_v (fm)	J_w (MeV fm^3)	R_w (fm)
WS1	77.1	13.32	0.987	1.209	0.703	0.723	3.09	225	4.480	68	5.206
WS2	118.7	14.15	0.927	1.191	0.690	0.739	3.4	292	4.275	69	5.182
WS3	162.4	15.03	0.891	1.169	0.674	0.767	3.59	357	4.132	71	5.169
WS4	203.1	16.04	0.894	1.133	0.627	0.825	3.6	438	4.038	71	5.183
WS5	248.8	16.66	0.885	1.115	0.606	0.848	3.65	516	3.965	72	5.180
DF	141.43	45.72	0.735	0.812	0.920	1.020	3.4				

The second approach to finding an OMP, the double folding calculation using the JLM effective interaction, utilized the optimal normalizations and ranges from [6]. These were four parameters were varied, but the best fit to the elastic scattering data was found with the values from [6]. The results are shown in Fig. 2 and the potential is given in Table I.

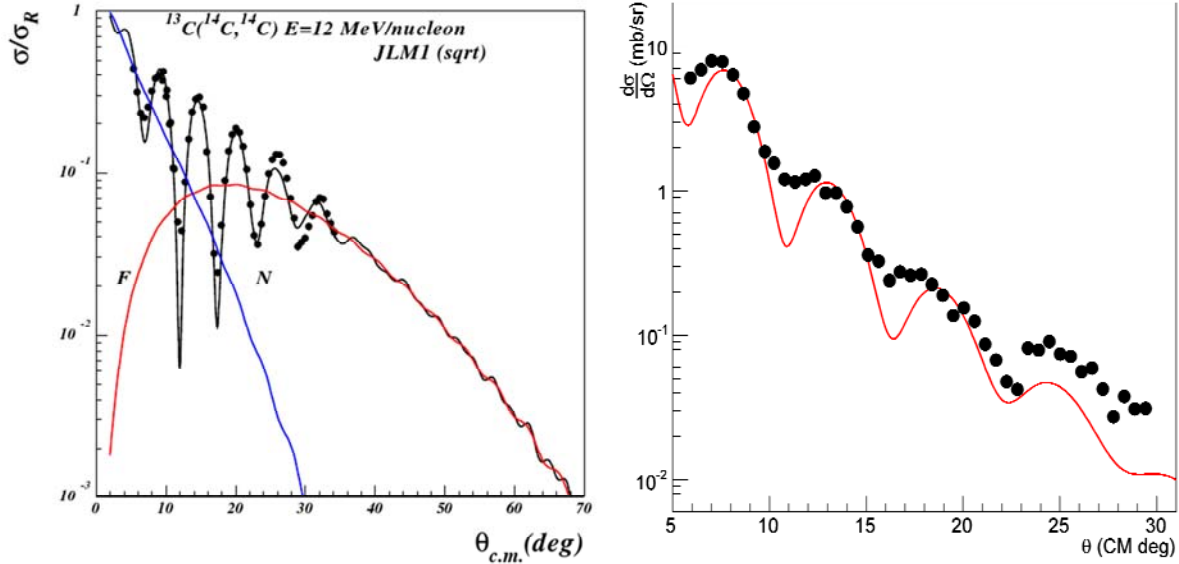


FIG. 2. On the left is the elastic scattering measurement (black dots) plotted with the results scattering calculation using the OMPs resulting from the double folding calculation (black line). Red and Blue lines are the near/far decomposition. On the right is the DWBA calculation for the neutron transfer utilizing this potential plotted along with the measured transfer distribution.

A summary of the ANCs obtained using these different DWBA calculations is given in Table II. The average value was $C^2=2.09\pm0.29 \text{ fm}^{-1}$ for transfer to the ground state, and $C^2=4.48\pm0.58\times10^{-3} \text{ fm}^{-1}$ for transfer to the 1st excited state.

Table II. Phenomenological SFs and ANCs obtained with DWBA calculation using the WS OMP fits.

	SF _{2s1/2}	$C^2_{2s1/2} \text{ (fm}^{-1}\text{)}$	SF _{1d5/2}	$C^2_{1d5/2} \times 10^{-3} \text{ (fm}^{-1}\text{)}$
WS1-WS1	1.22	2.30	1.13	4.45
WS2-WS2	1.16	2.18	1.02	4.03
WS3-WS3	1.04	1.95	1.13	4.46
WS4-WS4	0.98	1.83	1.20	4.74
WS5-WS5	1.14	2.14	1.25	4.94
DF	1.15	2.16	1.09	4.28
Average	1.12	2.09	1.14	4.48

b. Analysis of the $d(^{14}\text{C},p)^{15}\text{C}$ measurement

The inverse kinematics (d,p) on ^{14}C was measured using the Texas A&M Edinburg Catania silicon array (TECSA) [7] at TAMU-CI. A beam of 11.7 MeV/nucleon ^{14}C impinged on a $251 \pm 5 \mu\text{g}/\text{cm}^2$ CD_2 target and reaction products were measured in the backwards (lab) direction using the array of Micron YY1 detectors. The angular distributions were calculated using the code FRESKO [8]. The adiabatic distorted wave approximation (ADWA) [9] was used for the entrance channel utilizing CH89 [10] single nucleon potentials for the proton and neutron evaluated at half the deuteron energy. The finite range correction described in [11] was applied to the potential for the entrance channel. The experimental and renormalized calculations are shown in Figure 3. The ANC for the ground state was found to be $C_{2s_{1/2}}^2 = 2.01 \pm 0.24 \text{ fm}^{-1}$ and the first excited state $C_{1d_{5/2}}^2 = (4.06 \pm 0.49) \cdot 10^{-3} \text{ fm}^{-1}$, consistent with that found from $^{13}\text{C}(^{14}\text{C},^{15}\text{C})^{12}\text{C}$.

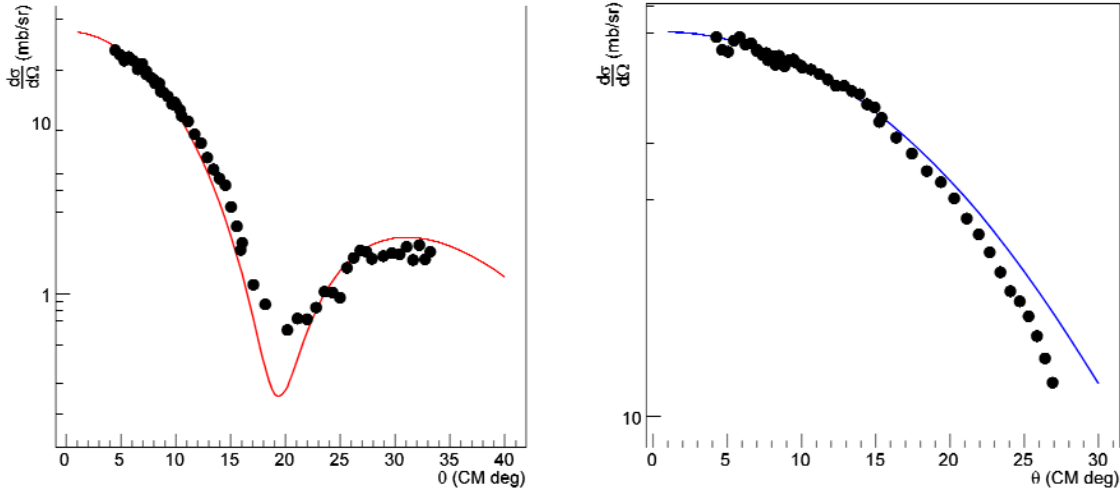


FIG. 3. On the left is the transfer to the $2s_{1/2}$ ground state. Black dots mark the experimental data points and the red line is the ADWA calculation. On the right is the 740 keV $1d_{5/2}$ first excited state, with experimental points shown as black dots and the ADWA calculation as a blue line.

c. $^{14}\text{C}(d,p)^{15}\text{C}$

The forward kinematics (d,p) on ^{14}C was measured at TAMU-CI with an incident deuteron energy of 60 MeV. As was the case in the measurement of $^{13}\text{C}(^{14}\text{C},^{15}\text{C})^{12}\text{C}$, the MDM spectrometer and Oxford detector were used. This experiment was described in [2], and only the new results from the analysis of the transfer will be presented here. The measurement of this reaction was motivated by the desire to evaluate the method outlined in [1] to determine SFs using ANCs, which will be discussed in the next section. Because of this motivation the deuteron energy of 60 MeV was selected in the hope of making this reaction non-peripheral, which would make it inappropriate for extracting the ANC.

However, the reaction turned out to be more peripheral than anticipated and as a result could be used to extract the ANC for transfer of a neutron to the ground state of ^{15}C .

The angular distribution for the transfer was calculated using the ADWA as described in the previous case of $d(^{14}\text{C},p)^{15}\text{C}$. CH89 potentials were again employed and the results are shown in Fig. 4, plotted against the experimental data. Both the ground state and first excited states are shown, however, only transfer to the ground state was sufficiently peripheral to satisfactorily extract the ANC, which was found to be $C^2=1.76\pm 0.29 \text{ fm}^{-1}$. A summary of the ANCs found from the three reactions presented here is given in Table III. The weighted average value was $1.96\pm 0.16 \text{ fm}^{-1}$ for the ground state and $4.23\pm 0.38 \cdot 10^{-3} \text{ fm}^{-1}$ for the first excited state.

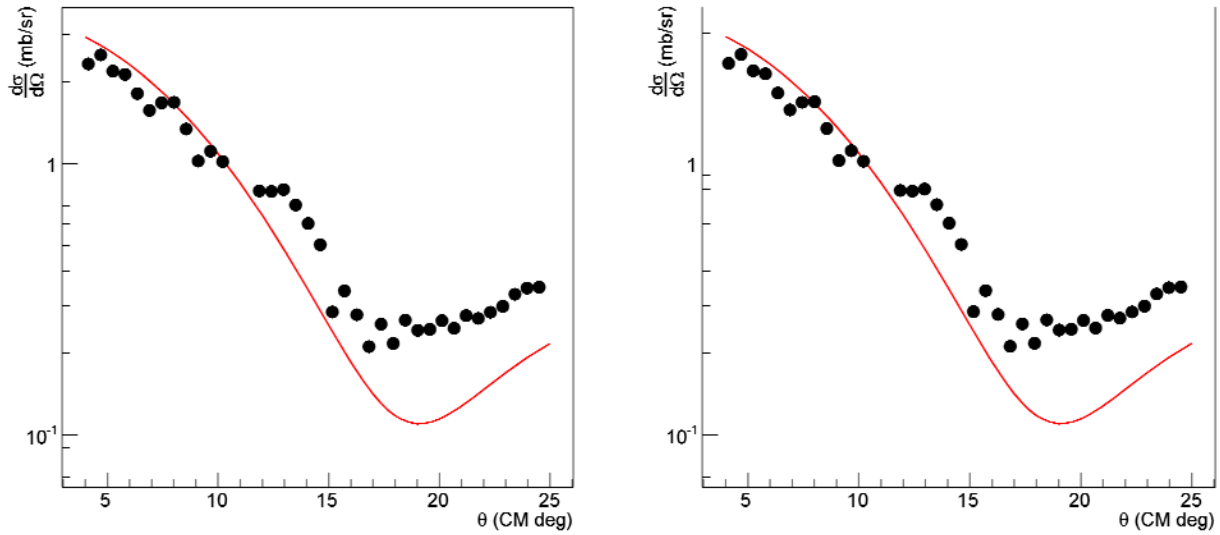


FIG. 4. On the left is the angular distribution for $^{14}\text{C}(d,p)^{15}\text{C}$ transfer to the ground state (black dots) and the ADWA calculation (red), the same is shown on the right for transfer to the $d_{5/2}$ excited state (black dots- experiment, green line ADWA).

Table III. Summary of ANCs found in the different measurements.

experiment	$C_{2s_{1/2}}^2 \text{ (fm}^{-1}\text{)}$	$C_{1d_{5/2}}^2 \text{ (fm}^{-1}\text{)}$
HI transfer	2.09 ± 0.29	$(4.48\pm 0.58)\cdot 10^{-3}$
TECSA $d(^{14}\text{C},p)^{15}\text{C}$	2.01 ± 0.24	$(4.06\pm 0.49)\cdot 10^{-3}$
60 MeV (d,p)	1.76 ± 0.29	
average	1.96 ± 0.16	$(4.23\pm 0.38)\cdot 10^{-3}$

Evaluation of a new method to extract SFs

In [1] a new method to extract SFs which used the ANC to experimentally fix the single particle ANC (SPANC) was presented. To do this a function

$$R^{DW}(b_{nlj}) = \left| \frac{\tilde{T}_{int}}{b_{nlj}} + \tilde{T}_{ext} \right|^2 \quad (5)$$

was defined where T stands for the transfer matrix element, and b is the SPANC. The transfer matrix element has been split into two parts, one which is integrated over the interior region (\tilde{T}_{int}) and is dependent on the SPANC and another \tilde{T}_{ext} which is integrated over the exterior and is not dependent on the SPANC. For a peripheral reaction, (\tilde{T}_{int}) is, by definition, negligibly small and R and thus the cross section is determined by \tilde{T}_{ext} . However, if a reaction has a non-negligible interior contribution, comparison of Eq. (5) to its experimental counterpart

$$R^{exp} = \frac{d\sigma^{exp}}{C_{lj}^2} \quad (6)$$

will fix the SPANC. This can then be used to calculate the SF using the relation

$$SF_{nlj} = \frac{C_{nlj}^2}{b_{nlj}^2} \quad (7)$$

Note that this procedure requires both a peripheral reaction to determine the ANC, and then a second, non-peripheral reaction to get the SF. R^{DW} is plotted against R^{exp} the 60 MeV $^{14}\text{C}(d,p)^{15}\text{C}$ reaction for both transfer to the ground state and first excited state in Fig.5. As can be seen, the uncertainties overlap for the entire range of SPANCs (which was varied by changing the radius parameter of the neutron binding potential which is the value plotted) for the ground state. Therefore, no information about the SF for

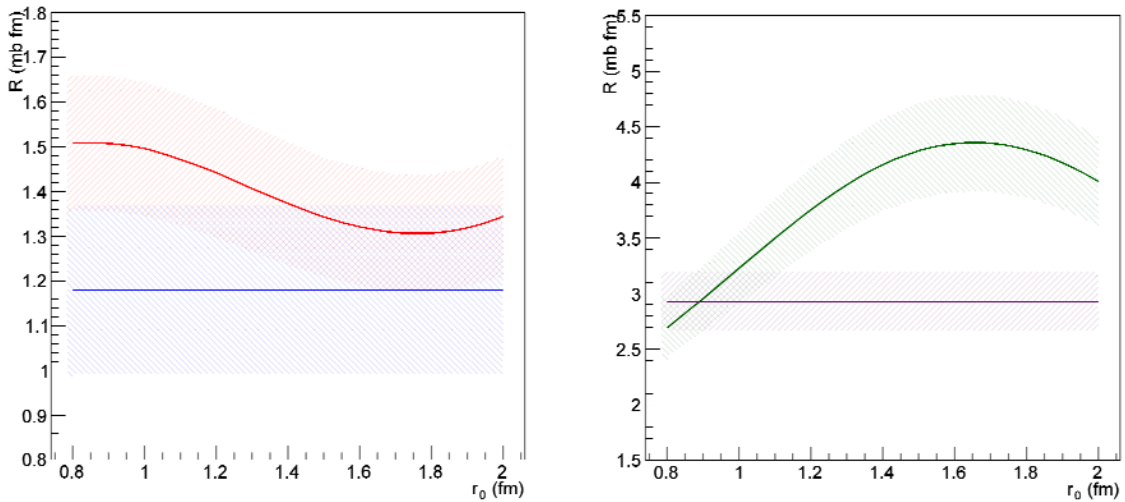


FIG. 5. R_{DW} (red) and R_{exp} (blue) for transfer to the ground state (left) and the $d_{5/2}$ first excited state (R_{DW} green, R_{exp} purple) (right). The uncertainties are shown by the hatched areas. In the calculation this is taken to be 10% and reflects the systematic uncertainty.

transfer to the ground state could be obtained for this reaction. In the plot for the first excited state, the two lines diverge around r_0 of ~ 1.15 fm, which corresponds to $b^2 = 4.01 \cdot 10^{-3} \text{ fm}^{-1}$. Using Eq. (7) one obtains a lower limit of $SF=1.05$. This is consistent with the expected single particle structure of ^{15}C . In summary, this test case highlights a significant problem with this method, namely, finding a reaction that is sufficiently non-peripheral to have a very strong dependence on the choice of SPANC, but that is still described well in the DWBA or ADWA.

Astrophysical $^{14}\text{C}(n,\gamma)^{15}\text{C}$ rate

The radiative neutron capture rates for $^{14}\text{C}(n,\gamma)^{15}\text{C}$ have been calculated using the code RADCAP [12] and the ANCs that were found in this work. At astrophysical energies only the first two states, the $2s_{1/2}$ ground state and the 740 keV $1d_{5/2}$ first excited state, contribute to the neutron capture cross section. The next state at 3.1 MeV and ~ 40 keV in width is too high to contribute [13]. S-wave neutron capture is not significant for the $^{14}\text{C}(n,\gamma)$ reaction due to parity conservation [14]. ^{14}C has $J^\pi=0^+$ and coupled with an s-wave neutron would give a system with $J^\pi=1/2^+$. Because the ground and first excited states in ^{15}C are $J^\pi=1/2^+$ and $J^\pi=5/2^+$, respectively this only allows for weak M1 and E2 transitions. Alternatively, a p-wave neutron would give the $^{14}\text{C}+n$ system $J^\pi=1/2^-$ or $3/2^-$, which would then be able to allow E1 transitions and thus a much higher cross section. For the first excited state E2 transitions should also be taken into account [14].

The neutron binding potential used was of the WS form with the real potential depth adjusted to reproduce the neutron binding energy for each state. The binding potential parameters were, for the ground state, $V_0=-54.71$ MeV, $r=2.8922$ fm, $a=0.60$ fm and $V_{SO}=-9.30$ MeV (using the SO convention described in [12]). The same geometry was used for the real and SO parts of the potential. The real depth was $V_0=-54.11$ MeV for the first excited state.

The cross section divided by the square root of the energy is given in Figure 6 for both capture to the ground state and the first excited state. The capture to the first excited state accounts for about 4% of the total (only the two states are considered). The sum of the two states is shown along with the recent direct measurement of Reifarth *et al.* [15] in Fig. 6.

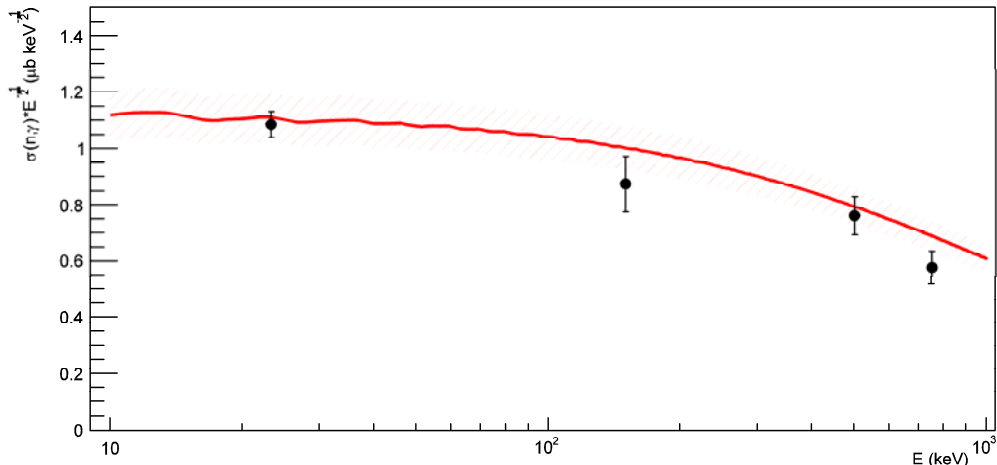


FIG. 6. Calculated cross section (sum of capture to gs and 1st exc. state, blue dots with red uncertainty) compared with Ref. [15] (black squares).

The calculated value for the cross section for capture to the ground state at 23 keV was $\sigma_{gs}(23 \text{ keV})=5.1\pm 0.4 \text{ } \mu\text{b}$ and to the first excited state was $\sigma_{exc}(23 \text{ keV})=0.19\pm 0.02 \text{ } \mu\text{b}$. The total cross section at 23 keV was found to be $\sigma(23 \text{ keV})=5.3\pm 0.5 \text{ } \mu\text{b}$, which is in good agreement with the most recent direct measurement [15].

Summary

The ANC for $^{15}\text{C}\leftrightarrow^{14}\text{C}+n$ has been determined for both the ground state and first excited state. The average values are $1.96\pm 0.16 \text{ fm}^{-1}$ for the ground state and $4.23\pm 0.38\cdot 10^{-3} \text{ fm}^{-1}$ for the first excited state. This was done as part of an effort to evaluate the new method of [1] to determine SFs with less uncertainty. The new method was found to not work at all for the GS due to a weak dependence on the neutron binding potential geometry and thus on the interior portion of the transfer matrix element for the non-peripheral reaction measured. The astrophysical $^{14}\text{C}(n,\gamma)$ rate was calculated using the determined ANCs and was found to be $\sigma(23 \text{ keV})=5.3\pm 0.5 \text{ } \mu\text{b}$, which is in good agreement with the most recent direct measurement.

- [1] A.M. Mukhamedzhanov and F.M. Nunes. *Phys. Rev. C* **72**, 017602 (2005).
- [2] M. McCleskey *et al.*, *Progress in Research*, Cyclotron Institute, Texas A&M University (2010-2011), p.I-5.
- [3] M. McCleskey *et al.*, *Progress in Research*, Cyclotron Institute, Texas A&M University (2009-2010), p.I-42.
- [4] A.M. Mukhamedzhanov, C.G. Gagliardi, and R.E. Tribble. *Phys. Rev. C* **63**, 024612 (2001).
- [5] T. Al-Abdullah *et al.*, *Phys. Rev. C* **81**, 035802 (2010).
- [6] L. Trache *et al.*, *Phys. Rev. C* **61**, 024612 (2000).
- [7] B.T. Roeder *et al.*, *Nucl. Instrum. Methods Phys. Res.* **A634**, 71 (2011).
- [8] I.J. Thompson, *Comput. Phys. Rep.* **7**, 167 (1988).
- [9] R.C. Johnson and P.J.R. Soper, *Phys. Rev. C* **1**, 976 (1970).
- [10] R.L. Varner, *Phys. Rep.* **201** (2), 57 (1991).
- [11] G.L. Wales and R.C. Johnson, *Nucl. Phys.* **A274**, 168 (1976).
- [12] C.A. Bertulani, *Comput. Phys. Commun.* **156**, 123 (2003).
- [13] A. Horvath *et al.*, *Astrophys. J.* **570**, 926 (2002).
- [14] M. Wiescher, J. Görres, and F.K. Thielemann, *Astrophys. J.* **363**, 340 (1990).
- [15] R. Reifarh *et al.*, *Phys. Rev. C* **77**, 015804 (2008).

Progress in the analysis of the beta delayed proton and gamma decay of ^{27}P for nuclear astrophysics

E. Simmons,¹ L. Trache,¹ A. Banu,¹ A. Saastamoinen,^{1,2} M. McCleskey,¹ B. Roeder,¹ A. Spiridon,¹ R.E. Tribble,¹ T. Davinson,³ P. J. Woods,³ G. J. Lotay,³ J. Wallace,³ and D. Doherty³

¹Cyclotron Institute, Texas A & M University, Texas, United States.

²If Department of Physics, University of Jyväskylä, Finland

³School of Physics, University of Edinburgh, Edinburgh, United Kingdom

Introduction & Astrophysical Motivation

When ^{26}Al is created in novae, the reaction chain is $^{24}\text{Mg}(p, \gamma)^{25}\text{Al}(\beta+\nu)^{25}\text{Mg}(p, \gamma)^{26}\text{Al}$, but this chain can be by-passed by another chain, $^{25}\text{Al}(p, \gamma)^{26}\text{Si}(p, \gamma)^{27}\text{P}$, and ^{26}Al can also be destroyed. One interesting feature of ^{26}Al is that its ground state has a large spin $J^\pi=5^+$ and, only 228 keV above it there is an isomeric state with $J^\pi=0^+$, which also beta decays, but has a much shorter life time than the ground state. In stars these two states behave as ‘different species’ until temperatures go beyond 1GK, and then they are correlated. Now, one of the ways ^{26}Al can be destroyed is by $^{26}\text{mAl}(p, \gamma)^{27}\text{Si}^*$, which is dominated by resonant capture. This was the focus of one of our experiments.

Energetically speaking, stars are too cold to study their reaction rates directly, that is, the actual cross sections are too low to allow us to measure them easily in the lab. So, we need to apply an indirect method in order to gain the information we require. In the case of interest here ($^{26}\text{Al}^m(p, \gamma)$), the indirect method we chose to use was the study of beta-delayed gamma ($\beta\gamma$) and proton (βp) decay. As shown in Fig. 1, the direct method involves a proton tunneling through the Coulomb barrier of $^{26}\text{Al}^m$ to form

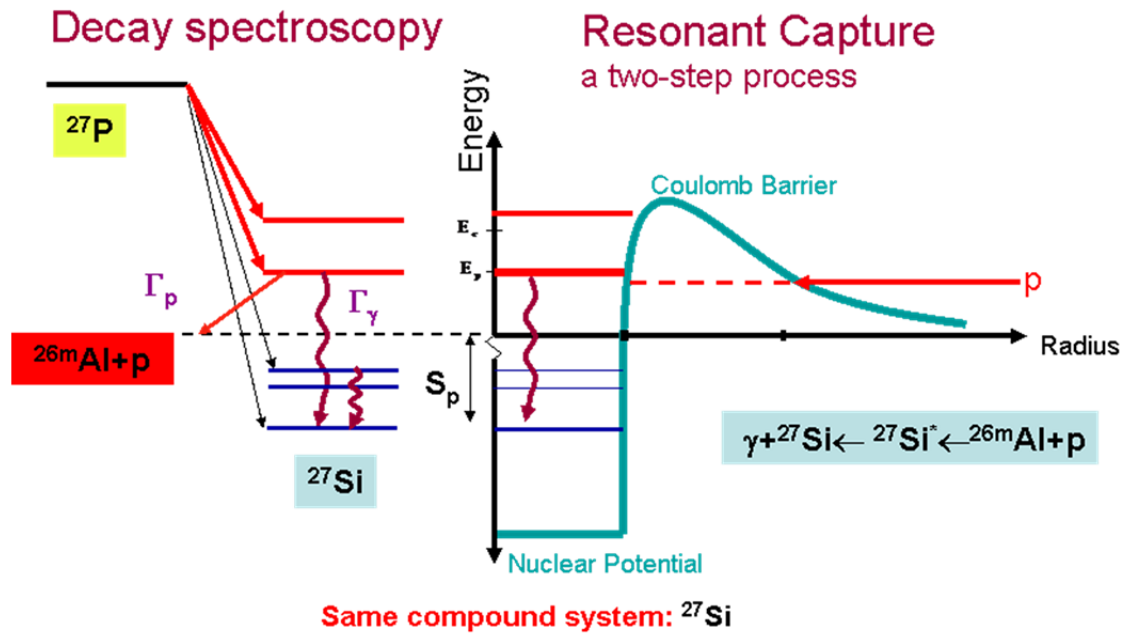


FIG. 1. Indirect method used to study resonances in the $^{26}\text{mAl}(p, \gamma)$ reaction. Note that they have the same compound system ^{27}Si .

excited states in ^{27}Si which then decay through gamma emission. Instead, starting with ^{27}P , it first β -decays to the same excited states in ^{27}Si (due to selection rules) and then decays through gamma emission. States populated above the proton threshold ($E^* > S_p + E(0^+) = 7.463 + 0.228 = 0.7661$ MeV) can decay by proton emission to $^{26}\text{Al}^m$ and these are the states of interest. In order to evaluate their contribution to the astrophysical reaction rate, we need to determine the position of the resonances and their partial gamma and proton widths.

Review of the Measurement

This experiment was run from Nov 24 to Dec 1 of 2010 using a primary beam of $^{28}\text{Si}^{+10}$ at 40 MeV/u obtained from the K500 superconducting cyclotron. A target of hydrogen gas, kept at LN₂ temps and 2 atm pressure, was used to create the desired ^{27}P by a (p, 2n) fusion evaporation reaction. After tuning and optimizing the secondary beam we ended up with about 11% total impurities, most of which was ^{24}Al .

The ^{27}P nuclei were implanted in the center of a thin detector where the decay occurred. A telescope combination of silicon detectors was used in this experiment. A thin (45 and later a 104 μm) double sided strip detector (DSSD), referred to here as the p-detector, was sandwiched between two thick (300 μm and 1 mm) silicon detectors, referred to as the β_1 and β_2 detectors respectively. The precise implantation in the middle of this very thin proton detector was possible due to the inherent high kinetic energy (30-40 MeV/u) of the exotic secondary beams produced using the in-flight technique and the good momentum control we have in MARS in combination with a rotating Al degrader foil, placed in front of the silicon detectors. By monitoring the two-dimensional histograms β_1 vs Proton detector and the Proton detector vs β_2 as the angle of the Al foil was changed, it was possible to see when the ^{27}P nuclei were implanted only in the center (proton) detector. This detector and degrader setup is shown below in Fig. 2.

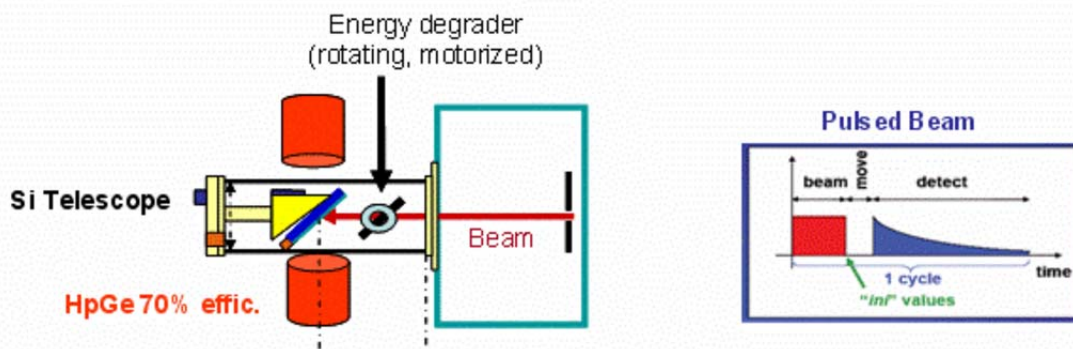


FIG. 2. Implantation and Decay Station Setup.

Using the β -detectors, p-detector and HpGe detectors, we measured, simultaneously, the β -p & β - γ coincidences. In order to do this the beam from the K500 cyclotron had to be pulsed, that is, ^{27}P was

implanted for a period of time, then the beam was switched off and the decay was measured before switching the beam back on and repeating the process.

Preliminary Results – Protons

The proton branching ratio for ^{27}P was known to be lower (0.07% total proton branching) compared to anything we had tried to measure before and was therefore, in many ways, a test run to see how far the β -background could be reduced. From preliminary analysis work it can be seen that, even though we were successful in substantially reducing the β -background from previous βp & $\beta\gamma$ experiments, we still have a background issue in the low energy region of interest, which is made even more troublesome in this case due to the very low total proton branching ratio. These features can be seen below in Fig. 3.

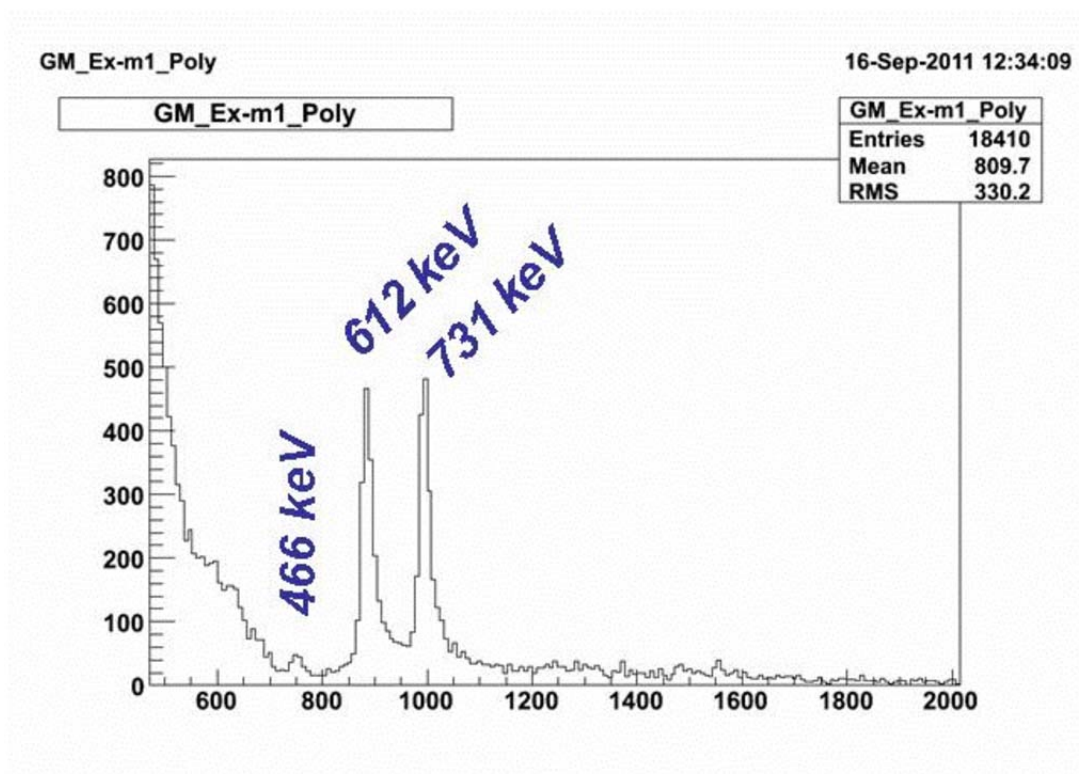


FIG. 3. Preliminary proton spectrum from the βp & $\beta\gamma$ experiment. A BB2-45 detector was used for this data.

The higher energy protons, originally identified by the Berkeley group, are clearly seen here but, in the low energy region we saw mostly β 's. As can be seen in Fig. 3, there is a clear structure above a continuous background in the low energy region 200 - 400 keV that suggests there is valuable information yet to be obtained. We have also determined that the total proton branching ratio is closer to 0.01% than the previous reported 0.07%.

Preliminary Results – Gammas

The gamma spectrum came out very nicely, especially in the high energy region, showing the payoff of having re-designed the implantation-decay station which allowed the HpGe's to be moved in as close as physically possible to the silicon detectors. The only impurities that were visible, due to our coincidence setup, came from impurities in the beam (^{22}Mg and ^{24}Al), see attached Fig 8. The ^{24}Al gammas were used, in addition to well known peaks identified in a background run, to create an extended energy calibration up to 8 MeV with residuals better than 2 keV for Germanium 1. It was found that the energy recoil had to be taken into account for the high energy gammas from ^{24}Al for the best calibration. Due to a non-linearity issue with Germanium 2, obtaining the best extended energy calibration requires using two separate fit ranges. That is, for energies up to about 1.7 MeV, one linear fit was used, and for energies 1.7 MeV to 8 MeV another linear fit was employed. Linear fits have so far proved slightly better than quadratic fits. Some work still needs to be done with these calibrations in order to get the residuals as good as Germanium 1. The current results for Germanium 2, with residuals for the major peaks, are shown below in Fig. 4.

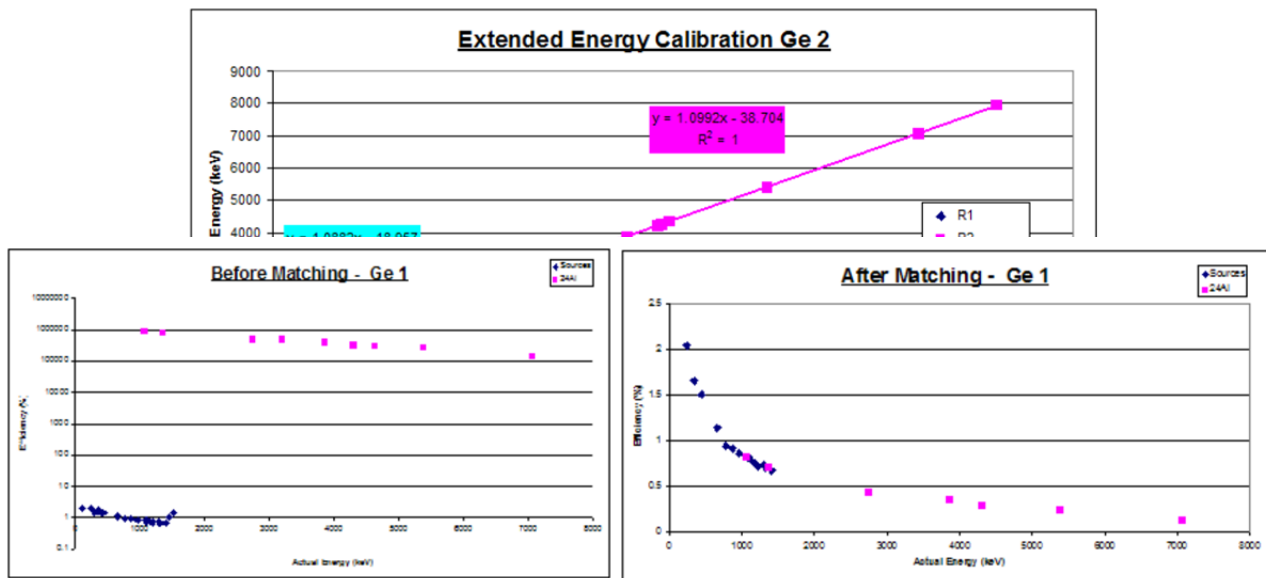


FIG. 5. Example of match ^{24}Al points to the efficiency curve created with the sources.

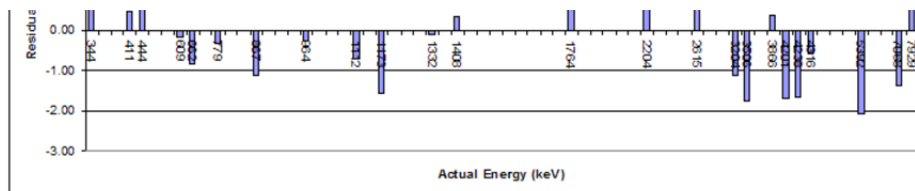


FIG. 4. Extended Energy Calibration for Germanium 2, showing the two ranges required.

An extended efficiency calibration was also obtained for each germanium detector using sources (^{152}Eu , ^{60}Co & ^{137}Cs) and the most intense peaks from ^{24}Al . This was done by first, using the source and

dead time information to create an efficiency calibration up to 1.4 MeV. Then, to include the ^{24}Al gammas, the sums (with background subtracted) divided by their absolute intensities were calculated for each peak, then, all of these values were multiplied by a common factor in order to match the efficiency points of the ^{24}Al to the curve created by the sources. This matching method is shown below in Fig. 5.

Further analysis at this point employed the use of the TAC data. Five TAC units were used to obtain information on the β_1 -p (TAC 1), β_2 -p (TAC 2), β_1 - γ (TAC 3), β_2 - γ (TAC 4) and the γ_1 - γ_2 (TAC 5) coincidences. By carefully gating on the peaks that appear in these histograms it is possible to cut out some background (and reduce the impurities) without losing real information. Several different gating conditions are shown in Fig. 6. A spectrum was created when gates were placed on each individual relevant TAC (3, 4 and 5) and also with a combination of relevant TACs (3 OR 4 and 3 OR 4 OR 5). Note that the single TAC condition on TAC 3 (β_1 - γ) has a larger reduction effect than TAC 4 (β_2 - γ), pointing to the fact that the thicker β -detector (β_2) was more efficient, as expected.

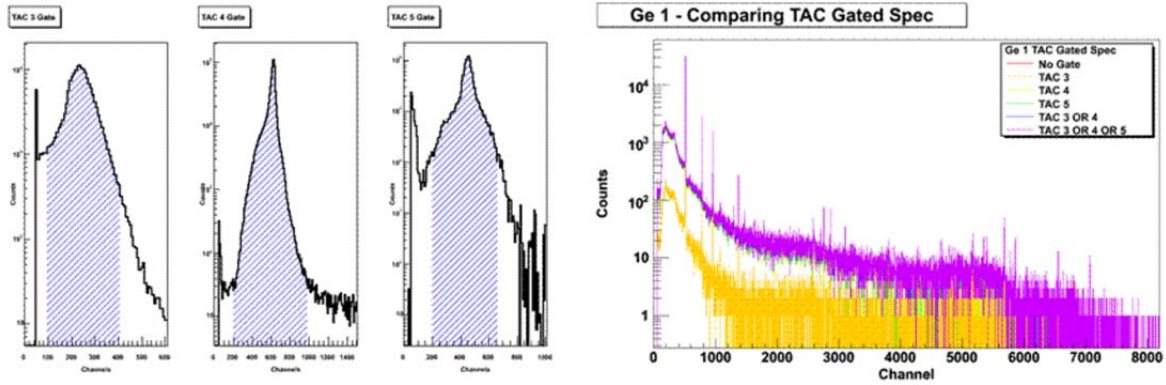


FIG. 6. TAC gates for the BB2-45 data on the left-hand side and various TAC-gated spectra on the right hand side.

The TAC-gated spectrum I will continue with at this point is the condition that an event corresponds within the (TAC 3 OR TAC 4 or TAC 5) gates. This spectrum is currently very similar to the original, non-TAC gated spectra, though it does seem to slightly reduce the impurities. Further analysis into these gates is needed to find the best results, that is, reducing the background as much as possible without compromising real counts.

The next step was to calculate the intensities of each gamma relative to the lowest gamma line (780 keV). First the background-subtracted sums have to be adjusted to take into account the efficiency of the detector. These numbers are then used to calculate the relative intensities. See equations below. Analysis of this is ongoing.

$$N_{\gamma}^i = \frac{A_{\gamma}^i}{\epsilon(E_{\gamma}^i)} \pm \delta N_{\gamma}^i$$

$$I_{\gamma}^i \equiv \frac{N_{\gamma}^i}{N_{\gamma}^1} \times 100$$

The results for the intensities of the major gammas are shown below in Table I in addition to the previously known values.

A preliminary decay scheme for these gamma lines is shown below in Fig 7. Many small peaks remain to be sorted out in order to determine if they are escape peaks or actual peaks, or maybe even a combination of the two cases. One method to help determine this is done by plotting the ratios for known cases where we have both the single escape (SE) and a double escape (SE) peak. That is, the ratio of the efficiency adjusted intensities of the SE to the original peak, and the DE to the original peak are plotted first, then, peaks that are suspected of being escape peaks are also plotted in this fashion (relative to their estimates original peaks). If the unknown points roughly follow the known points they are escape peaks, if they are very different, they are at least a combination of escape peaks and new peaks, if not entirely new peaks. Analysis on these data is currently ongoing.

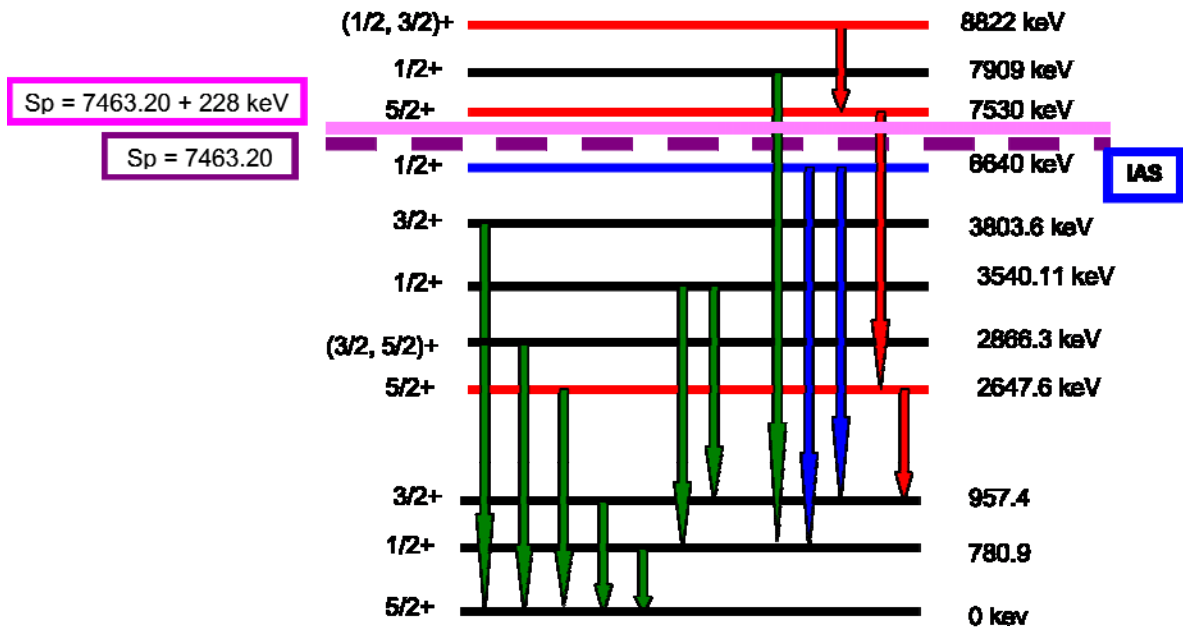


FIG. 7. Preliminary decay scheme for ^{27}Si . The blue lines come from the isobaric analog state, the green lines are the previously well known lines and the red are proposed new lines.

Future Plans

Future plans include finishing the analysis for the ^{27}P βp & $\beta\gamma$ experiment and understanding the method and results from a lifetime experiment. This involves finalizing the decay scheme for the gammas, calculating the branching ratios and estimating the logft values. Using this information we may be able to say something new about the overall picture of $^{26}\text{Al}^m$ in nuclear astrophysics.

[1] K. Krane, *Introductory Nuclear Physics*, (John Wiley & Sons, Inc., 1988).
 [2] D. Clayton, *Isotopes in the Cosmos*, (Cambridge University Press, 2003).
 [3] J.A. Caggiano *et al.*, *Phys. Rev. C* **64**, 025802 (2001).
 [4] T.J. Ognibene *et al.*, *Phys. Rev C* **54**, 1098 (1996).
 [5] A. Saastamoinen, L. Trache *et al.*, *Phys. Rev. C* **83**, 045808 (2011).

[6] L. Trache *et al.*, Proc. 10th Symposium on Nuclei in the Cosmos (NIC X), Mackinac Island, Michigan, July 2008, PoS 163.

Measurement of the $d(^{26m}\text{Al},p)^{27}\text{Al}$ reaction with TECSA

B.T. Roeder, M. McCleskey, L.Trache, S. Cherubini,¹V.Z. Goldberg, M. Gulino,¹ V.E. Iacob,
M. La Cognata,¹ G. Lotay,² R.G. Pizzone, G.G.Rapisarda,¹ E. Simmons,
R. Sparta,¹ A. Spiridon, C. Spitaleri,¹ and R.E. Tribble

¹INFN Laboratori Nazionali del Sud & DMFCI Università di Catania, 95123 Catania, Italy

²School of Physics and Astronomy, University of Edinburgh, Edinburgh, EH9 3JZ, United Kingdom

Following the success of the commissioning experiment for the Texas A&M-Edinburgh-Catania Silicon detector Array (TECSA) to measure the $d(^{14}\text{C},p)^{15}\text{C}$ reaction featured in last year's annual report [1] and in a published article [2], new experiments were planned during 2011 to measure reactions with rare isotope beams. It was found during the previous experiments that it would be difficult to observe reactions with beam rates less than 10^5 pps because of the background arising from the interacting of the primary beam on the primary target of MARS, and background from reactions associated with the secondary beam stopping in the end of the TECSA scattering chamber.

To prepare for these new measurements, some improvements were made to the TECSA scattering chamber and associated electronics. These improvements were carried out in order to shield the TECSA array from background reactions and β -decay of the rare isotope beams occurring inside the chamber and associated with stopping the beam. First, the TECSA detectors were shielded upstream of the target with a $\frac{1}{4}$ inch steel plate attached to the back of the mounting ring. The detectors were also shielded downstream of the target with a thick Al plate with a hole in the middle to allow the beam to pass through. To further reduce the background, the back flange of the TECSA scattering chamber was modified such that a section of 4" diameter beam pipe, approximately 1 m long, could be attached to the back of the chamber. With this addition to the setup, the beam was stopped 1m further away from the TECSA array than before, which further reduced the background from the decay of the beam. Finally, to improve the function of the scintillator-PMT detector with respect to the heavy-ion – proton coincidence in TECSA, the scintillator-PMT detector was moved from the front (upstream of the target) to the back of chamber. Fig. 1 shows the TECSA detector setup used in the rare isotope beam experiments after the improvements.

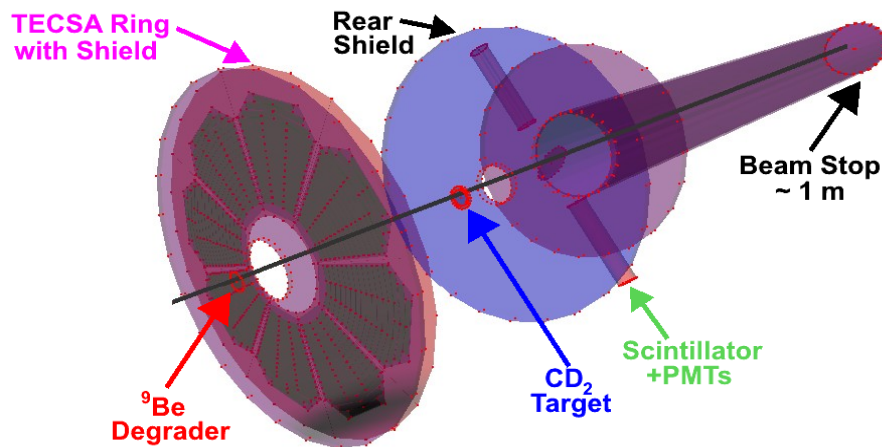


FIG. 1. Drawing of the TECSA setup for the rare isotope beam experiments

The first experiment with rare isotope beam carried out with the improved TECSA setup was a measurement of the $d(^{26}\text{Al},p)^{27}\text{Al}$ reaction in inverse kinematics. The ^{26}Al beam was produced in two forms which are relevant for this study: the ground state, ^{26g}Al with $J^\pi = 5^+$, and the isomeric state, ^{26m}Al with $J^\pi = 0^+$. Due to the short half-life of the ^{26m}Al (6.3 s), the $d(^{26m}\text{Al},p)^{27}\text{Al}$ reaction has not been studied previously. Both the $d(^{26g}\text{Al},p)^{27}\text{Al}$ and $d(^{26m}\text{Al},p)^{27}\text{Al}$ reactions could potentially populate ^{27}Al states that isobaric analogs of states in ^{27}Si that could be of importance in studying the $^{26g}\text{Al}(p,\gamma)$ and $^{26m}\text{Al}(p,\gamma)$ reactions that are important in stellar nucleosynthesis [3].

The ^{26m}Al and ^{26g}Al beams were produced in-flight with the $p(^{26}\text{Mg},^{26}\text{Al})n$ reaction using ^{26}Mg beam at 16 MeV/u from the K500 cyclotron at the Texas A&M University Cyclotron Institute (TAMU-CI). The ^{26}Al beam could be separated from other contaminate beams with the MARS spectrometer, but the ^{26m}Al and ^{26g}Al beams are only separated by 228 keV in mass and therefore are indistinguishable using normal mass separation and energy-loss techniques. However, it was expected that when the $p(^{26}\text{Mg},^{26}\text{Al})n$ reaction occurred with the “Transfer” reaction mechanism, it would produce mainly ^{26m}Al (0^+ to 0^+ spin-transfer) and when the reaction occurred with the “Fusion-Evaporation” reaction mechanism, it would produce mainly ^{26g}Al . As the reaction products of these two reaction mechanisms are transported through MARS at different magnetic rigidities, the ^{26m}Al and ^{26g}Al can be selected depending on which beam was needed. In order to test the above assumptions, the ^{26}Al beam was tested using the TAMU Tape Transport system [4] by measuring the number of β -decays to the number of ions. Since the ^{26g}Al is long-lived ($T_{1/2} \sim 7 \times 10^5$ years), measuring this ratio gives a direct measurement of the ^{26m}Al content of the beam. For the magnetic rigidity where the “Transfer” reaction mechanism dominated (MARS D1-2 = 420 A), it was found that the ^{26}Al beam intensity was 2×10^5 pps and had 66% ^{26m}Al and 33% ^{26g}Al . For the magnetic rigidity where the Fusion-Evaporation reaction mechanism dominated (MARS D1-2 = 402 A), it was found that the ^{26}Al beam intensity was 2×10^6 pps and had 36% ^{26m}Al and 64% ^{26g}Al . Spectra showing the ^{26}Al beam for both solutions measured with the MARS target detector are shown in Fig. 2.

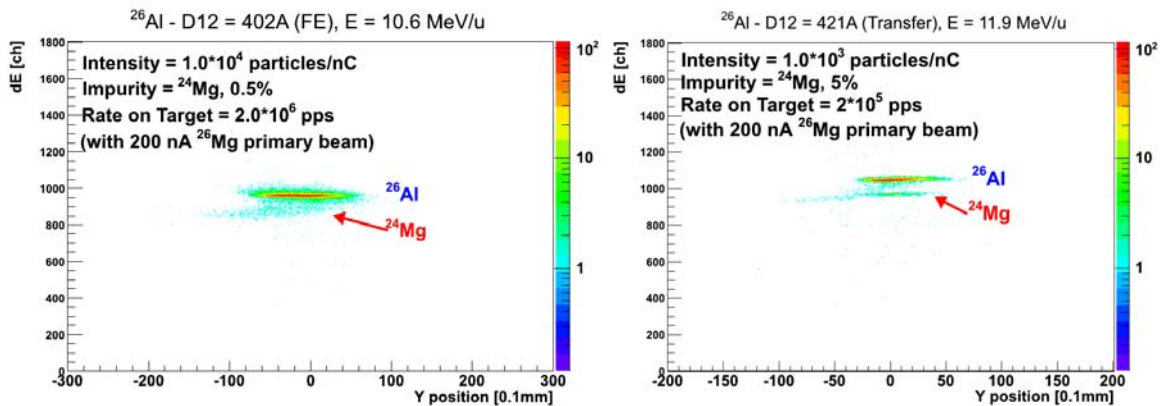


FIG. 2. MARS target detector spectra showing the separated ^{26}Al beam at the “Fusion-Evaporation” (left) and the “Transfer” (right) magnetic rigidity settings.

Following the beam tuning, the ^{26m}Al and ^{26g}Al beams were degraded in energy to ~ 5 MeV/u and ~ 3 MeV/u respectively by passing the beams through a $152\ \mu\text{m}$ ^9Be foil, located upstream of the TECSA array (see Figure 1). The beams were energy degraded to increase the cross sections for the (d,p) reactions and also to reduce the background from contaminate reactions. After passing through the degrader, the beams impinged on a target of deuterated-polyethylene (CD_2) with areal density of $451 \pm 5\ \mu\text{g}/\text{cm}^2$ and D:H ratio enriched to 98%. For this reaction, the protons from the forward center-of-mass angles would be detected at the backward lab angles. Thus, TECSA was mounted upstream of the CD_2 target in the flat configuration. The detector thickness of $\approx 300\ \mu\text{m}$ was sufficient to stop the protons from the reaction at all angles measured. Also, the detector ring had a hole in middle to allow the ^{26}Al beam to pass through it on its way to the target. The $d(^{26m}\text{Al},p)^{27}\text{Al}$ and $d(^{26g}\text{Al},p)^{27}\text{Al}$ reactions were measured with the CD_2 target distances of 21cm and 12cm to obtain angular distributions for the ^{27}Al states.

Typical spectra from TECSA for the $d(^{26m}\text{Al},p)^{27}\text{Al}$ and $d(^{26g}\text{Al},p)^{27}\text{Al}$ reactions for the TECSA ring positioned at 21cm from the target are shown in Figure 3. The spectra are shown in center-of-mass frame, which allows the addition of all the detectors and rings of TECSA in order to increase statistics. The background in these spectra was reduced by requiring a coincidence with a timing signal from a heavy-ion in the beam (^{26}Al) or from a reaction (^{27}Al) in the scintillator-PMT detector. Gating on this coincidence in the data analysis software, and the other improvements to the scattering chamber mentioned previously, reduced the background significantly. The remaining background under the peaks was due to reactions of the beam with the carbon in the CD_2 target that could not be removed, and some remaining background from the β -decay of the ^{26}Al beam stopped in the chamber. In Fig. 3, ^{27}Al states were observed from both the ^{26m}Al and ^{26g}Al beams. While similar states were populated in the two cases, it is expected that the angular distributions of these states will show which states were populated by the ^{26m}Al and which were populated by ^{26g}Al . Analyses of these angular distributions are currently underway.

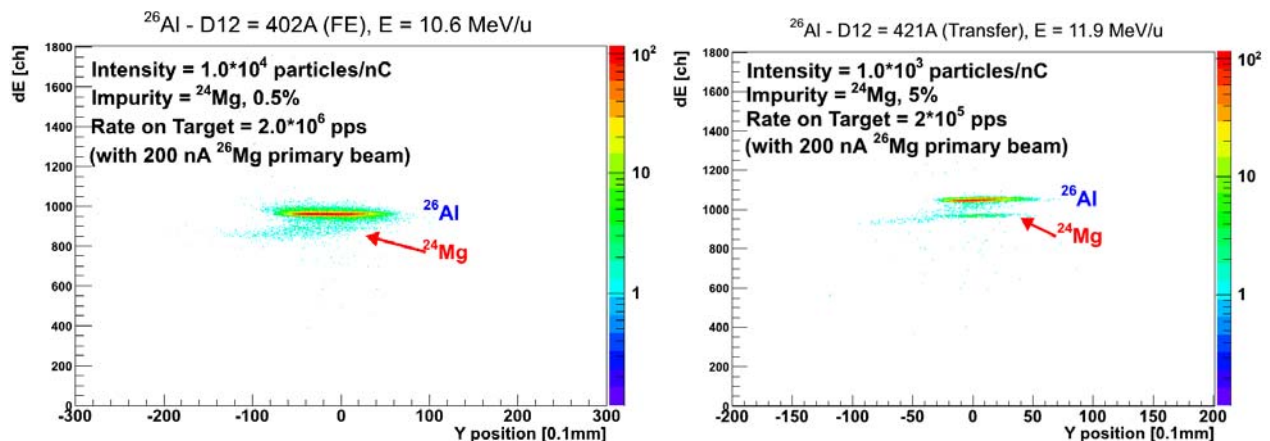


FIG. 3. Summed Center-of-Mass spectra for $d(^{26m}\text{Al},p)^{27}\text{Al}$ (left) and $d(^{26g}\text{Al},p)^{27}\text{Al}$ (right) obtained with TECSA at 21cm distance from the target.

In conclusion, the TECSA array was used to measure $d(^{26m}\text{Al},p)^{27}\text{Al}$ reaction at ~ 5 MeV/u and $d(^{26g}\text{Al},p)^{27}\text{Al}$ at ~ 3 MeV/u. Several states in ^{27}Al were selectively populated. In particular, the ^{27}Al level at 8.6 MeV excitation energy may be an isobaric analog state of a level in ^{27}Si , but further analysis of these data is needed.

- [1] B.T. Roeder *et al.*, Progress in Research, Cyclotron Institute, Texas A&M University (2010-2011), p.I-54;[http://cyclotron.tamu.edu/2011 Progress Report/index.html](http://cyclotron.tamu.edu/2011%20Progress%20Report/index.html).
- [2] B.T. Roeder *et al.*, Nucl. Instrum. Methods Phys. Res. **A634**, 71 (2011).
- [3] G. Lotay *et al.*, Phys. Rev. C **80**, 055802 (2009).
- [4] V.E. Iacob *et al.*, Phys. Rev. C **82**, 035502 (2010).

The $^{18}\text{F}(p,\alpha)^{15}\text{O}$ reaction studied via TECSA

R.G. Pizzone, B.T. Roeder, L. Trache, C. Spitaleri,¹ V.Z. Goldberg, M. Gulino, M. Kurokawa, I. Indelicato,¹ M. La Cognata,¹ M. McCleskey, G.G. Rapisarda,¹ E. Simmons, R. Spartà,¹ A. Spiridon, and R.E. Tribble

¹INFN Laboratori Nazionali del Sud & Università di Catania, Italy

Classical Novae gamma-ray emission is dominated, during the first hours of the explosion, by positron annihilation resulting from the beta decay of radioactive nuclei. The main contribution to this process arises from the decay of the ^{18}F [1]. Therefore the emission is directly related to ^{18}F production and destruction during the outburst. Among the physical inputs, which are necessary to evaluate the ^{18}F nucleosynthesis, a crucial role is played by the proton captures. The abundance of ^{18}F depends largely on few reaction rates highest, among which the $^{18}\text{F}(p,\alpha)^{15}\text{O}$ is one.

Measuring cross sections at astrophysical energies (in the case of novae nucleosynthesis few hundreds of keV) in the case of charged particle induced reactions is very difficult and this becomes an almost impossible task in the case of radioactive ion beams induced reactions. In order to by-pass these problems indirect methods are usually applied. One of the most powerful in the case of charged particle induced reactions is the Trojan Horse Method (THM) [2 - 4].

In particular, the THM selects the quasi-free (QF) contribution of an appropriate three-body reaction performed at energies well above the Coulomb barrier to extract a charged particle two-body cross section. The idea of the THM is to extract the cross section of an astrophysically relevant two-body reaction $A(x,c)C$ at low energies from a suitably chosen three-body quasi-free reaction $A(a,cC)S$. This is done with the help of direct theory assuming that the nucleus a has a strong $x+S$ cluster structure. In many applications this assumption is trivially fulfilled e.g. $a = \text{deuteron}$, $x = \text{proton}$, $S = \text{neutron}$. This three-body reaction can be described by a Pseudo-Feynman diagram, where only the first term of the Feynman series is retained.

The upper vertex describes the virtual break-up of the target nucleus a into the clusters x and S ; S is then considered to be spectator to the $A(x,c)C$ reaction which takes place in the lower pole. In the

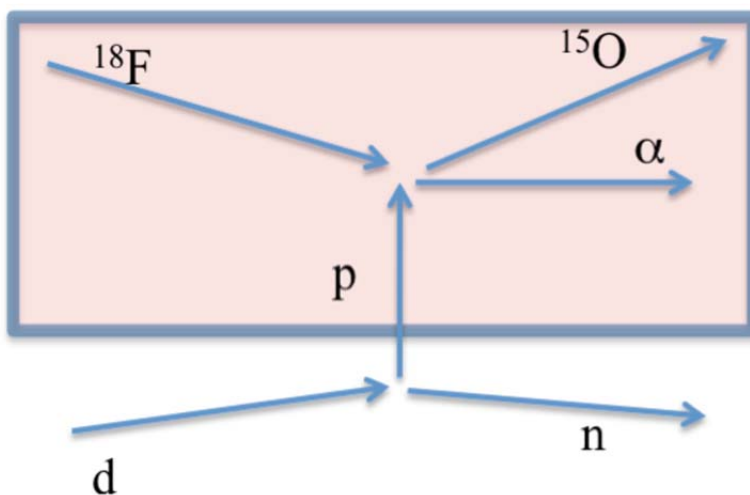


FIG. 1. Schematic sketch of the $^{18}\text{F}(p,\alpha)^{15}\text{O}$ studied by means of the THM.

present case we plan to study the $^{18}\text{F}(p,\alpha)^{15}\text{O}$ through the $^{18}\text{F}(d,\alpha)^{15}\text{O}n$ (see Fig. 1 for the present case); thus the deuteron will act like a Trojan Horse nucleus, the proton p as participant and the neutron as spectator.

Once the three body reaction cross section is determined (by means of ^{15}O and α detection in coincidence) it is possible to extract the binary reaction cross section of interest (in our case the $^{18}\text{F}(p,\alpha)^{15}\text{O}$) at the energies of astrophysical interest.

In the simplest approach, the plane wave impulse approximation, the three body cross section can be factorized as:

$$d^3\sigma/dE_a d\Omega_a d\Omega_{15\text{O}} \propto (KF) |\Phi(p_s)|^2 d\sigma^N/d\Omega$$

where KF is a kinematical factor containing the final state phase space factor, $|\Phi(p_s)|^2$ is the momentum distribution of the spectator *neutron* inside *deuteron*, and $d\sigma^N/d\Omega$ is the differential nuclear cross section for the two body reaction $^{18}\text{F}(p,\alpha)^{15}\text{O}$ [5,6].

The experiment was performed at the Cyclotron Institute of the Texas A&M University where the K500 cyclotron provided an ^{18}O beam as a primary beam at 9 A MeV. The K150 cyclotron was used in the beginning of the run for the same purpose, but problems to the injection line prevented to use this machine for the entire run. The MARS spectrometer was then used to get a ^{18}F beam via the $p(^{18}\text{O}, ^{18}\text{F})n$ reaction, after energy degrading of the primary beam by means of 1.25 mils Al degrader. The obtained secondary beam was tuned through MARS with a final energy of 56.7 MeV and then the beam-spot was tuned at the TECSA target position on a position sensitive detector. A beam-spot of 3 x 5 mm x mm was obtained after the tuning was completed. The energy spread of the beam was around 2%. The isotopic purity of the beam was checked during the tuning and it was found that the beam was 94% pure and the intensity of the beam was about $3\text{-}4 \times 10^5$ ions/sec. All these beam characteristics are clear from Fig. 2

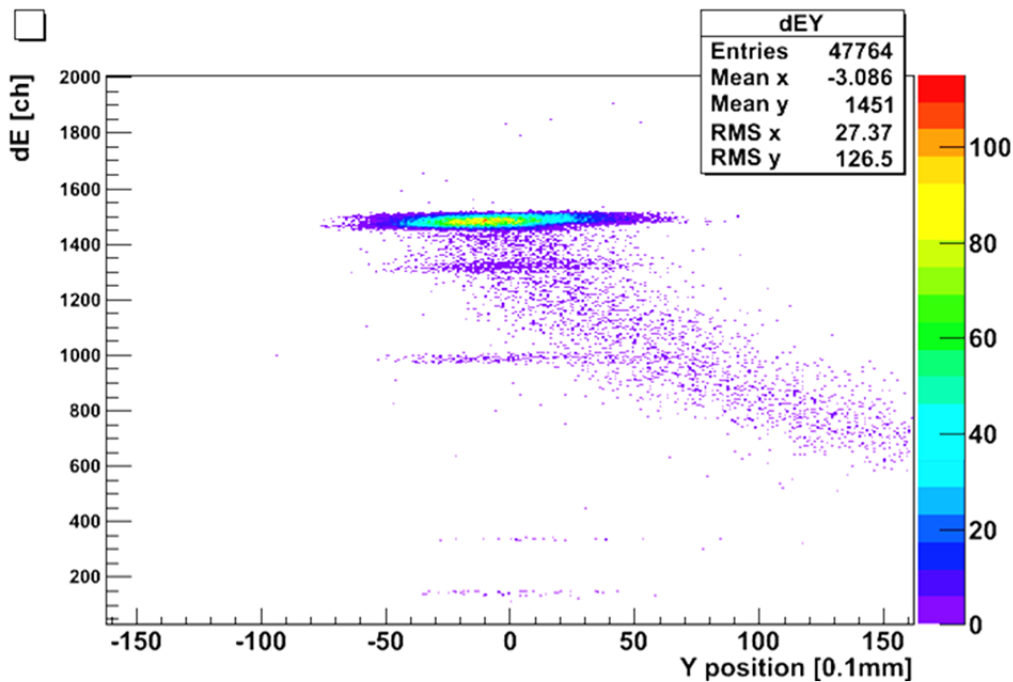


FIG. 2. Energy vs. y position plot for the target detector. A clear and more intense spot, related to ^{18}F is evident. Other isotopes represent only few percent of the total yield.

where the energy is reported as a function of y position in the target detector.

The beam impinged on an isotopically enriched deuterated polyethylene target (98% purity) around $800 \mu\text{g}/\text{cm}^2$ thick. The experimental set-up consisted of two detector arrays working in coincidence. The TECSA array (Texas Edinburgh Catania Silicon Array) [7], made up of 8 YY-1-300 Micron detectors (each one with 16 strips), was set at 190 mm from target covering angles in the range $\theta=15^\circ\text{-}40^\circ$. Closer to the beam axis a second detector array, the CROSS, is positioned, consisting of two position sensitive detectors (16 strips each), placed at 340 mm and covering angles from 3 to 12 degrees. The TECSA array was devoted to the detection of the alpha particles while the CROSS was used to detect the ^{15}O in coincidence. The experimental set-up is sketched in Fig. 3. The displacement of the experimental setup was chosen in order to cover the whole Quasi-Free angular range, known “a priori” from a Monte Carlo simulation. A scintillator was used to improve the definition of the timing of the experiment.

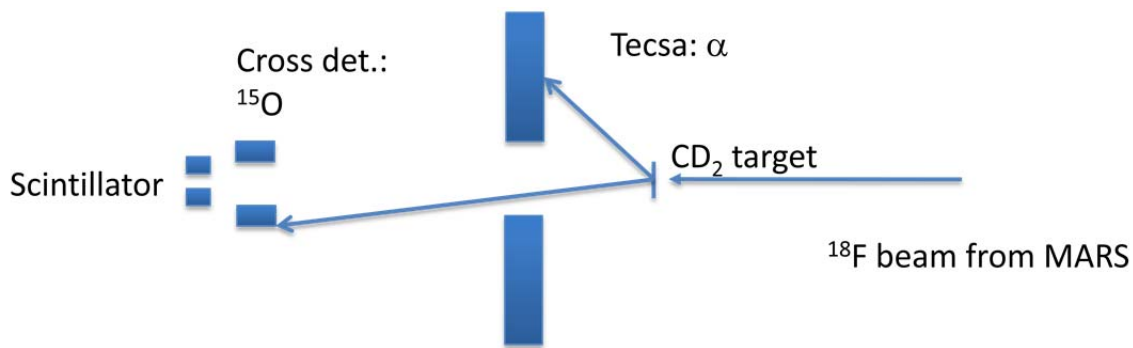


FIG. 3. Sketch of the experimental set-up described in the text.

The detectors were calibrated in energy by means of standard alpha sources and ^{18}F scattering off the CD_2 target. The CROSS detector was also calibrated in position by means of a mask which was used during the calibration runs. The measurement of the energy and position of the two ejectiles will give the possibility to calculate all the kinematic variables regarding the third, undetected, particle as well as other variables of interest for the following data analysis (e.g. Q-value, relative energy $\alpha\text{-}^{15}\text{O}$, spectator momentum).

After calibration (and taking into account the energy loss of beam and ejectiles in the target) the kinematic locus of $\alpha\text{-}^{15}\text{O}$ energy is studied and plotted in Fig. 4. At this time, only coincidences between detector number 4 of the TECSA array and the bottom detector of the CROSS have been partially examined. The data analysis is still going on and will study, as the next step, the presence of the quasi-free mechanism.

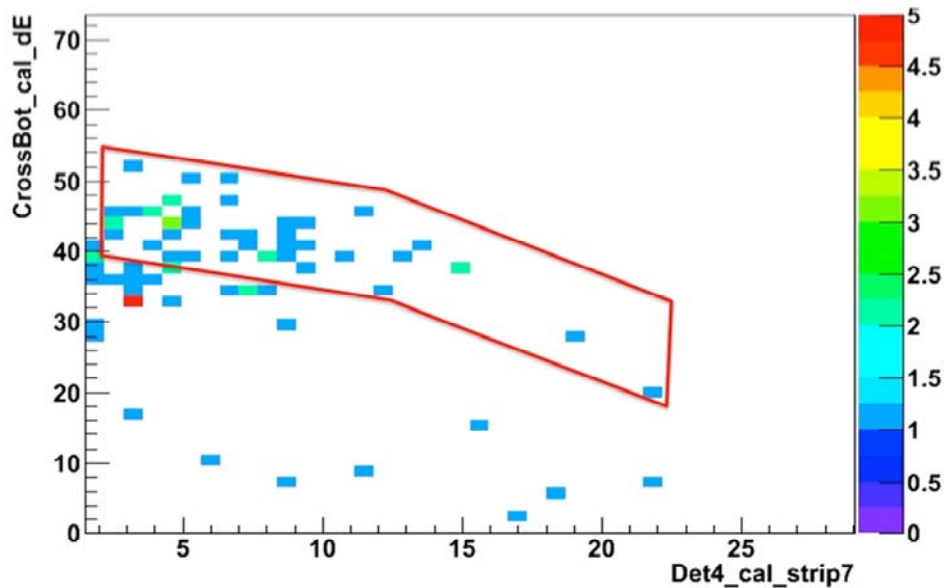


FIG. 4. Typical kinematic locus for the α - ^{15}O coincidence for one strip of detector #4 of TECSA and the bottom detector of the CROSS. The red curve marks the region where the three body reaction of interest is expected.

- [1] A. Coc *et al.*, *Astronomy & Astrophys. (A&A)* **357**, 561 (2000).
- [2] S. Cherubini *et al.*, *Astrophys. J.* **457**, 855 (1996).
- [3] C. Spitaleri *et al.*, *Phys. Rev. C* **60**, 055802 (1999).
- [4] R.G. Pizzone *et al.*, *Phys. Rev. C* **71**, 058801 (2005).
- [5] C. Spitaleri *et al.*, *Phys. Rev. C* **63**, 055806 (2004).
- [6] C. Spitaleri *et al.*, *Phys. Rev. C* **63**, 005801 (2001).
- [7] B.T. Roeder *et al.*, *Nucl. Instrum. Methods Phys. Res.* **A634**, 71 (2011).

The two-proton decay of ^{12}O and its isobaric analog state in ^{12}N

M.F. Jager,¹ R.J. Charity,¹ J.M. Elson,¹ J. Manfredi,¹ H. Mohammad,¹ L.G. Sobotka,¹
M. McCleskey, L. Trache, B.T. Roeder, A. Spiridon, E. Simmons,
R.G. Pizzone and M. Kurokawa²

¹*Departments of Physics and Chemistry, Washington University, St. Louis, Missouri*

²*RIKEN Nishina Center, Wako, Saitama 351-0198, Japan*

This report abstracts the results from a recent experiment with a ^{13}O secondary beam, using neutron and proton knockout reactions to populate $^{12}\text{O}_{gs}$ and its isobaric analog state (IAS) in ^{12}N [1]. The two-proton decays of these states were detected and used to deduce the masses and limit the decay widths of these states. The two-proton decay of $^{12}\text{N}_{IAS}$ is the second example of two-proton decay where all one-nucleon emissions are either energy or isospin forbidden. The energy of $^{12}\text{N}_{IAS}$ was unknown prior to this work and finding it completed the $A = 12$ quintet. The energy for this state and a new mass for $^{12}\text{O}_{gs}$ allowed for a fit of the Isobaric Multiplet Mass Equation (IMME) which showed no evidence of isospin symmetry breaking.

The Texas A&M University K500 cyclotron delivered a primary beam of $E/A=38$ MeV ^{14}N of intensity 80 pA. A secondary beam of 2000-4000 s^{-1} $E/A=30.34$ MeV ^{13}O was separated from the other reaction products using the MARS spectrometer. This secondary beam impinged on a 45.6 mg/cm^2 target of ^9Be . The beam and reaction products were incident on a 10 cm \times 10 cm 300 μm Si ΔE detector of type TTT manufactured by Micron Semiconductor. This detector has 128 strips on both the front and back sides. The particles of interest pass through this Si detector, which was located 18 cm from target, and are stopped by a 32 element array of CsI(Tl) scintillator E detectors located immediately behind it. These CsI(Tl) detectors were arranged in a 6x6 array with the corner locations vacant.

In order to have confidence in the masses and widths, it is useful to compare to well-known “calibrations” states. Figs. 1(a) and 1(b) show the ^{12}N and ^{13}N excitation-energy spectra deduced with the invariant mass method for detected $p+^{11}\text{C}$ and $p+^{12}\text{C}$ events respectively. The first spectrum (a) is dominated by a peak corresponding to the first-excited state of ^{12}N which is produced very strongly in proton-knockout reactions. The peak in the second spectrum (b) can be associated with a known $J^\pi = 3/2^-$ level in ^{13}N . From Gaussian fits with suitable background, we obtain centroids of 968 keV and 3496 keV with a 2 keV statistical error for these two states. These can be compared to the tabulated values of 960 ± 12 keV and 3502 ± 2 keV, respectively, listed in the ENSDF database. From these comparisons we assign a systematic error of 10 keV to all our extracted excitation energies and mass excesses.

The reconstructed spectrum of total kinetic energy E_T released in the decay of ^{12}O is shown in Fig. 1(c) after a small background removal. Particle identification was obtained with the $E-\Delta E$ method, but complete separation of C isotopes was not achieved. The most important contribution to this problem is from channeling interactions in the Si ΔE detector which result in 5% of ^{11}C fragments leaking into the ^{10}C gate. (The MICRON TTT detectors are not cut off axis and thus channeling should be avoided in subsequent uses of this detector by mounting it so that particles are not incident normal its front surface.)

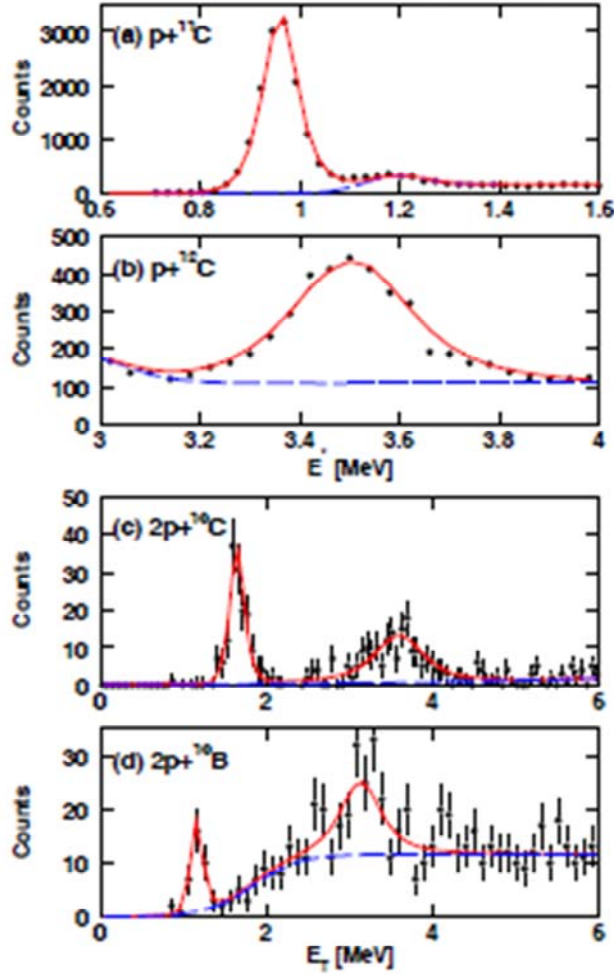


FIG. 1. Excitation-energy spectra of calibration peaks for (a) the 960-keV, $J^\pi = 2^+$ state in ^{12}N and (b) the 3.502 MeV, $J^\pi = 3/2^-$ level in ^{13}N . The solid curves show the results of Monte Carlo simulations of the peak shapes incorporating the detector response and the known level properties. The dashed curves indicate as estimation of the background under these peaks. Spectra of total kinetic energy released in the two-proton decay of (c) ^{12}O and (d) its analog in ^{12}N reconstructed from detected $2p+^{10}\text{C}$ and $2p+^{10}\text{B}$ events. The solid curves shows peak fits to these data with the dashed curves indicating the fitted background.

The solid curve in Fig. 1(c) shows a fit to the spectrum assuming Breit-Wigner line shapes for the ground and excited-state peaks and including the experimental resolution using the Monte Carlo simulations. The width of the ground-state peak was found to be consistent with the experimental resolution. An upper limit of 72 keV at the 3σ level was determined.

The ^{12}N E_T spectrum from $2p+^{10}\text{B}$ events, shown in Fig. 1(d), displays a peak at 1.165 MeV corresponding to an excitation energy of 10.45 MeV if ^{10}B was formed in its ground state. In principle, the detected ^{10}B fragment could have also been formed in more than 4 excited states, and thus its

excitation energy may be larger than 10.45 MeV. The two-proton decay of the isobaric analog state is expected to populate the 1.740 MeV ^{10}B state which subsequently decays by γ -ray emission, see Fig. 2(b). If the observed peak is the IAS, then the level energy would be 12.19 MeV, exactly at the energy expected by the IMME. A fit to this peak with an exponential background is shown by the solid curve in Fig. 1(d). The peak width is again consistent with the experimental resolution with an upper limit of $\Gamma < 110$ keV at the 3σ level. No such narrow ^{12}N levels are known above $E^*=10$ MeV and it seems highly likely this is the isobaric analog state.

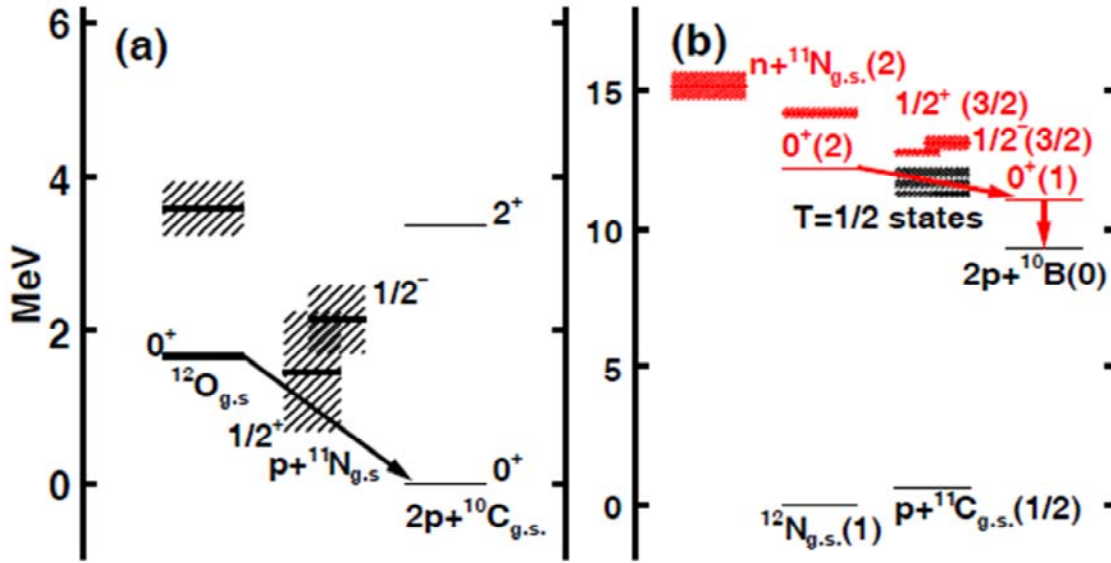


FIG. 2. Level diagrams showing the states of interest in the two-proton decays of (a) ^{12}O levels and (b) their isobaric analogs in ^{12}N . For the latter not all states are shown: The intermediate states that conserve isospin have their isospin indicated in the parenthesis (red). Also for ^{11}C , the possible isospin violating $T=1/2$ intermediate states are indicated. The ^{11}N levels in both (a) and (b) are not well determined.

Having completed the quintet (see Ref. [1]) quadratic, cubic, and quartic fits to the IMME were done. The mass excesses are clearly consistent with the quadratic form of the IMME expected for isospin symmetry. The d coefficient for the cubic fit is 0.4 ± 4.7 keV, a result consistent with zero. Although the IMME fits the data quite well this does not rule out all aspects of isospin asymmetries. For multiplets where the proton-rich members are at or near the continuum, the wavefunctions of the last proton extend further out compared to the analog neutrons in the bound neutron-rich members. This effect is enhanced for nucleons in s orbits where the effect is called the Thomas-Ehrman shift. These isospin asymmetries are mostly absorbed into the b and c coefficients of the IMME and produce very small d values.

In summary we have created ^{12}O fragments via neutron knockout from a ^{13}O projectile. The three decay products produced in the two-proton decay of the ground and an excited state were detected and the ^{12}O mass and width were determined with the invariant mass method. The width of the ground state was found to be less than 72 keV. The isobaric analog state of $^{12}\text{O}_{g.s.}$ in ^{12}N was observed for the first time.

Single-nucleon decay of this state cannot conserve both energy and isospin but two-proton decay to the isobaric analog in ^{10}B does. Thus to the extent that isospin is conserved, this represents a Goldansky type two-proton decay of a type previously seen only once before – the isobaric analog of ^8C in ^8B . No evidence for isospin symmetry breaking was found in $A = 12$.

[1] M.F. Jager *et al.*, Phys. Rev. C. **86**, 011304(R) (2012).

Preliminary results of the indirect study of the $^{12}\text{C}(^{12}\text{C},\alpha)^{20}\text{Ne}$ reaction via the THM applied to the $^{16}\text{O}(^{12}\text{C},\alpha)^{20}\text{Ne}$ reaction

G.G. Rapisarda,^{1,2,6} C. Spitaleri,^{1,2} C. Bordeanu,³ Z. Hons,⁴ G.G. Kiss,¹ M. La Cognata,¹ J. Mrazek,⁴
C. Nita,³ D. Pantelica,³ H. Petrascu,³ R.G. Pizzone,¹ S. Romano,^{1,2} T. Szücs,⁵
L. Trache,⁶ A. Tumino,^{1,7} and G. Velisa⁵

¹*INFN Laboratori Nazionali del Sud, Catania, Italy*

²*Dipartimento di Fisica e Astronomia Università di Catania, Italy*

³*NIPNE, Bucharest, Romania*

⁴*Nuclear Physics Institute of ASCR, Rez near Prague, Czech Republic*

⁵*ATOMKI, Debrecen, Hungary*

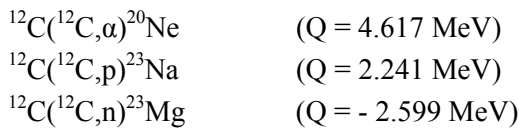
⁶*Cyclotron Institute – Texas A&M University, College Station, TX, USA*

⁷*Università degli studi di Enna “Kore,” Enna, Italy*

Abstract - The Trojan Horse Method was applied to the $^{16}\text{O}(^{12}\text{C},\alpha)^{20}\text{Ne}$ 2 to 3 body process to study the $^{12}\text{C}(^{12}\text{C},\alpha)^{20}\text{Ne}$ reaction within the energy range of astrophysical interest. This reaction bears a very important role in the advanced stages of massive star evolution, in particular during the carbon burning phase. The experiment was performed at the Horia Hulubei National Institute of Physics and Nuclear Engineering - IFIN HH (Bucharest, Romania). Preliminary results will be presented in this paper.

Astrophysical Context

The study of the $^{12}\text{C}+^{12}\text{C}$ reaction is of great interest in astrophysics. Carbon burning is connected with the third phase of massive star evolution [1]. When helium is consumed in the center of the star, the core mainly consists of ^{12}C and ^{16}O . Only in stars with $M > 8 M_{\odot}$ the gravitational contraction increases the central temperature up to trigger ^{12}C burning. In particular the first activated process is the $^{12}\text{C}+^{12}\text{C}$ fusion, the Coulomb barrier for carbon nuclei being the lowest. The most likely reaction channels are:



On one hand, these reactions are the key processes for the ^{20}Ne , ^{23}Ne and ^{23}Mg nucleosynthesis, on the other hand, they determine the successive stellar evolution. Carbon burning reaction rate is a fundamental parameter to determine the so-called M_{up} , that is, the minimum mass of a star for carbon ignition. Stars with $M < M_{\text{up}}$ evolve into CO White dwarf, while stars with $M > M_{\text{up}}$ conclude their life as core-collapse Supernovae [2].

The core carbon burning takes place in a temperature range of $T = 0.5 - 1.0$ GK. For a temperature of 0.5 GK, the corresponding Gamow energy for the $^{12}\text{C}+^{12}\text{C}$ fusion is $E_G = 1.5 \pm 0.3$ MeV. Accurate determination of the carbon burning reaction rate requires very precise measurement of the $^{12}\text{C}+^{12}\text{C}$ cross section down to this energy, well below the Coulomb barrier (about 8 MeV).

In spite of the key role of carbon fusion reactions in understanding stellar evolution, its reaction rate is not very well determined right at the energies relevant for astrophysics.

One of the main problem occurring in the experimental study of nuclear reactions of astrophysical relevance is the strong suppression of the cross section due to the Coulomb barrier that strongly decreases the signal-to-noise ratio.

In experiments performed so far ([3] and references therein), involving both charged particle and gamma ray spectroscopy, data were obtained down to carbon-carbon center of mass energy $E_{\text{cm}} = 2$ MeV, that is at the higher edge of the Gamow peak. Nevertheless, experimental data below $E_{\text{cm}} = 3$ MeV are rather uncertain [2]. For instance, a recent work [4] questions the presence of the claimed resonance at $E_{\text{cm}} = 2.14$ MeV [3].

Because of the experimental data uncertainty, up to now the only way to obtain the carbon-carbon fusion reaction rate at astrophysical energies has been the extrapolation from experimental data at higher energy [5]. In the present case, extrapolation might introduce systematic uncertainties owing to the presence of possible resonant structures in the astrophysical energy range as well, like the already mentioned 2.14 MeV or a theoretically predicted resonance at $E_{\text{cm}} = 1.5$ MeV [6].

New and accurate experimental data, down to the astrophysical energies, are strongly required.

In this paper, we report on the study of the $^{12}\text{C}(^{12}\text{C},\alpha)^{20}\text{Ne}$ reaction carried out applying the Trojan Horse Method (THM) to the three-body reaction $^{16}\text{O}(^{12}\text{C}, \alpha)^{20}\text{Ne}$. The THM features, briefly described below, allow us to obtain the $^{12}\text{C}(^{12}\text{C}, \alpha)^{20}\text{Ne}$ cross section in a wide energy range including the Gamov peak region.

The Trojan Horse Method

The THM [8-12] is a powerful indirect technique that allows one to extract a two-body reaction cross section, $t(p,a)b$, down to low energies of astrophysical interest by selecting the quasi-free break-up channel of an suitable three-body reaction $A(p,ab)s$. The so-called TH nucleus A should have a large probability for a $t \oplus s$ cluster configuration. The three-body reaction is performed at a beam energy larger than the Coulomb barrier in the entrance channel, where the electron screening effect is also negligible. The $p+A$ interaction produces A break-up into t and s ; in the quasi-free kinematical condition it is assumed that s behaves like a spectator while t interacts with the nucleus p leading to the astrophysically relevant reaction $t(p,a)b$. The high beam energy in the entry channel is compensated for by the $t \oplus s$ binding energy so that the two-boby reaction can takes place at the low astrophysical energies. Moreover, thanks to the $t \oplus s$ inter-cluster motion, the THM allows to measure the two-body cross section in a wide energy using a single beam energy.

The Experiment

The 9 MV Tandem accelerator of the Horia Hulubei National Institute of Physics and Nuclear Engineering - IFIN HH provided a 25 MeV ^{16}O beam with a spot size on the target of about 1 mm and an

intensity of about 8 nA. A natural carbon target, $100 \mu\text{g}/\text{cm}^2$ thick, was used to induce the $^{16}\text{O}+^{12}\text{C}$ reaction. ^{16}O was used as TH nucleus since it can be described in terms of a $^{12}\text{C}+\alpha$ configuration [13-15].

Energy and position of the outgoing particles were detected using six position sensitive silicon detectors (PSD) in a symmetric configuration to double the number of collected events (Fig. 1). In particular, PSD1 (PSD4), covering the 13° - 26° angular range, was devoted to the ^{20}Ne detection. To distinguish Ne from other nuclei produced in the oxygen-carbon interaction the ΔE -E technique was employed. To this aim an ionization chamber (IC) was placed in front of PSD1 (PSD4).

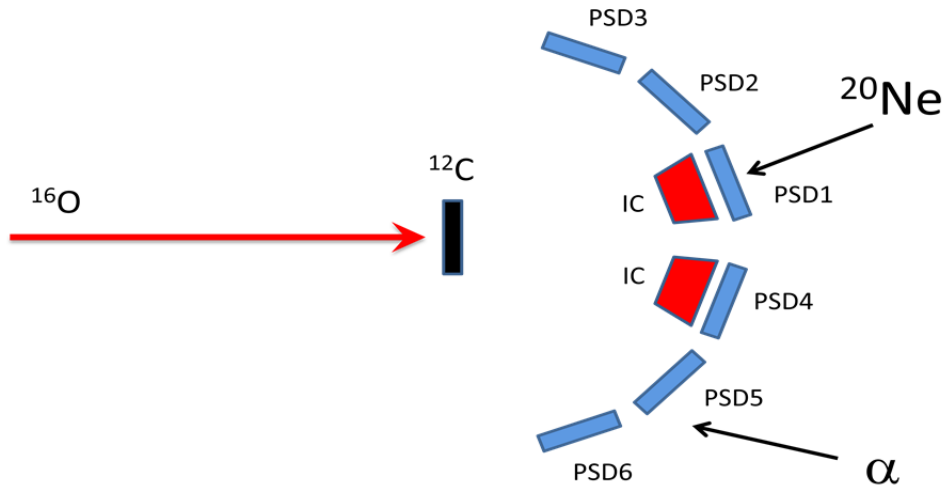


FIG. 1. Experimental set-up.

PSD5 (PSD2) and PSD6 (PSD3), covering the angular range $41^\circ - 55^\circ$ and $65^\circ - 80^\circ$ respectively, were placed on the other side with respect to the beam axis, and were dedicated to the α particles detection. ^{20}Ne nuclei and α particles were detected in coincidence. This experimental set-up allowed us to measure the $^{12}\text{C}(^{12}\text{C},\alpha)^{20}\text{Ne}$ excitation function in a wide range 0-3 MeV ($E_G = 1.5 \pm 0.3$).

In Fig. 2 the experimental ΔE -E 2D plot is shown. The Ne locus is highlighted by a red arrow. This locus is very well separated from loci due to lighter elements (in particular the most intense locus is due to the ^{16}O scattered beam), though it overlaps with the Mg one at low energy.

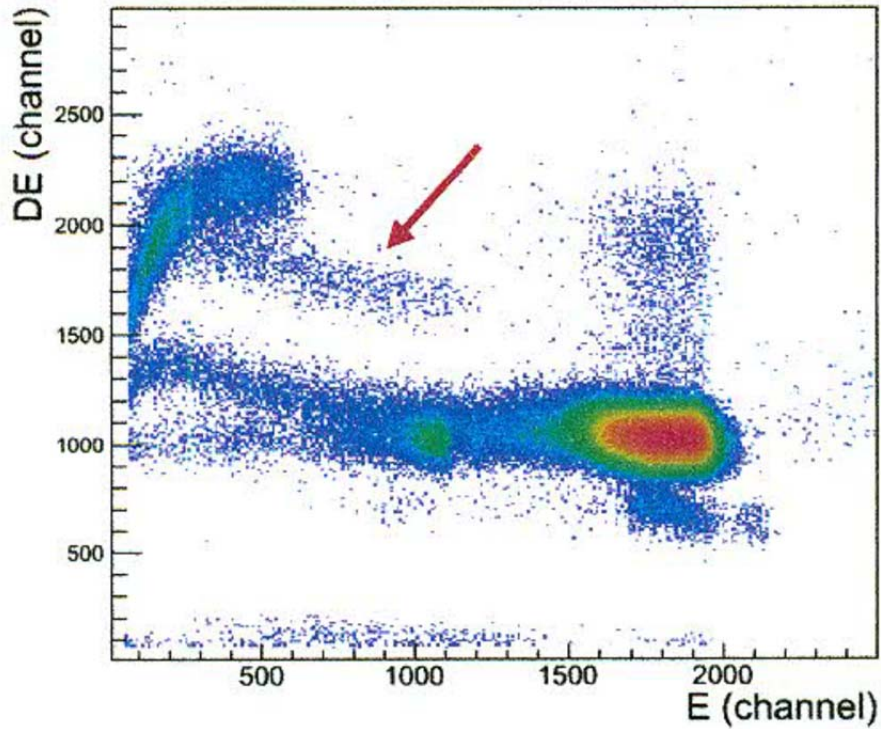


FIG. 2. ΔE -E 2D plot for Ne identification. The red arrow indicates the Ne locus.

To select the events due to the reaction channel $^{16}\text{O}(^{12}\text{C},\alpha^{20}\text{Ne})\alpha$, of our interest, a graphical cut was made around the Ne locus. For the selected data, the α energy (E_α) vs ^{20}Ne energy ($E_{20\text{Ne}}$) 2D plot was reconstructed and compared with the simulated kinematical locus (black dots), as shown in Fig. 3.

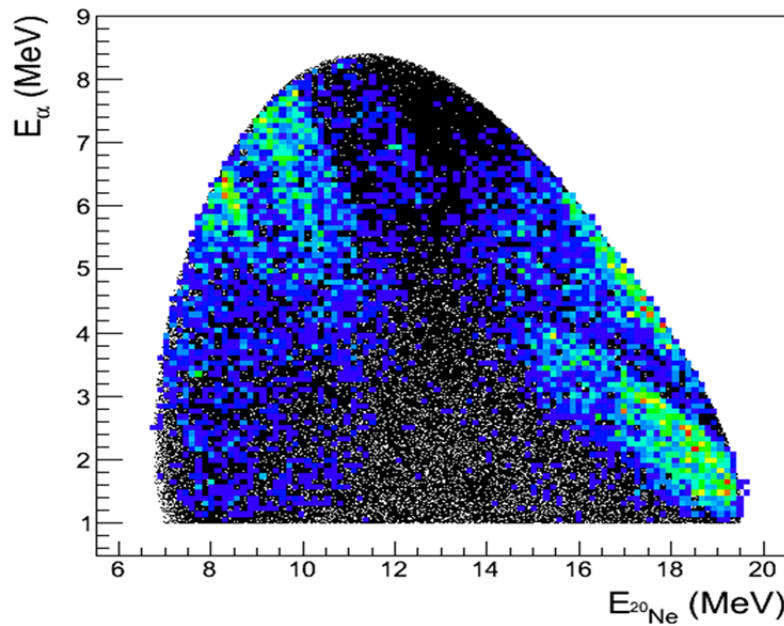


FIG. 3. Alpha particle energy (E_α) vs ^{20}Ne energy ($E_{20\text{Ne}}$). Experimental data are superimposed onto the simulated kinematical locus (black dots).

A good agreement shows up, making us confident on the calibration performed. Experimental data show the presence of additional loci due to two-body reactions as well as to the Mg contamination. An accurate procedure will be applied to disentangle the $^{16}\text{O}(^{12}\text{C},\alpha^{20}\text{Ne})\alpha$ events from background.

Then, next step of the analysis will be the selection of the quasi-free break-up mechanism and the study of the $^{20}\text{Ne}-\alpha$ relative energy spectrum.

- [1] C.E. Rolfs and W.S. Rodney *Cauldrons in the Cosmos* (University of Chicago Press) (1988).
- [2] F. Strieder J. Phys. Conf. Ser. **202**, 012025 (2010).
- [3] T. Spillane *et al.* Phys. Rev. Lett. **98**, 122501 (2007).
- [4] X.D. Tang *et al.* J. Phys. Conf. Ser. **337** 012016 (2012).
- [5] G.R. Caughlan and W.A. Fowler At. Data Nucl. Data Tables **40**, 283 (1988).
- [6] R.L. Cooper, A.W. Steiner and E.F. Brown Astroph. J. **702**, 660 (2009).
- [8] S. Cherubini *et al.*, Astrophys. J. **457**, 855 (1996).
- [9] C. Spitaleri, Proceedings of the 5th Winter School on Hadronic Physics, Folgaria, Italy, (1990).
- [10] C. Spitaleri *et al.*, Phys. Rev. C **60**, 055802 (1999).
- [11] C. Spitaleri *et al.*, Phys. Rev C **63**, 055801 (2001).
- [12] M. La Cognata *et al.*, Astrophys. J. **708**, 796 (2010).
- [13] E.B. Carter *et al.* Phys. Rev. **133**, B1421 (1964).
- [14] G.E. Mitchell *et al.* Phys. Rev. **133**, B1434 (1964).
- [15] H.Horiuchi and K. Ikeda Prog. Theor. Phys. **40**, 277 (1968).

Clustering in non-self-conjugate nuclei

V.Z. Goldberg, M. Avila,¹ S. Cherubini,² G.V. Rogachev,¹ M. Gulino,² E.D. Johnson,¹
A.N. Kuchera,¹ M. La Cognata,² L. Lamia,² S. Romano,² L.E. Miller,¹ R.G. Pizzone,² G.G. Rapisarda,²
M.L. Sergi,² C. Spitaleri,² R.E. Tribble, W.H. Trzaska,³ A. Tumino²

¹*Department of Physics, Florida State University, Tallahassee, Florida*

²*Istituto Nazionale di Fisica Nucleare- Laboratori Nazionali del Sud, Catania, Italy*

³*Physics Department, University of Jyväskylä, Jyväskylä, Finland*

1. Introduction

Clustering is a well established phenomenon in light $N=Z$ ($4N$) nuclei. The low excitation energy spectrum of ${}^8\text{Be}$ can be described as a two-center $\alpha - \alpha$ structure[1]. Strong α -cluster quasi-rotational bands (inversion doublets) are known in ${}^{16}\text{O}$ and ${}^{20}\text{Ne}$ [2, 3]. The members of these bands have large reduced α widths, comparable to the single particle limit, which is the maximum possible reduced width that a nuclear resonance can have if it has a pure α +core structure. The α -cluster structure of $4N$ ($N = Z$) nuclei has been studied extensively, however much less information is available on the α -cluster structure of non-self-conjugate $N \neq Z$ nuclei. Experimental study of clustering in $T=1$ spectrum of ${}^{10}\text{B}$ and is reported in this contribution.

2. $T=1$ states in ${}^{10}\text{B}$

The suggestion that the structure of certain states in ${}^{10}\text{Be}$ can be better described using two center model where "valence" nucleons are added to the system of two α -particles has been made in the early 1970s.[1] A semi-quantitative discussion of this subject can be found in [4] where the two-center molecular states in ${}^9\text{B}$, ${}^9\text{Be}$, ${}^{10}\text{Be}$, and ${}^{10}\text{B}$ nuclei were considered in the framework of a two-center shell model. An Antisymmetrized Molecular Dynamics plus Hartree-Fock (AMD+HF) approach was proposed in [5] as a theoretical tool to study the structure of low-lying levels in ${}^9, {}^{10}, {}^{11}\text{Be}$ isotopes. Deformation (distance between the two α for several low-lying states in Be isotopes has been studied. Very large deformation ($\beta=0.852$) for the 6.179 MeV 0^+ state in ${}^{10}\text{Be}$ was suggested which corresponds to an interalpha distance of 3.55 fm. This is 1.8 times more than the corresponding value for the ${}^{10}\text{Be}$ ground state. A similar result was obtained in [6] where the spectrum of ${}^{10}\text{Be}$ was reasonably well reproduced using a molecular orbit (MO) model. It was shown that the second 0^+ in ${}^{10}\text{Be}$ has an enlarged $\alpha - \alpha$ distance and that the highly deformed rotational band with large moment of inertia built on that configuration emerges. The two known states in ${}^{10}\text{Be}$, the 0^+ at 6.179 MeV and the 2^+ at 7.542 MeV are believed to be associated with this rotational band. The experimental evidence for the 4^+ member of this band is controversial. The state at excitation energy of 10.15 MeV was assigned spin-parity of 3^- in [7]. However, in [8, 9] the 4^+ spin-parity assignment was suggested for this state. It was argued in [9] that the 10.15 MeV state is the next member of the highly deformed $K^\pi=0^+$ rotational band built on the 0^+ state at 6.179 MeV and that the very large moment of inertia of this band indicates ($\alpha : 2n : \alpha$) configuration. If this

is the case then an analogous band with $(\alpha : np : \alpha)$ configuration should be found in the spectrum of T=1 states in ^{10}B . Properties of T=1 states in ^{10}B are studied in this contribution.

The experiment was performed at the INFN facility in Catania, Italy. T=1 resonances in ^{10}B were searched for in the excitation functions of $^1\text{H}(^9\text{Be}, \alpha)^6\text{Li}^*(\text{T}=1, 0^+, 3.56 \text{ MeV})$ reaction. While both T=0 and T=1 states can be populated in $^9\text{Be}+p$ scattering, only the T=1 states would predominantly decay to the T=1 state in ^6Li by α emission due to isospin conservation and the T=0 states would be strongly suppressed in the $^1\text{H}(^9\text{Be}, \alpha)^6\text{Li}^*(\text{T}=1, 0^+, 3.56 \text{ MeV})$ excitation function. Excitation functions of $^1\text{H}(^9\text{Be}, \alpha)^6\text{Li}^*(\text{T}=1, 0^+, 3.56 \text{ MeV})$ were measured by changing the beam energy from 22:3 up to 55:6 MeV with steps ranging between 0.12 and 5.75 MeV (0.012 MeV and 0.575 MeV in c.m.). Both reaction products, α and ^6Li , were detected. The $^1\text{H}(^9\text{Be}, \alpha)^6\text{Li}^*(\text{T}=1, 0^+, 3.56 \text{ MeV})$ events were selected using angle-energy correlation of ^6Li ions identified using $\Delta\text{E}-\text{E}$ 2-D spectra. The excitation functions for the $^1\text{H}(^9\text{Be}, \alpha)^6\text{Li}^*(\text{T}=1, 0^+, 3.56 \text{ MeV})$ reaction were measured in the c.m. energy range between 2.1 and 5.5 MeV (8.7 - 12.1 MeV excitation in ^{10}B). The excitation function at $55 \pm 2.5^\circ$ in c.m. is shown in Fig. 1. The narrow peak at $E_{\text{cm}} = 2.3 \text{ MeV}$ corresponds to the doublet of known T=1 states in ^{10}B , the 3^- and the 2^+ at $E_x = 8.9 \text{ MeV}$. Spin-parities and widths of these states are known, but the decay branching ratios are not. This data allows for direct measurement of the partial α -widths for these states.

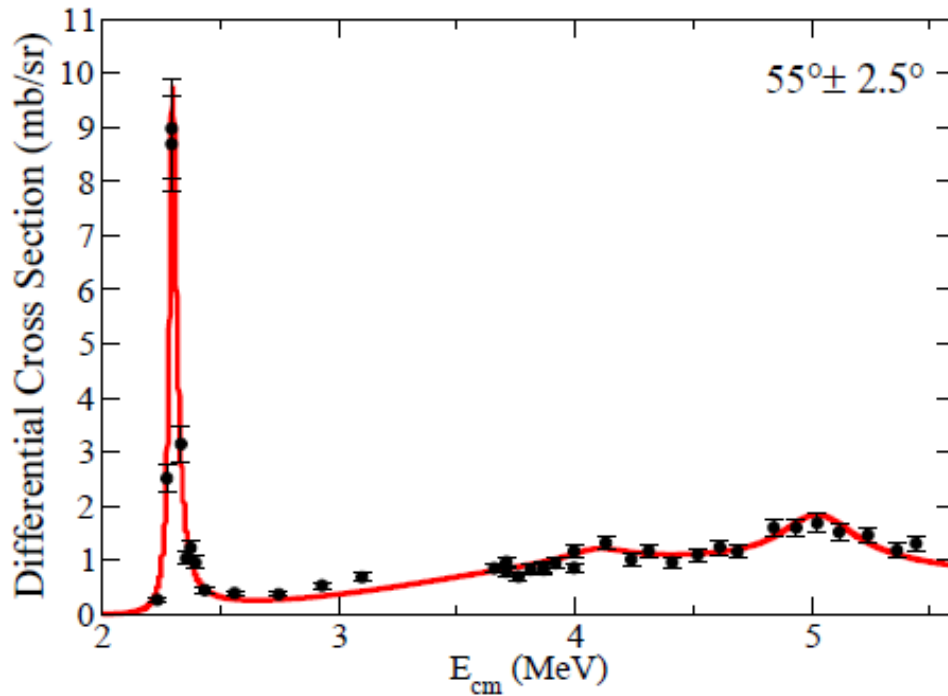


FIG. 1. $^1\text{H}(^9\text{Be}, \alpha)^6\text{Li}^*(\text{T}=1, 0^+, 3.56 \text{ MeV})$ excitation function at 55° in c.m. Solid (red) curve is the best R-Matrix fit.

A multi-channel, multi-level \mathbf{R} -matrix analysis of the excitation functions was performed. The reduced width amplitudes were constrained in the \mathbf{R} -matrix fit by requiring that corresponding proton and

neutron reduced width amplitudes are equal, as determined by the isospin Clebsch-Gordon coefficients for the T=1 states in ^{10}B . The parameters of the resonances are given in Table I. More details on this analysis can be found in [10].

Table I. Resonance parameters from the R -matrix fit.

J^π	E_{cm} (MeV)	E_x (MeV)	Γ_{tot} (keV)	Γ_α (keV)	Γ_p (keV)	Γ_n (keV)	θ_α^2
2^+	2.308(2)	8.894(2)	34(4)	$18 \pm 2.0 \pm 2.3$	7(4)	2(1)	1.1(2)
3^-	2.312(10)	8.898(10)	80(10)	0.57(5)	75(10)	4(3)	0.42(4)
2^+	4.1(1)	10.7(1)	300 ± 100	≈ 8	≈ 170	≈ 130	≈ 0.007
(0^+)	4.4(3)	11.0(3)	3700_{-600}^{+200}	2800_{-600}^{+200}	514(100)	414(100)	$0.97_{-0.20}^{+0.06}$
1^-	5.04(7)	11.63(7)	480(150)	13(6)	260(100)	210(120)	0.004(2)

As it was mentioned above, several theoretical approaches predict a developed α -2n- α structure for $0^+/2^+/4^+$ band with 0^+ bandhead at 6.179 MeV in ^{10}Be . The same should be true for the corresponding analog states in ^{10}B . The most direct experimental observable for the degree of clustering is the partial α width. The excitation energies of the 0^+ states in both ^{10}Be and ^{10}B are below the corresponding α decay thresholds. The partial α widths for the 2^+ states were unknown in both nuclei. The $18 \pm 2.0 \pm 2.3(\text{sys})$ keV partial α width for the 2^+ state at 8.89 MeV in ^{10}B determined in this experiment corresponds to the α single particle limit. In fact, this width can be well reproduced in the framework of a simple $^6\text{Li}(T=1)+\alpha$ potential model. The Woods-Saxon potential with depth of -119 MeV, radius and charge radius of 2.58 fm and 2.27 fm respectively, and diffuseness of 0.677 fm generates the 0^+ and the 2^+ α -cluster states in excellent agreement with the spectra of ^{10}B and ^{10}Be and predicts the 15 keV width for the purely α -cluster 2^+ state at 8.894 MeV in ^{10}B (0.870 MeV above the $^6\text{Li}(0^+, 3.56 \text{ MeV})+\alpha$ decay threshold).

The very large partial α width of the 2^+ state at 8.89 MeV measured in this work leaves no doubt about its α - $^6\text{Li}(T=1)$ molecular type nature. This confirms the assertion made in several theoretical and experimental works [5, 6, 9] that this state (or its analog at $E_x=7.542$ MeV in ^{10}Be) is a member of a highly clustered rotational band built on the 0^+ state at $E_x=7.56$ MeV in ^{10}B (6.179 MeV in ^{10}Be). The defining feature of this band is its high moment of inertia which is indicative of the large separation between the two α cores [5]. Assuming that the 10.15 MeV state observed in [9] is the 4^+ member of the analogous band in ^{10}Be it can be expected that the excitation energy of the corresponding 4^+ in ^{10}B is ~ 11.5 MeV. Indeed, if this state has a large dimensionless reduced α width as suggested in [9] for the presumably analogous 10.15 MeV state in ^{10}Be then there is a good chance to see it in the $^1\text{H}(^9\text{Be}, \alpha)^6\text{Li}(T=1)$ reaction. The 2^+ resonance at 8.89 MeV that is considered to be a member of the same rotational band as the aforementioned 4^+ is the dominant feature in the measured excitation function (Fig. 1). However, the 4^+ state has not been observed in this work. Besides a trivial reason for not seeing this state because it does not exist or is at higher excitation energy, we can offer another explanation. If this state corresponds to pure α - $^6\text{Li}(T=1)$ molecular configuration and the admixture of the $^9\text{Be}(\text{g.s.})+\text{p}$ configuration is too small then the cross section for the (p, α) reaction may be too small making this resonance "invisible" on top of the "background" of other T=1 states in ^{10}B . This may also explain the results of [11] where excited states of ^{10}B were populated in the $^{11}\text{B}(^3\text{He}, \alpha)^{10}\text{B}$ reaction and the 11.5 MeV

state was only observed in the ${}^6\text{Li} + \alpha$ decay channel, and not in the ${}^9\text{Be}(\text{g.s.}) + \text{p}$ channel. We estimate that the proton dimensionless reduced width for the 4^+ state has to be less than 2×10^{-4} to make it unobservable in our measurements. This is 0.6% of the proton dimensionless reduced width of the 2^+ that corresponds to the same rotational band. As shown in Fig. 2 the resonance structure at 11.6 MeV excitation in ${}^{10}\text{B}$ is evident, but it corresponds to the 1^- state with weak α -cluster component. It is possible that this state is the isobaric analog for the 10.57 MeV state with uncertain (≥ 1) spin-parity assignment in ${}^{10}\text{Be}$ [12]. The finding of a new broad $T=1$ 0^+ state at ~ 11 MeV was surprising. Its large partial α width is the direct evidence for the extreme α cluster structure of this state.

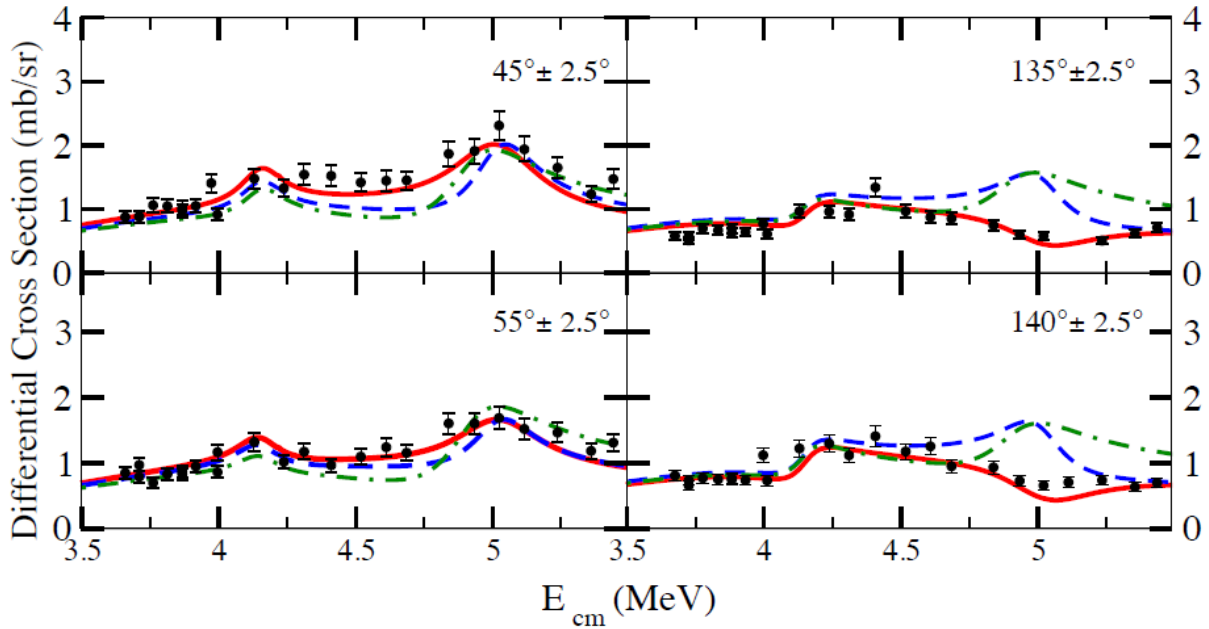


FIG. 2. Excitation functions of ${}^9\text{Be}(p, \alpha){}^6\text{Li}(T=1, 0^+, 3.56 \text{ MeV})$ and the R-matrix fits with three different spin-parity assignments for the state at 5 MeV (11.6 MeV excitation energy). The best fit has a 1^- spin-parity assignment, as shown by the solid (red) line, the fit with a 4^+ state is shown by the dashed (blue) line, and the fit with a 3^- state is shown by the dot-dash (green) line. All three fits agree with the data relatively well at lower angles, but only the fit with a 1^- state agrees well with higher angle data.

Acknowledgements

This work was supported in part by the National Science Foundation under Grant Nos. PHY-456463 and PHY-1064819 and by the US Department of Energy Grant Nos. DE-FG02-93ER40773 and DE-FG52-06NA26207.

- [1] J. Hiura and R. Tamagaki, Prog. Theor. Phys. Suppl. **52**, 25 (1972).
- [2] L.L. Ames *et al.*, Phys. Rev. C **25**, 729 (1982).
- [3] S.R. Riedhauser *et al.*, Phys. Rev. C **29**, 1991 (1984).
- [4] W. von Oertzen, Z. Phys. A **354**, 37 (1996).

- [5] A. Dote, H. Horiuchi, and Y. Kanada-Enyo, Phys. Rev. C **56**, 1844 (1997).
- [6] N. Itagaki and S. Okabe, Phys. Rev. C **61**, 044306 (2000).
- [7] N. Curtis *et al.*, Phys. Rev. C **64**, 044604 (2001).
- [8] M. Milin *et al.*, Nucl. Phys. **A753**, 263 (2005).
- [9] M. Freer *et al.*, Phys. Rev. Lett. **96**, 042501 (2006).
- [10] A.N. Kuchera *et al.*, Phys. Rev. C **84**, 054615 (2011).
- [11] M. Uroic *et al.*, AIP Conference Proceedings **1165**, 31 (2009).
- [12] D.R. Tilley *et al.*, Nucl. Phys. **A745**, 155 (2004).

Highly excited high spin states in ^{22}Ne

V.Z. Goldberg, S.Yu. Torilov,¹ M. Brenner,² K.A. Gridnev,¹ S.V. Khlebnikov,³ M. Mutterer,⁴ B.G. Novatski,⁵ Yu.G. Sobolev,⁶ W.H. Trzaska⁷, L.I. Vinogradov,¹ V.I. Zherebchevsky¹

¹*Department of Nuclear Physics, Saint-Petersburg State University, St. Petersburg 198504, Russia*

²*Department of Physics, Abo Akademi, FIN-20500, Turku, Finland*

³*V. G. Khlopin Radium Institute, St.-Petersburg, 194021 Russia*

⁴*Institut für Kernphysik, Technische Universität, 69289 Darmstadt, Germany*

⁵*Russian Scientific Centre “Kurchatov Institute”, 123182 Moscow, Russia*

⁶*Flerov Laboratory of Nuclear Reactions, JINR, Dubna 141980, Russia*

⁷*Department of Physics, P.O. Box 35 (YFL), FI-40014 University of Jyväskylä, Finland*

The main aim of this work is to study the high spin states of some highly excited levels in ^{22}Ne and to investigate their nature. The data on the presence of highly excited high-spin states in ^{22}Ne which decay by α -particles were obtained previously using the $^{18}\text{O}+^{12}\text{C}$ reaction (see [1] and references therein). However, in spite of a number of theoretical predictions for the properties of the ^{22}Ne quasimolecular bands [2], mainly experimental data are available only for the low lying levels which decay by γ -rays [3,4]. The scarce information on high-spin states in ^{22}Ne is in strong contrast with the data on ^{20}Ne , where many high-spin states were interpreted as members of ten rotational bands [5].

We used the $^{14}\text{C}(^{12}\text{C}, \alpha_1)^{22}\text{Ne}^* \rightarrow \alpha_2 + ^{18}\text{O}$ reaction to populate high spin states in ^{22}Ne . If α_1 detected at zero degrees, then the α_1 - α_2 angular correlations provide for a reliable way to make spin-parity assignment. The angular correlation function, $W(\theta)$, will be

$$W(\theta) \sim (2J + 1)/4\pi [P_J(\cos\theta)]^2$$

where θ is the angle of the second α -particle, J is the spin of the level in neon and P_J is the ordinary Legendre polynomials.

Experiment

The experiment was carried out using the K-130 Cyclotron of the University of Jyväskylä, Finland and a 44 MeV ^{12}C beam. The target was a self-supporting carbon foil with a thickness of 280 $\mu\text{g}/\text{cm}^2$ (80% of ^{14}C). A schematic of the experimental arrangement is shown in fig. 1. The primary α -particle was detected using two 10 mm^2 silicon detectors of 380 μm thickness placed at $\pm 3^\circ$ (below and above the horizontal plane) behind a 15 μm platinum foil used to absorb the elastically scattered ^{12}C ions. The α -particles were separated from other light products by pulse-shape discrimination techniques [6]. The α -particles from the decay of states in ^{22}Ne were detected in $dE - E$ detector telescopes. Each telescope consisted of a position-sensitive gas proportional counter used as the dE detector combined with 10 silicon PIN diodes as E detectors. The total active area of the $dE - E$ detectors is 18 cm^2 . The thickness of the fully depleted PIN diodes was 380 μm . The dE gas proportional counter has a single resistive wire and measures the energy loss of the particles and the X -coordinate of the points of

penetration. The counter was filled with Ar+10% CH₄ gas mixture (pressure 250 Torr). A continuous renewing of the gas in the counter volume was provided. The length of the detectors (100 mm) spanned 40° in the laboratory system. The angles at the center of each diode were measured with the precision of better than ±0.5°. The (α-α) double coincidence events were analyzed to generate the α₂ angular distributions for the decays to the ground state of ¹⁸O. The decay channel was selected using a two-dimensional plot Eα₂ versus Eα₁ at each α₂ angle as given by the position sensitivity of the α₂ detector.

Results

The measured angular correlation functions together with a fit by squared Legendre polynomials are shown in Fig. 1. Results of the analysis are summarized in Table I.

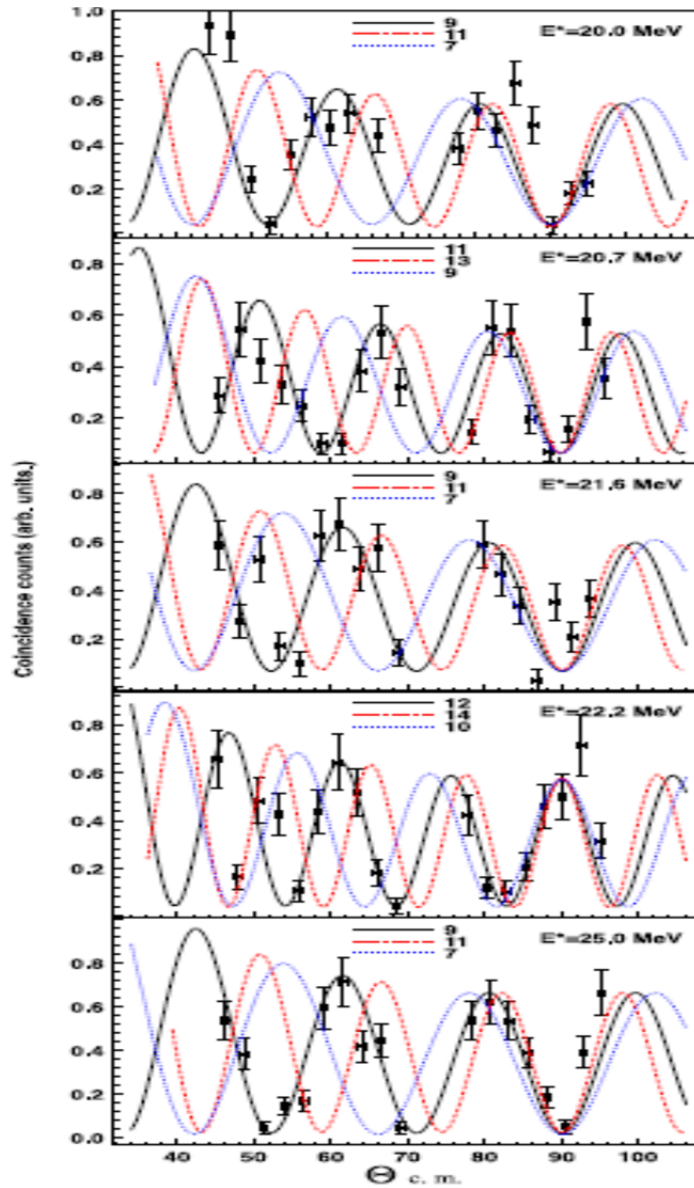


FIG. 1. Double angular correlations for the α decay of the 20.0MeV.

Table I. ^{22}Ne levels. Energy, spin and parity information from this and other work.

Present work	Adopted levels
17.0 MeV (unres. group)	17.05 MeV 7^- [23]
18.45 MeV $\Gamma \sim 330$ keV	18.42 MeV [22]
19.13 MeV (unres. group)	19.28 MeV 7^- [9]
20.0 MeV 9^- $\Gamma \sim 270$ keV	19.89 (10^+) [12]
20.7 MeV 11^- $\Gamma \sim 340$ keV	20.85 MeV 9^- [9]
21.6 MeV 9^- $\Gamma \sim 350$ keV	21.84 9^- [9]
22.2 MeV 12^+ $\Gamma \sim 250$ keV	(22.2) MeV [22]
22.9 MeV $\Gamma \sim 290$ keV	
24.0 MeV (unres. group)	24.14 MeV [24]
25.0 MeV 9^- $\Gamma \sim 350$ keV	
25.9 MeV (unres. group)	
27.0 MeV (unres. group)	26.89 MeV [24]

A very characteristic back bending observed for the high spin states with the positive parity in ^{22}Ne and the comparison with ^{20}Ne (Fig.2) evidences that new 12^+ level is the yrast level in ^{22}Ne .

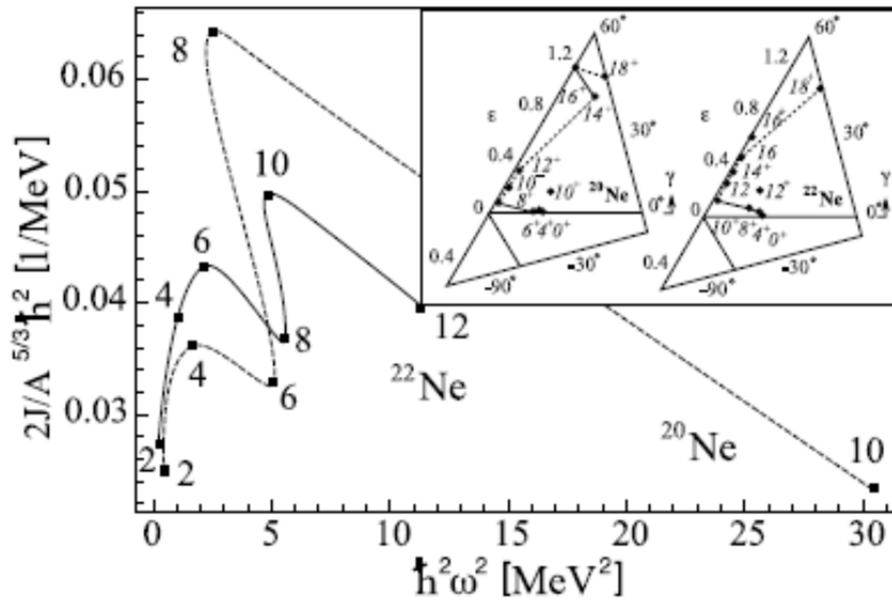


FIG. 2. Effective moment of inertia versus of the square of the rotational frequency for the ^{20}Ne and ^{22}Ne yrast lines. The inset compares the yrast-spin trajectories for these nuclei as was obtained in [10].

Summary

The spins of five highly excited states in ^{22}Ne were determined by measuring double α - α angular correlations $^{14}\text{C}(^{12}\text{C},\alpha_1)^{22}\text{Ne}^* \rightarrow \alpha_2+^{18}\text{O}$ reaction. The 22.2 MeV (12^+) state is assigned to the yrast line of ^{22}Ne in good agreement with theoretical prediction based on the Nilsson-Strutinsky formalism. The states at 20.7MeV (11^-) and 21.6MeV (9^-) were considered as members of the α -cluster rotational bands supporting the cluster model predictions.

- [1] S. Yildiz, M. Freer, N. Soic *et al.*, Phys. Rev. C **73**, 034601 (2006).
- [2] M. Kimura, Phys. Rev. C **75**, 034312 (2007).
- [3] K.L. Keyes *et al.*, J. Phys.G **31**, S1903 (2005).
- [4] K.L. Keyes *et al.*, Eur. Phys. J. A **25**, 431 (2005)
- [5] D.R. Tilley *et al.*, Nucl. Phys. **A636**, 249 (1998).
- [6] A.D. Panagiotou *et al.*, Phys. Rev. C **5**, 1995 (1972).
- [7] M. Mutterer, W. H. Trzaska, Yu. N. Kopatchet, et al., Nucl. Instrum. Methods Phys. Res. **A608**, 275 (2009).
- [8] R.M. Freeman *et al.*, Phys. Rev. C **46**, 589 (1992).
- [9] G.V. Rogachev, V.Z. Goldberg, T.Lonnroth *et al.*, Phys. Rev. C **64**, 051302 (2001).
- [10] Ragnarsson, S. Aberg, R.K. Sheline, Phys. Scr. **24**, 215

Resonance scattering to study exotic nuclei at the limits of stability

V.Z. Goldberg, B.T. Roeder, G.G. Chubarian, A.A. Alharbi, A. Banu, M. McCleskey, E. Simmons,
G. Tabacaru, L. Trache, R.E. Tribble, G.V. Rogachev,¹ E.D. Johnson,¹ C. Fu,²
M.L. Avila,¹ and J.P. Mitchell¹

¹Department of Physics, Florida State University, Tallahassee, Florida

²Indiana University, Bloomington, Indiana

1. Introduction

Examining nuclear matter under extreme conditions makes the most demanding test of our understanding of nuclear structure. A perfect opportunity is provided by the study of exotic nuclei which are far from the valley of stability. This is because the addition of a single nucleon can change the properties of a light nucleus, and because theoretical calculations, such as *ab-initio* calculations, can only be made for light nuclei at present. ¹⁴F and ⁹He, two exotic nuclei beyond the limits of stability, provide good systems to test the parameters of the nucleon-nucleon (NN) interactions used in these theoretical calculations. In the present work we consider application of the resonance scattering induced by rare isotope beams to obtain experimental data on both borders of nuclear stability.

2. ¹⁴F

Fig. 1 illustrates the typical experimental setup for the Thick Target Inverse Kinematics (TTIK) method [1]. In this method, a beam of heavy ions is stopped in the target material and the light recoil

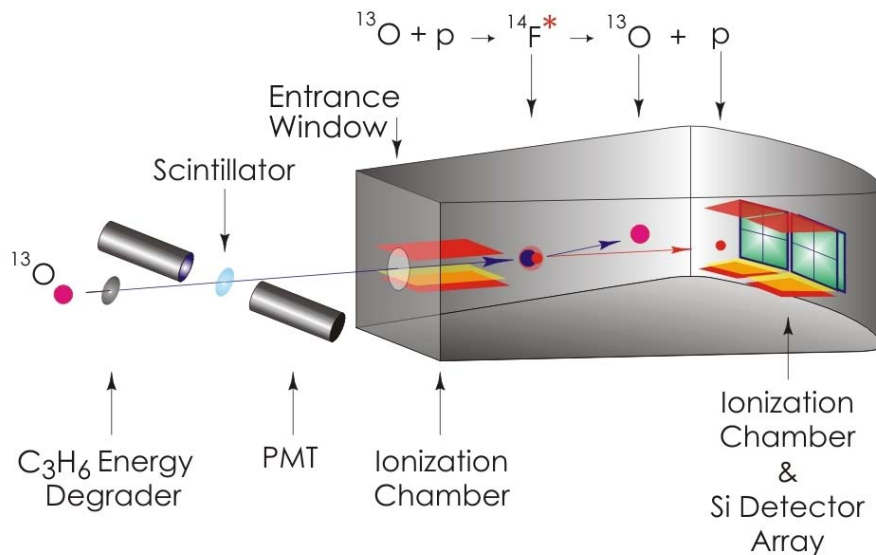


FIG. 1. The setup for the ¹⁴F experiment. The "gray box" is the scattering chamber. See explanation in the text and Ref. [5].

product of the elastic scattering reactions (protons in our case) comes out of the target due to much smaller specific energy loss and is detected.

At the Texas A&M University Cyclotron Institute, a 31 MeV/u ^{13}O beam was produced after MARS separation [2] for the ^{14}F experiment. The beam was then slowed down, close to the entrance to the scattering chamber, to minimize the loss of intensity. Stacks of 100 μm polypropylene (C_3H_6) foils (total thickness 1.5 mm) were used to degrade the energy of the beam of ^{13}O from 31 MeV/u to ≈ 11 MeV/u. A scintillating foil was placed before the entrance to the scattering chamber. The light signal from the particles passing through the foil was detected by a pair of photomultiplier tubes (PMTs). The signals from the PMTs were used to monitor the beam, to obtain a “start” signal for time-of-flight (TOF) measurements, and to identify the main beam contaminant, ^{10}C . Our experimental setup was similar to that used in [3,4]. The scattering chamber was filled with methane gas (CH_4) which was used as a safe substitute for hydrogen. The CH_4 was separated from the high vacuum of MARS by a 3 μm Havar foil. However, a few modifications made the target system more “active” than before. A windowless ionization chamber (ICE) was placed in the scattering chamber close to the entrance window (see Fig. 1) to measure the specific energy loss of incoming ions and discriminate protons related with the interaction of the beam with the degrader, which resulted in the destruction of ^{13}O . A pair of quadrant-silicon detector telescopes (QSDs) (the same as in [4]) was also mounted inside smaller windowless ionization chambers 515 mm from the entrance window. Each QSD consisted of four square detectors ($12.5 \times 12.5 \times 1 \text{ mm}^3$) and was followed by a similar veto detector to eliminate high-energy particles that passed through the first QSD. The role of the small ionization chambers was to allow $\Delta E-E$ analysis for the light ions that are not stopped in the gas and can reach the Si detectors. Further details about the experiment setup and data analysis are given in Ref. [5].

Fig. 2 presents the excitation functions for $^{13}\text{O} + p$ elastic scattering. A code of the complete R-matrix analysis was used [6]. The results of the analysis are summarized in Table I. As seen in Table I, ^{14}F is unstable by 1.56 MeV relative to proton decay, which corresponds to an atomic mass excess of $31\,960 \pm 50 \text{ keV}$ for ^{14}F using the mass tables in [7]. According to the recent *ab-initio* calculations [8], it is expected be unstable by $\sim 3 \text{ MeV}$. While new calculations are needed to specify the necessary corrections

Table I. Levels in ^{14}F .

$E_R \text{ (MeV)}^a$	$E_{\text{ex}} \text{ (MeV)}^b$	J^π	Γ	$\Gamma/\Gamma_{\text{sp}}$
1.56 \pm 0.04	0.00	2-	910 \pm 100	0.85
2.1 \pm 0.17	0.54	1-	\sim 1000	0.6
3.05 \pm 0.06	1.49	3-	210 \pm 40	0.55
4.35 \pm 0.10	2.79	4-	550 \pm 100	0.5

^a Energy above $^{13}\text{O}+p$ threshold.

^b Excitation Energy in ^{14}F .

to the theoretical approaches, part of the disagreement between the predictions and the present result should be related with the Thomas–Ehrman shift of levels in mirror nuclei. This shift down toward greater stability in proton rich nuclei is the largest (and therefore famous) for *s*-states. The shift is strongly

dependent upon the single particle structure of the state. As reported in Table I, the ground state in ^{14}F has nearly pure shell model structure, and thus the effect of the Thomas–Ehrman shift on the ^{14}F binding energy should be larger than normal.

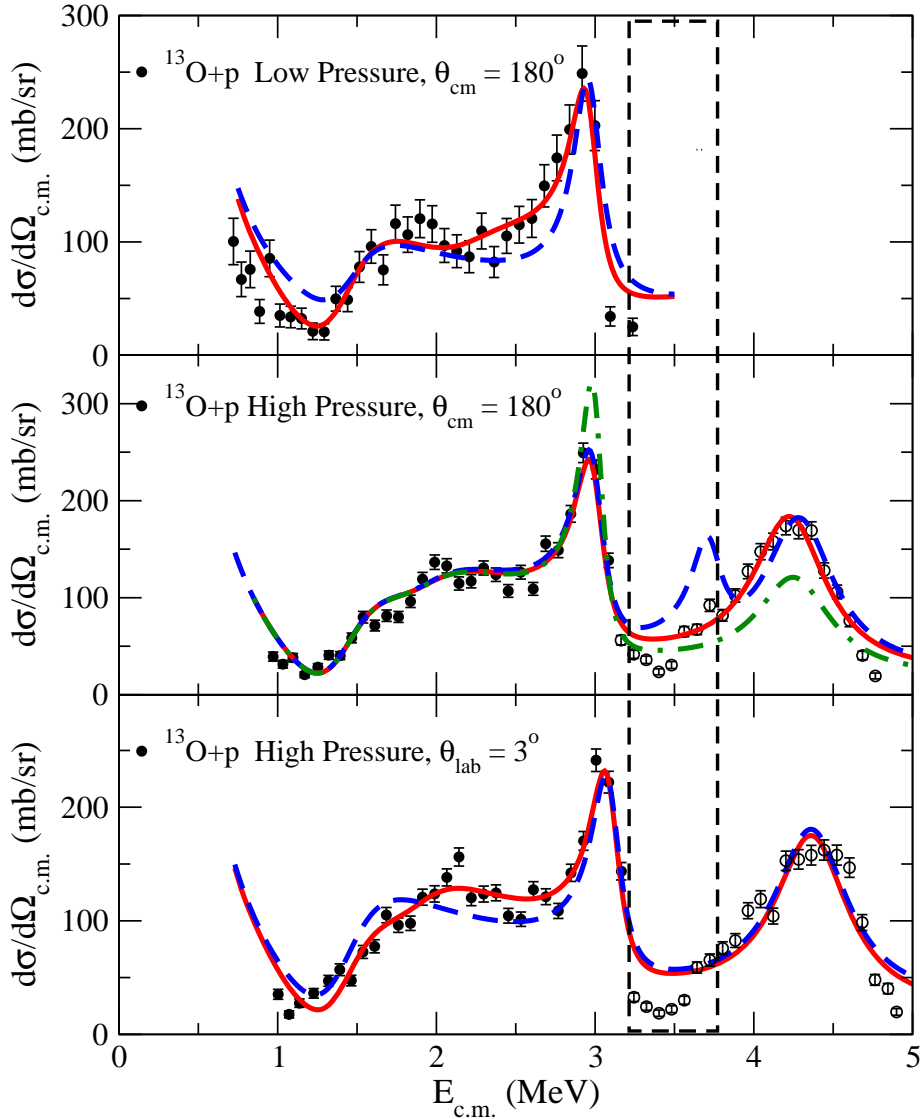


FIG. 2. Excitation functions for $^{13}\text{O}+p$ elastic scattering are given in comparison with R-Matrix calculations. The solid line (red) is the best fit calculation following the ^{14}F level scheme as given in Table 1. The dashed box shows the region where the data are distorted because the QSD detector was not fully depleted. Top Panel. The dashed line (blue) is a fit with 1^- as the ground state (instead of 2^-). Middle Panel. The dashed line (blue) is a calculation with a second hypothetical 2^- state at high energy. The dashed-dot line (green) is a calculation with a 4^- state at 3 MeV (instead of 3^-) and a 3^- state at 4.35 MeV (instead of 4^-). Bottom Panel. The dashed line (blue) is the fit without the 1^- first excited state. See text for further discussion.

It is easy to note looking at Fig. 3 that the shell model calculations produce a much more compressed level scheme than the *ab-initio* calculations. The latter are in better agreement with the

experimental data. We suppose that this indicates that the residual interactions should be modified in the shell model for a better description of these exotic nuclei.

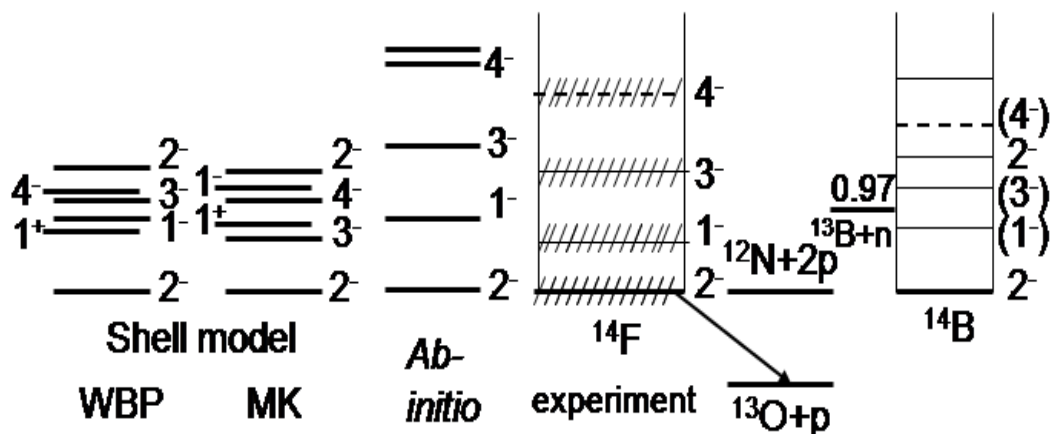


FIG. 3. ^{14}F level scheme from this work compared with shell-model calculations, ab-initio calculations [8] and the ^{14}B level scheme. See Ref. [5] for further explanation about these calculations.

3. A mystery in the structure of ^9He

The structure of ^9He , with its two protons and seven neutrons, could be expected to be simple: two protons fill the s -shell, while six neutrons fill the $p_{3/2}$ sub shell and the extra neutron should be in the $p_{1/2}$ shell. Since the time of its first observation in the $^9\text{Be}(\pi^+, \pi^-)$ reaction [9], a $(1/2^-)$ state, unstable by 1.1 MeV to neutron emission, was considered to be the ground state of ^9He . The authors compared the excitation energies of the observed levels with theoretical predictions of Ref. [10] and noted that these predictions, based on calculations for nuclei on the line of stability, “appear to be remarkably good for ^9He ”[9]. Then several high resolution measurements with heavy ion mass transfer reactions [11, 12] brought more exact data. A state of ^9He at 1.27 ± 0.10 MeV above the $^8\text{He} + n$ threshold with $\Gamma = 0.10 \pm 0.06$ MeV was found. It is remarkable that the width appeared to be more than ten times smaller than what could be expected from “naïve” shell model considerations. The narrow width of the $1/2^-$ state is direct evidence for its complicated, non shell-model structure, and could be a sign of unusual nuclear structure beyond the neutron dripline.

Then, a surprising result was obtained from neutron-fragment velocity difference measurements in the two-proton knockout reaction $^9\text{Be}(^{11}\text{Be}, ^8\text{He} + n)\text{X}$ [13]. The MSU group [13] found that the ground-state of ^9He was a virtual s -wave state within 0.2 MeV of the $^8\text{He} + n$ threshold. Evidently, this result is also in contradiction to the conventional shell structure, and can again be considered as a manifestation of unusual structure near the dripline. Additionally, this result is confusing when one considers the ground state in ^{10}He [14]. New predictions for the ground state of ^{10}He on the basis of new results for ^9He gave a much more tightly bound ^{10}He . Finally, the recent availability of a more intense, rare beam of ^8He made the long waited $^2\text{H}(^8\text{He}, \text{p})^9\text{He}$ experiment feasible [15]. The energy resolution and the counting statistics were poor in [15] due to evident experimental difficulties. Still, the authors claimed that their data exclude existence of the narrow $1/2^-$ resonances which have been previously observed [11,

12]. Simultaneously, Ref. [15] supported finding an s -state near the threshold for the ${}^9\text{He}$ decay into ${}^8\text{He}+n$ on the basis of the interference pattern between broad $l=0$ and $l=1$ structures, but it was noted that “the energy resolution and the quality of measured angular distributions are not sufficient to draw solid conclusions about the exact properties of the s -wave contributions”.

Probably the very confusing situation around ${}^{9,10}\text{He}$ should also be combined with the similar situation for the heavy hydrogen isotope, ${}^7\text{H}$. The possibility of observing ${}^7\text{H}$ as a sharp resonance was first stimulated by the unusual stability of ${}^8\text{He}$ [16]. The discovery of ${}^7\text{H}$ as a resonance in the ${}^{12}\text{C}({}^8\text{He}, {}^{13}\text{N}){}^7\text{H}$ reaction was claimed in Ref [17]. However, several more recent attempts to observe ${}^7\text{H}$ in the ${}^2\text{H}({}^8\text{He}, {}^3\text{He}){}^7\text{H}$ reaction with an expected higher yield were not successful [18].

Thus, there remain many problems to be resolved in the structure of ${}^9\text{He}$, and all evident nuclear reactions involving direct measurement of ${}^9\text{He}$ have been tried. However, resonance reactions again can be useful, but this time the study should be related with population of the ${}^9\text{He}$ analog states in ${}^9\text{Li}$.

In the ${}^8\text{He}+p$ resonance elastic scattering, excitations of ${}^9\text{Li}$ levels (see Fig.4) with $T=3/2$ or $T=5/2$ are allowed in accordance with isobaric spin conservation. Strong resonance population of (unknown) $T=3/2$ resonances at high excitation energy in ${}^9\text{Li}$ is not expected due to the small ratio of the proton width of the initial channel to the total width of the hypothetical $T=3/2$ resonances. However, only two decay channels are allowed by T conservation for the lowest states with $T=5/2$. These are the initial channel ${}^8\text{He}+p$, and its isobaric conjugate, ${}^8\text{Li}(T=2)+n$ (Fig.4). The analog of the “sharp” $1/2^-$ state in ${}^9\text{He}$ with $T=5/2$ [11,12] should be present at an excitation energy of 16.1 MeV in ${}^9\text{Li}$ [19]. As can be seen in Fig. 4, more than 2 MeV of energy interval below the $1/2^-$ ($T=5/2$) state in ${}^9\text{Li}$ are open for the investigation

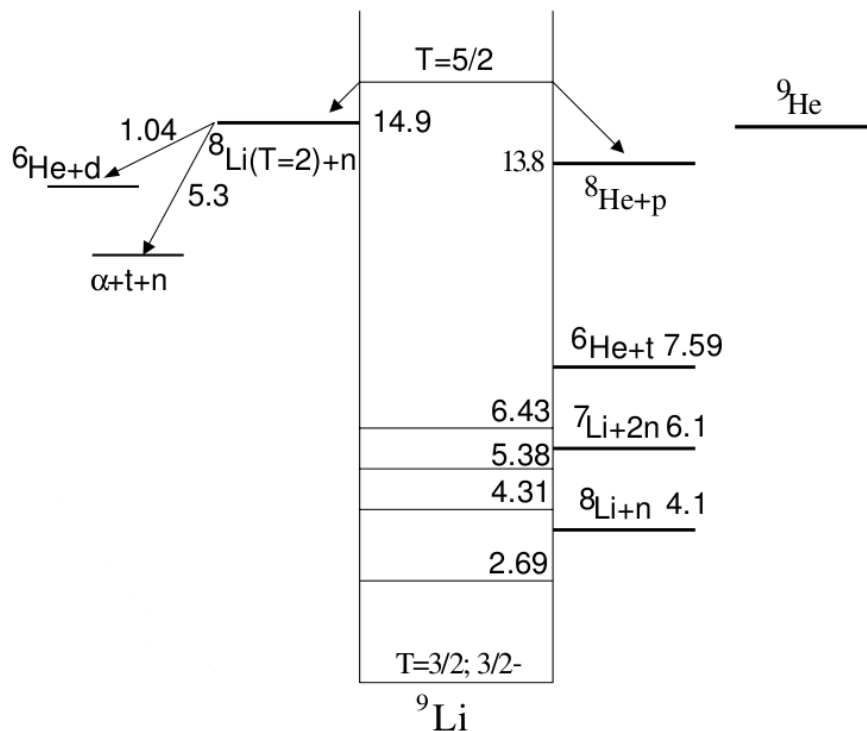
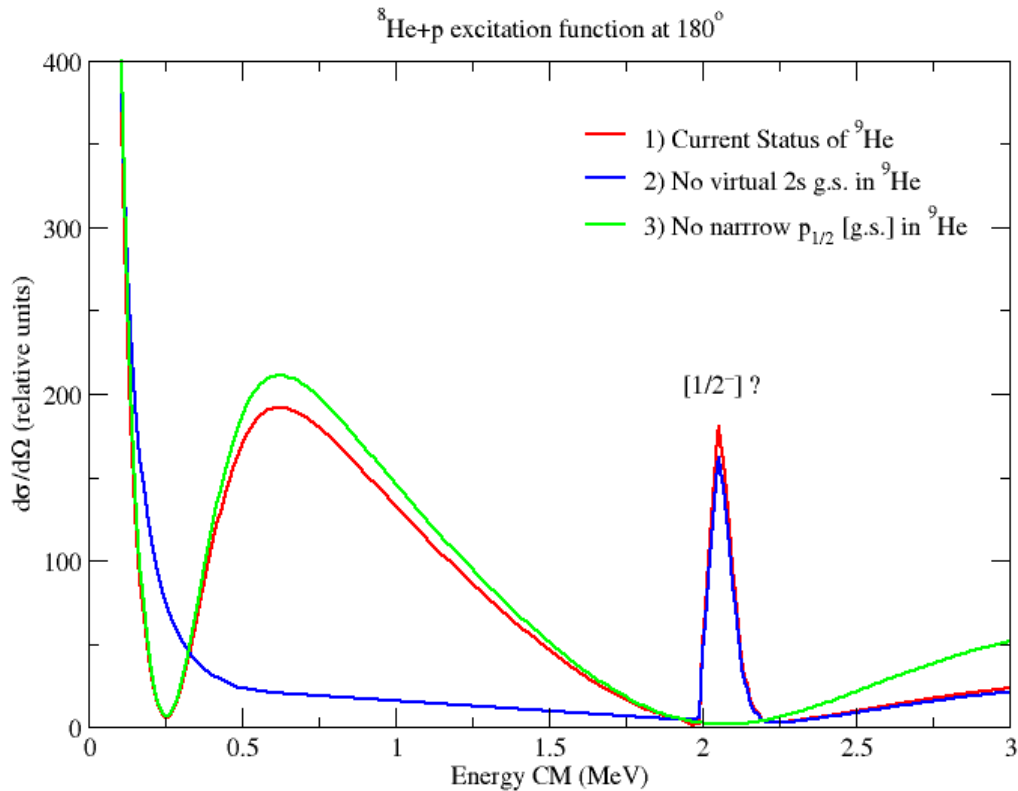


FIG. 4. Level scheme of ${}^9\text{Li}$ showing various possible decay channels for excited states.

in ${}^8\text{He}+p$ resonance scattering as a result of the Coulomb interaction and the p - n mass difference. Also the Coulomb interaction turns the virtual $\frac{1}{2}^+$ ground state in ${}^9\text{He}$ [13] into a quasi-stationary state in ${}^9\text{Li}$.

The first (and only) study of the ${}^8\text{He}+p$ resonance scattering found evidence for rather broad p and d states with $T=5/2$ at excitation energies above 17 MeV in ${}^9\text{Li}$ [19]. These findings appeared to be in agreement with the recent investigation of ${}^9\text{He}$ spectrum [7]. However, the most interesting region corresponding to the controversial lowest states in ${}^9\text{He}$ could not be investigated in [19]. The on-line beam of ${}^8\text{He}$ [19] separated at FLNR was of high energy and had a large energy spread. The poor parameters of the beam resulted in poor resolution (~ 400 - 500 keV) in the region of the possible $\frac{1}{2}^-$ sharp state. At present, there are reaccelerated low energy ${}^8\text{He}$ beams at SPIRAL (France) and TRIUMF (Canada), and it is possible to make TTIK measurements at the ${}^8\text{He}$ initial energy of ~ 4 MeV/A and energy spread of $<0.5\%$. Under these conditions, the energy resolution in the excitation region of ~ 16 MeV in ${}^9\text{Li}$ will be better than 50 keV, and one should easily observe a resonance peak with 100 keV width. It is well known that the elastic scattering cross sections are highly sensitive to the scattering phase. Therefore the parameters of the s -wave scattering near the threshold can be fixed. Fig. 5 illustrates the effect of the $2s$ virtual state in ${}^9\text{He}$ on the low energy ${}^8\text{He}+p$ resonance scattering at 180° . The strong effect of this state is obvious as a result of interference between the nuclear and the Coulomb scattering. We plan to make this measurement in the near future with a setup very similar to that used for the ${}^{14}\text{F}$ study.



4. **FIG. 5.** The effect of a possible $2s$ resonance (analog of the virtual ground state in ${}^9\text{He}$) on the excitation function of the ${}^8\text{He}+p$ elastic scattering. Also shown is the expectation for a narrow width $p_{1/2}$ first excited state.

Conclusion

In summary, we hope that we have demonstrated using the two examples above the importance of resonance reactions for exciting studies at both borders of nuclear stability.

- [1] K.P. Artemov *et al.*, Sov. J. Nucl. Phys. **52**, 406 (1990).
- [2] R.E. Tribble, R.H. Burch, and C.A. Gagliardi, Nucl. Instrum. Methods Phys. Res. **A285**, 441(1989).
- [3] V.Z. Goldberg, G.G. Chubarian, G. Tabacaru, L. Trache, R.E. Tribble, A. Aprahamian, G.V. Rogachev, B.B. Skorodumov, and X.D. Tang, Phys. Rev. C **69**, 031302(R) (2004).
- [4] C. Fu *et al.*, Phys. Rev. C **77**, 064314 (2008).
- [5] V.Z. Goldberg *et al.*, Phys. Lett. B **692**, 307 (2010).
- [6] G.V. Rogachev, Ph. D. Thesis, Kurchatov Institute, Moscow, 1999
- [7] G. Audi, A.H. Wapstra, and C. Thibault, Nucl. Phys. **A729**, 337 (2003).
- [8] P. Maris, A.M. Shirokov, and J.P. Vary, Phys. Rev. C **81**, 021301(R) (2010).
- [9] K.K. Seth, M. Artuso, D. Barlow, S. Iversen, M. Kaletka, H. Nann, B. Parker and R. Soundranayagam, Phys. Rev. Lett. **58**, 1930 (1987).
- [10] N.A.F.M. Poppelier, L.D. Wood and P.W.M. Glaudemans, Phys. Lett. B **157**, 120 (1985).
- [11] H.G. Bohlen, A. Blazevic, B. Gebauer, W. von Oertzen, S. Thummerer, R. Kalpakchieva, S.M. Grimes and T.N. Massey, Prog. Part. Nucl. Phys. **42**, 17 (1999).
- [12] W. von Oertzen *et al.*, Nucl. Phys. **A588**, 129c (1995).
- [13] L. Chen, B. Blank, B.A. Brown, M. Chartier, A. Galonsky, P.G. Hansen and M. Thoennessen, Phys. Lett. B **505** 21 (2001).
- [14] A.A. Korshennikov *et al.*, Phys. Lett. B **326**, 31 (1994).
- [15] M.S. Golovkov *et al.*, Phys. Rev. C **76**, 021605 (2007).
- [16] A.I. Baž , V.I. Goldansky, V.Z. Goldberg, and Y.B. Zeldovich, 1972 *Light and Intermediate Nuclei Near the Borders of Nucleon Stability* (Moscow: Nauka, 1972) [in Russian].
- [17] M. Caamano *et al.*, Phys. Rev. Lett. **99**, 062502 (2007).
- [18] E.Y. Nikolskii *et al.*, Phys. Rev. C **81**, 064606 (2010).
- [19] G.V. Rogachev *et al.*, Phys. Rev. C **67**, 041603(R) (2003).

**Resonances in elastic alpha-particle scattering as evidence of clustering at
high excitation in ^{34}S and ^{40}Ca**

V.Z. Goldberg, M. Norrby,¹ T. Lönnroth,¹ G.V. Rogachev,² M.S. Golovkov,³ K.-M. Källman,¹
S.V. Perov,³ M. Lattuada,^{4,5} S. Romano,⁵ B.B. Skorodumov,² G.P. Tiourin,⁶
W.H. Trzaska,⁶ and A. Tumino⁵

¹ *Department of Physics, Åbo Akademi, FIN-20500 Turku, Finland*

² *Department of Physics, Florida State University, Tallahassee, Florida*

³ *Joint Institute for Nuclear Research, Dubna, Russia*

⁴ *Istituto Nazionale di Fisica Nucleare - Laboratori Nazionali del Sud, Catania, Italy*

⁵ *Dipartimento di Fisica ed Astronomia, Università di Catania, Catania, Italy*

⁶ *Department of Physics, University of Jyväskylä, Jyväskylä, Finland*

The main goals of the present $^{30}\text{Si} + \alpha$ and $^{36}\text{Ar} + \alpha$ experiments were to find excitation functions for several angles in a large energy interval in highly excited ^{34}S and ^{40}Ca , to make approximate parameter assignments for the observed resonances and to compare the results to nearby nuclei. Data were collected using the time-saving Thick Target Inverse Kinematics (TTIK) technique [1,2]. The data were analyzed using a simplified R -matrix formalism [3–5], in the same manner as in [6] and similar to that of [7].

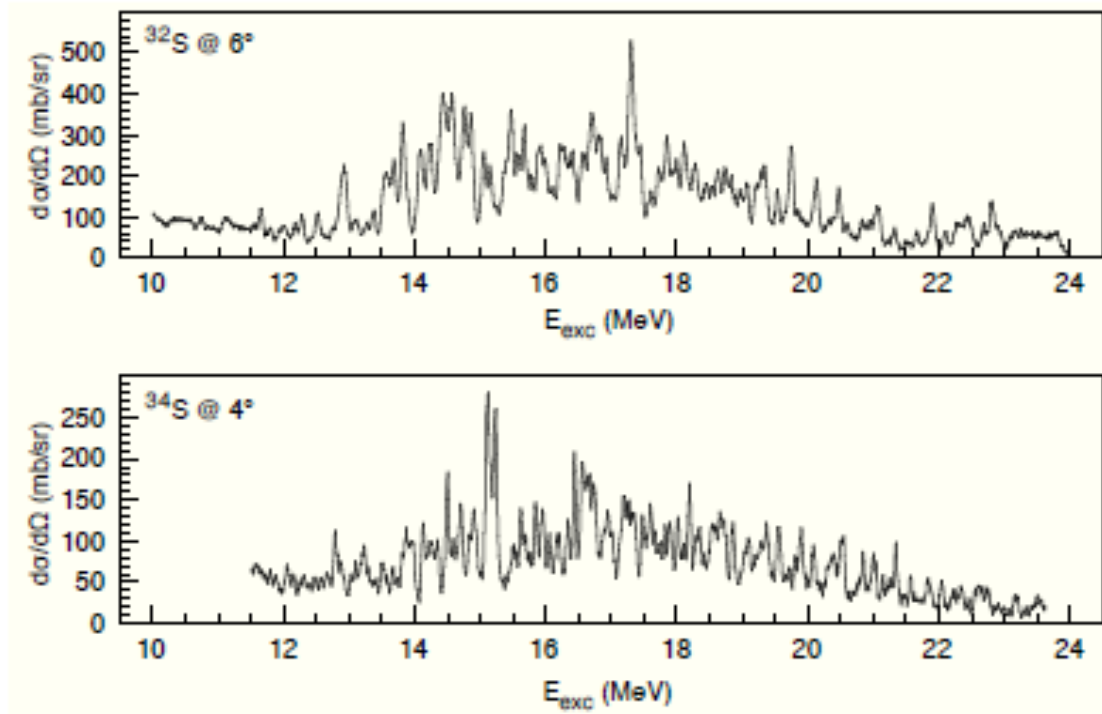


FIG. 1. The excitation function of ^{32}S from [6] (top), compared to the present data for ^{34}S (bottom).

The data collected for $^{30}\text{Si} + \alpha \rightarrow ^{34}\text{S}$ are shown in Fig.1 in comparison with the previous data for $^{28}\text{Si} + \alpha \rightarrow ^{32}\text{S}$ [6] and the data collected for $^{36}\text{Ar} + \alpha \rightarrow ^{40}\text{Ca}$ are shown in Fig. 2 at several angles. The elastic cross-sections are similar for ^{32}S and ^{40}Ca , but much lower in ^{34}S . This might in part be explained by the difference in threshold energies for α -decay, neutron decay and proton decay. Especially, the neutron partial widths should be larger in ^{34}S providing for a decrease in the probability to observe the α -decay. The density of resonances is clearly larger and their average width clearly smaller in ^{40}Ca compared to the sulphur isotopes, perhaps connected to its tightly bound doubly magic structure.

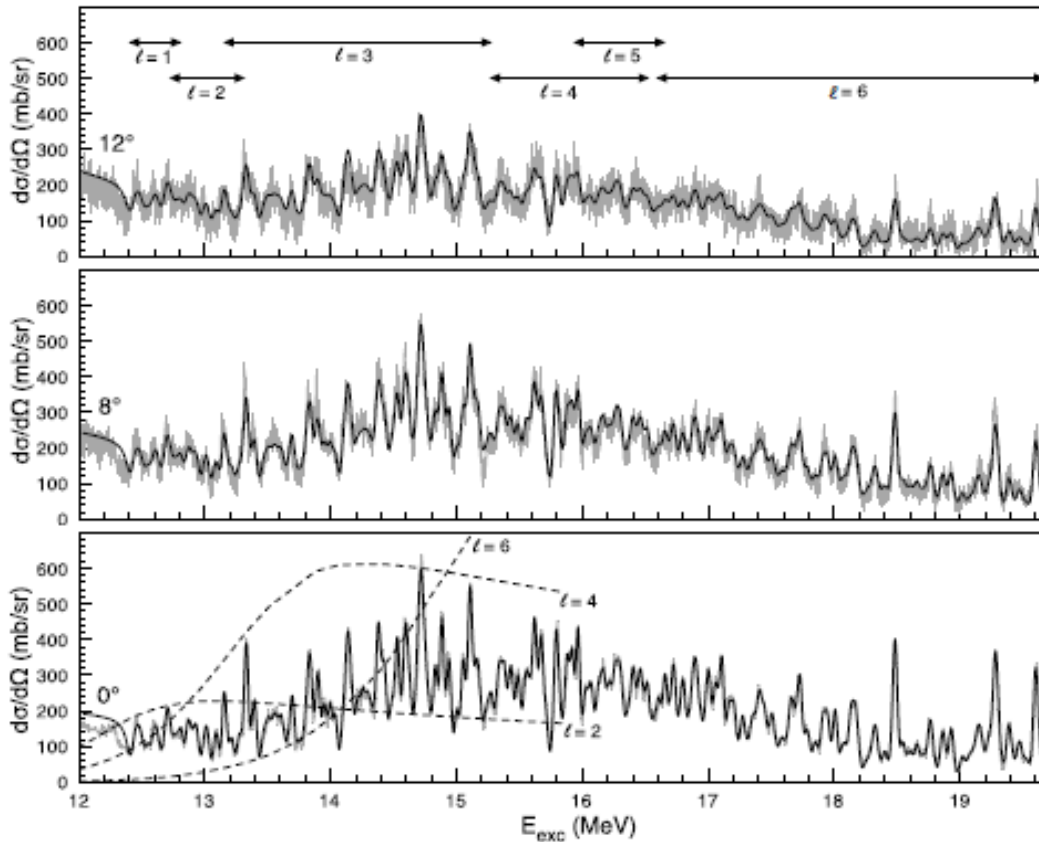


FIG. 2. Excitation functions including uncertainties for the $^{36}\text{Ar} + \alpha$ scattering measured by detectors at 0° , 8° , and 12° respectively. The black lines show the fits to the data. The regions where different spin groups are found are indicated with arrows in the top panel. In the bottom panel the dashed lines indicate the maximum theoretical cross-section for strong resonances of selected spins, detected with a resolution of 30 keV.

Fig. 3 shows resonances found in ^{32}S (from [6]), ^{34}S , ^{36}Ar [7] and ^{40}Ca plotted according to their respective excitation energy and spin. An average for each spin value has been obtained by weighting each level by its reduced width, illustrated by the diamonds in the figure. In all four cases a clear linear behavior is seen, indicative of quantum mechanical rotation. The moments of inertia can be extracted and for all four nuclei they lie between the values of a rotating “molecular” core + α -particle and a single α -particle orbiting an inert core.

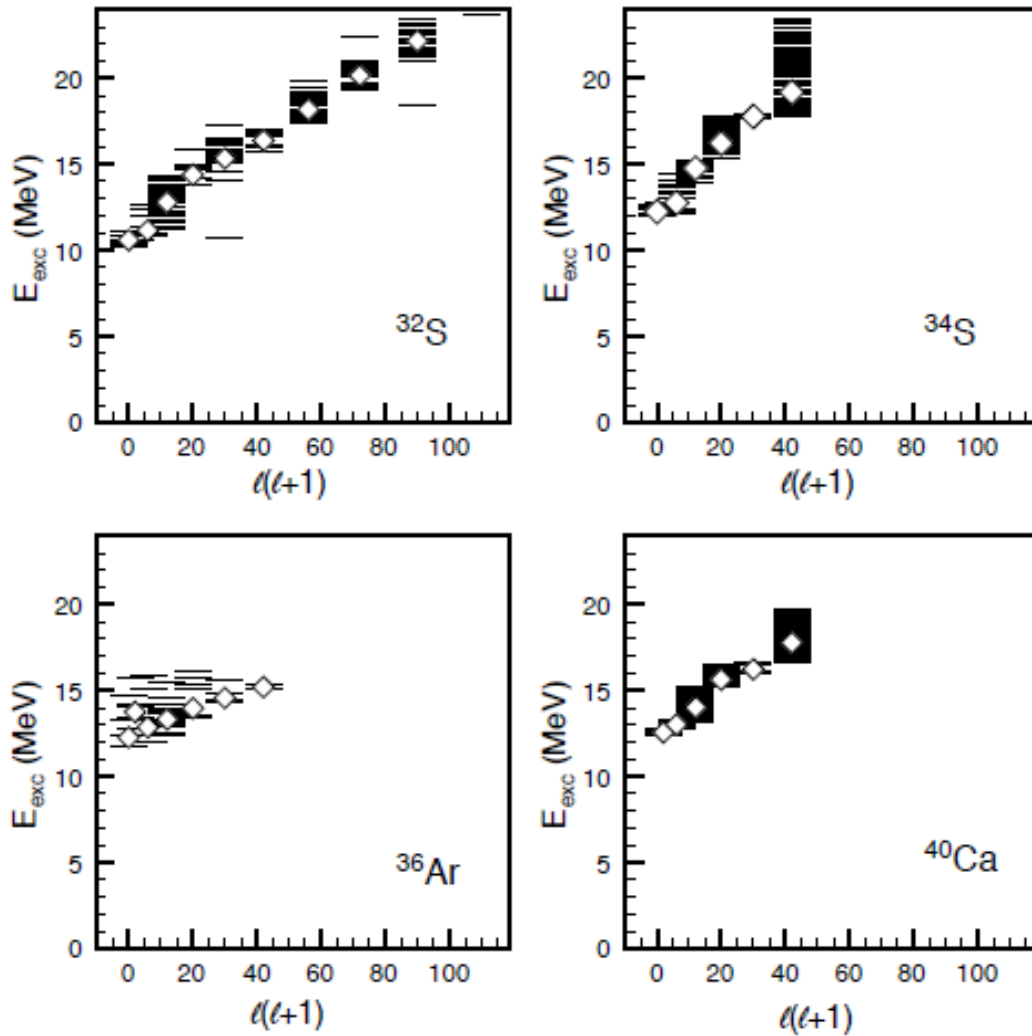


FIG. 3. The $l(l + 1)$ versus E_{exc} plot of resonances in ^{32}S (from [21]), ^{34}S , ^{36}Ar [23] and ^{40}Ca . The diamonds represent the weighted average energy for the levels of the same spin.

This work shows the importance of the α clusterization for the medium light nuclei even at high excitation energy.

- [1] K.P. Artemov *et al.*, Sov. J. Nucl. Phys. **52**, 406 (1990).
- [2] V.Z. Goldberg, A. Pakhomov, Phys. At. Nucl. **56**, 1167(1993).
- [3] A.M. Lane, R.G. Thomas, Rev. Mod. Phys. **30**, 257 (1958).
- [4] S.R. Riedhauser, Phys. Rev. C **29**, 1961 (1984).
- [5] G. Rogachev, *Simplified R-matrix code for spinless particles* (1999) unpublished.
- [6] T. Lönnroth *et al.*, Eur. Phys. J. A **46**, 5 (2010).
- [7] V.Z. Goldberg *et al.*, Phys. At. Nucl. **63**, 1518 (2000).

Spin physics with STAR at RHIC

Z. Chang, P. Djawotho, J.L. Drachenberg, C.A. Gagliardi, L. Huo, M.M. Mondal,
R.E. Tribble, and the STAR Collaboration

Our group continues to play major roles in STAR investigations of both longitudinal and transverse spin phenomena in polarized pp collisions at RHIC. During the past year, our analysis efforts have focused on the 200 GeV longitudinal spin data that were recorded by STAR during 2009 and 200 GeV transverse spin data that were recorded during 2008.

One of the primary goals of the RHIC spin program is to determine the gluon contribution to the proton spin. At RHIC energies, jet production at mid-rapidity is dominated by gg and qg scattering. This makes the double longitudinal-spin asymmetry A_{LL} for inclusive jet production a sensitive probe of gluon polarization. For several years, our group has carried a leading role in the STAR inclusive jet A_{LL} analyses. Just as this year began, STAR released preliminary measurements of A_{LL} for inclusive jets in 200 GeV pp collisions recorded during 2009, based on an analysis that we performed at Texas A&M [1]. Fig. 1 shows a comparison of the 2009 preliminary results with previous measurements from 2006 [2], together with theory predictions from GRSV [3] and DSSV [4]. The yellow triangular region in Fig. 1 shows the $\chi^2+2\%$ uncertainty region identified in the DSSV global analysis. The 2009 data are more

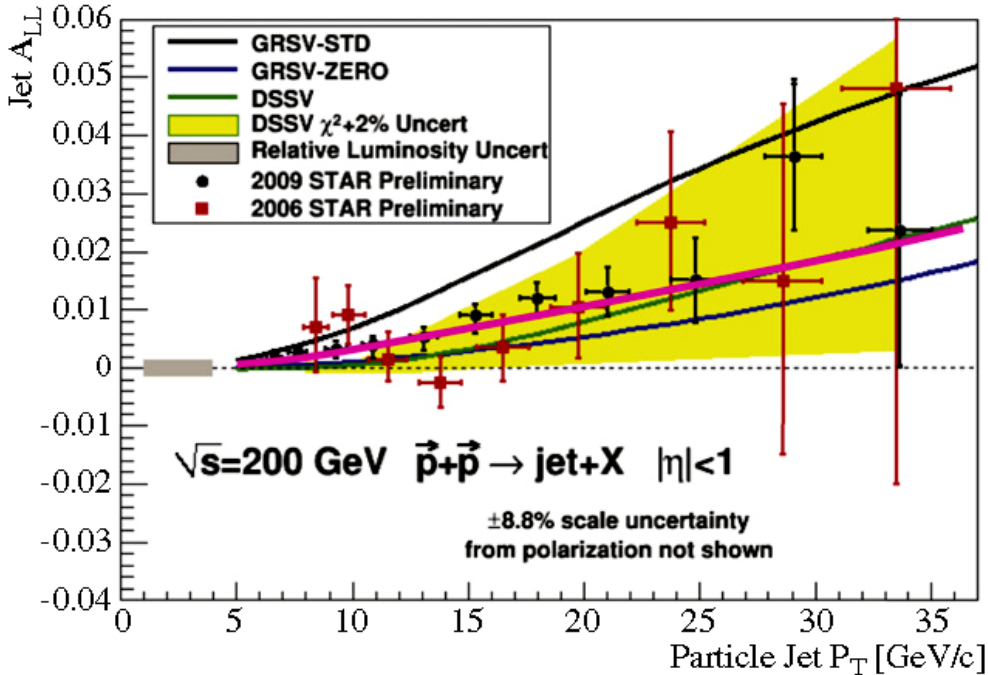


FIG. 1. 2009 (black circles) [1] and 2006 (red squares) [2] STAR measurements of the inclusive jet A_{LL} vs. p_T . The curves show predictions based upon the GRSV [3] and DSSV [4] polarized parton distributions. The yellow band shows the DSSV $\chi^2+2\%$ uncertainty region [4]. The magenta curve shows a new global fit by the DSSV group [5] that includes these preliminary 2009 results among the input

precise than the 2006 data by a factor of four in the low- p_T bins and a factor of three in the high- p_T bins. The STAR 2009 inclusive jet results fall between the predictions from DSSV and GRSV-STD.

DSSV was the first polarized parton distribution fit that included deep-inelastic scattering, semi-inclusive deep-inelastic scattering, and RHIC data on an equal footing [4]. The STAR 2005 and 2006 inclusive jet A_{LL} measurements played a significant role in constraining $\Delta g(x)$ in DSSV. Last summer we obtained a copy of the DSSV source code from the authors. The original DSSV analysis treated all STAR (and PHENIX) systematic uncertainties as point-to-point effects, added in quadrature with the respective statistical uncertainties. We revised the DSSV inclusive jet A_{LL} subroutines to treat properly our dominant correlated systematics: relative luminosity and the overall jet energy scale. We also included the new results from the 2009 STAR data. We then explored how the 2009 STAR data impact the best fit for the gluon polarization. We find that the new STAR data lead to an increase in the integral of $\Delta g(x)$ over the region $0.05 < x < 0.2$ and significantly reduce the uncertainty. We also find that the 2009 STAR results have a significant impact on the integral of $\Delta g(x)$ over the region $0.2 < x < 1$, in contrast to previous RHIC measurements. The DSSV group has now substituted our modified inclusive jet A_{LL} routines into their analyses. They have also substituted similar modified inclusive $\pi^0 A_{LL}$ routines from PHENIX, and added new results from COMPASS. The magenta curve in Fig. 1 shows a new preliminary best fit from the DSSV group [5] that incorporates these modifications. The integral of $\Delta g(x)$ over the region $0.05 < x < 0.2$ is approximately 0.13, consistent with the fits that we performed. This represents the first experimental evidence for non-zero gluon polarization in the proton.

The dominant systematic uncertainties in the 2009 measurement originate from differences between the true and reconstructed jet p_T , the non-uniform trigger sampling of the underlying partonic processes (gg , qg , and qq), and relative luminosities. During the past year, we have been working to reduce and finalize the trigger and reconstruction bias uncertainties. Previous STAR inclusive jet analyses have estimated trigger and reconstruction bias using samples of PYTHIA events processed through a GEANT model of the STAR detector. Such “pure simulation” events lack the pile-up backgrounds that are present in real data. Charged hadron tracks or electromagnetic calorimeter towers from pile-up can inadvertently be included in a jet. The pile-up can also reduce the tracking efficiency of the TPC by several percent [6]. In the early years of RHIC, the luminosities were low enough that pile-up backgrounds were not a significant problem in pp collisions. This is no longer true at current RHIC pp collision rates. For the 2006 and preliminary 2009 A_{LL} measurements, corrections were applied for the pile-up effects on the reconstructed jet energies. The corrections did a good job accounting for the average shift in the reconstructed jet energies. The uncertainties associated with the event-by-event fluctuations due to pile-up effects were larger.

During the past year, we have developed techniques to embed full PYTHIA+GEANT simulations into recorded STAR zero-bias events, thereby folding both the average and event-by-event effects of pile-up into our simulations without the need for external corrections. The cpu time required to produce microDST’s from the embedded events is at least an order of magnitude longer than is required for pure simulation samples. In order to keep the total cpu requirements tolerable, we modified the standard STAR embedding and event reconstruction procedure to occur in two passes, first simulating the electromagnetic calorimeters and trigger, then simulating the TPC only for those events that satisfy the

trigger requirements. The PYTHIA information is saved for all simulated events, including those that fail the trigger.

For the preliminary 2009 result, the systematic uncertainties from trigger and reconstruction bias were 50-100% of the statistical uncertainties for several low- to intermediate- p_T bins. For these jet p_T 's, the dominant effect arises from underlying event contributions that cause low- p_T parton jets to be reconstructed as higher- p_T particle and detector jets. Previous STAR jet analyses have used a STAR implementation of the mid-point cone algorithm that was developed for the Tevatron Run 2. The main external parameter, the cone radius R , has been chosen based on the physical coverage of the TPC and electromagnetic calorimeters combined with examinations of the recorded data. We adopted $R = 0.4$ for 2003-05 and $R = 0.7$ for 2006 and the preliminary 2009 analyses. The simulations required to estimate trigger and reconstruction bias were then done using those parameters. For the final 2009 analysis, we are turning this procedure around. We are performing a detailed comparison of the jets in our embedded PYTHIA+GEANT events at the parton, particle, and detector levels, using four different cone radii ($R = 0.4, 0.5, 0.6,$ and 0.7) and four different jet reconstruction algorithms (the STAR mid-point cone algorithm, plus the k_T , Anti- k_T , and CDF mid-point cone algorithms from the FastJet package). We have found that we can reduce the systematic bias substantially at the expense of a modest loss of jet statistics. We are now working to optimize of the total uncertainties.

Another major goal of the RHIC spin program is to unravel the origin of the large transverse single-spin asymmetries that have been seen at forward rapidities at RHIC [7]. The asymmetries have been attributed to the Sivers effect, a correlation between the spin of the incident proton and the transverse momentum of the quark or gluon that experiences the hard scattering, the Collins effect, which arises from the spin-dependent fragmentation of polarized scattered quarks, or a combination of the two. The Sivers effect provides a window into parton orbital motion because it requires interference between amplitudes involving partons with different orbital angular momenta. The Collins effect provides a means to explore quark transversity, the third collinear, leading-twist parton distribution function. (The other two are the unpolarized distribution and the helicity distribution, which is explored in longitudinally polarized collisions.)

This past year, we completed an exploratory study of spin-dependent two-particle correlations in transversely polarized proton collisions from the 2008 RHIC run [8]. By correlating trigger π^0 's from the STAR FMS with charged tracks at similar pseudorapidity measured with the STAR FTPC, we explored interference fragmentation functions (IFF) and Sivers asymmetries in a kinematic region where we have already measured large A_N for inclusive pions [7]. IFFs are sensitive to quark transversity and closely related to the Collins effect.

The Sivers asymmetry depends on the azimuthal distribution of di-hadron pairs about the beam axis. The IFF asymmetry depends on both the azimuthal location of the di-hadron pair about the beam axis and the azimuthal orientation of the pair. These two effects decouple when the di-hadrons are measured with an azimuthally symmetric detector. Unfortunately, the 2008 data have large, poorly understood acceptance distortions in both the FMS and the FTPC. These distortions coupled the Sivers and IFF asymmetries. We developed data-driven procedures to obtain the Sivers and IFF asymmetries in

the presence of these distortions. The procedures that we developed have now been adopted by other STAR collaborators to measure the Collins asymmetry in mid-rapidity jet production.

Fig. 2 shows the final results for the IFF and Sivers asymmetries. The asymmetries were measured as a function of the maximum separation distance ΔR_{max} between the π^0 and the charged hadron. Large ΔR_{max} maximizes the di-hadron yield. However, it also leads to a large underlying event background that dilutes the spin asymmetries of interest. Small ΔR_{max} maximizes the signal-to-background ratio, but with a much smaller di-hadron yield. The measured IFF asymmetries are close to expectations. However, the limited statistics available in the 2008 data set prevent any strong conclusions.

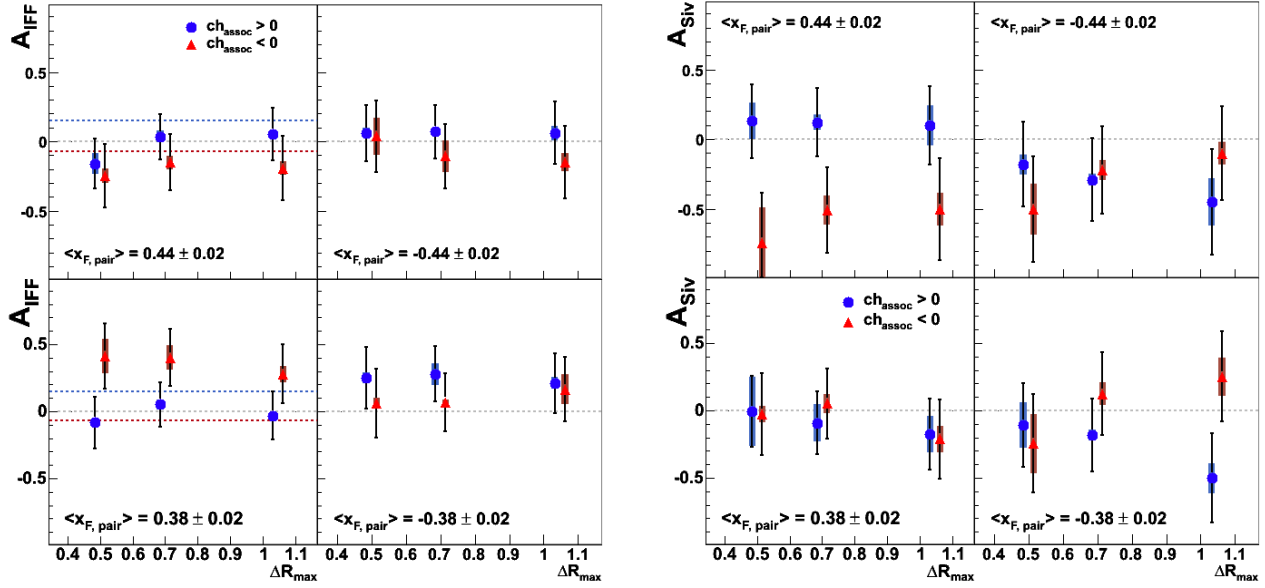


FIG. 2. The left four panels show forward π^0 -charged hadron IFF asymmetries, as a function of the maximum separation distance ΔR_{max} between the hadrons. The right four panels show forward π^0 -charged hadron Sivers asymmetries. Blue circles (red triangles) show results for positively (negatively) charged hadrons. Each individual panel shows results for the specified di-hadron Feynman- x . The dashed lines in the leftmost panels show the expected scale of the IFF asymmetries

More details regarding the spin-dependent di-hadron asymmetries can be found in [8].

- [1] P. Djawotho, for the STAR Collaboration, arXiv:1106.5769.
- [2] L. Adamczyk *et al.* (STAR Collaboration), arXiv:1205.2735.
- [3] M. Gluck, E. Reya, M. Stratmann, and W. Vogelsang, Phys. Rev. D **63**, 094005 (2001).
- [4] D. de Florian, R. Sassot, M. Stratmann, and W. Vogelsang, Phys. Rev. Lett. **101**, 072001 (2008); Phys. Rev. D **80**, 034030 (2009).
- [5] D. de Florian, R. Sassot, M. Stratmann, and W. Vogelsang, Prog. Nucl. Part. Phys. **67**, 251 (2012).
- [6] L. Huo, M.S. Thesis, Texas A&M University (2012).
- [7] B.I. Abelev *et al.* (STAR Collaboration), Phys. Rev. Lett. **101**, 222001 (2008).
- [8] J.L. Drachenberg, Ph.D. Thesis, Texas A&M University (2012).

SECTION II
HEAVY ION REACTIONS

A search for super heavy elements using a catcher foil

M. Barbui, K. Schmidt, J.B. Natowitz, H. Zheng, K. Hagel, A. Bonasera and M. Barbino

The search for super heavy elements (SHE) located on the predicted island of stability has a long history. The search usually involves an attempt at the direct detection of heavy elements that may have been produced. We made an attempt to collect SHE from the reactions of $^{197}\text{Au} + ^{232}\text{Th}$ using a magnet spectrometer and detect them at the focal point [1]. This experiment yielded a number of candidates but the results were not conclusive.

Super heavy elements are expected to be alpha-particle emitters. A calculation indicating alpha particle energies [2] expected for various heavy elements is shown in Fig. 1. We observe that with increasing charge that the alpha-particle Q-value increases. This suggests that it might be possible to search indirectly for super heavy elements and significantly improve the efficiency of the measurement.

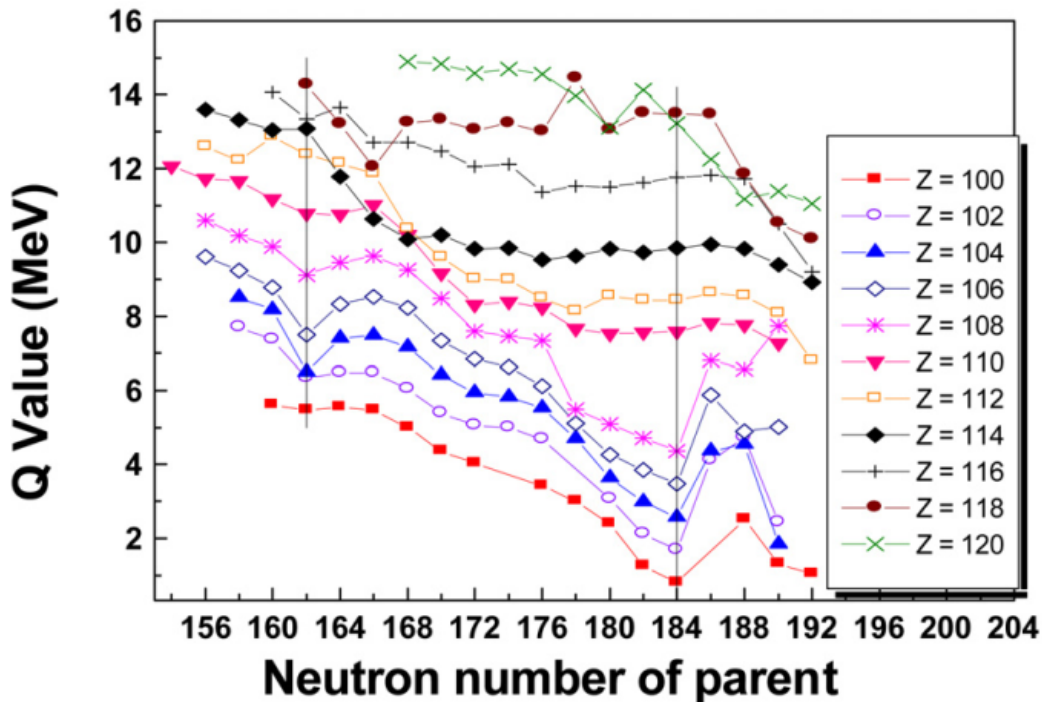


FIG. 1. Alpha Q-values for a range of heavy elements; from [2]

We have therefore embarked on a study to attempt to detect the alpha particles emitted from a super heavy element. The experimental setup is shown in Fig. 2. We note that the beam is incident on a ^{232}Th target. Immediately downstream of the target is a shield constructed of Borated Polyethylene with a conical hole that allows the products to travel to the catcher foil further downstream. Behind the blocker is a series of 7 strip silicon detectors that view only products that would be emitted from downstream, but not directly from the target. There were also two sets of thin silicon detectors placed in front of the strip detectors for the purpose of confirming particle identification for measured products.

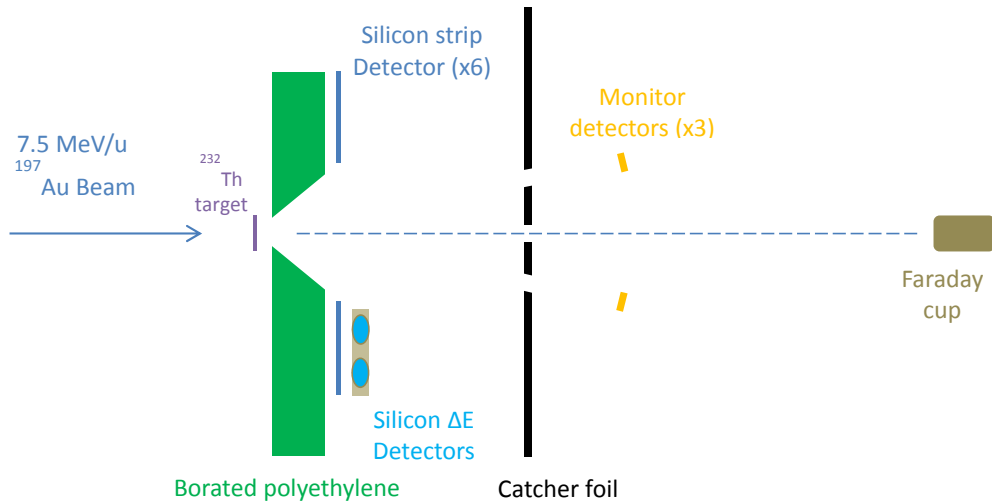


FIG. 2. Experimental Setup

The left two panels in Fig. 3 show the energy spectra and time distributions of particles detected in the silicon detectors when the beam was on. The relative time that the beam is on versus when it is off is indicated in the figure. We observe signals in the silicon detectors above 20 MeV with peaks around 6 MeV. When the beam was on, the time distributions show an increase with time. The high energy tail of the energy distributions are significantly suppressed when the beam is turned off as shown in the third column of Fig. 3. The peak of the distributions remains around 6 MeV and there are only a few signals

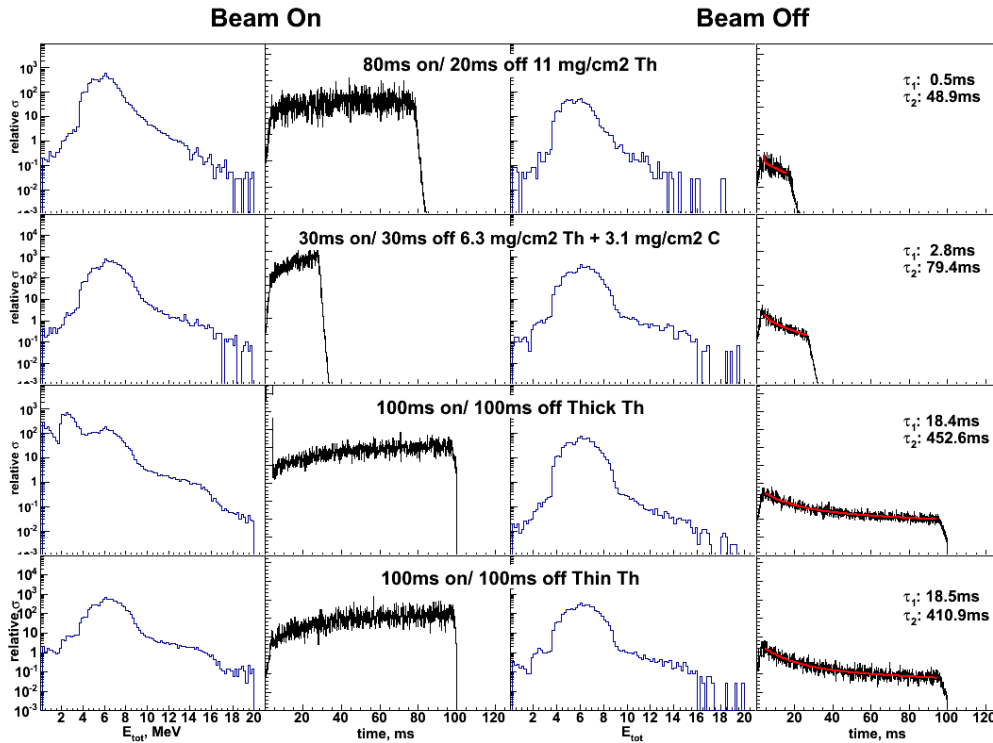


FIG. 3. Left two Columns: Energy distributions in the silicon detectors when beam was on (1st column) and time distribution of events from start of beam when beam was on. Right two columns: same for when beam was off. Time distributions in this column are measured from time beam was turned off.

above 15 MeV. The time distributions show a decay during the duration of no beam. In order to obtain an estimate of the lifetime of any heavy element decaying in the catcher foil, we performed a two component fit of the decay. A short as well as a long component is suggested. For the cases where the beam was off for 100ns, the short component is about 18ms and the decay of the long component is around 425ms.

We show the time distributions that are gated on the energy for the selected configuration of beam on/off of 100ms/100ms. These are shown in Fig. 4 along with the corresponding energy spectra shown at the top of the figure. The left side shows the time distributions when the beam was on and the right side shows the same when the beam was off. The two component fit shown on the right hand side hints at a decreasing lifetime for the higher energy window with the slow component decreasing from about 20ms at lower energies to about 3ms at the highest window and the long component decreasing from about 500ms at low energies to about 275ms at the higher energy window.

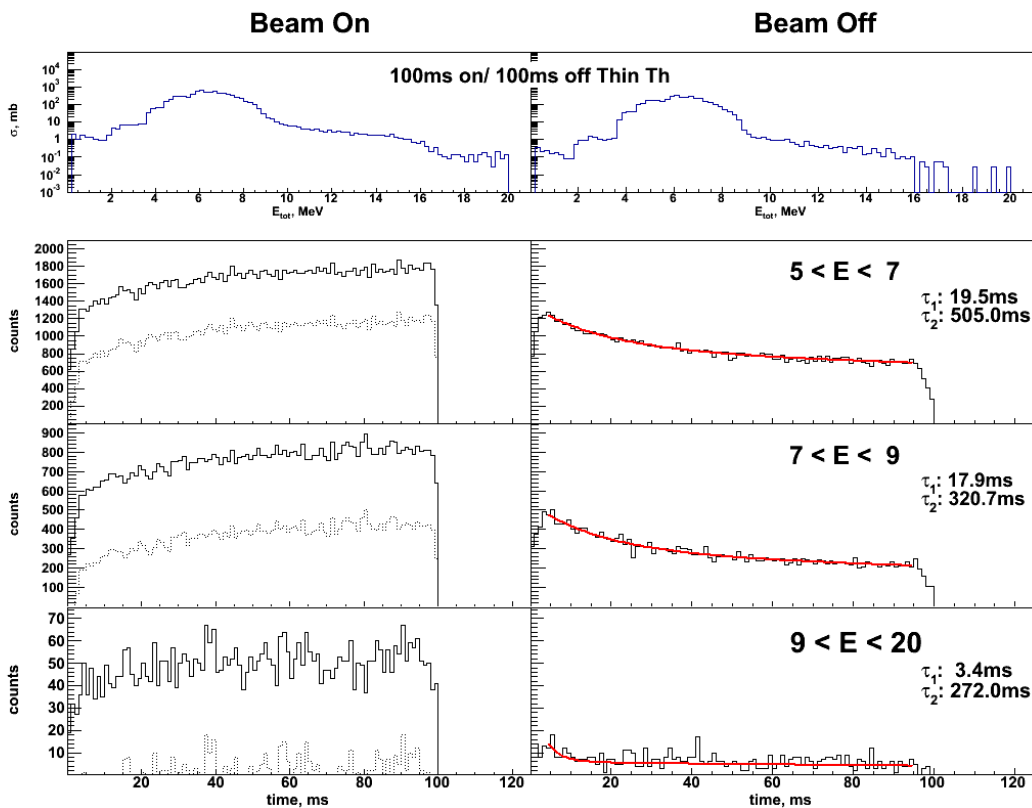


FIG. 4. Time distributions gated on energy for beam on (left) and beam off. The energy spectra that are gated are shown at the top.

The spectra obtained when a target was inserted, but the catcher foil was absent shows that the majority of events that are obtained when beam is off indeed result from decay from the catcher foil. This is demonstrated in Fig. 5. The top part of Fig. 5 shows the spectra obtained when a tantalum target thick enough to stop the beam was inserted. When the beam was on (left panels), events were observed that

probably result from neutron reactions with the silicon producing protons or alpha particles. When the beam was off, there were very few events and the events observed are less than 9 MeV.

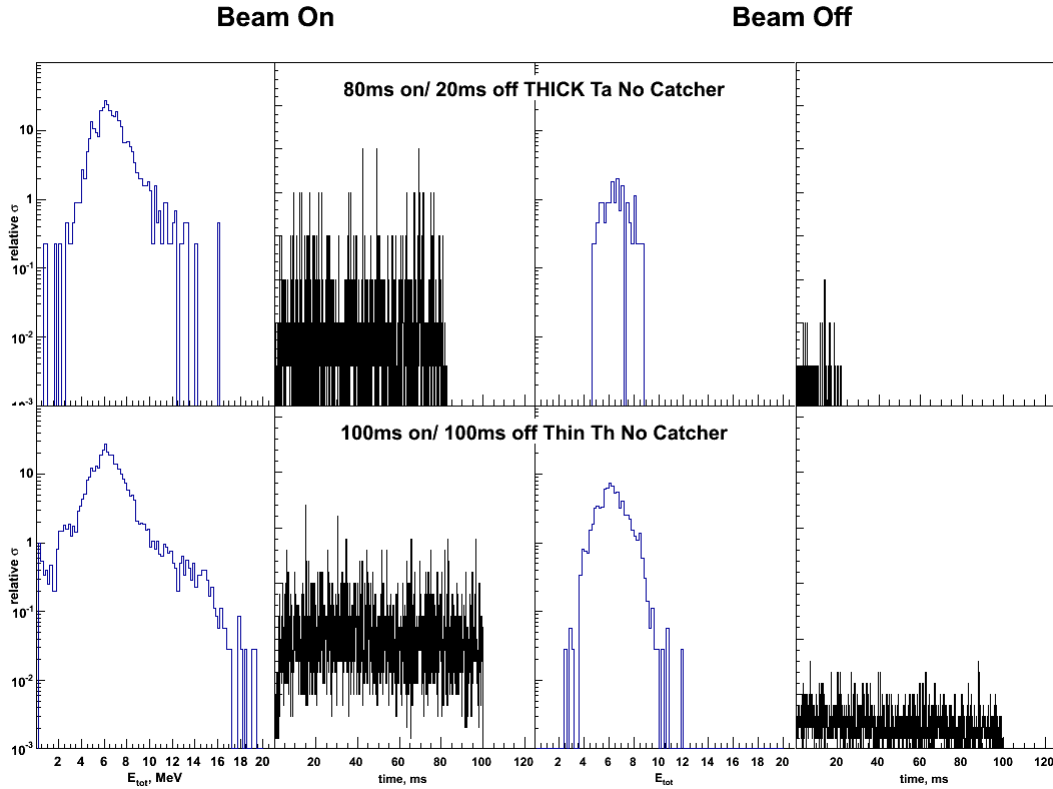


FIG. 5. Similar to Figs. 3 and 4, but for the cases where there was no catcher foil present. Top: beam on/off 80/20 ms with a Ta target thick enough to stop the beam. Bottom: beam on/off 100/100ms which a thin Th target that was used in the experiment.

The lower panel of Fig. 5 shows the measured quantities when the target is inserted, but no catcher foil present. In this case the beam was off for 100ms and the spectra extend to somewhat higher energies, but still remain below 12 MeV.

To determine whether the energy signals in the silicon detectors shown in figures 3-5 truly result from alpha particles, some 50um ΔE detectors were inserted in front of two of the silicon strip detectors. The ΔE -E maps that result from these measurements are shown in Fig. 6 where the left column, again, shows the maps with beam on and the right column shows the maps with beam off. The red curves show the alpha particle limits expected from range energy calculations. The lower limit results when the particle passes straight through the detector and the upper limit shows the range energy curve when the particle passes at the largest angle allowed by the geometry. The blue curves show the same quantity for protons. Any events falling inside the limits of the red curves are identified as alpha particles.

We observe two events that fall in the limits where alpha particles are expected when beam is off. We note a cluster of events just below the lower limit. It is not clear whether these could be alpha particles and the detector is thinner than advertised or perhaps not fully depleted or if they are not alpha particles. Further investigation is necessary.

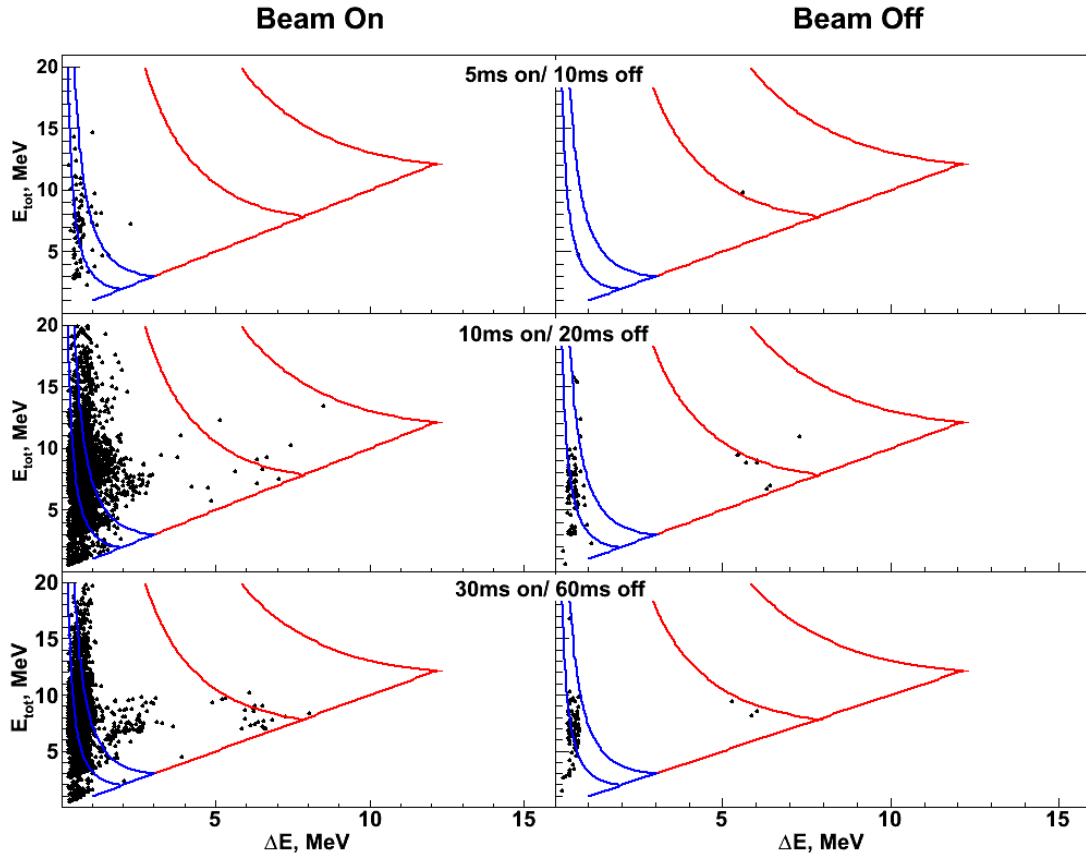


FIG. 6. ΔE - E maps for beam on (left) and beam off (right) for different beam on/off configurations.

To again ensure that the particles shown in Fig. 6 result from nuclei decaying in the catcher foil, we again inserted the beam stopping thick tantalum target and generated the ΔE - E maps. The catcher foil was inserted during this test. The result of this test is shown in the top row of Fig. 7. We observe a much smaller production of signals in the ΔE - E maps. There is, however, one event that is identified as an alpha particle. The bottom row of Fig. 7 shows a background where the data was acquired with no beam. In this case, beam on and beam off are the same. No alpha particles are observed in this background run.

In conclusion, we have observed decay of fragments from the catcher foil. This has been proven by background runs that show an absence of signals when the catcher foil is removed. The plethora of signals when beam is on as opposed to when beam is off indicate to us that neutrons interacting with silicon in the detector are a challenge. This means that pulsing the beam to observe the fragments decaying while beam is off is imperative. We have also observed alpha particles identified in ΔE - E maps.

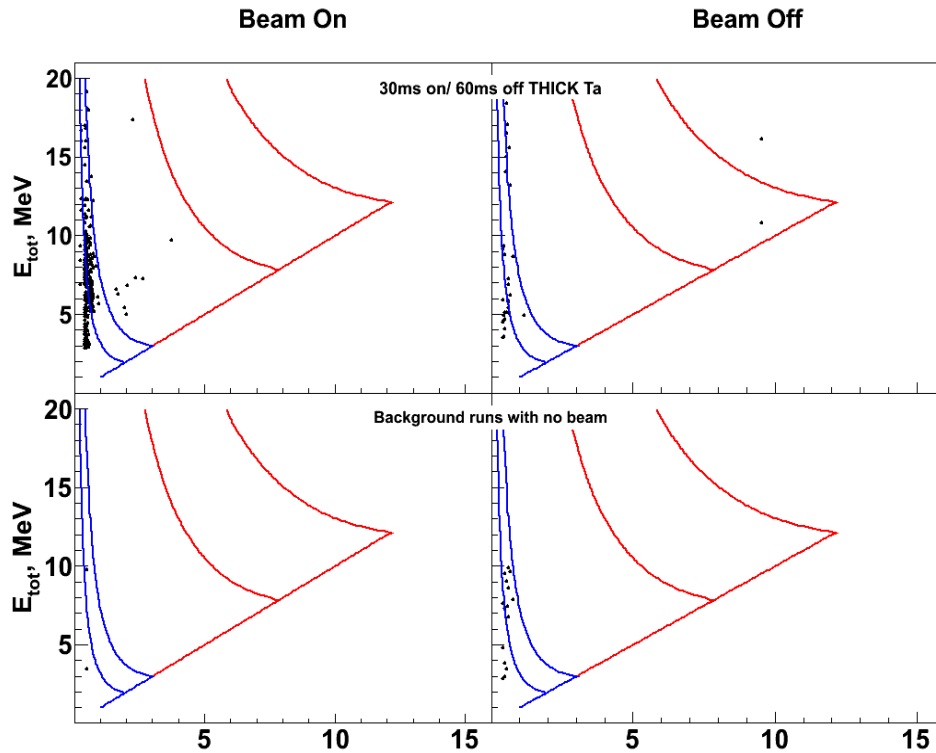


FIG. 7. ΔE -E maps for a run where the beam stopping thick Ta target is inserted (top) and for runs without beam (bottom). The catcher foil was inserted.

A number of improvements can be made in the search for super heavy elements. A larger efficiency of the ΔE -E maps is imperative as we note in the difference of signals between figures 3-5 versus what is observed in the ΔE -E maps. In order to reduce the contribution from neutron induced signals, a thinner ΔE detector needs to be implemented. We plan to accomplish this by using thinner strip detectors that will be placed in front of the thicker E detectors. In addition, we are designing a set of gas ionization chambers (ICs) which will be used either with the E detectors alone or along with the thinner ΔE detectors. Along with the ICs, we plan to implement a position sensitive parallel plate avalanche counter (PPAC). Together with the thin silicon strip detectors, the particles can be tracked to determine their origin.

Finally, we are investigating the possibility of an active catcher. This would allow us to identify where the heavy nucleus was implanted and together with the tracking capability of the position sensitive PPAC + silicon strip detectors we could confirm that the particles originate from the same position in the catcher foil where the heavy nucleus was implanted.

[1] J.B. Natowitz *et al.*, *Progress in Research*, Cyclotron Institute, Texas A&M University (2008-2009), p. II-1.

[2] K.P. Santhosh *et al.*, *Nucl. Phys.* **A825**, 159 (2009).

Probing clusterization in $^{40}\text{Ca} + ^{40}\text{Ca}$ reactions

K. Schmidt, M. Barbui, J. B. Natowitz, K. Hagel, A. Bonasera, G. Giuliani,
M. Rodrigues,¹ R. Wada,² M. Huang,³ C. Botosso,¹ G. Liu,³ G. Viesti,⁴ S. Moretto,⁴ G. Prete,⁵
S. Pesente,⁴ D. Fabris,⁴ Y. El Masri,⁶ T. Keutgen,⁶ S. Kowalski,⁷ and A. Kumar⁸

¹*Institute of Physics, University of Sao Paulo, Brazil*

²*Institute of Modern Physics HIRFL, Chinese academy of Science, Lanzhou, 73000, China*

³*Shanghai Institute of Applied Physics, Shanghai, China*

⁴*Dipartimento di Fisica dell'Universita di Padova and INFN Sezione di Padova, Italy*

⁵*INFN Laboratori Nazionali di Legnaro, Italy*

⁶*Universit'e Catholique de Louvain, Louvain-la-Neuve, Belgium,*

⁷*Institute of Physics, Silesia University, Katowice, Poland*

⁸*Nuclear Physics Laboratory, Department of Physics, Banaras Hindu University, Varanasi, India*

Given the high degree of alpha clustering which is expected for low mass alpha conjugate nuclei we previously initiated a search for evidence of cluster effects and possible Bose Condensates using the NIMROD array. Our experiments, carried out at the end of 2008 employed 10, 25, 35 MeV/u beams of ^{40}Ca and ^{28}Si incident on ^{40}Ca , ^{28}Si , ^{12}C and ^{180}Ta target. After completing the energy calibrations of the Si and CsI detectors we have initiated the physical analysis of the $^{40}\text{Ca} + ^{40}\text{C}$ reaction data at 35MeV/A in order to de-lineate the dominant reaction mechanisms present. We have also made comparisons with results of anti-symmetrized molecular dynamics (AMD) calculations. AMD calculations were performed up to 300 fm/c. The Gemini was employed as an afterburner to de-excite the fragments. All events were passed through an experimental acceptance filter. The goal of our analysis is to understand the mechanism of production of alpha conjugate products, similar to those shown in the Ikeda Diagram in Fig. 1.

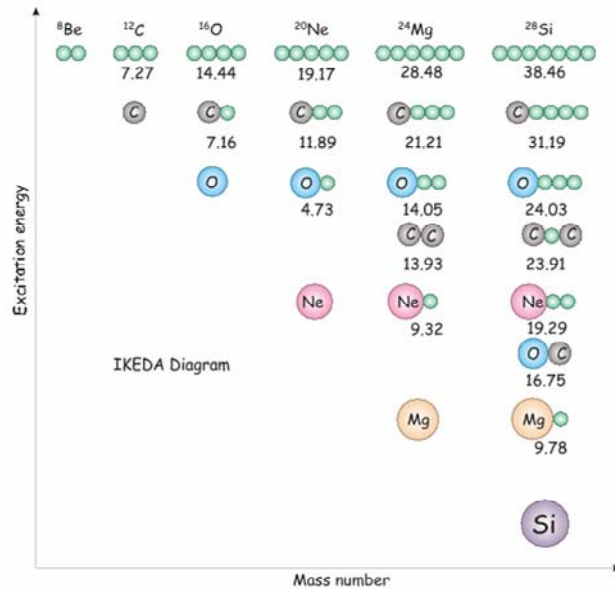


FIG. 1. Ikeda Diagram.

In order to find those various α -conjugate combinations it is necessary to define some observables. For each event we calculate the multiplicity of “ α -like fragments” and the total mass of those fragments as defined below.

$$\begin{aligned}\alpha\text{-like mult} &= \alpha \text{ mult} + {}^{12}\text{C mult} + {}^{16}\text{O mult} + \dots + {}^{40}\text{Ca mult} \\ \alpha\text{-like mass} &= 4(\alpha \text{ mult}) + 12({}^{12}\text{C mult}) + 16({}^{16}\text{O mult}) + \dots + 40({}^{40}\text{Ca mult})\end{aligned}$$

We define similar observables for “d-like fragments” as well:

$$\begin{aligned}\text{d-like mult} &= \text{d mult} + {}^6\text{Li mult} + {}^{10}\text{B mult} + \dots + {}^{22}\text{Na mult} \\ \text{d-like mass} &= 2(\text{d mult}) + 6({}^6\text{Li mult}) + 10({}^{10}\text{B mult}) + \dots + 30({}^{30}\text{P mult}).\end{aligned}$$

In Fig. 2 we show some preliminary results on the production of α (left) and d (right) conjugate fragments in the collisions of ${}^{40}\text{Ca}$ with ${}^{40}\text{Ca}$ at 35A MeV. The number of detected events with different multiplicities of α (d) conjugate nuclei is plotted against the total α (d) conjugate mass detected. No impact parameter selection is applied. A total mass as large as 85% of the entrance channel mass is observed. Given some detector inefficiency and energy thresholds this is a significant number. Also interesting is the limiting case, in which where all of the detected α (d) conjugate mass is in α -particles or deuterons. These are indicated by the large circles in Fig. 2.

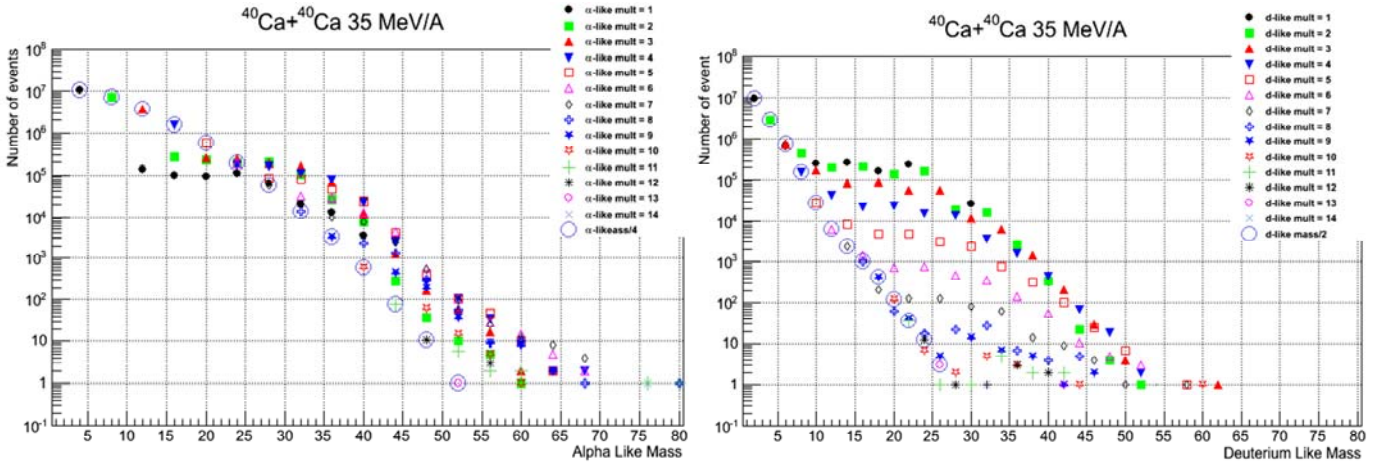


FIG. 2. α -like mass (left) and d-like mass (right) distribution for fixed α -like /d-like multiplicities.

Another interesting parameter, b_j is defined as follows:

$$B_j = \frac{1}{M} \sum_{i=1}^M \frac{(-1)^{Z_i} + (-1)^{N_i}}{2}$$

this parameter ranges from -1 to 1. The negative value indicates more d-like fragments in the event whereas positive value means more α -like fragments.

Fig. 3 shows the comparison between the experimental data (blue line) and AMD theoretical results (red line) for the the A and Z distributions and for the observables defined above. The model underestimates the production of heavier fragments starting from Z=15. We observe good agreement in the distributions of α -like and d-like multiplicity and their total masses. The theoretical distribution for the b_j parameter is narrower than that for the experiment, which might be due to the underestimate of heavier fragment production. It is also nearly symmetric, meaning that almost the same number of α -like and d-like fragments are predicted. The experimental distribution is weighted towards the positive values, which indicates that more α -like fragments have been created. The analysis is in progress and will explore source analyses, multiplicity fluctuations, multi-particle correlations and other observables.

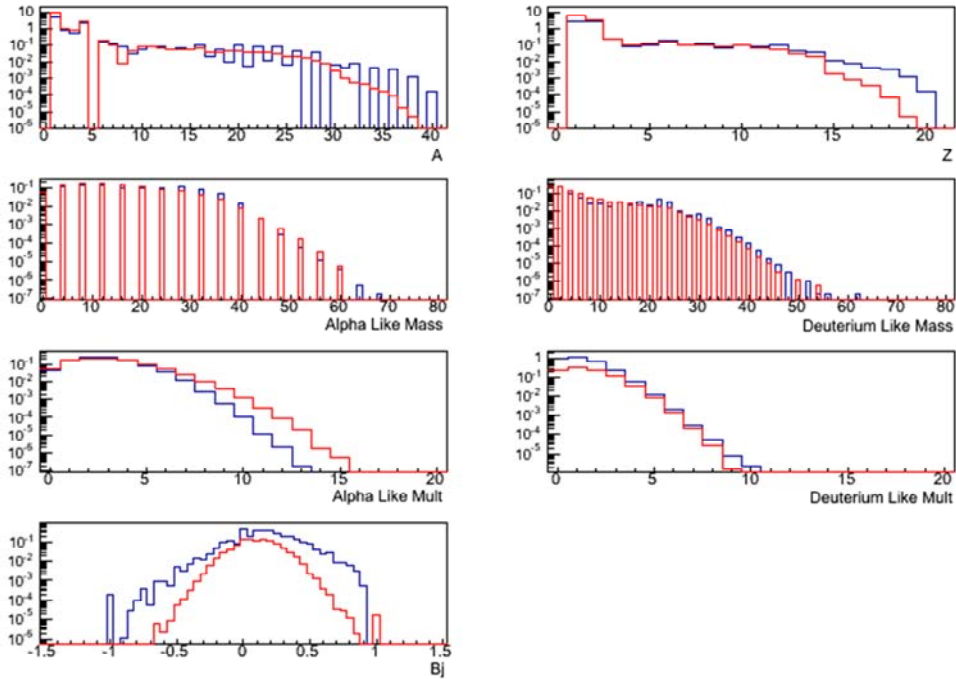


FIG. 3. A, Z, α -like mass, d-like mass, α -like multiplicity, d-like multiplicity, b_j distributions. Blue line – experimental data, red line – AMD calculations.

Yield of D-D and D-³He fusion reactions produced by the interaction of intense ultrafast laser pulses with molecular clusters

M. Barbui, A. Bonasera,¹ K. Hagel, J.B. Natowitz, K. Schmidt, W. Bang,² G. Dyer,² H. Quevedo,² A. Bernstein,² E. Gaul,² T. Borger,² A. Bernstein,² M. Martinez,² M. Donovan,² T. Ditmire,² F. Consoli,³ R. De Angelis,³ P. Andreoli³

¹*INFN Laboratorio Nazionale del Sud, Catania, Italy*

²*University of Texas, Austin, Texas*

³*Enea, Frascati, Italy*

The interaction of intense ultrafast laser pulses with molecular clusters produces a Coulomb explosion of the clusters. In this process, the positive ions from the clusters might gain enough kinetic energy to drive nuclear reactions [1-3]. The ratio of the yields of two reactions, with different cross section, occurring simultaneously can be used to determine the average temperature of the ions at the time when the reactions occurred.

A first experiment to measure the yield of D-D and D-³He fusion reactions was performed at University of Texas Center for High Intensity Laser Science. Laser pulses of energy ranging from 100 to 180 J and duration 150fs were delivered by the Petawatt laser. A layout of the experimental setup is given in Fig. 1.

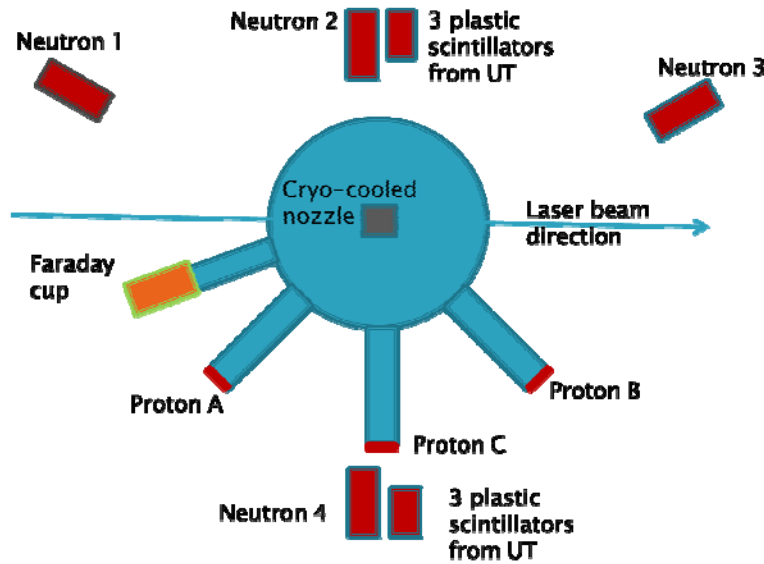


FIG. 1. Diagram of the experimental setup.

The experiment was divided in two parts. In the first part, pure D₂ clusters were used to optimize the yield of the D(D,n)³He and D(D,p)T fusion reactions. The temperature of the energetic deuterium ions was measured using a Faraday cup placed at 160° relative to the laser direction at a distance of about 1 m from the target. The yields of the D-D reactions were determined by detecting the characteristic 2.45 MeV neutrons and 3.02

MeV protons. In order to measure the 2.45 MeV neutrons, six plastic scintillators provided by the UT group were placed at 90° and -90° at distances of 2 m and 4 m from the target position. Four NE213 liquid scintillators of cylindrical shape (radius 7 cm and thickness 14 cm) were also placed at 36° , 90° , -90° , 151° and distances larger than 2 m.

The 3.02 MeV protons were detected using thin plastic scintillators (BC400) of thicknesses 254 μm ($\rho=1.03 \text{ g/cm}^3$) placed at 45° , 90° , 135° . Those detectors were placed at a distance of 106 cm from the target position. A 25.4 μm Al foil was placed in front of the detectors at a distance of about 5 cm in order to shield the detectors from the light and stop electrons of energy up to 50 keV.

Two Hamamatsu R1355 photo-multiplier tubes (PMT) were used to collect the scintillation light on both sides of the plastic scintillator. Home-made active bases were used to provide the high voltage to the PMTs and to derive the signal. The signals were recorded using three Tektronix TDS 3052 oscilloscopes. The time duration of a pulse signal was about 10 ns FWHM. The time difference between the signals produced by x-rays and by the proton was about 40 ns.

In the second part of the experiment, different concentrations of D_2 and ^3He or CD_4 and ^3He were mixed in the gas jet target to allow the simultaneous measurement of $^3\text{He}(\text{D},\text{p})^4\text{He}$ and D-D reactions. The 2.45 MeV neutrons from the $\text{D}(\text{D},\text{n})^3\text{He}$ reaction were measured as well as the 14.7 MeV protons from the $^3\text{He}(\text{D},\text{p})^4\text{He}$ reaction. The 14.7 MeV protons were detected using the same plastic scintillators used for the 3.02 MeV protons, but with a different degrader. The thin degrader was removed and replaced with a 1.1 mm thick Al degrader placed about 50 cm in front of the plastic scintillator. The energy of the protons was degraded to 4 MeV so that the time difference between the x-ray signal and the proton signal was about 25 ns. The detectors were calibrated using a 14 MeV proton beam delivered by the K500 superconducting Cyclotron at Texas A&M. Fig. 2 shows the typical signals produced by 3 MeV and 14.7 MeV protons.

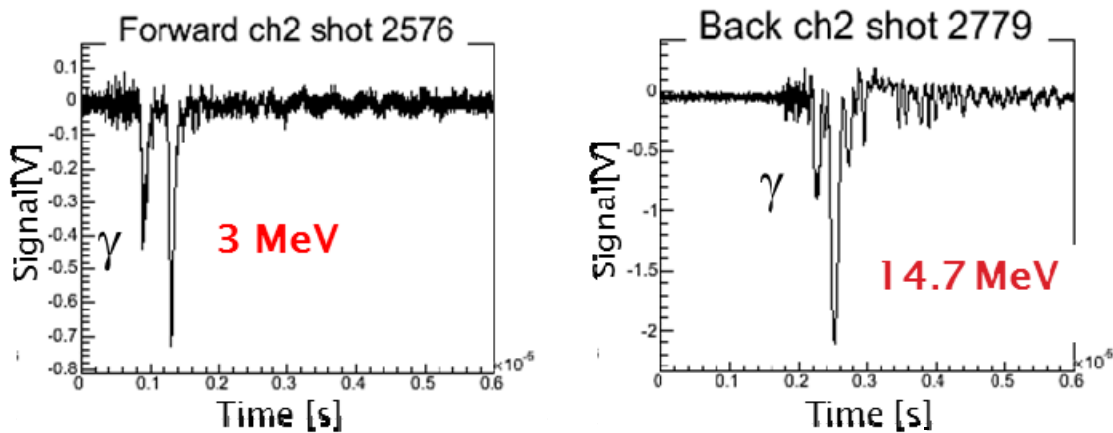


FIG. 2. Typical signals from the proton detectors. Left panel: 3 MeV protons from D-D fusion. Right panel: 14.7 MeV protons from D- ^3He fusion.

When ^3He was mixed with deuterium, the Faraday cup measurement showed no evidence of energetic ^3He ions, suggesting that the clusters were made of D_2 molecules and the ^3He was in the surrounding gas.

The preliminary results showing the ratio of the experimental yields as a function of the measured temperature are reported in Fig. 3. Within the experimental errors the temperature obtained from the yield ratio agrees with the temperature measured by the faraday cup.

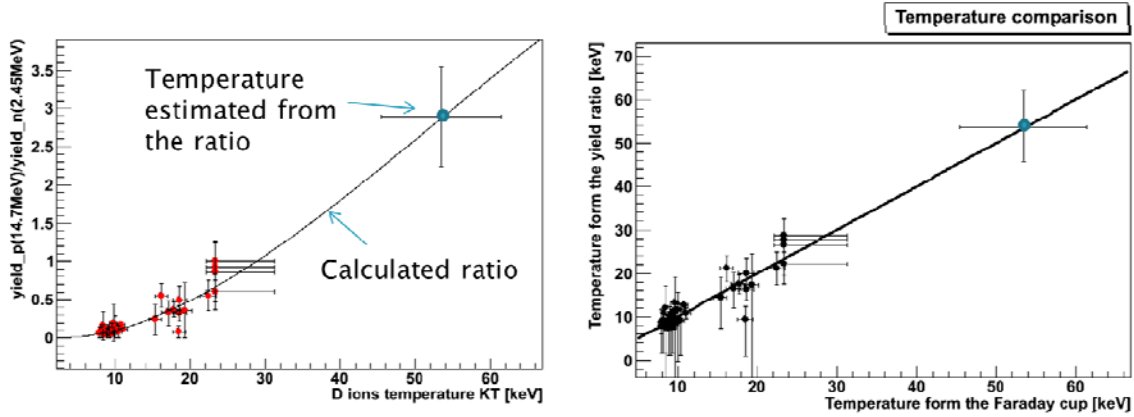


FIG. 3. Left panel: Ratio of the experimental yields as a function of the measured D ion temperature. The line shows the calculated ratio obtained using the cross-section parameterization from Bosch and Hale [4]. Right panel: D ion temperature estimated from the yield ratio plotted versus the D ion temperature measured using the faraday cup.

- [1] T. Ditmire, J. Zweiback, V.P. Yanovsky, T.E. Cowan, G. Hays, and K.B. Wharton, *Nature* **398**, 489 (1999).
- [2] J. Zweiback, R.A. Smith, T.E. Cowan, G. Hays, K.B. Wharton, V.P. Yanovsky, and T. Ditmire, *Phys. Rev. Lett.* **84**, 2634 (2000).
- [3] K.W. Madison, P.K. Patel, D. Price, A. Edens, M. Allen, T.E. Cowan, J. Zweiback, and T. Ditmire, *Phys. Plasmas* **11**, 270 (2004).
- [4] H.-S. Bosch, G.M. Hale, *Nucl. Fusion* **32**, 611 (1992)

Clusterization in low density nuclear matter

K. Hagel, R. Wada,¹ L. Qin, J. B. Natowitz, S. Shlomo, A. Bonasera,² G. Röpke,³ S. Typel,⁴ Z. Chen,¹ M. Huang,¹ J. Wang,¹ H. Zheng, S. Kowalski,⁵ C. Bottosso, M. Barbui, M. R. D. Rodrigues, K. Schmidt, D. Fabris,⁶ M. Lunardon,⁶ S. Moretto,⁶ G. Nebbia,⁶ S. Pesente,⁶ V. Rizzi,⁶ G. Viesti,⁶ M. Cinausero,⁷ G. Prete,⁷ T. Keutgen,⁸ Y. El Masri,⁸ and Z. Majka⁹

¹*Institute of Modern Physics HIRFL, Chinese Academy of Sciences, Lanzhou, 730000, China.*

²*Laboratori Nazionali del Sud, INFN, via Santa Sofia, 62, 95123 Catania, Italy*

³*University of Rostock, FB Physik, Rostock, Germany*

⁴*GSI Helmholtzzentrum für Schwerionenforschung GmbH,
Theorie, Planckstrae 1, D-64291 Darmstadt, Germany*

⁵*Institute of Physics, Silesia University, Katowice, Poland.*

⁶*Dipartimento di Fisica dell Università di Padova and INFN Sezione di Padova, Padova, Italy*

⁷*INFN Laboratori Nazionali di Legnaro, Legnaro, Italy*

⁸*FNRS and IPN, Universit'e Catholique de Louvain, B-1348 Louvain-Neuve, Belgium*

⁹*Smoluchowski Institute of Physics, Jagiellonian University, Krakow, Poland*

During the past year we completed three experimental investigations of low density nuclear matter. Papers on the first two have been published in Physical Review Letters. A paper on the third is in press in Physical Review C.

1. Experimental determination of in-medium cluster binding energies and Mott points in nuclear matter

In medium binding energies and Mott points for d, t, ³He and α clusters in low density nuclear matter have been determined at specific combinations of temperature and density in low density nuclear matter produced in collisions of 47A MeV ⁴⁰Ar and ⁶⁴Zn projectiles with ¹¹²Sn and ¹²⁴Sn target nuclei. The experimentally derived values of the in medium modified binding energies are in good agreement with recent theoretical predictions based upon the implementation of Pauli blocking effects in a quantum statistical approach (Phys. Rev. Lett. **108**, 062702 (2012)).

2. Laboratory tests of low density astrophysical equations of state

Clustering in low density nuclear matter has been investigated using the NIMROD multi-detector at Texas A&M University. Thermal coalescence modes were employed to extract densities, ρ , and temperatures, T, for evolving systems formed in collisions of 47 A MeV ⁴⁰Ar + ¹¹²Sn, ¹²⁴Sn and ⁶⁴Zn + ¹¹²Sn, ¹²⁴Sn. The yields of d, t, ³He, and ⁴He have been determined at $\rho = 0.002$ to 0.03 nucleons/fm³ and T = 5 to 11 MeV. The experimentally derived equilibrium constants for α particle production are compared with those predicted by a number of astrophysical equations of state. The data provide important new constraints on the model calculations (Phys. Rev. Lett. **108**, 172701 (2012)).

3. The nuclear matter symmetry energy at $0.03 \leq \rho / \rho_0 \leq 0.2$

Measurements of the density dependence of the Free symmetry energy in low density clustered matter have been extended using the NIMROD multi-detector at Texas A&M University. Thermal coalescence models were employed to extract densities, ρ , and temperatures, T , for evolving systems formed in collisions of 47 A MeV $^{40}\text{Ar} + ^{112}\text{Sn}$, ^{124}Sn and $^{64}\text{Zn} + ^{112}\text{Sn}$, ^{124}Sn . Densities of $0.03 \leq \rho / \rho_0 \leq 0.2$ and temperatures in the range 5 to 10 MeV have been sampled. The Free symmetry energy coefficients are found to be in good agreement with values calculated using a quantum statistical model. Values of the corresponding symmetry energy coefficient are derived from the data using entropies derived from the model (Phys. Rev. C (in press)).

Temperature measurements in reactions at low excitation energies to probe a possible phase transition

A. Raphelt, B. Stern, P.J. Cammarata, L. Heilborn, J. Mabiála, L.W. May, A.B. McIntosh,
A. Zarella, and S.J. Yennello

Exploration of the nuclear phase diagram provides for a way to explain the fundamental properties of nuclear matter. Searching for a possible liquid--gas phase transition requires a way to probe the temperature. Several thermometers have been developed to measure the temperature of nuclear systems. The quadrupole momentum fluctuation thermometer [1] calculates the temperature using a classical approach. The recently developed quantum thermometer [2] uses a quantum treatment of the quadrupole momentum fluctuation thermometer to derive the temperature, which allows for Fermi motion. This thermometer can be used with fermions such as neutrons, protons, and tritons. When the temperature is calculated using the quadrupole momentum fluctuation thermometer for various energy densities, the energy density is shown to decrease with decreasing temperature from higher temperature to around 3 MeV. The temperature then curves back as the energy density decreases, indicating a possible signature of a phase transition. This phase transition is shown in the Constrained Molecular Dynamics (CoMD) simulation [2] and hinted at by experimental data [3] shown in Fig. 1.

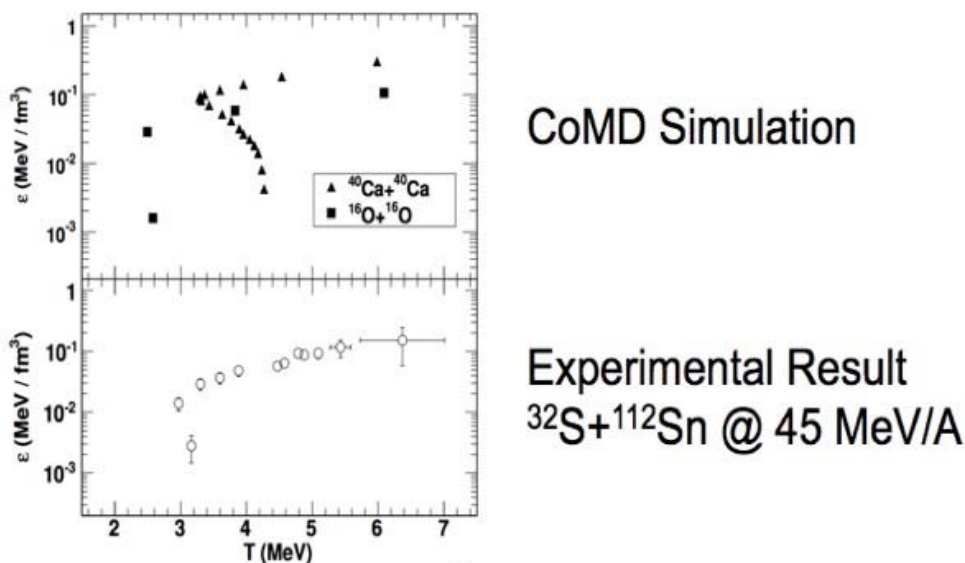


FIG. 1. Energy Density vs Temperature for CoMD Simulation of $^{40}\text{Ca} + ^{40}\text{Ca}$ and $^{16}\text{O} + ^{16}\text{O}$ at energies of 4 MeV/A to 100 MeV/A and impact parameter of 1 fm to a time of 1000 fm/c [4] and experimental data of $^{32}\text{S} + ^{112}\text{Sn}$ at 45 MeV/A [3]

A CoMD simulation of $^{64}\text{Ni} + ^{27}\text{Al}$ at 25 MeV/nucleon to 3000 fm/c was performed in order to observe what fragments are produced in the region near this phase transition. Determining what fragments are prevalent at these temperatures, and what properties they have, can help to provide a possible way to measure them in an experimental setup in order to probe the phase transition further using experimental data. Properties such as size, energy, and angle of detection can help to determine what

experimental setup could be used to best detect these fragments. A more complete detection of the fragments should lead to a better analysis and better understanding of the region at the phase transition. The phase transition is present at a relatively low temperature, which corresponds to low excitation energy. Shown in Fig. 2 are the products from the simulation that show how the excitation energy corresponds to other useful properties.

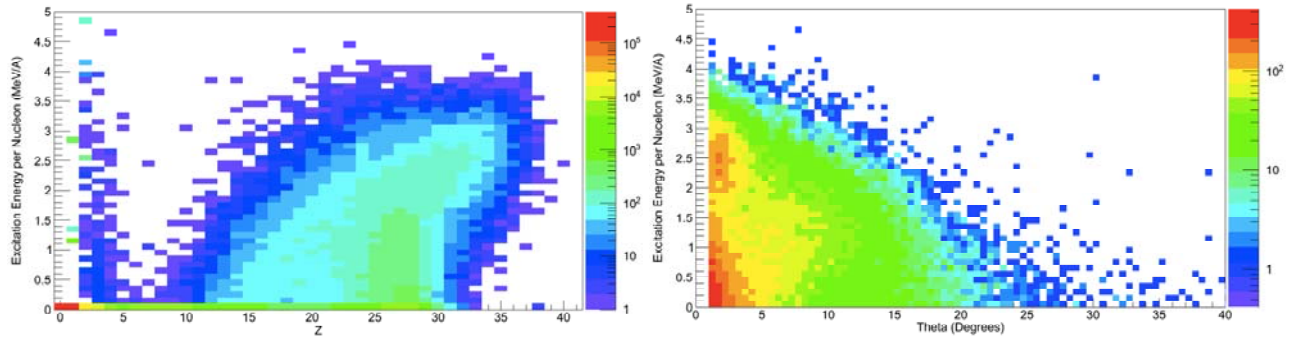


FIG. 2. Fragments from a CoMD simulation of $^{64}\text{Ni} + ^{27}\text{Al}$ at 25 MeV/A plotted as (left) excitation energy per nucleon vs the charge of the fragment and (right) excitation energy per nucleon vs the angle of the fragment relative to the beam axis.

In the plot on the left in Fig. 2, it is shown that the CoMD simulation produces fragments with low excitation energy mostly at high charge, close to the charge of the projectile. It should be noted that a majority of the fragments produced in this reaction are either very light, such as neutrons and protons, or large projectile--like residues. Light fragments with high excitation energy should also be produced in the reaction, but are absent in this plot due to a lack of yield. The plot to the right shows that low excitation energy fragments also occur at a very low theta angle relative to the beam axis. From these two figures, it can be seen that in the region of interest, the low excitation energy region, fragments with a large size and fragments close in angle to the beam axis are very prevalent and are of great interest for pursuit of information at low temperatures.

Determining the properties of the fragments that occur in the area near the phase transition will help to further the study of this area. Knowing the size and detection angle of the fragments of interest also provides information that can be used for experiments in the future in order to probe this interesting phase transition. Being able to explore this phase transition further by extracting temperatures from experimental data will allow for the study of the fundamental properties of nuclear matter.

- [1] S. Wuenschel *et. al.*, Nucl. Phys. **A843**, 1 (2010).
- [2] H. Zheng and A. Bonasera, Phys. Lett. B **696**, 178 (2011).
- [3] B. Stein, arXiv:1111.2965
- [4] H. Zheng and A. Bonasera, arXiv:1112.4098v1 [nucl---th] (2011)

Investigation of the nuclear phase transition using the Landau free energy approach

J. Mabilia, A. Bonasera, H. Zheng, A.B. McIntosh, L.W. May, P. Cammarata, Z. Kohley, K. Hagel, L. Heilborn, A. Zarrella, A. Raphelt, and S.J. Yennello

Nuclear multifragmentation is one of the most interesting phenomena in heavy-ion collisions, for studying the behavior of nuclear matter under extreme conditions of temperature and density, and possible phase transitions. In recent works [1,2,3] fragment yields have been used to investigate the nuclear liquid-gas phase transition using the Landau free energy approach, which is applicable to systems in the vicinity of a critical point. In the Landau free energy approach, the isospin asymmetry of a fragmenting source acts as an external field which can modify the fragment yields. In the present work, fragment yield data from $^{64}\text{Zn} + ^{64}\text{Zn}$, $^{64}\text{Ni} + ^{64}\text{Ni}$ and $^{70}\text{Zn} + ^{70}\text{Zn}$ reactions at 35 MeV/nucleon were analyzed within the framework of the Landau free energy approach.

The experiment was performed at the Texas A&M University Cyclotron Institute. Charged particles were measured using the NIMROD-ISiS 4π detector array, which was housed inside the TAMU Neutron ball. Details on the experiment are reported in Ref. [4]. In the analysis, quasi-projectile (QP) sources were reconstructed and selected by means of event-by-event cuts as in Ref. [5]. The QP mass was restricted to be in the range $54 \leq A \leq 64$. Its excitation energy was deduced using the measured free neutron multiplicity, the charged particle kinetic energies, and the Q-value of the breakup. Data were sorted into four different bins in QP source asymmetry ($m_s = (N - Z)/A$) ranging from 0.04 to 0.24 with bin width of 0.05. Effects of QP excitation energies on the thermodynamic quantities were investigated by gating the data into nine bins of 1 MeV in the range of 1-10 MeV/nucleon.

In the modified Fisher model, the fragment yield near the critical point is related to its free energy (F) normalized with respect to the temperature T by [6]

$$Y = y_0 A^{-\tau} e^{-\frac{F}{T}A} \quad (1)$$

with y_0 a constant, A the fragment mass number and τ a critical exponent. In the Landau approach, F/T can be written in terms of an order parameter m as given by [6]

$$\frac{F}{T} = \frac{1}{2}am^2 + \frac{1}{4}bm^4 + \frac{1}{6}cm^6 - \frac{H}{T}m \quad (2)$$

The parameters a , b and c contain information about the position of the fragmenting system with respect to the critical point. H is the external field due to the isospin asymmetry of the source (m_s). In the absence of any external field ($H/T=0$), Eq. (2) may predict three minima with $m=0$ the central minimum. The presence of an external field shifts the positions of these minima.

The free energy data were obtained by normalizing fragment yields with respect to ^{12}C yields to eliminate the constant y_0 . F/T values of $N=Z$ nuclei were observed to significantly deviate from the regular behavior of the $N \neq Z$ fragments. These so-called odd-even effects were corrected by a pairing

coefficient extracted from the analysis of $N=Z$ fragments. The following equation was used for the fragment yield to correct for pairing effects

$$Y = y_0 A^{-\tau} e^{-\left(\frac{F}{T} - \frac{a_p \delta}{T A^{3/2}}\right) A} \quad (3)$$

where a_p is the pairing coefficient. Fig. 1 shows free energy (F/T) values for different for different m_s bins. Solid lines (Fit1) are fit to the data using the Landau free energy (Eq. 2) with a , b , c and H/T as free parameters. Dashed lines (Fit2) are fit to data using only first and last terms of Eq. (2). It is seen from the figure that the Landau equation provides a better fit to the free energy data. The three minima seen in the free energy plot indicate the system to be in the regime of a first order phase transition. However, a more definitive conclusion on this aspect would require measurement of exotic fragments with large m to better constrain the fit.

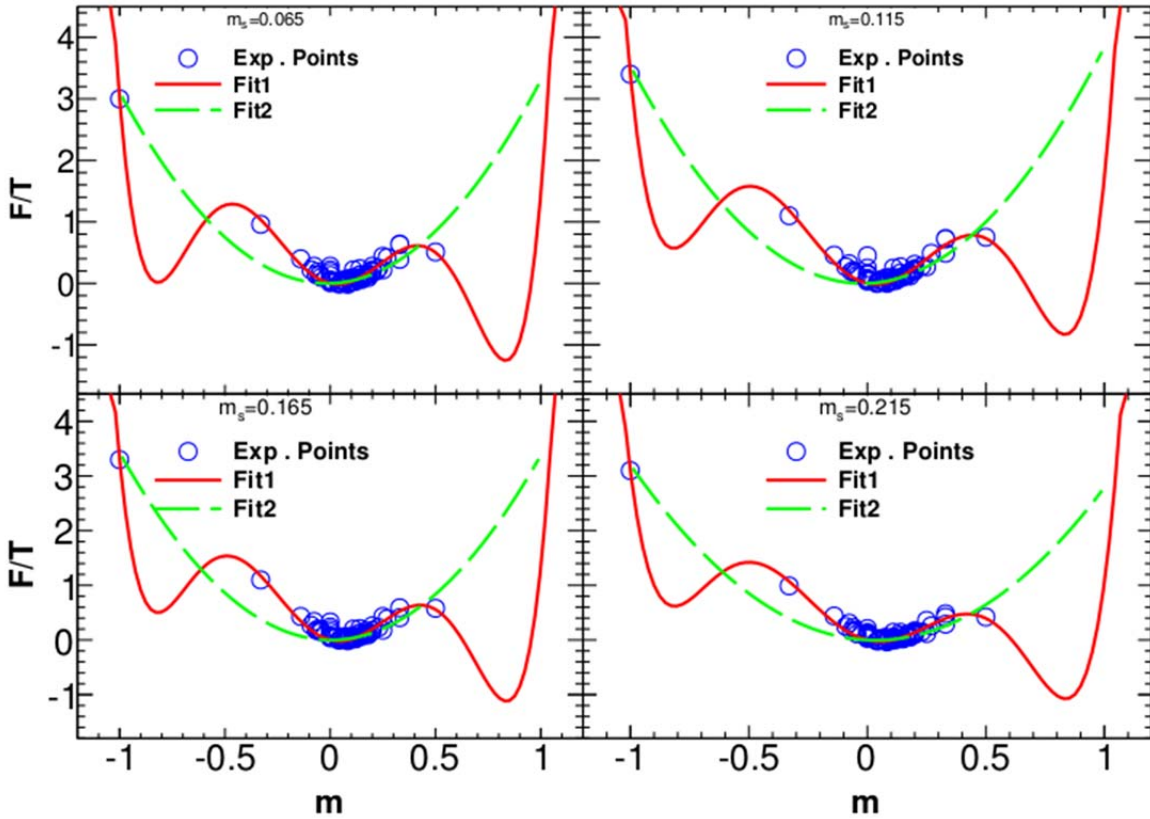


FIG. 1. F/T as a function of fragment isospin asymmetry m . Different panels correspond to different source asymmetry (m_s) bins.

In Fig. 2, the a_p/T values extracted for different m_s bins are plotted as a function of the QP excitation energy. It is observed that a_p/T values systematically decrease with increasing QP excitation energy. These a_p/T values are used to estimate the temperature of the QP for each m_s bin assuming $a_p=12$

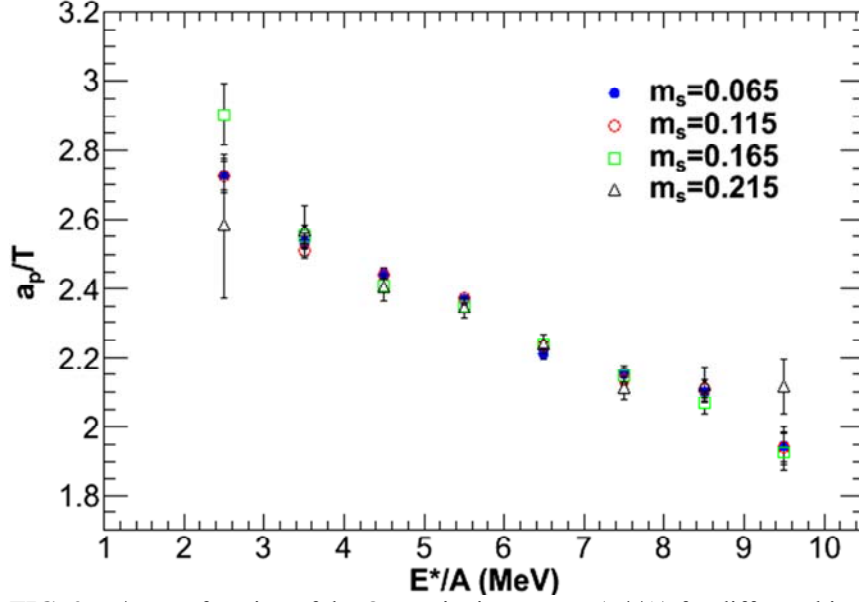


FIG. 2. a_p/T as a function of the QP excitation energy (E^*/A) for different bins in source asymmetry.

MeV. The fitting parameters a , b , c and H/T extracted for each m_s bin are plotted versus the QP excitation energy in Fig.3. The parameters a , b and c which are related to thermodynamic properties of the fragmenting system show a dependence on m_s in addition to their dependence on the excitation energy. H/T shows a systematic increase with increasing m_s . This verifies qualitatively that the external field H is the conjugate variable of m_s . The parameters a , b and c are very close to satisfying the condition for a first order phase transition $b = -4\sqrt{ac}/3$.

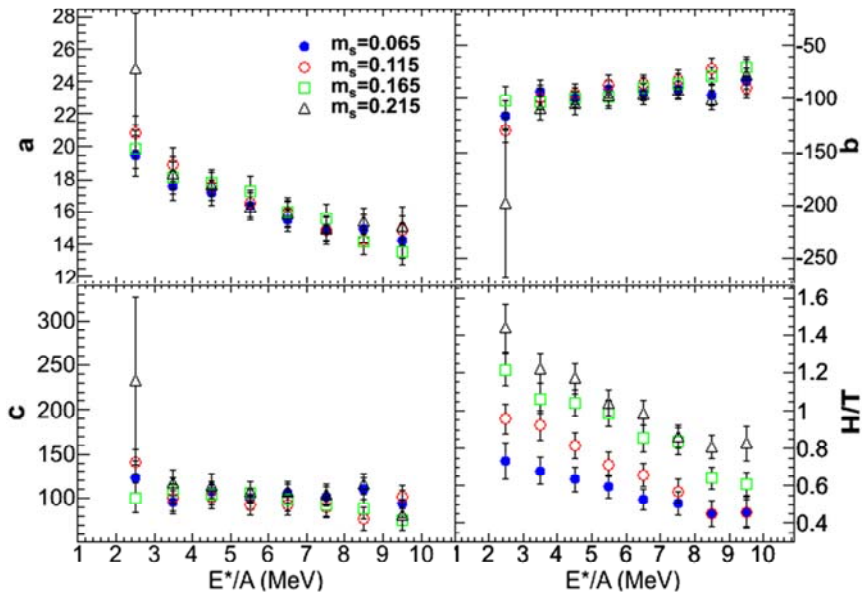


FIG. 3. Fitting parameters a , b , c and H/T obtained from fits to the free energy data as a function of E^*/A for different bins in m_s .

In summary, a detailed analysis of the data on fragment yields within the framework of the Landau free energy approach showed the signature of a first-order phase transition with respect to isospin asymmetry of the fragmenting source. Future work will be to complement these results and temperatures and densities extracted from the new quantum method by Zheng and Bonasera [7, 8].

- [1] A. Bonasera *et al.*, Phys. Rev. Lett. **101**, 122702 (2008).
- [2] M. Huang *et al.*, Phys. Rev. C **81**, 044618 (2010).
- [3] R. Tripathi *et al.*, Phys. Rev. C **83**, 054609 (2011).
- [4] Z. Kohley, PhD Thesis, Texas A&M University, 2010.
- [5] S. Wuenschel *et al.*, Nucl. Phys. **A843**, 1 (2010).
- [6] R. Tripathi *et al.*, Int. J. Mod. Phys. E **21**, 1250019 (2012).
- [7] H. Zheng and A. Bonasera, Phys. Lett. B **696**, 178 (2011).
- [8] H. Zheng and A. Bonasera, (2011), nucl-th/1112.4098.

Signatures of the liquid-gas phase transition from fermionic quantum fluctuations

J. Mabilia, A. Bonasera, H. Zheng, A.B. McIntosh, L.W. May, P. Cammarata, Z. Kohley, K. Hagel, L. Heilborn, A. Zarrella, A. Raphelt, and S.J. Yennello

Heavy-ion collisions at the Fermi scale are dominated by nuclear fragmentation, the breakup of a nuclear system into several intermediate sized pieces, and are often used to explore the phase diagram of nuclear matter. Because of the van der Waals nature of the nucleon-nucleon interaction, it is believed that nuclear matter is likely to exhibit a liquid-gas phase transition [1–3]. However, unlike van der Waals fluids, nuclei are finite two-component systems. Most of the divergences usually linked to a phase transition in macroscopic systems are washed out in these small systems [4]. Also, the additional degree of freedom which is related to proton and neutron concentrations makes phase transitions more complex [5]. The phase transition should therefore manifest itself through different signals. Several attempts were made in the past to investigate the relationship between multifragmentation and a liquid-gas phase transition. For example, caloric curves were examined [2, 6], critical exponents were determined [7] and negative heat capacities were observed [8]. However, because of the assumptions made in these studies the system could not be located in pressure-density-temperature space [9]. In the present study, the experimental temperatures and densities of the fragmenting systems are determined using a new quantum method presented in Ref. [10, 11]. Experimental pressures are extracted making use of the grand partition function of Fisher’s droplet model [12].

The experiment was performed at the Texas A&M University Cyclotron Institute. Beams of ^{64}Zn , ^{64}Ni and ^{70}Zn at 35 MeV/nucleon were incident on ^{64}Zn , ^{64}Ni and ^{70}Zn targets, respectively [13]. Charged particles and neutrons were measured using the NIMROD-ISiS 4π detector array [14]. The granularity and excellent isotopic resolution provided by the array enabled the reconstruction of the quasi-projectile (QP), the hot projectile-like source produced in the early stage of the collision, in both Z and A . The NIMROD-ISiS charged particle array is housed inside the TAMU Neutron Ball. The Neutron Ball provides experimental information on the free neutrons emitted during a reaction. The QP source was selected by means of event-by-event cuts on the experimental data as in Ref. [15] with its mass restricted to be in the range $54 \leq A \leq 64$. Its excitation energy was deduced using the measured free neutron multiplicity, the charged particle kinetic energies, and the Q -value of the breakup. Data were sorted into four different source asymmetry ($m_s = (N - Z)/A$) bins ranging from 0.04 to 0.24 with bin width of 0.05. In addition, effects of QP excitation energies on the thermodynamic quantities were investigated by gating the data into nine bins of 1 MeV in the range of 1-10 MeV/nucleon.

The temperatures and densities of the selected QP 's have been extracted from the momentum quadrupole and multiplicity fluctuations with protons as a probe particle. Full details of the calculations are reported in Refs. [10, 11]. The corresponding pressures were calculated by making use of the grand partition function from Fisher’s droplet model described in Ref. [12]. In Fig.1 (left panel), the critical exponent β which describes the nature of singularity in density (ρ) and temperature (T) at the critical point is determined by fitting $1-\rho/\rho_c$ versus $1-T/T_c$. The critical values ρ_c and T_c for each m_s bin are determined using Guggenheim's equation [9] to fit ρ versus T curves. Calculated pressures (P) normalized

to the critical values (P_c) are plotted versus the inverse of the reduced temperature (T_c/T) in Fig.1 (right panel).

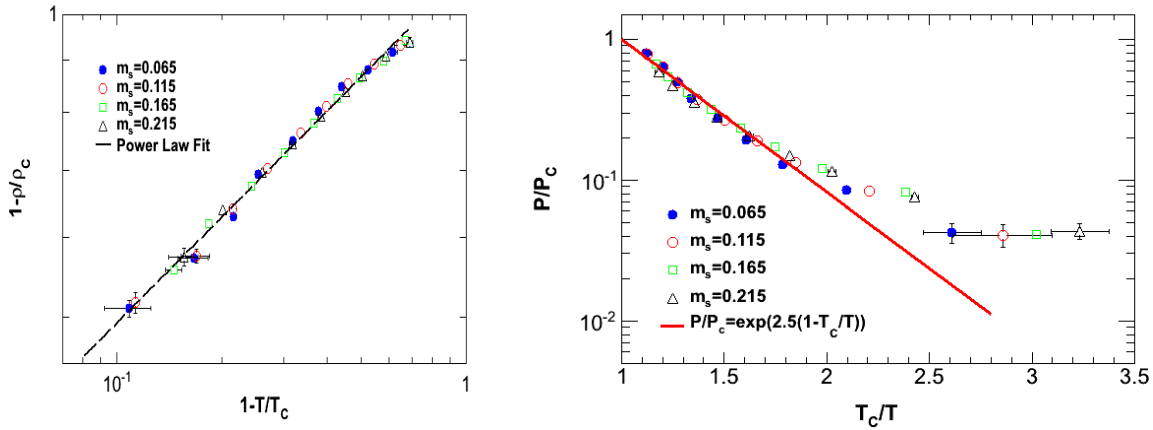


FIG. 1. (Left panel) The extraction of the critical exponent β . The dash line represents a fit to a power law. (Right panel) The reduced pressure as a function of the inverse of the reduced temperature. The solid line shows a fit to the Clausius-Clapeyron equation [9].

The temperature, the density and the pressure of the selected fragmenting sources and the corresponding critical values have shown a dependence on the source asymmetry. The extracted critical exponent $\beta = 0.355 \pm 0.014$ is in the range of extracted experimental values from a variety of systems [9]. Calculated critical compressibility factor values ($P_c/\rho_c T_c$) have shown an increase when increasing m_s and are very close to those for several fluids [9]. These results provide strong evidence for a signature of a nuclear liquid-gas phase transition.

- [1] H. Jaqaman, A.Z. Mekjian, and L. Zamick, Phys. Rev. C **27**, 2782 (1983).
- [2] J. Pochodzalla *et al.*, Phys. Rev. Lett. **75**, 1040 (1995).
- [3] L. Satpathy, M. Mishra, and R. Nayak, Phys. Rev. C **39**, 162 (1989).
- [4] P. Chomaz and F. Gulminelli, Nucl. Phys. **A749**, 3c (2005).
- [5] S.J. Lee and A.Z. Mekjian, Phys. Rev. C **68**, 014608 (2003).
- [6] J.B. Natowitz *et al.*, Phys. Rev. C **65**, 034618 (2002).
- [7] J. E. Finn *et al.*, Phys. Rev. Lett. **49**, 1321 (1982).
- [8] M. D'Agostino *et al.*, Phys.Lett. B **473**, 219 (2000).
- [9] J. B. Elliott *et al.*, Phys. Rev. C **67**, 024609 (2003).
- [10] H. Zheng and A. Bonasera, Phys. Lett. B **696**, 178 (2011).
- [11] H. Zheng and A. Bonasera, nucl-th/1112.4098 (2011).
- [12] P. Finocchiaro, M. Belkacem, T. Kubo, V. Latora, and A. Bonasera, Nucl. Phys. **A600**, 236 (1996).
- [13] Z. Kohley, PhD Thesis, Texas A&M University, 2010.
- [14] S. Wuenschel *et al.*, Nucl. Instrum.Methods Phys. Res. **A604**, 578 (2009).
- [15] S. Wuenschel *et al.*, Nucl. Phys. **A843**, 1 (2010).

Equation of state effects on Nucleon Transport

L.W. May, P. Cammarata, L. Heilborn, J. Mabiala, A. McIntosh, A. Rappelt,
A. Zarrella, and S. J. Yennello

The nuclear equation-of-state (EoS) has been well studied for symmetric nuclear matter at nuclear saturation densities. However, there are not strong constraints on the density dependence of the symmetry energy at sub-saturation densities. Nucleon transport, which includes isospin drift and diffusion, describes the interaction and movement of nucleons between projectile and target in a nuclear reaction. Isospin diffusion, the transport of nucleons due to differences in isospin content, can be used to further constrain the density dependence of the symmetry energy [1,2].

Transport calculations (like the isospin-dependent Boltzmann-Uehling-Uhlenbeck, or iBUU model) utilize test particles and a mean-field potential to simulate the interaction of particles during a nuclear reaction [3,4]. By examining the behavior of these test particles under different impact parameters for various inputs, information about the transport of nucleons can be determined. Reactions for 35 MeV/u $^{70,64}\text{Zn}$, $^{64}\text{Ni}+^{70,64}\text{Zn}$, ^{64}Ni as seen in Table 1 were modeled using iBUU04. The reactions were allowed to run out to 100 fm/c, where it was determined that the quasi-projectile (QP) and quasi-target (QT) were well separated while only a modest number of test particles had been lost outside of the bounding box of the model.

Table I. These reactions were simulated over a range of impact parameters at 35 MeV/u using the iBUU04 transport code. Listed are the N/Z content of the initial system projectile, target and composite system.

System	Projectile N/Z	Target N/Z	Composite System N/Z
$^{70}\text{Zn}+^{70}\text{Zn}$	1.333	1.333	1.333
$^{70}\text{Zn}+^{64}\text{Zn}$	1.333	1.133	1.233
$^{64}\text{Zn}+^{64}\text{Zn}$	1.133	1.133	1.133
$^{64}\text{Zn}+^{64}\text{Ni}$	1.133	1.286	1.207
$^{64}\text{Ni}+^{64}\text{Ni}$	1.286	1.286	1.286

The QP (and QT) is defined from the test particle output via an algorithm which cuts particles which do not match certain criteria. First, a geometry cut is defined by a line that connects the two highest test particle density centers (i.e. the centers of the QP and QT) located in the simulation. A perpendicular bisector of this line is calculated. Everything on the target side is tentatively identified with the QT while test particles on the projectile side are identified with the QP. A spherical density cut is then applied to the center of the QP (and QT) to better define a “source.” A set of vectors defining a spherical shell are matched in magnitude to the low density region radially away from the QP (QT) corresponding to $\rho_0/10$. These distances are then averaged, and a sphere of this radius is generated around the high-density center. All test particles inside the sphere are chosen as part of the QP (QT respectively).

The simulation is run over a large range in impact parameter, from 0fm (central collisions) out to 10fm (approximately touching-spheres for all systems). Small impact parameters (more violent collisions) correspond to increased exchange of matter. The QP exchanges matter with the target as you move to more central collisions while the QT exhibits similar behavior, exchanging matter with the projectile. Similar behavior for QP and QT of gain and loss of particles is largely independent of system and parameterization of EoS.

As seen in the top left panel of Fig. 1, the N/Z content mostly matches that of the composite system (black line) for the symmetric $^{70}\text{Zn}+^{70}\text{Zn}$ system for a “stiff” interaction ($x=-2$ parameter in iBUU). A slight dip in N/Z at mid-peripheral impact parameters could indicate loss of high N/Z content to the predicted high N/Z “neck” formation in collisions at these energies. Additionally, high N/Z at very central impact parameters could suggest that loss of nuclear matter to the surrounding “gas” may be rich in N=Z content.

In the middle left and lower left panels we see that for the asymmetric reactions, QP and QT N/Z begin near the value of the initial projectile and target N/Z contents, respectively. Decreased impact parameter (small b) implies longer contact time between projectile and target, which could allow more N/Z mixing to occur. While QP and QT N/Z do not approach composite system N/Z, the similarity between QP and QT N/Z at small impact parameters suggests N/Z equilibration. Deviation of the N/Z value from that of the composite system could be the result of nucleons migrating to the neck region and evaporating to the surrounding gas.

The top right panel of Fig. 1 (which is the same as the top left panel, but for “soft” interaction, iBUU MDI parameter $x=1$) shows that the N/Z content mirrors that of the composite system (black line) with a slight drop in N/Z. There is very little variation with impact parameter in the “soft” case. The middle right and lower right panels show the “soft” case for the asymmetric systems. Similar to the “stiff” case, the “soft” QP and QT N/Z begin near initial projectile and target N/Z values, respectively, while the QP and QT N/Z converge at small impact parameters to the values of the composite systems. The “soft” symmetry energy reaches N/Z equilibrium (convergence between QP and QT) at a much larger impact parameter than in the “stiff” case. This is similar to the effect seen by Tsang *et. al.* and Baran *et. al.* when looking at equilibration as a function of time[5,6]. We can see from comparing the left and right sides of Fig. 1 that the form of the symmetry energy has a large impact on the QP and its composition. Baran *et. al.* has also predicted the isospin dependence of neck formation/breakup and emission to the gas that is consistent with this work. It may be possible to examine the “neck” and “gas” emission experimentally, this will be investigated further. It is clear that impact parameter determination will also be critical for event characterization and analysis of these effects in the experimental data. Work will continue on the simulations to find a surrogate for the impact parameter, since impact parameter cannot be directly measured experimentally.

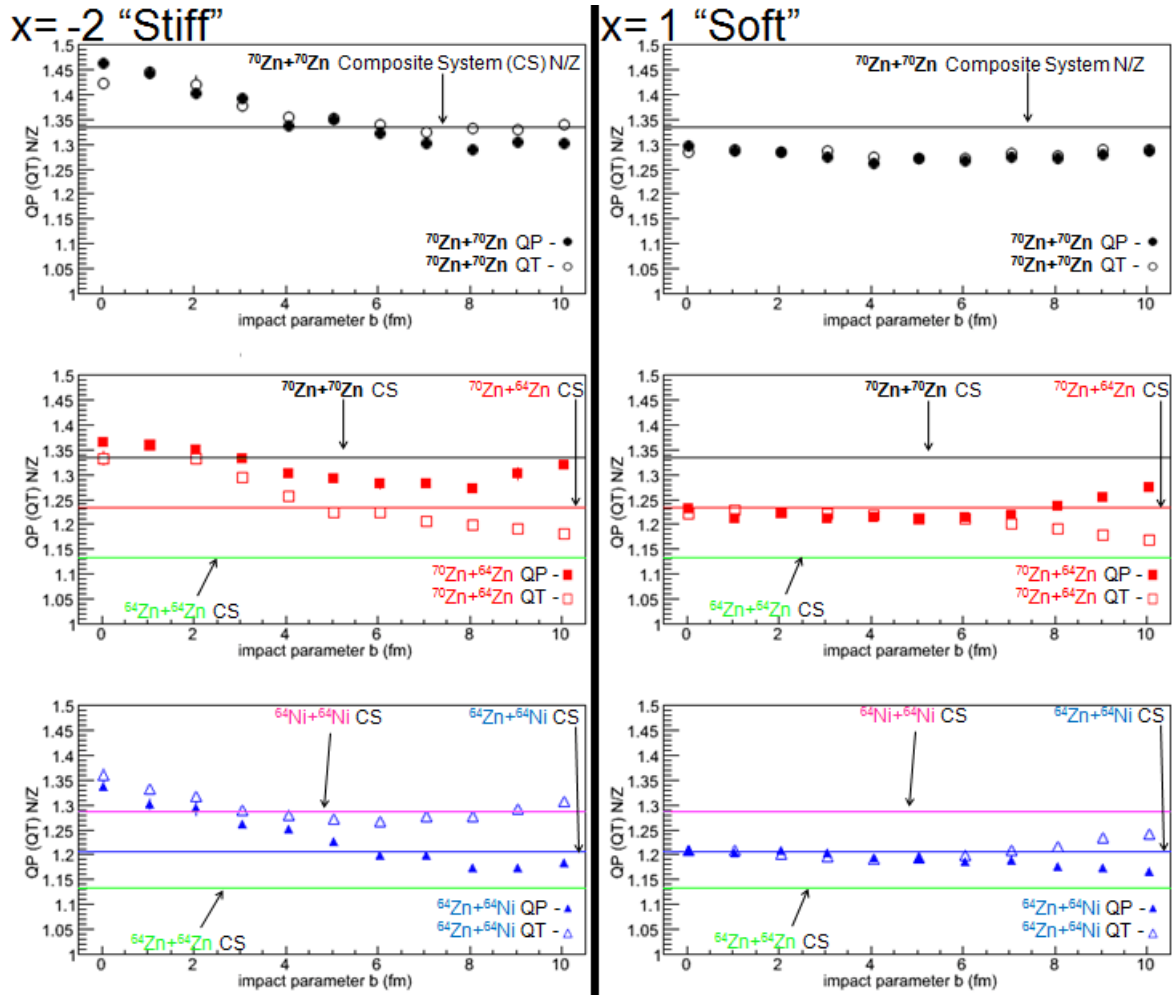


FIG. 1. The N/Z content of QP and QT by impact parameter for various systems and EoS. **Top panels:** For the symmetric $^{70}\text{Zn}+^{70}\text{Zn}$ reaction, the N/Z content of the QP (solid) and QT (open) are shown with the composite system (black line). **Middle panels:** For the mass asymmetric $^{70}\text{Zn}+^{64}\text{Zn}$ reaction, QP (solid red square) and QT (open red square) N/Z are shown with projectile (black line), target (green line) and composite system (red line) N/Z. **Lower panels:** For the charge asymmetric $^{64}\text{Zn}+^{64}\text{Ni}$ reaction, QP (solid blue triangle) and QT (open blue triangle) N/Z are shown with projectile (green line), target (pink line) and composite system (blue line) N/Z.

- [1] A.L. Keksis *et al.* Phys. Rev. C **81**, 054602 (2010).
- [2] M.B. Tsang *et al.* Phys. Rev. Lett. **92**, 062701 (2004).
- [3] Bao-An Li *et al.* Phys. Rev. C **69**, 011603 (2004).
- [4] Bao-An Li *et al.* Nucl. Phys. **A735**, 563 (2004).
- [5] M.B. Tsang, *et al.* Phys. Rev. Lett. **92**, 062701 (2004).
- [6] V. Baran, *et al.* Phys. Rev. C **72**, 064620 (2005).

Probing the symmetry energy at high energies with the ASY-EOS collaborations at GSI

Paul Cammarata, Lauren Heilborn, Larry May, Paola Marini, and S.J. Yennello
for Asy-EOS Collaboration

The nuclear equation of state (EoS) of asymmetric nuclear matter is also a quantity of crucial significance in understanding the physics of isolated and binary neutron stars, type II supernovae and neutron star mergers. Experimental information about the EoS can help to provide improved predictions for neutron star observables such as stellar radii and moments of inertia, crustal vibration frequencies and neutron star cooling rates [1, 2], which are currently being investigated with ground-based and satellite observatories. The symmetry energy is not well constrained at supra-saturation densities (Fig. 1). This is especially true in the range $\rho \geq 2\rho_0$ where there are the greatest theoretical uncertainties. The behaviour of the symmetry energy at supra-saturation densities can be explored in terrestrial laboratories by using relativistic heavy-ion collisions of isospin asymmetric nuclei. Elliptic neutron and proton flow, neutron-proton double yield and fragment ratios, as well as, flows in relativistic isospin-asymmetric heavy-ion collisions are predicted to be sensitive to the density dependence of the symmetry energy.

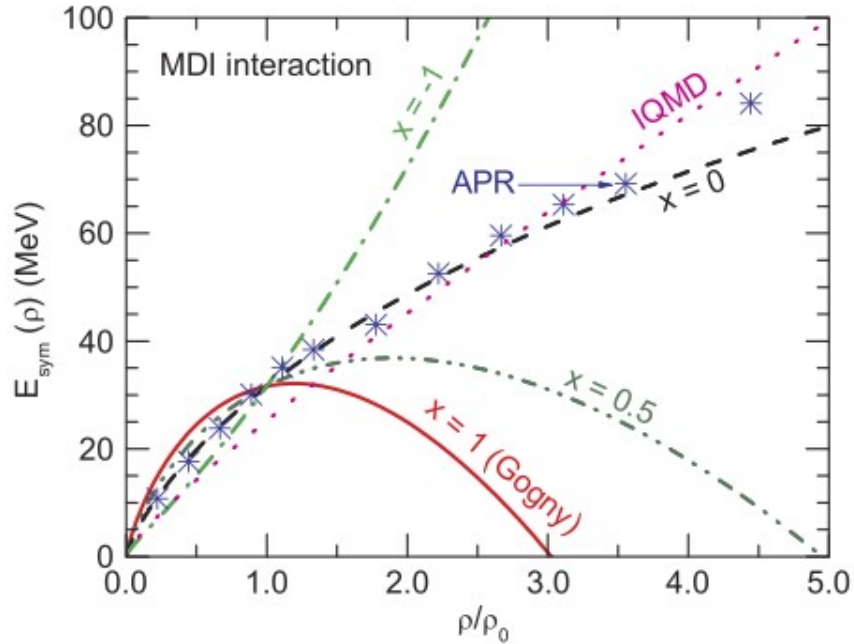


FIG. 1. Compilation of the theoretical symmetry energy vs normalized nuclear density [3].

For this experiment, the collaboration used reaction systems of $^{197}\text{Au}+^{197}\text{Au}$ at 800A MeV, $^{197}\text{Au}+^{197}\text{Au}$, $^{96}\text{Ru}+^{96}\text{Ru}$ (RuO_2), and $^{96}\text{Zn}+^{96}\text{Zn}$ (ZnO_2) at 400A MeV. Detector arrays from around the world were set up to collect data in a common trigger. The CsI(Tl) Rings 4-8 of MicroBall [4] were

installed around the target for multiplicity measurements to discriminate beam-target reactions from the reactions with lighter nuclei in air. Downstream (Fig. 2) CHIMERA [5] (Charge Heavy Ion Mass and Energy Resolving Array) was used for impact parameter determination and particle identification of reaction products from $7 - 20^\circ \theta$. To help veto reactions in air downstream of the target, a He pipe was installed before CHIMERA for the Ru and Zn systems.

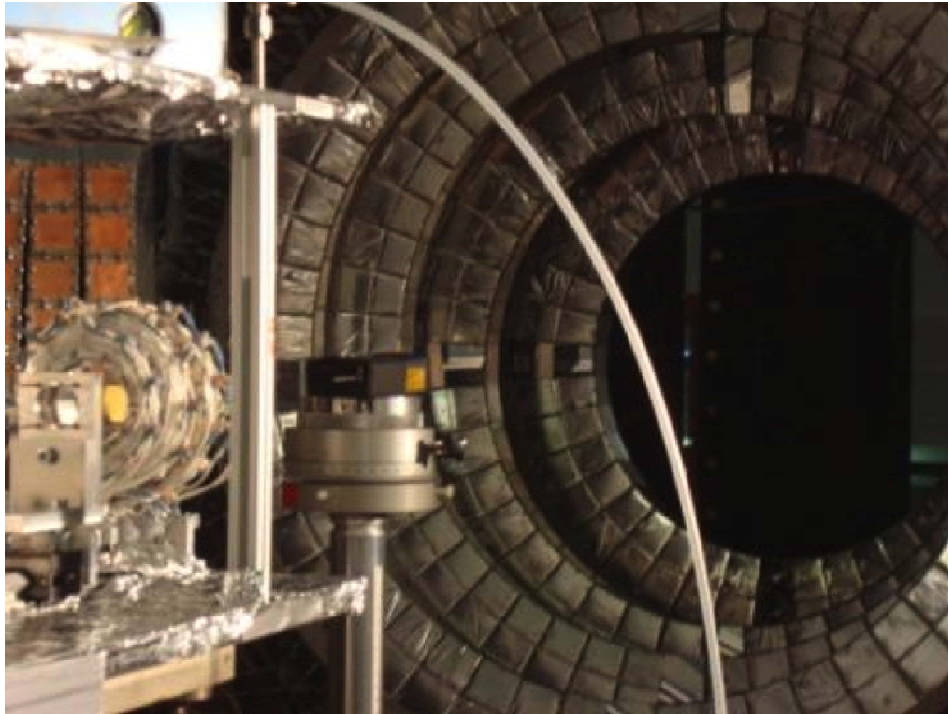


FIG. 2. MircoBall with CHIMERA downstream in the experimental configuration.

The ALADIN-ToF Wall [6] (Time of Flight Wall), constructed of dual-layered scintillator, was placed behind CHIMERA. The angular coverage of $0 - 8^\circ \theta$ overlapped with CHIMERA for particle identification of the reaction products. In addition, the Krakow PHOSwitch and LAND [7] (Large Area Neutron Detector) were placed at 60° and 45° off beam axis respectively. The PHOSwitch, located in close proximity to MicroBall and constructed of 35 Si-Si-Si-CsI stacked detectors, was used for mid-rapidity IMF (intermediate mass fragment) detection. LAND, constructed of plastic scintillator sandwiched Fe with 20 paddles per layer, was used to detect the neutrons in mid-rapidity complimentary to the IMFs in the PHOSwitch.

The American contingent, was responsible for the setup and operation of the MicroBall detector during the experiment, along with, the data analysis scripting after the experiment to analyze the data. Initial data suggests that the MicroBall should be successful in detecting reactions in air vs reactions between the beam and target based on multiplicities collected during the initial calibration runs (Fig. 3). The green lines shows $^{197}\text{Au} + ^{197}\text{Au}$ at 400A MeV with the target removed, thus yielding reaction products due to Au beam incident on air (N_2 and O_2).

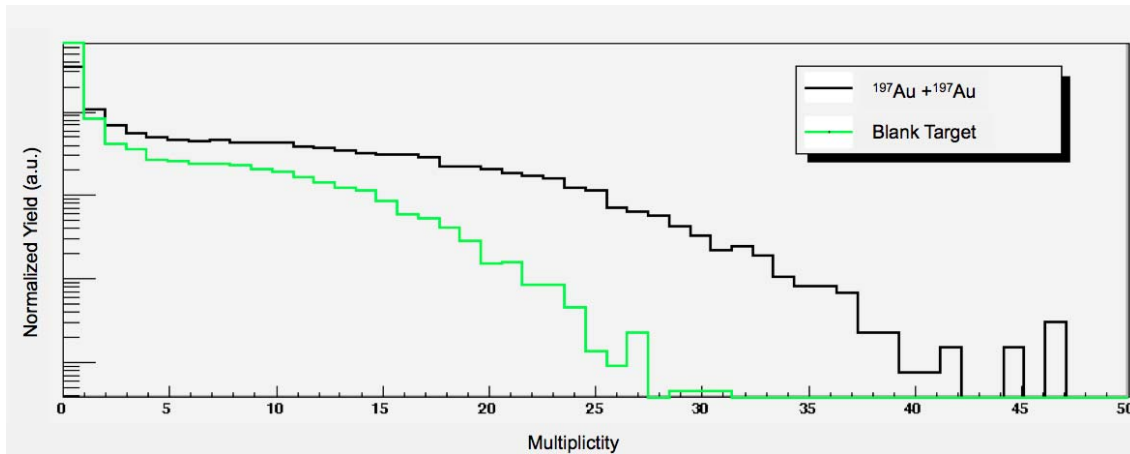


FIG. 3. Multiplicities from MicroBall calibration run. Green line shows multiplicity of beam in air (target removed) and black shows beam on target.

The collaboration has completed the synchronization of the data from each detector and has set up a computational scheme to read in synchronized data for combined analysis. The calibration of CHIMERA has been successful. As of the date of this report, we are continuing to calibrate the remaining detectors this summer and hope to begin data analysis later this fall.

- [1] J.M. Lattimer and M. Prakash, *Science* 304, 536 (2004); <http://www.sciencemag.org/content/304/5670/536.full.pdf>, URL <http://www.sciencemag.org/content/304/5670/536.abstract>.
- [2] A. Steiner, M. Prakash, J. Lattimer, and P. Ellis, *Phys. Rep.* 411, 325 (2005); ISSN 0370-1573, URL <http://www.sciencedirect.com/science/article/pii/S0370157305001043>.
- [3] B.-A. Li, L.-W. Chen, and C.M. Ko, *Phys. Rep.* 464, 113 (2008); ISSN 0370-1573, URL <http://www.sciencedirect.com/science/article/pii/S0370157308001269>.
- [4] D. Sarantites, P.-F. Hua, M. Devlin, L. Sobotka, J. Elson, J. Hood, D. LaFosse, J. Sarantites, and M. Maier, *Nucl. Instrum. Methods Phys. Res. A* 381, 418 (1996); ISSN 0168-9002, URL <http://www.sciencedirect.com/science/article/pii/S0168900296007851>.
- [4] D. Sarantites, P.-F. Hua, M. Devlin, L. Sobotka, J. Elson, J. Hood, D. LaFosse, J. Sarantites, and M. Maier, *Nucl. Instrum. Methods Phys. Res. A* 381, 418 (1996); ISSN 0168-9002, URL <http://www.sciencedirect.com/science/article/pii/S0168900296007851>.
- [6] J. Hubele, P. Kreuzt, J. C. Adloff, M. Begemann-Blaich, P. Bouissou, G. Imme, I. Iori, G. J. Kunde, S. Leray, V. Lindenstruth, *et al.*, *Z. Phys. A* 340, 263 (1991); ISSN 0939-7922, 10.1007/BF01294674, URL <http://dx.doi.org/10.1007/BF01294674>.
- [7] T. Blaich, T. Elze, H. Emling, H. Freiesleben, K. Grimm, W. Henning, R. Holzmann, G. Ickert, J. Keller, H. Klingler *et al.*, *Nucl. Instrum. Methods Phys. Res. A* 314, 136 (1992), ISSN 0168-9002, URL <http://www.sciencedirect.com/science/article/pii/016890029290507Z>.

Using break-up mechanisms in heavy ion collisions at low energies to constrain the symmetry energy at low nuclear density

Paul Cammarata, Alan McIntosh, Lauren Heilborn, Larry May, Andrew Raphelt,
Andrew Zarrella, and S.J. Yennello

Nuclear reactions just below the Fermi energy present a unique opportunity for probing the dynamics of nuclear matter below normal nuclear density using shape fluctuations, spin and relative multiplicities of the resulting fragments. The results of these interactions are theorized to be dependent upon and sensitive to the symmetry energy. Composite systems resulting from semi-peripheral collisions may exhibit prolate (elongated) shape with a large associated angular momentum. More neutron-rich nuclear reactions are expected to have a greater sensitivity to the density dependence of the symmetry energy through observing ternary or quaternary breaking after re-separation [1].

Using the results from DiToro *et al.* [1] (Fig. 1) as motivation, simulations using TWINGO code [2-7] (a stochastic mean field approach) have been used to calculate the fluctuations in quadrupole and octupole moments in momentum space. This was done in order to facilitate the prediction of

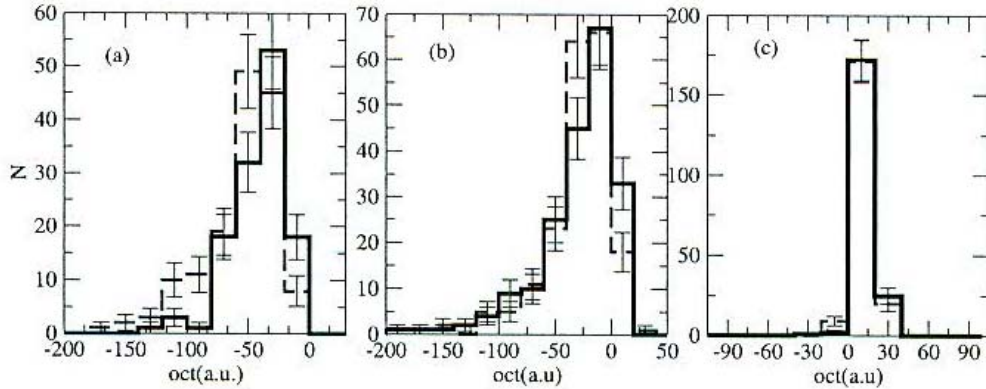


FIG. 1. Octupole fluctuations of the primary fragments (in position space) for $^{132}\text{Sn}+^{64}\text{Ni}$ at 10A MeV. In dashed = asy-stiff, solid= asy-soft [1]. (a) $b = 6$ fm (b) $b = 7$ fm (c) $b = 8$ fm.

the relative expected ternary (quaternary) breaking of the PLF (and TLF) resulting from semi-peripheral interactions of heavy nuclei below the Fermi energy. Using $^{124}\text{Sn}+^{64}\text{Ni}$ at 15A MeV, Fig. 2 shows the cluster identified results of TWINGO resulting from the mean field interaction. In this way we can see that there are noticeable differences in the quadrupole and octupole fluctuations with respect to the symmetry energy. It is expected that reactions using $^{124,136}\text{Xe}$ instead of ^{124}Sn should exhibit the same signatures. In addition, to gain an insight into the observables pertinent to the experiment on long time scales, CoMD (Constant rained Molecular Dynamics [8, 9]) has been used. In Fig. 3, we can see there is a noticeable difference in the multiplicity of the $Z \geq 3$ fragments.

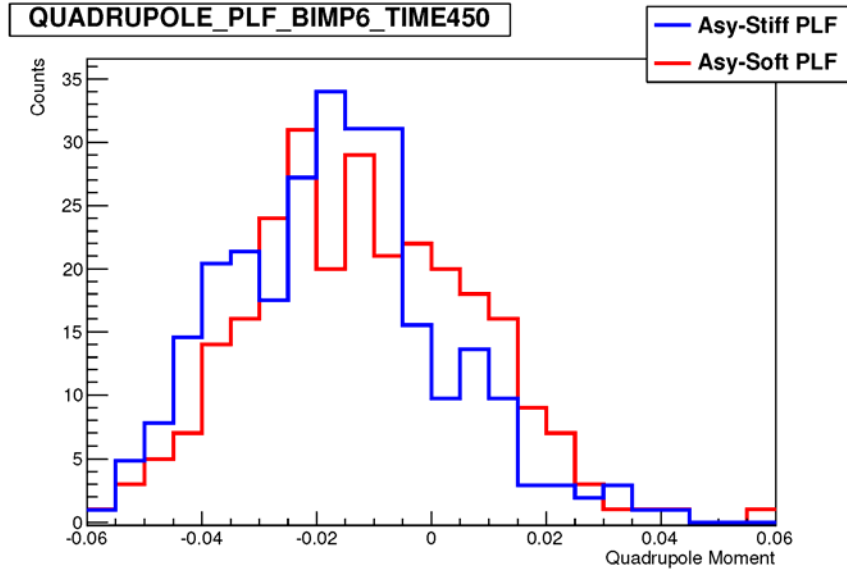


FIG. 2. Quadrupole fluctuation of the projectile-like-fragment (PLF) via TWINGO code.

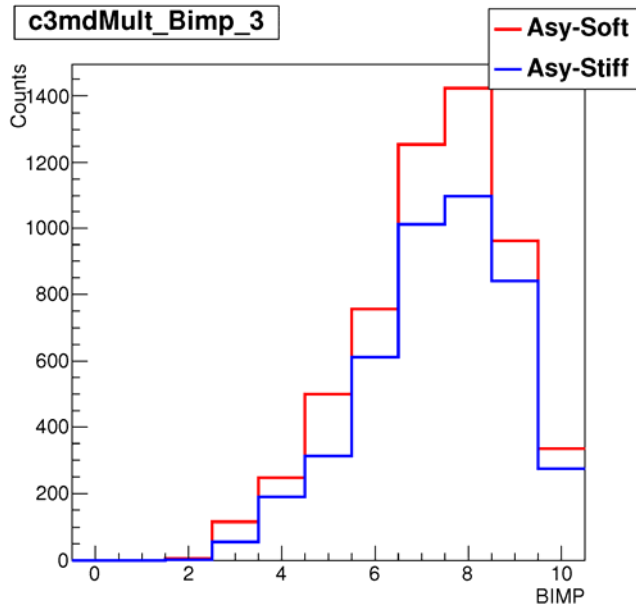


FIG. 3. CoMD events shown where the multiplicity = 3 for $Z \geq 3$ particles as a function of impact parameter and symmetry energy.

In order to probe these fluctuations in octupole and quadrupole moments and their effects on the breaking of the projectile-like-fragment (PLF), an experiment must be designed to specifically cater to the lower energy reaction products typically produced in the subsequent (dynamic) fission of the PLF. One of the observables, dependent on the multiplicity distribution from CoMD mentioned above, is a mass partitioning of the products emanating from the breakup of the PLF. Therefore, it will be

necessary to measure the mass of the fragments via time-of-flight techniques in this lower energy regime. Time-of-flight methods are necessary as Z identification will not be feasible using standard $\Delta E-E$ methods. To this end, we have conducted experimental tests using an accelerated beam of ^{129}Xe to measure the expected time and energy resolution of the timing pre-amplifier and silicon detector combination. Using the Forward Array Using Silicon Technology (FAUST) [10] in combination with the timing pick-off preamplifiers and a fast time zero detector (micro-channel plate detector), we expect to measure the symmetry energy dependence of the dynamic fission of the PLF. We have demonstrated (Fig. 4) that we were able to achieve a time resolution of 135ps (FWHM) corresponding to a mass resolution of 1 mass unit. In combination with the Si timing-pick off amplifiers, a micro-channel plate time-zero detector should provide the timing resolution to detect the mass of the expected heavy ions [11]. The retrofit upgrade of FAUST for Time-of-Flight (ToF) capabilities, with excellent timing resolution (100's of pico-seconds) is currently underway and is expected to be completed by mid-fall 2012.

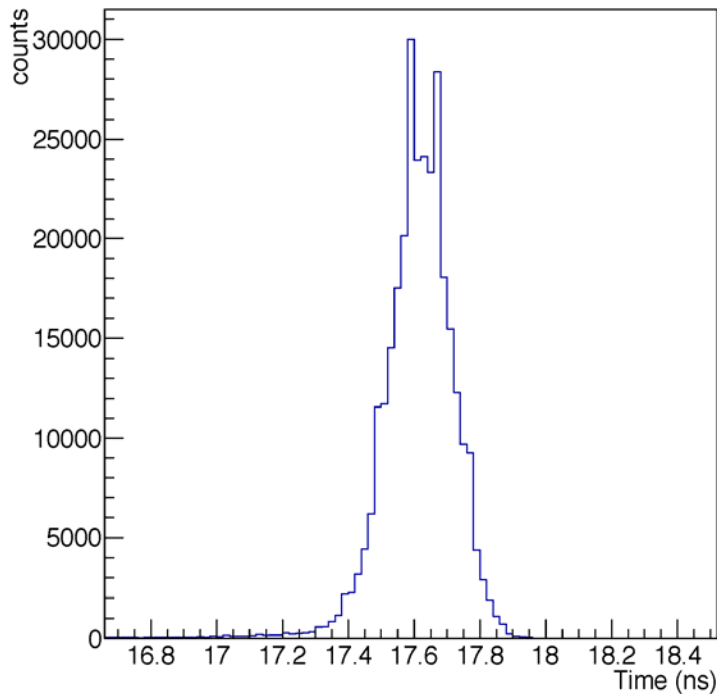


FIG. 4. Time resolution of the 300 μm Si detector with timing pick-off.

Based on the experimental and theoretical results, probing the fragmentation mechanism competition of the primary nuclei and neck fragmentation at low-intermediate energies in heavy, asymmetric systems could provide additional constraints on the symmetry energy at low nuclear density. Initial simulations have been performed using CoMD and TWINGO (a stochastic mean field simulations) to predict the prevalence of the reaction observables. However, because of the time intensive nature of the computations, more statistics are needed to enhance the effects of the symmetry energy.

- [1] M.D. Toro, V. Baran, M. Colonna, G. Ferini, T. Gaitanos, V. Greco, J. Rizzo, and H. Wolter, Nucl. Phys. **A787**, 585 (2007); URL <http://www.sciencedirect.com/science/article/pii/S0375947406010682>.
- [2] V. Greco, A. Guarnera, M. Colonna, and M. Di Toro, Phys. Rev. C **59**, 810 (1999); URL <http://link.aps.org/doi/10.1103/PhysRevC.59.810>.
- [3] A. Bonasera and F. Gulminelli, Phys. Lett. B **259**, 399 (1991).
- [4] A. Bonasera, G. Burgio, and M. D. Toro, Phys. Lett. B **221**, 233 (1989); ISSN 0370-2693, URL <http://sciencedirect.com/science/article/pii/0370269389917036>.
- [5] A. Bonasera, F. Gulminelli, and J. Molitoris, Phys. Rep. **243**, 1 (1994); ISSN 0370-1573, URL <http://www.sciencedirect.com/science/article/pii/0370157394901082>.
- [6] R.J. Lenk and V.R. Pandharipande, Phys. Rev. C **39**, 2242 (1989); URL <http://link.aps.org/doi/10.1103/PhysRevC.39.2242>.
- [7] A. Guarnera, Ph.D. Thesis, University of Caen, 1996.
- [8] M. Papa, T. Maruyama, and A. Bonasera, Phys. Rev. C **64**, 024612 (2001); URL <http://link.aps.org/doi/10.1103/PhysRevC.64.024612>.
- [9] M. Papa, G. Giuliani, and A. Bonasera, J. Comp. Phys. **208**, 403 (2005); ISSN 0021-9991, URL <http://www.sciencedirect.com/science/article/pii/S0021999105000847>.
- [10] F. Gimeno-Nogues, D. Rowland, E. Ramakrishnan, S. Ferro, S. Vasal, R. Gutierrez, R. Olsen, Y.-W. Lui, R. Laforest, H. Johnston *et al.*, Nucl. Instrum. Methods Phys. Res. **A399**, 94 (1997); ISSN 0168-9002, URL <http://www.sciencedirect.com/science/article/pii/S0168900297009236>.
- [11] W. Starzecki, A. Stefanini, S. Luardi, and C. Signorini, Nucl. Instrum. Methods Phys. Res. **193**, 499(1982); ISSN 0167-5087; URL <http://www.sciencedirect.com/science/article/pii/0029554X82902427>.

Temperature dependence of the nuclear caloric curve

A.B. McIntosh, A. Bonasera, Z. Kohley, S. Galanopoulos, K. Hagel, L.W. May,
P. Marini, D.V. Shetty, W.B. Smith, S.N. Soisson, G.A. Souliotis,
B.C. Stein, R. Tripathi, S. Wuenschel, and S.J. Yennello

The relation between temperature and excitation energy for nuclei has been studied in much detail to extract information on the properties of nuclear matter. Recently, a mass-dependence of the nuclear caloric curve has been demonstrated [1]. Dependence on the orthogonal degree of freedom, the neutron-proton asymmetry, is not constrained. Theoretical models differ on the magnitude and even the sign of the asymmetry dependence [2-6]. Observation of such dependence may provide insights into the mechanism of nuclear disassembly, allow for a refined interpretation of fragment yield information (e.g. in isoscaling), provide support for the interaction between a nuclear “gas” and a nuclear “liquid”, and provide a new way to access information on the nuclear asymmetry energy.

Quasi-Projectile (QP) sources produced in symmetric collisions of ^{70}Zn , ^{64}Zn and ^{64}Ni at $E/A = 35\text{MeV}$ were reconstructed event by event using the fragments and free neutrons measured in the NIMROD-ISiS detector array [7] to obtain the charge, mass and excitation energy. The uncertainty in the free neutron measurement has been investigated and does not significantly affect the results shown here. The excitation is determined from the charged particle kinetic energy, the free neutron multiplicity, and the Q-value of the QP breakup. Temperatures are calculated using the quadrupole momentum fluctuation thermometer [8] and the Albergo thermometer [9].

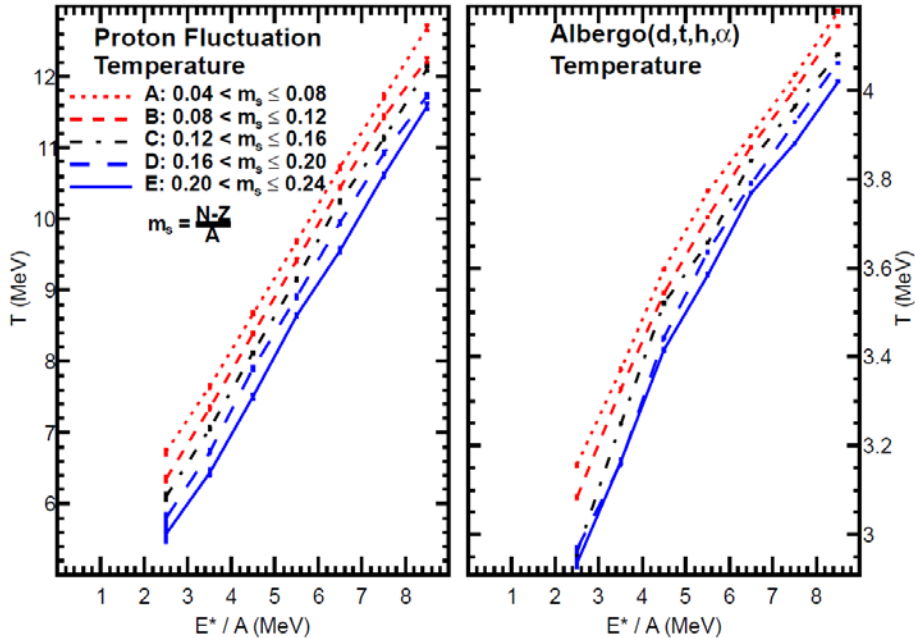


FIG. 1. Caloric curves for isotopically reconstructed sources with mass $48 \leq A \leq 52$. Each curve corresponds to a narrow range in source asymmetry, $m_s = (N-Z)/A$. Left Panel: Temperatures are extracted using the momentum quadrupole fluctuation method. Right Panel: Temperatures are extracted using the Albergo yield ratio method.

The left panel of Fig. 1 shows the caloric curves extracted with the quadrupole fluctuation thermometer using protons as the probe particle for QPs with mass $48 \leq A \leq 52$. Each series of points corresponds to a narrow selection in composition, $m_s = (N-Z)/A$. Increasing the neutron content of the QP shifts the caloric curve to lower temperatures. In fact, the caloric curves for different m_s bins are nearly equally spaced. The right panel of Fig. 1 shows the caloric curves obtained with the Albergo(d,t,h, α) thermometer with the same selections on m_s . Here too, increasing the neutron content lowers the temperature. For both of these thermometers, the change in temperature with changing m_s does not exhibit a dependence on excitation energy. The selection on the asymmetry of the QP rather than the asymmetry of the initial system is important since the initial systems each have broad and largely overlapping distributions of QP asymmetry.

The dependence of the change in temperature, ΔT , between two sources as a function of Δm_s , the difference in their compositions, is shown in Fig. 2. The change in temperature has been averaged over excitation. Both thermometers exhibit a negative correlation of ΔT with Δm_s , and both are well described by a linear fit over the broad range in source asymmetry, with slope -7.3 MeV for the momentum quadrupole fluctuation temperature and -1.2 MeV for the Albergo temperature. Other charged particle probes of the quadrupole momentum fluctuation temperature also show linear trends of ΔT with Δm_s with slopes of the same order of magnitude. This result may be compared to the recent result from the ALADIN collaboration [10]. How the asymmetry dependence changes as the reaction mechanism evolves from evaporation to multifragmentation will be the focus of future studies.

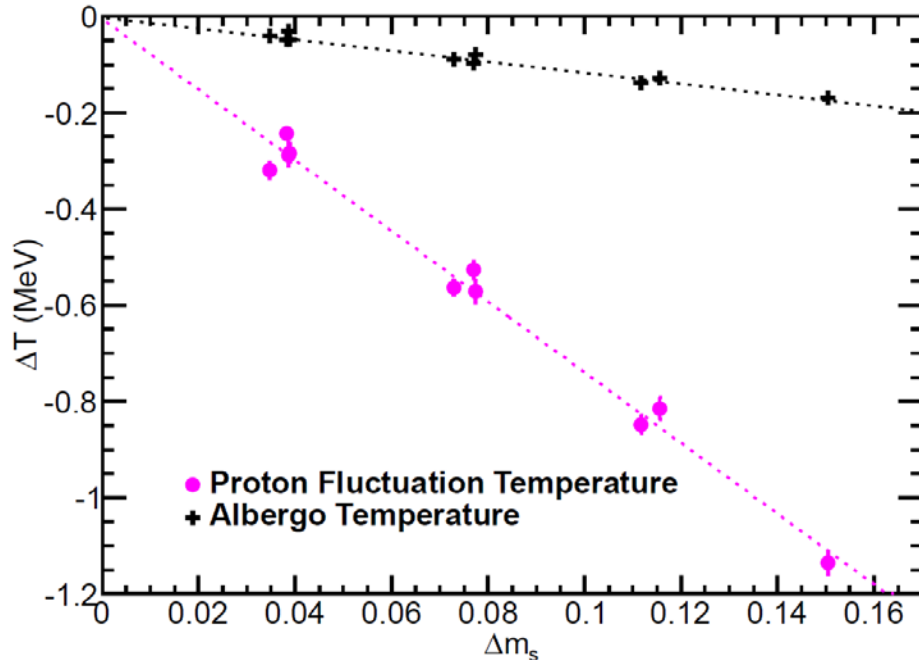


FIG. 2. Change in temperature as a function of the change in source asymmetry $m_s = (N-Z)/A$. The dashed lines are linear fits to the experimental data.

[1] J.B. Natowitz *et al.*, Phys. Rev. C **65**, 034618 (2002).

- [2] V.M. Kolomietz, A.I. Sanzhur, S. Shlomo and S.A Firin, Phys. Rev. C **64**, 024315 (2001).
- [3] C. Hoel, L.G. Sobotka and R.J. Charity, Phys. Rev. C **75**, 017601 (2007).
- [4] J. Besprosvany and S. Levit, Phys. Lett. B **217**, 1 (1989).
- [5] R. Ogul and A.S. Botvina, Phys. Rev. C **66**, 051601(R) (2002).
- [6] J. Su and F.S. Zhang, Phys. Rev. C **84**, 037601 (2011).
- [7] S. Wuenschel et al., Nucl. Instrum. Methods Phys. Res. **A604**, 578 (2009).
- [8] H. Zheng and A. Bonasera, Phys. Lett. B **696**, 178 (2011).
- [9] S. Albergo *et al.*, Il Nuovo Cimento **89**, 1 (1985).
- [10] C. Sfienti *et al.*, Phys. Rev. Lett. **102**, 152701 (2009).

Correlation functions in constrained molecular dynamics (CoMD)

Lauren Heilborn, H. Zheng, Z. Kohley and SJY Group

The interactions between nucleons (proton-proton, neutron-neutron, proton-neutron) are not particularly well constrained, and continue to be an area of study [1-3]. One method for characterizing these interactions is through correlation functions, which can graphically and numerically show the effects from quantum, Coulomb, and other interactions between nucleons. The shape of correlation functions is strongly influenced by these effects, and correlation functions have long been used to extract spatial and temporal information about the excited emitting sources [1,2,4,5]. Theoretical predictions have suggested that the contribution of the symmetry potential to the behavior of nucleon-nucleon interactions may be large enough that neutron-neutron, proton-proton, and neutron-proton correlation functions are sensitive to the size of the source and the timescale of particle emission [3]. The shape of the correlation functions may therefore be sensitive to the symmetry energy in the nuclear equation-of-state. Constrained Molecular Dynamics (CoMD) simulations of neutron-rich and neutron-poor calcium on nickel systems have been run using two different formulations of the aforementioned nucleon interactions to investigate the possibility of experimentally probing the density-dependence of the symmetry energy in these correlation functions using detectors with high angular resolution.

The correlation functions are defined and plotted in terms of the relative angular momentum (\vec{q}_{Rel}) of any two protons (\vec{p}_1, \vec{p}_2). Where

$$|\vec{q}_{Rel}| = \frac{1}{2} |\vec{p}_1 - \vec{p}_2|. \quad (1)$$

The correlation function can be written as [1]

$$C(p_1, p_2) = N \frac{A(p_1, p_2)}{B(p_1, p_2)}, \quad (2)$$

and plotted as a function of q_{Rel} . The correlation function is $C(p_1, p_2)$, N is a normalization coefficient defined to make $C(p_1, p_2) = 1$ at large values q_{Rel} (the protons are assumed to have very little correlation when separated by large momentum, and, therefore, space), $A(p_1, p_2)$ is the yield of pairs of protons at each q_{Rel} from the same event (which are defined to be correlated) and $B(p_1, p_2)$ is the yield of pairs of protons from different events (which are by definition uncorrelated) at each relative momentum point (q_{Rel}). This method of calculating the uncorrelated portion of the ratio is known as “event mixing” [1].

In this work, CoMD [6] simulations were used to simulate nucleus-nucleus reactions, and the resulting data were used to construct proton-proton correlation functions for 31 MeV/nucleon $^{40}\text{Ca}+^{40}\text{Ca}$ and 30 MeV/nucleon $^{48}\text{Ca}+^{64}\text{Ni}$ reactions. Fig. 1 demonstrates that CoMD is able to create a correlation function of an expected shape for charged fermions. A ratio $[C(q)]$ of greater than one means that there was a higher yield of correlated proton pairs than uncorrelated with that relative momentum. The $C(q)$ values at the lowest q_{Rel} in Fig 1 shows the Coulomb effects on the protons, they are less likely to have the

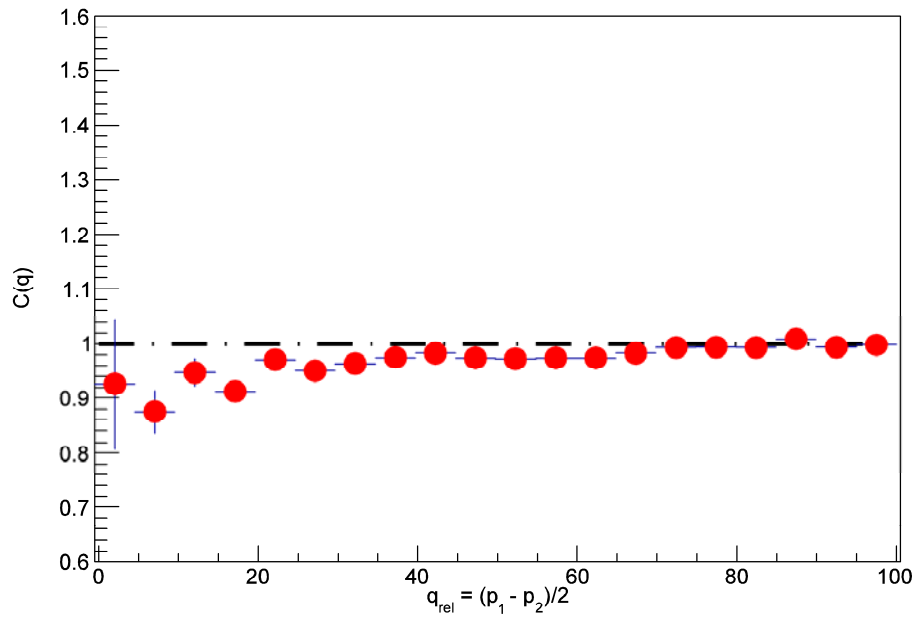


FIG. 1. Correlation function for protons, central impact parameter events of 31 MeV/u $^{40}\text{Ca}+^{40}\text{Ca}$ events.

same momentum if they are close in space and time. Fig. 2 shows the difference between a "stiff" and "soft" density-dependence of the symmetry energy. The bump towards more correlations at a relative momentum of about 20 MeV/c is caused by the Coulombic repulsion of proton-on-proton interactions. Protons that are near in space in the same event tend to repel each other to a relative momentum near 20

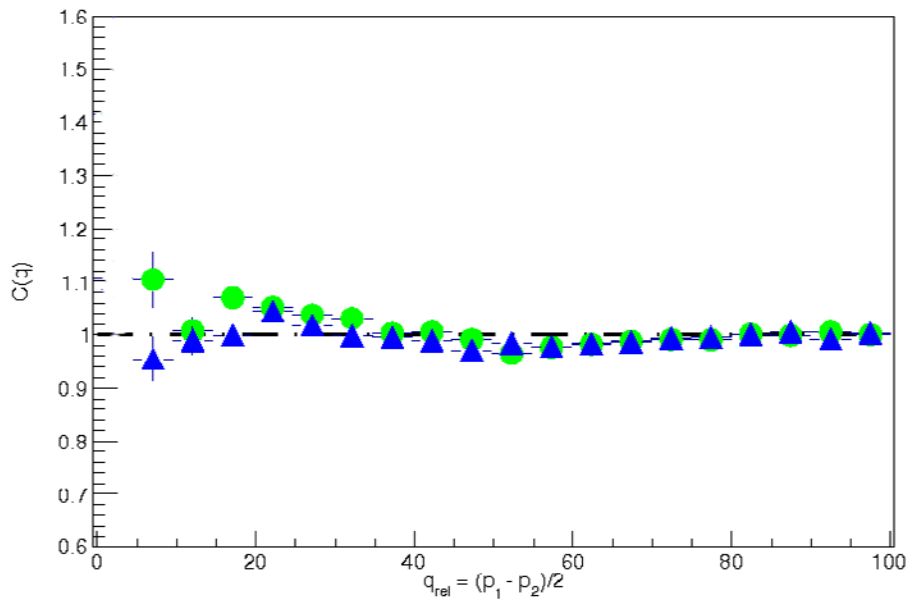


FIG. 2. Correlation function for protons for all impact parameter events of 30 MeV/u $^{48}\text{Ca}+^{64}\text{Ni}$ events. The green circles denote the "soft" implementation of the symmetry energy, while the blue triangles denote the "stiff".

fm/c.

More events are being run now in CoMD, in order to reduce the effects of statistical uncertainties. Transport models such as isospin-dependent Boltzmann-Uehling-Uhlenbeck (iBUU) have been used in the past to construct these correlation functions, which shows the relative correlation of pairs of protons at any relative momentum [3]. A transport model code will also be run, in order to compare with previously published simulations [3].

Position-sensitive dual-axis dual-lateral (DADL) silicon detectors will be incorporated in the Faust array to experimentally test these calculations [7]. The Faust array in its current configuration will be tested in-beam at the end of this summer, and tests with the DADL detectors are underway with a couple of different types of electronics.

[1] V. Henzl *et al.*, Phys. Rev. C **85** (2012).

[2] R. Ghetti *et al.*, Nucl. Phys. **A674**, 277 (2000).

[3] L.W. Chen, V. Greco, C.M. Ko, and B.A. Li, Phys. Rev. Lett. **90**, 162701 (2003).

[4] S. Koonin, Phys. Lett. B **70**, 43 (1977).

[5] S. Pratt *et al.*, Phys. Rev. C **36**, 2390 (1987).

[6] M. Papa, T. Maruyama, and A. Bonasera, Phys. Rev. C **64**, 024612 (2001).

[7] S. soisson, B. Stein, L. May, R. Diehoffer, M. Jandel, G. Souliotis, D. Shetty, S. Galanopoulos, A. Keksis, S. Wuenschel, Z. Kohley, S.J. Yennello, M. Bulloough, N. Greenwood, S. Walsh, C. Wilburn *et al.*, Nucl. Instrum. Methods Phys. Res. **A613**, 240 (2010).

Proximity effect in multifragmentation events

Lauren Heilborn, G. Souliotis, S. Soisson, P. Cammarata, P. Marini, L.W. May, A. McIntosh,
A. Raphelt, B. Stein, and S.J. Yennello

The relationship between the N/Z of the fragmenting source and the nature of its subsequent fragmentation was studied in the reaction of ^{32}S on ^{112}Sn at 45 MeV/nucleon. Isotopically resolved light charged particles (LCP) and intermediate mass fragments (IMF) were measured with the Forward Array Using Silicon Technology (FAUST) [1]. The velocity distribution of ^7Li was observed to be asymmetric and backward peaked in the frame of the moving quasiprojectile (QP) [2]. The QP consisted of all detected charged particles in a given event. The shape of the velocity distributions seemed inconsistent with dynamic effects, so a simple numerical ratio was determined between the number of particles emitted in the “forward” direction and the “backward” direction, in the frame of the QP. In this ratio, a value greater than 1 means there are more particles of a particular type emitted forward than back in multifragmentation events. The experimental data, shown in Fig. 1, demonstrates that lower neutron-content particles, as well as larger Z fragments, are emitted in a more forward direction, while lower Z and more neutron-rich fragments favored backward emission.

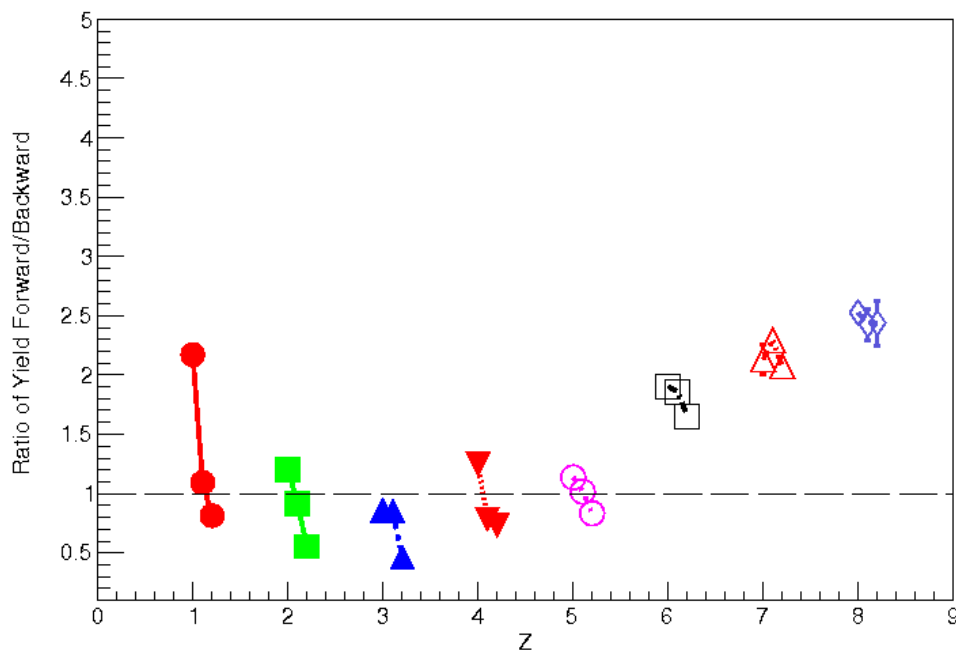


FIG. 1. Ratio of the number of low- Z particles emitted forward of the QP vs. the number emitted backward. Symbols represent fragments of the same Z , and within an element. For example, the circles represent, from left to right, protons, deuterons, and tritons.

In order to investigate the velocity distributions of the emitted fragments in the beam direction of the center-of-mass of the QP, and an effect caused by the Coulomb field of the quasitarget (QT). The Deep-Inelastic Transfer/Statistical Multifragmentation Model (DIT/SMM) code was run for this system at different distances between the QP and the QT at the time of breakup. The DIT creates an excited QP [3]. The SMM simulates the breakup of this excited QP [4]. The unfiltered DIT/SMM longitudinal velocity distribution was approximately Gaussian in shape, and the ratios for all fragments were centered about 1.

The proximity of the QP to the QT at the time of breakup in SMM does affect the distribution of fragments in the QP frame. When the QT is more than 60 fm/c from the QP at the time of the breakup, the ratios of forward to backward emitted particles remain centered at 1. When this SMM data is run through a software “filter,” for the purpose of emulating real collisions which are detected by the FAUST array, the ratios shift to higher values, as more of the forward particles may be geometrically accepted. As the QT is moved to a closer proximity, the SMM data matches the experimental data qualitatively more closely. Fig. 2 shows the ratios of particles emitted forwards vs. backwards in the frame of the QP, plotted as the experimental data in Fig. 1. Similar trends are observed in both; however, the SMM data does not match numerically. Below a distance of 20 fm/c in time, the ratios do not differ much, as the QP and QT may not have completely separated at the time of multifragmentation.

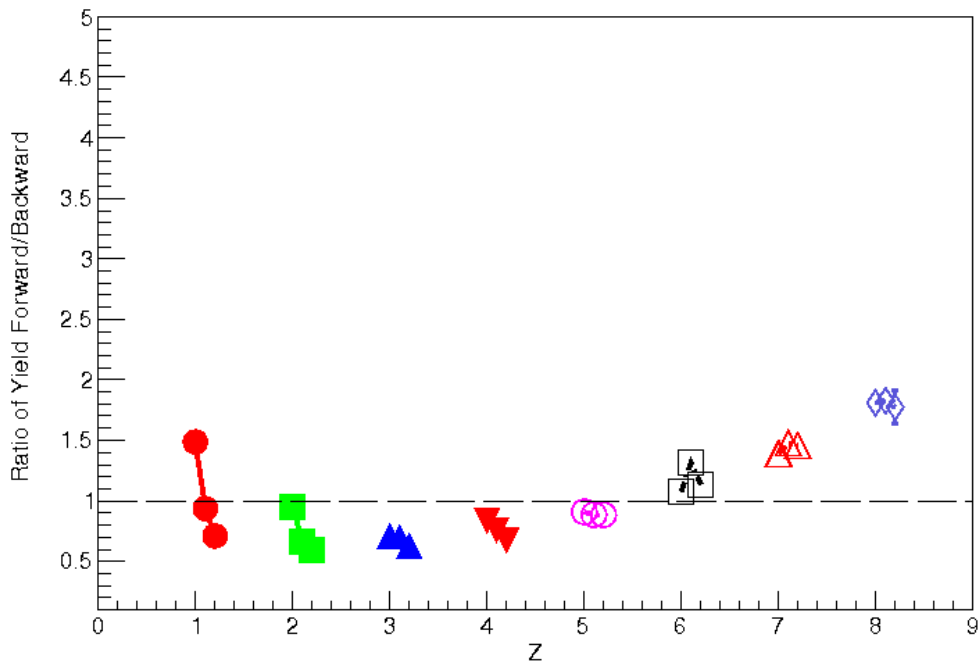


FIG. 2. Shows the same ratio and visualization scheme as used in Figure 1. These ratios were calculated for data from DIT+SMM simulation, with 20 fm/c between the QP and the QT, after the simulated data had been geometrically and energetically “filtered” to emulate actual data through the FAUST detector.

The effect is diminished when the experimental filter is applied. None of the proximity options shown scaled to the shapes of the originally observed distributions of ${}^7\text{Li}$ and other LCPs from the experimental data. Investigation of the source of the asymmetric velocity distributions of fragments is ongoing, and includes data from other systems of reactions.

- [1] F. Gimeno-Nogues, D. Rowland, E. Ramakrishnan, S. Ferro, S. Vasal, R. Gutierrez, R. Olsen, Y.-W. Lui, R. Laforest, H. Johnston, and S.J. Yennello, Nucl. Instrum. Methods Phys. Res. **A399**, 94 (1997), ISSN 0168-9002, <http://www.sciencedirect.com/science/article/pii/S0168900297009236>.
- [2] S. Soisson, Ph.D. Thesis, Texas A&M University, 2010.
- [3] L. Tassan-Got and C. Stephan, Nuclear Physics **A524**, 121 (1991).
- [4] A. Botvina, A. Iljinov, I. Mishustin, J. Bondorf, R. Donangelo, and K. Sneppen, Nucl. Phys. **A475**, 663 (1987).

Production of nuclides near the $N = 126$ shell in ^{48}Ca , ^{50}Ti , and ^{54}Cr induced reactions

D.A. Mayorov, T.A. Werke, M.C. Alfonso, M.E. Bennett, and C.M. Folden III

Modern theoretical calculations conclude that the most promising reaction pathway to the synthesis of elements heavier than 118 is fusion of ^{50}Ti with actinides [1]. At present, the low intensities of necessary beams in alternative production mechanisms (i.e. neutron-rich radioactive beams, low energy damped multi-nucleon transfer) make them inferior to “hot” fusion [2]. However, despite being most promising, the estimated cross sections for synthesis of element 120 in the $^{50}\text{Ti} + ^{249}\text{Cf}$ reaction are on the order of tens to hundreds of femtobarns, much lower than the picobarn-level observed for a number of its immediate lighter predecessors. The reduction in projectile-target asymmetry in the ^{50}Ti reaction, relative to the $^{48}\text{Ca} + ^{249}\text{Cf}$ fusion, and, possibly (likewise surprisingly), the proximity of its product to the predicted proton and neutron shell closures of the island of stability can be linked to this low prediction.

A series of reaction systems, with significantly higher product yield than the case of superheavy elements, were chosen for a study to better quantify the role the projectile plays on the reaction cross section (specifically a relative comparison among ^{48}Ca , ^{50}Ti , and ^{54}Cr). Table I summarizes these and draws attention to the systems explored to date (shown in bold). Furthermore, the reaction systems all produce residues in the vicinity of the $N = 126$ shell closure; the next closed neutron shell is predicted at $N = 184$ and is being approached with the search for element 120 [3]. This aids in determining the effect of the shell correction energy on the survival probability of the residue.

Table I. Comparison of reactions of interest in the current work. Data for the items in bold are presented in this report. Column 2 features a measure of the reaction projectile-target pair mass asymmetry. Values of the ground-state (equilibrium) quadrupole deformation, column 3, are taken from [13]. Fission barriers (B_f) are calculated according to [14] and neutron binding energies (B_n) are based on ground-state masses from [15].

Reaction $A_p + A_T \rightarrow A_{CN}$	$\eta = \frac{ A_p - A_T }{A_p + A_T}$	$\beta_{2,CN}^{eq}$	$[B_f - B_n]_{CN - to - 3n}$ (MeV)
$^{48}\text{Ca} + ^{159}\text{Tb} \rightarrow ^{207}\text{At}$	0.536	-0.035	7.20, 7.65, 4.71, 5.42
$^{48}\text{Ca} + ^{162}\text{Dy} \rightarrow ^{210}\text{Rn}$	0.543	-0.026	7.05, 7.50, 4.79, 5.49
$^{48}\text{Ca} + ^{165}\text{Ho} \rightarrow ^{213}\text{Fr}$	0.549	0.008	6.81, 7.27, 4.83, 5.19
$^{50}\text{Ti} + ^{159}\text{Tb} \rightarrow ^{209}\text{Fr}$	0.522	-0.044	2.75, 3.27, 0.69, 1.59
$^{50}\text{Ti} + ^{162}\text{Dy} \rightarrow ^{212}\text{Ra}$	0.528	-0.035	2.68, 3.25, 0.57, 1.49
$^{50}\text{Ti} + ^{165}\text{Ho} \rightarrow ^{215}\text{Ac}$	0.535	0.000	2.70, 3.13, 0.76, 1.17
$^{54}\text{Cr} + ^{159}\text{Tb} \rightarrow ^{213}\text{Ac}$	0.493	-0.044	0.76, 1.17, -1.29, -0.27
$^{54}\text{Cr} + ^{162}\text{Dy} \rightarrow ^{216}\text{Th}$	0.500	0.008	0.84, 1.45, -1.11, -0.34
$^{54}\text{Cr} + ^{165}\text{Ho} \rightarrow ^{219}\text{Pa}$	0.507	-0.008	-1.73, 0.80, -0.78, -0.37

Fig. 1 shows the preliminary measured excitation function for the (^{48}Ca , $4n$) reaction and the upper limits for the (^{54}Cr , $4n$) reaction on a ^{162}Dy target, with the experimental set-up details identical to

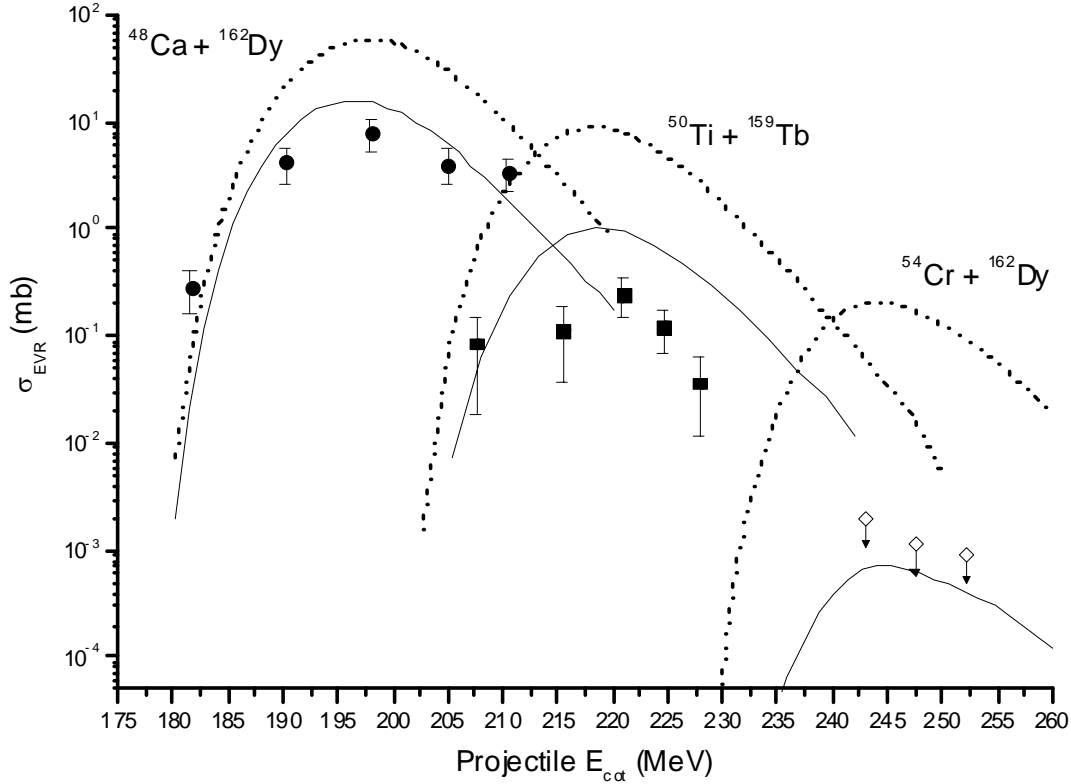


FIG. 1. Excitation functions for $^{162}\text{Dy}(^{48}\text{Ca}, 4n)^{206}\text{Rn}$ (circles), $^{159}\text{Tb}(^{50}\text{Ti}, 4n)^{205}\text{Fr}$ (squares), and $^{162}\text{Dy}(^{54}\text{Cr}, 4n)^{212}\text{Th}$ (diamonds). Upper limits for ^{212}Th are calculated with an 84% confidence interval according to [16]. A factor of over 7300 separates the $4n$ reaction products for the reactions involving ^{162}Dy target. Solid and dashed curves are theoretical calculations, with a distinction that the dashed curves exclude collective enhancements in the calculation [6].

those described in [4] (also see [5]). In addition, the most recent data from the $(^{50}\text{Ti}, 4n)$ reaction on ^{159}Tb is included for comparison. The dashed and solid curves are theoretical calculations based on the models of Zagrebaev et al. [6], with the distinction of the latter accounting for collective enhancements. Vermulen et al. [7] previously observed reduced survival probabilities of nuclides produced via fusion-evaporation near the $N = 126$ shell closure. This phenomenon was later explained by expanding the energy level density of the potential de-excitation modes of a “hot”, rotating compound nucleus to include collective nucleon excitations. In cases of weak nuclear deformation, the contribution from rotational excitation heavily favors the fission channel, meanwhile the contribution for the xn channels is at least an order of magnitude smaller [6, 8].

The much lower production cross section for $^{162}\text{Dy}(^{54}\text{Cr}, 4n)^{212}\text{Th}$ compared to $^{162}\text{Dy}(^{48}\text{Ca}, 4n)^{206}\text{Rn}$ is best explained by referring to column 4 of Table I, which summarizes for each respective compound nucleus the barriers encountered along the de-excitation cascade for the two primary decay modes of fission and neutron emission up to the $3n$ intermediate, which then leads to the $4n$ ground-state residue. Fission dominates for the heavier residue, suppressing its survival probability. In addition, the falling survival probability increasingly augments the magnitude of the effect from collective

enhancements as seen from the calculated solid curves from left to right in Fig. 1 [6]. This can be attributed to the growing magnitude of the product between a calculated enhancements factor and quickly rising fission probability for the heavier residues, which shifts the de-excitation in favor of fission.

Another key feature in Fig. 1 is the gap observed between the experimental points and the theoretical predictions (solid curves, which assume that probability of compound nucleus formation is unity [9]). This difference corresponds to the probability of complete fusion following projectile-target collision; the competing process is quasi-fission after collision resulting in re-separation of the nuclei before overcoming the saddle point. Preliminary analysis based on the approach employed in [10] suggests that the fusion probability (also probability of compound nucleus formation) falls from 0.50 to 0.25 to 0.10, for the ^{48}Ca to ^{50}Ti to ^{54}Cr reactions, respectively, at the maximum of each excitation function. An estimate for the peak cross section in the case of $^{162}\text{Dy}(^{54}\text{Cr}, 4n)^{212}\text{Th}$ was based on literature data for reactions with greater and lesser η (as defined in Table I), and forming the same compound nucleus and residue [7, 11]. These are $^{176}\text{Hf}(^{40}\text{Ar}, 4n)^{212}\text{Th}$, $^{154}\text{Sm}(^{68}\text{Ni}, 4n)^{212}\text{Th}$, and $^{92}\text{Zr}(^{124}\text{Sn}, 4n)^{212}\text{Th}$, all of which cluster at ≈ 100 nb for their excitation function maxima and is the value adapted for the estimate of fusion probability above for $^{54}\text{Cr} + ^{162}\text{Dy}$.

In the search for superheavy elements near the island of stability and with reactions involving projectile heavier than ^{48}Ca , the presently discussed effects are critical in determining experimental success. Although strong shell correction energies reduce the fissility of a nucleus, the collective excitation in weakly deformed nuclei is likely to cancel out this contribution and reduce survival of the residue. Even though the synthesis of element 120 is accompanied with these challenges and pushes the capabilities of modern instruments, it is not completely beyond reach as the record for lowest production cross section measured is purported to be 31 fb [12].

- [1] K. Siwek-Wilczynska, T. Cap, M. Kowal, A. Sobiczewski, and J. Wilczynski, *Phys. Rev. C* **86**, 014611 (2012).
- [2] V. Zagrebaev and W. Greiner, *Phys. Rev. C* **78**, 034610 (2008).
- [3] A. Sobiczewski and K. Pomorski, *Prog. Part. Nucl. Phys.* **58**, 292 (2007).
- [4] C.M. Folden III *et al.*, *Nucl. Instrum. Methods Phys. Res.* **A678**, 1 (2012).
- [5] D.A. Mayorov, M.C. Alfonso, T.A. Werke, and C.M. Folden III, *Progress in Research*, Cyclotron Institute, Texas A&M University (2010-2011), p. II-19.
- [6] V.I. Zagrebaev, Y. Aritomo, M.G. Itkis, Y.T. Oganessian, and M. Ohta, *Phys. Rev. C* **65**, 014607 (2001).
- [7] D. Vermeulen, H.G. Clerc, C.C. Sahm, K.H. Schmidt, J.G. Keller, G. Munzenberg, and W. Reisdorf, *Z. Phys. A.-Hadrons Nuclei* **318**, 157 (1984).
- [8] A.R. Junghans, M. de Jong, H.G. Clerc, A.V. Ignatyuk, G.A. Kudyaev, and K.H. Schmidt, *Nucl. Phys.* **A629**, 635 (1998).
- [9] V.I. Zagrebaev *et al.*, <http://nrv.jinr.ru/nrv/>.
- [10] K. Siwek-Wilczynska, A. Borowiec, I. Skwira-Chalot, and J. Wilczynski, *Int. J. Mod. Phys. E* **17**, 12 (2008).

- [11] C.C. Sahm, H.G. Clerc, K.H. Schmidt, W. Reisdorf, P. Armbruster, F.P. Hessberger, J.G. Keller, G. Münzenberg, and D. Vermeulen, Nucl. Phys. A **441**, 316 (1985).
- [12] K. Morita *et al.*, J. Phys. Soc. Japan. **76**, 045001 (2007).
- [13] P. Moller, J.R. Nix, W.D. Myers, and W.J. Swiatecki, At. Nucl. Data **59**, 185 (1995).
- [14] A.J. Sierk, Phys. Rev. C **33**, 2039 (1986).
- [15] National Nuclear Data Center (2011), <http://www.nndc.bnl.gov>.
- [16] K.H. Schmidt, C.C. Sahm, K. Pielenz, and H.G. Clerc, Z. Phys. A. **316**, 19 (1984).

Development of a gas stopper for heavy element chemistry

M.C. Alfonso and C.M. Folden III

Studying the chemistry of the transactinides is of particular interest due to relativistic effects. As Z (proton number) increases, the speed of the innermost electrons becomes increasingly more relativistic, changing the energies of the electron orbitals in the atom. This could lead to significantly different chemical and physical properties for heavy elements than expected. Transactinides ($Z > 103$) can only be created via fusion-evaporation reactions which produce evaporation residues (EVRs) with 30 – 50 MeV of kinetic energy. However, chemistry systems are studied at sub-eV energy levels. Therefore, these EVRs must be degraded before their chemistry can be studied.

Previous work in the field of heavy elements has used a combination of degraders and a gas cell, also known Recoil Transfer Chamber (RTC), to facilitate the chemical study of EVRs. Transactinides are produced with a very low rate and their half-lives can be very short so it is critical that the RTC be as efficient and fast as possible. An RTC for heavy elements has been designed and fabricated at the Cyclotron Institute (Fig. 1) that is a hybrid of gas cells used in the transactinides field [1] and one used at Michigan State University for stopping projectile fragmentation reaction products [2]. Our gas cell uses more laminar flow and a series of electrodes that create a potential gradient to efficiently transport the EVRs to the appropriate chemistry apparatus. The electrode system contains four rings with a decreasing potential that pulls the ion through; at the end there are four concentric spherical electrodes (so-called flower petals) that are used to focus the ions into the Extraction Nozzle. This electrode system is based on the gas cell from Michigan State University [2].

A two-chamber design was implemented in the RTC. In the Main Chamber, the electrode system and gas flow carry the ions through an Extraction Nozzle to a so-called Aerosol Chamber. In this chamber, ions attach to KCl aerosol clusters which aid in the transmission of the EVRs through the Transportation Capillary to the appropriate chemistry experiment. (Bare ions have a greater chance of getting trapped on the sides of the capillary than ion-aerosol clusters). The design of the gas cell was also driven by results from gas flow simulations by STAR-CCM++ (Fig. 2) [3]. It is critical that the gas flow in the Main Chamber does not hinder the focusing of the electrode system; by adding the Inner Chamber Groove (see Fig. 1) the flow in the region where the ions are thermalized and focused by the electric field is more laminar. A negative pressure differential between the two chambers is needed to limit the aerosol contamination in the Main Chamber, which may hinder the focusing ability of the electrode system. The gas flow in the Extraction Nozzle also had to be optimized since it is the dominate component in this region. Lastly, the gas flow in the Aerosol Chamber had to be optimized to carry the ion-aerosol clusters into the Transportation Capillary. The RTC has been fabricated and preliminary characterization results are presented here.

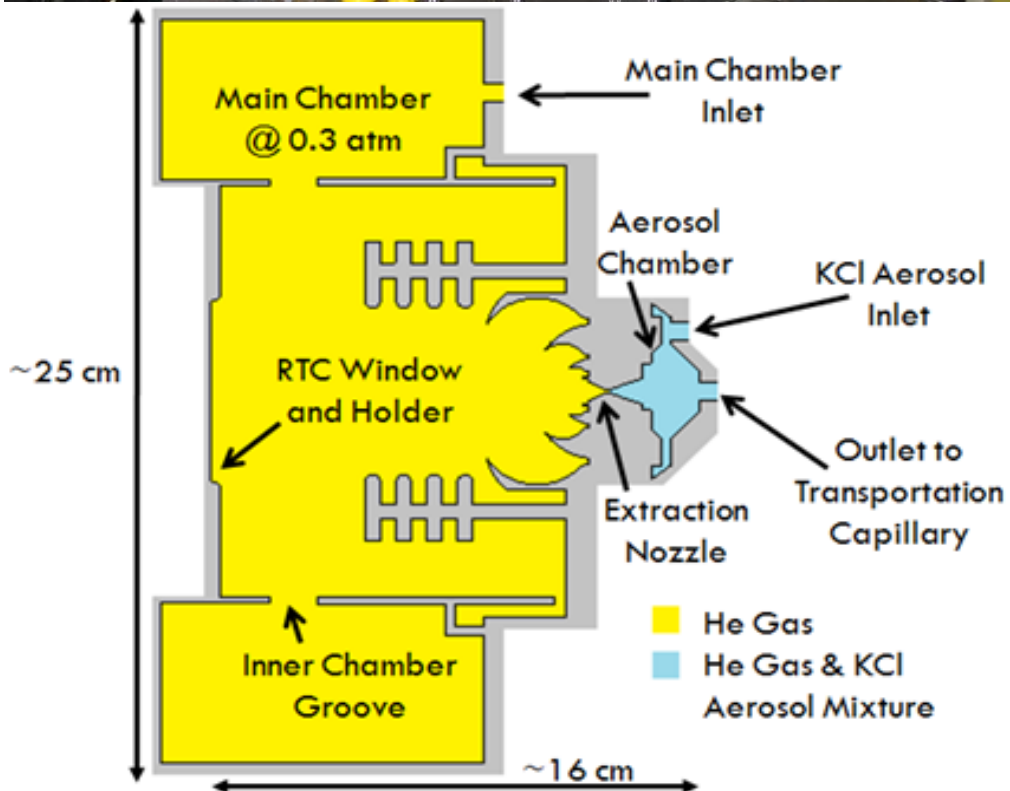
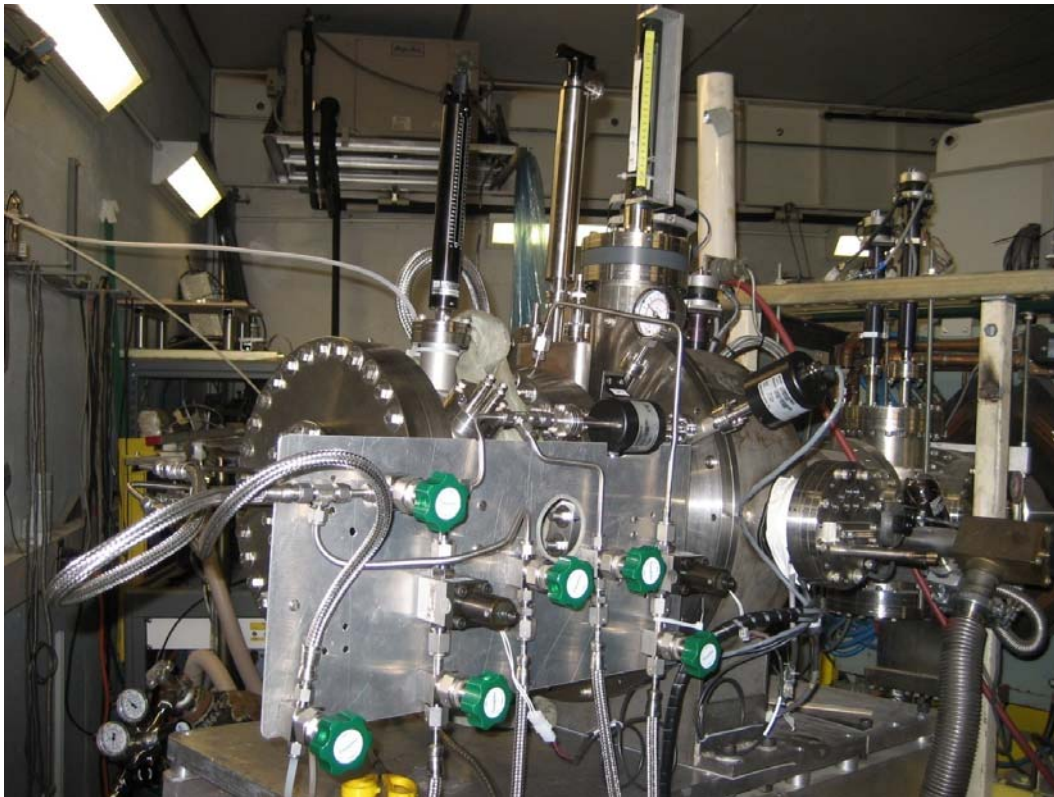


FIG. 1. Top: picture of the actual RTC attached to the detector chamber at end of the MARS beamline. Bottom: schematic picture of the RTC (see main text for more detail).

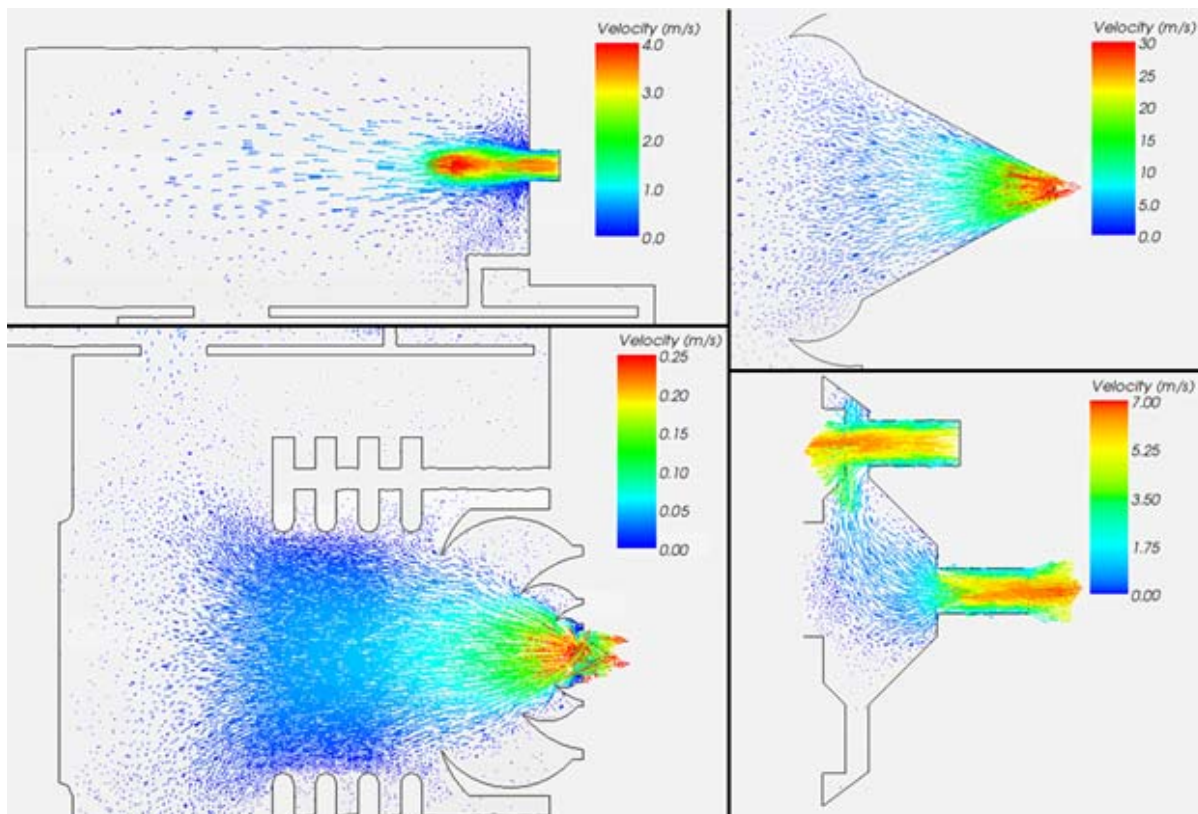


FIG. 2. Gas flow simulations of the finalized gas cell design. Pump speed simulated was 4 L/min with a -15 torr differential between the Main Chamber and Aerosol Chamber. The two quadrants to the left show how the Inner Chamber Groove creates a laminar flow in the critical region of the Main Chamber. The simulated gas flow in the Extraction Nozzle can be seen in the top right quadrant. In this region gas flow becomes the more dominate force and directs the ions through to the Aerosol Chamber. Lastly, the bottom right quadrant shows a favorable flow that carries the ions into the Transportation Capillary.

A two-detector system has been installed in the RTC to monitor the transportation of ions through the system. A large-area detector was placed where the peak of the stopped ion distribution is expected to be. This detector can be plunged in and out of the beam path and will make it possible to select the optimum degraders upstream of the RTC. An identical detector was placed directly downstream of the Extraction Nozzle, so the gas flow and electrode system in the Main Chamber could be optimized. The second detector requires that the Aerosol Chamber be on a retractable system.

The negative pressure differential (PD) between the Main Chamber and Aerosol Chamber also affects the magnitude of the flow in the Main Chamber. As the PD between the two chambers is increased the flow in the Main Chamber becomes increasingly more forceful. This is very important in the Extraction Nozzle where there is minimal focusing due to the electrode system. STAR-CCM+ simulations indicated there was a maximum possible flow out of the Main Chamber of 2.9 L/min. During offline testing it was discovered that the maximum PD possible depended strongly on the conductance of the system. The most important factor influencing the conductance is the inner diameter of the Transportation Capillary. Thus, capillaries with varying inner diameters (1/16", 3/32", 1/8", 5/32") and a constant length (25 ft) were tested. The maximum PD for the individual capillaries was determined by

closing the Aerosol Chamber inlet and holding the Main Chamber at a constant 228 torr (0.3 atm) with flow only from the Main Chamber inlet. The data (Table I) suggest that a capillary with an inner diameter smaller than 1/8" cannot be used because no PD is possible with these smaller capillaries.

Table I. Maximum achievable PD as a function of the inner diameter of the Transportation Capillary. As the inner diameter of the capillary increases the maximum PD increases. Capillaries with a maximum DP 0 torr cannot be used on the RTC.

Inner Diameter of Capillary	Maximum PD
1/16"	0 torr
3/32"	0 torr
1/8"	24 torr
5/32"	56 torr

The effects of inner diameter of the capillary and PD on transmission through the Main Chamber were tested using positively charged ^{216}Po recoils from a ^{228}Th source to simulate thermalized EVRs. Almost all recoils formed in the ^{228}Th source are neutral. However, a small amount of ^{220}Rn , a gaseous element, constantly emanates out of the source. ^{216}Po daughters from the emanated ^{220}Rn remain in a positive charge state and can be transported through the RTC. A ^{228}Th source with an activity of 2.3×10^3 Bq was attached to the linear actuator in the Main Chamber and the detector downstream of the Extraction Nozzle was used to measure the transmission of ^{216}Po recoils. SIMION [4] was used to determine the optimum electric field settings shown in Fig. 3; this voltage distribution was held constant while both the 1/8" and 5/32" inner diameter capillary were tested with varying PDs. As shown in Fig. 4, the transmission is constant with a PD of ≥ 15 torr. Also, the difference in transmission between the two different capillaries is not significant. Previous experiments on other RTCs suggest that the flow becomes turbulent in the Transportation Capillary at high flow rates [5]; this may decrease the transmission of the ion-aerosol

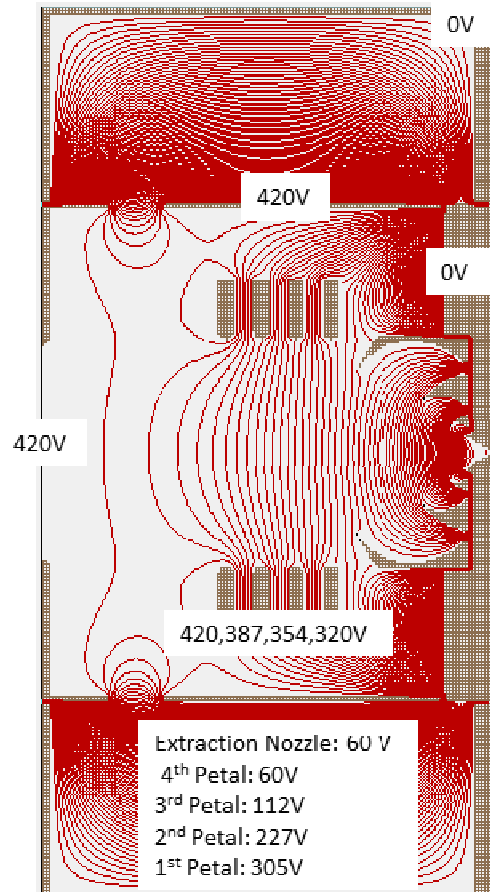


FIG. 3. Equipotential lines diagrams from an optimized SIMION simulation. Ions travel perpendicular to these lines.

clusters through the capillary. Therefore, the 1/8" inner diameter capillary was selected for further studies.

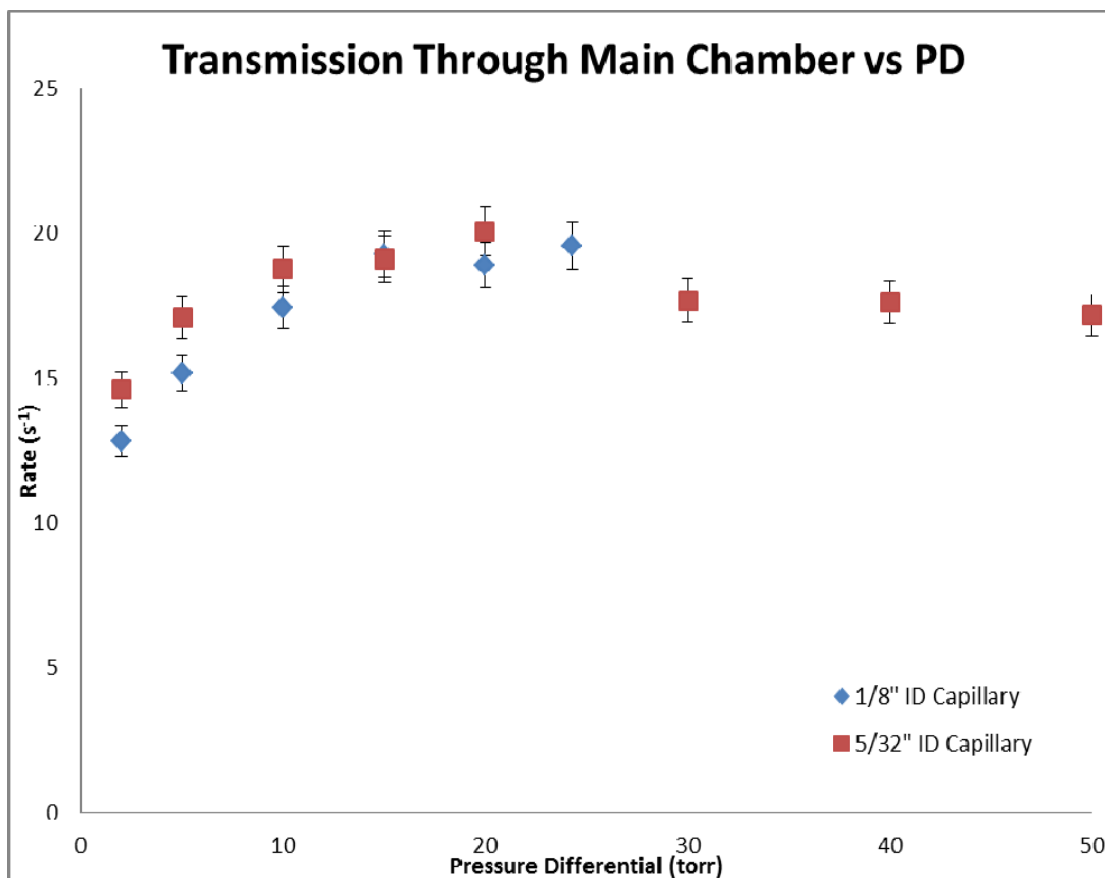


FIG. 4. Transmission through the Main Chamber as a function of PD between the two chambers and inner diameter (ID) of the capillary. A systematic error of 4.2% was calculated and applied to all data points.

Lastly, the effects of the electric field and gas flow on transmission were separately measured. This was first done by measuring the transmission without gas flow but with optimum electric field settings (Fig. 3); a transmission of less than 1% of the maximum transmission was detected. Also, tests were conducted with gas flow (PD set to 15 torr) and the electric field off; a transmission of less than 3% of the maximum transmission was detected. This is evidence that both gas flow and the electric field are needed to efficiently transmit the ions through the Main Chamber.

Assuming that the fraction of ^{220}Rn emitting from the source is 3% [6], the RTC has an efficiency of approximately 70%. Also the half life of ^{216}Po is 150 ms, which is short enough that the transportation time in the RTC is significant. Simulations from SIMION show a time-of-flight of approximately 20 ms for these electric field settings (Fig. 3). Decay loss corrections are included in the efficiency quoted above.

Currently, the RTC has been fabricated and offline tests of the RTC's electric field with ^{228}Th recoils will continue. A beam experiment is planned for the end of May 2012 to test the gas stopper's

efficiency. The reaction $^{118}\text{Sn}(^{40}\text{Ar}, 6n)^{152}\text{Er}$ will be used since the Momentum Recoil Achromat Spectrometer (MARS) has already been optimized in previous experiments; this reaction also has orders of magnitude higher cross section than transactinide production reactions [7]. Commissioning experiments of the RTC with this high cross section reaction will be completed by Fall 2012. Then the RTC will be used to facilitate the testing of new chemical systems for transactinides.

[1] C.E. Düllmann *et al.*, Nucl. Instrum. Methods Phys. Res. **A551**, 528 (2005).

[2] L. Weissman *et al.*, Nucl. Instrum. Methods Phys. Res. **A540**, 245 (2005).

[3] STAR-CCM+ 5.02.010, CD-adapco, www.cd-adapco.com.

[4] SIMION, www.simion.com.

[5] R. Sudowe, private communication.

[6] A. Sakoda *et al.*, Applied Radiation Isotopes **69**, 1422 (2011).

[7] R.L. Hahn *et al.*, Phys. Rev. Lett. **42**, 218 (1979).

Improvements to the heavy elements program aimed toward reaching lower cross-sections at the Texas A&M University Cyclotron Institute

T.A. Werke,^{1,2} M.C Alfonso,^{1,2} M.E. Bennett,^{1,2} D.A. Mayorov,^{1,2} and C.M. Folden III¹

¹*Cyclotron Institute, Texas A&M University, College Station, Texas, 77843*

²*Department of Chemistry, Texas A&M University, College Station, Texas, 77842*

With the discovery of elements up to $Z = 118$, heavy elements scientists have reached the current limit of the chart of the nuclides. Future discovery will require reaching cross-sections on the level of tens of femtobarns or below [1], requiring either an extremely lengthy beam time, or an advancement in technology that allows us to reach these incredibly small cross-sections in a reasonable timeframe. Also, projectiles heavier than the doubly-magic ^{48}Ca need to be developed due to the lack of sufficient target material of elements beyond Cf.

In the Heavy Elements group, we are interested in studying lighter system with higher cross-sections and then drawing analogies to the superheavy systems. The study of projectiles ranging from $Z = 20-24$ reacting with lanthanide targets provides a suitable system of reactions to measure excitation functions within a seven day period. However, as the atomic number of the projectile increases, the cross-section decreases to the point where the reaction of ^{54}Cr with ^{162}Dy is on the level of microbarns and below our current sensitivity limits. One factor that limits sensitivity is the need to pulse the beam. Beam pulsing greatly reduces background, but also cuts sensitivity by a factor of four. To allow the study of smaller cross-sections, improvements are being made to the detection capabilities of the Heavy Elements group that will eliminate the need for beam pulsing. Additionally, improvements are being made to the cyclotron ion source that will increase beam intensities.

MCP:

The microchannel plate (MCP) detector is a widely used type of radiation detector that consists of a series of channels that serve as continuous electron multipliers [2]. As shown in Fig. 1, when a

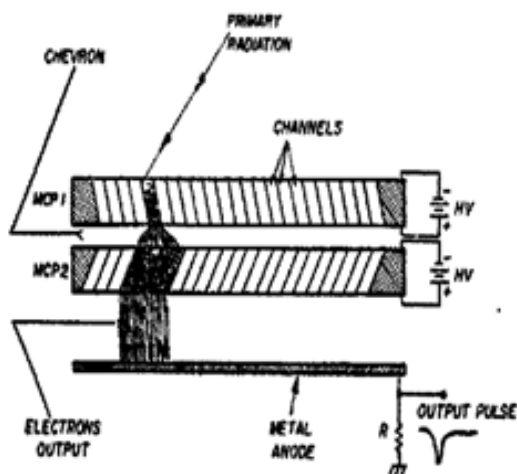


FIG. 1. Electron path and amplification through an MCP detector [2].

quantum of radiation impacts the active area of the detector, it creates a few electrons that are accelerated by a large voltage applied across the plate. Each electron collides with the walls of a channel, creating a cascade with an electron multiplication factor of 10^3 to 10^4 . In a standard detector configuration, two plates are stacked together in a chevron configuration. The two plates have a combined multiplication of 10^6 to 10^7 . After exiting the channels, the electrons are accelerated toward an anode, usually metal or a resistive material. The anode collects the electrons and creates a charge pulse.

An MCP detector was installed in the detector chamber in MARS below and parallel to the beam axis as shown in Fig. 2. The MCP detector was biased to +1800 V on the anode, and +1425 V across the plates. Ions that traverse MARS and reach the detector chamber pass through a 0.6 μm Al foil and an

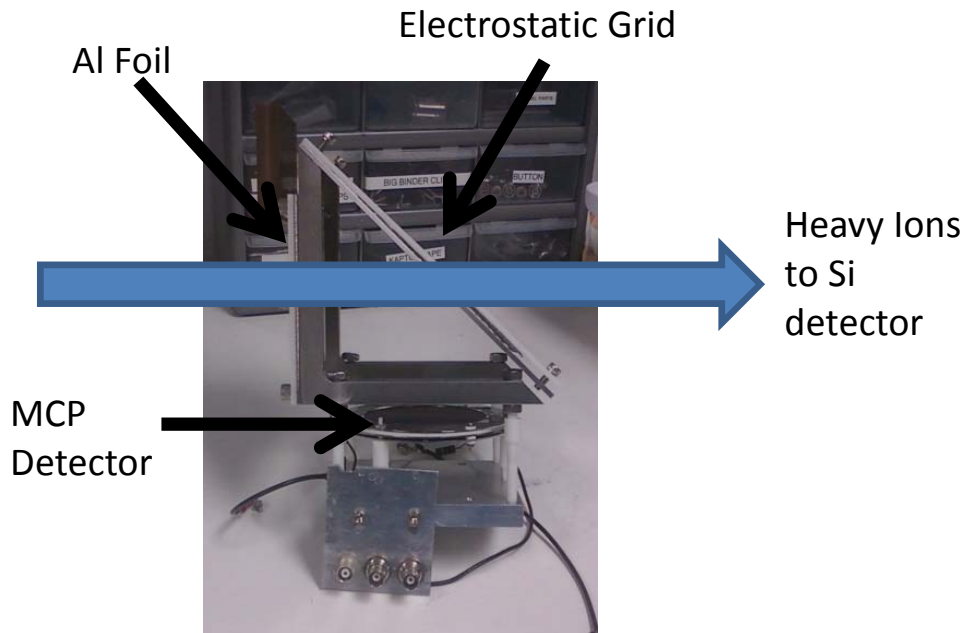


FIG. 2. Picture of the MCP detector assembly. Heavy ions (Scattered beam, scattered target, evaporation residues) pass through the Al foil. The foil ejects a few electrons, which are steered downward by the electrostatic grid.

85% transparent electrostatic grid before reaching the focal plane silicon detector. The foil and grid are each biased to -200 V. As the ions pass through the foil, several electrons are knocked off the Al and accelerated toward the MCP by the field created by the foil, grid, and the detector. The silicon signal is used as the ‘Start’ signal for a Time-to-Amplitude Converter (TAC). The MCP detector signal is delayed and used as the ‘Stop’ signal. The TAC records the time difference between the two pulses and digitizes the signal as a voltage pulse. This creates a unique signal for all ions that implant in the silicon detector and can be used to separate out radioactive decays from these implantation events, significantly reducing background as shown in Fig. 3. Thus, using the MCP detector allows us to eliminate the need to pulse the beam, giving a factor of two increase in beam dose, and a factor of two increase in the collection time where alpha decays of the evaporation residue (EvR) can be observed. Analysis of the data suggests that the efficiency of the MCP detector for EvRs is at least 99%.

Series of Si energy spectra with unpulsed beam and gating on MCP

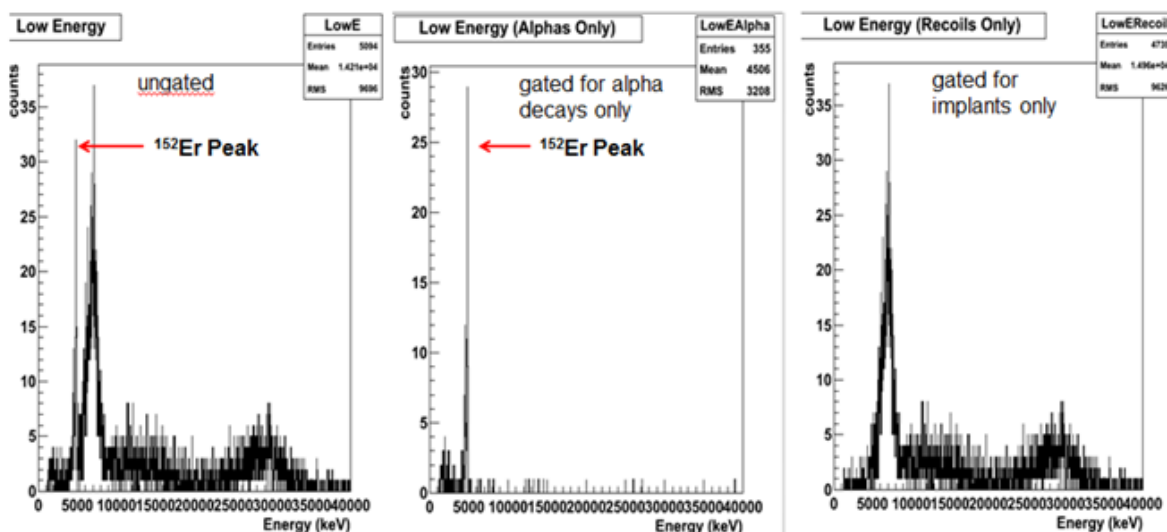


FIG. 3. Representative energy spectra for the products of the $^{40}\text{Ar} + ^{118}\text{Sn}$ reaction without beam pulsing, but instead using the MCP to gate on the alpha decays. ^{152}Er is the product of interest. *Left:* Ungated spectrum including implants and radioactive decays. *Middle:* Spectrum gated for only radioactive decays in the silicon detector. *Right:* Spectrum gated for only implants in the silicon detector.

Oven and Target Wheel:

The development of a high-temperature oven is in progress and should be completed by the summer of 2012. The design is similar to the oven constructed for use with the Electron Cyclotron Resonance (ECR) source for the 88-inch cyclotron at Lawrence Berkeley National Laboratory [3]. The oven should provide higher beam intensities than currently available techniques such as metal sputtering. The higher intensities will increase our sensitivity to low cross-section exit channels.

With the expected higher beam intensities, we need a target system that can tolerate the larger beam power. To accomplish this, a rotating target wheel has been designed, is under construction and is discussed in a separate contribution to this report. The wheel is based on the design used in the TASCAs separator at GSI, Darmstadt, Germany [4]. The wheel will consist of three, banana-shaped holes that hold the targets and will rotate at a maximum of 1700 rpm.

Conclusions

Due to the incredibly tiny cross-sections for producing superheavy elements, our group's focus is on producing lighter nuclei with higher cross-sections, then drawing meaningful analogies to superheavy nuclei. To reach the required sensitivities for our reactions, a microchannel plate detector was developed and implemented to differentiate implantation events from alpha decays, thus eliminating the need for beam pulsing. The detection efficiency for the implanting ions is at least 99%. Additional improvements

are being made to reach even lower cross-sections. These include a high-temperature oven that will provide higher beam intensities, and a rotating target wheel to tolerate the high power from the beam.

- [1] V. Zagrebaev and W. Greiner, Phys. Rev. C **78**, 034610 (2008).
- [2] J.L. Wiza, Nucl. Instrum. Methods Phys. Res. **162**, 587 (1979).
- [3] T. Loew *et al.*, Proceedings of PAC07, Albuquerque, New Mexico, USA, p.1742; <http://accelconf.web.cern.ch/AccelConf/p07/PAPERS/TUPAS044.PDF>
- [4] E. Jäger *et al.*, *Aretesia – A Rotating Target Wheel for Experiments with Superheavy-Element Isotopes at GSI Using Actinides as Target Material*, TASCA Target Meeting, Mainz, Germany, 2 March 2005, http://www-win.gsi.de/tasca/publications/task_groups/target_group/Target_Meeting_March05/Target_Meet_05_03_02_E_Jaeger.pdf

Extraction chromatographic studies of Rf homologs with TEVA resin

Megan E. Bennett, Marisa C. Alfonso, and Charles M. Folden III

1. Introduction

It is of great interest to determine the chemical properties of the transactinide elements ($Z > 103$). These studies can help to assess the influence of relativistic effects on the chemical properties of the heaviest elements. The influence of relativistic effects is expected to result in deviation of periodic group trends [1]. In order to assess deviation of chemical behavior of the heaviest elements their chemical behavior should be compared to that of their lighter homologs that reside in the same periodic group. However, developing chemical systems suitable for study of the heaviest elements presents several challenges which stem from the short half-lives and low production rates of transactinide elements (TAns). The short-half lives of the TAns require the chemical system to be fast. Cross sections of nanobarns and smaller result in TAns being produced one atom-at-a-time. Since there is only a single atom present at a given time the atom can only interact with its surroundings and not with atoms of the same element. This makes development of chemical systems in which the single atom undergoes many exchange steps necessary [2]. Column chromatographic systems lend themselves well to this need and have successively been used for the study of the lightest TAns [3].

1.2 TEVA resin

The TEtraVAlent, TEVA, resin is commercially available from Eichrom Technologies, inc. with trialkyl methylammonium chloride sorbed to an inert polymeric substrate, where the alkyl chain lengths are C8 and C10 [4]. The TEVA resin, shown in Fig.1, is similar to an anionic exchange resin; however instead of the extractant molecule being chemisorbed to an inert support it is physisorbed to the inert support. Batch studies were conducted using 0.1 M to concentrated HCl, HNO₃, and H₂SO₄. Based upon

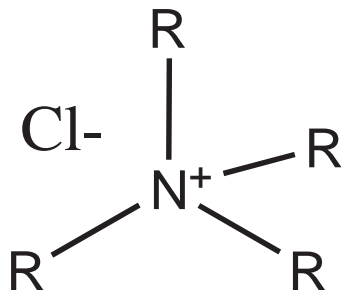


FIG. 1. The structure of the trialkyl methylammonium extractant on the TEVA resin.

the results of the batch study dynamic column studies were conducted.

1.3. HCl System

Hulet *et al.* previously showed that Rf in 12 M HCl behaves similarly to Hf on trioctylmethylammonium chloride (Aliquat 336) sorbed onto an inert support [5]. However, the chemical behavior of Rf has never been compared to that of Zr in HCl media on an Aliquat 336 resin. It was shown by Cerrai and Ghersini that a Whatman No. 1 CRL/1 type filter paper impregnated with Aliquat 336 showed separation of Zr and Hf at 1-4 and 8-10 M HCl in a thin-layer-chromatography-type experiment [6].

1.4 HNO₃ System

Lister and McDonald found an anionic specie(s) of Zr to exist in solutions above 4 M HNO₃ [7]. Faris and Buchanan found that Hf slightly adsorbs to Dowex 1x10, indicating the presences of an anionic species, while Zr exhibited a definite adsorption to the resin [8]. Recently Haba *et. al.* investigated the behavior of Zr, Hf and Rf on the anion exchange resin MCI GEL CA08Y and found that in nitric solutions ranging from 1.1 to 13.1 M Zr and Hf have lower adsorption to the anion exchange resin, indicating that Zr and Hf have a lower tendency to form anionic species compared to neutral or cationic species [9]. Haba and co-workers also found that Rf exhibited a similar chemical behavior to that of Zr and Hf, while Pu and Th formed $[M(NO_3)_6]^{2-}$ species, where M is Pu or Th [9]. This indicates that the anion exchange resin MCI GEL CA08Y could be used to remove actinides in a catcher block type experiment. For a discussion on catcher block experiments please see Ref. [10].

1.5 H₂SO₄ System

Ryabchikov and co-workers determined that the stability of inorganic complexes with Zr and Hf decrease in the order of $F^- > SO_4^{2-} \gg Cl^- > NO_3^-$ [11]. This indicates that SO_4^{2-} should bind Group 4 elements stronger than chloro or nitrate systems, which have been extensively studied for Rf. The sulfate systems of Rf should be of interest when assessing the chemical behavior of Rf compared to its homologs, Zr and Hf. Because the sulfate ion binds Group 4 elements so tightly it could provide insight into any relativistic effects that maybe affecting the chemical properties of Rf.

Recently, Li and co-workers investigated the ion-exchange behavior of Zr and Hf in 0.018-0.99 M H₂SO₄ for application to Rf chemistry. It was found that over this concentration range Zr and Hf adsorbed to both cation and anion exchange resins. In batch studies Zr and Hf behaved similarly on anion exchange resin and had a separation factor, $SF_{Zr/Hf}$, of 3 to 4. The dominant species that adsorbed to the anion exchange resin was $M(SO_4)_3^{2-}$, where M is Zr or Hf [12].

2. Experimental

2.1 Materials

The TEVA resin was purchased from Eichrom Technologies Inc. The concentrated HCl, HNO₃ and H₂SO₄ used for solution preparation were purchased from VWR. All chemicals were used without further purification. The actual concentrations of acid solutions were determined via titration with standardized 0.4895 M NaOH using a Class A buret and phenolphthalein indicator.

2.2 Radionuclide Solutions

⁹⁵Zr ($t_{1/2} = 64$ d) was obtained from Eckert and Ziegler Isotope Products in the oxalate form in 0.5 M oxalic acid (1 mCi). The ⁹⁵Zr oxalate was converted to the chloride form and purified upon receipt. The conversion from oxalate to chloride was done by precipitating Zr in the hydroxide form using concentrated ammonium hydroxide and lanthanum carrier. The precipitation was followed by dissolution in concentrated hydrochloric acid. The dissolved product was then passed over a Dowex 1 x 8 anion exchange column. The column was flushed with concentrated HCl to remove any impurities from the Zr. The Zr was then stripped from the anion exchange column using 2 M HCl. The resulting solution was diluted in 2 M HCl to a volume that resulted in an approximately 3 cps/mL ⁹⁵Zr solution.

The ¹⁷⁵Hf ($t_{1/2} = 70$ d) was produced from proton bombardment of lutetium foil, ^{nat}Lu(p,x)¹⁷⁵Hf, at the Center for Accelerator Mass Spectrometry (CAMS) at Lawrence Livermore National Laboratory (LLNL). The ^{nat}Lu foil contained approximately 0.1 mCi ¹⁷⁵Hf. Upon receipt the foil underwent dissolution in aqua regia (1:1). The resulting solution was then loaded onto a Dowex 1 x 8 anion exchange column conditioned with concentrated HCl. The column was then rinsed with copious amounts of concentrated HCl to remove all impurities. The Hf was then eluted with 4 M HCl. The purified ¹⁷⁵Hf fraction was diluted in 2 M HCl and had an activity concentration of approximately 5 cps/mL.

2.3 Batch Studies

All tracer solutions were stored in 2 M HCl acid. An appropriate amount (3 to 5 cps) of each radionuclide to be studied was transferred to a clean, dry 12 x 55 mm plastic sample tube. This was then counted using a Perkin-Elmer Wizard² 2480 automatic NaI gamma counter for 30 minutes to establish the initial activity of each radionuclide of interest in the sample. The samples were then evaporated to dryness in a water bath with a jet of compressed air flowing over each sample, and reconstituted in 1 mL of the solution to be studied. 10-20 mg of the desired resin was quantitatively weighed into the 12 x 55 mm plastic sample tube containing the radionuclides. Samples were then placed on a shaker for one hour. The liquid sample was then extracted from the sample tube using a syringe equipped with a needle. The liquid sample was then passed through a syringe tip filter set-up and into a clean, dry 12 x 55 mm plastic sample tube. The sample was then counted using the same gamma counter as above for 1 hour to determine the quantity of activity taken up by the resin.

The activity on the resin is taken as the difference between final and initial activity in solution. The weight distribution, D_w , of the element of interest can be obtained using Equation 1. In Equation 1 A_0 is the initial activity of the solution; A_s is the activity on the solid phase; W is the mass of the resin in

grams and V is the volume of solution in milliliters. Once D_w is calculated k' , free column volume to peak maximum, can be found using Equation 2, where F is the resin factor. The resin factor, F, is available from Eichrom.

$$D_w = \left(\frac{A_p - A_s}{W} \right) + \left(\frac{A_s}{V} \right) \quad (1)$$

$$k' = D_w \times F \quad (2)$$

2.4 Column Studies

Column extraction of mixed radionuclides was performed with pre-packed 2 mL columns containing the TEVA resin. An appropriate volume of each stock solution was transferred to a clean, labeled 12 x 15 mm sample tube, and used as-is. The sample was evaporated to dryness in a water bath with a jet of compressed air flowing over each sample, reconstituted in 1 mL of the desired acid solution. The sample was then counted for 30 minutes on the same automatic gamma counter to determine the initial activity of each radionuclide present.

During the column extraction studies a vacuum box set-up was used, available from Eichrom International, Inc. The vacuum box set-up consisted of a 24-hole polycarbonate vacuum box equipped with a pressure regulator was used to accelerate the elution process. A pressure between 8 and 15 in Hg was maintained. The column was conditioned with the appropriate solution and then the 1 mL solution containing the radionuclides of interest was then loaded on the column. The elution profile of each radionuclide was then determined in 0.5 mL increments. The samples were then brought up to a volume of 1 mL to maintain counting geometry. The samples were then counted on the same Wizard² automatic gamma counter for 30 minutes to determine the quantity of radionuclides in each fraction.

3. Results and Discussion

3.1 HCl Solutions

3.1.1 Batch Studies

Preliminary results are discussed in the remainder of this report. The extraction behavior of Zr and Hf from 0.1 to 11.5 M HCl with the commercially available extraction chromatographic resin TEVA was studied. The results from this batch study are shown in Fig. 2.

It is apparent from Fig. 2 that both Zr and Hf have virtually no affinity for the TEVA resin below approximately 6 M HCl. This is expected, as it is well documented that Group 4 metals do not form an anionic complex below 6 M HCl, however above 6 M HCl the MCl_6^{2-} complex is formed, where M is Zr

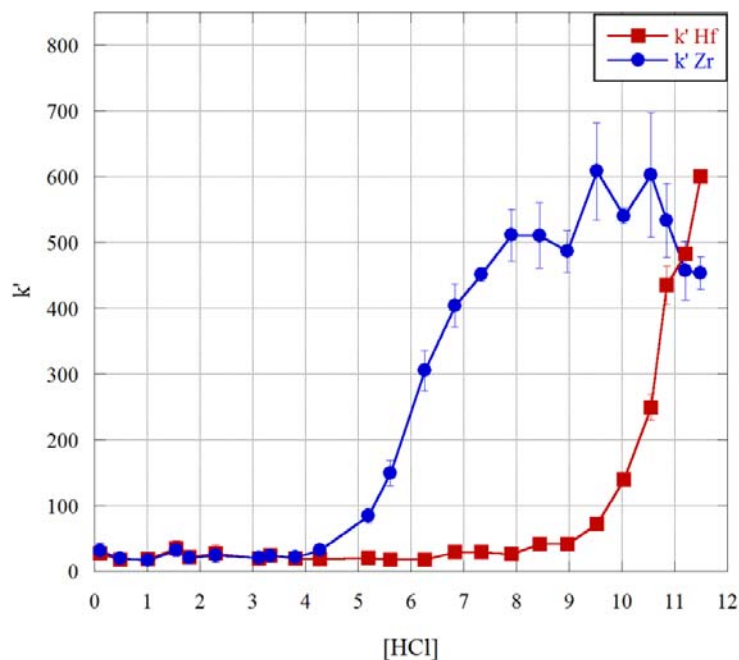


FIG. 2. The separation behavior of Zr and Hf on Eichrom's TEVA resin. The error bars are population standard deviations.

or Hf [13,14]. Zr has a much stronger affinity for the TEVA resin than does Hf, until 11 M HCl is reached. Above 11 M HCl the affinity trends appears to invert and Hf has a stronger affinity for the TEVA resin than Zr. This is most likely due to the presence of a large number of chloride anions, which causes increased formation of the HfCl_6^{2-} species. The largest separation of Zr from Hf occurs between 6 and 8.5 M HCl, as indicated by the separation factors for Zr and Hf ($\text{SF}_{\text{Zr/Hf}}$) listed in Table I. Based upon these results 6.256, 6.839, 7.332 and 7.900 M HCl were chosen for further investigation in a dynamic column study. It was believed that these concentrations would allow Hf to be eluted from the TEVA column while leaving Zr adsorbed to the column from a load solution of concentrated HCl (11.49 M).

Table 1. TEVA separation factor for Zr and Hf as a function of HCl concentration obtained in batch studies.

[HCl]	$\text{SF}_{\text{Zr/Hf}}$
0.1036	1.13±0.13
0.4886	1.13±0.11
1.005	0.95±0.09
1.549	0.93±0.04
1.792	1.00±0.13
2.297	0.90±0.04
3.118	1.03±0.01
3.335	0.99±0.04
3.811	1.13±0.23
4.273	1.77±0.27
5.189	3.96±0.50
5.600	8.24±0.40
6.256	17.0±4.8
6.830	14.0±1.11
7.332	15.5±2.87
7.900	19.2±3.26
8.432	12.1±1.35
8.956	11.7±1.74
9.516	8.39±0.93
10.00	3.85±0.16
10.45	2.41±0.33
10.84	1.22±0.05
11.20	0.94±0.06
11.49	0.75±0.03

3.1.2 Dynamic Column Studies

The column was loaded and then eluted with 6 aliquots of 0.5 mL of 6.256, 6.839, 7.332 or 7.900 M HCl. Based on the batch results it was believed that this would elute the Hf off the column while leaving Zr adsorbed to the column. Zr was then eluted with 6 aliquots of 0.5 mL of 3 M HCl. The elution curves of each Hf elution condition are shown in Fig. 3.

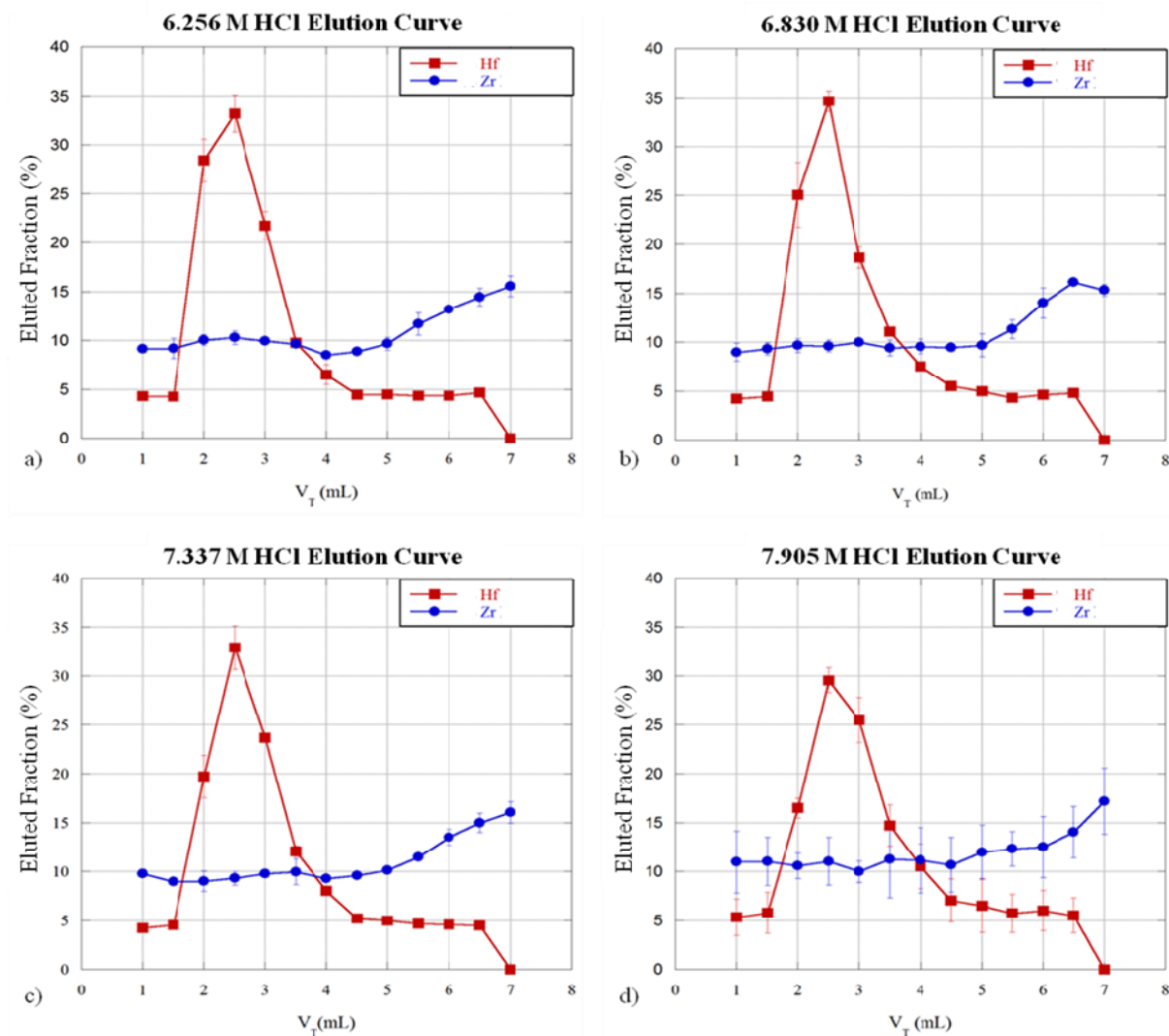


FIG. 3. The HCl elution profiles for Zr and Hf on Eichrom's TEVA resin, where V_T is the total solution volume passed through the column. All columns were loaded using a concentrated HCl solution. a) The elution profile using an eluent of 6.256 M HCl to elute Hf. b) The elution profile using an eluent of 6.830 M HCl to elute Hf. c) The elution profile using an eluent of 7.337 M HCl to elute Hf. d) The elution profile using an eluent of 7.905 M HCl to elute Hf. Zr was eluted from all columns using 3 M HCl.

In Fig. 3 the first data point at 1 mL indicates the load fraction and is not included in the eluted percentages below. In panel a there is separation of Hf and Zr. $104 \pm 3\%$ of Hf is eluted with the 3 mL of 6.256 M HCl, while $57.7 \pm 1.5\%$ of Zr is eluted with the Hf. This indicates a $SF_{Hf/Zr}$ of 1.80 ± 0.04 . In

panel b there is also separation of Hf and Zr. $101 \pm 4\%$ of Hf is eluted with 3 mL of 6.830 M HCl, while $57.6 \pm 1.5\%$ of Zr is eluted with the Hf. This indicates a $SF_{Hf/Zr}$ of 1.76 ± 0.04 . In panel c there is again separation of Hf and Zr. $101 \pm 3\%$ of Hf is eluted with 3 mL of 7.337 M HCl, while $57.4 \pm 1.6\%$ of Zr is eluted with the Hf. This indicates a $SF_{Hf/Zr}$ of 1.79 ± 0.05 . In panel d there, yet again, appears to be separation of Hf and Zr. $103 \pm 5\%$ of Hf is eluted with 3 mL of 7.905 M HCl, while $65.0 \pm 6.4\%$ of Zr is eluted with the Hf. This indicates a $SF_{Hf/Zr}$ of 1.58 ± 0.11 .

Based on these results if an experiment were to be done with Rf it would be recommended that the radioactivity be loaded onto the column from concentrated HCl, followed by an elution of Hf with 6.256, 6.830 or 7.337 M HCl; Zr could then be eluted from the column using 3 M HCl. Under these conditions the experiment would have to be conducted many times in order to minimize the effects of statistical fluctuations on the separation of Rf from its homologs.

3.1.3. Conclusions

The extraction chromatographic behavior of Zr and Hf in HCl has been investigated using the commercially available TEVA resin. Batch studies using carrier free ^{95}Zr and ^{175}Hf indicated Zr and Hf were best separated between 6 and 8.5 M HCl with separation factors of Zr from Hf ($SF_{Zr/Hf}$) exceeding 10. This result was then used during dynamic column studies to preferentially elute Hf and determine the optimal conditions for separating Hf from Zr. It was determined that a maximum separation factor of Hf from Zr ($SF_{Hf/Zr}$) was 1.89 at 6.3 M HCl, in dynamic column studies.

Based on these results it is recommended that the radioactivity be loaded on to the column from concentrated HCl, followed by an elution of Hf with 6.256, 6.830 or 7.337 M HCl, Zr could then be eluted from the column using 3 M HCl. Following this recommended separation procedure there would need to be many experiments to ensure proper chemical characterization of Rf, with respect to Zr and Hf, and not draw a conclusion based upon statistical fluctuation.

3.2 HNO₃ System

3.2.1 Batch Studies

The extraction behavior of Zr and Hf from 0.1 to 15.9 M HNO₃ with the commercially available extraction chromatographic resin TEVA was studied. The results from this batch study are shown in Fig. 4.

It is apparent from Fig. 4 that Zr and Hf have identical behavior on the TEVA resin, within error bars. Horwitz and co-workers report a k' for Th that is greater than 10^2 and k' for Pu that is greater than 10^4 [14]. Here, it is shown that the highest k' value for Zr and Hf is < 50 at 7.367 M HNO₃. Upon comparison of the k' values reported here for Zr and Hf and those reported for Th and Pu by Horwitz and co-workers it appears that the TEVA resin would work well for removal of actinides in a catcher block type experiment by sorbing the actinide elements and allowing Zr and Hf to pass through the resin. However, based on Fig.4 the TEVA resin is not a good candidate for intra-Group 4 separations and thus not a good candidate for chemically characterizing Rf with respect to its homologs, Zr and Hf.

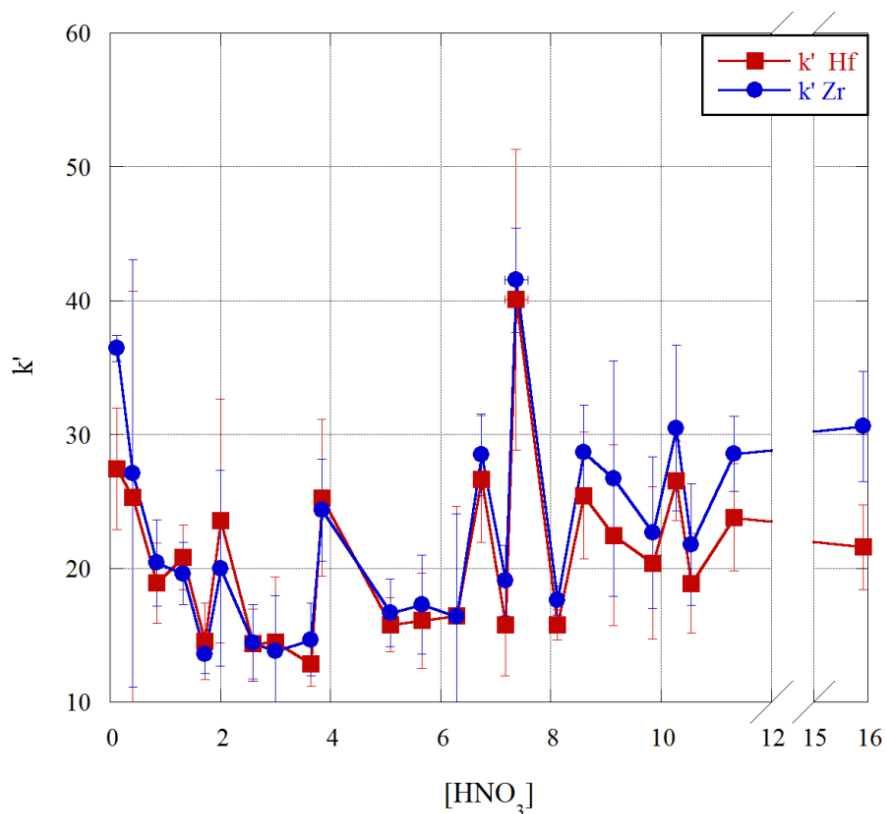


FIG. 4. The separation behavior of Zr and Hf in a nitric matrix on Eichrom’s TEVA resin. The error bars are population standard deviations.

Similar k' values are found in this study as in the study by Haba and co-workers [9], implying a similar speciation of Zr and Hf. It appears from these results that Zr and Hf have a lower tendency to form anionic species in nitric matrices and a higher tendency to form neutral or cationic species.

The separation factors for Zr from Hf ($SF_{Zr/Hf}$) at their respective acid concentrations are shown in Table II. It is apparent from the $SF_{Zr/Hf}$ values reported in Table II that there is virtually no separation of Zr from Hf. Even though little separation was found dynamic column studies were conducted to ensure that the static batch system is representative of the dynamic column system.

Table II. TEVA separation factor for Zr and Hf as a function of HNO₃ concentration obtained in batch studies

[HNO ₃]	SF _{Zr/Hf}
0.1199	1.35±0.21
0.4120	1.08±0.04
0.8452	1.08±0.04
1.324	0.94±0.02
1.712	0.95±0.13
1.995	0.85±0.11
2.589	1.01±0.11
2.992	0.96±0.03
3.642	1.13±0.13
3.840	0.98±0.08
5.083	1.05±0.05
5.653	1.08±0.10
6.285	1.00±0.08
6.734	1.08±0.10
7.173	1.23±0.14
7.367	1.06±0.20
8.119	1.12±0.02
8.530	1.14±0.10
9.134	1.18±0.05
9.843	1.12±0.07
10.28	1.14±0.15
10.55	1.15±0.06
11.33	1.21±0.09
15.91	1.42±0.09

3.2.2 Dynamic Column Studies

Each resin was pre-treated with 3 mL of concentrated HNO₃ prior to loading the column with 1 mL of solution containing Zr and Hf. The column was then loaded with the radionuclides of interest. The load solution containing Zr and Hf was in concentrated HNO₃; this was chosen to ensure if an anionic complex could form there would be enough nitrate ion present to bind Zr and/or Hf. The column was the eluted with 6 aliquots of 0.5 mL of 7.173, 8.119 or 11.325 M HNO₃. From the results of the batch studies it was expected that under all of these elution conditions both Zr and Hf would co-elute. However, to ensure all Zr and Hf were eluted off of the column 6 aliquots of 0.5 mL of 3 M HNO₃ were then taken after the initial elution solution of high molarity nitric acid. 3 M HNO₃ was chosen based on the batch studies; Zr and Hf had little affinity for the TEVA resin under these conditions. The elution curves for Zr and Hf under various HNO₃ elution conditions can be seen in Fig. 5.

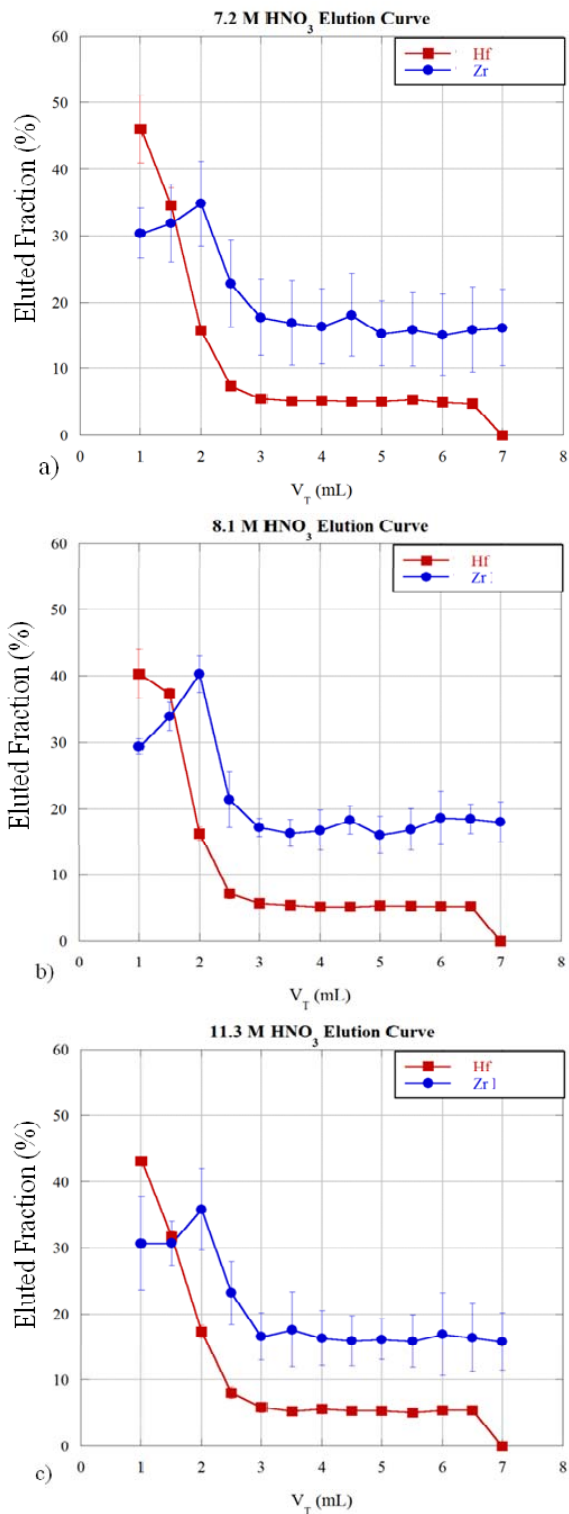


FIG. 5. The elution profiles for Zr and Hf on Eichrom's TEVA resin. All samples were loaded using a concentrated HNO₃ solution. a) The elution profile using an eluent of 7.173 M HNO₃. b) The elution profile using an eluent of 8.119 M HNO₃. c) The elution profile using an eluent of 11.325 M HNO₃. All errors are reported as population standard deviations.

In Fig. 5 the first data point at 1 mL indicates the load fraction. Despite the indications in the batch study that Zr and Hf behaved identically in a nitric matrix on the TEVA resin, Fig. 5 shows that Zr consistently elutes later than Hf. This indicates that Zr has a slightly higher affinity for the TEVA resin, in a nitric matrix, than does Hf. However, there is still little separation between the two elements. Under the 7.173 M HNO₃ elution conditions 140.±15% of the Zr is eluted with the 3 mL elution fraction and 73.4±2.7% of the Hf is eluted, Fig. 5a. Under the 8.119 M HNO₃ elution conditions 146±7% of the Zr is eluted with the 3 mL elution fraction and 76.9±1.7% of the Hf is eluted, Fig. 5b. Under the 11.325 M HNO₃ elution conditions 152±12% of the Zr is eluted with the 3 mL elution fraction and 73.7±9.1% of the Hf is eluted, Fig. 5c.

If the total elution fraction is summed over the entire elution curve a number >100% results. In order to explain this deviation the following is proposed: For Zr, the background levels in the counting windows of the automated gamma counter are approximately 0.3 cps and for Hf the background is approximately 0.2 cps. Generally, this small of a background would not be a problem however, being that the solution concentrations used in these studies are so low the 0.3 and 0.2 cps background becomes approximately 10% and 4% of the signal for Zr and Hf, respectively. Increasing the counting time of the sample to decrease the background is not a feasible option due to the number of samples processed. Increasing the quantity of activity in solution is also not an option, as this could lead to polynuclear formation, which is in turn not representative of atom-at-a-time chemistry [15,16,17].

Despite this rather large error it can still be seen that TEVA does not separate Zr and Hf in a nitric matrix that is suitable for chemically characterizing Rf with respect to its homologs. It is still possible to use the TEVA resin in a catcher block setup to purify the element of interest from tetravalent actinides.

3.2.3 Conclusions

The extraction chromatographic behavior of Zr and Hf in HNO₃ has been investigated using the commercially available TEVA resin. Batch studies using carrier-free ⁹⁵Zr and ¹⁷⁵Hf indicated that Zr and Hf behave identically in a nitric matrix and cannot be separated using the TEVA resin. Despite this dynamic column studies were carried out to ensure that static batch studies were representative of dynamic column studies.

In the dynamic column study it was found that Zr has a slightly higher affinity for TEVA than does Hf. However, there is not enough separation between Zr and Hf to render it useful for the chemical characterization of Rf with respect to its lighter homologs, Zr and Hf.

Both the batch and dynamic column studies indicates that Zr and Hf have a tendency to form an cationic or neutral species even in high nitric acid concentrations, an observation that has been noted by Haba and co-workers [9].

Despite not being useful for the chemical characterization of Rf with respect to Zr and Hf it is possible that TEVA could be used to separate out tetra- and hexavalent actinides from Group 4 elements in a catcher-block-type chemistry experiment.

3.3.1 H₂SO₄ System

3.3.1 Batch Studies

The extraction behavior of Zr and Hf from 0.1 to 15.9 M H_2SO_4 with the commercially available extraction chromatographic resin TEVA was studied. The results from this batch study are shown in Fig. 6.

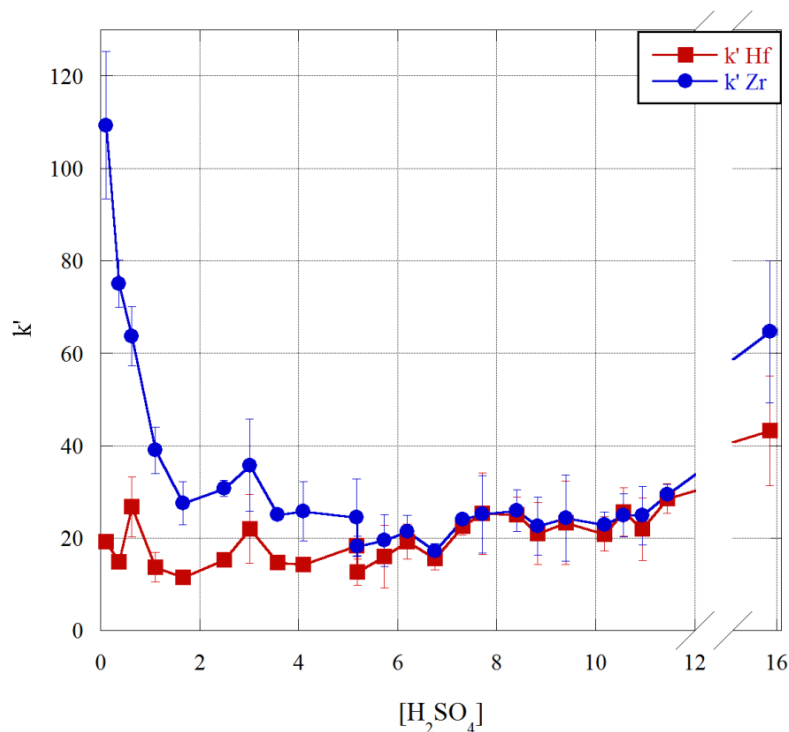


FIG. 6. The separation behavior of Zr and Hf in a sulfuric matrix on Eichrom's TEVA resin. The error bars are population standard deviations.

It can be seen from Fig. 6 that above 3 M H_2SO_4 Zr and Hf have nearly identical behavior to one another. The 3 – 15.9 M concentration regime is inadequate to chemical characterize Rf with respect to Zr and Hf. The behavior of Zr and Hf below 3 M is much more interesting for the chemical characterization of Rf. At 0.1069, 0.3696 and 0.6315 M H_2SO_4 Zr has a much higher affinity for the TEVA resin than Hf and shows promise for the separation of Zr and Hf and in turn investigation of relativistic effects in Rf.

The separation factors for Zr from Hf ($\text{SF}_{\text{Zr/Hf}}$) at their respective acid concentrations are shown in Table III. It is apparent from the $\text{SF}_{\text{Zr/Hf}}$ values reported in Table I that there is some separation of Zr from Hf at the lowest $[\text{H}_2\text{SO}_4]$. Based on the results of the batch study a load solution of concentrated (15.86 M) H_2SO_4 was chosen due to Zr and Hf both having similar and high adsorption to the TEVA resin from this solution. Elutions solutions of 0.1069, 0.3696, 0.6315 and 1.101 M H_2SO_4 were chosen to elute Hf from the column while leaving Zr on the column. Finally, an elution solution of 6.5 M H_2SO_4 was chosen to elute Zr and any remaining Hf from the column.

Table III. TEVA separation factor for Zr and Hf as a function of H₂SO₄ concentration obtained in batch studies.

[H ₂ SO ₄]	SF _{Zr/Hf}
0.1069	5.71±0.83
0.3696	5.10±0.56
0.6315	2.45±0.45
1.101	2.89±0.32
1.656	2.41±0.46
2.488	2.02±0.15
3.007	1.67±0.34
3.575	1.72±0.15
4.093	1.79±0.31
5.167	1.34±0.11
5.186	1.47±0.16
5.733	1.26±0.25
6.192	1.12±0.04
6.753	1.11±0.10
7.309	1.07±0.08
7.714	1.00±0.02
8.408	1.03±0.09
8.831	1.09±0.11
9.397	1.05±0.10
10.18	1.11±0.13
10.56	0.98±0.16
10.94	1.15±0.18
11.45	1.04±0.11
15.86	1.51±0.17

3.3.2 Dynamic Column Studies

Each resin was pre-treated with 3 mL of concentrated H₂SO₄ prior to loading the column with 1 mL of solution containing Zr and Hf. The column was then loaded with the radionuclides of interest. The load solution containing Zr and Hf was in concentrated H₂SO₄; this was chosen to ensure if an anionic complex could form there would be enough sulfate ion present to bind Zr and/or Hf. The column was eluted with 6 aliquots of 0.5 mL of 0.1069, 0.3696, 0.6315 or 1.101 M H₂SO₄. From the results of the batch studies it was expected that below 1 M H₂SO₄ Hf would elute leaving Zr on the column. To ensure all Zr and Hf were eluted off of the column 6 aliquots of 0.5 mL of 6.5 M H₂SO₄ were also eluted. This was chosen based on the batch studies; Zr and Hf had little affinity for the TEVA resin under these conditions. The elution curves for Zr and Hf under various H₂SO₄ elution conditions can be seen in Fig. 7.

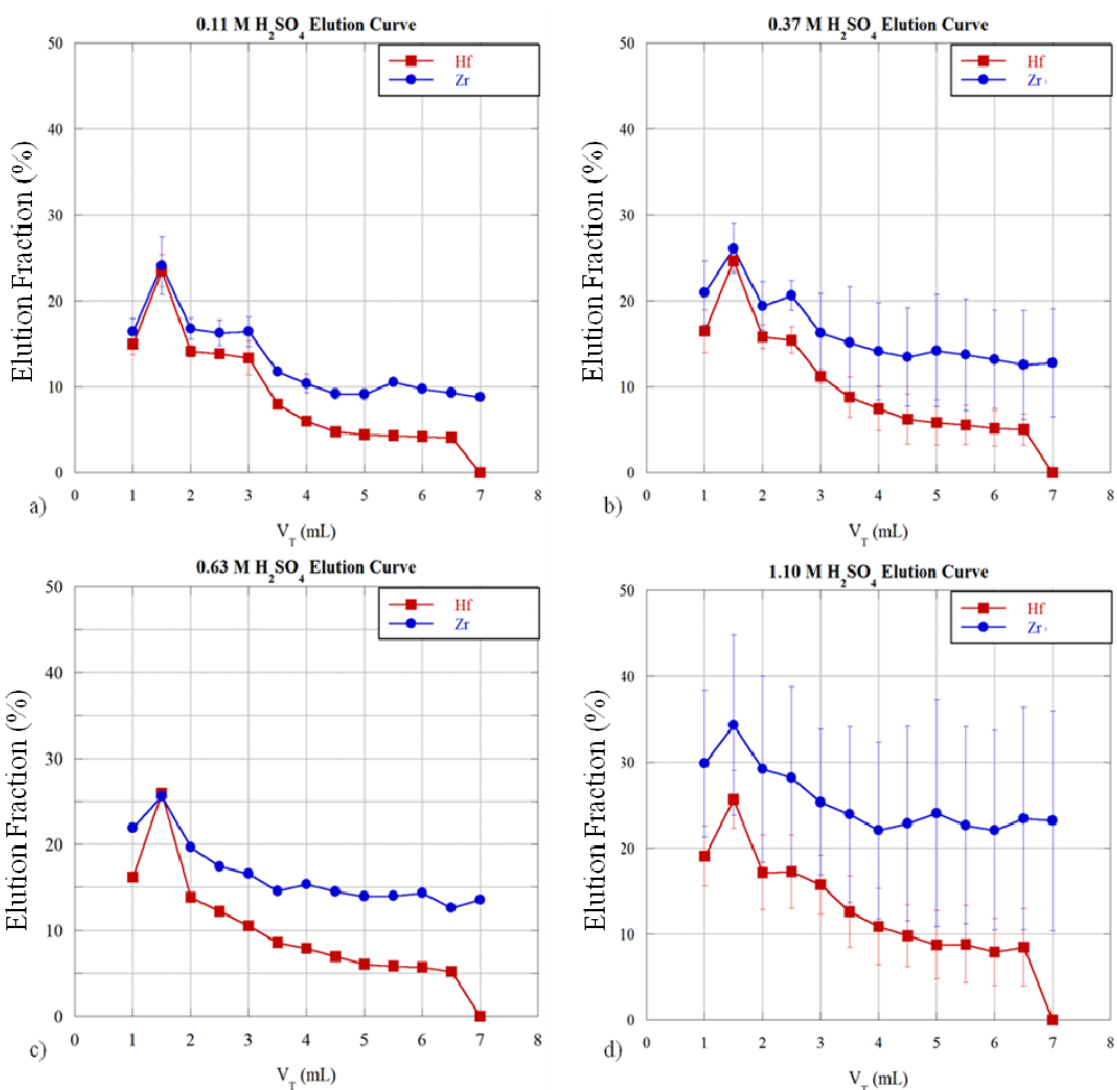


FIG. 7. The elution profiles for Zr and Hf on Eichrom's TEVA resin. All samples were loaded using a concentrated H_2SO_4 solution. a) The elution profile using an eluent of 0.1068 M H_2SO_4 followed by 6.5 M H_2SO_4 . b) The elution profile using an eluent of 0.3696 M H_2SO_4 followed by 6.5 M H_2SO_4 . c) The elution profile using an eluent of 0.6315 M H_2SO_4 followed by 6.5 M H_2SO_4 . d) The elution profile using an eluent of 1.101 M H_2SO_4 followed by 6.5 M H_2SO_4 . All errors are reported as population standard deviations.

In Fig. 7 the first data point at 1 mL indicates the load fraction. In the batch studies the $SF_{Zr/Hf}$ for 0.1036 and 0.3696 M H_2SO_4 were found to be > 5 , however it can be seen from Fig 7 a and b there is little separation of Zr and Hf on the dynamic column. Under the 0.1068 M H_2SO_4 elution conditions $95.7 \pm 4.3\%$ of the Zr eluted with the 3 mL elution fraction and $78.8 \pm 2.6\%$ of the Hf eluted, Fig. 37a. Under the 0.3696 M H_2SO_4 elution conditions $112 \pm 11\%$ of the Zr eluted with the 3 mL elution fraction and $83.4 \pm 4.3\%$ of the Hf eluted, Fig. 37b. Under the 0.6315 M H_2SO_4 elution conditions $109 \pm 15\%$ of the Zr eluted with the 3 mL elution fraction and $79.0 \pm 7.8\%$ of the Hf eluted, Fig 7c. Under the 1.101 M H_2SO_4 elution conditions $163 \pm 25\%$ of the Zr eluted with the 3 mL elution fraction and $98.9 \pm 9.9\%$ of the

Hf eluted, Fig 7d. Despite this rather large error it can still be seen that TEVA does not separate Zr and Hf in a sulfuric matrix that is suitable for chemically characterizing Rf with respect to its homologs.

3.3.3. Conclusions

The extraction chromatographic behavior of Zr and Hf in H₂SO₄ has been investigated using the commercially available TEVA resin. Batch studies using carrier free ⁹⁵Zr and ¹⁷⁵Hf indicated that Zr and Hf in a low molarity sulfuric matrix could be separated adequately for use in chemically characterizing Rf using the TEVA resin. This also indicates that Zr has a higher tendency to form an anionic species in a sulfuric matrix, than does Hf. Based on the batch study results dynamic column studies were carried out.

In the dynamic column study it was found that Zr has a slightly higher affinity for TEVA than does Hf. However, there was not enough separation between Zr and Hf to render it useful for the chemical characterization of Rf with respect to its lighter homologs, Zr and Hf.

Acknowledgements. The authors would like to thank the heavy elements group at LLNL for providing the ¹⁷⁵Hf and the Welch Foundation for funding grant number A-1710.

- [1] V. Pershina, Chem. Rev. **96**, 1977 (1996).
- [2] R. Guillaumont, J.P. Adloff, A. Penelozu, Radiochim. Acta **46**, 169 (1989).
- [3] M. Schädel, Angew. Chem. Int. Edit. **45**, 365 (2006).
- [4] E.P. Horwitz, M.P. Dietz, R. Chiarizia, H. Diamond, S.L. Maxwell III, M.R. Nelson, Anal. Chem. Acta **310**, 310 (1995).
- [5] E.K. Hulet, R.W. Lougheed, J.F. Wild, J.H. Landrum, Inorg. Nucl. Chem. **42**, 79 (1980).
- [6] E. Cerrai, G. Ghersini, Energia Nucleare **11**, 441 (1964).
- [7] B.A.J. Lister, L.A. McDonald, J. Chem. Soc.; **1952**, 4315 (1952).
- [8] J.P. Faris, R.F. Buchanan, Anal. Chem.; **36**, 1147 (1964).
- [9] H. Haba *et. al.*, J. Nucl. Radiochem. Sci.; **3**, 143 (2002).
- [10] N.J. Stoyer *et. al.*, Nucl. Phys. **A787**, 388c (2007).
- [11] D.I. Ryabchikov, I.N. Marov, A.N. Ermakov, V.K. Belyaeva, J. Inorg. Nucl. Chem.; **26**, 965 (1964).
- [12] Z.J. Li, A. Toyoshima, K. Tuskada, Y. Nagame, Radiochim. Acta; **98**, 7 (2010).
- [13] A. Clearfield, Rev. Pure Appl. Chem. **14**, 91 (1964).
- [14] *Comprehensive Coordination Chemistry, Vol. 3*, edited by G. Wilkinson, (Oxford, Pergamon Press, 1987) p. 384.
- [15] B. Noren, Acta Chemica Scandinavica **27**, 4 (1973).
- [16] J.S. Johnson, K.A. Kraus, Hydrolytic Behavior of Metal Ions. VI. Ultracentrifugation of Zirconium(IV) and Hafnium(IV); J. Am. Chem. Soc. **78**, 16, (2002).
- [17] A.K. Mukherji, Analytical Chemistry of Zirconium and Hafnium. 1st edition (Pergamon Press: Oxford, New York, 1970), p. 281.

Measurement of the $^{nat}\text{Lu}(p,x)^{175}\text{Hf}$ excitation function

Megan E. Bennett, Dmitriy A. Mayorov, Kyle D. Chapkin, Marisa C. Alfonso,
Tyler A. Werke, and Charles M. Folden III

1. Introduction

It is of great interest to study the chemical properties of the transactinide elements ($Z > 103$) due to the influence of relativistic effects on the chemical properties. These effects are expected to result in deviation of periodic group trends [2]. In order to assess this deviation of chemical behavior for the heaviest elements, their chemical behavior should be compared to that of their lighter homologs that reside in the same periodic group. However, chemically studying the heaviest elements presents several challenges which stem from the short half-lives and extremely low production rates [3]. In order to determine the suitability of a chemical system for transactinide chemistry, off-line experiments are first performed with the homologs and pseudo-homologs of the element of interest, at sub-tracer scale levels. In order to perform experiments with sub-tracer scale concentrations, radionuclides are used, some of which are not commercially available. Here we report the measurement of the $^{nat}\text{Lu}(p,x)$ excitation function for production of ^{175}Hf ($t_{1/2} = 70$. d) for off-line chemical studies of Group IV homologs.

2. Experimental methods

Long-lived ^{175}Hf was produced using the $^{nat}\text{Lu}(p,x)$ reaction at the Single Event Effects (SEE) beam line of the K500 cyclotron at the Texas A&M University Cyclotron Institute. The stacked foil activation technique is commonly used to experimentally determine excitation functions [4,5,6] and has been used in this study. The extensively measured $^{nat}\text{Ti}(p,x)^{48}\text{V}$ reactions were used as monitor reactions [7] to assess the beam energy and intensity. A schematic of the target stack and target holder is shown in Fig. 1 a and b, respectively. A HD^+ beam was accelerated in the K500 cyclotron and underwent stripping via an Al stripper foil to H^+ before being delivered into the SEE beam line target chamber. A proton beam with an energy of 22.1 ± 0.05 MeV, one of the lowest achievable proton energies for the K500 cyclotron, was incident on the target stack. A stack of three ^{nat}Ta foils, each ~ 81 μm thick, was placed in front of the first Lu foil in order to degrade the beam to a lower, more appropriate energy, 16.7 MeV. Energy losses of the proton beam through each degrader and target were calculated using SRIM-2008 [9]. The average beam current was 1.85 μA . The geometry of the aluminum target holder ensured that nearly the whole beam passed through each target.

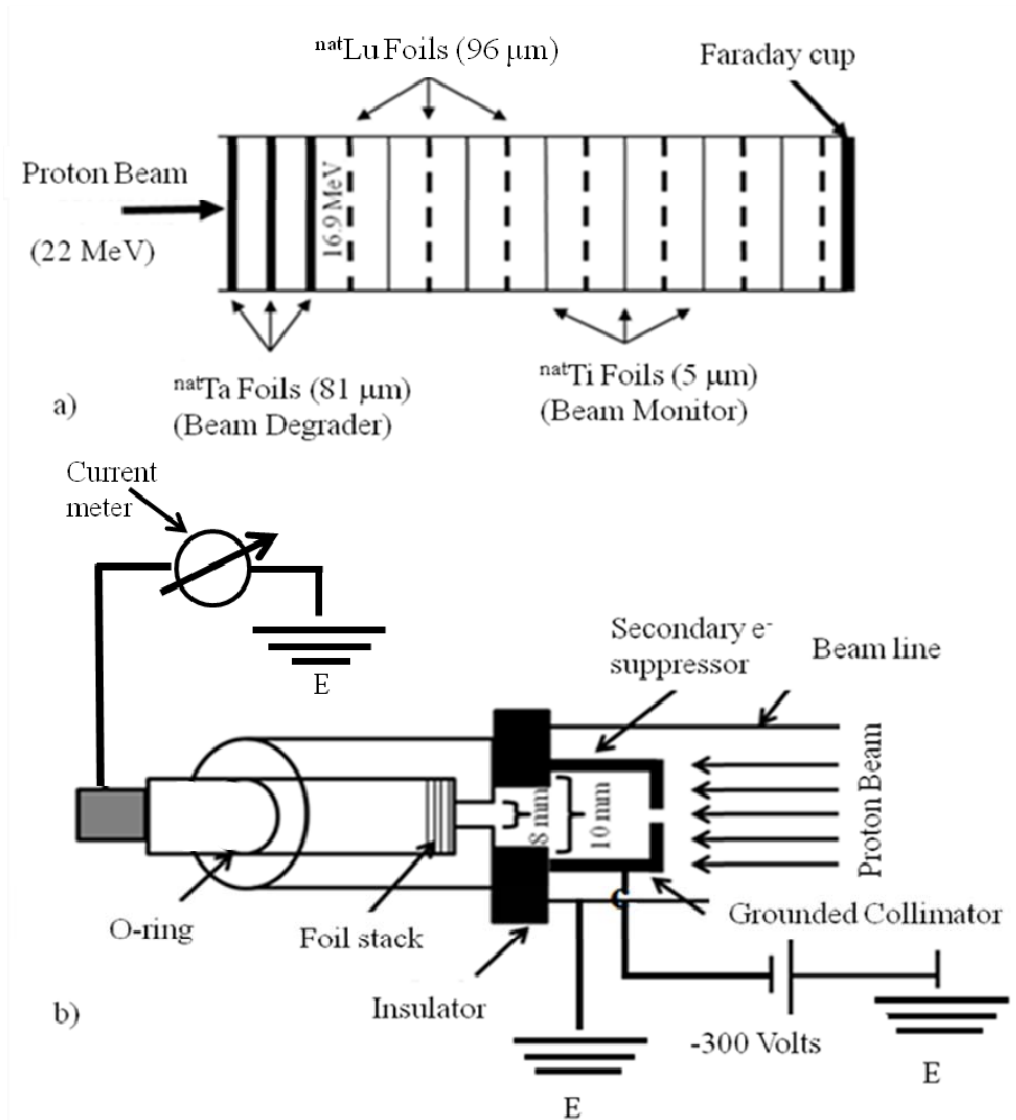


FIG. 1. Schematic drawings of the experimental setup. a) The foil degrader proceeding from left to right. b) The custom aluminum target holder mounted on the beam line [8].

The beam energy in the center of each target is shown in Table I. These values have an estimated 0.2 % error due to the error associated with the reported initial beam energy and an estimated 4% error associated with the energy loss calculations. The beam dose was determined using a current integrator connected to the back end of the target chamber, which also held the targets in place. The data from the current integrator was used to determine the reaction cross sections. At the end of irradiation, the target foils were allowed to cool for approximately 90 minutes to allow for the decay of short-lived products, transportation, and preparation of targets for γ -ray measurements. The foils were then carefully removed from the target holder in irradiation order. Each foil was then counted on a 70% HPGe γ -ray detector that

was energy calibrated using a National Institute of Standards and Technology (NIST) traceable ^{152}Eu point source and efficiency calibrated using a polynomial fit. The 343 and 983.5 keV lines were monitored for ^{175}Hf and ^{48}V , respectively. The resulting spectra were processed using the GF3 module within RadWare [10]. The cross sections were then calculated based on the obtained results.

Table I. Calculated beam energy on the center of each target (E_{cot}) with an estimated error of 0.2% and 4% from the initial beam energy and energy loss calculations, respectively.

Target	Thickness (μm)	E_{cot} (MeV)
Ta-1	80.8±1.5	21.3
Ta-2	80.8±1.5	19.8
Ta-3	80.8±1.5	18.1
Lu-1	96 ±7	16.7
Ti-1	4.9±0.2	16.0
Lu-2	96 ±7	15.3
Ti-2	4.9±0.2	14.6
Lu-3	96 ±7	13.8
Ti-3	4.9±0.2	13.1
Lu-4	96 ±7	12.2
Ti-4	4.9±0.2	11.5
Lu-5	96 ±7	10.6
Ti-5	4.9±0.2	9.7
Lu-6	96 ±7	8.7
Ti-6	4.9±0.2	6.9
Lu-7	96 ±7	5.2

3. Results and Discussion

3.1 γ -ray measurements of proton irradiated $^{\text{nat}}\text{Ti}$ and $^{\text{nat}}\text{Lu}$ target foils

The spectra collected from the peak of the excitation functions are shown in Fig. 2 a and b, respectively. All unlabeled peaks can be attributed to the minor products of the irradiation, minor gamma rays of ^{175}Hf , the natural decay series, background or electronic noise. The lack of γ -rays should be noted in the Lu foil spectrum. This indicates that ^{175}Hf is free of γ -ray interferences and can be produced for off-line chemical studies.

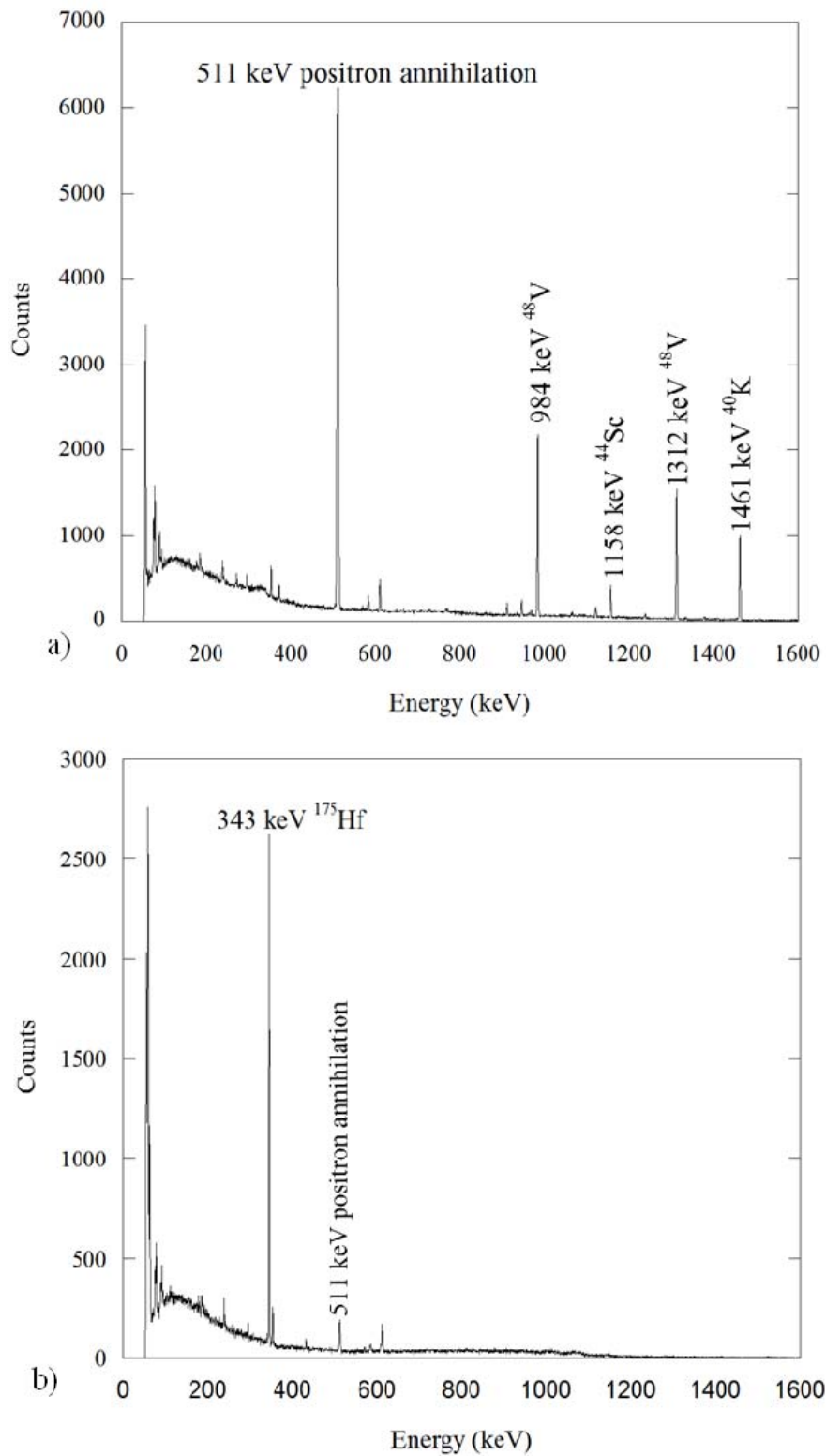


FIG. 2. The γ -ray spectra for proton irradiated foils at the peak of the excitation function. a) The spectrum from the ^{nat}Ti foil that was bombarded with 13.1 MeV protons in the center of the target. b) The spectrum from the ^{nat}Lu foil that was bombarded with 10.6 MeV protons in the center of the target

3.2 Excitation function for the $^{nat}\text{Ti}(p,x)^{48}\text{V}$ reaction

The measured excitation function for the $^{nat}\text{Ti}(p,x)^{48}\text{V}$ reaction is shown in Fig. 3 and the resulting cross sections and associated errors are listed in Table II. All cross sections were calculated based on the absolute detector efficiency, γ -ray intensity, decay corrections to the produced activity, beam intensity and the areal density of the target. For the $^{nat}\text{Ti}(p,x)^{48}\text{V}$ reaction the cross section was based upon the 983.5 keV γ -ray line which has an intensity of 99.98% [11]. All data points within the measured cross section were systematically high compared to the recommended data available through the International Atomic Energy Agency (IAEA) [7]. The cross sections were shifted down based on a χ^2 minimization fit. The correction lowered the cross sections by 27.32%. The error in the cross section is likely due to a systematically low output reading of the beam current integrator. The shape of the excitation function is in excellent agreement with the recommended data without further corrections, when the error bars of the reported data are considered. The maximum cross section was 368 ± 26 mb and occurred at proton energy of 13.1 MeV.

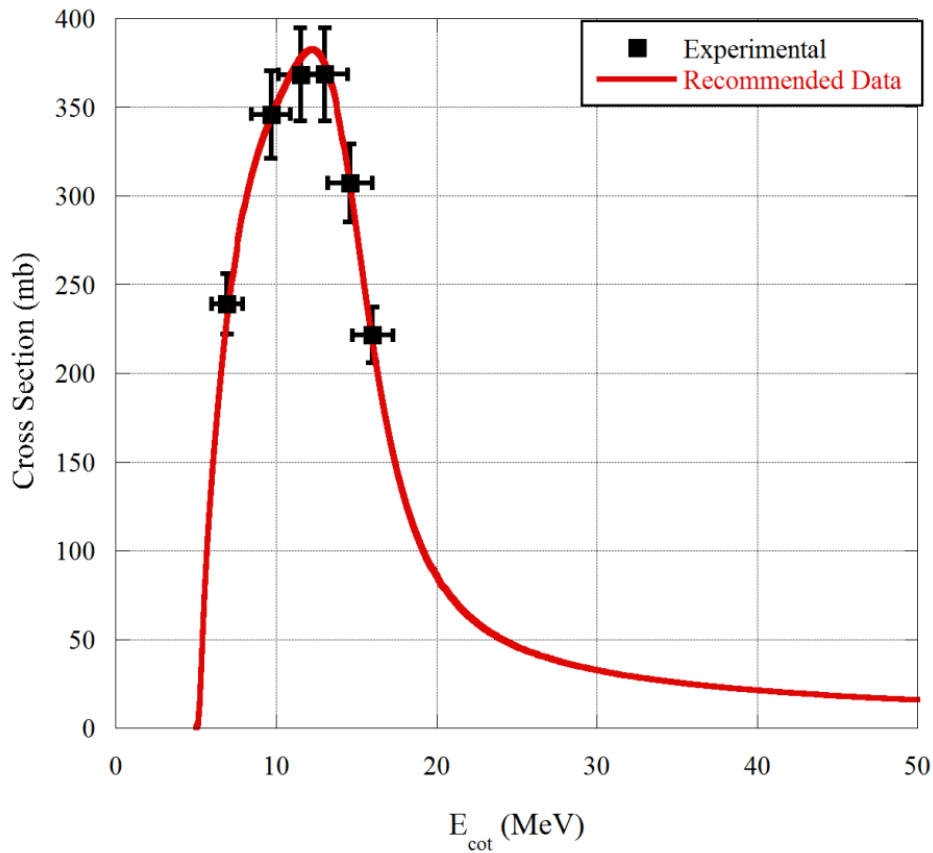


FIG. 3. The excitation function for the $^{nat}\text{Ti}(p,x)^{48}\text{V}$ reaction, systematically corrected and plotted as the squares, compared to the recommended data from the IAEA, plotted as a solid line [7].

Table II. Experimentally determined cross sections for the ${}^{\text{nat}}\text{Ti}(p,x){}^{48}\text{V}$ reaction with their associated error. These data have been corrected with an experimentally determined correction factor of 27.32%; see the main text for a discussion.

Target	E_{cot} (MeV)	Cross section (mb)
Ti-6	6.9	239±17
Ti-5	9.7	346±25
Ti-4	11.5	368±26
Ti-3	13.1	368±26
Ti-2	14.6	307±22
Ti-1	16.0	221±16

3.3 Excitation function for the ${}^{\text{nat}}\text{Lu}(p,x){}^{175}\text{Hf}$ reaction

The measured and predicted excitation functions for the ${}^{\text{nat}}\text{Lu}(p,x){}^{175}\text{Hf}$ reaction are presented in Fig 4. The 27.32% systematic error correction that was applied to the ${}^{\text{nat}}\text{Ti}(p,x){}^{48}\text{V}$ reaction was also applied to the ${}^{\text{nat}}\text{Lu}(p,x){}^{175}\text{Hf}$ cross section data. The resulting cross sections and associated errors are

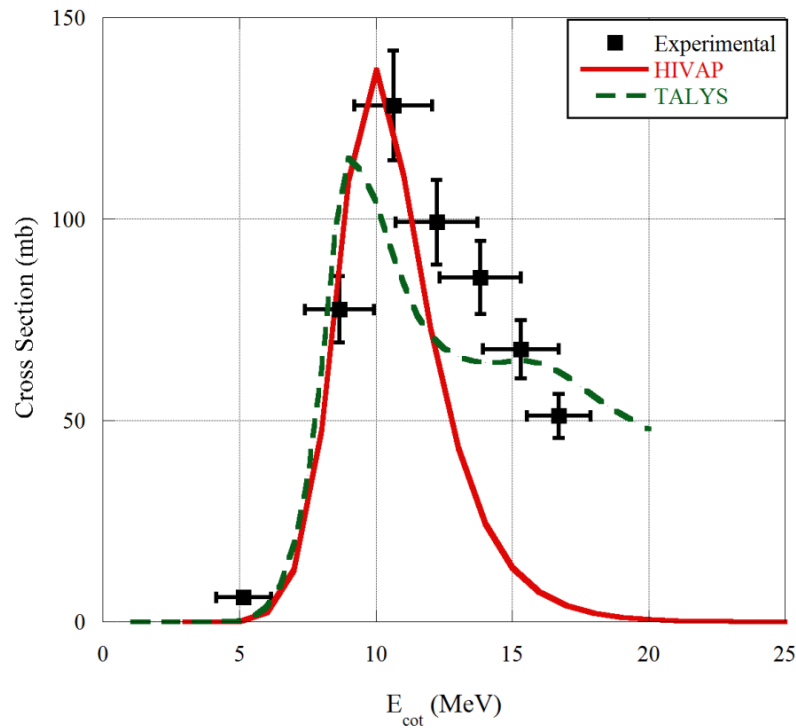


FIG. 4. The measured excitation function for the reaction ${}^{\text{nat}}\text{Lu}(p,x){}^{175}\text{Hf}$ compared to that calculated with the HIVAP and TALYS codes. The reported error bars (shown in Table 1) are largely due to the error in the target thickness. The error at 5.2 MeV is smaller than the data point.

listed in Table III. The cross section was calculated based on the 343 keV γ -ray line which has an intensity of 84% [11]. Experimentally, the maximum cross section is 128 ± 14 mb and is observed at a proton energy of 10.6 MeV.

Both the HIVAP and TALYS codes were used to model the excitation function for the ${}^{\text{nat}}\text{Lu}(p,x){}^{175}\text{Hf}$ reaction [12,13]. Within the experimental error bars, both the HIVAP and TALYS codes predict the peak of the excitation function accurately. This indicates that both the HIVAP and TALYS codes predict particle evaporation from the compound nucleus accurately. The overall shape of the excitation function is poorly predicted by the HIVAP code, which can be explained by the fact that the HIVAP code does not account for the pre-equilibrium decay process (see [14] for a review). In this case, a localized region of high energy density is formed as the projectile interacts with the target nucleus, and particles can be emitted from this region before the dinuclear system can fully equilibrate to become a compound nucleus. Due to the high local temperature, these particles are emitted with significant kinetic energies; when the compound nucleus finally forms it has a relatively low excitation energy. In this way, reaction products can be formed at projectile energies greater than those normally expected from the traditional compound nucleus reaction mechanism, and the measured excitation function extends to higher projectile energies [14]. This can be seen both in the recommended excitation function for ${}^{\text{nat}}\text{Ti}(p,x){}^{48}\text{V}$ in Fig. 3 and the experimental data for ${}^{\text{nat}}\text{Lu}(p,x){}^{175}\text{Hf}$ in Fig. 4. [14]. The TALYS code predicts the shape of the ${}^{175}\text{Hf}$ excitation function much better than the HIVAP code, as the TALYS code accounts for the pre-equilibrium decay process, although a pronounced shoulder is not observed.

It will be necessary to use the K150 cyclotron to achieve higher beam intensities desired for the larger scale production of ${}^{175}\text{Hf}$ (not the K500, as used in this experiment) [15]. Based on the measured excitation function, a beam intensity of 10 μA and a target thickness of 300 μm , approximately 0.5 mCi of ${}^{175}\text{Hf}$ can be made in an 8 hour irradiation period using the K150 cyclotron.

Table III. Experimentally determined cross sections for the ${}^{\text{nat}}\text{Lu}(p,x){}^{175}\text{Hf}$ reaction. These data have been corrected with an experimentally determined correction factor of 27.32%; see the main text for a discussion.

Target	E_{cot} (MeV)	Cross section (mb)
Lu-7	5.2	6.0 ± 0.5
Lu-6	8.7	77 ± 8
Lu-5	10.6	128 ± 14
Lu-4	12.2	99 ± 11
Lu-3	13.8	85 ± 9
Lu-2	15.3	67 ± 7
Lu-1	16.7	51 ± 5

4. Conclusions

The $^{nat}\text{Lu}(p,x)^{175}\text{Hf}$ excitation function has been measured. During the γ -ray measurements, very little γ -ray contamination was seen, indicating that relatively clean ^{175}Hf can be produced at the Cyclotron Institute at Texas A&M University for use in off-line chemical studies of Rf homologs. The maximum cross section was determined to be 128 ± 14 mb, observed at a proton beam energy of 10.6 MeV. A complete description of this work has been published in Ref [1].

- [1] M. E. Bennett, D.A. Mayorov, K.D. Chapkin, M.A. Alfonso, T.A. Werke. Nucl. Instrum. Methods Phys. Res. **B276**, 62 (2012).
- [2] V. Pershina, Chem. Rev. **96**, 1977 (1996).
- [3] M.Schädel, Angew. Chem. Int. Ed. **45**, 368 (2006).
- [4] F. Tárkányi, F. Szelecsényi, S. Takács, A. Hermanne, M. Sonck, A. Thielemans, M.G. Mustafa, Yu. Shubin, Z. Youxiang. Nucl. Instrum. Methods Phys. Res. **B168**, 144 (2000).
- [5] M.A. Avila-Rodriguez, J.S. Wilson, M.J. Schueller, S.A. McQuarrie. Nucl. Instrum. Methods Phys. Res. **B266**, 3353 (2008).
- [6] S. Takács, F. Tárkányi, A. Hermanne, R.A. Rebeles. Nucl. Instrum. Methods Phys. Res. **B269**, 2824 (2011).
- [7] F. Tárkányi, S. Takács, K. Gul, G. Hermanne, M.G. Mustafa, M. Nortier, P. Obložinský, S.M. Qaim, B. Scholten, Yu.N. Shubin, Z. Youxiang, *Beam Monitor Reactions*, IAEA document number IAEA-TECDOC-1211, 49 (2001).
- [8] A.A. Alharbi, M. McCleskey, G. Tabacaru, B. Roeder, A. Banu, A. Spiridon, E. Simmons, L. Trache, R.E. Tribble, *Progress in Research*, Cyclotron Institute, Texas A&M University (2008-2009), p.V-19.
- [9] J.F. Ziegler, Computer Code SRIM-2008, www.srim.org (accessed June 2011).
- [10] D.C. Radford, RadWare Software Package, <http://radware.phy.ornl.gov> (accessed June 2011)
- [11] R.B. Firestone, L.P.Ekström, Table of Radioactive Isotopes, <http://ie.lbl.gov/toi/index.asp> (accessed June 2011).
- [12] W. Reisdorf, Z. Phys. A **300**, 227 (1981).
- [13] A.J. Koning, S. Hilaire and M.C. Duijvestijn, .TALYS-1.0., *Proceedings of the International Conference on Nuclear Data for Science and Technology*, April 22-27, 2007, Nice, France, editors O.Bersillon, F.Gunsing, E.Bauge, R.Jacqmin, and S.Leray, EDP Sciences, 2008, p. 211-214.
- [14] M. Blann, Ann. Rev. Nucl. Sci. **8**, 886 (1975).
- [15] Cyclotron Institute: Cyclotron Institute Proposed Upgrade, http://cyclotron.tamu.edu/facility_upgrade.pdf (accessed July 2011)

Toward understanding relativistic heavy-ion collisions with the STAR detector at RHIC

M. Cervantes, M. Coddington, A. Hamed, S. Mioduszewski, Y. Mohammed, and the STAR Collaboration

We have advanced the following physics analyses: I) understanding the bottomonium (Upsilon) production mechanism via Upsilon+hadron correlations and a spin-alignment measurement, II) long-range pseudorapidity correlations in heavy-ion collisions via high- p_T π^0 and direct γ triggers, and III) the energy loss mechanism in heavy-ion collisions via γ -jet correlations. Finally, we have performed simulation studies for a STAR upgrade project, the Muon Telescope Detector.

Upsilon Production Mechanism:

We have performed the Upsilon+hadron correlation analysis on the Run-9 p+p data set, as well as the Run-8 d+Au data set, and the spin-alignment measurement on the Run-9 p+p data. Fig.1 shows the reconstructed mass from e^+e^- pairs (black) and like-sign pairs (red) from our Run-9 p+p analysis. The blue lines indicate his mass cuts for the Upsilon-hadron correlations and the spin-alignment analysis. The high signal to background ratio enables us to perform the analyses with high purity.

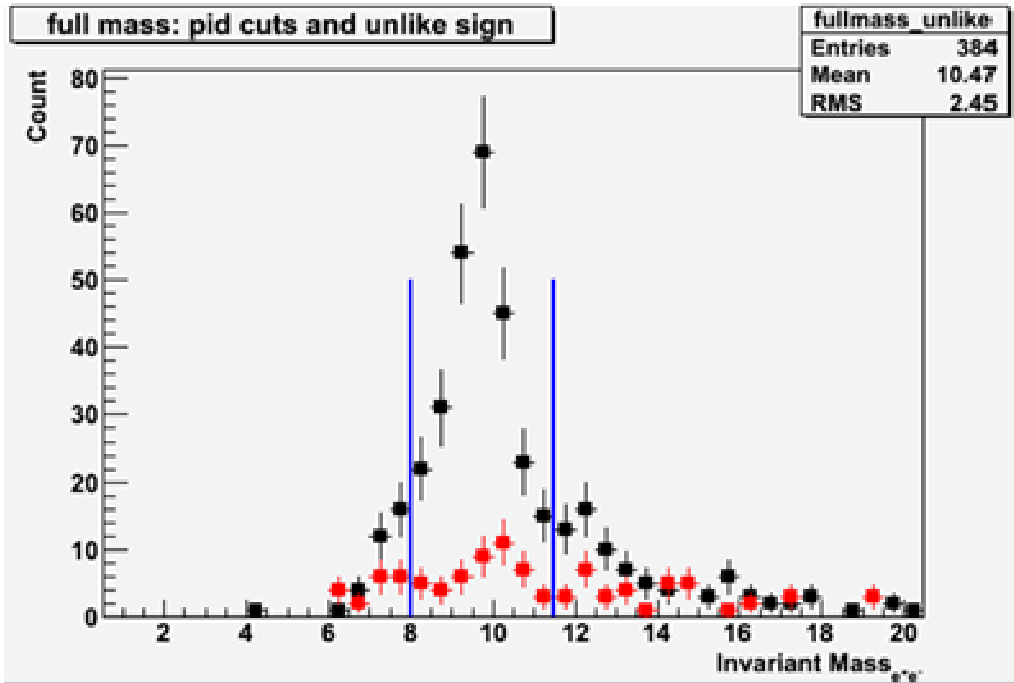


FIG. 1. Invariant mass distribution of e^+e^- pairs (black) and like-sign pairs (red) calculated in p+p events. The blue lines indicate the mass cuts used for the analyses.

Possible insight into the prompt production mechanism of heavy quarkonium can be obtained from hadronic activity measured near the Upsilon. Since more soft gluons are produced together with the Upsilon in the Color Octet model, one would expect more soft hadrons to be correlated with the Upsilon at close azimuthal angle ($\Delta\Phi \sim 0$). Fig. 2 shows the results for the azimuthal correlation between hadrons

and the Upsilon in p+p events. In the past year, the results have been corrected for the tracking efficiency determined from pions embedded into p+p events. Additionally, the cuts have been optimized for pile-up rejection using the comparison of the effect of cuts on embedded pions vs. the effect on data. We found that the most effective cut for rejecting pile-up was a cut on the distance of closest approach of the track to be within 1 cm of the primary vertex.

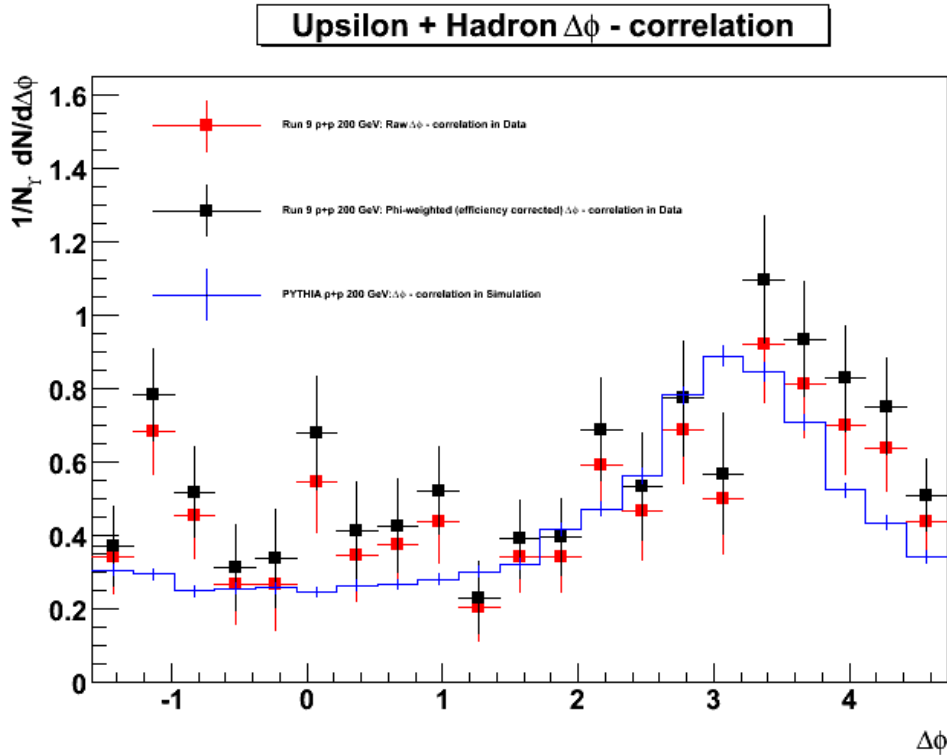


FIG. 2. Efficiency-corrected $\Delta\Phi$ -correlation (black squares) of hadrons with respect to the Upsilon in p+p events. The raw $\Delta\Phi$ -correlation is also shown (red squares). The result is compared to PYTHIA (blue).

The spin alignment measurement is parameterized as $dN/d(\cos\theta)=1+\alpha(\cos^2\theta)$, where θ is the angle between the direction of the decay e^+ momentum, measured in the Upsilon's rest frame with respect to the Upsilon's direction of motion, i.e. the polarization axis. This measurement contributes to the understanding of the production mechanism of heavy quarkonia because the Color Octet Model predicts a sizable non-zero polarization ($\alpha>0$), while the Color Singlet Model predicts a value of ~ 0 . We performed this measurement on Run-9 p+p collisions and corrected the measured distribution (Fig. 3) using Upsilon's embedded into p+p events. Checks are currently being made to finalize these results.

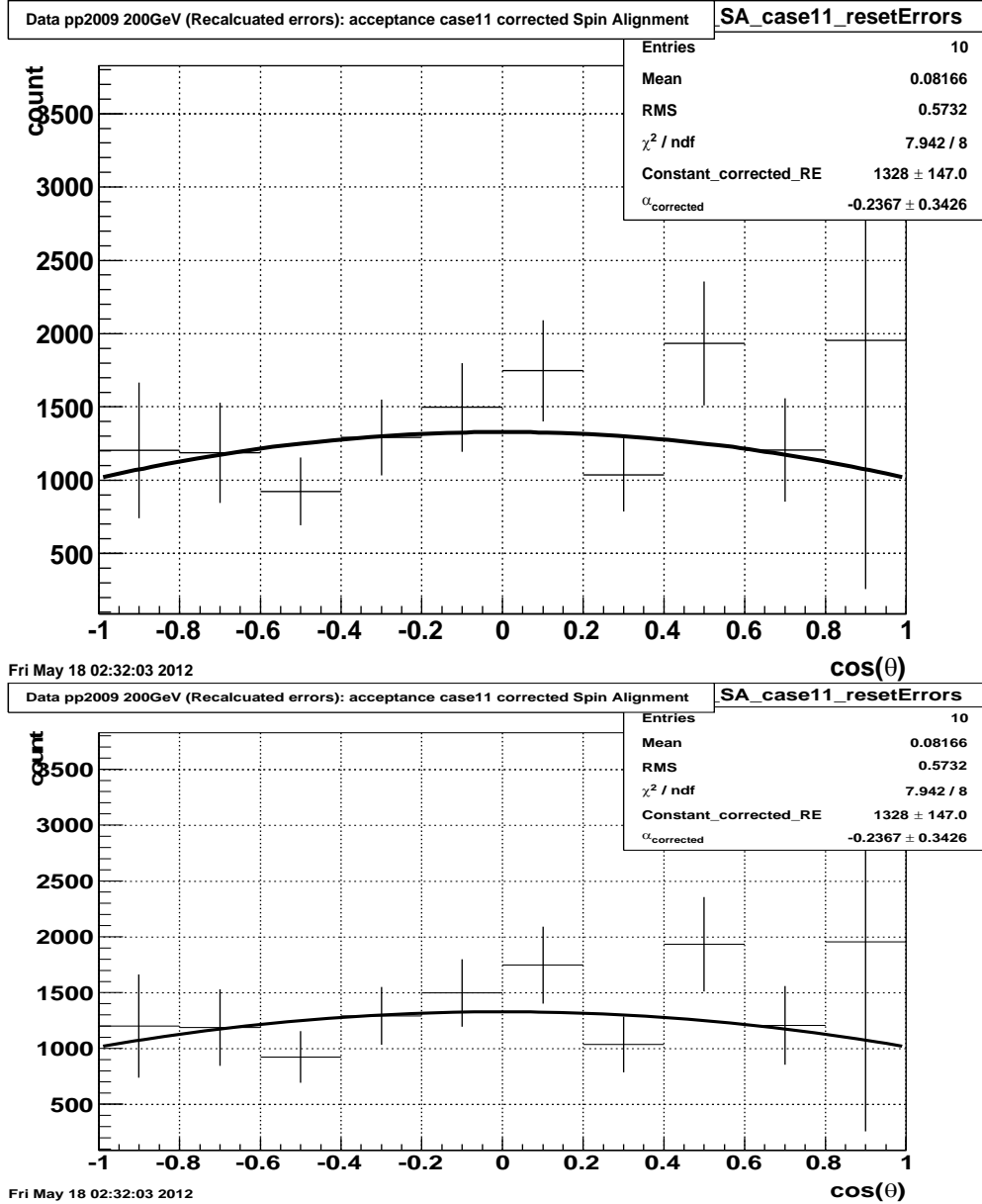


FIG. 3. Raw (upper panel) and acceptance-corrected (lower panel) spin-alignment measurement $dN/d(\cos\theta)$ fit with function $C[1+\alpha(\cos^2\theta)]$.

The “ridge” via high- p_T γ/π^0 triggers:

The “ridge” has been observed as a long-range correlation in $\Delta\eta$ with respect to a high p_T trigger. It has previously only been measured in correlations with charged hadron triggers. This previous measurement has large uncertainties (including large statistical errors for $p_T > 5$ GeV/c) making it difficult to conclude whether the ridge persists up to trigger p_T exceeding 5 GeV/c. However, it was concluded that within the uncertainties, the ridge yield is constant as a function of trigger p_T . We extended the measurement of the ridge to higher p_T using π^0 triggers. As a consistency check, we first performed the

measurement using charged-particle triggers to compare with previously published results. Fig. 4 shows his results for two different methods of extracting the ridge yields from the correlation in $\Delta\Phi-\Delta\eta$ using Run-7 and Run-10 central Au+Au collision data, and compares to previous STAR results using Run-4 central Au+Au collision data.

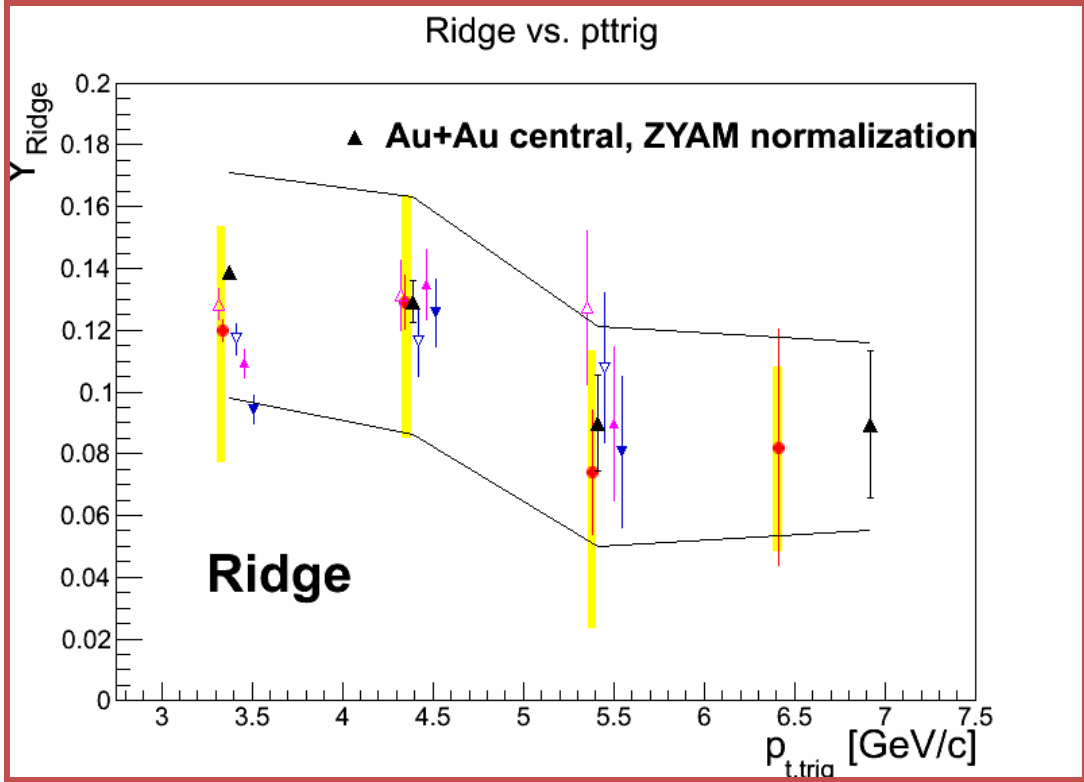


FIG. 4. The “ridge” yields measured in central Au+Au collisions (Run 7 and Run 10) via charged-particle triggered correlations, as a function of trigger-particle p_T , compared with results from Run 4. The black triangles are the Run-4 published result. The red circles are also from Run 4, from the Ph.D. thesis of Christine Nattrass, and the blue and magenta points are from this analysis of Run-7 (open triangles) and Run-10 (closed triangles) data for the two different methods of extracting the ridge yield.

Fig. 5 shows the ridge yield in central Au+Au events, extracted by two different methods, as a function of trigger p_T , for π^0 triggers. The direct γ/π^0 discrimination is performed using the transverse shower profile measured with the Barrel Shower Maximum Detector (BSMD), and was shown to be $>90\%$ pure for π^0 with $p_T > 8$ GeV/c for a previous publication on γ -jet correlations.

Although the statistical errors are still large (even in the Run-10 data set), we performed a χ^2 analysis, testing the consistency of the results at higher p_T ($p_T > 6$ GeV/c) with a constant value fit to the lower p_T ($p_T < 6$ GeV/c) yields vs. the consistency with zero yield. We found that the higher p_T yields, which were not previously measured by STAR, were more consistent with zero, than with a constant value of ~ 0.1 . We also concluded that combining the Run-7, Run-10, and Run-11 data sets would result in an increase in statistics, relative to Run-7 data alone, of a factor of 6.

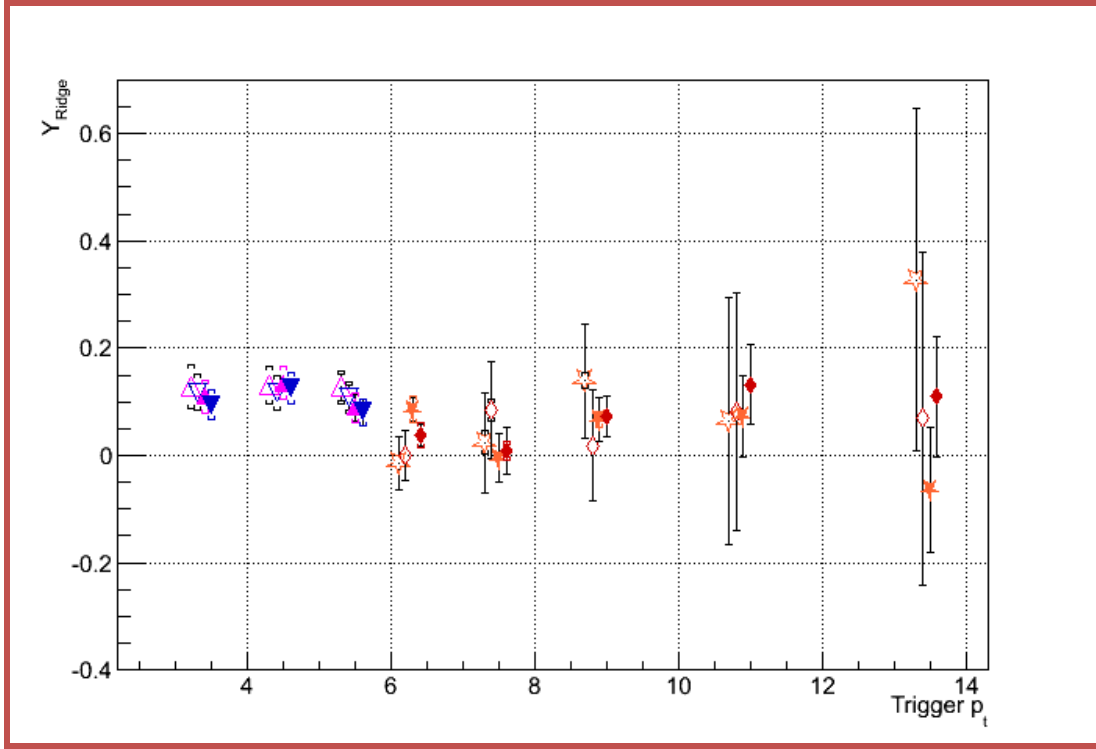


FIG. 5. Ridge yields shown for charged-charged correlations (blue) and π^0 -charged correlations (red), for Run-7 (closed symbols) and Run-10 (open symbols) central Au+Au collisions, all from this analysis.

γ -Jet Correlations:

We are currently repeating the γ -jet analysis on Run-10 and Run-11 data, aiming to reproduce the published results and then extending the measurement to 1) lower $z_T = p_{T,assoc}/p_{T,trig}$ (i.e higher $p_{T,trig}$), 2) more centralities, and 3) the 2+1 correlations. Because of adjustments to the BSMD settings to prevent saturation, the transverse shower profile cut (on the quantity of $E_{cluster}/(\sum E_{i,r_1})^{1.7}$), used for distinguishing single photons from π^0 , needed to be adjusted accordingly. Before adjustments, the π^0 trigger sample had more contamination from direct γ , reducing the near-side associated yields. With the current cuts, we found agreement between Run-7 and Run-11 yields associated with π^0 triggers, shown in Fig. 6.

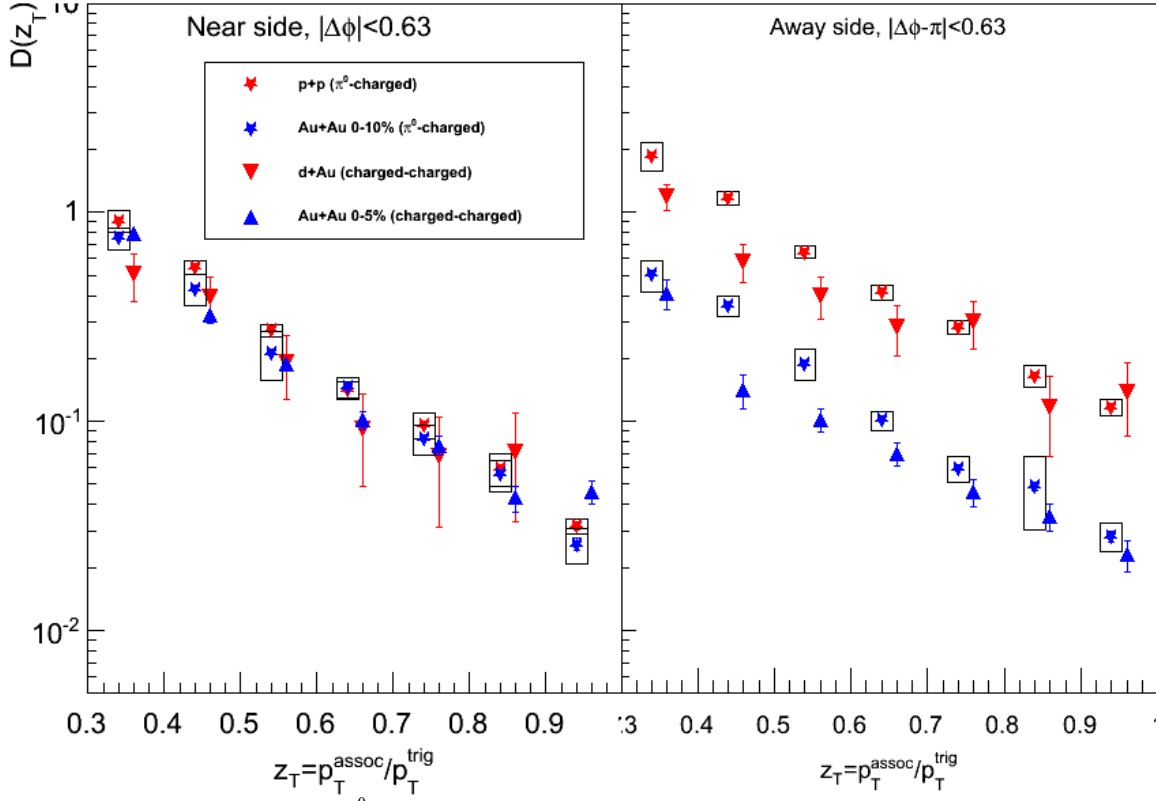


FIG. 6. Yields associated with π^0 triggers on the near side (left panel) and away side (right panel). The blue stars are Run-11 central Au+Au collisions and the blue triangles are Run-4 central Au+Au collisions (published results used for comparison). The red triangles are d+Au collisions and red stars are p+p collisions, as the baseline.

MTD-Related Research:

We studied the feasibility of using the Muon Telescope Detector (MTD), together with the Heavy Flavor Tracker (HFT), for separating J/Ψ particles from B-meson decays from primordial J/Ψ particles. The B-meson has a decay channel into a J/Ψ particle together with a kaon, and the J/Ψ decay channel that will be reconstructed is the two-muon decay. The B-meson has a lifetime large enough to allow the reconstruction of a decay vertex (displaced from the primary event vertex), with fine enough position resolution. The MTD is used to identify the muons from the $J/\Psi \rightarrow \mu^+ \mu^-$, and the HFT is a silicon detector with the necessary resolution to reconstruct a displaced vertex. The simulation used simulated B-mesons and primordial J/Ψ in this study. Our study concluded that a cut on the decay-length (as measured using hits in the HFT) to be greater than 0.15 mm results in nearly 100% rejection of primordial J/Ψ and a B-meson reconstruction efficiency of approximately 7%.

SECTION III
NUCLEAR THEORY

High order corrections to density and temperature of fermions and bosons from quantum fluctuations and the CoMD- α Model

Hua Zheng,^{1,2} Gianluca Giuliani,¹ Matteo Barbarino,¹ and Aldo Bonasera^{1,3}

¹*Cyclotron Institute, Texas A&M University, College Station, Texas 77843*

²*Department of Physics and Astronomy, Texas A&M University, College Station, Texas 77843*

³*Laboratori Nazionali del Sud, INFN, via Santa Sofia, 62, 95123 Catania, Italy*

Fragmentation experiments could provide information about nuclear matter properties and constrain the nuclear equation of state (EOS) [1-4]. Long ago, W. Bauer stressed the crucial influence of Pauli blocking on the momentum distributions of nucleons emitted in heavy ion collisions near the Fermi energy [5]. We have recently proposed a method to estimate the density and temperature based on fluctuations estimated from an event by event determination of fragment momenta and yields arising after the energetic collision [6]. A similar approach has also been applied to experimentally observe the quenching of fluctuations in a trapped Fermi gas [7] and the enhancement of fluctuations in a Bose condensate [8]. We go beyond the method of [7, 8] by including quadrupole fluctuations as well to have a direct measurement of densities and temperatures for subatomic systems (Fermions or Bosons). We recently extend the method to derive the entropy of the system and have shown how to recover the classical limit for fermions when the temperatures are large compared to the Fermi energy. Furthermore, we have also shown how to derive the density and temperature for bosons in the same scenario. We examine the collision dynamics by means of the Constrained Molecular Dynamics (CoMD) model, which allows an event-by-event analysis of the reaction mechanisms that is necessary in order to calculate fluctuations.

Following [10] a quadrupole $Q_{xy} = \langle p_x^2 - p_y^2 \rangle$ is defined in a direction transverse to the beam axis (z-axis) and the average is performed, for a given particle type, over events. Such a quantity is zero in the center of mass of the equilibrated emitting source. Its variance is given by the simple formula:

$$\sigma_{xy}^2 = \int d^3p (p_x^2 - p_y^2)^2 n(p) \quad (1)$$

where $n(p)$ is the momentum distribution of particles. In [10] a classical Maxwell-Boltzmann distribution of particles at temperature T_{cl} was assumed which gives: $\sigma_{xy}^2 = \bar{N}(2mT_{cl})^2$, m is the mass of the fragment. \bar{N} is the average number of particles.

In heavy ion collisions, the produced particles do not follow classical statistics, thus the correct distribution function must be used in Eq. (1). Protons(p), neutrons(n), tritium etc. follow the Fermi statistics while, deuterium, alpha particles etc., even though they are constituted of nucleons, should follow the Bose statistics.

For fermions, we will concentrate on, in particular, p and n which are abundantly produced in the collisions thus carrying important informations on the densities and temperatures reached. Using a Fermi-Dirac distribution $n(p)$,

$$\sigma_{xy}^2 = \bar{N}(2mT)^2 F_{QC}\left(\frac{T}{\epsilon_f}\right) \quad (2)$$

Where $F_{QC} \left(\frac{T}{\varepsilon_f} \right) = 0.2 \left(\frac{T}{\varepsilon_f} \right)^{-1.71} + 1$ is the quantum correction factor which should converge to one for high T (classical limit).

Within the same framework we can calculate the fluctuations of the p, n multiplicity distributions. These are given by [11]. Since in experiments or modeling one recovers the normalized fluctuations, it is better to find a relation between the normalized temperatures as function of the normalized fluctuations. It is useful to parameterize the numerical results as:

$$\frac{T}{\varepsilon_f} = -0.442 + \frac{0.442}{\left(1 - \frac{\langle(\Delta N)^2\rangle}{\bar{N}}\right)^{0.656}} + 0.345 \frac{\langle(\Delta N)^2\rangle}{\bar{N}} - 0.12 \left(\frac{\langle(\Delta N)^2\rangle}{\bar{N}}\right)^2 \quad (3)$$

which is practically indistinguishable from the numerical result. Since from experimental data or models it is possible to extract directly the normalized fluctuations, one can easily derive the value of $\frac{T}{\varepsilon_f}$ from Eq. (3). Substituting Eq. (3) into Eq. (2), the temperature and fermi energy for the fermion system can be obtained. Then the density of the system can be extracted from

$$\varepsilon_f = 36 \left(\frac{\rho}{\rho_0} \right)^{\frac{2}{3}} \quad (4)$$

Where $\rho_0 = 0.16 \text{ fm}^{-3}$ is the normal density. Once the density and the temperature of the system have been determined it is straightforward to derive other thermodynamical quantities. One such quantity is the entropy:

$$S = \frac{U-A}{T} \quad (5)$$

U and A are the internal and Helmotz free energy respectively[11]. For practical purposes it might be useful to have a parameterization of the entropy in terms of the normalized fluctuations, which is physically transparent since entropy and fluctuations are strongly correlated [11]:

$$\frac{S}{N} = -41.68 + \frac{41.68}{\left(1 - \frac{\langle(\Delta N)^2\rangle}{\bar{N}}\right)^{0.022}} + 2.37 \frac{\langle(\Delta N)^2\rangle}{\bar{N}} - 0.83 \left(\frac{\langle(\Delta N)^2\rangle}{\bar{N}}\right)^2 \quad (6)$$

For bosons, in the same scenario, we use a Bose-Einstein distribution $n(p)$ for the particles. But we need to consider the cases above or below the critical temperature $T_c = \frac{2\pi}{[2.612(2s+1)]^{2/3}} \frac{\hbar^2}{m} \rho^{2/3}$ at a given density ρ with spin s, we obtain [11]:

$$\sigma_{xy}^2 = \bar{N} (2mT)^2 \frac{g_7(1)}{g_3(1)} \quad (T < T_c) \quad (7)$$

$$\sigma_{xy}^2 = \bar{N} (2mT)^2 \frac{g_7(z)}{g_3(z)} \quad (T > T_c) \quad (8)$$

where the $g_n(z)$ functions are well studied in the literature [11] and $z = e^{\mu/T}$ is the fugacity which depends on the critical temperature for Bose condensate and thus on the density of the system and the chemical potential μ [11]. The quadrupole fluctuations depend on temperature and density through T_c , therefore we need more information in order to be able to determine both quantities for $T > T_c$.

We can calculate the multiplicity fluctuations of d , α etc in the same framework again. Fluctuations are larger than the average value and diverge near the critical point. We will show the results later. Interactions and finite size effects will of course smooth the divergence [4]. These results are very important and could be used to pin down a Bose condensate.

Two solutions are possible depending whether the system is above or below the critical temperature for a Bose condensate. Below the critical point, Eq. (7) can be used to calculate T and then multiplicity fluctuation gives the critical temperature and the corresponding density. Above the critical point it is better to estimate the chemical potential first and then derive the temperature, critical temperature and density. The details can be seen in coming paper.

The CoMD- α Model has been developed to study collisions between alpha cluster candidates and to search for Bose condensates in alpha-clustered nuclear systems. In CoMD- α case, the nuclear ground states have an alpha-clustered structure. The boson nature of alpha-clusters is taken into count in the two-body collision term by means of the Bose-Einstein blocking factor $\Pi = (1 + \bar{f}_1)(1 + \bar{f}_2)$, where \bar{f}_i is the average occupation probability for alpha $i=1, 2$. We calculate this factor Π before the collision and Π' after the collision. If $\Pi' > \Pi$, the collision will be accepted, otherwise, the collision will be rejected. We will look at the multiplicity fluctuations for alpha particles. Later, we can select the particular events from experimental data which only have alpha like mass fragments. Then we can compare the model data with experimental data.

To illustrate the strength of our approach we have performed calculations for the system $^{40}\text{Ca} + ^{40}\text{Ca}$ at fixed impact parameter $b=1$ fm and beam energies E_{lab}/A ranging from 4 MeV/A up to 100 MeV/A. Collisions were followed up to a maximum time $t=1000$ fm/c in order to accumulate enough statistics. A complete discussion of these simulations can be found in [6], here we will use the results to compare the different approximations.

In Fig. 1 we plot the temperature versus density as obtained from the quadrupole and multiplicity fluctuations. The top panel refers to protons while the bottom to neutrons. As we can see from the figure, the results obtained using the fit functions, Eqs.(2) and (3), deviate slightly from the lowest order approximations [6]. This is a signature that we are in the fully quantum regime for the events considered. For comparison, in the same plot we display the classical temperatures which are systematically higher than the quantum ones[10].

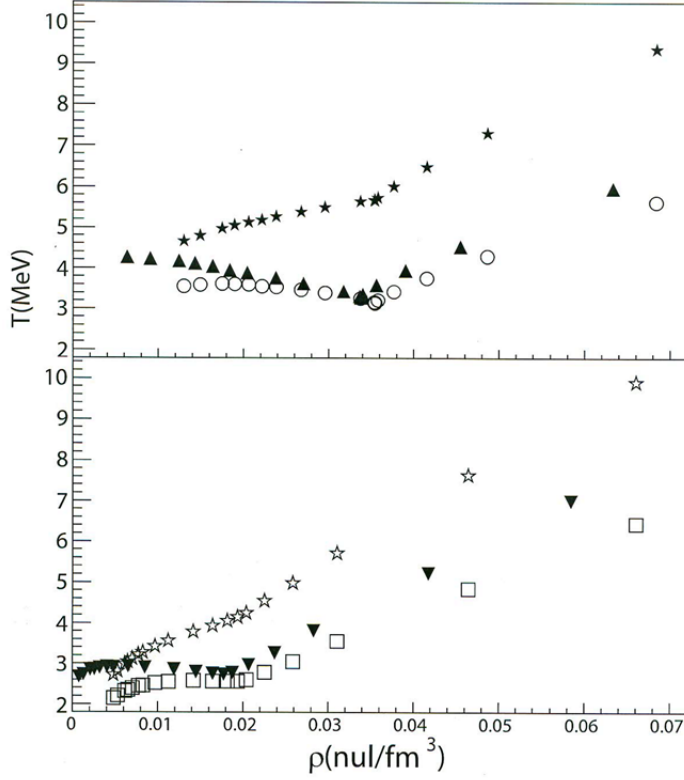


FIG. 1. Temperatures versus density normalized to the ground state density $\rho_0 = 0.16\text{fm}^{-3}$, derived from quantum fluctuations, Eqs. (2, 3). Open dots and open squares are the approximation at the lowest order in $\frac{T}{\epsilon_f}$, full stars and open stars are the classical cases similar to [10], the full triangles are the numerical results. The top panel refers to protons and the bottom panel refers to neutrons.

To better summarize the results we plot in Fig. 2 (top panel), the energy density $\epsilon = \langle \frac{E_{\text{th}}}{A} \rangle \rho$ versus temperature [6]. Different particle types scale especially at high T where Coulomb effects are expected to be small. A rapid variation of the energy density is observed around $T \sim 2\text{MeV}$ for neutrons and $T \sim 3\text{MeV}$ for protons which indicates a first order phase transition, or a crossover. As we see from the figure, the numerical solution of the Fermi integrals gives small corrections while keeping the relevant features obtained in the lowest approximation intact. This again suggests that in the simulations the system is fully quantal. We also notice that Coulomb effects become negligible at $T \gg 3\text{MeV}$ where the phase transition occurs. The smaller role of the Coulomb field in the phase transition has recently been discussed experimentally in the framework of the Landau's description of phase transitions [12].

In order to confirm the origin of the phase transition, it is useful to derive the entropy density $\Sigma = \langle \frac{S}{N} \rangle \rho$ which is plotted in the bottom panel of Fig. 2. The rapid increase of the entropy per unit volume is due to the sudden increase of the number of degrees of freedom (fragments) with increasing T . The entropy can be also derived using the law of mass action from the ratio of the produced number of deuterons to protons (or neutrons) $R_{d,p(n)}$ [4, 13]:

$$\frac{S}{N} \ln |d/p(n)| = 3.95 - \ln R_{d/p(n)} - 1.25 \frac{R_{d/p(n)}}{1+R_{d/p(n)}} \quad (9)$$

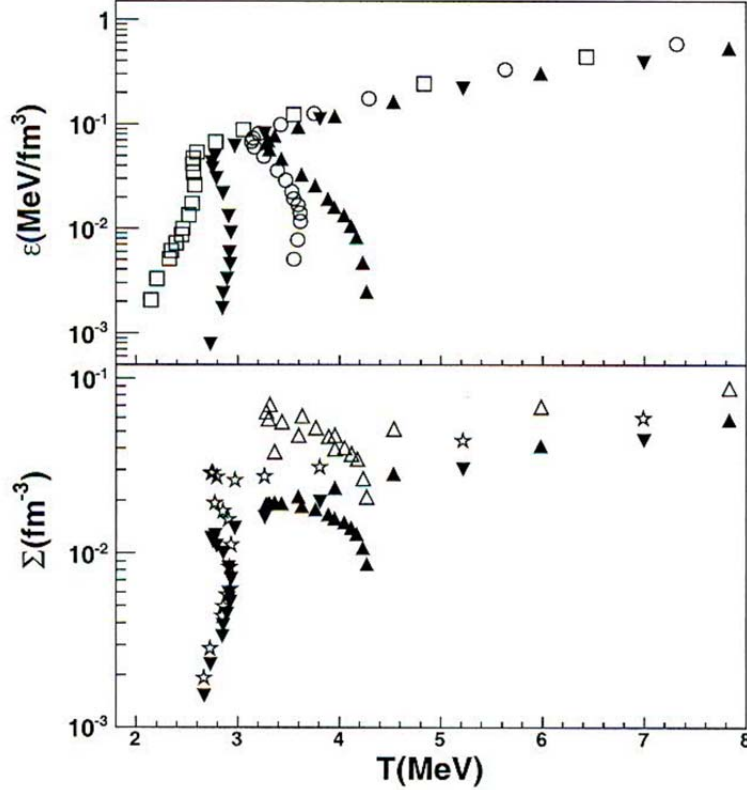


FIG. 2. (Top) Energy density versus temperature. Symbols as in Fig.1; (Bottom) entropy density versus temperature. The opens symbols refer to the entropy density calculated from the ratios of the produced number of deuterons to protons (triangles) (neutrons-stars), Eq. (9).

We find an overall qualitative good agreement of the entropy density to the quantum results, especially for neutrons. Very interesting is the good agreement for neutrons at low T where the particles are emitted from the surface of the nuclei which are at low density, see also Fig.1. Such a feature is not present for the protons due to larger Coulomb distortions. There is a region near the transition ($T \sim 3$ MeV), where both ratios do not reproduce the quantum results. However, at large temperatures it seems that all methods converge as expected. Recall that this method is valid only if d , n and p are produced in the reactions. If different fragments are produced then the entropy derivation should be modified to include more complex nuclei [4]. The CoMD model favors the formation of deuterium since it is over bound. We expect data to be quite different since alpha production is important but qualitatively we expect a similar behavior as discussed here.

In Fig 3, we plot the multiplicity fluctuation versus reduced temperature $t = \frac{T-T_c}{T_c}$. The multiplicity fluctuations diverge at the critical temperature where $t=0$. One can calculate the multiplicity fluctuation numerically above the critical temperature. Below the critical temperature, one can obtain the

behavior of the multiplicity fluctuation according to Landau's theory. It is driven by the interaction but doesn't depend on the detail of interaction.

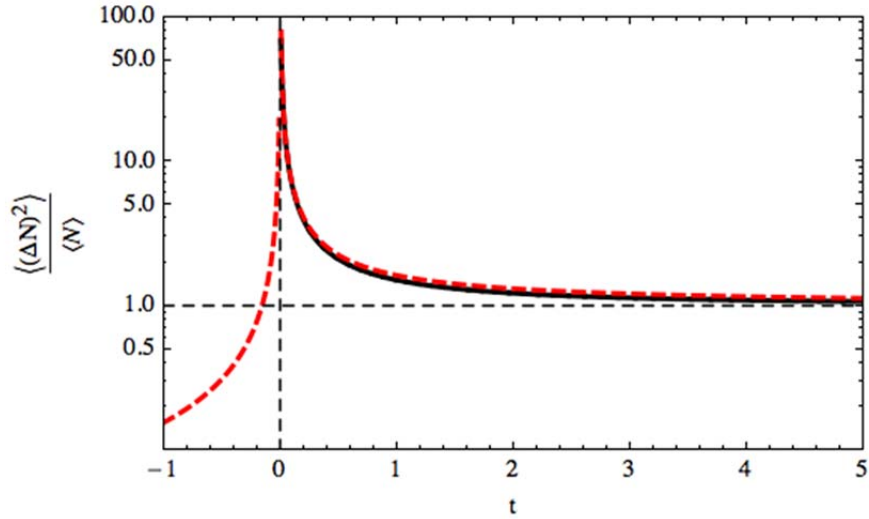


FIG. 3. Multiplicity fluctuation versus reduced temperature t .

In Fig 4, we plot the multiplicity fluctuations for alpha particle versus E_{cm}/A . As one can see, the

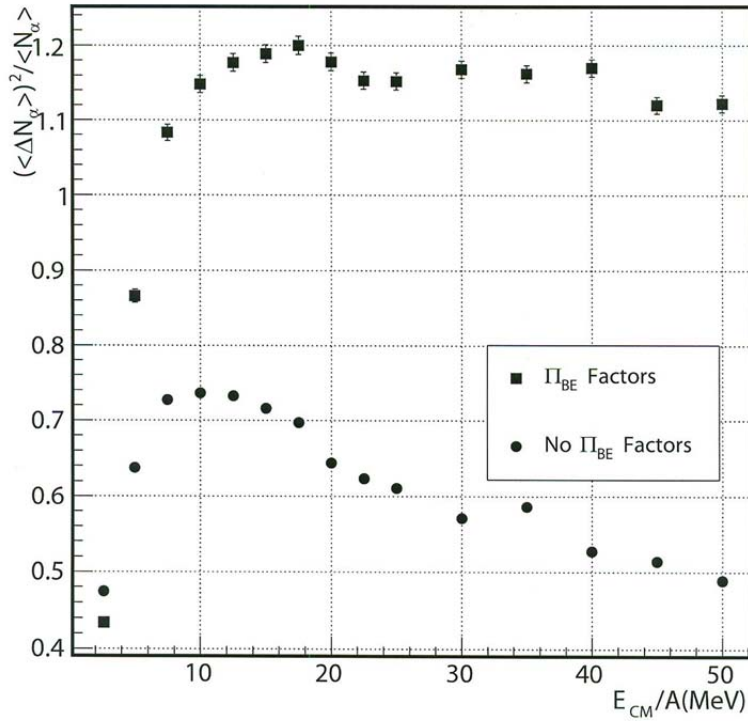


FIG. 4. Multiplicity fluctuation versus energy per nucleon in center of mass in CoMD- α . The square is with Bose-Einstein blocking factor and the circle is without Bose-Einstein blocking factor.

multiplicity fluctuations of alpha particle are systematically larger in the Bose-Einstein blocking case. This means the multiplicity fluctuations can be used as a probe to study Bose condensate phenomena in nuclear physics. Of course, the interactions and finite size effects will smooth the divergence, this may be the reason we don't see the divergence in the model.

In conclusion, in this work we have addressed a general method for deriving densities and temperatures of weakly interacting fermions and bosons. For high temperatures and small densities the classical result is recovered as expected. We have shown in CoMD calculations that the effect of higher order terms give small differences in the physical observables considered in this paper but they could become large when approaching the classical limit. To overcome this problem we have produced suitable parameterizations of quadrupole and multiplicity fluctuations which are valid at all temperatures and densities. The results obtained in this paper are quite general and they could be applied to other systems. The CoMD- α results show that the multiplicity fluctuations are a good probe to investigate boson condensate.

- [1] A. Bonasera, F. Gulminelli and J. Molitoris, Phys. Rep. **243**, 1 (1994).
- [2] G. Bertsch and S. Dasgupta, Phys. Rep. **160**, 189 (1988).
- [3] A. Bonasera *et al.*, Rivista del Nuovo Cimento **23**, 1 (2000).
- [4] L.P. Csernai, Introduction to Relativistic Heavy Ion Collisions, Wiley, New York, 1994.
- [5] W. Bauer, Phys. Rev. C **51**, 803 (1995).
- [6] H. Zheng and A. Bonasera, Phys. Lett. B **696**, 178 (2011); H. Zheng and A. Bonasera, arXiv: 1112.4098 [nucl-th]; H. Zheng and A. Bonasera, arXiv: 1105.0563 [nucl-th].
- [7] T. Mueller *et al.*, Phys. Rev. Lett. **105**, 040401 (2010); C. Sanner *et al.*, Phys. Rev. Lett. **105**, 040402 (2010); C. I. Westbrook, Physics **3**, 49 (2010).
- [8] J. Esteve *et al.*, Phys. Rev. Lett. **96**, 130403 (2006); J.B. Trebbia *et al.*, Phys. Rev. Lett. **97**, 250403 (2006).
- [9] A. Bonasera, Phys. Rev. C **62**, 052202 (R) (2000); M. Papa, T. Maruyama, A. Bonasera, Phys. Rev. C **64**, 024612 (2001); A. Bonasera, Nucl. Phys. **A681**, 64c (2001); S. Terranova, A. Bonasera, Phys. Rev. C **70**, 024906 (2004); S. Terranova, D.M. Zhou, A. Bonasera, Eur. Phys. J. A **26**, 333 (2005).
- [10] S. Wuenschel *et al.*, Nucl. Phys. **A843**, 1 (2010).
- [11] L. Landau, F. Lifshits, Statistical Physics, Pergamon, New York, 1980; K. Huang, Statistical Mechanics, second edition, John Wiley and Sons, New York, 1987.
- [12] A. Bonasera *et al.*, Phys. Rev. Lett. **101**, 122702 (2008); M. Huang *et al.*, Phys. Rev. C **81**, 044618 (2010). M. Huang *et al.*, Nucl. Phys. **A847**, 233 (2010) 233.
- [13] P.J. Siemens and J.L. Kapusta, Phys. Rev. Lett. **43**, 1486 (1979).

New insight into deuteron stripping to bound states and resonances

A.M. Mukhamedzhanov, I. Thompson,¹ and J. Escher¹

¹Lawrence Livermore National Laboratory, Livermore, California 94550

Surface integral formalism and generalized R-matrix approach [1] applied to deuteron stripping reactions $A(d,p)B$ provide a new insight into the physics of these reactions. In this approach both post and prior forms of the DWBA amplitude can be written as

$$M^{DW} = M_{\text{int}}^{DW(\text{post})}(0, a) + M_{\text{surf}}(a) + M_{\text{ext}}^{DW(\text{prior})}(a, \infty) \quad (1)$$

The first term is the internal post form amplitude, the second term is the surface integral and the last one is the external prior form. The dominant contribution comes from the surface term, while the internal and external terms are typically small. By proper using of the core-core (p - A) optical potential the internal

Peak cross section relative to full calculation

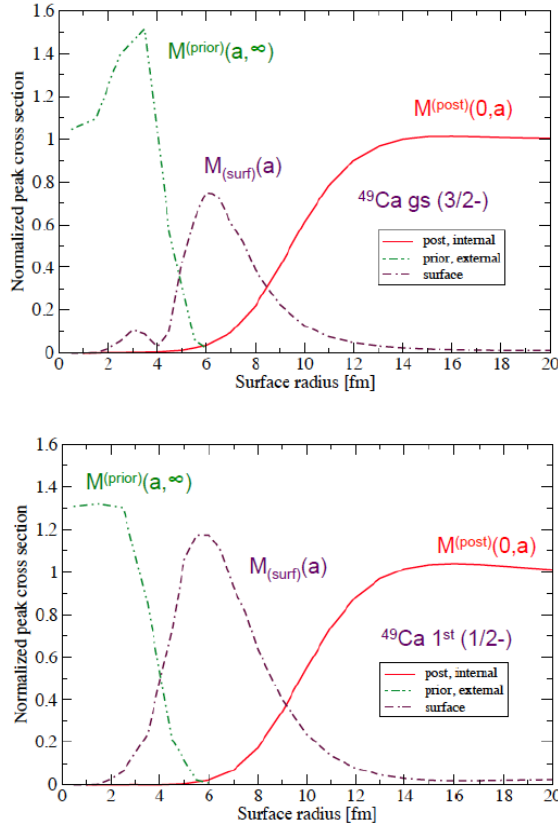


FIG. 1. Peak values of the differential cross sections for the deuteron stripping $^{48}\text{Ca}(d,p)^{49}\text{Ca}$ to the ground bound state (upper panel) and first excited state (bottom panel) of ^{49}Ca as a function of the channel radius. The green line is the prior external cross section, the blue line is the surface cross section and the red line is the post external cross section.

part can be significantly minimized. FRESKO code has been modified to take into account Eq. (1). The calculations have been done for different reactions including stripping to bound states and resonances.

In Fig. 1 we present the calculations of the $^{48}\text{Ca}(d,p)^{49}\text{Ca}$ reaction populating the ground and the first excited state of ^{49}Ca at the deuteron energy of 13 MeV. As we can see, if the channel radius is taken to be $a = 6\text{fm}$, the surface term is totally dominant and both internal and external terms can be neglected. Because the surface term is parameterized in terms of the ANC, only the ANC rather than the spectroscopic factor can be determined from the analysis of the deuteron stripping

[1] A.M. Mukhamedzhanov, Phys. Rev. C **84**, 044616 (2011).

Asymptotic normalization coefficients from the $^{14}\text{C}(d, p)^{15}\text{C}$ reaction

A.M. Mukhamedzhanov, V. Burjan,¹ M. Gulino,² Z. Hons,¹ V. Kroha,¹ J. Mrazek,¹ J. Novak,¹ S. Piskor,¹
S. Romano,² M.L. Sergi,² C. Spitaleri,² and R.E. Tribble

¹ *Nuclear Physics Institute, Czech Academy of Sciences, 250 68 Rez-Prague, Czech Republic*

² *Universita di Catania and INFN Laboratori Nazionali del Sud, Catania, Italy*

The $^{14}\text{C}(d, p)^{15}\text{C}$ reaction plays an important role in inhomogeneous big bang models. In [1] it was shown that the $^{14}\text{C}(n, \gamma)^{15}\text{C}$ radiative capture at astrophysically relevant energies is peripheral, that is the overall normalization of its cross section is determined by the asymptotic normalization coefficient (ANC) for $^{15}\text{C} \rightarrow ^{14}\text{C} + n$. Here we present new measurements of the $^{14}\text{C}(d, p)^{15}\text{C}$ differential cross sections at the deuteron incident energy of 17.06 MeV and the analysis to determine the ANCs for neutron removal from the ground and first excited states of ^{15}C . The measurement of the differential cross section of the $^{14}\text{C}(d, p)^{15}\text{C}$ reaction was carried out at the U-120M cyclotron isochronous cyclotron at the Nuclear Physics Institute of the Czech Academy of Sciences. The deuteron beam with the energy of 17.06 MeV was led into a target chamber with ^{14}C and mylar targets. Reaction products were measured by four $\Delta E - E$ telescopes assembled from thin surface barrier silicon and thick Si(Li) detectors with thickness about 200 μm and 4 mm respectively

The angular distributions of deuterons from the reaction $^{14}\text{C}(d, p)^{15}\text{C}$ corresponding to the two bound states in ^{15}C calculated using adiabatic wave Born approximation, which is the simplified version of the CDCC and determined ANCs compared with existing data. The paper has been published in [2].

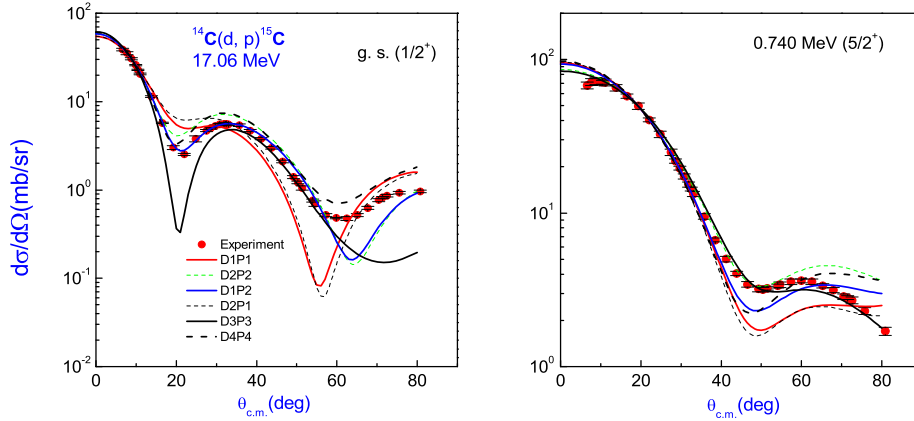


FIG. 1. Angular distributions from the $^{14}\text{C}(d, p)^{15}\text{C}$ reaction for the transitions leading to the ground and 0.740 MeV states in ^{15}C . DWBA calculations were made with optical model parameter sets given in [2].

- [1] N.K. Timofeyuk, D. Baye, P. Descouvemont, R. Kamouni, and I.J. Thompson, Phys. Rev. Lett. **96**, 162501 (2006).
- [2] A.M. Mukhamedzhanov *et al.*, Phys. Rev. C **84**, 024616 (2011).

Electron - and photon - impact atomic ionization

I. Bray,¹ D.V. Fursa,¹ A.S. Kadyrov,¹ A.S. Kheifets,² A.M. Mukhamedzhanov,
and A.T. Stelbovics¹

¹*ARC Centre for Antimatter-Matter Studies, Curtin University, Perth, WA 6845, Australia*

²*Research School of Physical Sciences, The Australian National University, Canberra
ACT 0200, Australia*

The last decade has seen extraordinary theoretical progress in the field of fully kinematically resolved atomic electron-impact ionisation, and its closely related field of double photoionisation. These processes were challenging to calculate due to formal and computational difficulties associated with breakup problems involving the long-range Coulomb potential. Presently, however, these processes can be calculated accurately for simple targets such as atomic hydrogen and helium, irrespective of the kinematics considered or the geometry of detectors. The purpose of this work is to review the recent progress in formal ionisation theory, and show how it relates to the successful computational techniques, which aim to fully solve the ionisation problems without resorting to approximations that limit the applicability of the methods. Such issues are best addressed using relative simple targets such as atomic hydrogen and helium, where we can be very confident in the accuracy of the calculated target structure. Our report addresses also the computational progress, and how it has resulted in a deeper understanding of the formalism of Coulomb few-body problems. The review paper will be published in Phys. Rep.

Generalized Faddeev equations in the AGS form for deuteron stripping with explicit inclusion of the Coulomb interactions

A.M. Mukhamedzhanov, V. Eremenko, and A.I. Sattarov¹

¹*Department of Physics and Astronomy, Texas A&M University, College Station, Texas 77843*

Deuteron stripping provides a unique tool for determining information on the neutron capture. Deuteron stripping processes off a target nucleus consisting of A nucleons are treated within the framework of the few-body integral equations theory. The theoretical description of reactions in general, and the theory for (d, p) reactions in particular, needs to advance into the new century.

The generalized Faddeev equations in the AGS form, which takes into account the target excitations, with realistic optical potentials provide the most advanced and complete description of the deuteron stripping. The main problem in practical application of such equations is the screening of the Coulomb potential, which works only for light nuclei. In this paper we present the AGS equations taking into account the target excitations with explicit inclusion of the Coulomb interaction. By projecting the $(A + 2)$ -body operators onto target states, matrix three-body integral equations are derived which allow for the incorporation of the excited states of the target nucleons. Using the explicit equations for the partial Coulomb scattering wave functions in the momentum space we present the AGS equations in the Coulomb distorted wave representation without screening procedure. The derived equations are compact in the Hilbert space. We also use explicit expressions for the partial Coulomb scattering wave function and for the off-shell two-body Coulomb scattering T-matrix, which are needed to calculate the effective potentials in the AGS equations. We present the regularization of the effective potentials in the AGS equations to make the integration converged. For NN and nucleon- target nuclear interactions we use the separable potentials.

Reexamination of the astrophysical S factor for the $\alpha+d\rightarrow{}^6\text{Li}+\gamma$ reaction

A.M. Mukhamedzhanov, L.D. Blokhintsev,¹ and B.F. Irgaziev²

¹*D.V. Skobeltsyn Institute of Nuclear Physics, Lomonosov Moscow State University, Moscow, Russia*

²*GIK Institute of Engineering Sciences and Technology, Topi, Pakistan*

Recently, a new measurement of the ${}^6\text{Li}$ (150 A MeV) dissociation in the field of ${}^{208}\text{Pb}$ has been reported [1] to study the radiative capture $\alpha+d\rightarrow{}^6\text{Li}+\gamma$ process. However, the dominance of the nuclear breakup over the Coulomb one prevented the information about the $\alpha+d\rightarrow{}^6\text{Li}+\gamma$ process from being obtained from the breakup data. The astrophysical $S_{24}(E)$ factor has been calculated within the α - d two-body potential model with potentials determined from the fits to the α - d elastic scattering phase shifts. However, the scattering phase shift, according to the theorem of the inverse scattering problem, does not provide a unique α - d bound-state potential, which is the most crucial input when calculating the $S_{24}(E)$ astrophysical factor at astrophysical energies. In this work, we emphasize the important role of the asymptotic normalization coefficient (ANC) for ${}^6\text{Li}\rightarrow\alpha+d$, which controls the overall normalization of the peripheral $\alpha+d\rightarrow{}^6\text{Li}+\gamma$ process and is determined by the adopted α - d bound-state potential. Since the potential determined from the elastic scattering data fit is not unique, the same is true for the ANC generated by the adopted potential. However, a unique ANC can be found directly from the elastic scattering phase shift, without invoking intermediate potential, by extrapolation the scattering phase shift to the bound-state pole [2]. We demonstrate that the ANC previously determined from the α - d elastic scattering s -wave phase shift [2], confirmed by *ab initio* calculations, gives $S_{24}(E)$, which at low energies is about 38% less than the other one reported [1]. We recalculate also the reaction rates, which are lower than those obtained in that same study [1]. The paper has been published in Phys. Rev. C **83**, 055805 (2011).

[1] Hammache *et al.*, Phys. Rev. C **82** 065803 (2010).

[2] Blokhintsev *et al.*, Phys. Rev. C **48** 2390 (1993).

Theory of deuteron stripping: From surface integrals to a generalized R-matrix approach

A.M. Mukhamedzhanov

There are two main reasons for the absence of a practical theory of stripping to resonance states that could be used by experimental groups: The numerical problem of the convergence of the distorted-wave Born approximation (DWBA) matrix element when the full transition operator is included and the ambiguity over what spectroscopic information can be extracted from the analysis of transfer reactions populating the resonance states. To address both questions in this paper a new theory of the deuteron stripping based on the surface integral formalism [1] and generalized R-matrix approach is developed. The theory uses post continuum discretized coupled channels (CDCCs) formalism going beyond of the DWBA. First, the formalism is developed for the DWBA and then it is extended to the CDCC formalism, which is the ultimate goal of this work. The CDCC wave function takes into account not only the initial elastic $d + A$ channel but also its coupling to the deuteron breakup channel $p + n + A$ missing in the DWBA. Stripping to both bound states and resonances is included. The convergence problem for stripping to resonance states is solved in the post CDCC formalism. The reaction amplitude is parametrized in terms of the reduced width amplitudes (asymptotic normalization coefficients), inverse level matrix, boundary condition, and channel radius, which are the same parameters used in the conventional R-matrix method. For stripping to resonance states, many-level and one- and two-channel cases are considered. The theory provides a consistent tool to analyze both binary resonant reactions and deuteron stripping in terms of the same parameters. The paper was published in *Phys. Rev. C* **84**, 044616 (2011).

[1] A.S. Kadyrov *et al.*, *Ann. Phys.* **324**, 1516 (2009).

Skyrme-Hartree-Fock calculations of isospin-symmetry breaking

I.S. Towner and J.C. Hardy

The isospin-symmetry breaking correction, δ_C , required in the analysis of superallowed Fermi beta decay is discussed in Ref. [1]. For practical reasons, the correction is divided into two components: $\delta_C = \delta_{C1} + \delta_{C2}$, where δ_{C1} incorporates isospin mixing with neighboring states of the same spin and parity and δ_{C2} expresses the difference between the proton and neutron radial functions.

For δ_{C2} we have used both Saxon-Woods radial functions [1] and Hartree-Fock-potential eigenfunctions [2]. The Hartree-Fock calculation is based on the Skyrme zero-range, nucleon-nucleon, density-dependent interaction, for which ten parameters have to be specified. As these parameters are highly correlated in their contributions to nuclear-matter properties, we make no attempt to adjust any of them singly. Rather, our approach is to choose from the more than 400 parameter sets available in the literature a selection that is representative of the field. In this report, we will highlight one of the ten parameters, x_0 , which governs the amount of spin exchange – or, equivalently, for an antisymmetric zero-range interaction, the amount of isospin-exchange – in the attractive short-range S-wave part of the interaction. So far, we have considered in detail 16 sets of Skyrme parameters.

For each set of parameters we have computed the δ_{C2} correction for 20 superallowed Fermi decays, from ^{10}C to ^{74}Rb . We add to these values, the δ_{C1} corrections given in Ref. [2] to arrive at the total isospin-symmetry-breaking correction, δ_C . Then these δ_C values were subjected to a test [3] based on the requirement that the δ_C values should lead to corrected Ft values that satisfy the requirements of the Conserved Vector Current (CVC) hypothesis. The test is based on the equation

$$\delta_C = 1 + \delta_{NS} - \frac{K}{ft(1+\delta'_R)}, \quad (1)$$

where ft is the experimental ft -value and δ_{NS} and δ'_R are previously-computed nucleus-dependent contributions to the radiative correction. Thus, to test a set of n calculated δ_C values, we treat K as a simple adjustable parameter and use it to bring the n results from the right-hand side of Eq. (1), which are based predominantly on experiment, into the best possible agreement with the n values of δ_C . The normalized χ^2 (*i.e.* $\chi^2/(n-1)$), minimized by this process, then provides a figure of merit for that set of calculations. Of the three such tests described in [3], we just consider the first test, in which only statistical errors are included on experimental measurements and no errors are included on theoretical quantities. In column two of Table I we list the normalized χ^2 for the 16 sets of Skyrme parameters based on 13 experimental ft values. In all cases, the fit is barely adequate with the normalized χ^2 ranging from 4.9 to 16.1. These values are some distance from the result, 1.2, obtained with Saxon-Woods radial functions. That the Hartree-Fock calculations cannot do better on this test is something of a puzzle.

Table I. Figure of merit, $\chi^2/(n-1)$, for the test [3] discussed in the text and the slope Δ_0 defined in Eq. (2) for 16 Skyrme-potential parameter sets. For comparison, the results with Saxon-Woods functions are shown in the bottom row.

Force	$\chi^2/(n-1)$ 13 data	$\chi^2/(n-1)$ 11 data	Δ_0
SkV	4.92	4.08	1.06
Ska	6.45	3.44	1.01
SGII	8.60	4.09	0.94
SkM*	9.03	4.47	1.00
SKT5	10.40	3.63	1.05
SkR σ	9.87	4.18	0.97
SkG σ	10.32	4.64	0.98
Sly4	10.19	7.45	0.93
SKX	16.12	4.85	0.72
SKXce	14.81	4.97	0.82
KDE0	12.46	6.02	0.77
KDE	12.18	7.36	0.86
SV-min	12.49	4.18	0.87
SV-bas	12.40	4.85	0.86
BSk17	11.33	5.23	0.86
MSL0	9.91	3.44	1.00
Saxon-Woods	1.22	1.39	1.32

The principal defect in the Hartree-Fock results is their failure to obtain a large enough δ_C value for the high-Z cases of ^{62}Ga and ^{74}Rb . Indeed, of the 13 nuclear decays included in the test, the largest contribution to the χ^2 for every choice of Skyrme parameter set comes from ^{62}Ga . Given this difficulty, it is of interest to see how well the Hartree-Fock calculations perform in the lighter nuclei only. Thus in column three of Table I we give the normalized χ^2 values based on 11 experimental fit values, excluding ^{62}Ga and ^{74}Rb . Although the χ^2 values are much better, ranging from 3.4 to 7.5, they are still considerably worse than the 1.4 value obtained with Saxon-Woods radial functions. One of the main contributors to the χ^2 for these Hartree-Fock calculations is ^{26}Al , for which the δ_{C2} values obtained are consistently larger than those obtained with Saxon-Woods radial functions. Another way to quantify this under-prediction for high-Z cases and over-prediction for ^{26}Al is to focus on their difference. We define

$$\Delta_0 = \delta_C(A = 74) - \delta_C(A = 26) \quad (2)$$

and list this quantity in Table I. This slope lies between 0.7 and 1.1 for the 16 Skyrme parameter sets, while the equivalent result from Saxon-Woods radial functions is 30% larger, $\Delta_0 = 1.32$, in agreement with experiment. To date, we have failed to identify any component of the Skyrme force that could be said to be responsible for this defect.

Another curious result is that the correction δ_{C2} computed with Hartree-Fock functions for the decay of a $T_z = -1$ nucleus depends approximately linearly on the Skyrme parameter, x_0 , while in the decay of a $T_z = 0$ nucleus the δ_{C2} value is independent of x_0 . In Fig. 1, we show this dependence for three cases of $T_z = -1$ emitters, ^{10}C , ^{26}Si and ^{42}Ti , and for three cases of $T_z = 0$ emitters, ^{26}Al , ^{46}V and ^{62}Ga . We

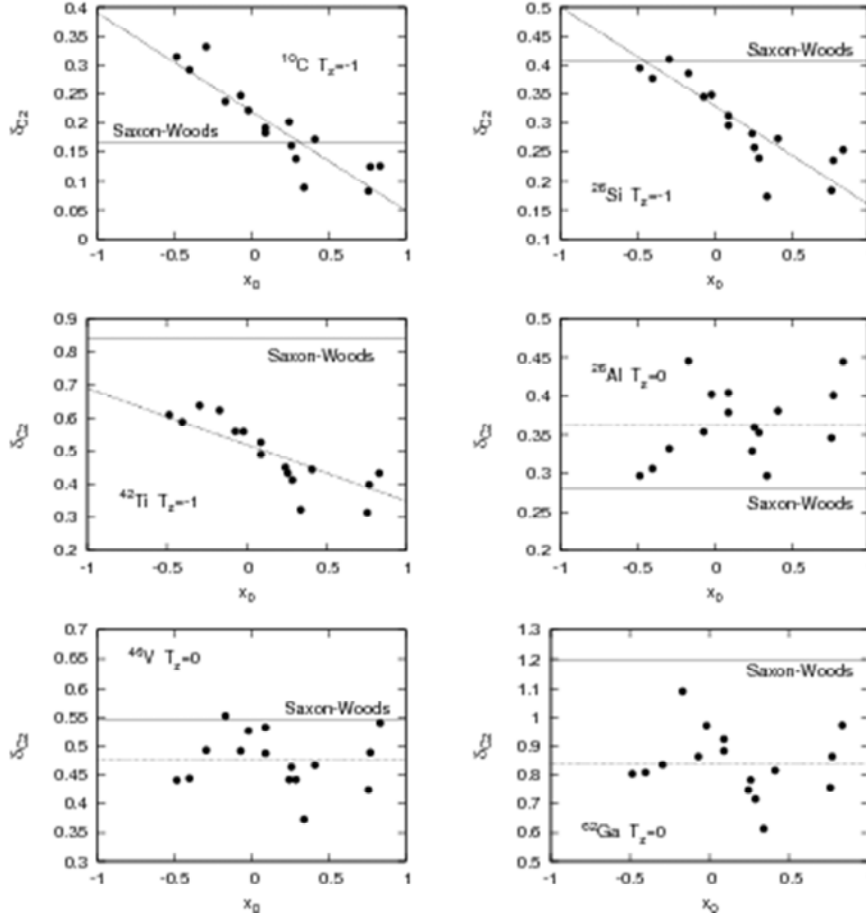


Figure 1. δ_{C2} values in percent units for three $T_z = -1$ and three $T_z = 0$ emitters. The black dots are from Hartree-Fock calculations showing the results as a function of the Skyrme asymmetry parameter, x_0 . The solid horizontal line is the result obtained with Saxon-Woods radial functions. The dotted line has no physical significance: it is merely to guide the eye. The Skyrme interactions from left to right are: SkG σ , SkR σ , SkT5, SkV, SGII, MSL0, Ska, SkM*, SV-min, SV-bas, SKXce, SKX, BSk17, KDE0, KDE, SLy4.

make the following observations:

- Only the $T_z = -1$ emitters show a linear dependence on the x_0 parameter.
- A best-fit line, linear in x_0 , has the same slope for all the $T_z = -1$ emitters.
- The average δ_{C2} value from the Hartree-Fock calculations over-predicts, relative to the Saxon-Woods calculation, in light nuclei, and under-predicts in heavier nuclei. More specifically in the $T_z = -1$ emitters, Hartree-Fock over-predicts for ^{10}C , is comparable to Saxon-Woods for ^{14}O , and under-predicts in all heavier cases. For the $T_z = 0$ emitters,

Hartree-Fock over-predicts for ^{26}Al , is comparable to Saxon-Woods for ^{34}Cl and ^{38}K , and under-predicts in all heavier cases.

- We have found no other correlation between the δ_{C2} value and any of the other 10 Skyrme parameters.

At the time of writing, we have no explanation for these observations, but investigations are continuing.

[1] I.S. Towner and J.C. Hardy, Phys. Rev. C **77**, 025501 (2008).

[2] J.C. Hardy and I.S. Towner, Phys. Rev. C **79**, 055502 (2009).

[3] I.S. Towner and J.C. Hardy, Phys. Rev. C **82**, 065501 (2010).

Approximate expressions for the beta-neutrino angular correlation coefficient

I.S. Towner and J.C. Hardy

Recently [1], an ‘exact’ calculation of the beta-neutrino angular correlation coefficient for ^{21}Na was published. The coefficient is defined as

$$a_{ev}(W) = a_{ev}^0 + \Delta a_{ev}(W) \quad (1)$$

with $a_{ev}^0 = (a_1^2 - \frac{1}{3}c_1^2)/(a_1^2 + c_1^2)$ being the major contribution, where $a_1 = g_V M_F$ and $c_1 = g_A M_{GT}$ with M_F and M_{GT} being the Fermi and Gamow-Teller matrix elements and g_V and g_A their respective coupling constants. Here W is the electron total energy expressed in electron rest-mass units. We computed the correction Δa_{ev} using the exact formalism of Behrens and Bühring (BB) [2] and found Δa_{ev} , when averaged over the electron energy spectrum, gave a correction of order 1%. Alternatively computing the correction with the formalism of Holstein [3] we found the correction to be much smaller, of order 0.1%. To try and resolve this discrepancy we have been working with the BB formalism, identifying the leading order terms and comparing them with those of Holstein.

The beta decay differential decay rate is written in Holstein [3] as

$$d^5\Gamma = \frac{G^2}{(2\pi)^5} F(Z, W)(W_0 - W)^2 p W dW d\Omega_e d\Omega_\nu \left(f_1(W) + f_2(W) \frac{p}{W} \hat{\mathbf{p}} \cdot \hat{\mathbf{k}} + \dots \right) \quad (2)$$

where $\hat{\mathbf{p}}$ and $\hat{\mathbf{k}}$ are unit vectors in the directions of the electron and neutrino respectively. Here W_0 is the maximum value of W , p is the electron momentum, with $p^2 = W^2 - 1$ in electron rest-mass units, and $F(Z, W)$ is the Fermi function. The beta-neutrino angular correlation coefficient is defined as

$$a_{ev} = \frac{f_2(W)}{f_1(W)} \quad (3)$$

In BB [2] the same decay rate is written

$$d^5\Gamma = \frac{G^2}{(2\pi)^5} F_0 L_0 (W_0 - W)^2 p W dW d\Omega_e d\Omega_\nu \left(C(W) + D(W) \frac{p}{W} \hat{\mathbf{p}} \cdot \hat{\mathbf{k}} + \dots \right) \quad (4)$$

and

$$a_{ev} = \frac{D(W)}{C(W)} \quad (5)$$

Here $F_0 = 2F(Z, W)/(1 + \gamma_1)$ with $\gamma_1 = (1 - (\alpha Z)^2)^{1/2}$; α is the fine-structure constant and Z is the charge number of the daughter nucleus, taken positive in electron decay and negative in positron decay.

Note the two expressions Eqs. (2) and (4) have different normalizations. This is because BB prefer to normalize their electron wave functions to the value obtained at the origin (L_0 represents the electron density at the origin), whereas Holstein uses the historical normalization at a radius R ($F(Z, W)$ represents the electron density at radius R). The relationship between the two is

$$f_1(W) = \frac{2}{(1+\gamma_1)} L_0 C(W) \quad f_2(W) = \frac{2}{(1+\gamma_1)} L_0 D(W) \quad (6)$$

If it is assumed that the electron moves in the Coulomb field of a uniform nuclear charge-density distribution of radius R , then to second order in (WR) and (αZ) , the relationship is [2]

$$\frac{2}{(1+\gamma_1)} L_0 = 1 - (\alpha Z)(WR) - \frac{1}{2} \frac{(\alpha Z)R}{W} + \frac{7}{15} (\alpha Z)^2, \quad (7)$$

where R is given in electron Compton wavelength units. Note that the dimensionless R is a small quantity, such that (WR) and (αZ) can be considered expansion parameters.

In Holstein's formalism all the aspects of nuclear-structure physics are encoded in terms of a few form factors, $a(q^2)$, $b(q^2)$, $c(q^2)$, $d(q^2)$, $h(q^2)$. . . , where q^2 is the square of the four-momentum transfer. On invoking the impulse approximation these can be related to nuclear-structure matrix elements calculable in the shell model. The important ones are: $M_F = \langle 1 \rangle$, $M_{r^2} = \langle r^2 \rangle \cong \frac{3}{5} R^2 \langle 1 \rangle$, $M_{GT} = \langle \sigma \rangle$, $M_{\sigma r^2} = \langle r^2 \sigma \rangle \cong \frac{3}{5} R^2 \langle \sigma \rangle$, $M_{1y} = (16\pi/5)^{1/2} \langle r^2 [Y_2 \times \sigma] \rangle$ and $M_L = \langle L \rangle$. It is convenient to express M_{1y} in terms of M_{GT} (valid only for allowed transitions for which M_{GT} does not vanish) by defining x as

$$x = -\sqrt{10} \frac{M_{1y}}{M_{\sigma r^2}} \quad (8)$$

Our goal is to write the spectral functions $f_1(W)$ and $f_2(W)$ introduced in Eq. (2) in terms of the four parameters: a_1 , c_1 , the weak-magnetism form factor b , and x . For the present time, we have left out the relativistic matrix elements denoted in [3] as $M_{r,p}$ and $M_{\sigma p}$, while the matrix element $M_{\sigma L}$ vanishes in diagonal matrix elements as would occur in a mirror transition between isobaric analogue states. We have also dropped the small pseudoscalar term in $h(q^2)$ and the second-class current term in $d(q^2)$.

In the method of Behrens and Bühring [2], all beta-decay observables are given in terms of quantities $M_K(k_e, k_\nu)$ and $m_K(k_e, k_\nu)$, which are linear combinations of form factor coefficients F_{KLS} and electron and neutrino radial wave functions. To the extent that these radial wave functions can be computed exactly, by solving the appropriate Dirac equation, the formalism can be considered exact. Here K is the multipolarity of the transition, L and s are the orbital and spin quantum numbers characterising the transition, and k_e and k_ν are the partial-wave counting indices for the electron and neutrino radial functions. For allowed transitions, it is usually sufficient to consider the two lowest partial waves, $k_{e,\max} = 2$, $k_{\nu,\max} = 2$. The strength of BB's work, however, is that they give expansions of the electron and neutrino wave functions in power series of (αZ) , (WR) and $(p_\nu R)$, where W and $p_\nu =$

$W_0 - W$ are the electron and neutrino energies in electron rest-mass units. These expansions should enable us to make contact with the expressions of Holstein. We will quote formulae to second order in the quantities.

The form factor coefficients, F_{KLs} , are very similar to Holstein's form factors and by invoking the impulse approximation they too can be related to nuclear-structure matrix elements. To show the relationships between Holstein and BB's expressions it is convenient to separate the Fermi and Gamow-Teller pieces, $f_1(W) = f_1^F(W) + f_1^{GT}(W)$ and $f_2(W) = f_2^F(W) + f_2^{GT}(W)$. Further, we display their electron energy dependence explicitly by writing them as

$$f_\alpha^F(W) = a_1^2 k_\alpha^F (1 + A_\alpha^F W + \frac{B_\alpha^F}{W} + C_\alpha^F W^2)$$

$$f_\alpha^{GT}(W) = c_1^2 k_\alpha^{GT} (1 + A_\alpha^{GT} W + \frac{B_\alpha^{GT}}{W} + C_\alpha^{GT} W^2), \alpha = 1, 2 \quad (9)$$

Expressions for the parameters of these expansions are given in Table I for $f_1(W)$ and in Table II for $f_2(W)$.

Table I. Expressions for the spectral function $f_1(W)$ derived from the formulations of Holstein and Behrens-Bühring.

	Holstein	Behrens-Bühring
Fermi terms		
k_1	$1 - \frac{1}{5}(W_0 R)^2 + \frac{1}{15}R^2 - \frac{6}{35}(\alpha Z)(W_0 R)$	$1 - \frac{1}{5}(W_0 R)^2 + \frac{1}{15}R^2 - \frac{6}{35}(\alpha Z)(W_0 R)$
$k_1 A_1$	$\frac{4}{15}(W_0 R)R - \frac{48}{35}(\alpha Z)R$	$\frac{4}{15}(W_0 R)R - \frac{48}{35}(\alpha Z)R$
$k_1 B_1$	$\frac{2}{15}(W_0 R)R - \frac{18}{35}(\alpha Z)R$	$\frac{2}{15}(W_0 R)R - \frac{18}{35}(\alpha Z)R$
$k_1 C_1$	$-\frac{4}{15}R^2$	$-\frac{4}{15}R^2$
Gamow-Teller terms		
k_1	$1 - \frac{1}{5}(W_0 R)^2 + \frac{11}{45}R^2(1 - \frac{1}{10}x)$ $+ \frac{2}{35}(\alpha Z)(W_0 R) - \frac{2}{3}(W_0 R)\frac{b}{Ac_1}\frac{1}{MR}$	$1 - \frac{1}{5}(W_0 R)^2 + \frac{11}{45}R^2(1 - \frac{2}{11}x)$ $+ \frac{2}{35}(\alpha Z)(W_0 R)(1 - x) - \frac{2}{3}(W_0 R)\frac{b}{Ac_1}\frac{1}{MR}$ $+ \frac{22}{25}(\alpha Z)\frac{b}{Ac_1}\frac{1}{MR}$
$k_1 A_1$	$\frac{4}{9}(W_0 R)R(1 - \frac{1}{10}x) - \frac{8}{5}(\alpha Z)R$ $+ \frac{4}{3}R\frac{b}{Ac_1}\frac{1}{MR}$	$\frac{4}{9}(W_0 R)R(1 - \frac{1}{10}x) - \frac{8}{5}(\alpha Z)R(1 - \frac{1}{28}x)$ $+ \frac{4}{3}R\frac{b}{Ac_1}\frac{1}{MR}$
$k_1 B_1$	$-\frac{2}{45}(W_0 R)R(1 - \frac{11}{20}x) - \frac{18}{35}(\alpha Z)R$ $- \frac{2}{3}R\frac{b}{Ac_1}\frac{1}{MR}$	$-\frac{2}{45}(W_0 R)R(1 - x) - \frac{18}{35}(\alpha Z)R$ $- \frac{2}{3}R\frac{b}{Ac_1}\frac{1}{MR}$
$k_1 C_1$	$-\frac{4}{9}R^2(1 - \frac{1}{10}x)$	$-\frac{4}{9}R^2(1 - \frac{1}{10}x)$

Table II. Expressions for the spectral function $f_2(W)$ derived from the formulations of Holstein and Behrens-Bühring.

	Holstein	Behrens-Bühring
Fermi terms		
k_2	$1 - \frac{1}{5}(W_0R)^2 + \frac{1}{5}R^2 - \frac{6}{35}(\alpha Z)(W_0R)$	$1 - \frac{1}{5}(W_0R)^2 + \frac{1}{5}R^2 - \frac{6}{35}(\alpha Z)(W_0R)$
k_2A_2	$-\frac{48}{35}(\alpha Z)R$	$-\frac{48}{35}(\alpha Z)R$
k_2B_2	0	$-\frac{1}{2}(\alpha Z)R$
k_2C_2	0	0
Gamow-Teller terms		
k_2	$-\frac{1}{3} + \frac{1}{15}(W_0R)^2(1 + \frac{1}{5}x) - \frac{1}{15}R^2(1 - \frac{1}{10}x) - \frac{6}{35}(\alpha Z)(W_0R) + \frac{2}{3}(W_0R)\frac{b}{Ac_1}\frac{1}{MR}$	$-\frac{1}{3} + \frac{1}{15}(W_0R)^2(1 - \frac{2}{5}x) - \frac{1}{15}R^2(1 - \frac{2}{5}x) - \frac{6}{35}(\alpha Z)(W_0R) + \frac{2}{3}(W_0R)\frac{b}{Ac_1}\frac{1}{MR} - \frac{22}{75}(\alpha Z)\frac{b}{Ac_1}\frac{1}{MR}$
k_2A_2	$-\frac{8}{15}(W_0R)R(1 - \frac{1}{10}x) + \frac{24}{35}(\alpha Z)R - \frac{4}{3}R\frac{b}{Ac_1}\frac{1}{MR}$	$-\frac{8}{15}(W_0R)R(1 - \frac{13}{180}x) - \frac{68}{105}(\alpha Z)R(1 + \frac{61}{1190}x) - \frac{4}{3}R\frac{b}{Ac_1}\frac{1}{MR}$
k_2B_2	0	$-\frac{1}{2}(\alpha Z)R$
k_2C_2	$\frac{8}{15}R^2(1 - \frac{1}{10}x)$	$\frac{8}{15}R^2(1 - \frac{13}{180}x)$

For the Fermi terms, it is noted there is almost complete agreement between the Holstein and BB formalisms; the only difference is in a small B_2 coefficient in $f_2(W)$. For the Gamow-Teller terms, we note the following:

- There are no electromagnetic (αZ) corrections to the weak-magnetism terms, b , in coefficients k_1 and k_2 ;
- The coefficient of the matrix-element ratio, x (see Eq. (8)) is in many, but not all, instances different.

These differences do not represent errors, but reflect different approximations made in the derivations. There is little numerical consequence from these differences. The correction to the beta-neutrino correlation coefficient, Δa_{ev} , is likely to be small and of order 0.1% from these formulae.

However, we have not yet included the relativistic terms: the matrix elements $M_{r,p}$ and $M_{\sigma p}$. These could lead to terms of comparable size to the terms considered so far. We also need to do some numerical studies on the exact formulation to understand their differences from the approximate formulae. Further study is underway.

- [1] V.E. Iacob, J.C. Hardy, C.A. Gagliardi, J. Goodwin, N. Nica, H.I. Park, G. Tabacaru, L. Trache, R.E. Tribble, Y. Zhai and I.S. Towner, *Phys. Rev. C* **74**, 015501 (2006).
- [2] H. Behrens and W. Bühring, *Electron Radial Wave Functions and Nuclear Beta-decay* (Clarendon Press, Oxford, 1982); H. Behrens, H. Genz, M. Conze, H. Feldmeir, W. Stock and A. Richter, *Ann. of Phys.* **115**, 276 (1978).
- [3] B.R. Holstein, *Rev. Mod. Phys.* **46**, 789 (1974).

Isoscalar and isovector giant resonances in ^{40}Ca and ^{48}Ca

M.R. Anders, S. Shlomo, T. Sil,¹ D.H. Youngblood, Y.-W. Lui, Krishichayan and J. Button

¹*Indian Institute of Information Technology Design and Manufacturing,
Kancheepuram, Chennai 600 036, Tamil Nadu, India*

Very recently the giant resonance region from $9.5 \text{ MeV} < E_x < 40 \text{ MeV}$ in ^{48}Ca has been studied with inelastic scattering of 240 MeV α particles at small angles, including 0° . Close to 100% of the ISGMR (E0), ISGDR (E1) and isoscalar giant quadrupole resonance (E2) strengths have been located between 9.5 and 40 MeV in ^{48}Ca [1]. To study the effect of neutron-proton asymmetry, a comparison with the available data for ^{40}Ca , as well as with the results obtained within the HF based RPA, was carried out in Ref. [1]. The ISGMR has been found at somewhat higher energy in ^{48}Ca than in ^{40}Ca , whereas self consistent HF-RPA calculations obtained using the SGII, KDE0, SKM* and SK255 Skyrme interactions predict a lower centroid energy in this neutron rich Ca isotope. This precipitated the thorough study of isoscalar and isovector giant resonances of ^{40}Ca and ^{48}Ca for multipolarities: $L=0-3$.

In this work we extend our theoretical investigation by considering the isoscalar and isovector giant resonances of multipolarities $L = 0 - 3$ in ^{40}Ca and ^{48}Ca . For this purpose, we have carried out [2] fully self-consistent Hartree-Fock (HF) based RPA calculations of the isoscalar ($T = 0$) giant monopole resonance (ISGMR), dipole (ISGDR), quadrupole (ISGQR), and the octopole (ISGOR) strength functions, and for the isovector ($T = 1$) giant monopole resonance (IVGMR), dipole (IVGDR), quadrupole (IVGQR) and octopole (IVGOR) strength functions, for ^{40}Ca and for ^{48}Ca , using a wide range of over 15 commonly employed Skyrme type interaction. These interactions, which were fitted to ground state properties of nuclei, are associated with a wide range of nuclear matter properties such as incompressibility coefficient $K_{\text{NM}} = 200 - 255 \text{ MeV}$, effective mass $m^* = 0.6 - 1.0$, and symmetry energy $J = 27 - 37 \text{ MeV}$. We consider, in particular the issue of self-consistency and investigate the sensitivities of E_{CEN} and of the isotopic differences $E_{\text{CEN}}(^{48}\text{Ca}) - E_{\text{CEN}}(^{40}\text{Ca})$ to physical quantities, such K_{NM} , m^* , J and the symmetry energy density, associated with the effective nucleon-nucleon interactions and compare the results with available experimental data. As examples we present below results of our calculations [2] for the ISGMR and IVGDR.

In Fig. 1. we compare the experimental data of the ISGMR centroid energies E_{CEN} of ^{40}Ca (a), ^{48}Ca (b), and the energy difference $E_{\text{CEN}}(^{48}\text{Ca}) - E_{\text{CEN}}(^{40}\text{Ca})$ between ^{48}Ca and ^{40}Ca (c), shown as the regions between the dashed lines, with the results of fully self consistent HF based RPA calculations (full circles), using the Skyrme type interactions having nuclear matter incompressibility coefficients in the range of, $K_{\text{NM}} = 201-258 \text{ MeV}$. The results obtained with violation of self-consistency by the neglecting the Coulomb and the spin orbit particle-hole interactions in the RPA calculations, are shown in (d). The energies shown were calculated over the experimental excitation energy range of $0 - 60 \text{ MeV}$. A clear correlation between E_{CEN} of ^{40}Ca and E_{CEN} of ^{48}Ca can be seen with K_{NM} . We point out that we have that $E_{\text{CEN}}(^{48}\text{Ca}) - E_{\text{CEN}}(^{40}\text{Ca}) < 0$ for all the interactions used in our work, in disagreement with the experimental data. Note that for not self-consistent RPA calculations, the results of some interactions lead to spurious agreement with the experimental data.

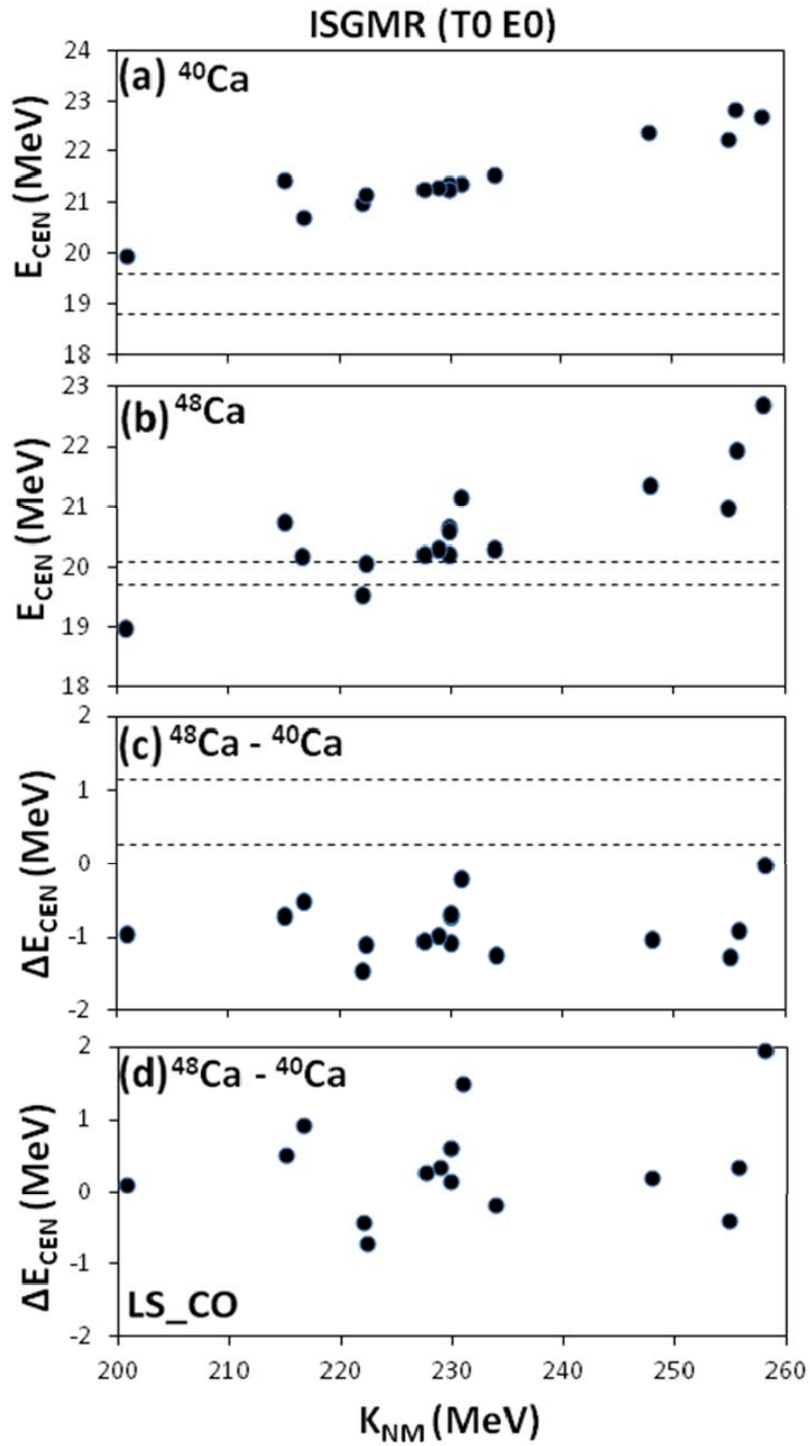


FIG. 1. Comparison between calculated centroid energies and experimental data (region between the dashed lines) for the ISGMR in ^{40}Ca and ^{48}Ca

In Fig. 2, we show our results for the centroid energies of the IVGDR in ^{40}Ca and ^{48}Ca as a function of $J(0.1)/J$, the ratio between the symmetry energy at 0.1 fm^{-3} (about $(2/3)\rho_0$) and the symmetry energy at saturation density ρ_0 . An agreement with experimental data is obtained for several interactions. However, weak correlation is obtained between the centroid energy and $J(0.1)/J$. We point out that similar results were obtained when using, instead of $J(0.1)/J$, the first or the second derivative of the symmetry energy at saturation density.

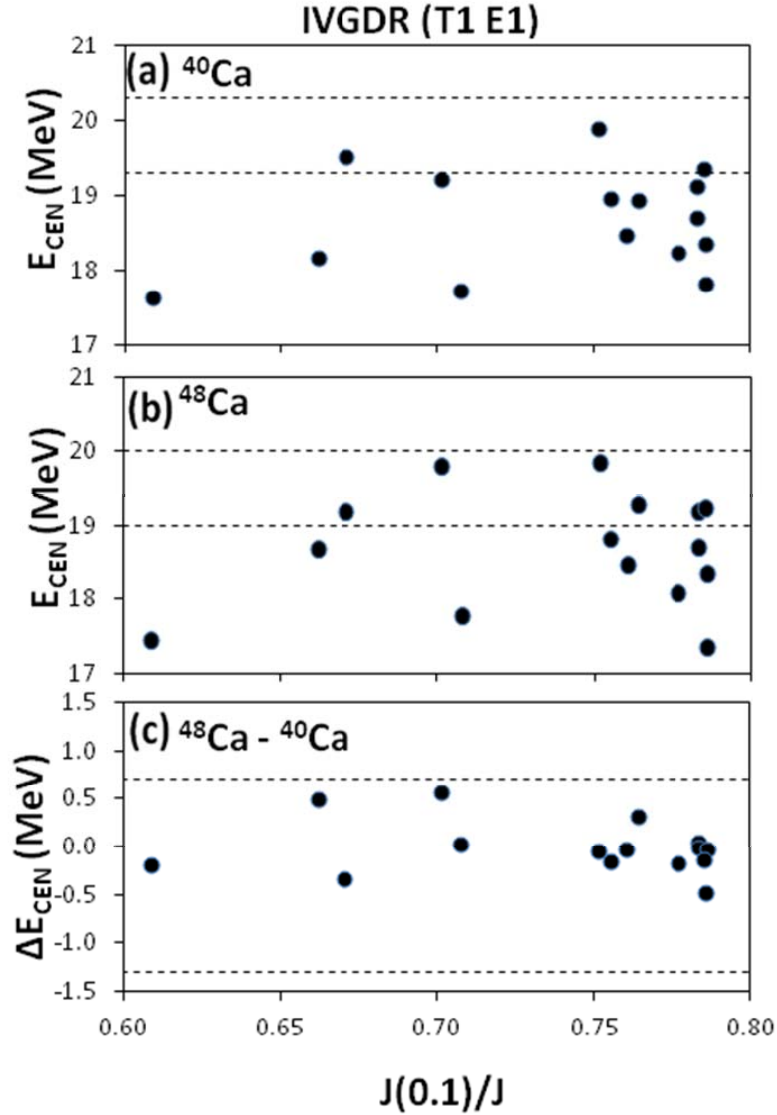


FIG. 2. Comparison between calculated centroid energies and experimental data (region between the dashed lines) for the IVGDR in ^{40}Ca

- [1] Y.-W. Lui, D.H. Youngblood, S. Shlomo, X. Chen, Y. Tokimoto, Krishichayan, M. Anders, and J. Button, Phys. Rev. C. **83**, 044327 (2011).
 [2] M. R. Anders *et al.*, in preparation.

Nuclear matter properties from energies of giant resonances

M.R. Anders and S. Shlomo

The development of a modern and more realistic nuclear energy density functional (EDF) for accurate predictions of properties of nuclei is the subject of enhanced activity, since it is very important for the study of properties of rare nuclei with unusual neutron-to-proton ratios that are difficult to produce experimentally and likely to exhibit interesting new phenomena associated with isospin, clusterization and the continuum. Adopting the standard parametrization of the Skyrme type interactions, it is common to determine the parameters of the EDF within the Hartree-Fock (HF) mean-field approximation by carrying out a fit to an extensive set of data on; (i) binding energies, (ii) single-particle energies, and (iii) charge root-mean-square (rms) radii. This approach has resulted with over 200 EDFs associated with the Skyrme type effective nucleon-nucleon interaction.

To better determine the values of the Skyrme parameters, we investigate the sensitivities of the centroid energies E_{CEN} of the isoscalar and isovector giant resonances of multipolarities $L = 0 - 3$ in ^{40}Ca and ^{48}Ca . For this purpose, we have carried out fully self-consistent Hartree-Fock (HF) based RPA calculations of the isoscalar ($T = 0$) giant monopole resonance (ISGMR), dipole (ISGDR), quadrupole (ISGQR), and the octopole (ISGOR) strength functions, and for the isovector ($T = 1$) giant monopole resonance (IVGMR), dipole (IVGDR), quadrupole (IVGQR) and octopole (IVGOR) strength functions, for ^{40}Ca and for ^{48}Ca , using a wide range of over 15 commonly employed Skyrme type interaction. These interactions, which were fitted to ground state properties of nuclei are associated with a wide range of nuclear matter properties such as incompressibility coefficient $K_{\text{NM}} = 200 - 255$ MeV, symmetry energy $J = 27 - 37$ MeV and effective mass $m^* = 0.6 - 1.0$. We investigate the sensitivities of E_{CEN} and of the isotopic differences $\Delta E_{\text{CEN}} = E_{\text{CEN}}(^{48}\text{Ca}) - E_{\text{CEN}}(^{40}\text{Ca})$ to physical quantities of nuclear matter (NM), such as the effective mass m^* ; the incompressibility coefficient $K_{\text{NM}} = -9\rho_0^2 \left. \frac{d^2(E/A)}{d\rho^2} \right|_{\rho_0}$; the symmetry energy coefficient $J = E_{\text{sym}}(\rho_0)$; the symmetry energy at 0.1 fm^{-3} , $J(0.1) = E_{\text{sym}}(0.1)$ the coefficient proportional to the slope, $L = 3\rho_0 \left. \frac{d(E_{\text{sym}})}{d\rho} \right|_{\rho_0}$, and the curvature $K_{\text{sym}} = 9\rho_0^2 \left. \frac{d^2(E_{\text{sym}})}{d\rho^2} \right|_{\rho_0}$ of the density dependence of the symmetry energy, respectively, κ , the enhancement factor of the energy weighted sum rule for the IVGDR, and the strength of the spin-orbit interaction W_0 .

In Table I and II we present the Pearson Correlation Coefficients between the values of E_{CEN} and ΔE_{CEN} of the isoscalar and isovector giant resonances, respectively, and the properties of NM. It is seen from the Tables that strong correlations were found between the energies of compression modes (ISGMR and ISGDR) and K_{NM} , and between the energies of the ISGQR (and ISGOR) and m^* . However, weak correlations were found between IVGDR in ^{40}Ca and ^{48}Ca and the values of J , L , or K_{sym} .

Table I. Pearson's correlation coefficient between the energies of Isoscalar (T=0) giant multipole (L=0-3) resonances and NM properties

		m^*/m	K_{NM}	J	J(0.1)	L	K_{sym}	J(0.1)/J	κ	$W_0(X_W=1)$	
L0 T0	Ca 40	E_{CEN}	-0.71	0.95	0.39	-0.29	0.76	0.86	-0.65	-0.02	0.02
L0 T0	Ca 48	E_{CEN}	-0.85	0.85	0.29	-0.41	0.73	0.87	-0.66	0.16	0.30
L0 T0		ΔE_{CEN}	-0.59	0.13	-0.07	-0.40	0.21	0.36	-0.29	0.41	0.69
L1 T0	Ca 40	E_{CEN}	-0.86	0.88	0.35	-0.38	0.77	0.92	-0.69	0.05	0.23
L1 T0	Ca 48	E_{CEN}	-0.94	0.82	0.25	-0.26	0.58	0.82	-0.50	0.03	0.43
L1 T0		ΔE_{CEN}	-0.71	0.32	-0.07	0.12	-0.10	0.24	0.16	-0.02	0.53
L2 T0	Ca 40	E_{CEN}	-0.96	0.76	0.29	-0.25	0.61	0.85	-0.53	-0.04	0.50
L2 T0	Ca 48	E_{CEN}	-0.98	0.68	0.25	-0.25	0.54	0.80	-0.48	0.03	0.57
L2 T0		ΔE_{CEN}	-0.56	-0.04	-0.10	-0.14	-0.03	0.18	-0.02	0.32	0.48
L3 T0	Ca 40	E_{CEN}	-0.96	0.77	0.30	-0.19	0.58	0.83	-0.49	-0.03	0.41
L3 T0	Ca 48	E_{CEN}	-0.98	0.68	0.20	-0.27	0.51	0.79	-0.45	0.06	0.59
L3 T0		ΔE_{CEN}	-0.25	-0.17	-0.32	-0.33	-0.13	0.01	0.03	0.35	0.56

Table II. Pearson's correlation coefficient between the energies of Isovector (T=1) giant multipole (L=0-3) resonances and NM properties

			m^*/m	K_{NM}	J	J(0.1)	L	K_{sym}	J(0.1)/J	κ	$W_0(X_W=1)$
L0 T1	Ca 40	E_{CEN}	-0.43	0.69	0.09	-0.41	0.48	0.48	-0.43	0.43	0.01
L0 T1	Ca 48	E_{CEN}	-0.56	0.58	-0.03	-0.60	0.46	0.52	-0.48	0.63	0.36
L0 T1		ΔE_{CEN}	-0.36	-0.06	-0.21	-0.47	0.09	0.20	-0.21	0.51	0.70
L1 T1	Ca 40	E_{CEN}	-0.03	0.08	-0.27	0.03	-0.30	-0.32	0.32	0.58	-0.01
L1 T1	Ca 48	E_{CEN}	-0.17	0.07	-0.32	-0.15	-0.24	-0.21	0.21	0.70	0.25
L1 T1		ΔE_{CEN}	-0.42	0.00	-0.20	-0.49	0.11	0.24	-0.24	0.47	0.68
L2 T1	Ca 40	E_{CEN}	-0.68	0.51	-0.01	-0.19	0.20	0.33	-0.15	0.60	0.43
L2 T1	Ca 48	E_{CEN}	-0.70	0.39	-0.14	-0.32	0.14	0.31	-0.13	0.64	0.66
L2 T1		ΔE_{CEN}	-0.47	-0.03	-0.37	-0.47	-0.06	0.14	-0.04	0.47	0.71
L3 T1	Ca 40	E_{CEN}	-0.71	0.58	0.13	-0.21	0.38	0.53	-0.30	0.40	0.37
L3 T1	Ca 48	E_{CEN}	-0.73	0.53	0.01	-0.22	0.26	0.43	-0.19	0.48	0.42
L3 T1		ΔE_{CEN}	0.30	-0.38	-0.33	0.06	-0.45	-0.45	0.39	-0.02	-0.11

[1] M.R. Anders *et al.*, in preparation.

**Clusters in nuclei, nuclear matter, heavy ion collisions and astrophysics- report on the ECT*
workshop, June 13-17, Trento, Italy**

Gerd Roepke,¹ David Blaschke,² Thomas Klähn,² Shalom Shlomo and Stephan Typel³

¹*Rostock University, Rostock, Germany*

²*Wroclaw university, Wroclaw, Poland*

³*GSI, Darmstadt, Germany*

Correlations in nuclear systems are of fundamental interest for different phenomena in nuclear structure and reaction physics, but also for the nuclear matter equation of state which is crucial for the modeling of astrophysical systems. A better understanding of correlations and more realistic descriptions are crucial since usually the described systems are very complex and subject to many uncertainties. Therefore, understanding and applying state of the art techniques with respect to cluster formation promise to give much better insight into the physics of the investigated phenomena.

Nuclear systems are important examples for strongly interacting quantum liquids. New experiments in nuclear physics and observations of compact astrophysical objects require an adequate description of correlations, in particular with respect to the formation of clusters and the occurrence of quantum condensates in low-density nuclear systems. An important task is to join different approaches such as virial expansions and the nuclear statistical equilibrium, valid in the low-density limit, with approaches that are applicable near the saturation density, such as Dirac-Brueckner-Hartree-Fock or relativistic mean-field (RMF) approximations. A quantum statistical approach has been elaborated that allows to include few-nucleon clusters like deuterons, tritons, ³He, and ⁴He embedded in nuclear matter, but can also be extended to describe the formation of larger nuclei in low-density matter. The final goal is the formulation of a unified approach which describes the properties of nuclear matter and bound states over the whole range of relevant temperatures, densities and asymmetries.

We have discussed important issues related to three fields where correlations in nuclear systems are of fundamental interest: nuclear structure and reaction physics, heavy-ion collisions and the structure and evolution of compact astrophysical objects. In particular, we focused on bound states (clusters) in nuclear matter. We discussed the issues of:

1. Correlations in nuclear matter: nuclei in matter, quantum condensates: pairing, quartetting.
2. Clusters and the equation of state (EoS): nuclear statistical equilibrium, virial expansion, RMF, quantum statistical approach to clusters in the low-density EoS; astrophysical applications: supernovae, neutron stars.
3. Heavy-ion collisions: symmetry energy.
4. Clusters in nuclei: Alpha cluster and Hoyle state, tritons and further clusters; reactions and astrophysical applications.

In the following we summarize some results and highlights of the workshop which serve as motivations for further work:

1. Correlations, in particular cluster formation, has to be considered in low-density nuclear systems. Any single-nucleon quasiparticle approach fails in that region. A possible approach is the introduction of clusters as effective degrees of freedom in the model description. The full antisymmetrization (Pauli blocking) is indispensable at increasing densities.
2. Nuclear structure: pairing is well accepted. We need a theory that includes quartetting, i.e. four-particle correlations. First steps have been done for ^8Be and ^{12}C (Hoyle state) and related low-density state in light nuclei. Similar to Hartree-Fock-Bogoliubov theory, we need an approach that joins shell structure calculations and alpha cluster-like correlations. Promising approaches such as Fermionic Molecular Dynamics should be studied further. At present, one can use a local density approach to estimate the role of four-nucleon correlations.
3. Heavy ion collisions: the formation of light elements is a nonequilibrium process that has to be described with adequate equilibrium approaches as inputs (freeze-out, coalescence, transport codes). The extraction of thermodynamic parameters, including the symmetry energy, should go beyond the nuclear statistical equilibrium (NSE) taking into account in-medium effects.
4. Astrophysics: we need improved equations of state (EOS) to analyse the evolution of supernovae, including neutrino transport. At present, different attempts are performed to include few-nucleon correlations (light elements) as well as the full table of all known nuclei. The unification of mean-field approaches and NSE (in-medium description of clusters) as well as the contribution of continuum states (virial coefficients) has to be implemented.

Deducing the neutron skin thickness in ^{208}Pb from the strength function distribution of the isovector giant dipole resonance

M.R. Anders and S. Shlomo

An accurate knowledge of the density dependence of the symmetry energy coefficient, E_{SYM} , is needed for the equation of state (EOS) of asymmetric nuclear matter (NM). It is well known that the energies of the isovector giant resonances, in particular, the isovector giant dipole resonance (IVGDR), are sensitive to the density dependence of the symmetry energy E_{sym} , commonly parameterized in terms of the quantities J , L and K_{sym} which are the symmetry energy at saturation density of symmetric NM, and the quantities directly related to the derivative and the curvature of $E_{\text{sym}}(\rho)$ at the saturation density, respectively. Furthermore, information on the density dependence of E_{SYM} can also be obtained by studying the isotopic dependence of strength functions, such as the difference between the strength functions of ^{40}Ca and ^{48}Ca and between ^{112}Sn and ^{124}Sn . Other physical quantities that are sensitive to the $E_{\text{sym}}(\rho)$ below the saturation density are: the neutron skin thickness, $r_n - r_p$, the difference between the root mean square radii (rms) of the neutron and proton density distributions; and the electric dipole polarizability α_D , which is related to the inverse energy moment (m_1) of the strength function of the IVGDR.

Recent high-resolution measurement [1] of α_D in ^{208}Pb was used to determine the value of the neutron skin thickness in this nucleus, resulting in the value of $r_n - r_p = 0.156$ (.025) fm . However, the analysis in this work was based on only one form of energy density functional (EDF), associated with the Skyrme SV-min interaction. Here we examine the conclusion of the work of Ref. [1]. For this purpose, we have carried out fully self-consistent Hartree-Fock (HF) based RPA calculations of the isovector ($T = 1$) giant dipole resonance (IVGDR) in ^{208}Pb , using over 27 commonly employed Skyrme type interaction, which were deduced by carrying out HF based fits to wide ranges of experimental data on binding energies and radii.

In Fig. 1 we present the predictions [2] of these interactions for α_D and $r_n - r_p$. The experimental data on α_D is shown as the region between the dashed lines. Also shown is the Pearson correlation coefficient $C_{AB} = 0.55$, which indicates a weak correlation between α_D and $r_n - r_p$. We thus conclude that EDFs associated with theoretical predictions of values of $r_n - r_p$ in the range of 0.14 to 0.20 fm are consistent with the experimental data on α_D .

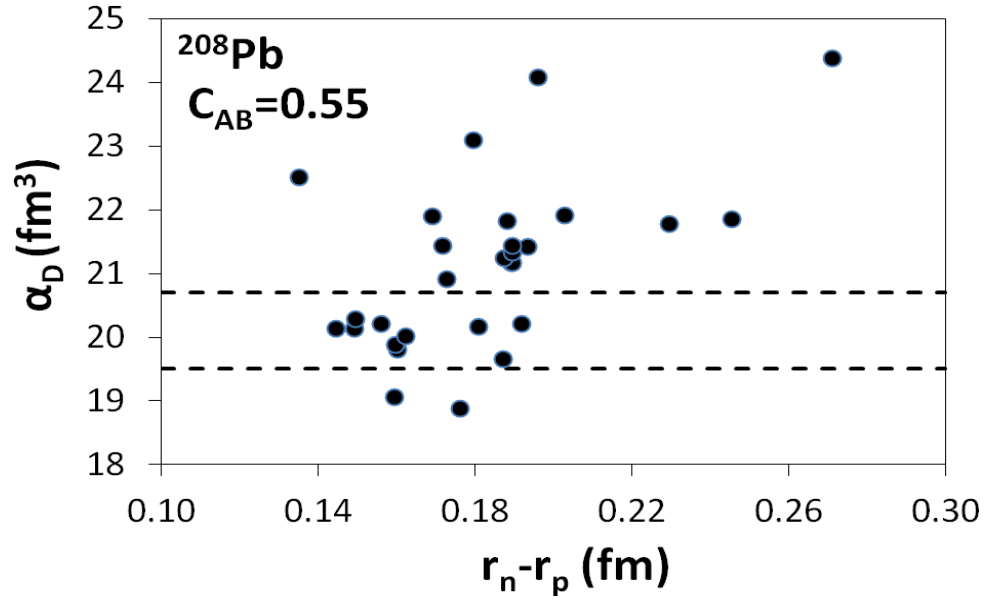


FIG. 1. The IVGDR polarizability α_D and the corresponding values of $r_n - r_p$ for various interactions. The experimental data on α_D is shown as the region between the dashed lines.

[1] A. Tamii *et al.*, Phys. Rev. Lett. **107**. 062502 (2011).

[2] M.R. Anders and S. Shlomo, in preparation.

Hadronic potential effects in elliptic flow in heavy ion collisions

J. Xu, L.W. Chen,¹ C.M. Ko, and Z.W. Lin²

¹*Department of Physics, Shanghai Jiao Tong University, Shanghai 200240, China*

²*Department of Physics, East Carolina University, C-209 Howell Science Complex, Greenville, North Carolina 27858*

We have studied the elliptic flows of p , K^+ , π^+ and their antiparticles in heavy ion collisions at energies of $\sqrt{s_{NN}} = 7.7, 11.5$ and 39 GeV, where a baryon-rich hot dense matter is produced, by extending the string melting AMPT model [1] to include their mean-field potentials in the hadronic stage [2]. Because of the more attractive potentials for proton than antiproton [3], the attractive K^- and repulsive K^+ potentials [3], and the slightly attractive π^+ and repulsive π^- potentials in the baryon- and neutron-rich matter [4] formed in these collisions, smaller elliptic flows are obtained for antiproton, K^- , and π^+ than for proton, K^+ , and π^- . Also, the difference between the elliptic flows of particles and their antiparticles is found to decrease with increasing collision energy as a result of the decreasing baryon chemical potential of hadronic matter as shown in Fig. 1. Although our results are qualitatively consistent with the experimental observations from the STAR Collaboration at RHIC [5], they somewhat underestimated the relative elliptic flow difference between proton and antiproton as well as that between π^- and π^+ , and overestimated that between K^+ and K^- . Studies including different quark and antiquark potentials in the baryon-rich quark gluon plasma are being carried out to investigate their effects on the quark and antiquark elliptic flow before hadronization in order to understand more quantitatively the different

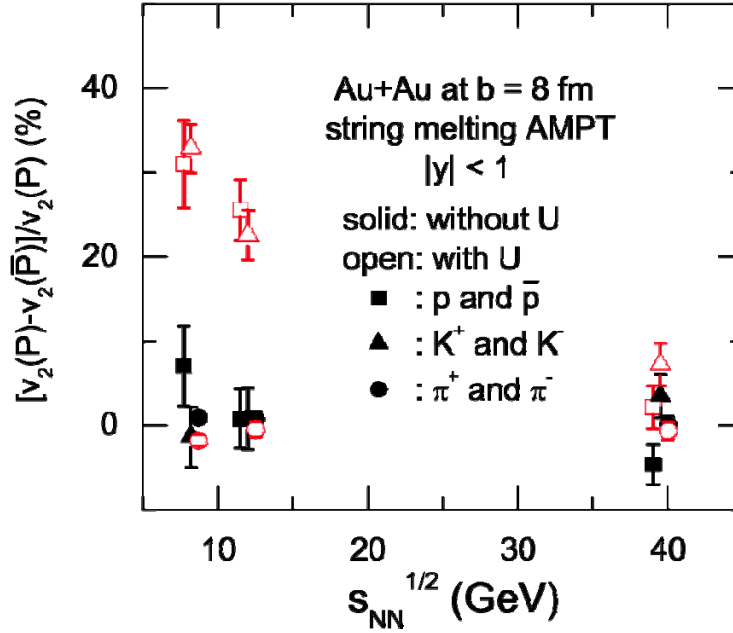


FIG. 1. Relative elliptic flow difference between proton and antiproton, K^+ and K^- , and π^+ and π^- with and without hadronic potentials U at three different energies from the string melting AMPT model. Results for different species are slightly shifted in energy to facilitate the presentation.

elliptic flows between particles and their antiparticles observed in relativistic heavy ion collisions.

[1] Z.W. Lin, C.M. Ko, B.A. Li, B. Zhang, and S. Pal, Phys. Rev. C **72**, 064901 (2005).

[2] J. Xu, L.W. Chen, C.M. Ko, and Z.W. Lin, Phys. Rev. C (in press).

[3] C.M. Ko and G.Q. Li, J. Phys. G **22**, 1673 (1996).

[4] N. Kaiser and W. Weise, Phys. Lett. B **512**, 283 (2001).

[5] B. Mohanty for the STAR Collaboration, arXiv:1106.5902 [nucl-ex].

Charmonium production in relativistic heavy ion collisions

T. Song, K.C. Han, and C.M. Ko

Using the two-component model that includes charmonium production from both initial nucleon-nucleon hard scattering and regeneration in the produced quark-gluon plasma, we have studied J/ψ production in heavy-ion collisions at the Super Proton Synchrotron (SPS), Relativistic Heavy Ion Collider (RHIC), and Large Hadron Collider (LHC) [1]. For the expansion dynamics of produced hot dense matter, we have used a schematic viscous hydrodynamic model [2] with the specific shear viscosity in the quark-gluon plasma and the hadronic matter taken, respectively, to be two and ten times the lower bound of $1/4\pi$ suggested by the anti-de Sitter/conformal field theory (AdS/CFT) correspondence. For the initial dissociation and the subsequent thermal decay of charmonia in the hot dense matter, we have used the screened Cornell potential to describe the properties of charmonia and the perturbative QCD to calculate their dissociation cross sections [3]. Including regeneration of charmonia in the quark-gluon plasma via a

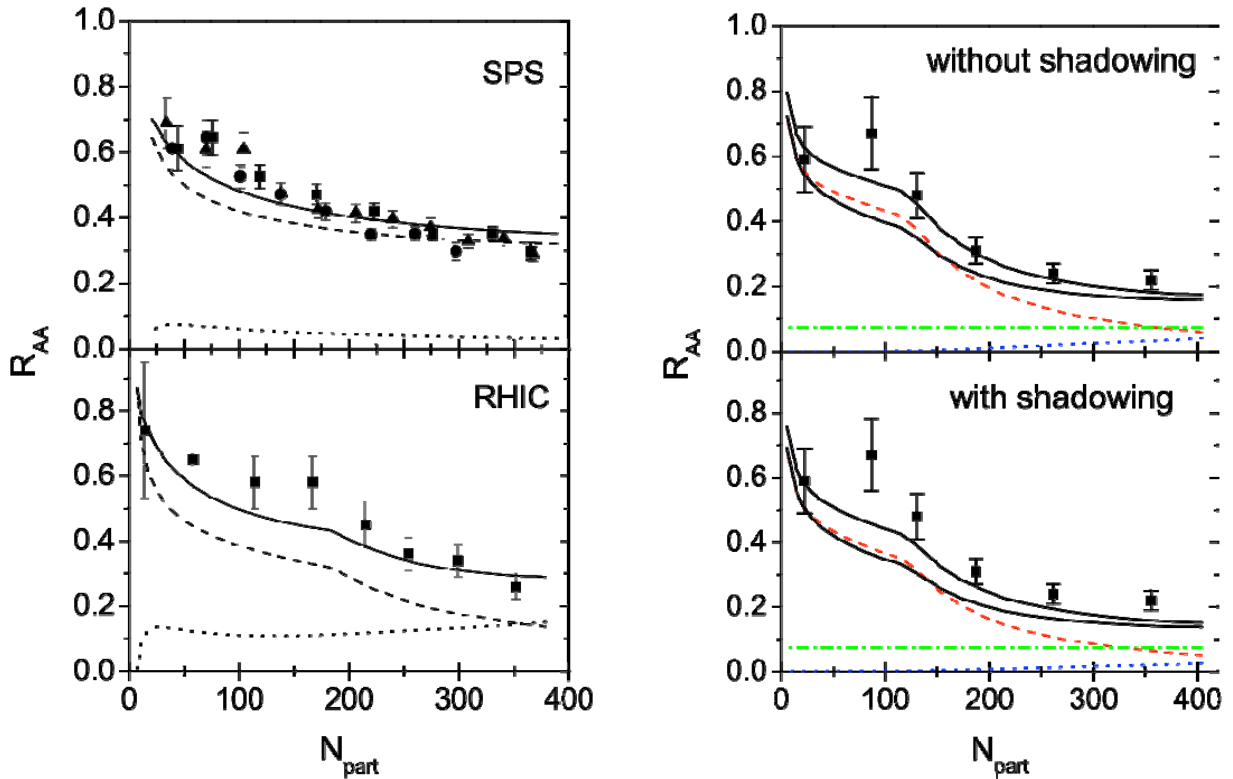


FIG. 1. Left window: Nuclear modification factor R_{AA} of J/ψ (solid line) as a function of the participant number N_{part} in Pb + Pb collisions at $\sqrt{s_{NN}} = 17.3$ GeV at SPS (upper panel) and in Au + Au collisions at $\sqrt{s_{NN}} = 200$ GeV at RHIC (lower panel). Dashed and dotted lines represent, respectively, the contributions to J/ψ production from primordial hard nucleon-nucleon scattering and regeneration in the QGP. Experimental data are from Refs. [4,5]. Right window: Same as left window for J/ψ of transverse momentum larger than 6.5 GeV/c without (upper panel) and with (lower panel) the shadowing effect in Pb + Pb collisions at $\sqrt{s_{NN}} = 2.76$ TeV at LHC. Dot-dashed line represents the contributions to J/ψ production from decay of bottom hadrons. Upper and lower solid lines are the total R_{AA} obtained with the nuclear absorption cross section of 0 and 2.8 mb, respectively. Experimental data shown by solid squares are from the CMS Collaboration [6].

kinetic equation with in-medium charmonium decay widths, we have obtained a good description of measured J/ψ nuclear modification factors in Pb + Pb collisions at $\sqrt{s_{NN}} = 1.73$ GeV at SPS and in Au + Au collisions at $\sqrt{s_{NN}} = 200$ GeV at RHIC as shown in the left window of Fig.1. A reasonable description of the measured nuclear modification factor of high transverse momenta J/ψ in Pb + Pb collisions at $\sqrt{s_{NN}} = 2.76$ TeV at LHC is also obtained as shown in the right window of Fig.1.

- [1] T. Song, K.C. Han, and C.M. Ko, Phys. Rev. C **84**, 034907 (2011).
- [2] T. Song, C.M. Ko, S.H. Lee, and J. Xu, Phys. Rev. C **83**, 014914 (2011).
- [3] Y. Park, K.I. Kim, T. Song, S.H. Lee, and C.Y. Wong, Phys. Rev. C **76**, 044907 (2007).
- [4] B. Alessandro *et al.* (NA50 Collaboration), Eur. Phys. J. C **39**, 335 (2005).
- [5] A. Adare *et al.* (PHENIX Collaboration), Phys. Rev. Lett. **98**, 232301 (2007).
- [6] V. Khachatryan *et al.* (CMS Collaboration), Eur. Phys. J. C **71**, 1575 (2011).

Nuclear symmetry energy and single-nucleon potential in asymmetric nuclear matter

C. Xu,¹ B.A. Li,² L.W. Chen,³ and C.M. Ko

¹*Department of Physics, Nanjing University, Nanjing 210008, China*

²*Department of Physics and Astronomy, Texas A&M University-Commerce, Commerce, TX 75429-3011,*

³*Department of Physics, Shanghai Jiao Tong University, Shanghai 200240, China*

Using the Hugenholtz–Van Hove theorem [1], we have derived general expressions for the quadratic and quartic symmetry energies in terms of the isoscalar and isovector parts of the single-particle potentials in isospin asymmetric nuclear matter [2]. These expressions allow us to connect directly the symmetry energies with the underlying isospin dependence of strong interactions. Since the single-particle potentials are direct inputs in both shell and transport models, the derived expressions facilitate the extraction of symmetry energies from experimental data. They thus help constrain the corresponding energy density functionals. As two examples, the BGBD [3] and the MDI [4] potentials are used in deriving the corresponding symmetry energies. For both interactions, the isovector potential is responsible for the uncertain high density behavior of the quadratic symmetry energy. The analytical formulas for the nuclear symmetry energies in terms of the isoscalar and isovector potentials are expected to be useful for extracting reliable information about the EOS of neutron-rich nuclear matter from experimental data. Also, the magnitude of the quartic symmetry energy is found to be generally small compared to the quadratic term. However, it could be important for determining the compositions and the core-crust transition densities of neutron stars.

[1] N.M. Hugenholtz and L. Van Hove, *Physica* **24**, 363 (1958).

[2] C. Xu, B.A. Li, L.W. Chen, and C.M. Ko, *Nucl. Phys.* **A865**, 1 (2011).

[3] I. Bombaci, Chapter 2 in “Isospin Physics in Heavy-Ion Collisions at Intermediate Energies”, edited by Bao-An Li and W. Udo Schröder, (Nova Science Publishers, Inc., New York, 2001).

[4] C.B. Das, S. Das Gupta, C. Gale, and B.A. Li, *Phys. Rev. C* **67**, 034611 (2003).

Bottomonium suppression in relativistic heavy ion collisions

T. Song, K.C. Han, and C.M. Ko

Using the two-component model that includes both initial production from nucleon-nucleon hard scattering and regeneration from produced quark-gluon plasma [1], we have studied bottomonium production in heavy-ion collisions at RHIC and LHC by including medium effects on the thermal properties of bottomonia and their dissociation cross sections [2]. With the expansion dynamics of produced hot dense matter described by a schematic viscous hydrodynamics and including the thermal dissociation of bottomonia as well as the regeneration of bottomonia by using a rate equation, our model describes successfully the experimental data from RHIC and reasonably those from LHC on bottomonium suppression as shown in Fig.1. Our results indicate that the contribution of regenerated bottomonia is small. We have also studied the cold nuclear matter effect due to the shadowing at LHC or antishadowing

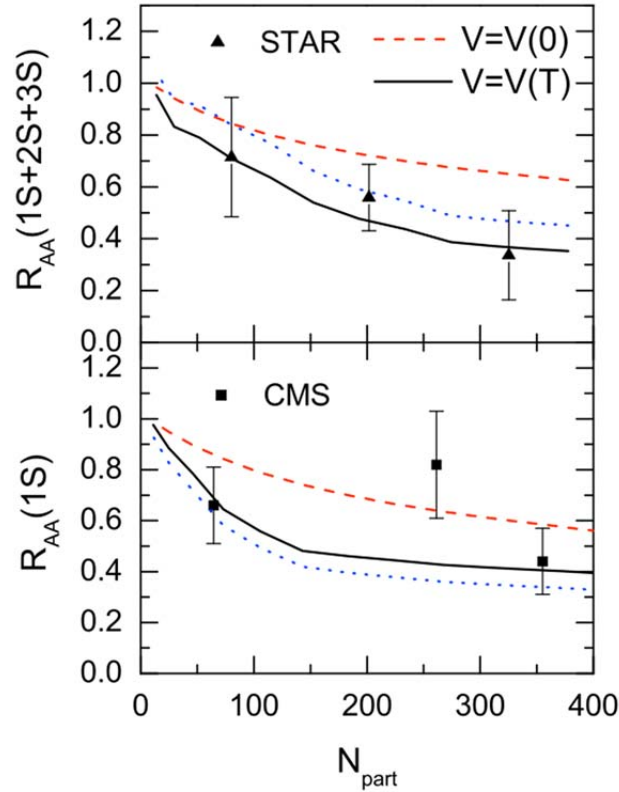


FIG. 1. Nuclear modification factor R_{AA} of the sum of $Y(1S)$, $Y(2S)$, and $Y(3S)$ in Au + Au collisions at $\sqrt{s_{NN}} = 200$ GeV at RHIC (upper panel) and that of $Y(1S)$ in Pb+Pb collisions at $\sqrt{s_{NN}} = 2.76$ TeV at LHC (lower panel) as functions of the participant number. Solid and dashed lines are, respectively, results with and without medium effects on bottomonia. Dotted lines are results including also the shadowing effect. Experimental data are from Ref. [3] for RHIC and Ref.[4] for LHC.

at RHIC of the parton distribution function in the nucleus. This was found to increase the nuclear modification factor of bottomonia at RHIC but decrease that at LHC. Our results with and without the cold nuclear matter effect are, however, both consistent with the experimental data because of their large errors. Furthermore, our study shows that the inclusion of medium effects on bottomonia is essential for describing the experimental observations at both RHIC and LHC.

- [1] T. Song, C.M. Ko, S.H. Lee, and J. Xu, Phys. Rev. C **83**, 014914 (2011).
- [2] T. Song, K.C. Han, and C.M. Ko, Phys. Rev. C **85**, 014902 (2012).
- [3] R. Reed *et al.* (STAR Collaboration), J. Phys. G **38**, 124185 (2011).
- [4] CMS Collaboration, CMS-PAS-HIN-10-006, 2011 (unpublished).

Subthreshold cascade production in heavy ion collisions

L. Feng, L.W. Chen,¹ C.M. Ko, and S.H. Lee²

¹INPAC, Department of Physics and Shanghai Key Laboratory for Particle Physics and Cosmology, Shanghai Jiao Tong University, Shanghai 200240, China

²Institute of Physics and Applied Physics, Yonsei University, Seoul 120-749, Korea

We have calculated the cross sections for the reaction $YY \rightarrow N\Xi$ ($Y = \Lambda, \Sigma$) based on a gauged SU(3)-invariant hadronic Lagrangian in the Born approximation [1] and found that these cross sections, given in the left window of Fig. 1, are almost four times the cross sections for the reaction $KY \rightarrow \pi\Xi$ that was considered in previous studies [2]. We then used these cross sections to study Ξ production in $^{40}\text{Ar} + \text{KCl}$ collisions at the subthreshold energy of 1.76 AGeV within the framework of a relativistic transport model that includes explicitly the nucleon, delta, pion, and perturbatively the kaon, antikaon, hyperons, and Ξ [3]. We found that the reaction $YY \rightarrow N\Xi$ would enhance the abundance by a factor of about 16 compared to that from the reaction $KY \rightarrow \pi\Xi$ [4] as shown in the right window of Fig. 1, resulting in an abundance ratio $\Xi^-/(\Lambda + \Sigma^0) = 3.38 \times 10^{-3}$ that is essentially consistent with that measured by the HADES Collaboration at GSI [5]. Our study has thus helped in resolving one of the puzzles in particle production from heavy ion collisions at subthreshold energies.

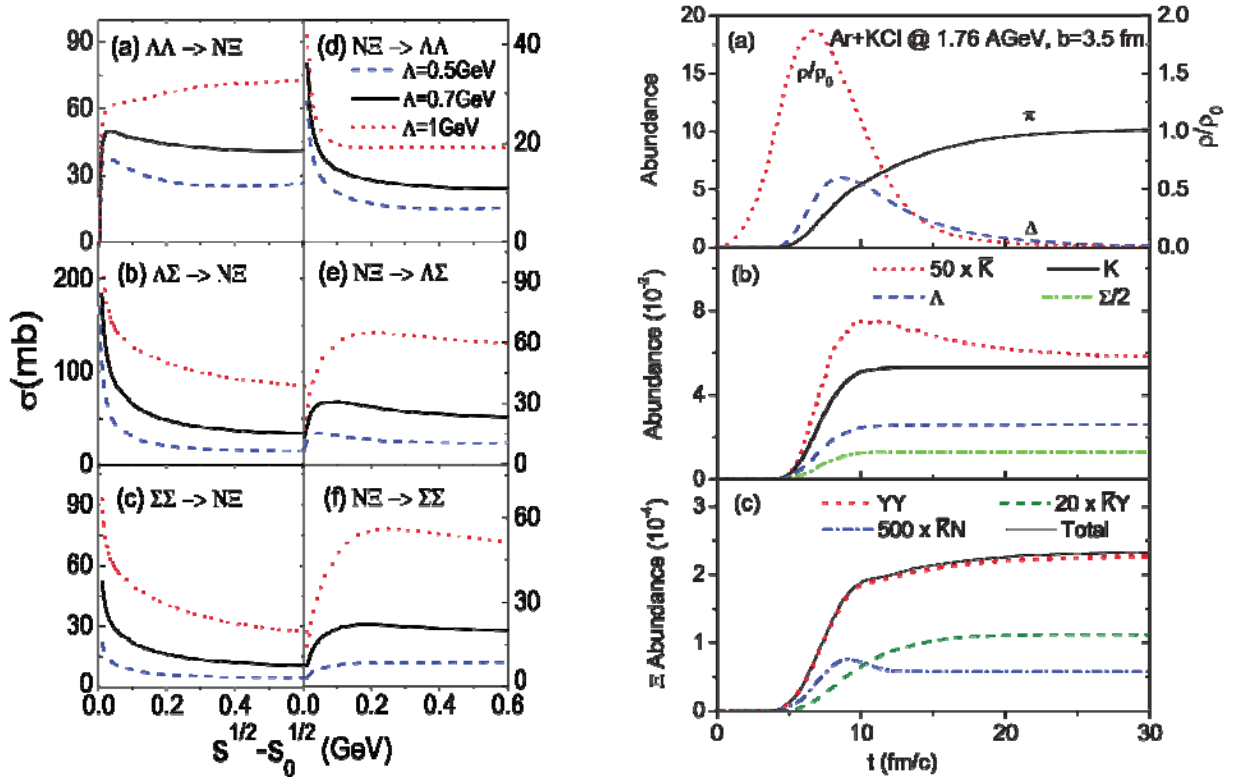


FIG. 1. Left window: Cross sections for (a) $\Lambda\Lambda \rightarrow N\Xi$, (b) $\Lambda\Sigma \rightarrow N\Xi$, (c) $\Sigma\Sigma \rightarrow N\Xi$, (d) $N\Xi \rightarrow \Lambda\Lambda$, (e) $N\Xi \rightarrow \Lambda\Sigma$, and (f) $N\Xi \rightarrow \Sigma\Sigma$ as functions of the center-of-mass energy from the Born approximation with cutoff parameters $\Lambda = 0.5$ GeV (dashed lines), $\Lambda = 0.7$ GeV (solid lines), and $\Lambda = 1$ GeV (dotted lines). Right window: Time evolutions of (a) central baryon density (right scale) and the abundances (left scales) of π and Δ , (b) K , Λ , Σ , and antikaon, and (c) Ξ produced from different reactions.

- [1] L. Feng, L.W. Chen, C.M. Ko, and S.H. Lee, Phys. Rev. C (in press).
- [2] C.H. Li and C.M. Ko, Nucl. Phys. **A712**, 110 (2002).
- [3] C.M. Ko and G.Q. Li, J. Phys. G **22**, 1673 (1996).
- [4] L.W. Chen, C.M. Ko, and Y. Tzeng, Phys. Lett. B **584**, 269 (2004).
- [5] G. Agakishiev et al. (HADES Collaboration), Phys. Rev. Lett. **103**, 132301 (2009).

Exotic hadrons in heavy ion collisions

S. Cho,¹ T. Furumoto,^{2,3} T. Hyodo,⁴ D. Jido,² C.M. Ko, S.H. Lee,¹
M. Nielsen,⁵ A. Ohnishi,² T. Sekihara,^{2,6} S. Yasui,⁷ and K. Yazaki^{2,3}

¹*Institute of Physics and Applied Physics, Yonsei University, Seoul 120-749, Korea*

²*Yukawa Institute for Theoretical Physics, Kyoto University, Kyoto 606-8502, Japan*

³*RIKEN Nishina Center, Hirosawa 2-1, Wako, Saitama 351-0198, Japan*

⁴*Department of Physics, Tokyo Institute of Technology, Meguro 152-8551, Japan*

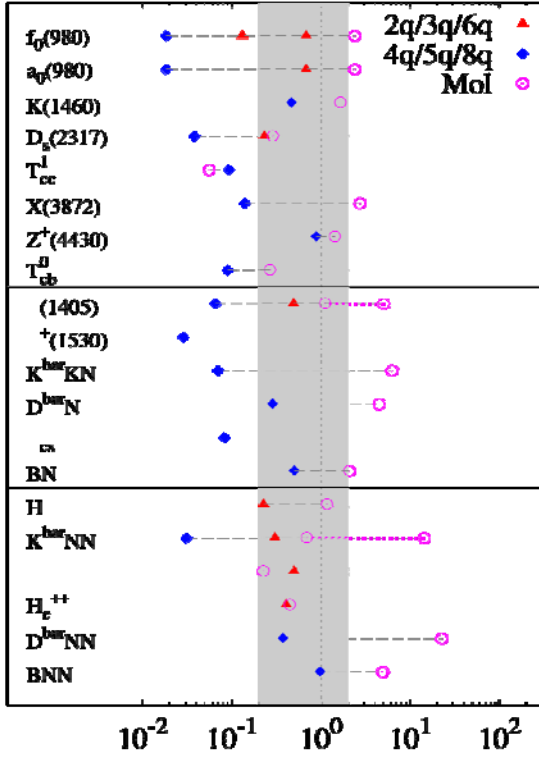
⁵*Instituto de Fisica, Universidade de Sao Paulo, C.P. 66318, 05389-970 Sao Paulo, SP, Brazil*

⁶*Department of Physics, Graduate School of Science, Kyoto University, Kyoto 606-8502, Japan*

⁷*Institute of Particle and Nuclear Studies, High Energy Accelerator Research Organization (KEK), 1-1,
Oho, Ibaraki 305-0801, Japan*

We have continued to investigate the possibilities of using measurements in present and future experiments on heavy ion collisions to answer some longstanding problems in hadronic physics, namely identifying hadronic molecular states and exotic hadrons with multiquark components [1]. Specifically, we considered the yields of following proposed exotic hadrons: $f_0(980)$, $a_0(980)$, $K(1460)$, $D_s(2317)$, T_{cc}^1 , $X(3872)$, $Z^+(4430)$, and T_{cb}^0 for exotic mesons; $\Lambda(1405)$, $\Theta^+(1530)$, KKN , DN , D^*N , Θ_{cs} , BN and B^*N for exotic baryons; H , KNN , $\Omega\Omega$, H_c^{++} , DNN and BNN for exotic dibaryons. To obtain the yields of these exotic multiquark hadrons or hadronic molecular states, we used the coalescence model based on either the quark degrees of freedom or the hadronic degrees of freedom. Our results indicate that the yields of many exotic hadrons are large enough to be measurable in experiments. In particular, heavy exotic hadrons containing charm and bottom quarks as well as strange quarks can be possibly observed at RHIC and especially at LHC. Therefore, relativistic heavy ion collisions will provide a good opportunity to search for exotic hadrons. In particular, it may lead to the first observation of new exotic hadrons. Also, we have found that the structure of light exotic hadrons has a significant effect on their yields in heavy ion collisions. As shown in Fig.1, for a hadron of normal quark structure, its production yield relative to the statistical model prediction is found in the range of 0.2-2. The yield ratio is smaller if a hadron has a compact multiquark configuration. For a hadron of molecular configuration with an extended size, its yield is, on the other hand, larger than the normal values. Therefore, the ratios of measured yields from experiments on heavy ion collisions to those predicted by the statistical model provides a new method to discriminate the different pictures for the structures of exotic hadrons.

Coalescence / Statistical model ratio at RHIC



Coalescence / Statistical model ratio at LHC

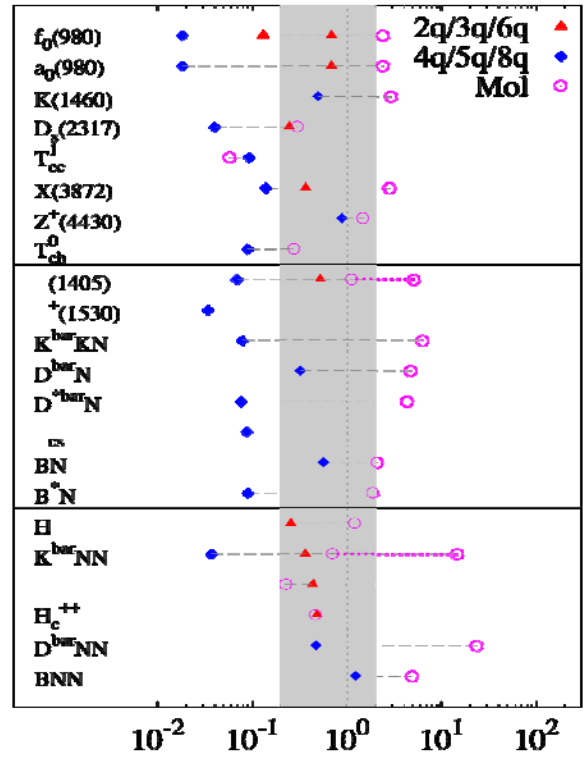


FIG. 1. Ratios of hadron yields at RHIC (left window) and LHC (right window) in the coalescence model to those in the statistical model for normal hadrons (gray band), hadronic molecules (above gray band), and multiquark states (below gray band).

[1] S. Cho, T. Furumoto, T. Hyodo, D. Jido, C.M. Ko, S.H. Lee, M. Nielsen, A. Ohnishi, T. Sekihara, S. Yasui, and K. Yazaki, Phys. Rev. C **84**, 064910 (2011).

Higher-order flows and dihadron correlations in heavy ion collisions at LHC

J. Xu and C.M. Ko

We have studied higher-order anisotropic flows and dihadron correlations in Pb-Pb collisions at $\sqrt{s_{NN}} = 2.76$ TeV within a multiphase transport model [1] with parameters fitted to reproduce the measured multiplicity density of mid-pseudorapidity charged particles in central collisions and their elliptic flow in midcentral collisions in a previous work [2]. We have found that the resulting higher-order anisotropic flows slightly overestimate the experimental data [3] at small centralities, but are consistent with them at other centralities as shown in the left window of Fig. 1. For the dihadron correlations, we have obtained a ridge structure along the pseudorapidity direction in the near side as shown in the right window of Fig. 1, and it disappears when final-state interactions are turned off in our model. We have also studied both the short-range and long-range dihadron azimuthal correlations for different transverse momenta of trigger particles, and they are seen to be qualitatively consistent with experimental results. We have further attempted to determine the background-subtracted short-range dihadron azimuthal correlations by taking the long-range dihadron azimuthal correlations as the background, and they are found to be similar to those obtained previously using a different method [4].

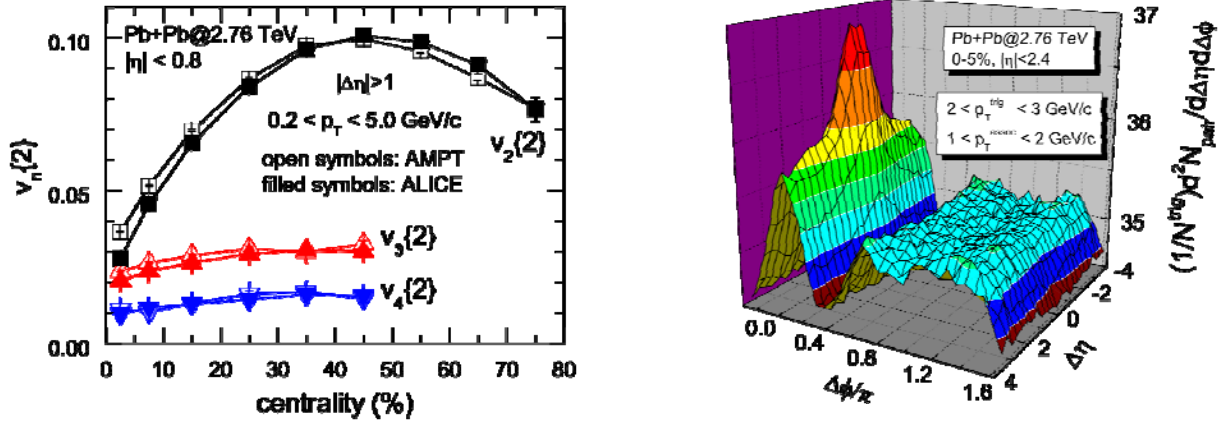


FIG. 1. Left window: Centrality dependence of v_n ($n=2,3,4$) for mid-pseudorapidity ($|\eta|<0.8$) charged particles obtained from the two-particle cumulant method in Pb-Pb collisions at $\sqrt{s_{NN}} = 2.76$ TeV from the string melting AMPT model. The ALICE data (filled symbols) are taken from Ref.[3]. Right window: Two-dimensional dihadron correlations per trigger particle as a function of $\Delta\eta$ and $\Delta\phi$ for $1 < p_T^{\text{assoc}} < 2$ GeV/c and $2 < p_T^{\text{trig}} < 3$ GeV/c for 0-5% most central collisions.

- [1] Z.W. Lin, C.M. Ko, B.A. Li, B. Zhang, and S. Pal, Phys. Rev. C **72**, 064901 (2005).
- [2] J. Xu and C.M. Ko, Phys. Rev. C **84**, 014903 (2012).
- [3] K. Aamodt *et al.* (ALICE Collaboration), Phys. Rev. Lett. **107**, 032301(2011).
- [4] J. Xu and C.M. Ko, Phys. Rev. C **83**, 021903 (R) (2011).

Triangular flow and dihadron correlations in heavy ion collisions at RHIC

J. Xu and C.M. Ko

Using the default values for the parameters in the Lund string fragmentation function and a smaller but more isotropic parton scattering cross section than previously used in the AMPT model [1] for heavy ion collisions at RHIC, we have obtained a good description of both the charged particle multiplicity density and the elliptic flow measured in Au + Au collisions at $\sqrt{s_{NN}} = 200$ GeV, although the transverse momentum spectra are still softer than the experimental results [2]. With these constrained parameters, the magnitude of the triangular flow in these collisions was predicted as shown in the left window of Fig.1. We have also studied the dihadron azimuthal correlations triggered by energetic hadrons at impact parameters of $b = 0$ and 8 fm and found that the double-peak structure at the away side of triggered particles, which is seen after subtracting the background contributions due to the elliptic flow, is largely due to the triangular flow as shown in the right window of Fig.1. However, the residual correlations shown in our study after the subtraction of the flow contribution might still contain the contribution from flow fluctuations in addition to the nonflow contribution that we are interested.

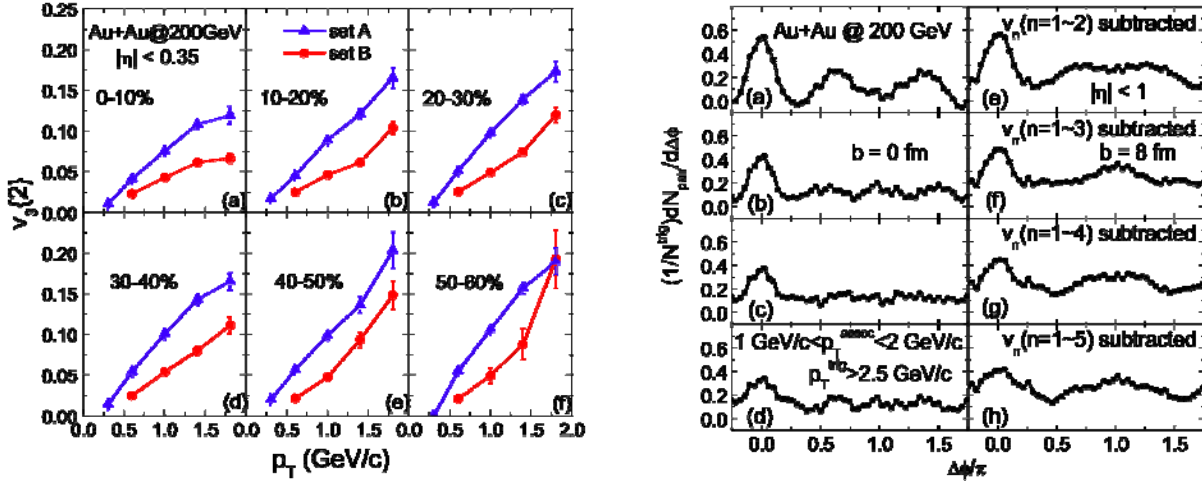


FIG. 1. Left window: Transverse momentum dependence of the triangular flow of mid-pseudorapidity ($|\eta| < 0.35$) charged particles by using parameter sets A (solid triangles) and B (solid circles) Au collisions at $\sqrt{s_{NN}} = 200$ GeV in Au+Au collisions from the two-particle cumulant method. Right window: Dihadron correlations per trigger particle after subtracting background correlations up to different orders in same collisions for $b=0$ fm (a-d) and $b=8$ fm (e-h) from parameter set B.

[1] Z.W. Lin, C.M. Ko, B.A. Li, B. Zhang, and S. Pal, Phys. Rev. C **72**, 064901 (2005).

[2] J. Xu and C.M. Ko, Phys. Rev. C **84**, 014903 (2012).

Dilepton production in relativistic heavy ion collisions

E.L. Bratkovskaya,^{1,2} W. Cassing,³ C.M. Ko, O. Lynn,³ J. Manninen,^{1,2} and V. Ozvenchuk²

¹*Institut für Theoretische Physik, Johann Wolfgang Goethe University, 60438 Frankfurt am Main, Germany*

²*Frankfurt Institute for Advanced Studies, DE-60438 Frankfurt am Main, Germany*

³*Institut für Theoretische Physik, Universität Giessen, DE-35392 Giessen, Germany*

Using the Parton-Hadron-String Dynamics (PHSD) approach [1], which consistently describes the full evolution of a relativistic heavy-ion collision from the initial hard scatterings and string formation through the dynamical deconfinement phase transition to the quark-gluon plasma as well as hadronization and to the subsequent interactions in the hadronic phase, we have studied dilepton production in In+In collisions at 158 AGeV at SPS [2] and Au+Au collisions at $\sqrt{s_{NN}} = 200$ GeV [3] by including a collisional broadening of vector mesons, microscopic secondary multi-meson channels, and the strongly interacting QGP radiation, which is described by the interactions of dynamical quasiparticles in line with the degrees of freedom propagated in the transport approach. As shown in the left window of Fig.1, the data of the

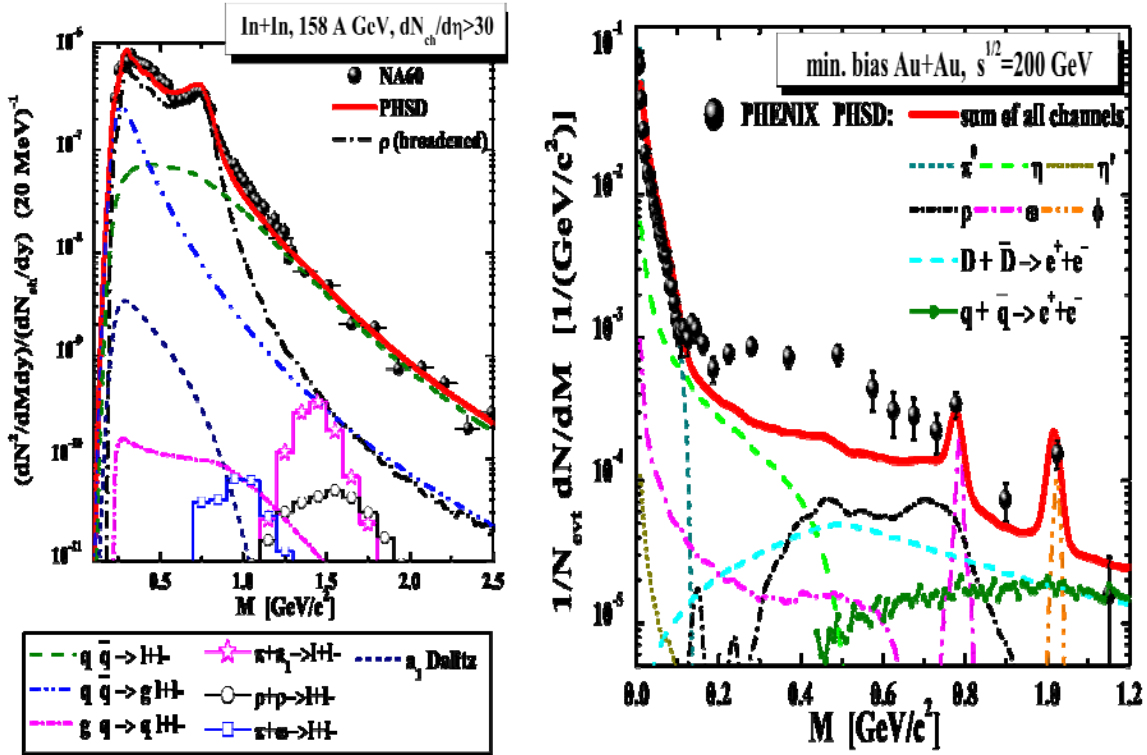


FIG. 1. Left window: Acceptance corrected mass spectra of excess dimuons from In+In at 158 AGeV integrated over p_T in $0.2 < p_T < 2.4$ GeV from PHSD compared to the data of NA60 [4]. Dash-dotted line shows the dilepton yield from the in-medium rho with broadened spectral function, dashed line presents the yield from the quark-antiquark annihilation, dash-dot-dot line gives the contribution of the gluon Bremsstrahlung process, solid line is the sum of all contributions. For the description of the other lines, which correspond to the non-dominant channels, we refer to the figure legend. Right window: Same as left window for Au+Au collisions at $\sqrt{s_{NN}} = 200$ GeV within the PHENIX acceptance cuts in comparison to the data from the PHENIX Collaboration [5] for invariant masses $0 \leq M \leq 1.2$ GeV.

NA60 Collaboration on the dilepton yield [4] is well described by including the collisional broadening of vector mesons, while simultaneously accounting for the electromagnetic radiation of the strongly coupled quark-gluon plasma (sQGP) via off-shell quark-antiquark annihilation, quark annihilation with gluon Bremsstrahlung and the gluon-Compton scattering mechanisms. In particular, the spectra in the intermediate mass range ($1 \text{ GeV} \leq M \leq 2.5 \text{ GeV}$) are dominated by quark-antiquark annihilation in the nonperturbative QGP. Also, the observed softening of the transverse mass spectra in this region is approximately reproduced. For the dilepton data from the PHENIX Collaboration [5] shown in the right window of Fig. 1, our studies have demonstrated that the observed excess in the low mass dilepton region from 0.15 to 0.6 GeV cannot be described by either the hadronic or the partonic reaction channels. Similar to our findings at SPS energies, the partonic dilepton production channels are visible in the intermediate-mass region between the ϕ and J/ψ peaks. Their contribution is about the same as the correlated background from D-meson decays. On the other hand, our results are in a rough agreement with the preliminary data from the STAR Collaboration [6].

- [1] W. Cassing and E. L. Bratkovskaya, Nucl. Phys. A **831**, 215 (2009).
- [2] O. Lynnk, E.L. Bratkovskaya, V. Ozvenchuk, W. Cassing, and C.M. Ko, Phys. Rev. C **84**, 054917 (2011).
- [3] O. Lynnk, W. Cassing, J. Manninen, E.L. Bratkovskaya, and C.M. Ko, Phys. Rev. C **85**, 024910 (2012).
- [4] R. Arnaldi *et al.* (NA60 Collaboration), Eur. Phys. C **59**, 607 (2009).
- [5] A. Adare *et al.* (PHENIX Collaboration), Phys. Rev. C **81**, 034911 (2010).
- [6] J. Zhao *et al.* (STAR Collaboration), arXiv:1106.6146[nucl-ex].

Energy release from hadron-quark phase-transition in neutron stars

W. Lin,¹ B.A. Li,¹ J. Xu, C.M. Ko, and D.H. Wen²

¹*Department of Physics and Astronomy, Texas A&M University-Commerce, Commerce, Texas*

²*Department of Physics, South China University of Technology, Guangzhou 510641, China*

Using an isospin- and momentum-dependent effective interaction for the baryon octet and the MIT bag model to describe, respectively, the hadronic and quark phases of neutron stars [1], we have investigated the maximum available energy for gravitational wave emission owing to the microcollapse triggered by the hadron-quark phase transition in neutron stars [2]. Moreover, the frequency and damping time of the first axial w mode of gravitational waves have been studied for both hadronic and hybrid neutron stars. Since the most uncertain part of the equation of state of a neutron star is the density dependence of the nuclear symmetry energy in the neutron-rich nucleonic matter and the bag constant in the quark matter within the MIT bag model, we have studied their effects on the energy release as well as the frequency and damping time of the first axial w mode of gravitational waves from neutron stars. We have found that the energy release is much more sensitive to the bag constant than to the density dependence of the nuclear symmetry energy. Also, the frequency of the w mode has been found to be significantly different with or without the hadron-quark phase transition and to depend strongly on the bag constant. Moreover, the effects of the symmetry energy and bag constant on the damping time have been found to be appreciable but not as strong as those on the frequency. We have further found that the effect of the symmetry energy on the frequency becomes stronger with a larger value of the bag constant that leads to a higher hadron-quark transition density. While the predicted frequency of the w mode is significantly above the bands of operating frequencies of the existing gravitational wave detectors, our results have indicated that the frequency of the w mode can indeed carry important information about the internal structure of neutron stars and the properties of dense neutron-rich matter.

[1] J. Xu, L.W.Chen, C.M. Ko, and B.A. Li, *Phys. Rev. C* **81**, 055803 (2010).

[2] W. Lin, B.A. Li, J. Xu, C.M. Ko, and D.H. Wen, *Phys. Rev. C* **83**, 045802 (2011)

Thermal photons and collective flow at RHIC

H. van Hees,¹ C. Gale,² and R. Rapp

¹*Frankfurt Institute for Advanced Studies, Frankfurt, Germany,*

²*McGill University, Montreal, Canada*

Electromagnetic radiation (photons and dileptons) in heavy-ion collisions is emitted throughout the evolution of the hot and dense fireball created in these reactions. To extract quantitative information about the strongly interacting medium from electromagnetic observables, such as the in-medium vector spectral function or the (evolving) temperature of the matter, it is of prime importance to reliably understand the contributions from the different phases of the fireball. In this context, a recent first measurement of the elliptic flow of direct photons in Au-Au collisions at the Relativistic Heavy-Ion Collider has yielded a surprising result [1]: the data for the pertinent anisotropy coefficient, $v_2(p_T)$, are comparable to those of pions, even though the latter are only emitted at the end of the fireball evolution where the elliptic flow has fully built up. In particular, the v_2 from thermal photons emitted from the Quark-Gluon Plasma (QGP), when evaluated in standard hydrodynamic evolution models [2, 3], has been predicted to lead to much smaller values, reflecting the early fireball phases during which the momentum anisotropy is still rather small.

In the present work we have revisited this problem by (i) utilizing our earlier calculated photon emission rates from hadronic matter [4] which are significantly larger than those currently employed in hydrodynamic evolutions; (ii) constructing a thermal fireball expansion where the bulk elliptic flow (as observed through the final hadron spectra) is built up by the time the system reaches the QGP-hadron phase transition; in particular, the spectra and v_2 of multistrange hadrons (Φ , Ξ , Ω) are quantitatively constrained by the common assumption that their kinetic freezeout occurs close to the quark-hadron phase boundary. These two components lead to a significant increase of hadronic radiation and pertinent elliptic flow in the total photon spectra in 0-20% Au-Au collisions compared to previous calculations, cf. Fig. 1. In particular, the thermal hadronic component turns out to be the largest contribution in the p_T spectra out to momenta of 2-3 GeV. The large elliptic flow carried by this component leads to a total v_2 of direct photons (including QGP radiation and primordial emission from binary NN collisions upon first impact of the colliding nuclei) which reaches into the lower part of the error bars of the experimental data. These calculations suggest that the dominant emission source of thermal photons in ultrarelativistic heavy-ion collisions is not from the early QGP phases but from the medium right around the transition regime. This conclusion is corroborated by the rather small slope parameter in the excess spectra (above the primordial component), which approximately reproduces the experimentally measured effective temperature of only about $T_{\text{eff}} \approx 220 \pm 20$ MeV [6] which is quite close to the (pseudo-) critical temperature of 170 MeV but well above typical initial temperatures of 350-400 MeV. Note also that the true medium temperature is smaller due to the spectral blue shift induced by the radially expanding medium (“Doppler effect”).

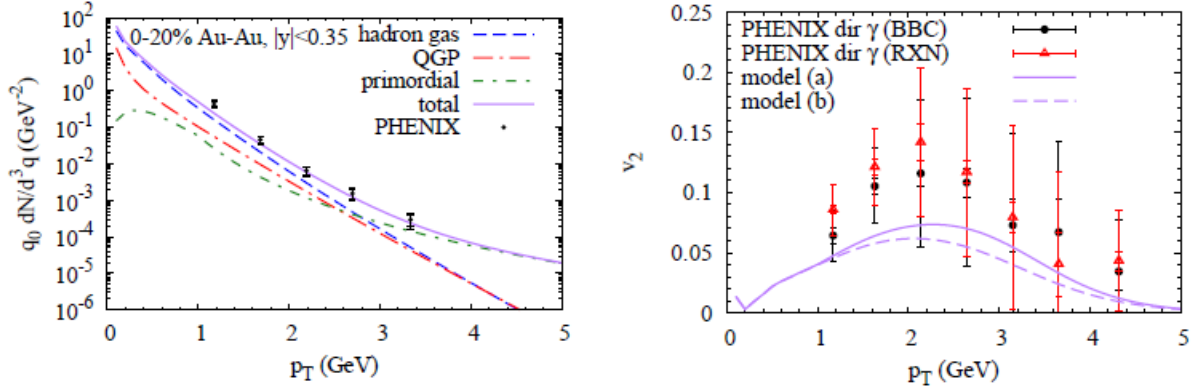


FIG. 1. Transverse-momentum spectra (left panel) and elliptic flow (right panel) of direct photons in 0-20% central Au-Au ($\sqrt{s_{NN}}=200$ GeV) collisions at RHIC. Our calculations of thermal radiation from QGP and hadronic phases are added to a primordial contribution from binary NN collisions estimated from the spectra in elementary pp collisions. The two curves in the right panel indicate the uncertainty of the primordial contribution in the total elliptic flow. The data are from the PHENIX collaboration [1,6].

- [1] A. Adare *et al.* (PHENIX Collaboration), LANL e-print arXiv:1105.4126 [nucl-ex].
- [2] R. Chatterjee, E.S. Frodermann, U.W. Heinz and D.K. Srivastava, Phys. Rev. Lett. **96**, 202302 (2006).
- [3] H. Holopainen, S. Räsänen and K. Eskola, Phys. Rev. C **84**, 064903 (2011).
- [4] H. van Hees, C. Gale and R. Rapp, Phys. Rev. C **84**, 054906 (2011).
- [5] S. Turbide, C. Gale and R. Rapp, Phys. Rev. C **69**, 014903 (2003).
- [6] A. Adare *et al.* (PHENIX Collaboration), Phys. Rev. Lett. **104**, 132301 (2010).

Bottomonia in the quark-gluon plasma and their production at RHIC and LHC

A. Emerick, X. Zhao and R. Rapp

Bound states of bottom and anti-bottom quarks (bottomonia) are valuable probes to investigate the formation and properties of deconfined matter as believed to be formed in ultra-relativistic collision of heavy nuclei. They excellently complement the widely discussed charmonium production [1], due to their different binding energies and smaller bottom-quark production cross sections. The latter presumably imply less contributions from recombination into bottomonia, thus facilitating the study of the Debye screening through a cleaner window on suppression effects.

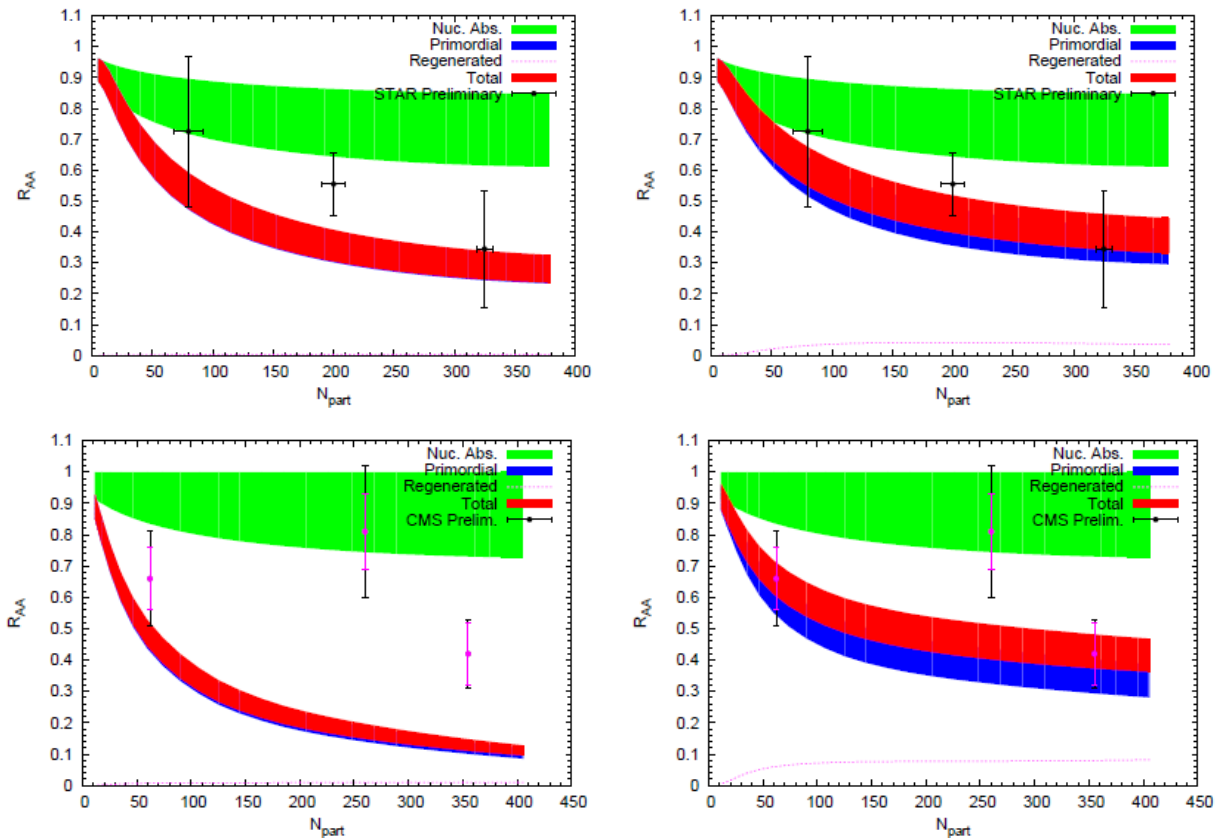


FIG. 1. Centrality dependence of the nuclear modification factor for the combined $\Upsilon(1S+2S+3S)$ yield in Au-Au at RHIC (upper panels) and for the $\Upsilon(1S)$ in Pb-Pb at LHC, compared to STAR [5] and CMS [6] data. Left and right panels correspond to the strong- and weak-binding scenarios, respectively. The green bands indicate uncertainties in pre-equilibrium nuclear absorption and shadowing effects.

In the present work [2] we have studied the suppression and regeneration of bottomonia at RHIC and LHC employing our previously developed thermal rate-equation approach for charmonia [3]. Paralleling the latter work, the bottomonium yields are evolved through an expanding thermal fireball model with input cross sections for bottomonia and bottom quarks extracted from existing data in p-p collisions, appropriately extrapolated to the heavy-ion collision energies and centralities under

consideration. In addition, the main microscopic ingredients to the bottomonium rate equation, i.e. the inelastic reaction rates and the equilibrium limit, are deduced from spectral functions which are constrained by Euclidean correlator ratios computed in thermal lattice QCD. As in our systematic charmonium studies [3], we evaluate two binding scenarios, i.e. a strong- and a weak-binding one, corresponding to the use of internal and free energies from lattice QCD, respectively, in an underlying potential model [4]. This also determines the prevailing dissociation mechanism as gluo-dissociation and quasi-free destruction, respectively. In Fig. 1 we display our results for the centrality dependence of the combined $\Upsilon(1S+2S+3S)$ yield for Au-Au($\sqrt{s}=0.2A\text{TeV}$) at RHIC and for the ground-state $\Upsilon(1S)$ in Pb-Pb($2.76A\text{TeV}$) at LHC in the two scenarios. The feed-down from the excited states, which are fully evolved through the rate equation as well, is included. We find that the weak-binding scenario appears to induce too much suppression, especially in comparison to the CMS data at the LHC. The strong-binding scenario leads to a more stable $\Upsilon(1S)$ well into the QGP, resulting in a better agreement with the current data. We also note a small but significant contribution from regeneration contributions in the strong-binding case, which becomes even more relevant for the more strongly suppressed excited states. Overall, the preference for the strong binding scenario is reassuring as it also was favored in the analysis of charmonium data [3] as well as in the calculations of heavy-quark diffusion coefficients [4].

- [1] R. Rapp, D. Blaschke and P. Crochet, *Prog. Part. Nucl. Phys.* **65**, 209 (2010).
- [2] A. Emerick, X. Zhao and R. Rapp, *Eur. Phys. J.* **A48**, 72 (2012).
- [3] X. Zhao and R. Rapp, *Phys. Rev. C* **82**, 064905 (2010); *Nucl. Phys.* **A859**, 114 (2011).
- [4] F. Riek and R. Rapp, *Phys. Rev. C* **82**, 035201 (2010).
- [5] R. Reed *et al.* (STAR Collaboration), *Nucl. Phys.* **A855**, 440 (2011).
- [6] S. Chatrchyan *et al.* (CMS Collaboration), *JHEP* **1205**, 063 (2012).

Heavy-quark diffusion and hadronization in quark-gluon plasma

Min He, Rainer J. Fries, and Ralf Rapp

Heavy quarks (charm and bottom) in ultra-relativistic heavy-ion collisions (URHICs), produced in primordial nucleon-nucleon collisions, act as impurities in the subsequently formed quark-gluon plasma (QGP) and are not expected to fully equilibrate with the medium. Due to their large masses, a memory of their interaction history may be preserved, providing a direct probe of the medium properties [1].

In the present work [2], we calculate diffusion and hadronization of heavy quarks in URHICs by implementing the notion of a strongly coupled QGP in both micro- and macroscopic components. The diffusion process is simulated using relativistic Fokker-Planck dynamics for elastic scattering in a hydrodynamic background. The heavy-quark transport coefficients in the medium are obtained from non-perturbative T-matrix interactions which build up resonant correlations close to the transition temperature [3]. The latter also form the basis for hadronization of heavy quarks into heavy-flavor mesons via resonance recombination [4] with light quarks from the medium. This formalism satisfies energy conservation and provides an equilibrium mapping between quark and meson distributions.

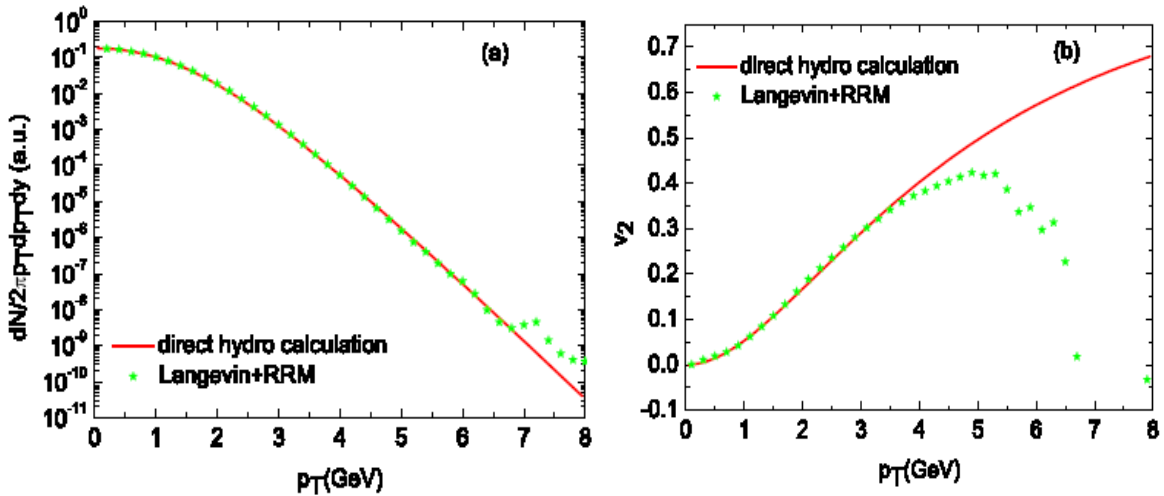


FIG. 1. (a) D-meson p_T -spectrum (stars) calculated from RRM on the hadronization hypersurface applied to charm-quark spectra from hydro+Langevin simulations in the large-drag coefficient limit. It is compared to the D-meson spectrum directly calculated from AZHYDRO on the same hypersurface. (b) Same as in panel (a) but for D-meson elliptic flow.

We first verified the equilibrium mapping (see Fig.1) using charm-quark Langevin diffusion simulations with an artificially large thermal relaxation rate, followed by resonance recombination with light quarks from the hydro medium. In realistic calculations, the relative partition of charm quark hadronization between recombination and independent fragmentation is determined by the coalescence probability based on the charm-quark reaction rate. Consequently, recombination dominates at low transverse momentum (p_T) and yields to fragmentation at high p_T (see Fig. 2). Our resonance recombination model respects kinetic equilibrium and drives D mesons closer to equilibrium as signaled

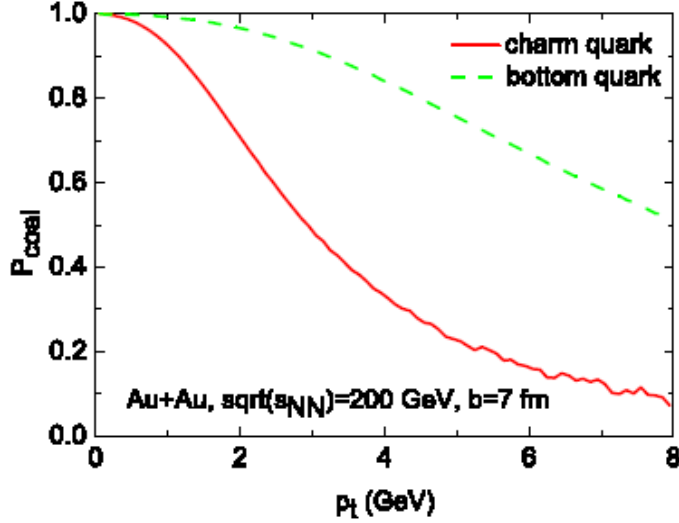


FIG. 2. Charm and bottom quark coalescence probability vs. lab frame transverse momentum.

by the flow bump developing in the nuclear modification factor (see Fig. 3) when going from charm quarks to D mesons.

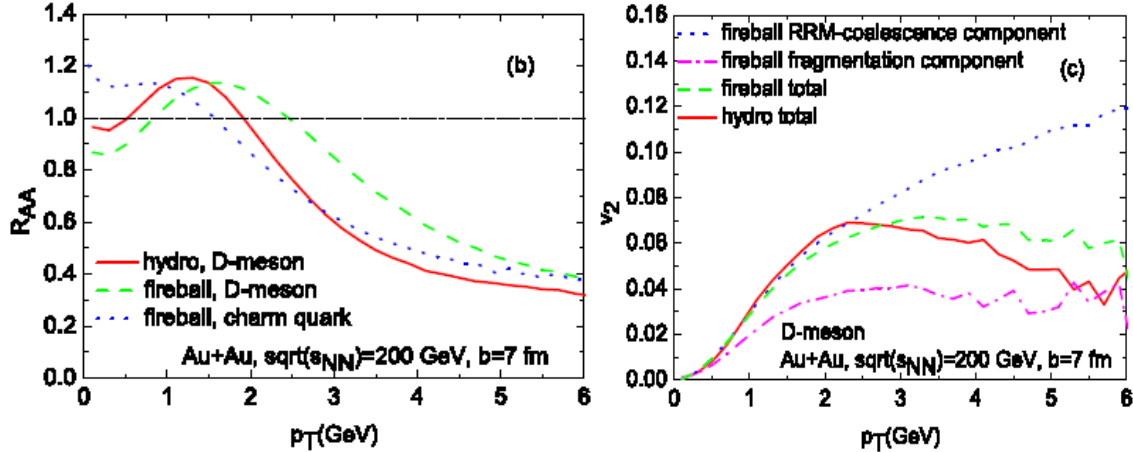


FIG. 3. Comparison of D-meson spectra and v_2 from AZHYDRO and an elliptic fireball with large flow in semi-central ($b=7$ fm) Au+Au collisions. Left panel: Nuclear modification factor for D-mesons (coalescence + fragmentation) and charm quarks. Right panel: Elliptic flow from coalescence, fragmentation and their weighted sum.

This work represents a further step toward a self-consistent and comprehensive description of open heavy flavor in a strong coupling framework of URHICs.

- [1] R. Rapp and H. van Hees, in Quark-Gluon Plasma 4 (edited by R. Hwa and X.N. Wang), (World Scientific, Singapore, 2010), p.111; and LANL eprint arXiv:0903.1096 [hep-ph].
- [2] M. He, R.J. Fries and R. Rapp, Phys. Rev. C (in press); arXiv:1106.6006[nucl-th].
- [3] F. Riek and R. Rapp, Phys. Rev. C **82**, 035201 (2010).
- [4] L. Ravagli anf R. Rapp, Phys. Lett. B **655**, 126 (2007).

Ideal hydrodynamics for bulk and multistrange hadrons in $\sqrt{s_{NN}} = 200$ A GeV Au-Au collisions

Min He, Rainer J. Fries, and Ralf Rapp

Relativistic hydrodynamics has been successfully applied to model the bulk evolution of the hot and dense matter created in relativistic heavy-ion collisions [1,2]. Hydrodynamic modeling now often includes viscous corrections [2]; however, it remains important to improve our understanding to which extent ideal hydrodynamics is capable of providing a realistic description of existing and new bulk-hadron data. This requires a consistent description of yields, transverse momentum spectra and elliptic flow for light, as well as multistrange, hadrons. The latter are interesting as they are expected to freeze out close to the phase transition from a quark-gluon plasma (QGP) to hadronic matter [3].

We have tuned the 2+1-D hydro code AZHYDRO [1] to reproduce bulk and multistrange hadron observables in nuclear collisions at the Relativistic Heavy Ion Collider [4]. We have used an equation of state based on recent lattice-QCD computations matched to a hadron-resonance gas with chemical decoupling at $T_{\text{ch}}=160$ MeV (see Fig. 1). We have also introduced a compact initial-density profile and an

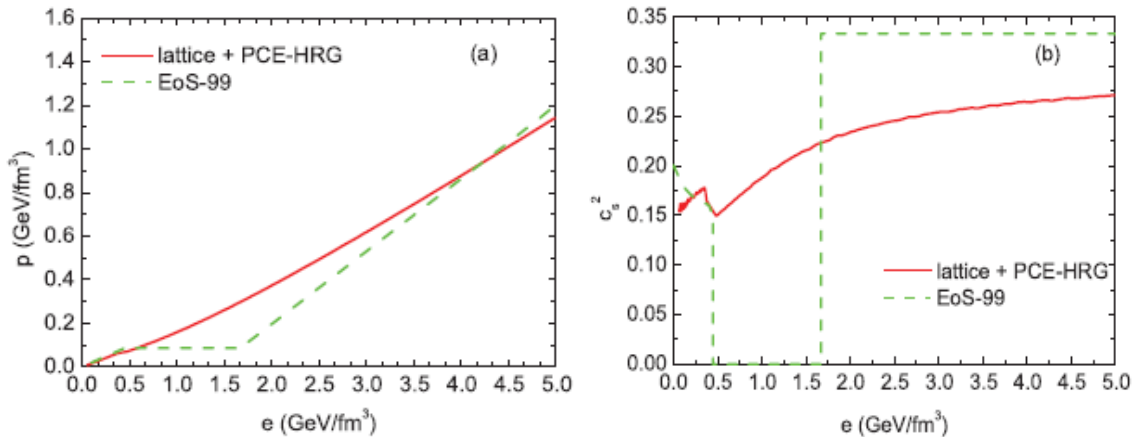


FIG. 1. Comparison of pressure (left panel) and speed of sound squared (right panel) vs. energy density as obtained from AZHYDRO with EoS-99 [1] (dashed lines) and our new equation of state (solid lines).

initial-flow field including azimuthal anisotropies, as motivated, e.g., by HBT analysis [5]. Our resulting hydrodynamic evolution features a fast build-up of radial flow, and the bulk elliptic flow saturates close to the phase transition temperature, $T_c=170$ MeV (see Fig. 2).

We find that this scheme allows for a consistent description of the observed chemistry, transverse-momentum spectra, and elliptic flow of light and multistrange hadrons (see Fig. 3) at a typical kinetic-freezeout temperature of $T_{\text{kin}}=110$ MeV and chemical-freezeout temperature $T_{\text{ch}}=160$ MeV, respectively. An important point is that the hydrodynamic evolution of the system is much more tightly constrained than if only light hadron data at T_{kin} are fitted. The thus constructed bulk-matter evolution model can be used as a realistic background medium in the exploration of heavy-flavor and electromagnetic probes of the quark-gluon plasma.

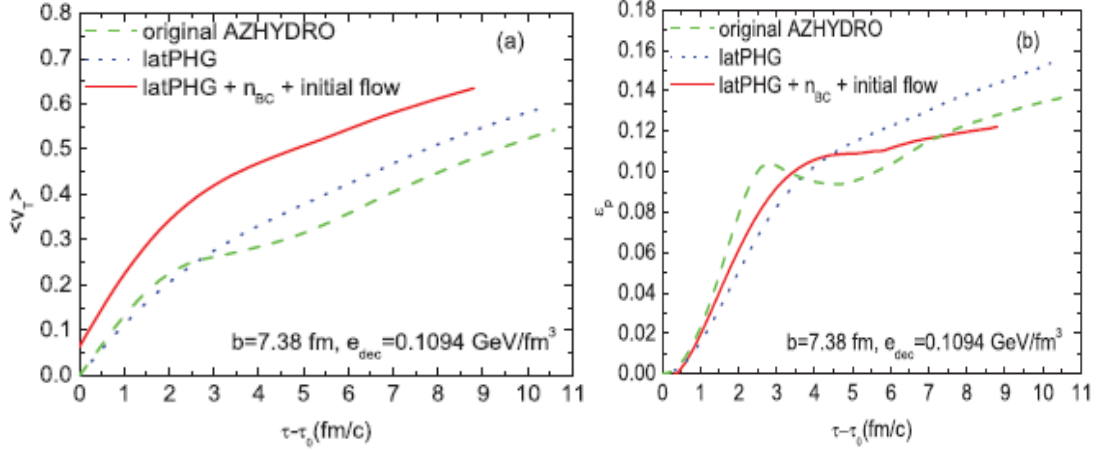


FIG. 2. (a) Proper-time evolution of the average transverse radial velocity for different hydrodynamics scenarios: default AZHYDRO with EoS-99 (green dashed curve), default AZHYDRO with the new EOS (blue dotted curve), and the new EoS with initial flow and compact initial density profile (red solid curve). (b) The same comparison for the time evolution of the energy-momentum anisotropy.

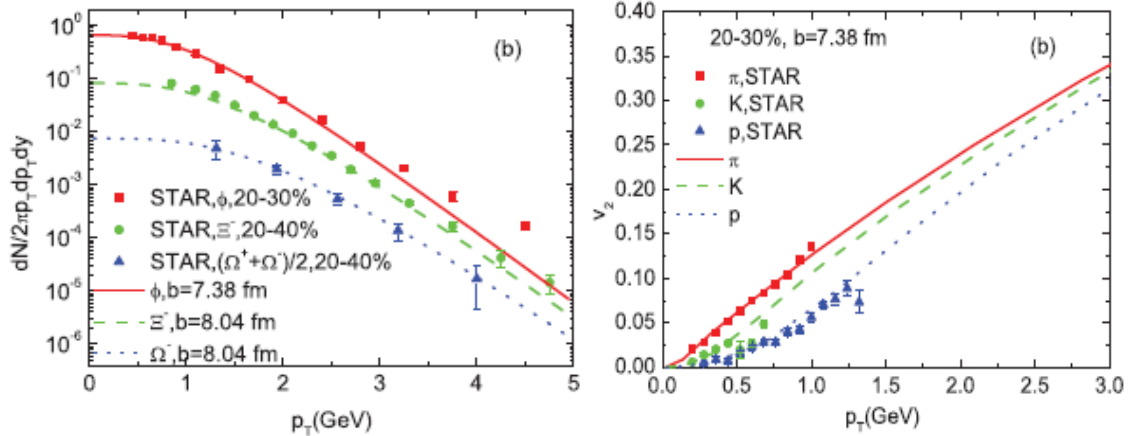


FIG. 3. Multistrange hadron transverse-momentum spectra (left panel) at $T_{ch}=160$ MeV and light hadron elliptic flow (right panel) at $T_{kin}=110$ MeV.

- [1] P.F. Kolb and U.W. Heinz, *Quark gluon plasma 3*, edited by R. C. Hwa and X.-N.Wang (World Scientific, Singapore, 2003), p. 634; arXiv:nucl-th/0305084.
- [2] U. Heinz, in *Relativistic Heavy Ion Physics*, edited by R. S. Stock, (Landolt-Boernstein New Series, I/23 Springer Verlag, New York, 2010).
- [3] B. I. Abelev *et al.* (STAR Collaboration), *Phys. Rev. C* **79**, 064903 (2009).
- [4] Min He, Rainer J. Fries, and Ralf Rapp, *Phys. Rev. C* **85**, 044911 (2012).
- [5] S. Pratt, *Phys. Rev. Lett.* **102**, 232301 (2009).

Directed flow from color glass condensate

R.J. Fries and G. Chen

The initial state of nuclear collisions at very high energies is thought to be a phase of Quantum Chromodynamics (QCD) called the Color Glass Condensate. We use a generalization of the McLerran-Venugopalan (MV) model and an expansion of the classical gluon field around the time of collision ($t=0$) to calculate the evolution of the energy momentum tensor in Color Glass Condensate.

In the past reporting period we have used this technique to investigate the early flow of energy which is encoded in the Poynting vector of the Yang-Mills energy momentum tensor. We have found, as shown in Fig. 1 that there is an unexpected (i.e. not driven by gradients of the energy density) flow component which is odd in rapidity. This phenomenon could translate to a significant directed flow (v_1) in the final observables. Such directed flow has been observed in heavy ion collisions and exhibits the right sign and roughly the right shape compared to our results. Since the origin of this directed flow is more elusive in other approaches this could be an important signature for the existence of color glass condensate at RHIC and LHC energies.

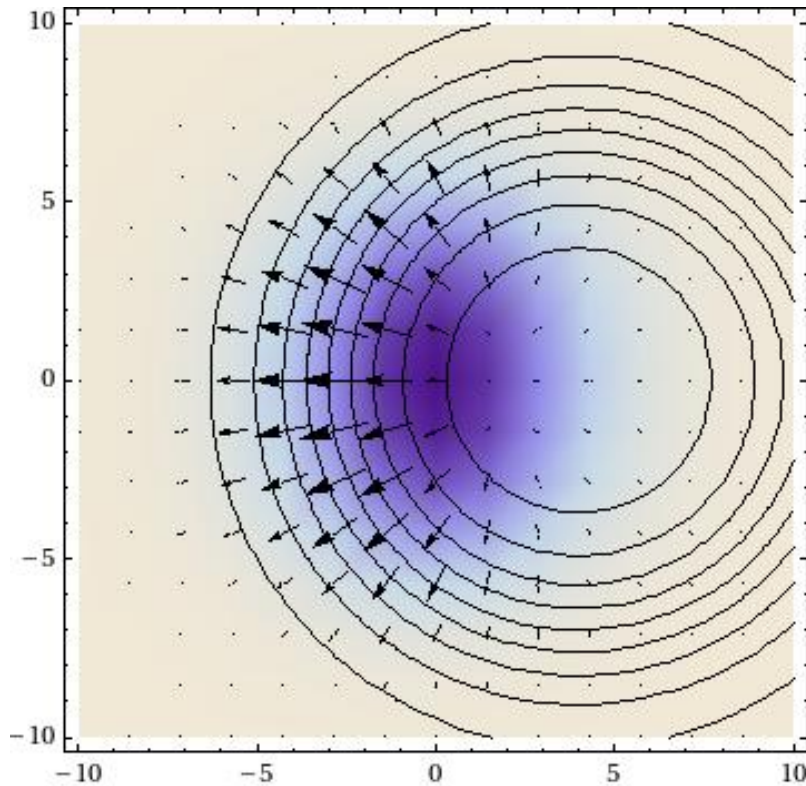


FIG. 1. The energy flow field (black arrows) in the transverse plane of the collision, showing preference for energy flow to the right at rapidity $\eta=1$. Blue shade: energy density of the fireball; black contours: baryon density of one of the colliding nuclei going into the plane.

Dileptons from the deconfinement phase transition

R.J. Fries and G. Chen

Photons and dileptons are excellent probes of the hot and dense matter formed in high energy collisions of heavy nuclei. Due to their large mean free path thermal radiation from both quark gluon plasma and the hot hadronic gas are accessible to experiment. Their spectra and other properties not always match expectations, indicating that we do not yet fully understand the emission processes. E.g. the yield of dileptons at RHIC with masses below the ρ meson is larger than expected in most calculations. We have embarked on a project to identify additional sources of electromagnetic radiation that have not been taken into account in previous theoretical calculations. In particular, we have calculated rates of radiation that is emitted during hadronization processes. This includes photons associated with recombination, $q+qbar \rightarrow \gamma + \pi$, and $q+qbar \rightarrow \gamma + \rho$ (where γ could be either a real or virtual photon, the latter decaying into dileptons), as well as recombination and direct decay, $q+qbar \rightarrow \rho \rightarrow$ dileptons.

We find that the rates of these processes are competitive with both quark gluon plasma and hot hadronic gas emission. We have plugged the rates into a hydrodynamic fireball simulation tuned to RHIC energies, and find that photon yields from hadonization are suppressed compared to other thermal emission because of the short duration of the emission process (just above the critical temperature). However we find that they make a sizable contribution to dileptons with masses below the ρ peak.

SECTION IV
MISCELLANEOUS

Ernest Rutherford and the origins of nuclear physics

J.C. Hardy

At the invitation of the Canadian Association of Physicists I presented a talk at their annual congress in St. John's Newfoundland on the subject, "Ernest Rutherford and the Origins of Nuclear Physics." I was subsequently asked to write an article on the same subject for *Physics in Canada*, which will appear in volume 68, number 1 (Jan-Mar 2012). A brief synopsis follows.

Rutherford was born in 1871 under very humble and remote circumstances in pioneering country on New Zealand's South Island. With intelligence and spunk he won scholarships, first to college in nearby Nelson, then to university in Christchurch; and finally landed an 1851 Exhibition Scholarship to Cambridge, where he arrived in 1895 just after Roentgen had reported from Germany on the mysterious new X radiation and just before Becquerel in France announced that uranium spontaneously emitted radiation. Working with J.J. Thomson, Rutherford was soon studying the nature of the radiation emitted from uranium and was the first to report (and name) [1] the two different types of rays – α and β – that he observed.

By 1898, at the age of 27, Rutherford had been appointed Macdonald Professor of Experimental Physics at McGill University in Canada, where he spent 9 years. During this time, with a series of ingenious experiments, he cracked the puzzle of radioactivity and determined that "... the succession of chemical changes taking place in radioactive bodies is due to the succession of α rays, i.e. the projection of a heavy charged mass from the atom" [2]. For his work at McGill he received the 1908 Nobel Prize in Chemistry.

By the time he received the prize he had already moved on to Manchester University, where he continued the experiments that led to his discovery that the atom had a hard core. The famous alpha scattering experiment by Geiger and Marsden (proposed by Rutherford), which gave the crucial evidence, was published in 1909 [3] but not understood for nearly two years. It was in 1911, one hundred years ago, that Rutherford first stated [4] that, "The ... atom ... consists of a central electric charge concentrated at a point and surrounded by a uniform spherical distribution of opposite electricity equal in amount."

The first mention of the word "nucleus" did not come for two more years, during which time a young postdoc at Rutherford's lab had weighed in on the problem. That postdoc was Niels Bohr, and it was he who first used the word in a published paper [5] although he gave full credit to Rutherford for proposing the atomic model with a charged nucleus at its center.

Rutherford's accomplishments were by no means over. After the interruption of the First World War, he moved to Cambridge, where he and the young scientists he attracted to work with him were the first to initiate a nuclear reaction using alpha particles from a radioactive source. They were then the first to build an accelerator to produce a beam of high speed hydrogen nuclei, which were projected onto a lithium target causing a nuclear reaction that "split the atom." Along the way, it was Rutherford who suggested that a special name – "protons" – be given to hydrogen nuclei to acknowledge the wide role they played in the nuclear structure of all species. It was also he who proposed in 1920 the existence of

an atom of mass one and zero nuclear charge, and it was in his lab 12 years later that this particle, the neutron, was first observed.

Although technology has improved enormously since Rutherford's day, nuclear physics – and particle physics for that matter – still follows the path well begun by Ernest Rutherford.

[1] E. Rutherford, *Phil. Mag. Ser. 5*, xviii, 109 (1899).

[2] E. Rutherford, *Phil. Mag. Ser. 6*, v, 177 (1903).

[3] H. Geiger and E. Marsden, *Proc. Roy. Soc. A 82*, 485 (1909).

[4] E. Rutherford, *Proc. Manchester Literary and Philosophical Soc. IV*, 55, 18 (1911).

[5] Niels Bohr, *Phil. Mag. Ser 6*, xxvi, 1, 476, 857 (1913).

SECTION V

SUPERCONDUCTING CYCLOTRON, INSTRUMENTATION AND RIB UPGRADE

K500 Operations and Development

D.P. May, G.J. Kim, H.L. Clark, and F.P. Abegglen

Introduction

During the 2011-2012 reporting period a total of 22 different beams, including 7 newly developed beams, were used for experiments, and there were a total of 29 beam tunings for these experiments. The SEE program is treated separately in this progress report.

Ion Source

During the shutdown ECR1 was opened for examination, and it was found that there had been no further deterioration in the damaged spot that had developed over a plasma flute on the aluminum wall. A beam of scandium was produced using ECR2. The material was sputtered into the source with a particularly high sputtering voltage of 3.5 kV. This was similar to titanium.

Cyclotron Beams

New beams of HD⁺ (hydrogen-deuterium molecular ion) at 22 AMeV, ¹⁸O at 10 AMeV, ²⁰Ne at 40 AMeV, ²⁶Mg at 16 AMeV, ⁴⁸Ca at 4.6 and 5.0 AMeV, and ⁵⁰Ti at 5.0 AMeV were developed for experiments.

Operations

For the period April 1, 2011 through March 31, 2012, the operational time is summarized in Table I, while Table II lists how the scheduled time was divided. There was an unusually large amount of unscheduled maintenance, the bulk of which involved water leaks into the K500 vacuum. The greatest time was lost in April and May to a leak in a dee, while somewhat less time was lost during December to a leak in the upper liner because the final repair was accomplished during the annual shutdown.

Table I. 2011-2012 Operational Time.

Time	Hrs.	%Time
Beam on target	5639.58	76.8
Tuning, optics, set-up	10.00	0.1
Beam development	634.92	8.7
Scheduled maint.	106.00	1.5
Unscheduled maint.	938.75	12.8
Idle time	10.75	0.1
Total	7440.00	100.0

Table II. 2011-2012 Scheduled Beam Time.

Time	Hrs.	%Time
Nuclear physics	1973.25	29.7
Nuclear chemistry	964.50	14.5
Atomic physics	0.00	0.0
Outside collaboration	0.00	0.0
Outside users	3079.58	46.3
Beam development	634.92	9.5
Total	6652.25	100.0

Texas A&M cyclotron radiation effects facility
April 1, 2011 – March 31, 2012

H.L. Clark, J. Brinkley, G. Chubarian, V. Horvat, B. Hyman, B. Roeder, and G. Tabacaru

The activity of the Radiation Effects Facility (REF) decreased compared to the previous reporting year. In this reporting period, the facility was used for 2,673 hours, which is a ~12% decrease over the 3,042 hours used in the 2010-2011 reporting period. However this year had the second highest usage ever. Nearly 250 hours were lost in December 2011 to unscheduled maintenance. Users of the facility (and hours used) over the past year were: SEAKR (381), NAVSEA (331.5), NASA GSFC (192), Lockheed Martin (181), Xilinx Corp (156.5), Sandia Nat Lab (120), NASA JPL (118.5), Boeing Satellite Systems (115.25), Aeroflex (114.25), JD Instruments (112), BAE Systems (81.25), Honeywell (72), International Rectifier (68), Maxwell Technologies (67), CEA - France (58), Intel Corp (56.25), Thales Alenia - France (56), Sun Tronics (51.5), Radiation Assured Dev (48), Stapor Research (38), Air Force (32), Johns Hopkins (24), MicroSemi (23.5), SEMICOA (22), TAMU Physics (18.25), University of Michigan (17.5), White Sands AFRL (16), Peregrine Semi (15.5), AMTEC (14.25), Texas Instruments (12), HIREX - France (11.5), EM Photonics (8), Montana State University (8), Northrop Grumman (8), Save Inc (8), University of Texas - El Paso (8) and Vanderbilt University (8). New users included CEA - France, MicroSemi, SEMICOA, University of Michigan, EM Photonics, Montana State University, Save Inc and University of Texas - El Paso.

Table I. Radiation Effects Facility usage by commercial and government customers for this and previous reporting years.

Reporting Year	Total Hours	Commercial Hours (%)	Government Hours (%)
2011-2012	2,673	1,630 (61%)	1,043 (39%)
2010-2011	3,042	1,922 (63%)	1,121 (37%)
2009-2010	2,551	1,692 (66%)	859 (34%)
2008-2009	2,600	1,828 (70%)	772 (30%)
2007-2008	2,373	1,482 (62%)	891 (38%)
2006-2007	2,498	1,608 (64%)	890 (36%)
2005-2006	2,314	1,314 (57%)	1,000 (43%)
2004-2005	2,012	1,421 (71%)	591 (29%)
2003-2004	1,474	785 (53%)	689 (47%)
2002-2003	1,851	1,242 (67%)	609 (33%)
2001-2002	1,327	757 (57%)	570 (43%)
2000-2001	1,500	941 (63%)	559 (37%)
1999-2000	548	418 (76%)	131 (24%)
1998-1999	389	171 (44%)	218 (56%)
1997-1998	434	210 (48%)	224 (52%)
1996-1997	560	276 (49%)	284 (51%)
1995-1996	141	58 (41%)	83 (59%)

Table I compares the facility usage by commercial and government customers. The ratio from this reporting year (61% to 39%) is similar to the trend seen in previous reporting periods, and commercial hours still dominate (see Fig 1). Commercial hours decreased by 15% and government hours decreased by 7% over hours from 2010-2011. 15 and 25 MeV/u Kr and Xe were most utilized as well as 15 MeV/u Au. No new beams were added to SEELine users list. Much of the testing conducted at the facility continues to be for defense systems by both government and commercial agencies. It is expected that the facility will continue to be as active in future years.

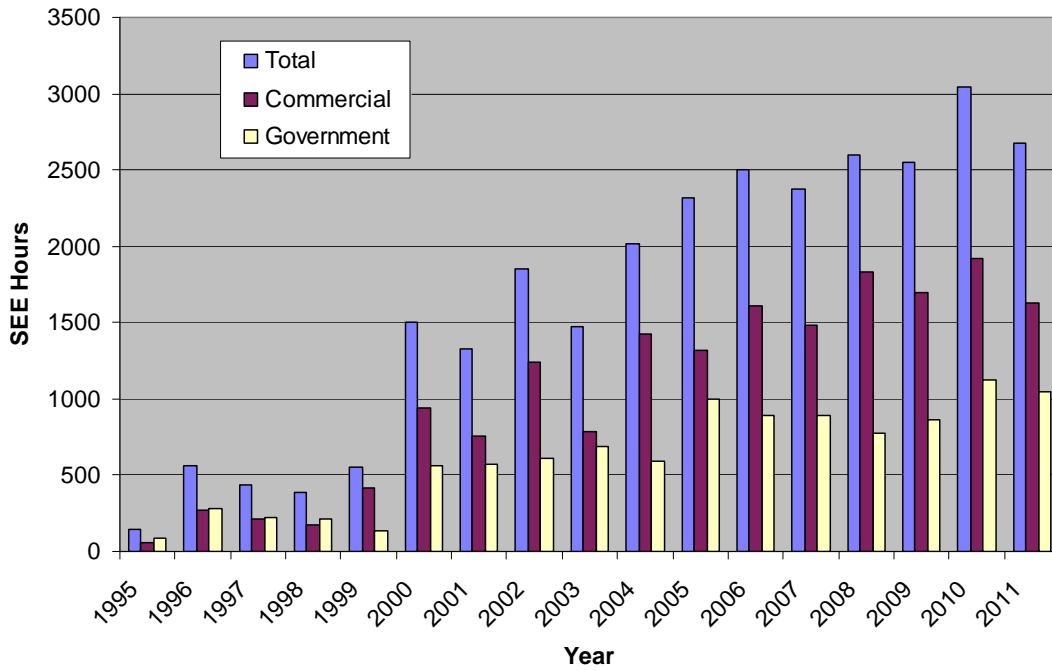


FIG. 1. Radiation Effects Facility usage by commercial and government customers for this and previous reporting years. Despite the decrease in total hours by 12%, the ratio from this reporting year (61% to 39%) is similar to the trend seen in previous reporting periods where commercial hours still dominate.

Cyclotron computing

R. Burch and K. Hagel

Our mission is to provide the Cyclotron Institute personnel with stable, fast, secure computational and network resources necessary for their research programs. This past year we upgraded the mail, firewall, list-server, and the password change service servers. We stopped the pursuit of virtualizing¹ due to difficulties with logistics including provisioning, maintenance, disaster-recovery and fail-over redundancy. We switched to using 35 Watt fan-less small form-factor PC's thus allowing us to better utilize server room rack space, power and cooling.

Further responding to user comments, we analyzed the mail server/mail client responsiveness¹ and found it lacking in its ability to handle the large graphics intensive emails utilized today. We replaced the aging mail server with a new stronger Dell PowerEdge server with dual quad core processors, 16GByte of RAM, RAID drives, and are running the Zimbra open-source mail system on a Ubuntu Long Term Support operating system. User mail was migrated to the new system with little or no loss. The new system currently handles the load without noticeable strain.

During the past year, the lab suffered a power-outage (voltage swings) which caused the primary firewall's disk to die. We switched to our secondary firewall which spontaneously rebooted every several days with increasing frequency. This was determined to be a hardware problem. To solve the problem, we built two new "twin" firewalls utilizing the 35 Watt fan-less small form-factor PC's mentioned above. These PC's appear to easily handle the network load providing full bandwidth on request with little to no processor load.

We also moved the data acquisition firewall, list-serve, syslog and web-password-change services each to 35 Watt small form-factor PC's. These changes help to reduce our power and cooling footprint and allow the reallocation of power and cooling to future new computational servers.

New hardware for mail, firewall, syslog, list-serve, and web-password-change servers as well as running the Zimbra for the mail service, and general maintenance allows us to continue to supply the Institute with stable, fast, and secure resources it needs to execute its mission.

[1] R. Burch and K. Hagel, *Progress in Research*, Cyclotron Institute, Texas A&M University (2010-2011), p.V-5

Cyclotron institute upgrade project

H.L. Clark, F. Abegglen, G. Chubarian, G. Derrig, G. Kim, D. May, and G. Tabacaru

On January 3, 2005 the Cyclotron Institute Upgrade Project (CIUP) began with the approval of the CIUP management plan by the Department of Energy Nuclear Physics Office. The project will extend at least to the second quarter of calendar year 2013. When completed, the upgraded facility will provide high-quality re-accelerated secondary beams in a unique energy range. Funding for the upgrade comes from several sources: the Department of Energy, matching support from TAMU, the Robert A. Welch Foundation and beam time sales for testing electronics components at the Cyclotron Institute.

The CIUP is divided into three major tasks: (1) Re-commission of the existing K150 (88") cyclotron and refurbish beam lines; (2) Construct light-ion and heavy-ion guides and produce 1+ radioactive ions; (3) Transport and charge boost radioactive ions and accelerate in the K500 cyclotron.

As detailed in the Management Plan, effort made during this year on Task 1 included,

- Construction of internal cryopanels for the K150 high vacuum system and
- Development of high energy proton, deuteron beams and heavy-ion beams.

Progress was also made on Tasks 2 and 3. This included,

- Placement of the ion guide equipment on the ion guide roof planks,
- Rebuild of Big Sol, restart of the CB-ECR ion source,
- Construction of the Heavy Ion Guide gas cell and transport system, and
- Assembly and installation of the n+ transport system. Below we report on a few of the accomplishments listed above.

K150 Cyclotron Development

After the successful acceleration and strip extraction of the first H- and D- beams last year, we have extended the range of energies for H- and D- beams, and after repairing the water leak on the deflector we have also accelerated and extracted several positively charged beams.

The energy range achieved for protons from H- acceleration is from 15 to 40 MeV, and for deuterons from D- acceleration is from 6.5 to 20 AMeV. We worked on 20 AMeV D- beam last year, but had trouble extracting it. This year we were able to extract the beam by more aggressively varying some of the trim coils from the CYDE calculated values. The differences in 3 trim coils (out of 17) from the CYDE values to the final tuned values ranged from 130 to 430 amps. These differences may indicate some problems with the CYDE field maps. However, we do not want to abandon CYDE, it is certainly good enough to find the beam at inner radii of the cyclotron. So for the near future, we will need to tune the beams with the idea that some trim coils may be adjusted as much as a few hundred amps from the CYDE trim coil values.

For the positively charged beam accelerations, we have so far worked mostly with light ion beams: 7 and 8 AMeV $^{16}\text{O}^{6+}$, 9 AMeV $^{18}\text{O}^{7+}$ and 10 AMeV $^{18}\text{O}^{8+}$, and 7.5 AMeV $^{28}\text{Si}^{9+}$ beams. The RF dee voltage ranged from 30 to 40 kV and the E1 deflector needed from 46 to 56 kV to extract these

beams. The extraction efficiency was better than 65% for all these beams. The deflector will need to be conditioned for higher voltages in order to extract higher energy beams.

We have also worked on a few third harmonic beams, but we have not had much success in developing them. One experiment requested a 5 AMeV ^{40}Ar beam, but because the beam orbital frequency turned out to be below our RF frequency range, it was tried as a third harmonic 15 MHz beam. At this high frequency, conditioning the RF dee was found to be very slow and difficult. After several days of conditioning the dee, the voltage was not high enough and the injection into cyclotron was poor and ultimately the beam could not be extracted. Then, shifting to a lower energy and hence to a lower frequency, we were able to accelerate and extract a low energy third harmonic beam, namely 3.2 AMeV $^{16}\text{O}^{4+}$ beam at 12 MHz. However, this beam will need much more work to improve the beam intensity, as the injection into the cyclotron and the internal transmission of the beam was poor.

We have also begun development for the 13.7 AMeV $^{40}\text{Ar}^{13+}$ beam in the anticipation of the heavy ion guide program. We have accelerated $^{40}\text{Ar}^{13+}$ ions to 10 and 12 AMeV, and $^{40}\text{Ar}^{14+}$ to 13.7 AMeV, but they were not extracted. The needed deflector voltages to extract the beams were beyond what the deflector could presently hold. Typically the injection efficiency from ILC02 into the cyclotron (as measured at 6" on the beam probe) was only about 10%, and the internal transmission from 6" to 39" was 70%. To get to the beam intensity goal of 0.9 μA on FC02, it is obvious that the ECR2 output must be increased by employing two frequency heating, the cyclotron vacuum must be improved, and the deflector must be conditioned to hold high voltages. Fig. 1 shows all the beams, both internal and extracted, that we have run since Dec. 2009, after the installation of the dee inserts.

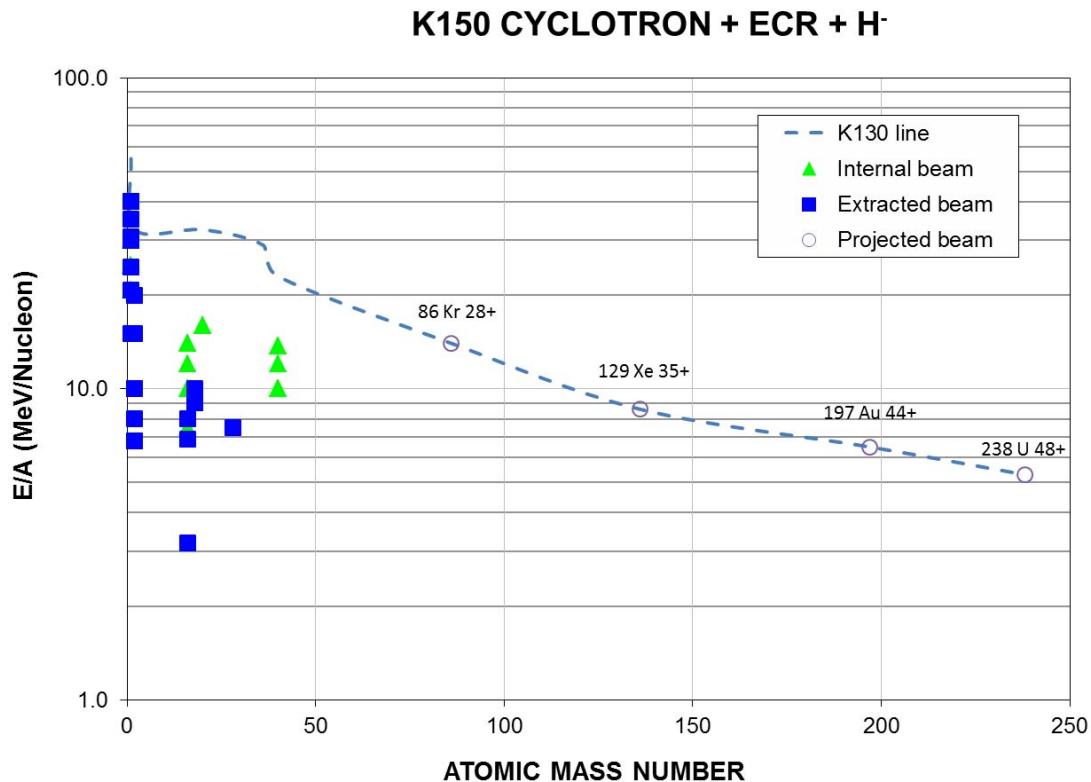


FIG. 1. Beams that ran on the K150 cyclotron with H⁻ and ECR2 sources since Dec. 2009.

Comparing the throughputs (ILC02 to FC02 transmission) of the H- beams and the ECR2 beams, it is clear that H- beams have much better throughputs, getting about 30% for the H- beams, 15 to 20% for D-, and 10 to 15% for the ECR2 beams, all with the first and second harmonic bunchers turned on. In a direct H- versus ECR2 test, with the cyclotron set for 25 MeV acceleration for 1H- and proton, for the H- beam up to 50% of the injected beam was measured at 10'' on the beam probe, whereas only 10% of the injected H+ was found on the beam probe. The internal transmission was about the same at 95% for both the H- and H+. (The H+ was not extracted.) The D- beams also had good injection efficiency of around 30 to 50%, but the internal transmission struggled from 30 to 60% for 6.5 to 20 AMeV accelerations. The obvious difference between the H- beams and the ECR2 beams is the emittance. The H- beams enjoy much a smaller emittance and a smaller beam spot on the inflector.

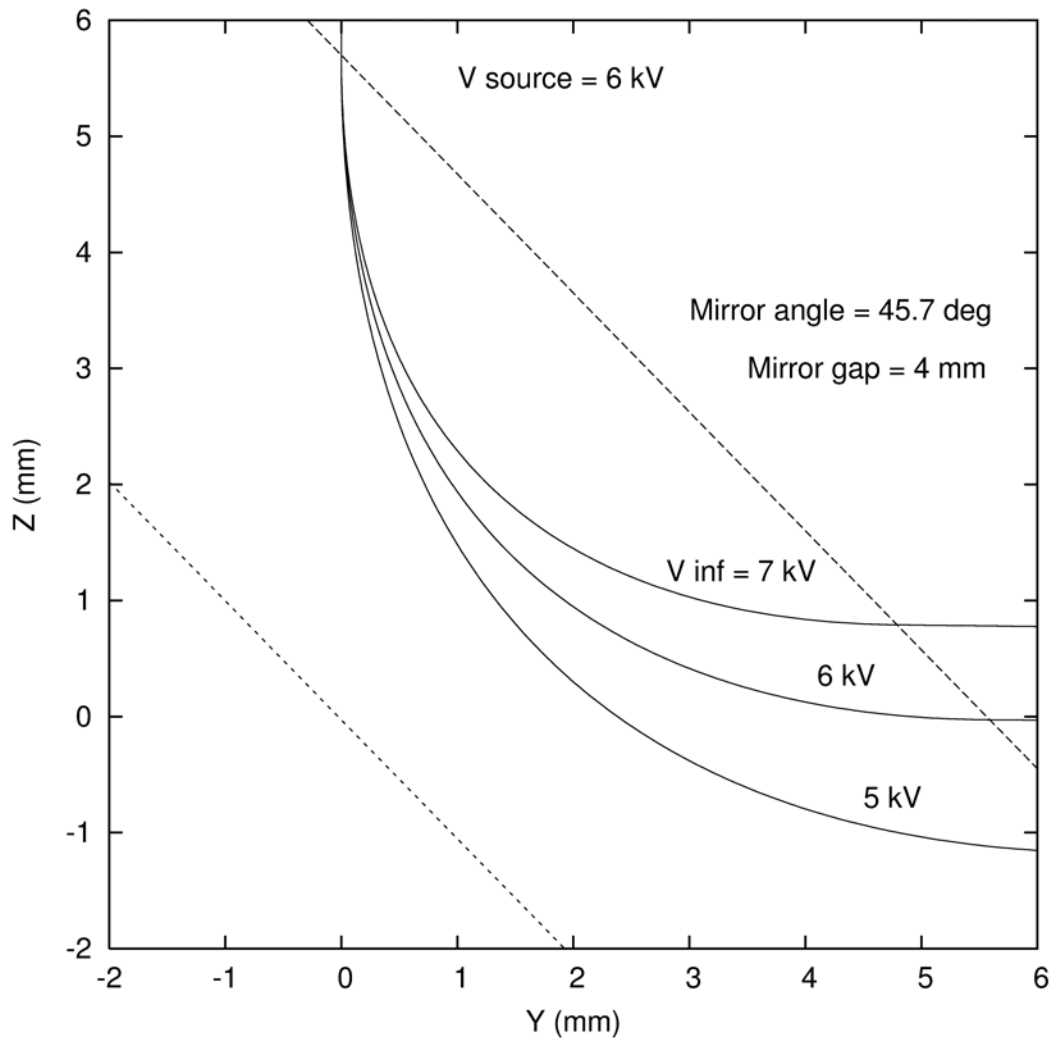


FIG. 2. Y-Z projection of a vertically injected particle through the mirror inflector. The dashed lines represent the grounded grid on the top and the HV electrode on the bottom. The three curves show the trajectories from three different inflector voltages.

The mirror inflector gap, from the electrode to the grounded grid, was increased from 1 mm to 4 mm in April 2012, and this has helped to increase the beam injection into cyclotron by doubling the beam intensities for some beams. Because the gap widening was obtained by lowering the electrode while keeping the grid the same position, there are some concerns about the z position of the injected beam. Fig. 2 shows the importance of having a small spot at the mirror inflector. The finite extent of the beam spot at the inflector translates into the vertical size into the cyclotron. Thus, having a small emittance helps to achieve a small spot at the inflector and a small vertical size and a larger acceptance into the cyclotron.

We met the proton beam intensity milestone by transporting 10 μ A of 30 MeV protons into the Light Ion Guide cave in April, 2011. The beam transport efficiency was good (for a large emittance beam), transporting 91% of 11 μ A on FC02 into the LIG cave.

We transported a K150 beam into the MARS cave for the first time in Nov. 2011. The beam height of various magnets through the 12° dipole to the Indiana magnet, which bends the beams into the MARS spectrometer, needs to be re-aligned. One benefit that came from sending a beam to MARS was that using the calibrated MARS dipole the energy of the K150 beam was determined, and this in turn was used to calibrate the 160° dipole magnet.

We have also re-configured the old ion interaction beam line to accommodate the STAR/LIBERACE experiment staged in cave 4. We have of course had several K150 beam into the BM04 (the Maryland dipole), however the difficulty of this beam transport was with the steep 53 degree bending through the BM04, which produced asymmetric focusing for x and y, see Fig. 3. To partially

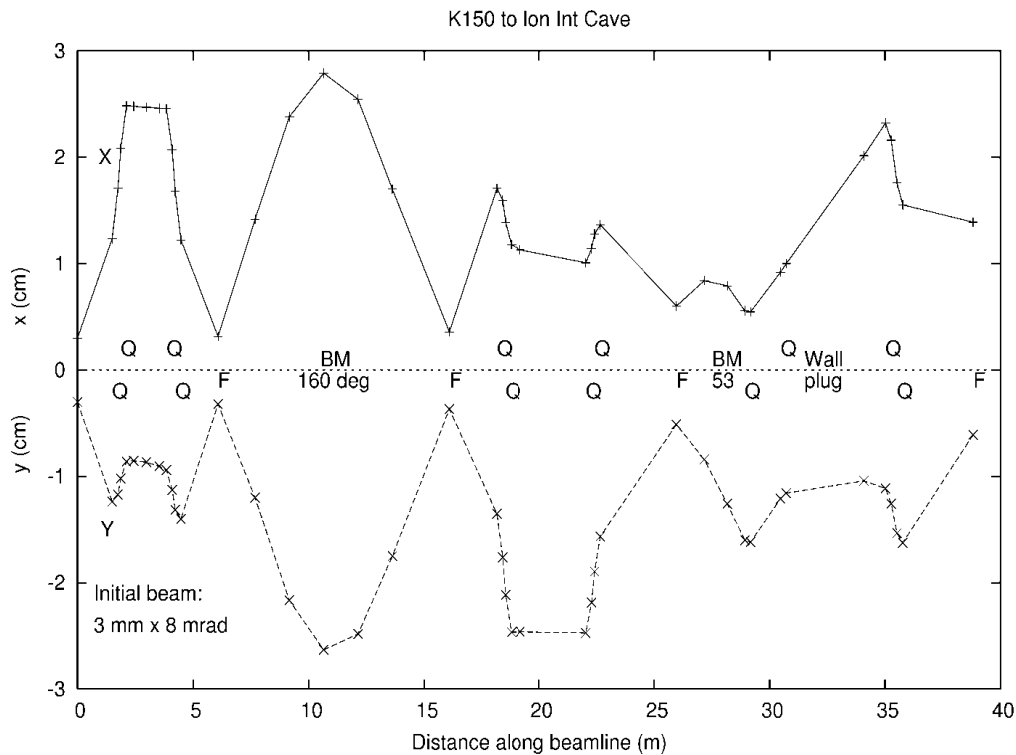


FIG. 3. TRANSPORT calculated X and Y beam profiles through to the newly re-configured Ion Interaction cave.

correct for this, we installed two separated quadrupoles just after BM04, first one to refocus the y side then to slightly focus x and also to parallelize the y side going into the cave. In the cave the experimenter's target was positioned about 3 m downstream of the last quadrupole doublet, in order to control the divergence of the beam through the target chamber. At the experimenter's target position the x-beam magnification is large, so in order to achieve a small beam spot the object slits need to be very small; while this reduces the beam, the experiment only needs a few of nA of proton or deuteron beams.

Ion Guide Hall

All power supplies, transmitters, HV transformers, and control equipment for the Ion Guides, CB-ECR ion source and n+ transport system have been positioned above the roof planks of the ion guide hall (Fig. 4). The safety interlock system to protect the cyclotron personnel from electrical and radiation hazards posed by the CB-ECR ion source and high voltage platform have been installed and tested. Final coupling of the Light Ion Guide to the CB-ECR ion source is under development.



FIG. 4. Left: Equipment for the light ion guide shown positioned above the roof planks of the ion guide hall. Placement above the roof planks removes the equipment from the high radiation environment of the ion guide hall. **Right:** The three tier roots blower system and high voltage safety cage for the light ion guide system shown completed in the ion guide cave.

Big Sol Rebuild

The repair of Big Sol involved a complete rebuild of the cryostat. The superconducting bobbin was the only original piece to be reused. In the spring of 2011, Big Sol was transported to a local machine shop and the cryostat was carefully cut open to remove the bobbin. The entire rebuild of the cryostat has occurred at the cyclotron lab.

Fig. 5 shows the original superconducting bobbin being fit into its new cryostat and the final assembly of Big Sol installed in Cave 2 and connected to its original cryogenics and power supply systems. The cryostat was cleaned with dry nitrogen gas and pumped down several times. The cryostat

was then cooled down with LN2 and finally filled with LHe from the cryogenics transfer system from the K500 cyclotron. Initial testing shows that the liquid helium leak rate has diminished substantially from the rebuild project.

One problem that was found was the LN2 feed line freezes if the nitrogen liquid flow is stopped. The problem is believed to exist in the chimney where cold helium gas meets the LN2 lines and can be fixed by cutting into chimney and rerouting the LN2 feed lines.



FIG. 5. Left: The original superconducting bobbin fit into its new cryostat. Right: Final assembly of Big Sol positioned back in its original location in cave 2 and reconnected with its original cryogenics and power supply systems.

Heavy Ion Guide and Gas Cell

The Gas Catcher has been completely assembled including the Cone and the three Body sections. A diagram of the system is shown in Fig. 6. Pictures of the Body and Cone sections of the RF Gas

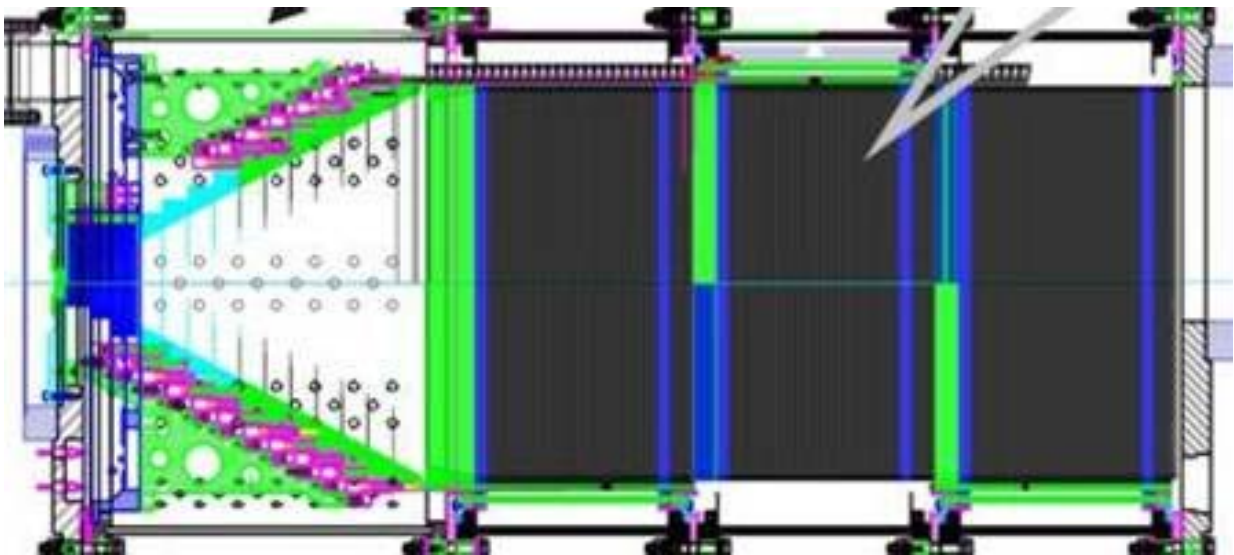


FIG. 6. Diagram of the RF gas catcher which includes the RF Cone and three Body Sections. The Cone, two Body sections and 1/2 of the third Body section have been assembled.

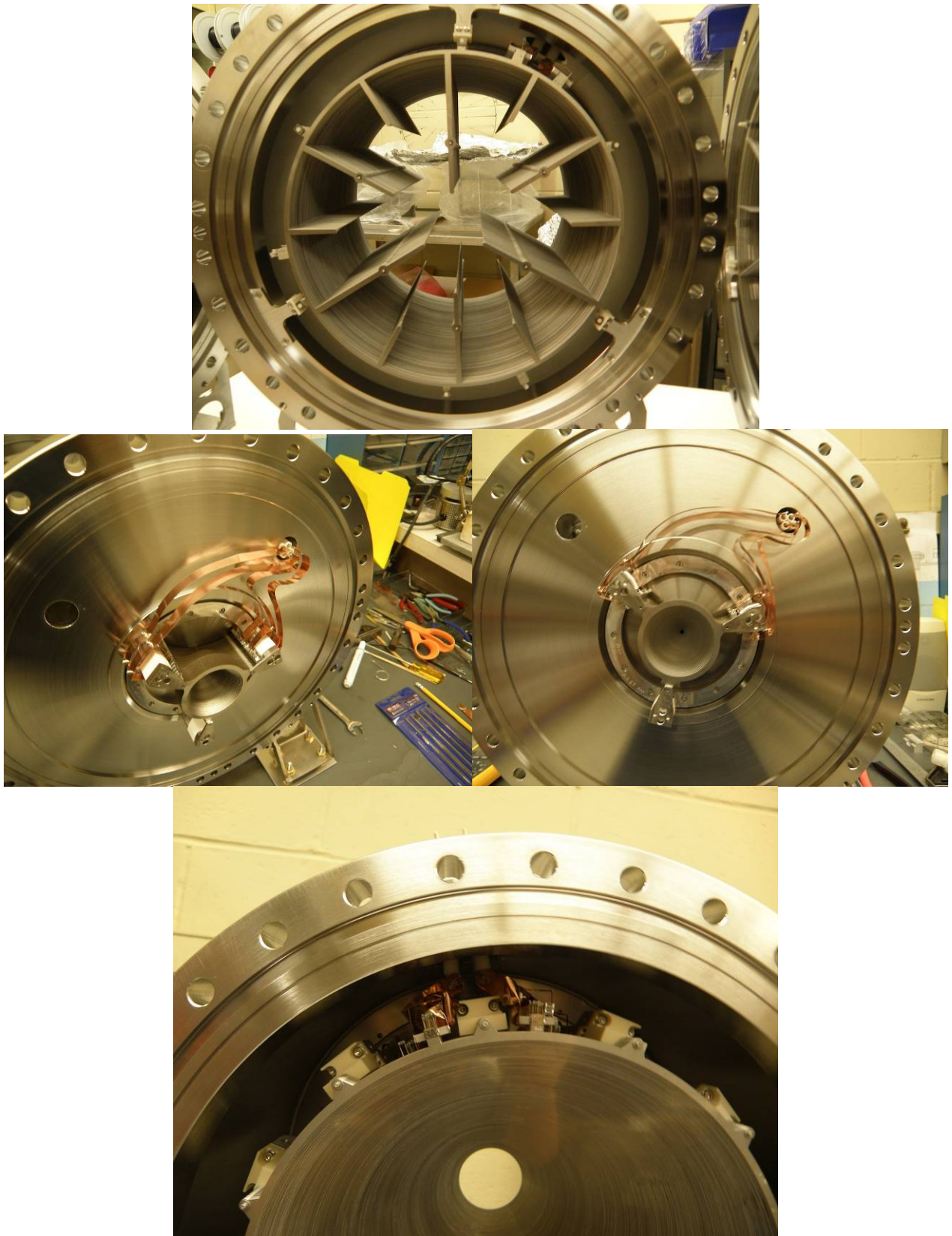


FIG. 7. Pictures of the Body and Cone sections of the RF Gas Catcher. Top picture: RF-Body section, Middle: Front part of the RF Cone, and Bottom: Main Part RF Cone.

Catcher are shown in Fig. 7. The entire gas cell assembly is planned to be moved to TAMU in the fall of 2012. The chamber for the Branching System has been completed and delivered. Beam optics components including Einzel lenses and X-Y steering elements are under construction. Preparation of the heavy ion guide cave is underway. The arch crane and flooring material for the HV platform have been installed.

n+ Transport System

The section of the n+ transport system below the roof planks was installed in the fall of 2011. This section included a Glazer lens, x-y steering magnet, 90° analyzing magnet, two diagnostic stations, two cryopump systems and control system. Assembly of the section of the n+ transport system above the roof planks that connects the CB-ECR ion source to the top of the K500 cyclotron is underway. The radiation shielding around the top of the K500 cyclotron was removed during the January maintenance period and n+ Solenoid #5, new BM2 and new BM3 magnets were installed (Fig. 8). The remaining components are now being installed and the entire n+ transport system is nearly completed. Fig. 8 shows the installation of the n+ BM2 magnet and its support structure with staircase. The n+ transport system should be completed and tested with beams by the fall of 2012.

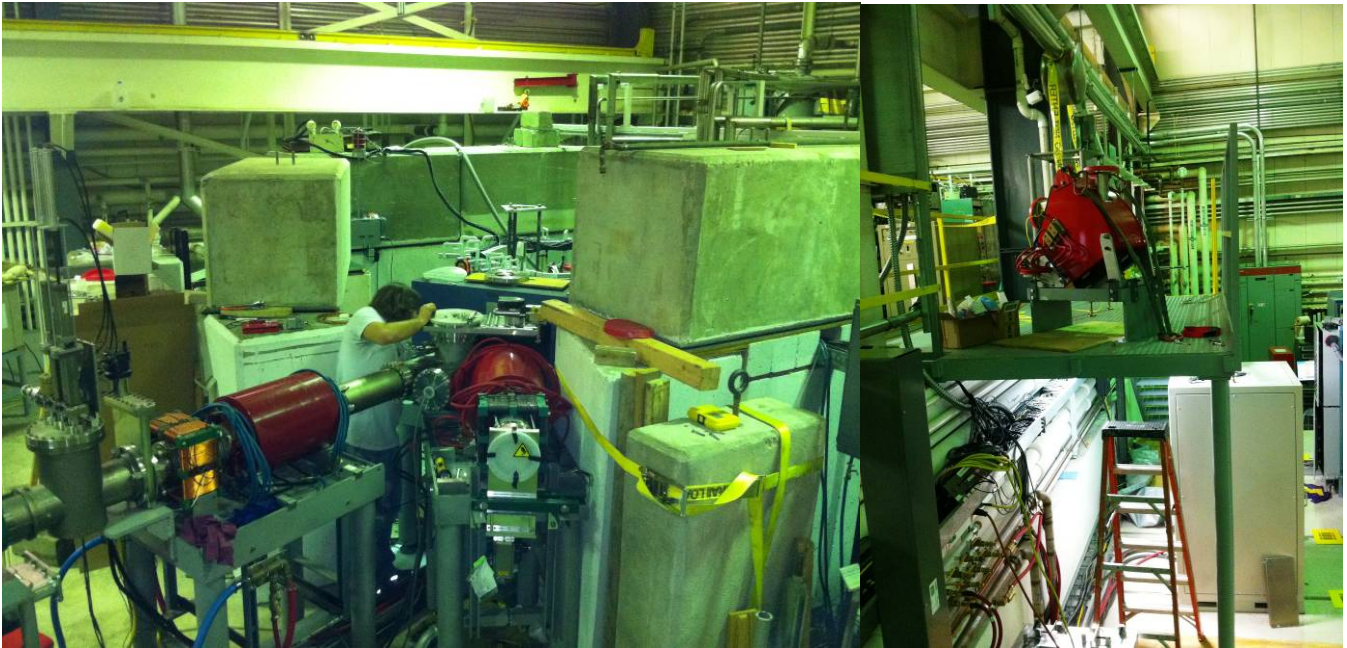


FIG. 8. Left: The construction of the horizontal section of the n+ transport system that connects the CB-ECR ion source to the top of the K500 cyclotron has begun with the placement of the N+ Solenoid #5, new BM2 and new BM3 magnets. **Right:** The installation of n+ BM2 magnet and its support platform with staircase. The n+ transport system should be completed and tested with beams from the CB-ECR ion source by the fall of 2012.

Restart of the CB-ECR Ion Source

After a break in operation of nearly 6 months, the CB-ECRIS was turned on in the fall of 2011 with the coil power supplies and RF microwave transmitter mounted on the roof planks above the ion guide hall (Fig. 9). The extraction plate of the CB-ECR ion source has been modified. The diameter of the extraction opening was increased from 5 mm to 8 mm and three additional holes were made in order to increase the pumping speed of the plasma chamber. The locations of the holes were carefully chosen not to interfere with the shape of plasma.

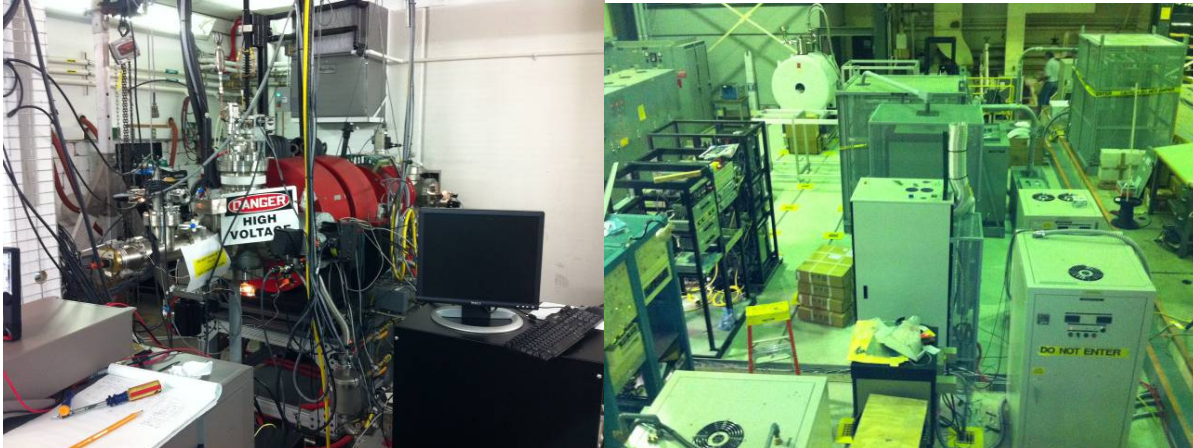


FIG. 9. CB-ECR ion source (left) has been restarted with its support equipment mounted above the ion guide hall roof planks (right).

Initial tests showed an improved ECR ion source performance; most likely from better pumping of the plasma chamber through the extraction plate. It was found that the ion source also accepted higher

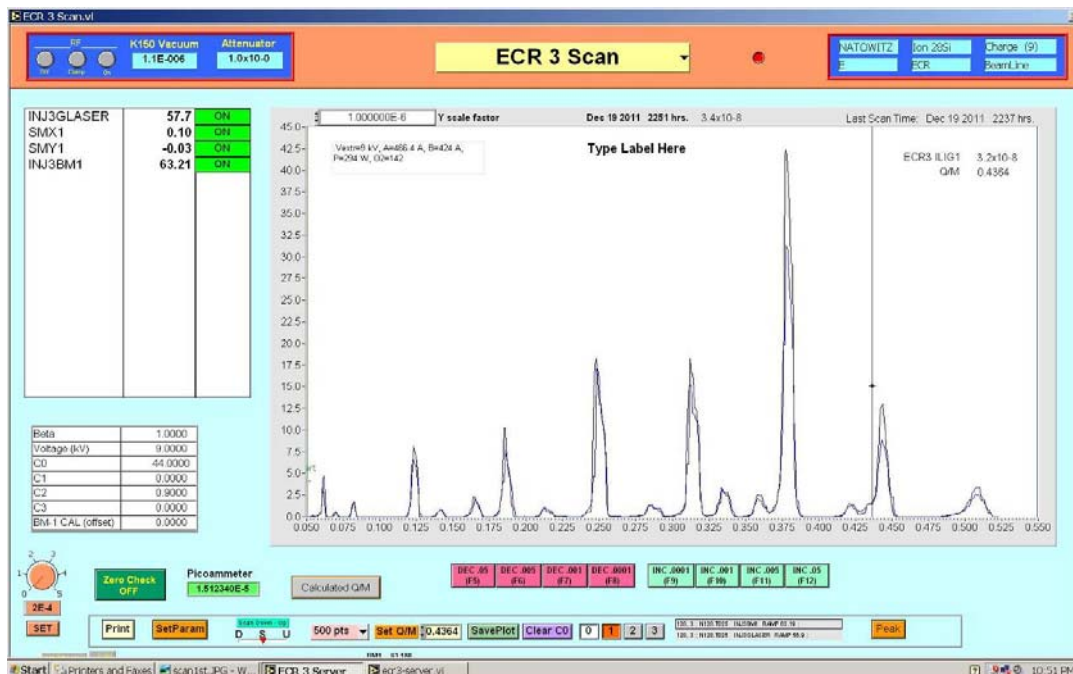


FIG. 10. The “best performance” of the CB-ECR ion source after startup – producing 40 μA of $^{18}\text{O}^{6+}$ with only ~250 watts of microwave power.

microwave power, but that higher power did not always produce optimal performance – indicating that the ion source needs further conditioning time to clean up the plasma chamber walls. Fig. 10 shows the “best performance” of the CB-ECR ion source – producing 40 μA of $^{18}\text{O}^{6+}$ with only ~ 250 watts of microwave power.

The ion gun was loaded with rubidium and installed with the Argonne electrostatic steerer, Einzel lens and the Faraday cup array to the entrance of the CB-ECR ion source. New power supplies for the injection system that can be remotely controlled from above the ion guide hall have been installed. The first tests showed an improved transmission rate of 50 % of the 1+ rubidium beam into the CB-ECR ion source – where prior tests without the Argonne steerer showed less than 1% transmission. SIMION calculations show that a transmission rate of 90 % rate could be reached. This reduction in our transmission is probably from slight misalignments in the system. Fig. 11 shows a screen shot of the acquisition program for the Faraday cup array – showing the majority of the 1+ rubidium beam being focused on a ~ 7 mm diameter spot.

Unfortunately, no evidence of “charge breeding” has been found so far. The injection system of the CB-ECR ion source is suspect and will be developed further.

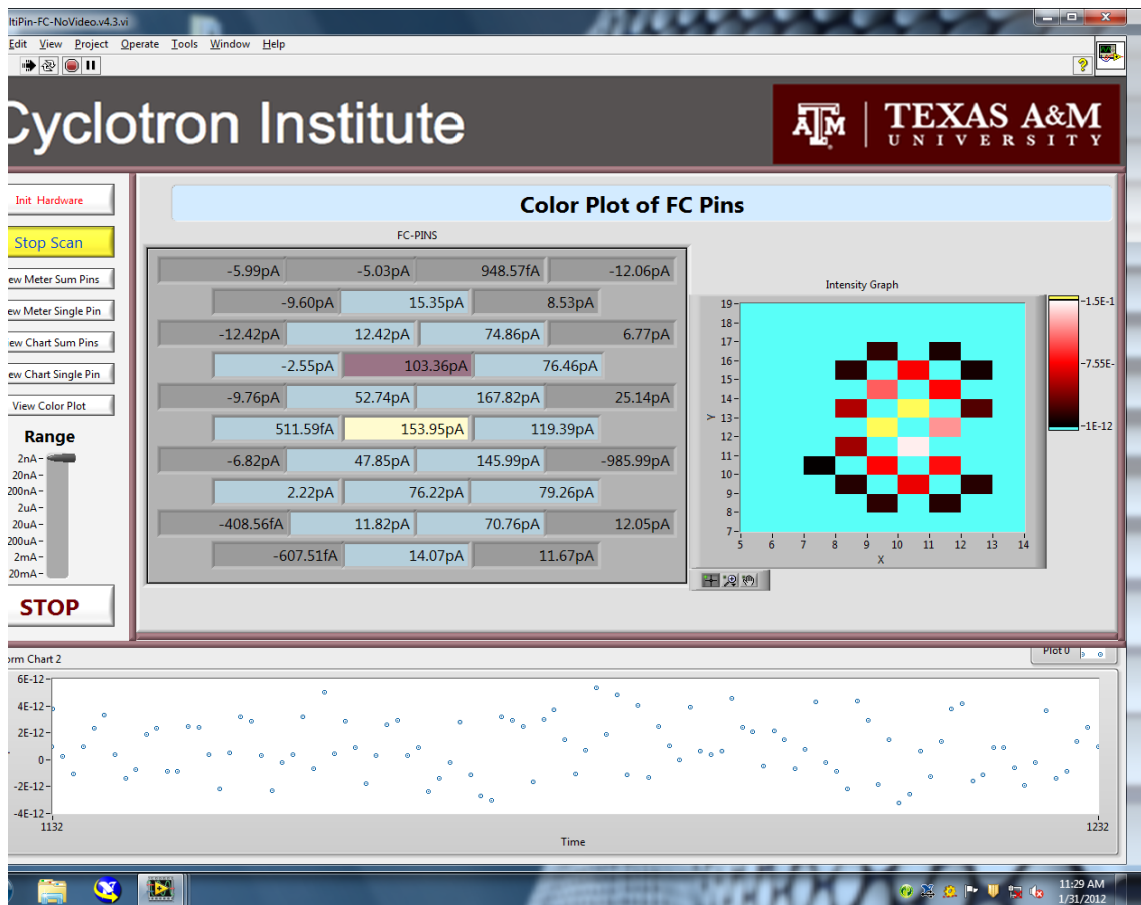


FIG. 11. Screen shot of the acquisition program of the Faraday cup array – the data shows that the majority of the 1+ Rubidium beam was focused on a ~ 7 mm diameter spot.

The charge breeding ECR ion source at the Cyclotron Institute

G. Tabacaru and D.P. May

The goal of the Upgrade Project of the Cyclotron Institute is to reaccelerate beams of radioactive ions for the exploration of the vast area of experimental nuclear physics using unstable nuclei. Ion guide techniques stop fast collision products in helium. These products are removed from the production target by helium flow and are subsequently formed into radioactive ion beams (RIB) of low charge state. Reacceleration to energies higher than 3 – 5 AMeV requires much higher charge states. These can be achieved using the charge-breeding process predicted in the late '90s for modified ECR ion sources. The PIAFE project [1] first proved this experimentally.

Charge breeding is defined as the process where low charge state ions, 1^+ or 2^+ , are trapped by the plasma of an ECR ion source and subsequently further ionized before being extracted. The process is complex and very difficult to approach from a theoretical point of view; extensive experimental work needs to be performed in order to achieve the goal of charge-breeding.

One of the key components of the Upgrade Project is the commissioning of the Charge Breeder ECR Ion Source designed, fabricated and delivered by Scientific Solutions, San Diego, California [2]. The injection of the 1^+ ions into the plasma chamber is critical in that the energy of the incoming beam must match the extraction potential of the ECR ion source plus the plasma potential (a few tens of volts)

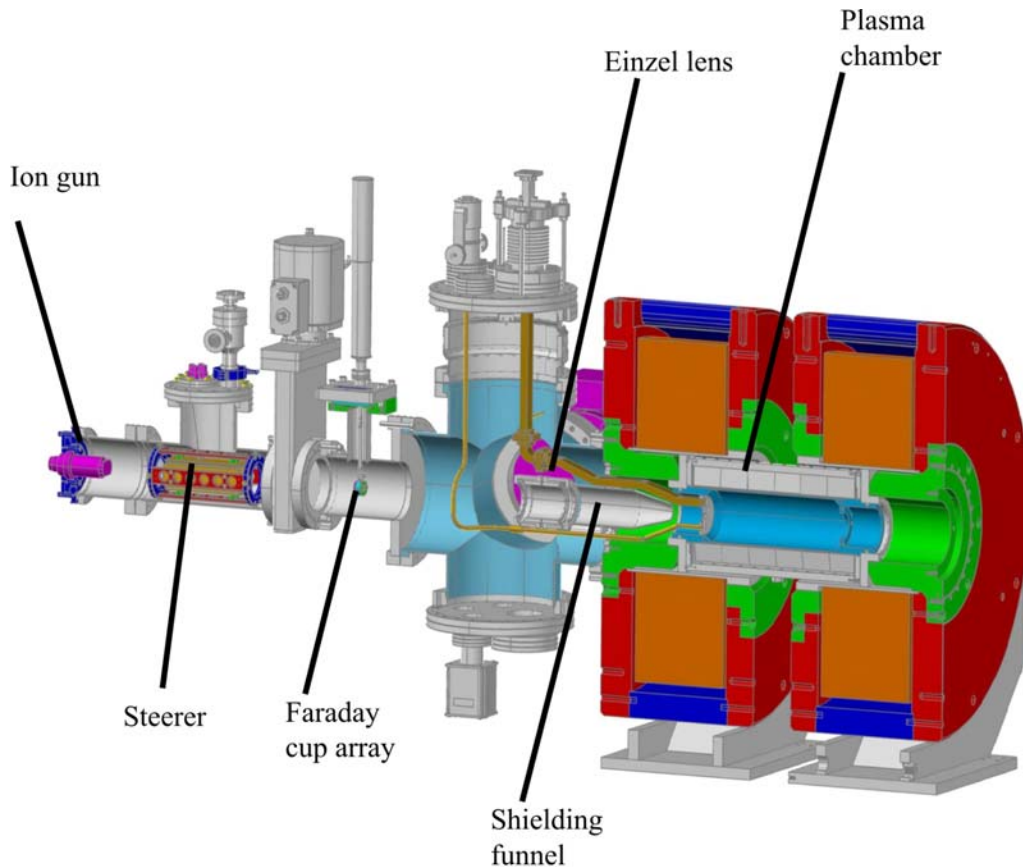


FIG. 1. Engineering drawing of the CBECR depicting the injection system.

in order for the ions to be trapped. Fig. 1 illustrates our testing scheme. The initial 1^+ ions (alkali metals) are produced using the HeatWave Labs ion gun and an electrostatic steerer corrects for any misalignment of the optical axis. The injection system of our Charge Breeder ECR consists of an einzel lens, a funnel, shielding the the 1^+ ions from the microwave guide held at the same potential as the plasma chamber, and a tube placed at the entrance of the plasma chamber. This end tube can be biased or grounded via an external high voltage feedthrough.

The work effort was concentrated in creating a remote control configuration of the ion source together with the ion gun and the electrostatic steerer. All the power supplies were moved out from the vicinity of the source, and they are completely remote controlled, making troubleshooting and monitoring much easier. A Faraday cup array (FCA) was developed together with the control software. The FCA consists of 35 pins embedded inside an insulator (ceramic) structure and covered by a copper mask. Current hitting each pin is measured using a low-current scanner card (model 7158) installed inside a programmable switch unit (model 7002) from Keithley Instruments. LabView based software was designed to read the digital picoammeter and to provide an image of the beam (see Fig. 2). A slight steering effect was observed when either the ion gun extractor or lens is tuned, an effect which was canceled by adjusting the voltage on the horizontal or vertical plates of the electrostatic steerer. The image also provided us with an estimated beam spot size of about 7 mm at the FCA's location, approximately 400 mm from the exit aperture of the ion gun.

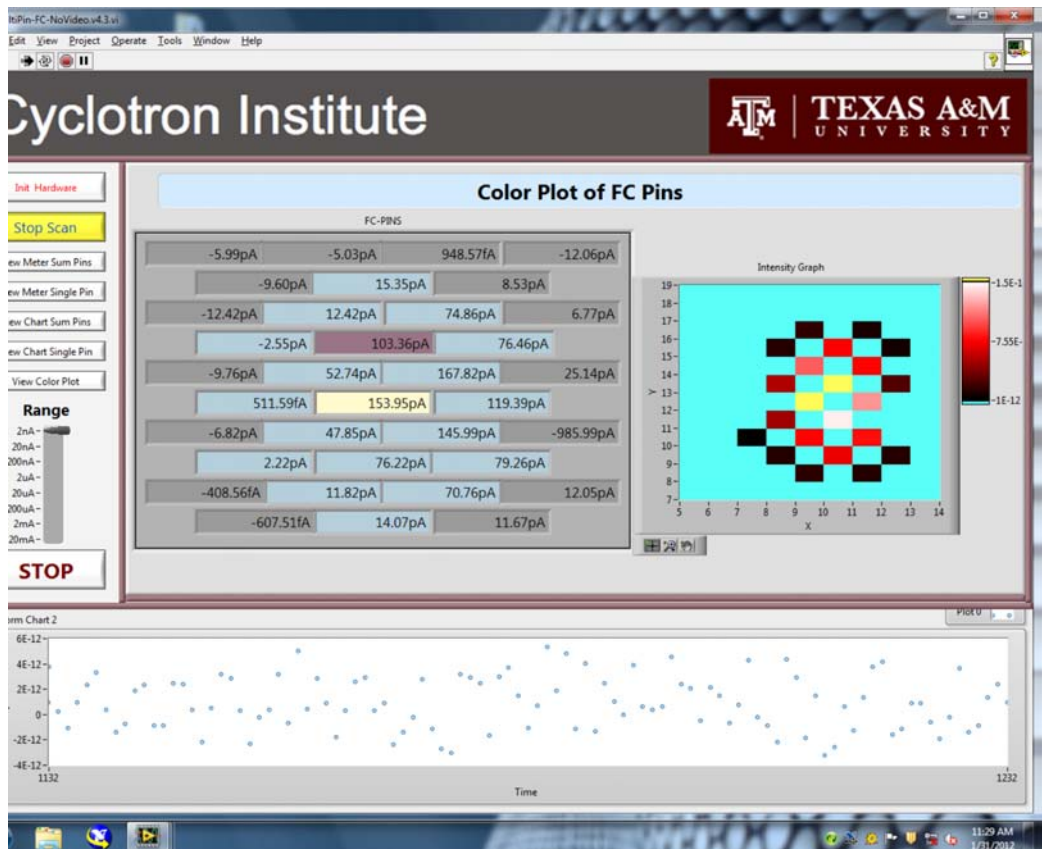


FIG. 2. Screenshot of the controlling software for the Faraday Cup Array. The circle diameter represents approximately 7 mm.

SIMION calculations were performed for various conditions, taking into account the solenoidal magnetic field of the two coils. Calculations show the ions are slowing down at the entrance of the plasma chamber and move inside the plasma chamber following a spiral trajectory. Depending on their velocity, the ions are captured by the plasma and suffer multiple ionizations changing their charge state.

Future tests will be focused on finding the right parameters for transporting the 1^+ ions into the chamber and search for sign of higher charge states, respectively charge breeding.

- [1] J.L. Belmont *et al.*, Proceedings of the 13th International Workshop on ECR Ion Sources, Texas A&M University, College Station, Texas, February 1997.
- [2] W.D. Cornelius, ECRIS 2008, 18th International Workshop on ECR Ion Sources, Chicago, Illinois USA; <http://accelconf.web.cern.ch/AccelConf/ecris08/papers/weco-b01.pdf>.

Radiation monitor data logging

R. Burch, F. Abegglen, L. Gathings, and D. Menchaca,

Our mission is to provide the Cyclotron Institute accelerator users with the accelerator control system and networking resources necessary for the Institute research and development programs. This past year we developed preliminary display, logging and archiving of both the Canberra stack monitor and the Ludlum Measurements Inc (LMI) Radiation Monitor systems with injection of important events into the electronic logging system. A backup system was also implemented to maintain several years of history for the stack monitor archive, the LMI RAD monitor archive, and the electronic log as well as backups of accelerator control runtime and development software.

The Canberra stack monitor system utilizes the Canberra iCAM software to monitor the stack emissions. We set the iCAM software to write both the spectra snapshot file and the measurements file at once per minute. A new snapshot file is written every minute while the measurements file is appended. We wrote a small LabVIEW program which reads the snapshot file, plots the spectra and other snapshot values, moves the file into an archive directory which has the structure: /canberra/History/YYYY/MM/DD/. The LabVIEW program also moves the measurements file into the same directory as the snapshot files but at the beginning of each new day.

The LMI RAD system utilizes LMI detectors to monitor radiation levels in areas of interest. The LMI units broadcast their values. We wrote a small LabVIEW program which collects and plots these values and an erlang program which collects and logs values in an archive which has the directory structure: /rad/repo/YYYY/MM/DD/ with the file name CHXXX.HRYY.cvs, where XXX is the channel number and the YY is the hour.

A backup system for both the Canberra stack monitor and the LMI RAD system archives was implemented to provide adequate storage for several years of history. The backup system (Fig. 1) is a four tier system and includes the original archives, a primary NAS (Network Attached Storage) unit, a secondary NAS unit, and an eSATA disk attached to the secondary NAS for offsite backups.

The archives are remotely mounted to the primary NAS which takes snapshots every 4 hours and keeps the last 6 copies for 24 hours. Daily, weekly and monthly snapshots are also maintained. These copies are then synced to the secondary NAS for archival redundancy and again to the external disk for off-site backups. Control system accelerator control runtime and development software are also backed up in a similar manner.

Further development and refinements for the Canberra stack monitor and the LMI RAD area monitor system may include redundancy and report generation. These developments and those envisioned allows us to continue to supply the Institute with a stable, fast, and secure control system and radiation monitoring system.

Synology DS211+ Based Backup

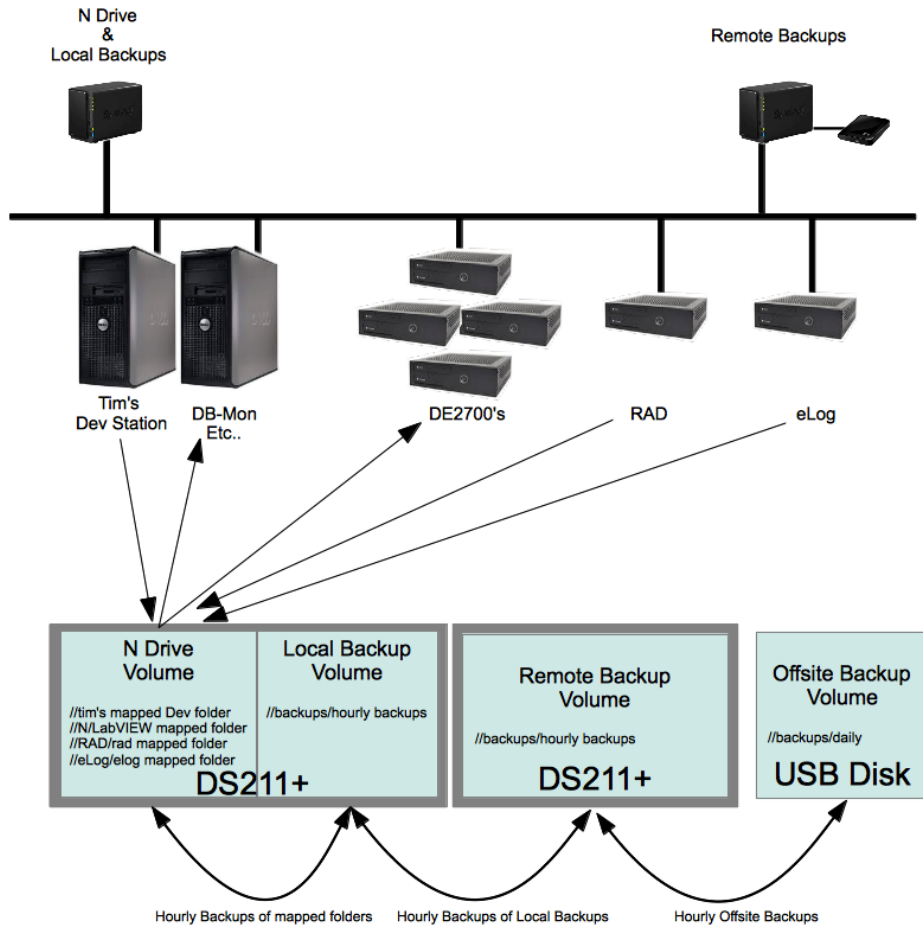


FIG. 1. Four tier Cyclotron Computer Control System Backup.

Upgrade of equipment to measure precise β -decay branching ratios

V.E. Iacob, J.C. Hardy, and H.I. Park

Our program [1] to test the Electroweak Standard Model via the unitarity of the Cabibbo-Kobayashi-Maskawa matrix requires precise measurements of the Q_{EC} -value, half life ($t_{1/2}$), and branching ratio (BR) for superallowed $0^+ \rightarrow 0^+ \beta^+$ decays. We make the $t_{1/2}$ and BR measurements by producing a pure sample of the activity of interest with the MARS spectrograph, collecting it on the tape of our fast tape transport and moving it rapidly to a shielded counting location. A high purity radioactive beam with energy of about 30 A MeV is extracted from the MARS focal plane into air and, after it passes through a 0.3-mm-thick BC-404 plastic scintillator and aluminum degraders, it is implanted into the 76- μ m-thick Mylar tape of the tape-transport system for up to two half lives. Then the beam is turned off and the activity is moved in less than 0.2 s to the center of the counting station, where the decays are measured. For branching-ratio measurements the counting station consists of a 1-mm-thick BC-404 plastic scintillator very close to one side of the tape and a HPGe detector located 15 cm away on the other side of the tape. The beam-on/move/detect cycles are repeated until the desired statistics have been acquired. While the measurements themselves are superficially simple, the required accuracy (better than 0.1%) is very demanding. The desired accuracy demands a series of reliability tests that must be as complete as possible. Thus all parameters that could possibly affect the result are monitored continuously, on a cycle-by-cycle basis, and, wherever possible, redundancy is incorporated.

We reported in Ref. [2] a β - γ coincidence setup, based on FERA modules and KmaxNT [3] software, able to perform a precise BR measurement. We first used this equipment to measure the branching ratio of the superallowed decay of ^{22}Mg [4]. The setup records two types of events:

- Those observed during the implantation of the heavy ions. For each event of this type we record the energy deposited in the 0.3-mm-thick plastic scintillator, ΔE_{HI} , and the time of its implantation, t_{HI} , relative to the beginning of the cycle.
- Those observed during the “detect” portion of the cycle: *viz.* beta-gamma coincidences. For each such event we record: 1) the energy deposited in the HPGe detector, E_γ ; 2) the energy deposited by the beta particle in the 1-mm-thick plastic scintillator, ΔE_β ; 3) the time, t_{decay} , that the decay is recorded relative to the beginning of the detect period; and 4) the “coincidence time,” $t_{\beta-\gamma}$, which is the time difference between the β and γ signals from the two detectors.

In an ideal case, all the events in the HPGe detector are gammas and all those in the 1-mm-thick plastic scintillator are betas originating in decays of the implanted source; then the BR can be extracted from the formula:

$$\text{BR} = N_{\beta-\gamma}/(N_\beta \varepsilon_\gamma), \quad (1)$$

where $N_{\beta-\gamma}$ is the number of observed beta-gamma coincidences, N_β is the number of observed beta singles and ε_γ is the absolute efficiency of the HPGe detector. In the real case, corrections must be applied for dead-time losses, for real and random coincidence gains and losses, for gamma events appearing in the

plastic scintillator and for small differences in the detection efficiencies for betas originating from different branches with different end-point energies. (The denominator in Eq. 1 incorporates all branches while the numerator involves only one.)

As is evident from Eq. 1, to obtain high precision in the measurement of BR, one requires comparable precision in the absolute efficiency, ϵ_γ , of the HPGe detector. The precise calibration of our HPGe detector [6-8] was accomplished using sources that were positioned at a well defined position relative to the HPGe detector, which had an uncertainty of ± 0.1 mm or better. Our on-line measurements use the tape transport system, which cannot be positioned repeatedly with the same precision. To overcome this limitation, we have placed a laser sensor next to the HPGe detector and pointing to the Mylar tape; with this device we can read the distance between source and detector to 0.05-mm precision and record that distance on a cycle-by-cycle basis. Note that control over the transport length (i.e. the source positioning in the tape direction) can be accomplished by recording the ratio of beta-singles to implanted-heavy-ions, N_β/N_{HI} , for each cycle since an incorrect position results in a reduced value of the ratio. This, of course, requires us to scale the beta singles and implanted heavy ions for each cycle.

Using the experience gathered over years of operation, we have now made a major upgrade to the BR setup. Now, in addition to the information related to the two types of events (ΔE_{HI} , t_{HI}) and (ΔE_β , E_γ , $t_{\beta-\gamma}$, t_{decay}), we also record the following for each cycle:

- the number of implanted heavy ions, N_{HI} ,
- the number of beta singles N_β ,
- the number of gamma singles N_γ ,
- the number of beta-gamma coincidences,
- the tape-to-HPGe distance,
- integrated dead-time in the beta-singles channel,
- integrated dead-time in the gamma-singles channel, and
- integrated dead-time in the beta-gamma coincidence channel.

Moreover, the new configuration has added significant redundancy: all the “per-cycle” totals are scaled in parallel chains (FERA and CAMAC).

Finally, the coincidence electronics has been optimized to minimize the event losses due to “underflows” in the ΔE_β and E_γ channels. Such underflows can happen if the analog-to-digital convertor (ADC) abandons the conversion (having assessed a too low value in the given channel) or if the signal presented to the ADC sits on the tail of a preceding one, thus preventing the ADC from rearming. Both cases result in events with incomplete information, and eventually in a lost event. The new setup reduces these losses from about 7-10% to less than 0.1% in the ΔE_β channel, and from 3-5% to about 0.3% in the E_γ channel.

With added controls, improved efficiency of the coincidence electronics, and continuous monitoring of the source-detector position, the new setup is expected to let us reach the desired 0.1% precision in BR measurements.

- [1] J.C. Hardy, I.S. Towner, V.E. Iacob, H.I. Park, L. Chen, V. Horvat, N. Nica, J. Goodwin, M. Bencomo, L. Trache and R.E. Tribble, *Progress in Research*, Cyclotron Institute, Texas A&M University (2011-2012), p I-3.
- [2] V.E. Iacob and J.C. Hardy, *Progress in Research*, Cyclotron Institute, Texas A&M University (1999-2000), p. V-22.
- [3] <http://www.sparrowcorp.com>
- [4] J.C. Hardy *et al.*, Phys. Rev. Lett. **91**, 082501 (2003).
- [6] J. C. Hardy *et al.*, J. Appl. Radiat. Isot. **56**, 65 (2002).
- [7] R.G. Helmer *et al.*, Nucl. Instrum. Methods Phys. Res. **A511**, 360 (2003).
- [8] R.G. Helmer *et al.*, J. Appl. Radiat. Isot. **60**, 173 (2004).

Precision measurement of $^{26}\text{Al}^m$ half-life with digital β^+ counting method

L. Chen and J.C. Hardy

On-line experiments have been made in the past year to characterize our newly developed digital β counting system [1]. In particular, the half-life of the superallowed β^+ emitter $^{26}\text{Al}^m$ was measured at Cyclotron Institute with the digital β^+ counting method. The half-life of $^{26}\text{Al}^m$ is already rather well known ($t_{1/2} = 6.345 \pm 0.002$ s) [2] and is thus suitable for testing purposes. In our experiments the $^{26}\text{Al}^m$ beam was produced by impinging a 23-MeV/u ^{27}Al primary beam, delivered from the superconducting cyclotron at Texas A&M University, on a liquid-nitrogen cooled hydrogen gas target. The reaction products were analyzed by the MARS spectrometer and purified $^{26}\text{Al}^m$ ions were extracted out of vacuum at the MARS focal plane through a 51- μm -thick Kapton window. The extracted beam then passed through a 0.3-mm-thick plastic scintillator where the ions were counted and a set of degraders, which further purified the beam and reduced its energy so that it stopped in the center of a 76- μm -thick aluminized Mylar tape. The purity of $^{26}\text{Al}^m$ at the MARS focal plane was about 40%, with the main contamination being the ^{26}Al ground state, which has a half-life of 7.4×10^5 years and consequently plays no role in our measurement. As seen from the particle identification spectrum at the MARS focal plane, shown in Fig.1, all other impurities are stable.

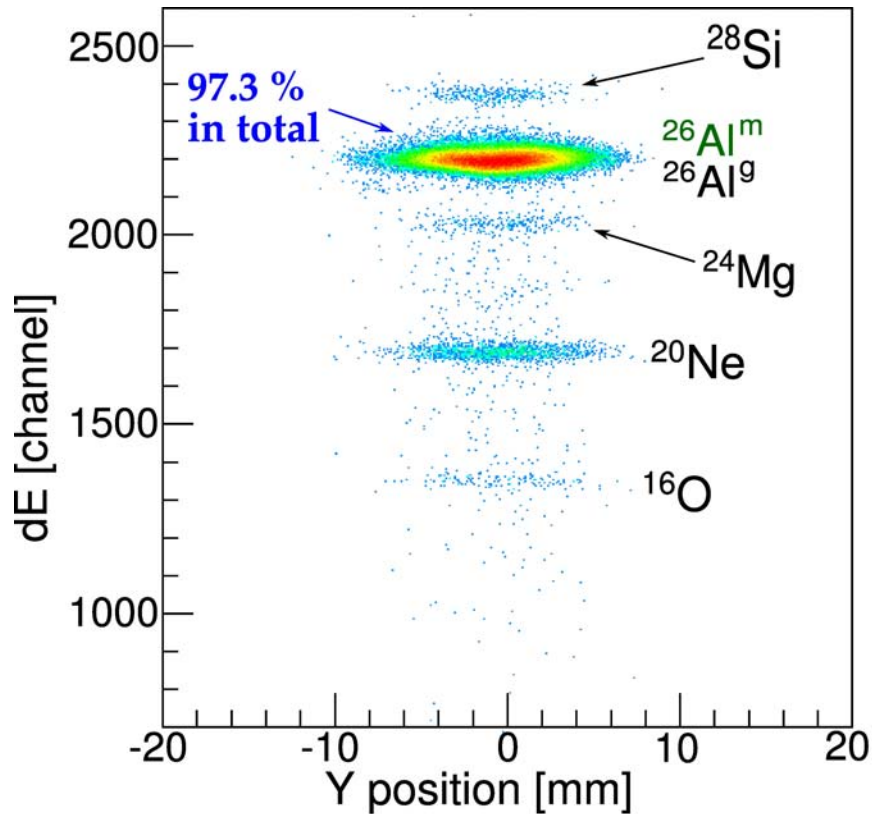


Figure 1. The particle identification spectrum taken at the MARS focal plane. All contaminants are stable isotopes and thus have no impact on the data

After implantation for 2-10 s (depending on the beam intensity and the desired count rate), the collected sample was moved in 185 ms to the center of the 4π gas proportional counter, where its decay was followed for 20 half-lives, after which the cycle was repeated. The signal from the gas proportional counter was amplified by two cascaded fast amplifiers with total gain of 1000, before being sent to a high-speed digitizer (NI-5154) for digitizing and pulse capture. The operation of the digitizer is illustrated in Fig.2. After being configured and initialized, the digitizer waits for an acquisition-start trigger from the tape-drive system indicating that the sample is ready to be counted. The digitizer then starts digitizing the pre-trigger samples continuously and, at the same time, monitors for the occurrence of reference (stop) triggers. A reference trigger is generated whenever the pulse-capture trigger condition is satisfied. As soon as a reference trigger is recognized the corresponding waveform is captured. This pulse-capture process is repeated until the counting period is over. The captured pulses are saved temporarily in the on-board 256-MB memory and then transferred to the host PC via a high-speed PCI bus in parallel to the pulse capture. In our experiment the reference trigger was configured to use an analog edge trigger method and the digitizer trigger level was set to -120 mV. The trigger level was chosen well above the background noise ($\sim 50\text{mV}$) and is low enough to ensure a high efficiency for β particle detection.

The tape transport system and the digital devices were synchronized by TTL signals generated by

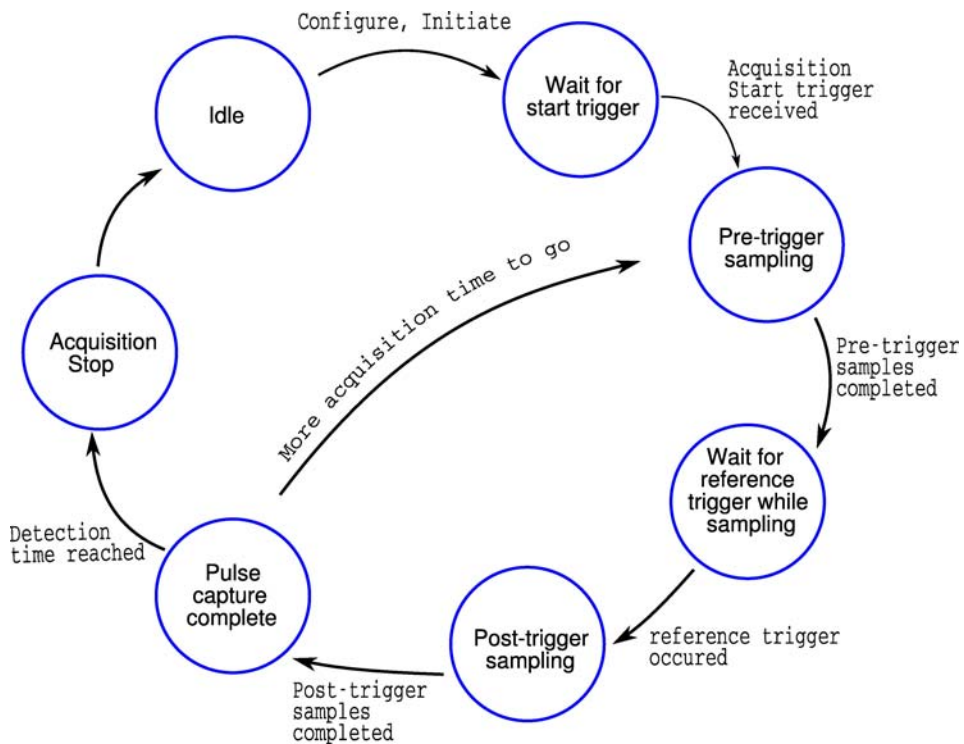


Figure 2. Schematic diagram of the digitizer operation our in on-line experiment.

the tape transport control system. In a cycle-by-cycle mode, two TTL signals were sent in each cycle from the tape system to control the data acquisition: the first triggered the DAQ to count the heavy ions (^{26}Al) using a digital counter (NI PCIe-6320); the second was the acquisition start trigger for the digitizer, which

indicated that the collected sample was positioned at the center of the proportional counter ready for counting.

In this experiment data were taken under different initial β -decay rates, from 4 kHz to about 10 kHz. In principle, higher rates up to ~ 40 kBq can be handled by the digitizer, which was actually only limited by the data transfer speed from the digitizer to the host PC. But, as our on-line tests have revealed, our gas proportional counter cannot handle counting rates above 10 kHz. At such high counting rates the change in gas-counter gain as the activity decays precludes high precision half-life measurements. Also, four different gas-counter biases, 2650V, 2700V, 2750V and 2800 V, were used to test for bias dependence. In total we collected about 100 million waveforms from 1700 cycles.

The on-line data processing procedure is quite different from that of our previous lifetime experiments [3]. Here, first we need to use software to distinguish true β pulses from “spurious” pulses. After pulse discrimination, we then impose an artificial dead time for all pulses. The intrinsic dead time of data acquisition is 870 ns. An imposed dead time can help us test for any systematic changes in extracted half-life as a function of the dead time correction. In this study, the imposed dead time was corrected using a “shadow window” technique, with which the loss of real β events in a dead-time window is compensated by the observed β events in a “shadow window” of identical length at a different (but nearby) time in the same decay spectrum. Our shadow window was located 10 ms away, at time that is negligible with respect to the half-life of $^{26}\text{Al}^m$. We tested imposed dead times from 2 to 10 μs and found that the corresponding half-lives are quite consistent within error bars. After the dead time correction, the decay spectra were built for each cycle. The fitting procedure was the same as used in our previous half-life measurements. In Fig.3 a summed decay spectrum is shown. In this experiment, we preliminarily obtained a half-life for $^{26}\text{Al}^m$ to be 6.3462(10) s.

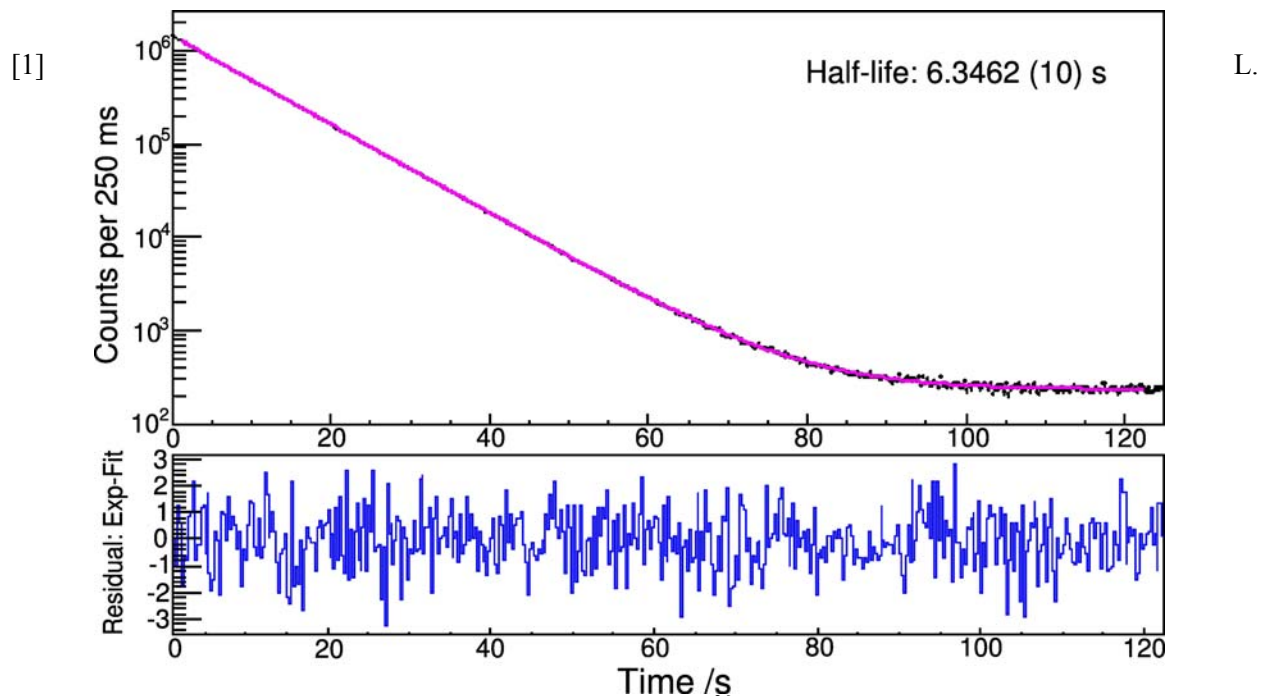


Figure 3. Decay spectrum of the sum of all data from the $^{26}\text{Al}^m$ measurement as obtained from the digital counting system. Residuals of the fit are shown at the bottom.

Chen and J. C. Hardy, *Progress in Research*, Cyclotron Institute, Texas A&M University (2010-2011), p. V-46.

[2] J.C. Hardy and I.S. Towner, *Phys. Rev. C* **79**, 055502 (2009).

[3] V.E. Jacob, J.C. Hardy, A. Banu, L. Chen, V.V. Golovko, J. Goodwin, V. Horvat, N. Nica, H.I. Park, L. Trache, and R.E. Tribble, *Phys. Rev. C* **82**, 035502 (2010).

Event analysis of β decay

V. Horvat, J.C. Hardy, and V.E. Iacob

Normally, the β -decay half-life of a nuclide is determined by measuring the number of decay events in a series of consecutive time intervals (channels) and presenting the results as a function of elapsed time in the form of a histogram known as the decay spectrum. In the *histogram analysis* that follows, the half-life is evaluated based on the known time-dependence of the event rate expected under ideal conditions (i.e., in the absence of the detection system's dead time), as described by a function that will be denoted by ρ and referred to as the *ideal rate function*. For example, in the case of a single-component decay in the presence of a constant background B ,

$$\rho = A \exp(-\lambda t) + B, \quad (1)$$

where A is the initial ideal rate (at time $t = 0$) in the absence of background, and

$$\lambda = \ln(2) / T_{1/2} \quad (2)$$

is the nuclide-specific decay constant, which is related to the nuclide's half-life $T_{1/2}$. In this report it is assumed that the system's detection efficiency does not depend on ρ . Specifically, in the *maximum-likelihood* method of histogram analysis, the best estimates of the parameters A , $T_{1/2}$, and B are taken to be those that maximize the resulting probability of obtaining the actual β -decay spectrum as a result of a measurement.

In high-precision work, there are three major disadvantages of histogram analysis. The first one is related to the fact that ρ changes as a function of time within each channel. Although this effect can be easily accounted for under ideal conditions, it cannot be otherwise: the statistics of actual events are distorted by the unavoidable presence of the detection system's dead time. All theoretical results that are relevant and apply under these circumstances have been derived assuming that ρ is constant. While the range of ρ values within a channel can be limited by decreasing the channel width, ρ varies by about 3 % per channel in typical measurements (for various technical reasons).

The second major disadvantage of histogram analysis is related to the fact that the probability (on which the maximum-likelihood method is based) of obtaining the measured number of events in a given channel, can be calculated exactly (based on ρ) only under ideal conditions. In the presence of a fixed non-extendable dead time this is possible only if ρ is constant. The theoretical results for other conditions (including the case of a fixed extendable dead time) are not available. Furthermore, the actual dead time is not likely to be fixed and non-extendable, and it is not even likely to be accurately predictable [1]. In a typical attempt to work around this problem, a known fixed non-extendable dead time is inserted in the detection system (preferably at an early stage) before the measurement starts. This dead time is set to be dominant, so that other contributions to the detection system's dead time are expected to become negligible. Consequently, only the dominant dead time is considered in the analysis. The remaining

problem is that the dominant dead time should be set to a minimum effective value, which is hard to predict. Therefore, the measurements must be repeated with different values of the dominant dead time in order to examine their effect on the results. However, even if it is found that an increased dominant dead time does not change the best estimates of the parameters of ρ (within their statistical uncertainties), that does not imply that the detection system's dead time can be accurately described as being fixed and non-extendable, and for high counting rates does not justify basing the analysis on this assumption. One way of mitigating this deficiency is to reduce the β -decay rate enough to make the uncertainties of the dead-time corrections negligible. However, in that case, the number of events in the spectrum is reduced, so that the measurements have to be repeated in order to reduce the uncertainty of the results, which increases the time it takes to complete the measurements and the analysis.

The third major disadvantage of histogram analysis is related to the required numerical accuracy and the desired speed of the calculations involved. Both issues become critical when the dead-time effect is significant and the number of counts in a single channel is relatively high (more than 1,000). This problem can be reduced by decreasing the channel width and/or by decreasing the β -decay rate.

With the TDC-based data acquisition system [1], the arrival time of each β -decay event is measured individually, and so the β -decay spectra can be constructed on-line or off-line, using any chosen value for the channel width. This chosen value can be set as low as needed in order to sufficiently reduce the effect of rate change within each channel and the numerical error in the calculations. Likewise, the effect that the dominant dead time would have if inserted at the final stage of event-detection can be simulated by software, which eliminates the need to insert the dominant dead time by hardware as well as the need for repeated measurements at different dominant dead times.

Ultimately, taking advantage of the available individual event timing information provided by the TDC-based system [1], the data can be analyzed event by event, without the need to construct the β -decay spectra (except for the sake of visualization). This report describes the principles behind such an analysis as well as some of the results. The method proposed here will be referred to as *event analysis*.

To begin with, let us assume that ρ is constant and that the conditions are ideal. In this case, based on Poisson statistics, the probability dp that an event occurring at time zero will be followed by the next event in the time interval $[t, t + dt)$ is given by

$$dp = P_0 \rho dt, \tag{3}$$

where

$$P_0 = \exp(-\rho t) \tag{4}$$

is the probability that no events occur in the time interval $[0, t)$, while ρdt is the probability that an event occurs in the time interval $[t, t + dt)$. Therefore,

$$dp = \exp(-\rho t) \rho dt. \tag{5}$$

If ρ is not constant, then eq.(4) must be generalized, so that, exactly,

$$P_0 = \exp(- \langle \rho \rangle t) , \quad (6)$$

where

$$\langle \rho \rangle = \frac{1}{t} \int_0^t \rho dt \quad (7)$$

is the average value of ρ over the time interval $[0, t)$. Accordingly, eq.(5) becomes

$$dp = \exp(- \langle \rho \rangle t) \rho_t dt , \quad (8)$$

where ρ_t is the value of ρ at time t .

In the presence of a known detection system's dead time per pulse τ , eq.(8) becomes (exactly)

$$dp = \Theta(t - \tau) \exp[- \langle \rho \rangle_\tau (t - \tau)] \rho_t dt , \quad (9)$$

where

$$\langle \rho \rangle_\tau = \frac{1}{t - \tau} \int_\tau^t \rho dt , \quad (10)$$

and $\Theta(t - \tau)$ is the Heaviside (unit-step) function.

The goal of data analysis is to determine the best estimates and uncertainties of the parameters of ρ . In event analysis, this is accomplished by choosing time zero at the time of detection of the first β -decay event and calculating, for each event i , the time $\Delta t_i = t_i - t_{i-1}$ elapsed since the previous event ($i-1$). Here i ranges from 2 to the index N of the last event in the current measurement cycle. This is followed by calculating the quantity W , which is proportional to the probability that the entire set of time differences Δt_i ($i = 2, \dots, N$) is measured as it was, using

$$W = \prod_{i=2}^N \rho_{ii} \exp[- \langle \rho_i \rangle_{\bar{a}} (\Delta t_i - \tau_i)] . \quad (11)$$

Note that the Heaviside functions were left out because, for real events and correctly determined dead times, their values must always equal 1. Finally, the parameters of ρ are varied iteratively in order to minimize the quantity E , defined as the natural logarithm of W multiplied by -2, i.e.,

$$E = -2 \sum_{i=2}^N [\ln(\rho_{ii}) - \langle \rho_i \rangle_{\bar{a}} (\Delta t_i - \tau_i)] . \quad (12)$$

In each iteration, the value of ρ can be calculated for any instant and its average value can be calculated for any time interval based on the current values of its parameters. The error of any parameter

of ρ can be calculated as the square root of the corresponding diagonal element of the inverse of the Hessian matrix of E .

For a fixed non-extendable dead time per pulse, τ does not depend on i , so its index can be dropped, while for the case of a fixed extendable dead time, eq.(9) must be replaced by the corresponding expression that applies to that case and eqs.(11-12) must be modified accordingly.

One way of assessing the quality of the results is to construct the histograms (β -decay spectra) of the measured events, compare them with the predictions based on the best estimate of ρ , and then proceed using the methods of histogram analysis. This has been done in order to compare the results of the event analysis with those of the histogram analysis for an extensive set of simulated ideal data on which a fixed non-extendable dead time was imposed. It was found that the two sets of results are identical for all practical purposes. However, the event analysis was found to be faster by a factor of 6. Also, using simulated data, the event analysis was confirmed to produce the expected results at high counting rates (more than 100,000 per second), and in the case of fixed extendable dead time.

In addition, the data collected using the TDC-based system and subject to the event analysis offer

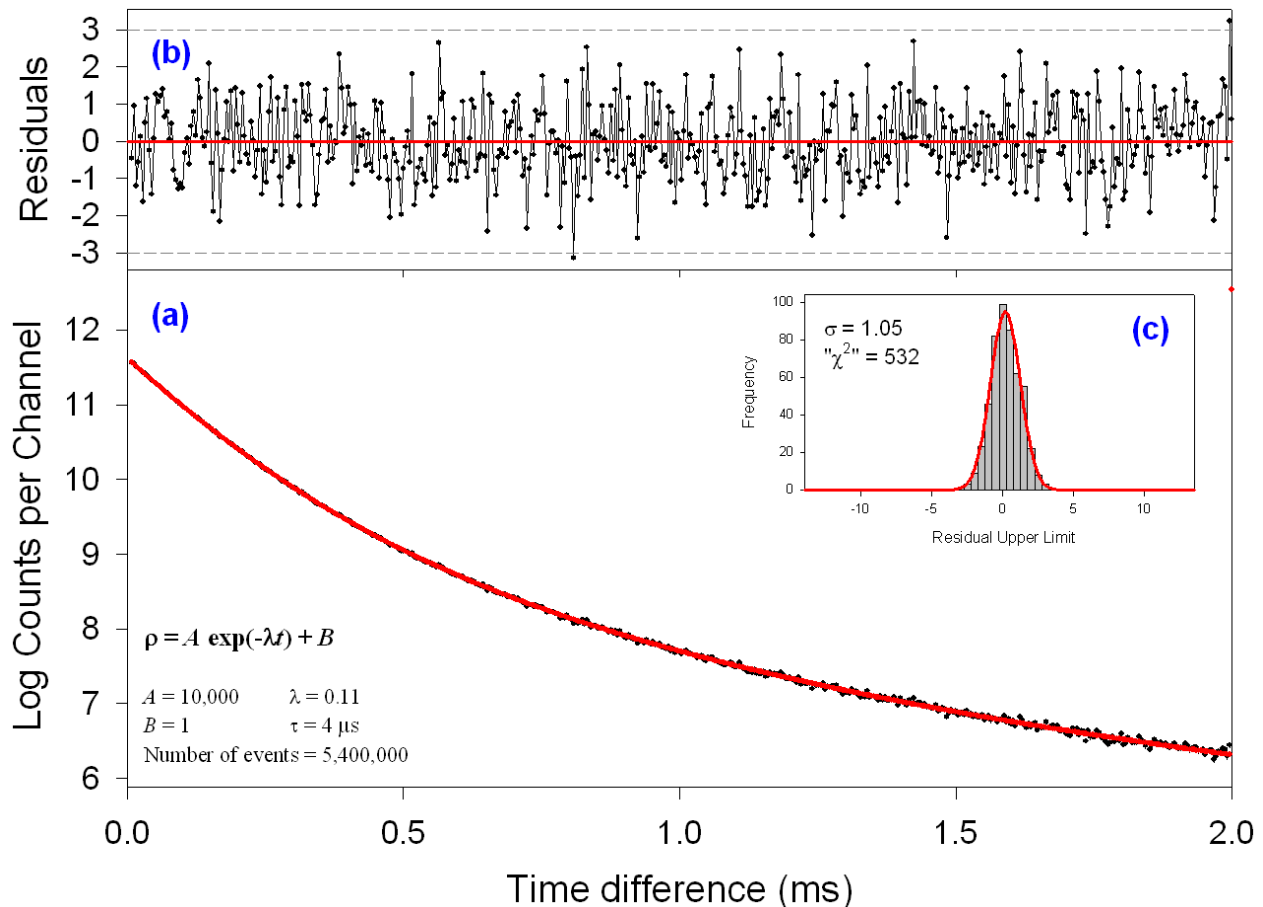


FIG. 1. (a) Time-difference spectrum (shown by black circles) of simulated ideal data to which a fixed non-extendable dead time of $4 \mu\text{s}$ was imposed. The red circles represent the values predicted based on ρ (as defined in the text). The last data point includes the contribution for all the events with time-difference exceeding 2 ms. (b) Spectrum of the residuals. (c) Histogram of the distribution of the residuals (shown by grey bars). The red line represents the best-fit Gaussian curve.

another method of result-quality assessment. Namely, the measured events can be used to construct a histogram of Δt values (i.e., the Δt spectrum, or the time-difference spectrum), and the result can be compared with the prediction based on the best estimate of ρ . By looking at the spectrum and the distribution of the residuals, it is possible to assess whether the predicted Δt spectrum provides an accurate description of the measured Δt spectrum for all values of Δt . If this is not the case, the assumed parameterization and time-dependence of ρ , as well as the assumptions regarding the nature and extent of the dead time must be questioned. As an example, results of the event analysis of a set of simulated ideal data with a fixed non-extendable dead time imposed on them are shown in Figure 1. Here it should be noted that the measured Δt spectrum was not fitted in the analysis. Instead, the predicted Δt spectrum was calculated based on ρ , where the best estimates of its parameters were obtained by minimizing the function E of eq.(12).

[1] V. Horvat and J.C. Hardy, *Progress in Research*, Cyclotron Institute, Texas A&M University (2010-2011), p. V-51.

TAMUTRAP facility status report

R.S. Behling, B. Fenker, M. Mehlman, D. Melconian, and P.D. Shidling

Significant progress has been made toward the completion of the Texas A&M University Penning Trap facility (TAMUTRAP). TAMUTRAP is a new ion trap facility dedicated to the study of fundamental symmetries of the weak interaction and for providing a low-energy radioactive ion beam (RIB) for various other applications. Electrostatic transport elements and a gas-filled radio frequency quadrupole (RFQ) Paul trap are planned to achieve efficient transport and preparation of the beam for the measurement trap. The design requirements of the TAMUTRAP beam line are twofold: first, the beam must be transported efficiently from the distribution point of the heavy-ion guide to the Penning trap system; second, the beam must be prepared in such a way that it can be accepted by the Penning trap, *i.e.* it must be bunched and have a low emittance (narrow energy, angular, time-of-flight and spatial distributions).

Initial simulations were performed with the SIMION ion trajectory simulation software¹. After this, mechanical designs were detailed using the 3D CAD software Autodesk Inventor as shown in Fig. 1. These models were optimized within the framework of the existing cyclotron facilities to ensure that the final design would be feasible in terms of space constraints and assembly. Following is a brief description of the beamline, highlighting several central components.

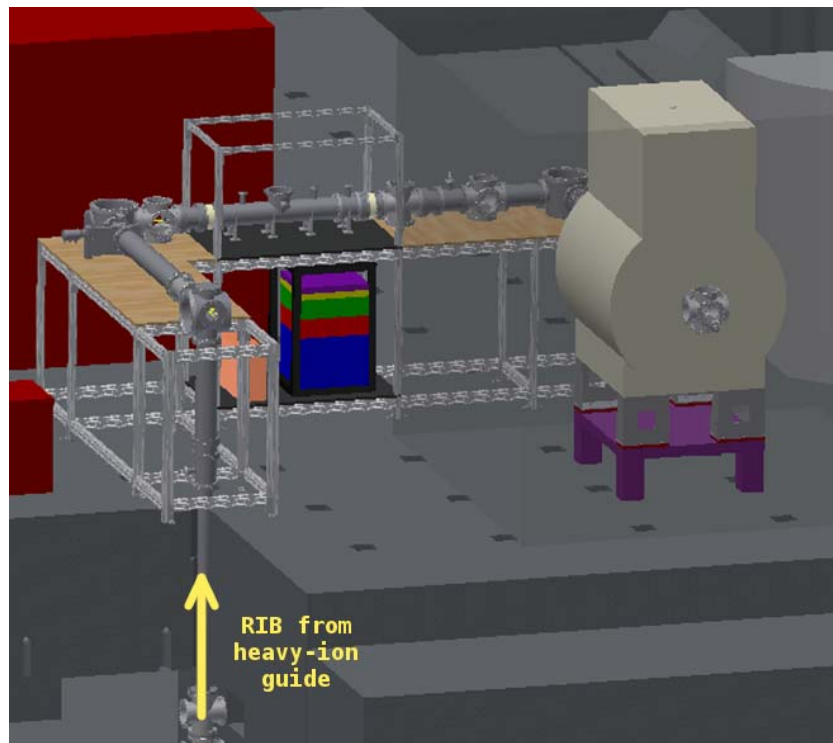


FIG. 1. 3D design of the TAMUTRAP facility.

¹ SimION—Industry standard charge particle optics simulation software (<http://simion.com>).

Upon leaving the high voltage platform of the heavy-ion guide, the radioactive ion beam (RIB) will be accelerated to 10-15 keV for transport up through the TAMUTRAP beamline. The RIB will be guided vertically by an x-y electrostatic steerer and a 3 electrode Einzel lens (a CAD drawing of this component is shown in Fig. 2).

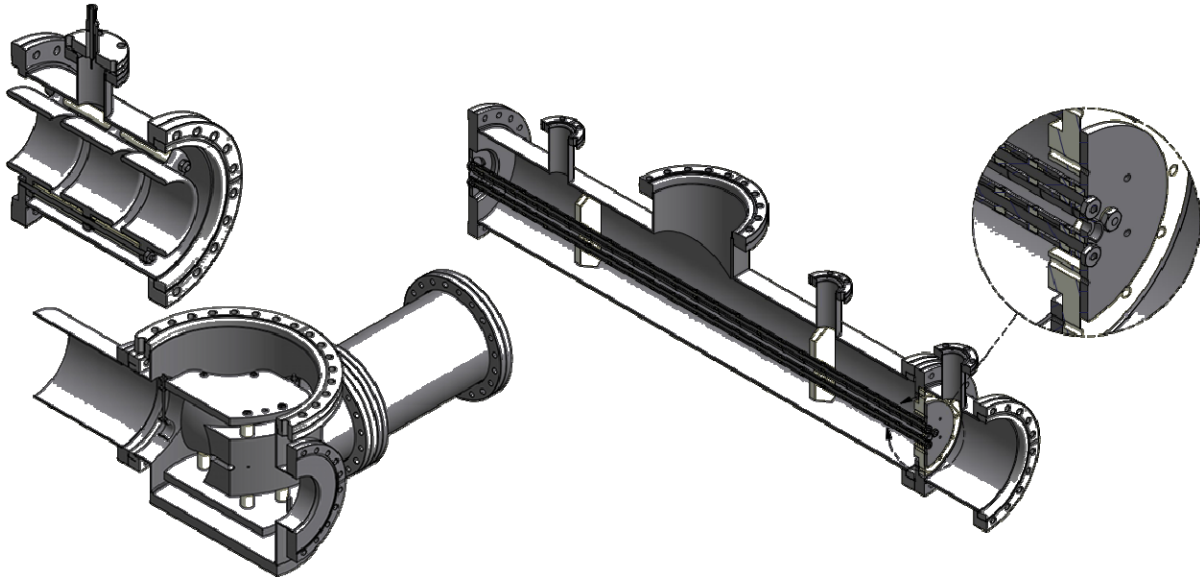


FIG. 2. CAD drawings of some of the beamline components of TAMUTRAP: an Einzel lens in a 3-electrode configuration (top-left); the spherical deflector with through holes in the outer electrode (bottom-left); and the gas-filled RFQ Paul trap used to cool and bunch the radioactive ion beam (right).

Once through the shielding blocks, which separates the heavy-ion guide system from the high bay experimental area, the RIB will undergo a 90° bend achieved by a spherical deflector (also depicted in Fig. 2). The outer electrode of the deflector has been designed with through holes along each beam axis such that it can also be used as a switchyard in the absence of an applied voltage. This feature also provides the ability to inject an offline ion source into the beam line. In addition, the through holes will aid optical alignment of the beam pipe. Following the 90° bend, the RIB will be guided in the horizontal direction using an additional x-y steerer, lens, and diagnostic section, before reaching a second 90° deflector.

After the 2nd deflection, the ion beam will be collinear with the axis of the RFQ cooler/buncher, which is depicted in Fig. 2. The beam will pass through a vacuum station and be reduced to several eV kinetic energy by specifically designed decelerating optics. The last element of these optics is situated on a high-voltage platform, which is held at a potential slightly below the beam energy. The beam will be bunched and cooled in a gas-filled RFQ Paul trap, which will be operated at room temperature with a gas pressure ranging from 10^{-2} to 10^{-4} mbar of ultra-pure helium. Simulations indicate that the bunched beam will have an energy spread of 5-10 eV and a time spread of 1.0-1.5 μ s upon exiting the high-voltage platform, and will be further guided by an x-y steerer and Einzel lens. The RIB will then enter the first pulsing cavity which is held at a potential that results in the kinetic energy of the beam being lowered to ≈ 2.7 keV. While it is within this cavity, the voltage on the electrode will be switched to ground, resulting

in a final beam kinetic energy of ≈ 2.7 keV relative to the beam pipe. The bunched beam will then be deflected by 90° for a final time in order to become collinear with the Penning trap axis. After encountering an additional Einzel lens, x-y steerer, and a diagnostic/pumping station, the beam energy will be lowered to a few tens of eV relative to ground by a second pulsing cavity. As the beam enters the magnet, it will become confined radially due to the ions' Larmor precession within the 7T magnetic field, and will be ready for subsequent loading in the Penning trap.

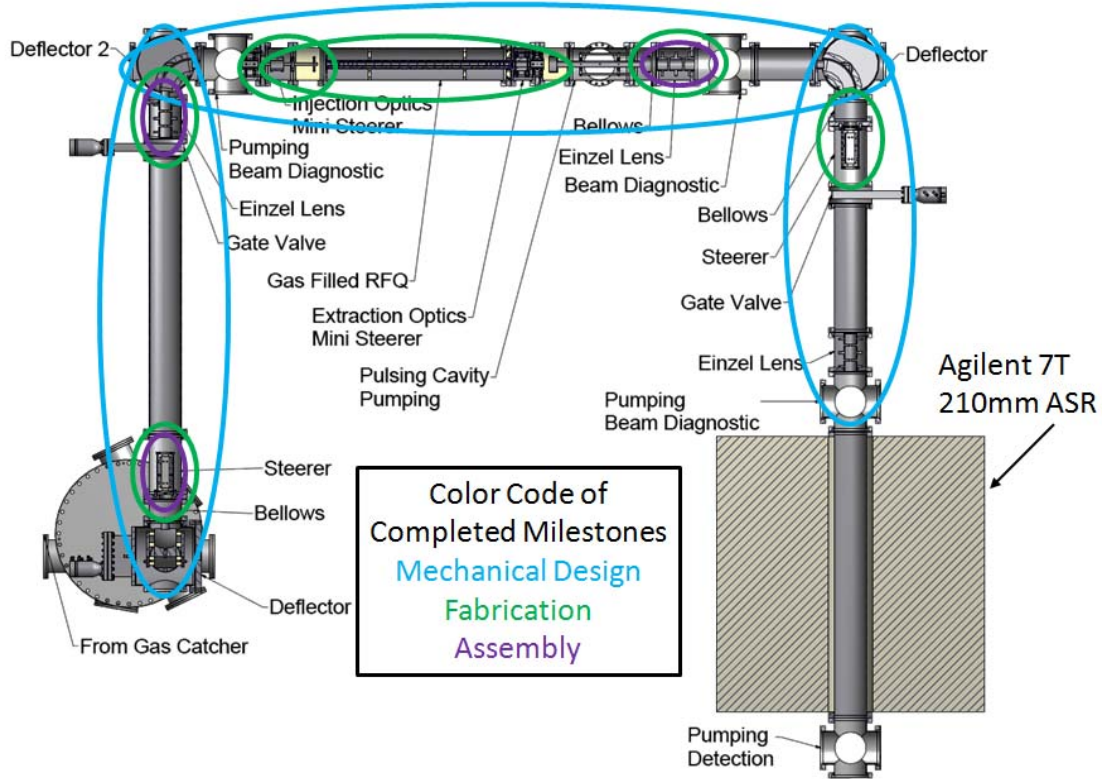


FIG. 3. Current progress towards completion of the TAMUTRAP beamline.

Fig. 3 highlights the current progress of the TAMUTRAP beam line that has been described. Geometrical optimization in SIMION and mechanical designs using Autodesk Inventor has been completed for the entire beam line up to the entrance of the Penning traps. Mechanical drawings have been finalized and submitted to different sources for fabrication, including our in-house machine shop. Fabrication has been completed on several Einzel lenses, beam steerers, and all elements composing the RFQ. Additionally, many standard vacuum components such as crosses, bellows, and beam pipe have been purchased and are ready for installation. A custom beam support and mounting table has been designed and installed using extruded aluminum profiles. Photos of several assembled components can be seen in Fig. 4.



FIG. 4. Pictures of some completed beamline components: an Einzel lens (left), the x-y steerer (middle) and the chamber for the RFQ (right).

In addition to beam line hardware, progress has been made on several critical systems. A pressure maintenance controller for the gas-filled RFQ has been characterized, and many of the high-voltage electronics have been specified and tested. Electronics for the RFQ have been developed and tested. The power supplies necessary for the beam elements are in place. The immediate outlook for the TAMUTRAP facility involves continued assembly of the beam line and its constituent elements. Initial placement and alignment of components at their final locations will begin within this year.

Upgrade of the ^{37}K asymmetry measurement experiment

R.S. Behling, B. Fenker, M. Mehlman, D. Melconian, and P.D. Shidling

Over the past year, we have continued working to upgrade the experimental apparatus to prepare for a measurement of the β -asymmetry in the decay of ^{37}K . The new ultra high vacuum (UHV) chamber that will house the experimental setup is now complete and has been attached to the TRINAT beam line at TRIUMF in preparation for the upcoming experiment. We are also currently developing a new data acquisition scheme that will accompany the new nuclear detectors described last year. In addition, we have improved our theoretical model of the optical pumping process that polarizes the trapped ^{37}K atoms, allowing a more precise determination of the degree of nuclear polarization. We plan to complete a short trial run of the experiment in October 2012 in fulfillment of a TRIUMF prerequisite to installing a dedicated TiC target for our experiment in December 2012.

With the new chamber in place, we have begun installing further components of the apparatus inside and around the chamber. The completed chamber is shown in Fig. 1 prior to its installation on the TRINAT beam line. Specifically, we have finished fabricating a series of electrostatic hoops that are

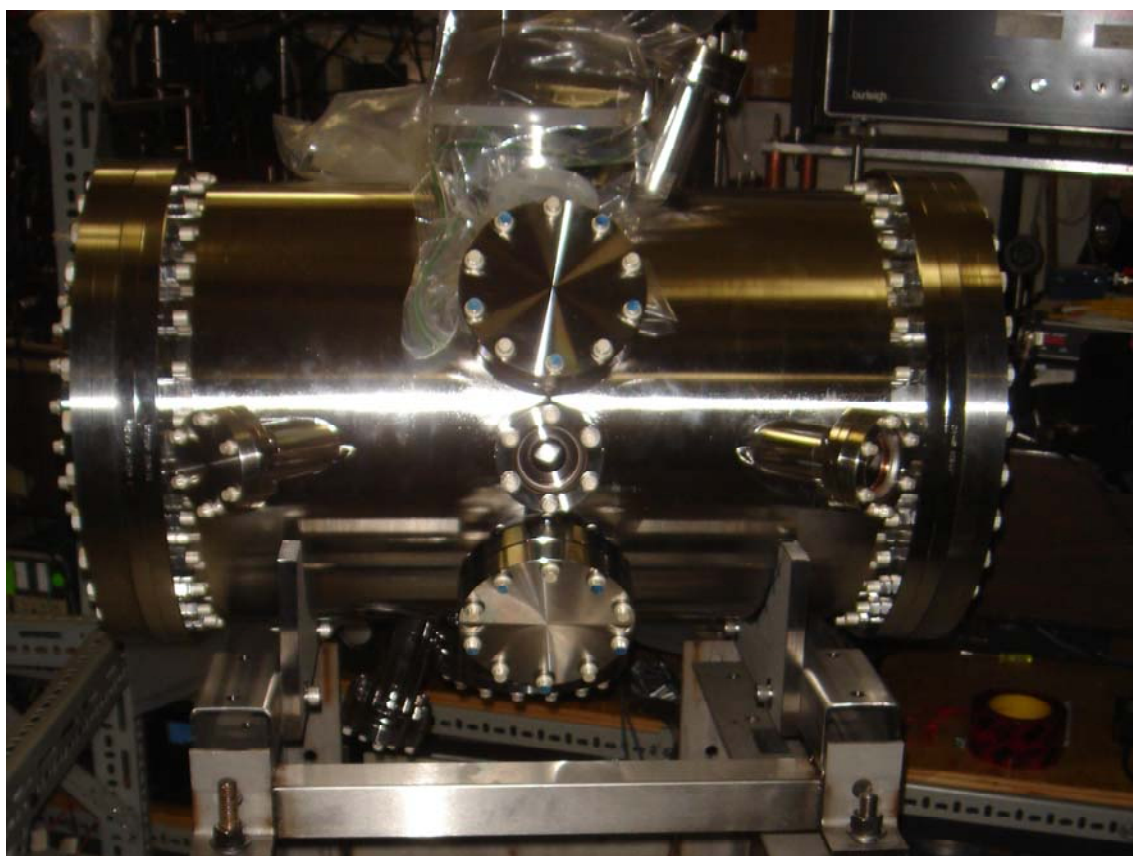


FIG. 1. The UHV chamber before being attached to the beamline. The various ports on the exterior accommodate the laser setup, detector electronics and vacuum requirements.

designed to establish a constant electric field while staying out of the likely path of recoiling ions as much

as possible. These hoops are made from glassy carbon and had to be entirely machined on an electron discharge machine because the material is too brittle to withstand traditional machining. We have also installed a set of Helmholtz coils inside the chamber as depicted in Fig. 2. These coils will be operated in the Helmholtz arrangement to produce a constant magnetic field at the trap location, lifting the degeneracy of the magnetic sublevel energies and allowing efficient optical pumping. They will also be operated with current flowing in an anti-Helmholtz arrangement to produce a quadrupole magnetic field, which is necessary for the magneto-optical trap (MOT) to operate. At this point, we have tested the coils in both the Helmholtz and anti-Helmholtz arrangements, and have also successfully tested our ability to efficiently switch from one mode to the other. We have also completed work on the UHV feedthroughs that will carry our MCP signals out of the vacuum chamber. These feedthroughs have been custom designed to satisfy the requirements that the MCP be floated at 10 kV, operate in a UHV setting and have a characteristic impedance of 50Ω to avoid reflecting the signal. We have also recently installed the necessary flow meters and pumps to run cooling water into our magnetic field coils and have also begun the task of installing and aligning all of the optics necessary for the trapping and optical pumping of the ^{37}K .

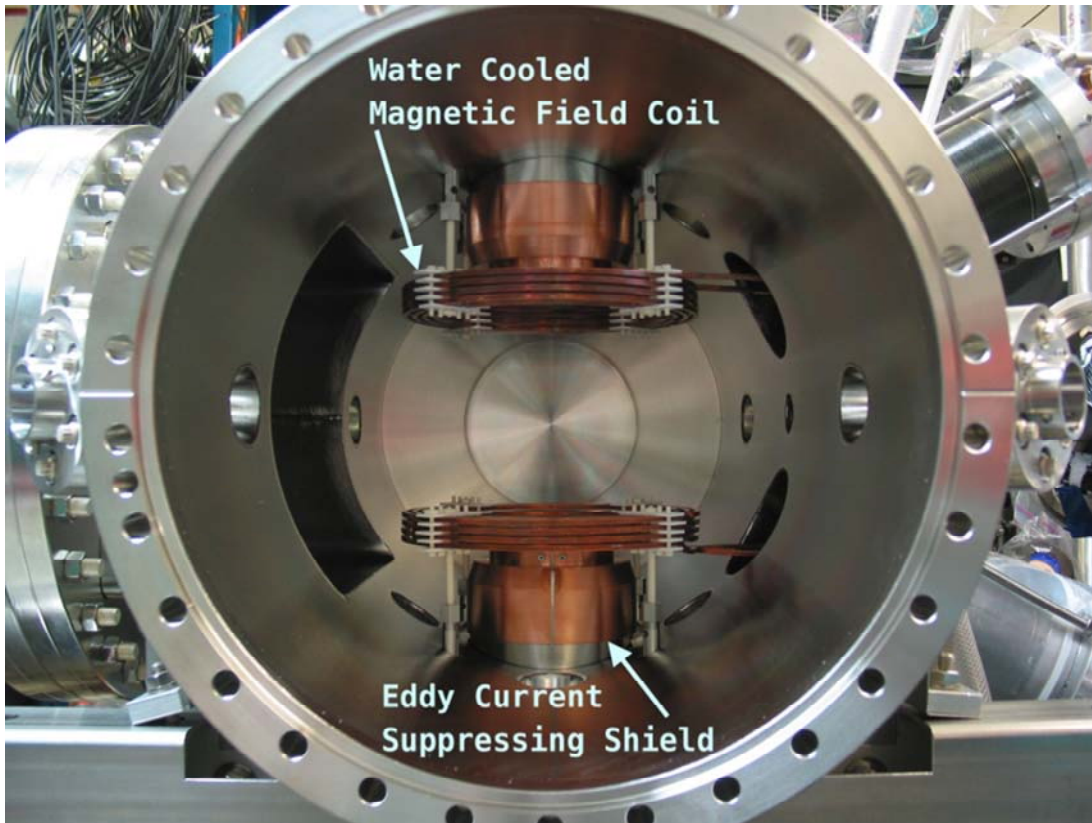


FIG. 2. The chamber with the magnetic field coils installed and the eddy current suppressing shields covering the detector ports and mirror mounts. It became apparent that these shields would be needed after testing the AC-MOT power dissipation from the oscillating magnetic field caused the mirror mounts to heat to 40°C while the thinner beryllium foils remained at 21°C . This large temperature gradient could stress and break the delicate diffusion bond between the stainless steel and beryllium. With the shields in place we saw no measurable heating.

The data acquisition plan for this experiment has now been fully developed and most of the

necessary modules acquired. Currently we have built a parallel test setup that allows us to take data from our strip detectors and digitize the signals with a VF48 digitizer that was developed by the DAQ group at TRIUMF. The firmware has been programmed in the module so that if any one of the strips is above a global threshold the module will send a logic signal to a NIMIO32 module that handles coincidence conditions between the front and back of the silicon detector. The NIMIO32 module has multiple slots that can be easily be programmed and will eventually handle the coincidence signals between the strip detector and scintillator.

We have also begun developing a more complete theoretical model for the optical pumping process that is responsible for polarizing the ^{37}K nuclei. The idea of optical pumping is to use circularly polarized light to manipulate the Zeeman sublevel populations, and through the hyperfine coupling of the atomic and nuclear angular momentum, attain both atomic and nuclear polarization. Previously, a phenomenological rate-equation approach has been used to model the optical-pumping process. However, this approach is essentially semi-classical in nature and neglects quantum coherences between atomic states. To account for these effects, we have developed a model using the full density matrix formalism that accounts for quantum coherences and provides a more realistic physical description of the optical-pumping process. The improved model will allow a more precise determination of the polarization of the sample and reducing an important systematic uncertainty from previous experiments.

In the coming months, we plan to complete work on the data acquisition system as well as install the silicon strip detectors and scintillators in the new vacuum chamber. With this complete we will test off-line the new components of the experiment including the new AC-MOT, detectors, and data acquisition hardware and electronics. We have scheduled a short test run in Oct. 2012 as a final test of the apparatus, and a longer production run in December 2012.

TAMUTRAP—Design of the cylindrical Penning trap system

R.S. Behling, B. Fenker, M. Mehlman, D. Melconian, and P.D. Shidling

The initial experimental program for the Texas A&M University Penning Trap facility (TAMUTRAP) will be centered on measuring the beta-neutrino correlation parameter, $a_{\beta\nu}$, in $T=2, 0^+$ to 0^+ superallowed β -delayed proton decays. In these experiments, $a_{\beta\nu}$ will be determined by observation of the proton energy distribution, which imposes three primary constraints on the design geometry of the apparatus: (i) the trap must provide a cold (few tens of eV), spatially localized source of ions with a minimal spread in time and energy; (ii) the geometry must allow for the full containment of the primary decay products of interest, in this case protons and positrons, which is facilitated by the Larmor precession of the particles within the trapping magnetic field; and (iii) provision should be made for flat disk-shaped position sensitive detectors held at arbitrary voltage to be placed at the ends of the measurement trap in order to detect the decay products.

In addition, the design of the TAMUTRAP facility has been optimized for precision mass measurements which requires that the trap geometry be both “tunable” and “orthogonalized” [1]. A quadrupole electric field is required for such measurements since the mass is related to the measured frequency of oscillation by the strength of the quadrupole component of the electric field. The geometry of a tunable trap includes compensation electrodes in order to produce the required quadrupole electric field at the trap center. An orthogonalized trap is one which employs a geometry in which adjustment of the voltages on the compensation electrodes does not affect the amplitude or shape of the quadrupole component of the electric field.

Additional measurement-independent constraints are also placed on the design of the trap geometry. The electrodes must be able to be machined and assembled taking into account real world fabrication precision. Furthermore, spacing should be allotted to prevent sparking between electrodes held at different voltages. And, finally, the entire trap must fit within the 210-mm diameter bore of the existing solenoidal magnet.

Calculated dimensions:

- Ring: 1.15×2 cm
- Compensation: 8.423 cm
- Endcap: 8 cm
- Gaps: 0.05 cm
- Radius: 9 cm

Calculated tuning ($C_4=0$)
condition: $V_c/V_o = -0.37088$

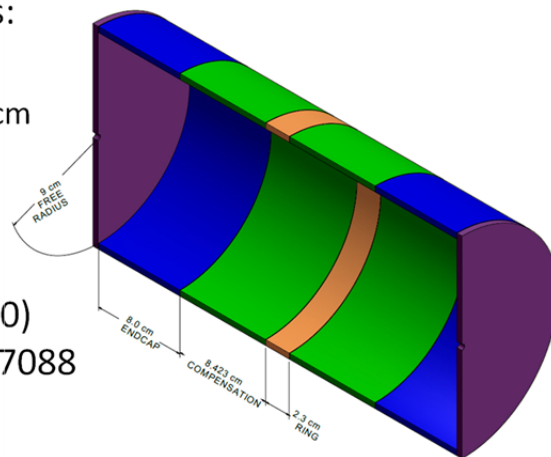


FIG. 1. Geometry of the large-bore cylindrical measurement trap.

Taking into account these constraints, the TAMUTRAP Penning trap system incorporates two cylindrical Penning traps within a large-bore superconducting solenoidal magnet having a field strength of 7 T. The first “purification” trap is similar to ISOLTRAP, and will be used optionally to further purify the incoming ion beam. The second “measurement” trap employs five electrodes with an inner radius of 90 mm. Since no existing Penning trap design could be modified or scaled to fulfill the design constraints for the measurement trap, the geometry was calculated from first principles. Using electrostatic techniques, an analytic description of a cylindrical, five electrode Penning trap of any electrode dimensions including gaps between electrodes, with endcaps of arbitrary voltage (to approximate detectors) was determined. Expanding the resulting potential at the trap center in Legendre polynomials and identifying the quadrupole term, the geometry was made both tunable and orthogonal. The trap design is shown in Fig. 1, and a cross section including the resulting field lines and the corresponding expansion coefficients can be found in Fig. 2. The 90 mm free radius of the measurement trap will be the largest of any existing Penning trap.

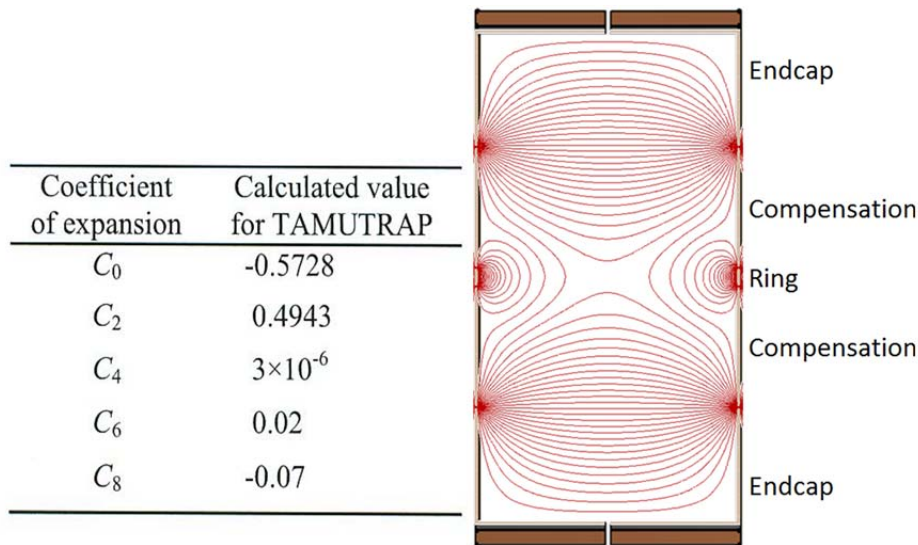


FIG. 2. Values of non-zero expansion coefficients (left) and a cross-sectional view of the measurement trap geometry with field lines superimposed (right).

[1] G. Gabrielse, L. Haarsma and S. Rolston, *Int. J. Mass Spectrom. and Ion Processes* **88**, 319 (1989).

Source specific neutron detection efficiencies of the TAMU Neutron Ball

Andrew Zarrella, P. Marini, A.B. McIntosh, P. Cammarata, L. Heilborn, J. Mabilia, L.W. May,
A. Raphelt, and S.J. Yennello

The NIMROD-ISiS detector array has been used to study the symmetry energy contribution to the nuclear equation of state [1,2]. The energy of nuclear matter can be represented as the sum of two terms, shown below, the first corresponding to the energy of symmetric nuclear matter and the second corresponding to the energy due to the asymmetry of the matter [3].

$$\frac{E}{A}(\rho, I) = \frac{E}{A}(\rho) + \frac{E_{sym}}{A}(\rho)I^2 \quad (1)$$

In equation 1, E_{sym} is the symmetry energy, I is the isospin ($I = \frac{N-Z}{A}$) and ρ is the density. In order to constrain the effects of the symmetry energy, we need to be able to study nuclear matter away from normal nuclear densities. Many experimental analyses of nucleus-nucleus collisions have relied on precise reconstruction of the Quasi-Projectile (QP) – the highly excited, forward-moving remnant of the projectile immediately after the reaction. By studying these QP's we can access the properties of exotic forms of nuclear matter at lower-than-normal nuclear densities. As shown in Fig. 1, for a QP with a given Z there is a distribution of masses.

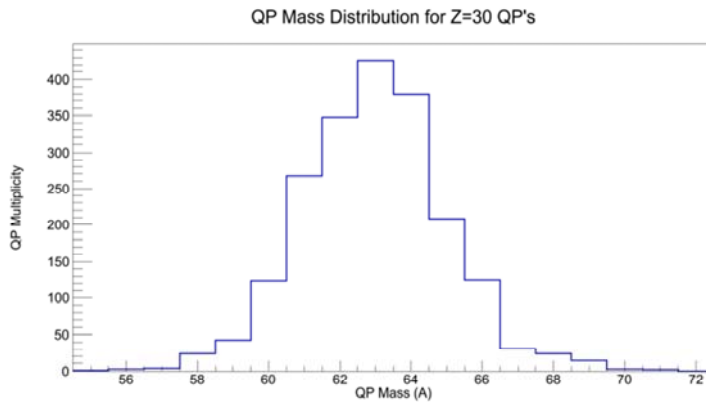


FIG. 1. HIPSE-SIMON simulation results for a $^{70}\text{Zn} + ^{70}\text{Zn}$ reaction at 35 MeV/nucleon beam energy. For QPs with a fixed Z ($Z=30$ is shown in the figure), there is a distribution of masses. On the y-axis is the QP multiplicity and on the x-axis is the QP mass. The QP's are determined by a sum over charged particle fragments and free neutrons that we associate with the QP using velocity cuts.

Because of this QP mass distribution, it is important to know how many neutrons to associate with the QP during reconstruction. Using the Neutron Ball which surrounds the NIMROD-ISiS array, we can measure the event-by-event number of neutrons. An estimate of the number of neutrons emitted from

the QP, though, requires source-specific neutron efficiencies. In order to accomplish this, we utilized the HIPSE (Heavy-Ion Phase Space Exploration) [4] event generator with the SIMON [5] statistical deexcitation code in conjunction with a software filter which simulates the geometric and energetic restrictions of the Neutron Ball. HIPSE is especially suited for this project due to its ability to keep track of the sources of all emitted particles.

Table I and Fig. 2 below give source-specific neutron detection efficiencies obtained using HIPSE-SIMON for the reaction $^{86}\text{Kr} + ^{64}\text{Ni}$ at 35 MeV/nucleon. This is a system for which there is NIMROD experimental data already and on which QP reconstruction has been performed. The source numbers are defined in the first column of the table.

Table I. Source-specific neutron detection efficiencies. These efficiencies were produced using the data from Fig. 2.

Source	Source Number	Efficiency
Fusion	0	70.96%
QP	1	78.11%
QT	2	64.51%
IMFs	3	70.36%
	4	70.57%
	5	70.84%
	6	70.66%
	etc	71.00%
	total	72.17%

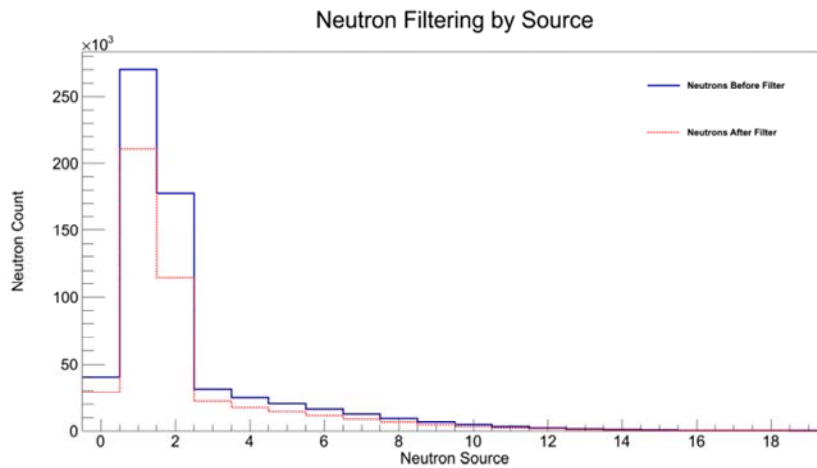


FIG. 2. Source specific neutron yield before and after the neutron filter.

Once we have the neutron efficiencies they can be used to find an estimate for the total number of neutrons emitted from the QP given the total number of neutrons measured and the following equation [1]:

$$n_{\text{det}} = n_{\text{QT}} \text{eff}_{\text{QT}} + n_{\text{QP}} \text{eff}_{\text{QP}} + n_{\text{IMFs}} \text{eff}_{\text{IMFs}} \quad (2)$$

where n_{det} is the detected number of free neutrons in the event, $n_{\text{QT/QP/IMFs}}$ is the number of neutrons emitted by the QT/QP/IMFs, and the $\text{eff}_{\text{QP/QT/IMFs}}$ terms are the respective, source specific neutron detection efficiencies. By neglecting the IMF neutrons and simplifying the equation based on the approximation that the ratio of free neutrons from the QP to the free neutrons from the QT is equal to the ratio of neutrons in the projectile to neutrons in the target, it is possible to extract the approximate number of neutrons that should be associated with the QP during reconstruction [1]:

$$n_{\text{QP}} = \frac{n_{\text{det}}}{\frac{N_{\text{tgt}}}{N_{\text{proj}}} \text{eff}_{\text{QT}} + \text{eff}_{\text{QP}}} \quad (3)$$

Currently, we are working towards a complete description of the neutron detection and reconstruction process using symmetric reactions of ^{70}Zn , ^{64}Ni , and ^{64}Zn [2]. In this work, we are also comparing the HIPSE-SIMON results with CoMD, a dynamical model.

- [1] S. Wuenschel. Ph.D. Thesis, Texas A&M University 2009.
- [2] Z. Kholey. Ph.D. Thesis, Texas A&M University 2010.
- [3] V. Baran *et al.*, Phys. Rep. **410**, 335 (2005).
- [4] D. Lacroix *et al.*, Phys. Rev. C **69**, 054604 (2004).
- [5] D. Durand. Nucl. Phys. **A541**, 266 (1992).

SAMURAI TPC: detailed design and construction of a time projection chamber

A.B. McIntosh, J. Barney, J. Dunn, J. Estee, T. Isobe, M. Famiano, W.G. Lynch, T. Murakami,
R. Olsen, R. Shane, A. Taketani, M.B. Tsang, and S.J. Yennello

The detailed design and fabrication of a new time projection chamber, the SAMURAI TPC, has progressed rapidly, and continues to do so. The utility of the device and specifications have been previously described [1, 2]. The detailed designs have been posted online [3].

The fabrication of the enclosure, motion chassis and hoisting structure is completed; see photograph in Fig. 1. The fabrication of the top plate (a critical element) is also completed, as are the structural ribs mounted to it. The angle iron skeleton was welded together at the TAMU chemistry machine shop, including the load-bearing legs along the four vertical edges. After polishing the outer surfaces, we expect no difficulty sealing the gas volumes with an O-ring across the weld seams.



FIG. 1. Photograph of the SAMURAI TPC enclosure with motion chassis attached.

Imperfections in the surface (gouges, scratches) were filled in with Hysol epoxy, which was allowed to cure for 3 days before being sanded smooth with 600-grit sandpaper. The side plates, fabricated on the large mill at the NSCL Machine Shop, were shipped to TAMU. The hole pattern on these plates was used as a template to tap matching holes in the angle iron skeleton. These plates each have two dovetail O-rings grooves for 0.139" rope. Custom length vulcanized O-rings were procured inexpensively from American Packing. After lightly sanding the joints smooth, the O-rings were covered with Apiezon-M vacuum grease and inserted into the grooves. The motion chassis and hoisting structure were machined and welded at the TAMU Cyclotron Institute Machine Shop. The ribs, bars between 58" and 82" long,

were machined at the TAMU Wind Tunnel Machine Shop. These were assembled, checked for accuracy, and shipped to MSU to be assembled on the top plate, which was fabricated by Digitrace in Michigan. The parts for the cooling of the front-end electronics were also fabricated at the TAMU wind tunnel machine shop.

The assembled enclosure skeleton with side plates and the motion chassis, as well as the parts for the front-end electronics cooling system, were inspected by the US project manager at the May 2012 fabrication deadline, and received a highly favorable review. Testing of the manipulation of the TPC with the motion chassis and hoisting structure is underway; following completion of this, the entire enclosure, motion chassis and hoisting structure will be shipped to Michigan for mating with the top plate.

Fabrication of the field cage, wire planes, and pad plane is underway at Michigan State. Design of the readout electronics is underway at RIKEN. Testing of the front-end electronics is underway at Western Michigan and Michigan State. Fabrication of the target mechanism and simulations (detector response to ionizing radiation and track reconstruction) will commence shortly at TAMU.

[1] http://rarfaxp.riken.go.jp/RIBF-TAC05/10_SAMURAI.pdf

[2] A.B. McIntosh *et al.*, *Progress in Research*, Cyclotron Institute, Texas A&M University (2010-2011) p. V-33.

[3] <http://groups.nscl.msu.edu/hira/sep/sepwiki/doku.php/start>

On-line transactinide homolog chemistry

Megan E. Bennett and Charles M. Folden III

1. Introduction

Chemical studies of the transactinide elements ($Z > 103$) can help assess the influence of relativistic effects within the heaviest elements. It is expected that relativistic effects will result in deviation of periodic group trends [1]. To determine the extent of deviation and where the deviation begins, the chemical behavior of the heaviest elements should be compared to that of their lighter homologs that reside in the same periodic group.

Currently there are 6 facilities in the world, located at the Gesellschaft für Schwerionenforschung in Darmstadt, Germany; The Japan Atomic Energy Research Institute in Tokai, Japan; The Joint Institute for Nuclear Research in Dubna, Russia; The University of Oslo in Oslo, Norway; Lawrence Berkeley National Laboratory in Berkley, California, USA; and at RIKEN in Wako, Sairama, Japan, that allow for the chemical study of transactinide elements and their short-lived accelerator produced homologs. With the exception of the University of Oslo and Japan Atomic Energy Research Institute these facilities perform gas phase chemistry. This presents a worldwide need, in the field of transactinide chemistry, for the development of an additional facility for liquid phase chemistry. Texas A&M University Cyclotron Institute is working to fulfill this need. Recently, a state-of the-art, custom modular radiochemical laboratory was built at the Cyclotron Institute.

2. Customization and Compliance of Laboratory

The modular laboratory is customized with the following: 1) chemically resistant walling, flooring and ceiling 2) non-slip flooring 3) GFI rated outlets, lights and switches 4) isolated waste system with high level alarm, sampling and neutralization capability 5) completely washable interior 6) chemically resistant sink, basin and laboratory benches 7) HClO_4/HF compatible radiological fume hood 8) 3 phase 120/220 V electrical panel and wiring 9) climate control 10) movable via overhead crane, forklift or wheeling 11) auditory and visual fire alarm compliant with the State of Texas building code 12) OSHA and State of Texas compliant safety shower and eyewash 13) OSHA and State of Texas building code stairs 14) NRC compliant. The laboratory is movable due to space constraints within the cyclotron and to allow for 18-wheeler access to the MARS cave and the K500 high-bay. The laboratory is in the process of being installed. A picture of the laboratory can be seen below in Fig. 1.



FIG. 1. A picture of the new, custom, state-of-the-art modular radiochemical laboratory at Texas A&M University Cyclotron Institute.

[1] V. Pershina, *Chem. Rev.* **96**, 1977 (1996).

Heavy element targetry

Megan E. Bennett, Charles M. Folden III, and J.P. Greene

1. Introduction

It is of great interest to determine the chemical and physical properties of the transactinide elements ($Z > 103$). These studies can allow for assessment of the influence of relativistic effects on the properties of the heaviest elements, refinement of nuclear theory and to probe where the end of the periodic table may be [1].

The transactinide elements have such low cross sections (nb to fb) that they are produced on an atom-at-a-time basis. For elements produced an atom-at a-time ($Z > 100$) a thin target, 0.8 mg/cm^2 , is necessary to allow for the fused nuclei to recoil out of the target and be collected. The target is typically bombarded with a beam intensity of approximately 3×10^{12} ions per second. This beam and target combination result in a production rate of a few atoms per minute (Rf and Db production) to an atom every week or lower (upper transactinide elements) [2,3,4].

2. Targetry

Currently, in the world there are very few facilities that have the capability to produce customized thin targets by means other than electrodeposition. One of the facilities with such capabilities is the Target Laboratory at Argonne National Laboratory (ANL), which has an electron beam gun evaporator, thermal evaporators, and a rolling system, in addition to electrodeposition techniques. Due to the need of the Heavy Elements Group at the Texas A&M University Cyclotron Institute a collaboration with the Target Laboratory at ANL has been established. To date 4- $\sim 300 \text{ nm}$ $^{\text{nat}}\text{Ge}$ foils on $3 \text{ }\mu\text{m}$ Ti, 4- $\sim 300 \text{ nm}$ $^{\text{nat}}\text{Gd}$ foils on $3 \text{ }\mu\text{m}$ Ti and 4 mixed targets with $\sim 300 \text{ nm}$ each of $^{\text{nat}}\text{Ge}$ and $^{\text{nat}}\text{Gd}$ on $1 \text{ }\mu\text{m}$ Ti have been produced through this collaboration.

3. Rotating Target Wheel

Rotating target wheels are currently used at all 5 major transactinide accelerator facilities (LBNL, GSI, JINR, RIKEN, JAERI). The targets are typically an electrodeposited actinide with a backing of $1\text{-}5 \text{ }\mu\text{m}$ $^{\text{nat}}\text{Ti}$, are banana shaped, and rotate between 900-1700 rpm. The purpose of the banana shape is to maximize the amount of target exposed to the beam. The purpose of rotating a target is to assist in cooling the targets from long exposure to particle nanoamperes of heavy ion beam (typically ^{48}Ca). Recently, Texas A&M Cyclotron Institute has commissioned a similar rotating target wheel that can be used in the MARS spectrometer. The Cyclotron Institute rotating target wheel, while similar to those used at LBNL, GSI, JAEA, JINR and RIKEN had to be designed to rotate at pressures of 10^{-7} torr. LBNL, GSI, JINR and RIKEN all have separators where the pressure inside the target chamber is orders of magnitudes higher. In order to accommodate pressures of 10^{-7} torr a ferrofluidic flange is employed.

In addition to this, a fiber optic system has been installed to pulse the beam when the beam would interact with the target frame. A picture of the new rotating target wheel can be seen in Fig. 1.

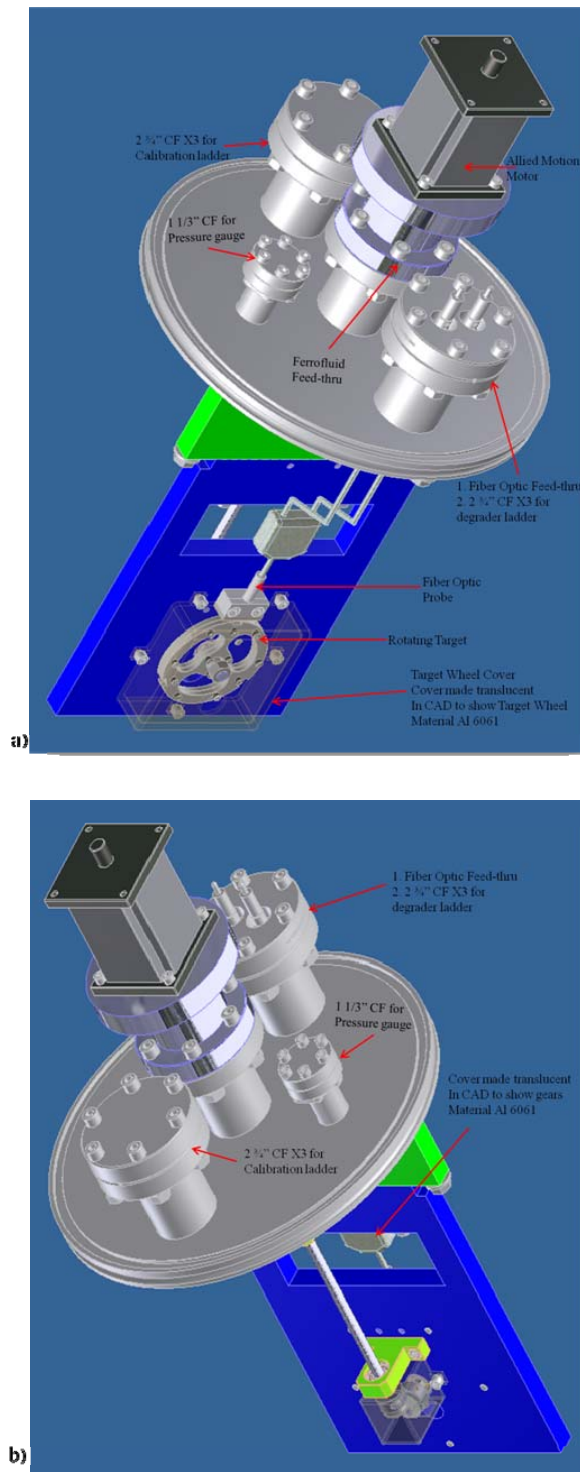


FIG. 1. Texas A&M Cyclotron Institute’s Heavy Elements Group’s new rotating target wheel. The rotating target wheel has been ordered from Ferrortec and is expected to be delivered in August of 2012.

- [1] V. Pershina, *Chem. Rev.* **96**, 1977 (1996).
- [2] G.T. Seaborg, W.D. Loveland, *The Elements Beyond Uranium*, (John Wiley & Sons, Inc.: United States of America, 1990).
- [3] M. Schadel, *The Chemistry of Superheavy Elements*, (Kluwer Academic Publishers: Boston, 2003).
- [4] M. Schadel, *Chemistry of superheavy elements*, *Angew. Chem. Int. Ed. Engl.* **45**, 368 (2006).

AstroBox – a new type of low energy proton detector

L. Trache, E. Simmons, A. Spiridon, M. McCleskey, B.T. Roeder, R.E. Tribble, E. Pollacco,¹

G. Pascovici,² Marc Riallot,¹ Jean Philippe Mols,¹ and Mariam Kebbiri¹

¹IRFU, CEA Saclay, Gif-sur-Yvette, France

²Institut fuer Kernphysik der Universitaet zu Koeln, D-50937 Koeln, Germany

We have recently started collaboration with CEA Saclay and IKP Koln on a new detector for very low energy protons from beta-delayed proton decays. This was motivated by results obtained in an ongoing study of such decays relevant for nuclear astrophysics. Previously the study was done with a setup of Si detectors [1]. In an effort to lower the beta background in the 100-400 keV region and increase the energy resolution we designed the AstroBox, a detector based on a gas medium and Micromegas [2].

The first test was done in March 2011 with a beam of ^{23}Al . A detailed description of the experiment and the detector is given in the corresponding report [3]. We obtained a significant reduction of the beta background. The low energy proton peaks detected were well separated and had good resolution (**Error! Reference source not found.**).

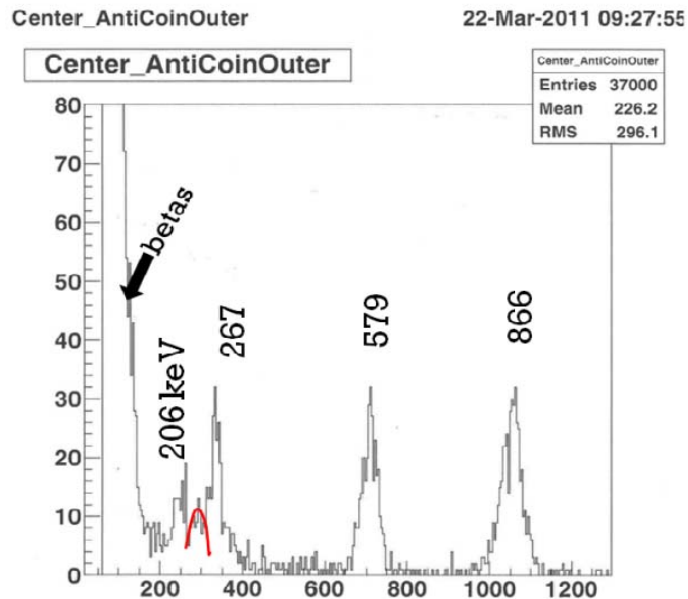


FIG. 1. Proton spectrum obtained in the first test experiment.

We have continued to work on improving the design and have conducted a second test in October 2011. For consistency, we used the same nuclide, ^{23}Al , under similar beam conditions. The AstroBox detector was used in a slightly different setup. We changed the gas medium from P10 (90% Argon, 10% Methane) to P5, keeping the same pressure and flow rate. We also chose to have 3 output signals, instead of 2. In the first test, we had only one signal from the 4 outer pads. In this experiment we split them in 2,

one signal from the two upstream pads and one signal from the two downstream pads, giving us, with the center, 3 regions of detection. The electronics setup was changed correspondingly.

We then followed the same experimental procedure. First, we implanted the ^{23}Al nuclei in the active region of the detector. We used 2-dimensional histograms showing the central signal versus the outer signals to determine when the implantation was done correctly (**Error! Reference source not**

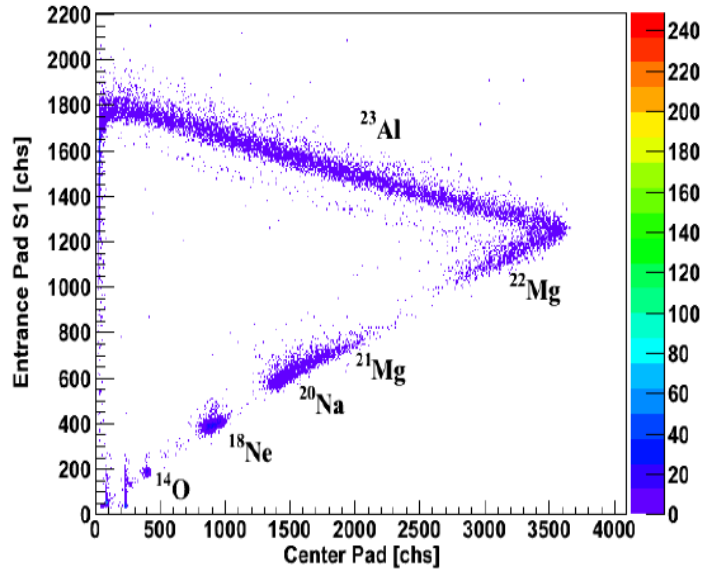


FIG. 2. Histogram showing the implantation spectrum at the right position (middle of the active region).

found.)

Second, we measured the decay of the implanted nuclei with the AstroBox. We used a pulsed beam to alternate between implantation (beam on, detector off) and measurement (beam off, detector on). Several sets of electronic settings were tested. **Error! Reference source not found.** shows an example of

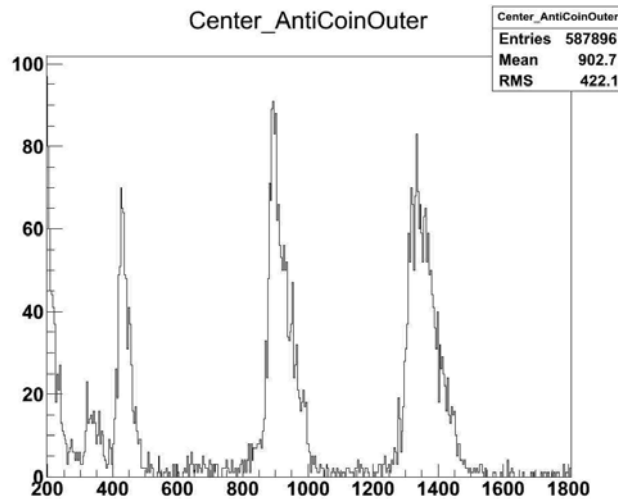


FIG. 3. Raw proton spectrum from the decay of ^{23}Al obtained in the second test experiment.

the raw proton spectra obtained.

The results confirmed the beta background reduction and improved resolution obtained in the first test. We also made further discoveries on the behavior of the detector and determined changes needed for a better design. The implementation of these observations is already in the works and we are hoping to test the upgraded version, AstroBox 2, in the following year.

- [1] A. Saastamoinen, L. Trache, A. Banu *et al.*, Phys. Rev. C **83**, 045808 (2011).
- [2] Y. Giomataris *et al.*, Nucl. Instrum. Methods Phys. Res. **A376** 29 (1996).
- [3] E. Simmons *et al.*, in *Progress in Research*, Cyclotron Institute, Texas A&M University (2010- 2011), p.V-31.

GEANT4 Simulations for the design of AstroBox2

B.T. Roeder, E. Pollacco,¹ and L. Trache

¹IRFU, CEA Saclay, Gif-sur-Yvette, France

During 2011, the “AstroBox2” detector was conceived in order to improve on the results obtained with the original “AstroBox” detector [1]. The purpose of AstroBox2 is to improve the implantation of the source in the active area of the detector and to reduce the background from the energy deposits of β -particles in the gas of the detector by modifying the detector geometry. While the background from the β -particles has already been reduced significantly using AstroBox [1], further reduction of the background is needed in order to carry out future measurements of β -delayed proton decay where the low-energy protons will have energies in the 100-400 keV and have very-low ($< 0.01\%$) relative intensities. AstroBox2 should be able to improve the measurements of the β -delayed proton decay of ^{23}Al , ^{31}Cl and ^{27}P for low proton energies.

A drawing of the design of AstroBox2 is shown in Figure 1. The chamber will be rectangular and will house a micromegas detector of the “Bulk” type [2] with 12 individual pads. Six of the pads will be arranged side-by-side along the beam-axis of the detector, and the remaining six pads will be arranged to surround the central pads on the top and bottom. The pads are configured such that a rare isotope beam produced and separated with the MARS spectrometer is fully stopped and contained, for a given gas pressure, within the four central pads along of the beam axis of the detector. The front and back pads along the beam are used to ensure that the beam implanted was in the center of the detector. In addition, the front pad is employed to count the number of implanted beam particles during the period of the experiment when the beam is on.

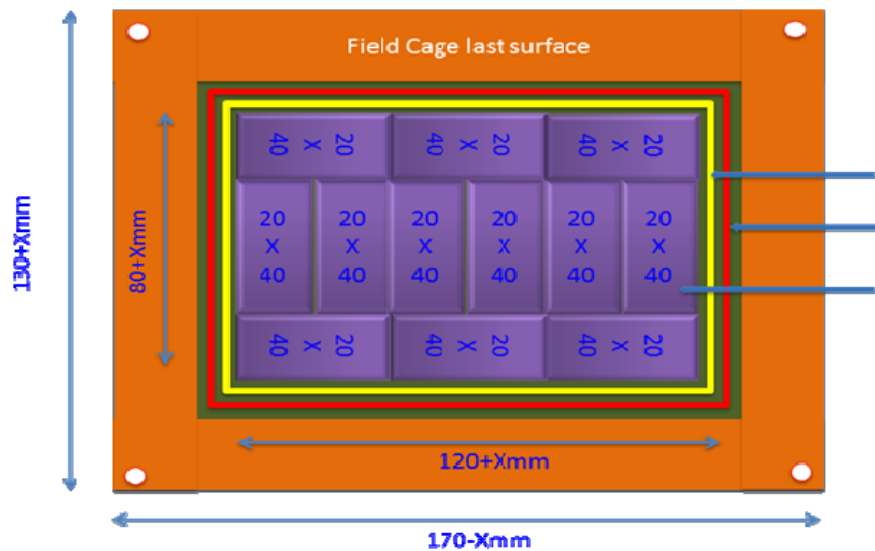


FIG. 1. Proposed design of AstroBox2. The beam enters the chamber from the right side and stops in the central pads. The outer pads are used to reduce the background from the β -particles and high-energy protons.

Once the general layout of the detector was determined, the design of AstroBox2 was simulated with Monte Carlo simulations using the GEANT4 toolkit [3]. A visualization of AstroBox2 simulated with GEANT4 is shown in Fig. 2. To optimize the dimensions and layout of the pads in the chamber, the geometry of AstroBox2 was fully described in GEANT4 and parameters such as the size of the micromegas pads, the gas pressure inside the AstroBox2 chamber and the gaps between the pads were varied. The simulations used the β -delayed proton decay of ^{23}Al [4] to test the response of AstroBox2 with the various detector dimensions and layouts. For most of the simulations, the detector was filled with P5 gas (95% Argon, 5% methane) at 800 torr.

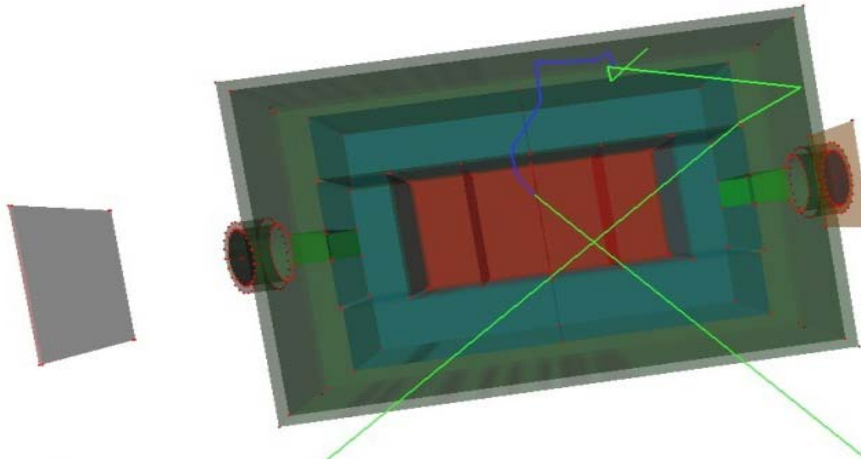


FIG. 2. AstroBox2 setup simulated in GEANT4. The blue and red blocks shown in figure represent the “active volumes” for each micromegas pad. One decay event occurring inside the chamber is also shown.

After testing several different configurations with larger and smaller pad sizes, it was found that a setup with dimensions similar to those in Fig. 1 with pad sizes of 20mm (length) \times 40mm (height) \times 40 mm (depth) gave the desired result of further reducing the background from the energy deposits from the

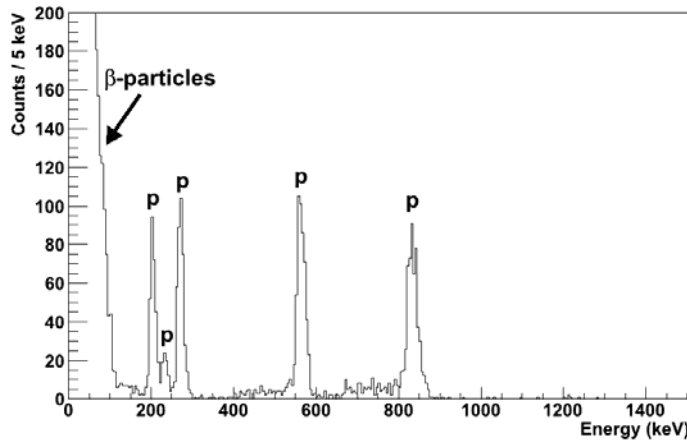


FIG. 3. ^{23}Al β -delayed proton decay as measured in AstroBox2 with the setup shown in Figure 1 simulated with GEANT4. The peaks marked “p” are proton peaks. The proton peaks are well-separated from the β -particle background at the low-energy side of the spectrum. The tail of the β -particle spectrum ends at ~ 110 keV.

β -particles. The simulated spectrum for ^{23}Al β -delayed proton decay for this setup is shown in Fig. 3. One should note in this figure that the tail of the β -particle distribution at low-energy ends abruptly at about 110 keV. This result is comparable with the one obtained with the original AstroBox detector. However, the advantage of AstroBox2 vs. the original AstroBox is that the ^{23}Al beam is fully implanted inside the central pads of the AstroBox2, even at gas pressures down to 600 torr, according to the simulations. At lower gas pressures, the simulations suggest that the tail of the β -particle distribution can be restricted to even lower energies, allowing for the possibility of observing low-energy protons well below 200 keV.

In conclusion, AstroBox2, a new detector using micromegas, has been designed. The response of the new detector to low-energy protons from ^{23}Al β -delayed proton decay was simulated with the GEANT4 toolkit. It was found that AstroBox2 would give similar results to the original AstroBox detector for the reduction of the background in the proton spectrum from the energy deposits of β -particles. However, the area for the implantation of the incoming beam particles will be larger and better controlled in AstroBox2. This should provide an improvement over the original AstroBox, and perhaps allow the gas pressure to be reduced in the detector which may further reduce the β -particle background.

- [1] E. Simmons *et al.*, Progress in Research, Cyclotron Institute, Texas A&M University (2010-2011), p. V-32; http://cyclotron.tamu.edu/2011_Progress_Report/index.html; E. Pollacco et al., Nucl. Instrum. Methods Phys. Res. (to be submitted).
- [2] Y. Giomataris, Ph. Rebourgeard, J.P. Robert, and G. Charpak, Nucl. Instrum. Methods Phys. Res. **A376**, 29 (1996).
- [3] GEANT4 version 4.9.4, S. Agostinelli *et al.*, Nucl. Instrum. Methods Phys. Res. **A506**, 250 (2003).
- [4] A. Saastamoinen *et al.*, Phys. Rev. C **83**, 045808 (2011).

STAR LiTe

M. McCleskey, G. Kim, R.E. Tribble, J.T. Burke,¹ R. Casperson,¹ and STARS Collaboration

¹*Lawrence Livermore National Laboratory, Livermore, California*

In November of 2011 work began on the installation of the silicon telescope array for reaction studies (STARS) and the Livermore-Berkeley array for collaborative experiments (LiBerACE) [1] at the Texas A&M Cyclotron Institute (TAMU-CI). The goal of this installation is to facilitate reaction studies making use of beams from the recently recommissioned K150 cyclotron. An official memorandum of understanding was signed in January of 2012. The new collaboration is referred to as STAR LiTe and consists of more than 55 researchers, post-docs, graduate and undergraduate students from five different countries and multiple national laboratories and universities.

Description of STARS

The silicon telescopes, reaction chamber and germanium clover array are as described in [1] and shown in Fig. 1. Briefly, a ΔE -E telescope of Micron S2 silicon detectors are placed in close proximity to the target, giving a large solid angle coverage. The Micron S2 detectors are annular silicon strip detectors which have 48 0.5 mm rings on the junction side and 16 wedge-shaped sectors on the ohmic side. Distance from the target to the detector determines the angular range covered, with approx. 30° to 62°

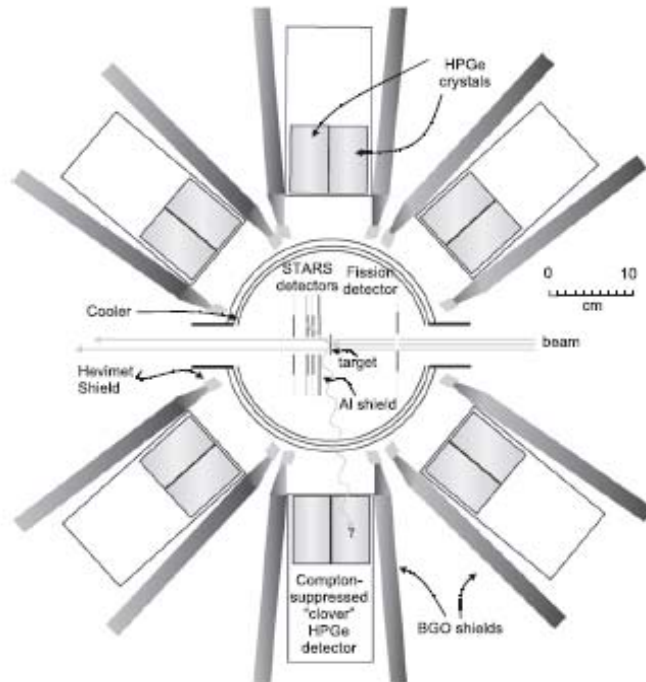


FIG. 1. STARS chamber and HPGe array [1].

being typical. An aluminum foil is placed in front of the ΔE detector in order to prevent δ electrons produced in the target from reaching the detectors. Additionally, an aluminum tunnel is used to block particles scattered at small angles (where the cross section is orders of magnitude larger than for the higher angles) from overwhelming the data acquisition system and damaging the inner rings of the detectors. An additional S2 detector is placed in the backward direction to detect fission fragments. γ -rays produced in the reactions are measured by a high efficiency array of segmented high purity germanium (HPGe) detectors. These detectors are Compton-suppressed by means of active bismuth germinate (BGO) shields. The signal of the each BGO shield is recorded for offline suppression.

A significant departure from the apparatus described in [1] is in the data acquisition system. CAMAC modules have been eliminated in favor of VME. CAEN N568B shaper-amplifiers are used for the silicon detectors as before, but now are also used for the BGO signals (one summed signal of the 16 individual BGO crystals is taken for each clover). For the silicon detector signals, discrimination of the N568B timing output is performed with CAEN V895 leading edge discriminators. The HPGe clover segment preamplifier outputs are fed into Mesytec MSCF-16s which act as both shaper amplifiers and discriminators. Digitization for all channels is by means of Mesytec MADC-32 VME ADCs. Timing information is through a CAEN V1190A TDC. An entirely new data acquisition software package has been developed which provides the user with comprehensive online data viewing and allows for a data rate in excess of 10 kHz. Currently the data rate is limited by the data network speed (10/100 Mbps), but near term plans to upgrade to a dedicated gigabit fiberoptic LAN should significantly raise this limit.

Installation at TAMU-CI

The new beamline was installed in Cave 4 in the place of the former Ion Interaction line. Special consideration was made to the quality of the beam spot that would be needed on target. Because of the close proximity of the silicon detectors to the target and the large solid angle covered, any beam halo that either hits the aluminum target frame or that scatters off the upstream collimators will have a significant impact on the data rate in the ΔE -E telescope and thus will severely limit the beam intensity that can be handled by the data acquisition system. This higher background rate has the effect of necessitating more beam time to achieve the same statistics for a given reaction being studied than would be the case with a better defined beam spot. Based on calculations performed by the accelerator physics group at TAMU-CI it was determined that two new quadrupoles would be necessary to achieve the desired beam spot quality. These consist of a y-focusing quadrupole immediately after the exit of the switching dipole (the Maryland magnet) at the beginning of line 7 and an x-focusing quadrupole just before the shield wall plug between the K150 vault and cave 4. These were in addition to the two existing quadrupoles that were part of the Ion Interaction line. An XY steering magnet was installed after the last quadrupole.

To aid in tuning the beam a large viewer was added just upstream of the chamber. Additionally, a series of targets are used to further improve the beam spot. First a solid phosphor target is used to focus the beam at the target position. This is then replaced by a phosphor with a 1/4" hole in the center that is used to check for any halo on the beam. Further refinement is then achieved by minimizing the rate in the

downstream silicon detector telescope while maximizing the current in the beam dump faraday cup with both the beam passing through the phosphor with the ¼” hole and also through an empty target frame.

A beam test was performed in February of 2012 with a 9 MeV/nucleon ^{18}O beam from the K150 cyclotron. A beam spot of 3mm at the target position was achieved and is shown in Fig. 2.

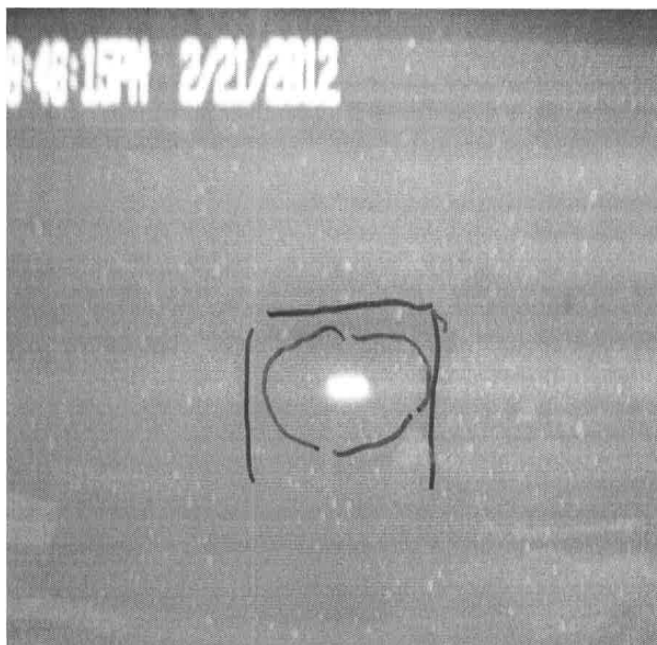


FIG. 2. First beam test on target. The target frame (with a ¼” hole) is drawn for reference.

Commissioning run: $^{240}\text{Am}(n,f)$

For the first experiment a measurement of the $^{240}\text{Am}(n,f)$ cross section via the surrogate reaction $^{243}\text{Am}(p,t)^{241}\text{Am}^*$ was performed. The beam of 34 MeV protons from the K150 cyclotron was used, with approximately 3.6 pA on target and an empty frame background rate in the silicon detectors of approximately 1.2 kHz. Particle identification is shown in Figure 3. Analysis of this experiment is ongoing.

Summary

The STARS-LiBerACE experimental setup has been relocated to TAMU-CI in an effort to further the already established experimental program of measuring reactions of interest for nuclear astrophysics, stockpile stewardship and nuclear energy. Installation is complete and as of May 2012 two data-taking experiments have been performed.

Acknowledgements

This research is funded by the Department of Energy and Lawrence Livermore National Laboratory under Contracts No.W-7405-Eng-48 and No. DE-AC52-07NA27344. A special thanks is extended to the cyclotron crew and staff for their significant efforts in this project.

[1] S.R. Lesher *et al.*, Nucl. Instrum. Methods Phys. Res. **A621**, 286 (2010).

Characterization of a front-end circuit for SAMURAI Si detection system

M. Kurokawa, M. McCleskey, B. Roeder, A. Saastamoinen, L. Trache, R.E. Tribble,
L. Sobotka,¹ and J. Elson¹

¹*Departments of Chemistry and Physics, Washington University, Saint Louis, Missouri 63130*

An array of silicon strip detectors will be installed between a secondary target and the Superconducting Analyzer for MULTiparticles from RADioactive Isotope beam (SAMURAI) at RIKEN Nishina Center for experiments performed to study the Coulomb breakup reaction of proton-rich nuclei [1]. The reaction products of the experiment are a proton and the residual heavy particle. The scattering angle must be detected for both particles with high accuracy. Therefore, a total number of silicon-strip electrodes will be more than 600. The large number of signal channels will be handled by an ASIC (Application-Specific Integrated Circuit) system called HINP (Heavy Ion Nuclear Physics) [2].

In order to distinguish an emitted proton and the residual heavy particle in coincidence, a larger dynamic range is necessary than that can be provided by the HINP system. To extend the range, a preamplifier ASIC called DGCSA (Dual Gain Charge Sensitive preAmplifier) has been developed at RIKEN [3]. This article reports the results on the range obtained by using the DGCSA at the input stage of a signal and the HINP at the following stage.

A fastest proton in the experiment will deposit the energy of around 200 keV in the Si detector. The charge equivalent to the energy was injected using a pulser into the system consisting of the DGCSA and the HINP for 30 s with a frequency of 50 Hz. To take into account the effect of the capacitive load attributed to the detector and the cables, a capacitor of 70 pF was placed at the input stage. In similar way, the output pulse heights were recorded for the different amount of the charge in steps of 100 keV equivalent except for the case of 500 keV, where the injection lasted for 60 s to make the corresponding peak dominant. The results are shown in Fig. 1. The lowest peak was generated by the noise. The detection efficiency of less than 100% is indicated for the peak at 752 ch corresponding energy of 100

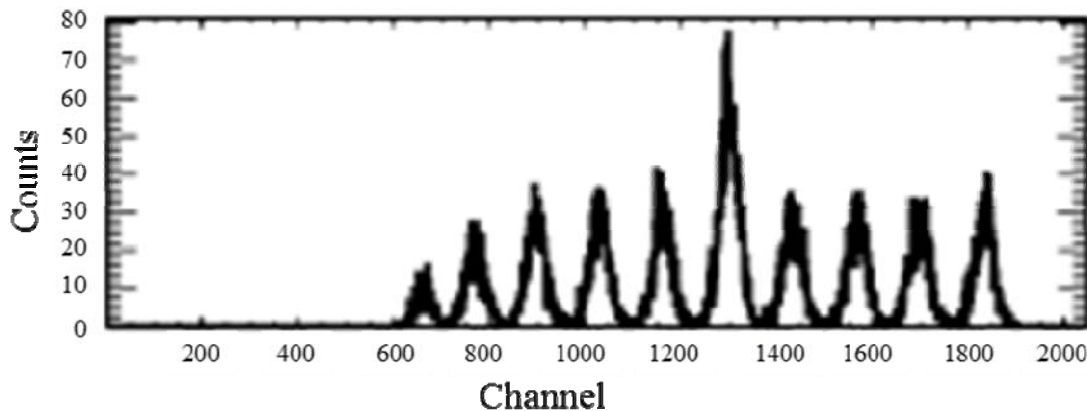


FIG. 1. The output pulse height for the charge injection using a pulser when the capacitive load was 70 pF.

keV because of its smaller counts compared with those for other peaks at larger channels. The result is consistent with the threshold of 762 ch estimated from the 5σ limit of the noise. The detection limit of lower than 200 keV is expected from this result

Another important parameter of the detection system is the higher detection limit of the energy. In order to enlarge the limit, the DGCSA employed a dual-gain system consisting of two charge-sensitive preamplifiers (CSAs). The result shown above was that obtained from the high-gain channel. Identical specifications were adopted for the two CSAs except for an FET that was installed in the high-gain channel. The dual-gain function was implemented by applying capacitive division to the input charge. The charge can be divided asymmetrically in proportion to the capacitance ratio of the two coupling capacitors and hence the range of the dual-gain system can be greater than that of the single-channel system as much as the ratio, if an input impedance of a CSA is negligibly small compared with that of the relevant capacitor.

The output pulse height of the system is shown as a function of the equivalent energy of the input charge in Fig. 2. For the high-gain channel given with red marks, the linearity between the energy and the pulse height degraded at the energy of less than 100 MeV as in the case of the single channel case. On the other hand, the range of the low-gain channel given with blue marks was larger than that was obtained for the high-gain channel about 10 times. The implementation of the dual-gain system successfully increased the range beyond the energy required for the detection of a heavy charged particle with the atomic number of 50. These tests were done at Texas A&M University using the ASICS system built for use with SAMURAI.

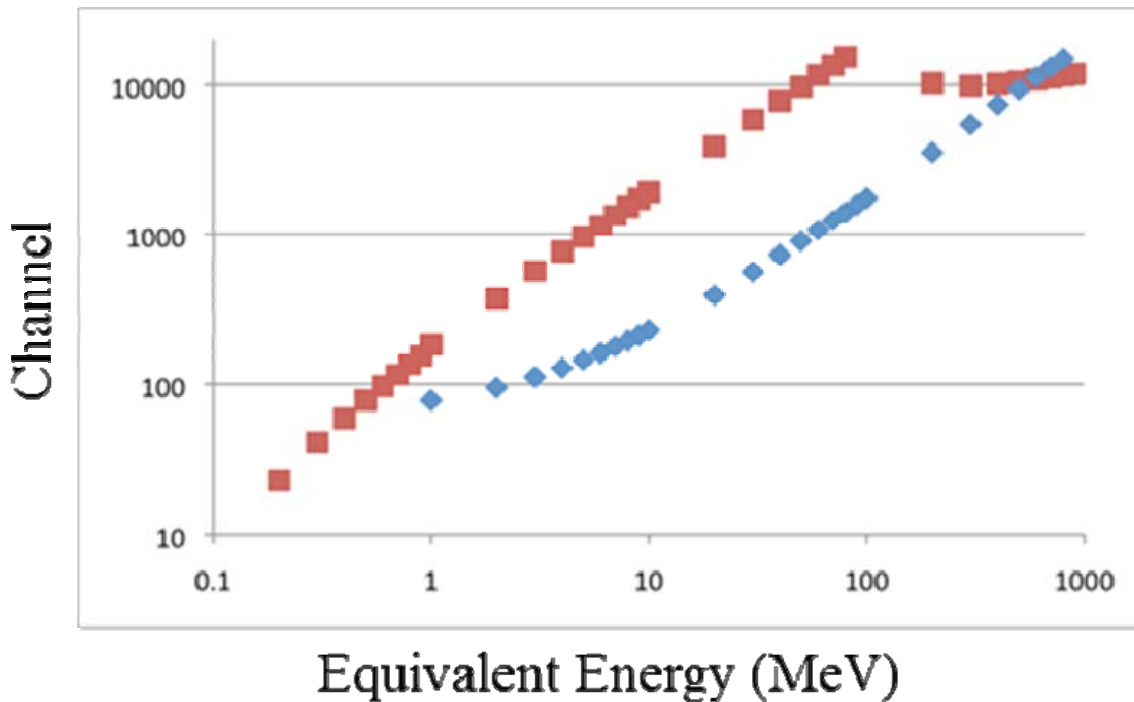


FIG. 2. Output pulse height of the system is shown as a function of the equivalent energy in MeV. The red and the blue marks indicate the results for the high and low gain channels, respectively.

In summary, the system consisting of DGCSA and HINP has been developed as a front-end circuit for SAMURAI Si detection system, which will be used for the Coulomb breakup reaction of proton-rich nuclei. The system is based on the ASIC chip and thus can handle enormous number of signal channels, which is necessary for the accurate measurement of the scattering angles of the reaction products. The lower and higher detection limits obtained for the system allows the coincidence detection of a proton and the residual heavy particle produced by the reaction of nuclei up to ^{100}Sn .

- [1] Y. Togano *et al.*, RIKEN Acc. Prog. Rep. **44** (2011).
- [2] G.L. Engel *et al.*, Nucl. Instrum. Methods Phys. Res. **A573** 418 (2007).
- [3] M. Kurokawa *et al.*, RIKEN Acc. Prog. Rep. **44** (2011).

Test of completed decay detector for ISGMR study

J. Button, Krishichayan, J. Shafer, Y.-W. Lui, and D.H. Youngblood

Introduction

In order to study the Isoscalar Giant Monopole Resonance in unstable nuclei, we have designed and built a ΔE - ΔE - E decay detector composed of plastic scintillator arrays. The elements of this detector and its parameters are described in Ref. [1].

In Ref. [2], the design for the optical connection between strip scintillators and their respective fiber optic bundles was shown to be adequate. A complete array of vertically ($\Delta E1$) and horizontally ($\Delta E2$) aligned strips was constructed and assembled. A reference for the naming system used to define the overlapping, square-pixel areas from $\Delta E1$ and $\Delta E2$ is provided in Fig.1. A reference for the E-Block array geometry and naming system is provided in Fig.2.

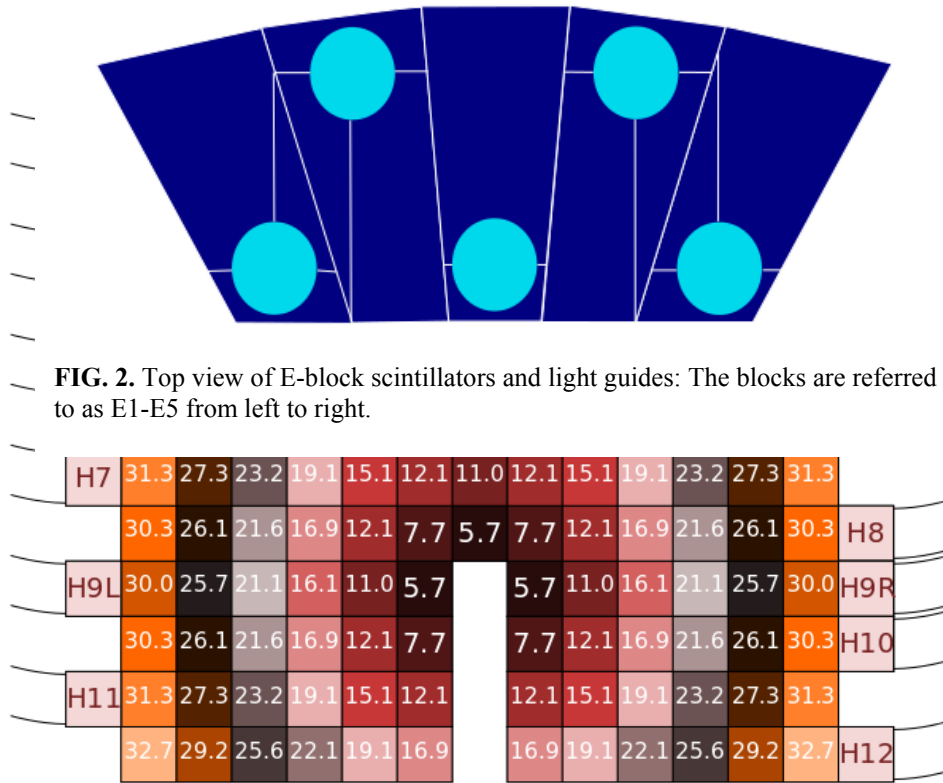


FIG. 2. Top view of E-block scintillators and light guides: The blocks are referred to as E1-E5 from left to right.

FIG. 1. Map of the $\Delta E1$ - $\Delta E2$ Pixel Geometry: The median accepted azimuthal angle in degrees with respect to the beam direction is written on each color-coded pixel. The location of the strip label on the diagram (V1, H1, etc.) indicates the location of the optical connection of the strip scintillator with its fiber bundle. V7 and H9L&R are half-length strips. H10-12 are full length strips, but no signal should come from the center of those strips because there is no vertical strip in front.

In-beam testing has since been done using 30 MeV protons incident on a ^{12}C target. Analysis of the recorded data is still ongoing. Preliminary results show that the decay detector is operating well and that an effective method for energy calibration of the scintillator light response signals has been devised.

In-Beam Test and Preliminary Results

A test run of the completed decay detector was done using a beam of 30 MeV protons on a ^{12}C target. As in prior test runs described in Ref. 2, data collection was triggered by signals from the strip layer $\Delta\text{E}2$. Since real proton events must also have a signal in E1, only events with both $\Delta\text{E}1$ and $\Delta\text{E}2$ signals were analyzed. Signals from all strip scintillators were amplified before being recorded by computer.

The $\Delta\text{E}2$ -E 2D-spectra (example shown in Fig. 3) show three distinct peaks due to protons of different energies from elastic scattering and excitation of the 4.4MeV (2+) and 9.6 MeV (3-) levels [3] in ^{12}C . To confirm this, $\Delta\text{E}2$ and E 1D-spectra (Fig. 4) corresponding to each of the three peaks visible in the 2D-spectra were produced. Each peak in the resulting 1D-spectrum was fit with a Gaussian. The average peak position was then compared with the expected light response of the $\Delta\text{E}2$ layer and E-Block (Tables I and II). The expected light response was calculated by first solving for the energies (corresponding to the spread in the azimuthal angle relative to the beam direction within the overlapping $\Delta\text{E}2$ -E area) of the incident proton on $\Delta\text{E}1$ using relativistic kinematics. The energy deposited in each layer was found by using the SRIM tables [4]. The EDSE model [5] was used to calculate the expected light response (Figs. 5 and 6).

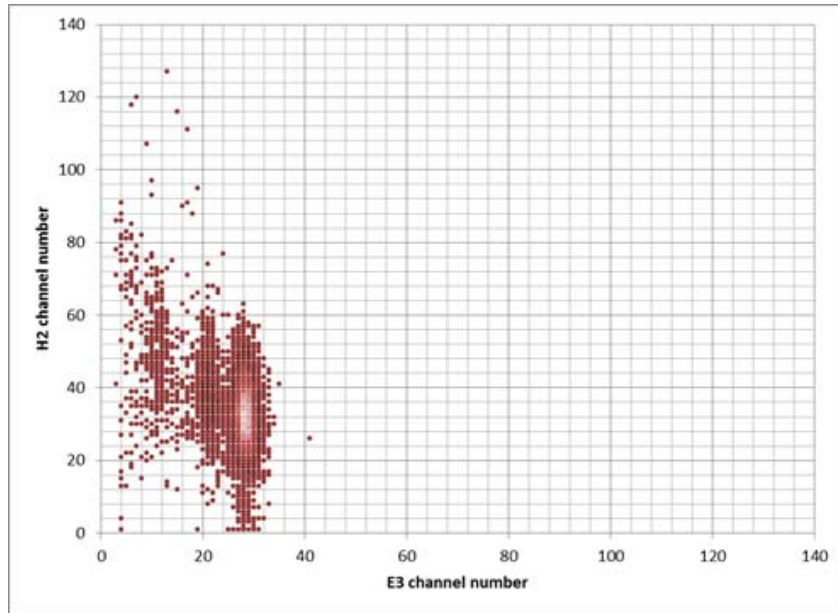


FIG. 3. Example ΔE -E 2D-spectrum: Lighter shades of red are used to indicate greater numbers of counts.

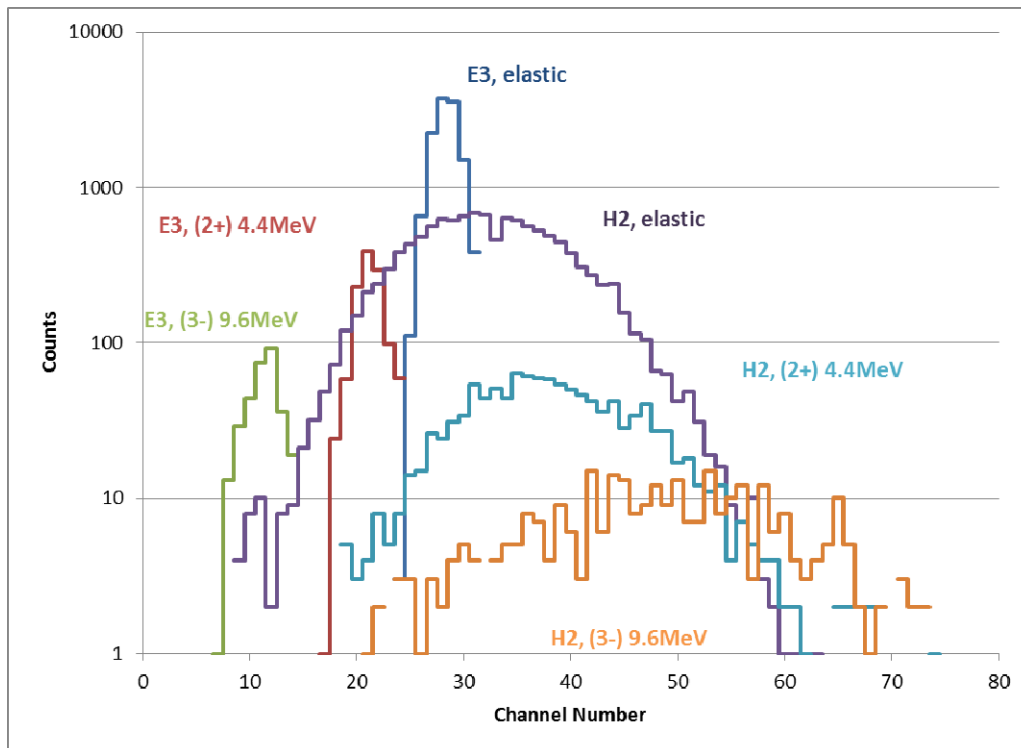


FIG. 4. Example 1D-spectra resulting from gates on peaks in the ΔE -E 2D-spectra (**Error! Reference source not found.**): Each peak is fit with a Gaussian. The extracted average peak positions are then compared to the expected light response calculated from the EDSE model.

Table I. Comparison of the light response in block E3 in coincidence with horizontal strip H2 at 3 different proton energies: The decay detector area corresponding to the overlap of E3 and H2 is at an azimuthal angle relative to the beam direction of $33\pm 2^\circ$. The uncertainty in the energy incident on $\Delta E1$ is due to the uncertainty of the proton angle. The energy deposited in E3 is found by consulting the SRIM tables [4].

	Energy incident on $\Delta E1$ MeV	Energy Deposited in E3 MeV	Exp. L.O. E3 (Ch. Number)	Relative Exp. L.O. E3	EDSE L.O. E3 (Arb. Unit)	Relative EDSE L.O. E3
Elastic	29±1	25±1	28.0 ± 2.0	1.0	660±4	1.0
2+ (4.4MeV)	24±1	20±1	21.1 ±0.1	0.8±0.1	498±5	0.8±0.1
3- (9.6 MeV)	19±1	13±1	12.0 ±3.0	0.4±0.1	279±4	0.4±0.1

Table II. Comparison of the light response in strip H2 in coincidence with E-block E3 at 3 different proton energies: The decay detector area corresponding to the overlap of E3 and H2 is at an azimuthal angle relative to the beam direction of $33\pm 2^\circ$. The uncertainty in the energy incident on $\Delta E1$ is due to the uncertainty of the proton angle. The energy deposited in $\Delta E2$ is found by consulting the SRIM tables [4].

	Energy Deposited in $\Delta E2$ MeV	Exp. L.O. H2 (Ch. Number)	Relative Exp. L.O. H2	EDSE L.O. H2 (Arb. Unit)	Relative EDSE L.O. H2
Elastic	2.0±1.0	32 ±5	1.0	76±3	1.0
2+ (4.4MeV)	2.5±1.0	38 ±4	1.2±0.3	93±4	1.2±0.1
3- (9.6MeV)	3.5±1.0	49 ±6	1.6±0.3	122±6	1.6±0.1

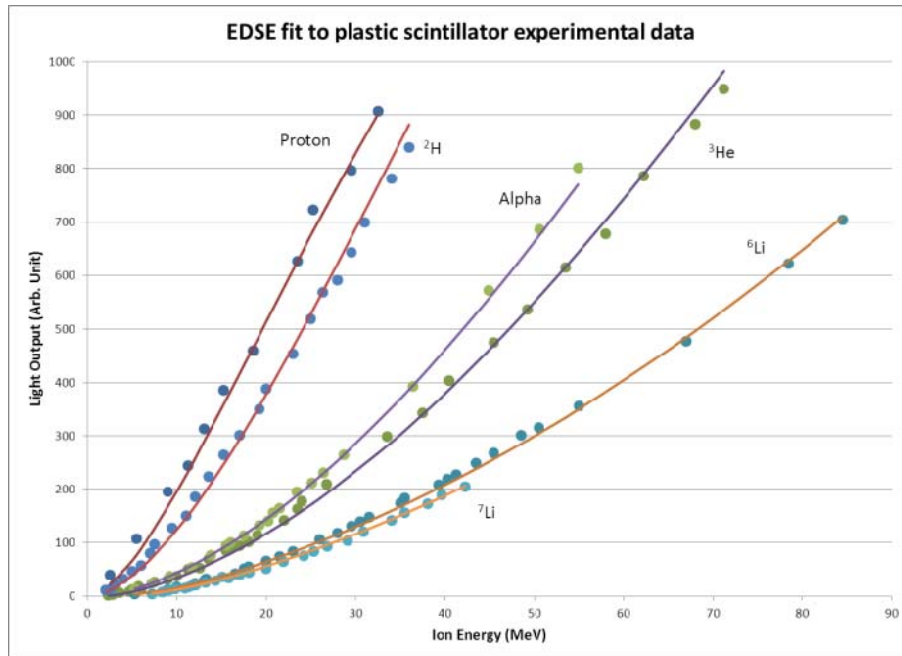


FIG. 5. Fit to published experimental data of the light response by plastic scintillator [6]: The parameters obtained by chi-square fit have the values $\rho_q = 99.7$ MeV/nm, $F = .998$, $A = 1E-4$, $C_{proton} = 1.14$, $C_\alpha = 1.96$, and $C_{6Li} = 2.90$.

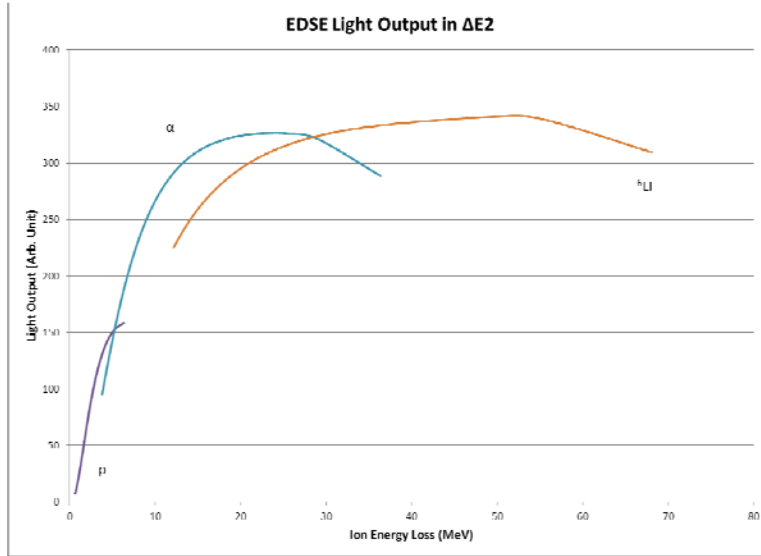


FIG. 6. Light response of the decay detector as a function of the energy deposited by various ions.

Conclusion

Comparison of the light output in the E3 and H2 scintillators for protons from the three groups shows good agreement between the expected and experimental relative values. This method of comparison could be extended by applying a similar procedure to the 2D-spectra generated by coincidences between the $\Delta E1$ and the E-Block layer. This would give an energy calibration for all scintillator signals.

The poorer resolution in the strip scintillators is probably due largely to energy straggling in the thin strips. Because of this, the three peaks are not resolved in the $\Delta E1$ - $\Delta E2$ 2D-spectra (Fig. 7).

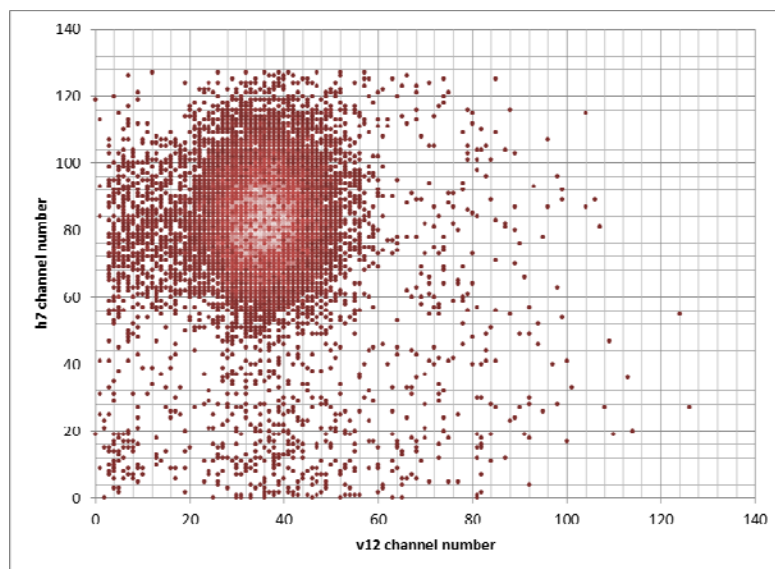


FIG. 7. An example $\Delta E1$ - $\Delta E2$ 2D-spectrum: The three peaks visible in the $\Delta E2$ -E 2D-spectra are not visible here due to the poorer energy resolution of the strip scintillators compared to that of the block scintillators.

- [1] J. Button, R. Polis et al., Progress in Research, Cyclotron Institute Texas A&M University (2008-2009), p.V-30.
- [2] J. Button, R. Polis et al., Progress in Research, Cyclotron Institute Texas A&M University (2010-2011), p.V-55.
- [3] National Nuclear Data Center, information extracted from the Chart of Nuclides database, <http://www.nndc.bnl.gov/chart/>
- [4] J.F. Ziegler, M.D. Ziegler and J.P. Biersack, Nucl. Instrum. Methods Phys. Res. **B268**, 1818 (2010).
- [5] K. Michaelian, A. Menchaca-Rocha, and E. Belmont-Moreno, Nucl. Instrum. Methods Phys. Res. **A356**, 297 (1995).
- [6] F.D. Becchetti, C.E. Thorn and M.J. Levine Nucl. Instrum. Methods **138**, 93 (1976).

SECTION VI
PUBLICATIONS

PAPERS PUBLISHED
April 1, 2011 – March 31, 2012

Isoscalar giant resonances in ^{48}Ca , Y.-W. Lui, D. H. Youngblood, S. Shlomo, X. Chen, Y. Tokimoto, Krishichayan, M. Anders, and J. Button, Phys. Rev. C **83**, 044327 (2011).

Experimental validation of the largest calculated isospin-symmetry-breaking effect in a superallowed Fermi decay, D. Melconian, S. Triambak, C. Bordeanu, A. Garcia, J.C. Hardy, V.E. Jacob, N. Nica, H.I. Park, G. Tabacaru, L. Trache, I.S. Towner, R.E. Tribble and Y. Zhai, Phys. Rev. Lett. **107**, 182301 (2011).

Precise half-life measurement of the superallowed β^+ emitter ^{38}Ca , H.I. Park, J.C. Hardy, V.E. Jacob, A. Banu, L. Chen, V.V. Golovko, J. Goodwin, V. Horvat, N. Nica, E. Simmons, L. Trache and R.E. Tribble, Phys. Rev. C **84**, 065502 (2011).

The β decay of ^{32}Cl : precision γ -ray spectroscopy and a measurement of isospin-symmetry breaking, D. Melconian, S. Triambak, C. Bordeanu, A. Garcia, J.C. Hardy, V.E. Jacob, N. Nica, H.I. Park, G. Tabacaru, L. Trache, I.S. Towner, R.E. Tribble and Y. Zhai, Phys. Rev. C **85**, 025501 (2012).

Decay spectroscopy for nuclear astrophysics: β and β -delayed proton decay, L. Trache, A. Banu, J.C. Hardy, V.E. Jacob, M. McCleskey, B.T. Roeder, E. Simmons, A. Spiridon, R.T. Tribble, A. Saastamoinen, A. Jokinen, J. Aysto, T. Davinson, G. Lotay, P.J. Woods and E. Pollacco, J. Phys: Conf. Series **337**, 012058 (2012).

Precise half-life measurement of the superallowed β^+ emitter ^{46}V , H.I. Park, J.C. Hardy, V.E. Jacob, L. Chen, J. Goodwin, N. Nica, E. Simmons, L. Trache and R.E. Tribble, Phys. Rev. C **85**, 035501 (2012).

V_{ud} from nuclear decays, I.S. Towner and J.C. Hardy, Proceedings of [CKM2010](http://www.slac.stanford.edu/econf/C100906), the 6th International Workshop on the CKM Unitarity Triangle, Warwick, United Kingdom, 2010; eConf/C100906 (<http://www.slac.stanford.edu/econf/C100906/>)

High precision Q_{EC} -value measurements for superallowed decays, T. Eronen and J.C. Hardy, Eur. Phys. J. A **48**, 48 (2012)

Nuclear Data Sheets for $A = 36$, N. Nica, J. Cameron and B. Singh, Nucl. Data Sheets **113**, 1 (2012).

α decay of the excited states in ^{12}C at 7.65 and 9.64 MeV, J. Manfredi, R.J. Charity, K. Mercurio, R. Shane, L.G. Sobotka, A.H. Wousmaa, A. Banu, L. Trache, R.E. Tribble, Phys. Rev. C **85**, 037603 (2012).

Molecular structures in T=1 states of ^{10}B , A.N. Kuchera, G.B. Rogachev, V.Z. Goldberg, E.D. Johnson, S. Cherubini, M. Gulino, M. La Cognata, L. Lamia, S. Romano, L.E. Miller, R.G. Pizzone, G.G. Rapisarda, M.L. Sergi, C. Spitaleri, R.E. Tribble, W.H. Trzaska, A. Tumino, Phys. Rev. C **84**, 054615 (2011).

Experimental validation of the largest calculated isospin-symmetry-breaking effect in a superallowed Fermi decay, D. Melconian, S. Triambak, C. Bordeanu, A. Garcia, J.C. Hardy, V.E. Iacob, N. Nica, H.I. Park, G. Tabacaru, L. Trache, I.S. Towner, R.E. Tribble, Y. Zhai, Phys. Rev. Lett. **107**, 182301 (2011).

Precise Determination of the Unperturbed ^8B Neutrino Spectrum, T. Roger, J. Büscher, B. Bastin, O.S. Kirsebom, R. Raabe, M. Alcorta, J. Äystö, M.J.G. Borge, M. Carmona-Gallardo, T.E. Cocolios, J. Cruz, P. Dendooven, L.M. Fraile, H.O.U. Fynbo, D. Galaviz, L.R. Gasques, G.S. Giri, M. Huyse, S. Hyldegaard, K. Jungmann, W.L. Kruithof, M. Lantz, A. Perea, K. Riisager, A. Saastamoinen, B. Santra, P.D. Shidling, M. Sohani, A.J. Sørensen, O. Tengblad, E. Traykov, D.J. van der Hoek, P. Van Duppen, O.O. Versolato, and H.W. Wilschut, Phys. Rev. Lett. **108**, 162502 (2012).

Specific mass shift measurements in rubidium by Doppler-free two-photon transitions, T. Kong, A. Gorelov, C. Höhr, T. Wiebe, A. Chatwin-Davies, A. Berman, S. Behling, D. Ashery, G. Gwinner, M.R. Pearson and J.A. Behr, J. Phys. B **44**, 215004 (2011).

Nuclear beta-decay measurements and $|V_{ud}|$, D. Melconian, Proceedings of [CKM2010](#), the 6th International Workshop on the CKM Unitarity Triangle, Warwick, United Kingdom, 2010; arXiv:1108.2530.

Asymptotic normalization coefficients from the $^{14}\text{C}(d,p)^{15}\text{C}$ reaction, A.M. Mukhamedzhanov, V. Burjan, M. Gullino, Z. Hons, V. Kroha, M. McCleskey, J. Mrazek, N. Nguyen, F.M. Nunes, S. Piskor, S. Romano, M.L. Sergi, C. Spitaleri, and R.E. Tribble, Phys. Rev. C **84**, 024616 (2011).

Structure of ^{23}Al from one-proton breakup and astrophysical implications, A. Banu, L. Trache, F. Carstoiu, N.A. Orr, N.L. Achouri, A. Bonaccorso, W.N. Catford, M. Chartier, B. Fernandez-Domínguez, M. Freer, L. Gaudefroy, M. Horoi, M. Labiche, B. Laurent, R.C. Lemmon, F. Negoita, S. Paschalis, N. Patterson, B. Piertras, B.T. Roeder, F. Rotaru, P. Roussel-Chomaz, E. Simmons, S. Thomas, and R.E. Tribble, Phys. Rev. C **84**, 015803 (2011).

Refractive versus resonant diffractive scattering of loosely bound nuclei, F. Carstoiu, S. Misicu, and L. Trache, Romanian J. Phys. **57**, 106 (2012).

Direct radiative proton capture $\text{Al-23}(p,\gamma)\text{Si-24}$ studied via one-proton nuclear breakup of Si-24 , A. Banu, F. Carstoiu, W.N. Catford, B. Fernandez-Domínguez, M. Horoi, N.A. Orr, B.T. Roeder, P. Roussel-Chomaz, L. Trache, and R.E. Tribble, 24th Nuclear Physics Conference – Nuclear Physics in

Astrophysics V (NPA5), J. Phys.: Conference Series **337**, 012059 (2012).

Resonance scattering to study exotic nuclei at the limits of stability, V.Z. Goldberg, B.T. Roeder, G.V. Rogachev, G.G. Chubarian, E.D. Johnson, C. Fu, A.A. Alharbi, M.L. Avila, A. Banu, M. McCleskey, J.P. Mitchell, E. Simmons, G. Tabacaru, L. Trache and R.E. Tribble, 24th Nuclear Physics Conference – Nuclear Physics in Astrophysics V (NPA5), J. Phys.: Conference Series **337**, 012008 (2012).

Decay spectroscopy for nuclear astrophysics: beta- and beta-delayed proton decay, L. Trache, A. Banu, J.C. Hardy, V.E. Iacob, M. McCleskey, B.T. Roeder, E. Simmons, A. Spiridon, R.E. Tribble, A. Saastamoinen, A. Jokinen, J. Aysto, T. Davinson, G. Lotay, P.J. Woods, E. Pollacco, 24th Nuclear Physics Conference – Nuclear Physics in Astrophysics V (NPA5), J. Phys.: Conference Series **337**, 012058 (2012).

Experimental study of beta-delayed proton decay of Al-23 for nucleosynthesis in novae, A. Saastamoinen, L. Trache, A. Banu, M.A. Bentley, T. Davinson, J.C. Hardy, V.E. Iacob, M. McCleskey, B.T. Roeder, E. Simmons, G. Tabacaru, R.E. Tribble, P.J. Woods, and J. Aysto, Phys. Rev. C **83**, 045808 (2011).

The Texas-Edinburgh-Catania Silicon Array (TECSA): A detector for nuclear astrophysics and nuclear structure studies with rare isotope beams, B.T. Roeder, M. McCleskey, L. Trache, A.A. Alharbi, A. Banu, S. Cherubini, T. Davinson, V.Z. Goldberg, M. Gulino, R.G. Pizzone, E. Simmons, R. Sparta, A. Spiridon, C. Spitaleri, J.P. Wallace, R.E. Tribble, and P.J. Woods, Nucl. Instrum. Methods Phys. Res. **A634**, 71 (2011).

Recent studies of Trojan Horse method, S. Cherubini, C. Spitaleri, M. Gulino, M. La Cognata, R.G. Pizzone, L. Lamia, G.G. Rapisarda, S. Romano, L. Sergi, A. Mukhamedzhanov, L. Trache, R.E. Tribble, S. Kubono, H. Yamaguchi, A. Tumino, Conference on Nuclear Physics - Extremes of the Nuclear Landscap, Acta Phys. Polonica B **42**, 769 (2011).

High accuracy O-18(p, alpha)N-15 reaction rate in the 8·10(6)-5 ·10(9) K temperature range, M. La Cognata, C. Spitaleri, A. Mukhamedzhanov, A. Banu, S. Cherubini, A. Coc, V. Crucilla, V.Z. Goldberg, M. Gulino, B. Irgaziev, G.G. Kiss, L. Lamia, J. Mrazek, R.G. Pizzone, S.M.R. Puglia, G.G. Rapisarda, S. Romano, M.L. Sergi, G. Tabacaru, L. Trache, R.E. Tribble, W. Trzaska, A. Tumino, In Frontiers in Nuclear Structure, Astrophysics and reactions (FINUSTAR 3), AIP Conference Proceedings **1377**, 195 (2010).

Study of excited states of S-31 through beta-decay of Cl-31 for nucleosynthesis in ONe novae, A. Saastamoinen, L. Trache, A. Banu, M.A. Bentley, T. Davinson, J.C. Hardy, V.E. Iacob, A. Jokinen, M. McCleskey, B. Roeder, E. Simmons, G. Tabacaru, R.E. Tribble, P.J. Woods, J. Aysto, in 4th International Conference on Proton Emitting Nuclei and Related Topics, AIP Conference Proceedings **1409**, 71 (2011).

Decay spectroscopy for nuclear astrophysics: β -delayed proton decay, L. Trache, E Simmons, A. Spiridon, M. McCleskey, B.T. Roeder, R.E. Tribble, A. Saastamoinen, A. Jokinen, J. Aysto, T. Davinson, P.J. Woods, E. Pollacco, M. Kebbiri, G. Pascovici, in 4th International Conference on Proton Emitting Nuclei and Related Topics, AIP Conference Proceedings **1409**, 67 (2011).

Indirect methods for nuclear astrophysics: reactions with RIBs. The ANC method, L. Trache, Proceedings of VI European Summer School on Experimental Nuclear Astrophysics, September 2011, St.Tecla Palace, Acireale, Italy (edited by M. LaCognata, L. Lamia, C. Rolfs and C. Spitaleri); http://pos.sissa.it/archive/conferences/148/030/ENAS%206_030.pdf.

Decay spectroscopy for nuclear astrophysics, L. Trache, Proceedings of VI European Summer School on Experimental Nuclear Astrophysics, September 2011, St.Tecla Palace, Acireale, Italy (edited by M. LaCognata, L. Lamia, C. Rolfs and C. Spitaleri); http://pos.sissa.it/archive/conferences/148/030/ENAS%206_033.pdf.

The beta-delayed proton and gamma decay of ^{27}P for nuclear astrophysics, E. Simmons, L. Trache, A. Banu, M. McCleskey, B. Roeder, A. Spiridon, R.E. Tribble, T. Davinson, P. J. Woods, G. J. Lotay, J. Wallace, D. Doherty, and A. Saastamoinen, Proceedings of VI European Summer School on Experimental Nuclear Astrophysics, September 2011, St.Tecla Palace, Acireale, Italy (edited by M. LaCognata, L. Lamia, C. Rolfs and C. Spitaleri); http://pos.sissa.it/archive/conferences/148/030/ENAS%206_038.pdf.

A new detection system for very low-energy protons from β -delayed p-decay, A. Spiridon, Proceedings of VI European Summer School on Experimental Nuclear Astrophysics, September 2011, St.Tecla Palace, Acireale, Italy (edited by M. LaCognata, L. Lamia, C. Rolfs and C. Spitaleri); http://pos.sissa.it/archive/conferences/148/030/ENAS%206_039.pdf.

Photoneutron cross sections for $^{118-124}\text{Sn}$ and the γ -ray strength function method, H. Utsunomiya, S. Goriely, M. Kamata, H. Akimune, T. Kondo, O. Itoh, C. Iwamoto, T. Yamagata, H. Toyokawa, Y.-W. Lui, H. Harada, F. Kitatani, S. Goko, S. Hilaire, and A. J. Koning, Phys. Rev. C **84**, 055805 (2011).

Highly excited alpha-cluster states in ^{34}S , M. Norrby, T. Lonnroth, V.Z. Goldberg, G.V. Rogachev, M.S. Golovkov, K.M. Kallman, M. Lattuada, S.V. Perov, S. Romano, B.B. Skorodumov, G.P. Tiourin, W.H. Trzaska, A. Tumino, A.N. Vorontsov, Eur. Phys. J. A **47**, 73 (2011).

Resonance Scattering to Study Exotic Nuclei at the Limits of Stability, V. Z. Goldberg, B. T. Roeder, G.V. Rogachev, G.G. Chubarian, E.D. Johnson, C. Fu, A. Alharbi, M.L. Avila, A. Banu, M. McCleskey, J.P. Mitchell, E. Simmons, G. Tabacaru, L. Trache, R.E. Tribble, J. Phys: Conference Series **337**, 012008 (2012).

Cluster states in the neutron excess nucleus ^{22}Ne , S.Yu. Torilov, M. Brenner, V.Z. Goldberg, K.A. Gridnev, S.V. Khlebnikov, T.V. Korovitskaya, T. Lonnroth, M. Mutterer, M. Norrby, B.G. Novatski, V.A. Rubchenya, JETP Lett. **94**, 6 (2011).

Elastic alpha-particle resonances as evidence of clustering at high excitation in ^{40}Ca , M. Norrby, T. Lonnroth, V.Z. Goldberg, G.V. Rogachev, M.S. Golovkov, K.-M. Kallman, M. Lattuada, S.V. Perov, S. Romano, B.B. Skorodumov, G.P. Tiourin, W.H. Trzaska, A. Tumino, A.N. Vorontsov, Eur. Phys. J. A **47**, 96 (2011).

High-spin states in ^{22}Ne populated in the $^{14}\text{C}(^{12}\text{C}, \alpha)$ reaction, S.Yu. Torilov, M. Brenner, V.Z. Goldberg, K.A. Gridnev, S.V. Khlebnikov, T.V. Korovitskaya, T. Lonnroth, M. Mutterer, M. Norrby, B.G. Novatski, V.A. Rubchenya, J.M.K. Slotte, Yu.G. Sobolev, W.H. Trzaska, G.P. Tyurin, L.I. Vinogradov, V.I. Zhrebchevsky, Eur. Phys. J. A **47**, 158 (2011).

The search for nuclear molecules in isobaric analog states of ^{10}B , A.N. Kuchera, G.V. Rogachev, V.Z. Goldberg, E.D. Johnson, S. Cherubini, M. Gulino, M. La Cognata, J. Hardy, L. Lamia, S. Romano, L.E. Miller, R.G. Pizzone, G.G. Rapisarda, M.L. Sergi, C. Spitaleri, R.E. Tribble, W.H. Trzaska, and A. Tumino, BAPS **56**, 12 (2011).

Medical radioisotopes production: a comprehensive cross-section study for the production of Mo and Tc radioisotopes via proton induced nuclear reactions on nat Mo, A.A. Alharbi, A. Azzam, M. McCleskey, B. Roeder, A. Spiridon, E. Simmons, V.Z. Goldberg, A. Banu, L. Trache and R. E. Tribble, Radioisotopes - Applications in Bio-Medical Science, edited by Prof. Nirmal Singh, ISBN: 978-953-307-748-2

Experimental determination of in-medium cluster binding energies and Mott points in nuclear matter, K. Hagel, R. Wada, L. Qin, J.B. Natowitz, S. Shlomo, A. Bonasera, G. Roepke, S. Typel, Z. Chen, M. Huang, J. Wang, H. Zheng, S. Kowalski, C. Bottosso, M. Barbui, M.R.D. Rodrigues, K. Schmidt, D. Fabris, M. Lunardon, S. Moretto, G. Nebbia, S. Pesente, V. Rizzi, G. Viesti, M. Cinausero, G. Prete, T. Keutgen, Y. El Masri, and Z. Majka, Phys. Rev. Lett. **108**, 062702 (2012).

Analysis of fragment yield ratios in the nuclear phase transition, R. Tripathi, A. Bonasera, S. Wuenschel, L.W. May, Z. Kohley, G.A. Souliotis, S. Galanopoulos, K. Hagel, D.V. Shetty, K. Huseman, S.N. Soisson, B.C. Stein, and S.J. Yennello, Phys. Rev. C **83**, 054609 (2011).

Use of the BigSol time of flight spectrometer in the study of superheavy element production, M. Barbui, K. Hagel, J.B. Natowitz *et al.*, Application of Accelerators in Research and Industry: 21st International conference, AIP Conference Proceedings **1336**, 594 (2011).

Search for heavy and superheavy systems in Au-197+Th-232 collisions near the Coulomb barrier, M. Barbui, K. Hagel, J.B. Natowitz *et al.*, International Nuclear Physics Conference 2010 (INPC2010), J. Phys. Conference Series **312**, 082012 (2011).

Neutron multiplicity from primary hot fragments produced in heavy ion reactions near Fermi energy, M.R.D. Rodrigues, R. Wada, K. Hagel *et al.*, International Nuclear Physics Conference 2010 (INPC2010), J. Phys. Conference Series **312**, 082009 (2011).

Evaporation and fission decay of ^{132}Ce compound nuclei at $E_x=122$ MeV: some limitations of the statistical model, A. Di Nitto, E. Vardaci, A. Brondi, G. La Rana, R. Moro, P.N. Nadtochy, M. Trotta, A. Ordine, A. Boiano, M. Cinausero, E. Fioretto, G. Prete, V. Rizzi, D.V. Shetty, M. Barbui, Fabris, M. Lunardon, G. Montagnoli, S. Moretto, G. Viesti, N. Gelli, F. Lucarelli, G.N. Knyazheva and E.M. Kozulin, Eur. Phys. J. A **47**, 83 (2011).

Secondary neutrons as the main source of neutron-rich fission products in the bombardment of a thick U target by 1 GeV protons, A.E. Barzakh, G. Lhersonneau, L.Kh. Batist, D.V. Fedorov, V.S. Ivanov, K.A. Mezilev, P.L. Molkanov, F.V. Moroz, S.Yu. Orlov, V.N. Panteleev, Yu.M. Volkov, O. Alyakrinskiy, M. Barbui, L. Stroe and L.B. Tecchio, Eur. Phys. J. A **47**, 70 (2011).

Constraining the symmetry term in the nuclear equation of state at subsaturation densities and finite temperatures, P. Marini, A. Bonasera, A. McIntosh, R. Tripathi, S. Galanopoulos, K. Hagel, L. Heilborn, Z. Kohley, L.W. May, M. Mehlman, S.N. Soisson, G.A. Souliotis, D.V. Shetty, W.B. Smith, B. C. Stein, S. Wuenschel, and S J. Yennello, Phys. Rev. C **85**, 034617 (2012)

Sensitivity of intermediate mass fragment flows to the symmetry energy, Z. Kohley, M. Colonna, A. Bonasera, L.W. May, S. Wuenschel, M. Di Toro, S. Galanopoulos, K. Hagel, M. Mehlman, W.B. Smith, G A. Souliotis, S.N. Soisson, B.C. Stein, R. Tripathi, S.J. Yennello, and M. Zielinska-Pfabe, Phys. Rev. C **85**, 064605 (2012)

Approaching neutron-rich nuclei toward the r-process path in peripheral heavy-ion collisions at 15 MeV/nucleon, G.A. Souliotis, M. Veselsky, S. Galanopoulos, M. Jandel, Z. Kohley, L.W. May, D.V. Shetty, B.C. Stein, and S.J. Yennello, Phys. Rev. C **84**, 064607 (2011).

Analysis of fragment yield ratios in the nuclear phase transition, R. Tripathi, A. Bonasera, S. Wuenschel, L.W. May, Z. Kohley, G.A. Souliotis, S. Galanopoulos, K. Hagel, D.V. Shetty, K. Huseman, S.N. Soisson, B.C. Stein, and S.J. Yennello, Phys. Rev. C **83**, 054609 (2011).

Transverse collective flow and mid-601rapidity emission of isotopically identified light charged particles, Z. Kohley, L.W. May, S. Wuenschel, M. Colonna, M. Di Toro, M. Zielinska-Pfabe, K. Hagel, R. Tripathi, A. Bonasera, G.A. Souliotis, D.V. Shetty, S. Galanopoulos, M. Mehlman, W.B. Smith, S.N. Soisson, B.C. Stein, and S.J. Yennello, Phys. Rev. C **83**, 044601 (2011).

Role of quasiprojectile isospin asymmetry in nuclear fragmentation, R. Tripathi, A. Bonasera, S. Wuenschel, L.W. May, Z. Kohley, P. Marini, A. McIntosh, G.A. Souliotis, S. Galanopoulos, K. Hagel, D.V. Shetty, K. Huseman, S.N. Soisson, B.C. Stein, and S.J. Yennello, *Int. J. Mod. Phys. E* **21**, 1250019, (2012).

Intermediate mass fragment flow as a probe to the nuclear equation of state, Z. Kohley, L.W. May, S. Wuenschel, M. Colonna, M. Di Toro, M. Zielinska-Pfabe, K. Hagel, R. Tripathi, A. Bonasera, G.A. Souliotis, D.V. Shetty, S. Galanopoulos, M. Mehlman, W.B. Smith, S.N. Soisson, B.C. Stein, and S.J. Yennello, *International Nuclear Physics Conference 2010 (INPC2010)*, *J. Phys. Conference Series* **312**, 082030 (2011).

Development of the MARS separator for heavy element studies, C.M. Folden III, M.C. Alfonso, D.A. Mayorov, K.R. Lawrence, A.A. Alharbi, E. Berdugo, P.J. Cammarata, A.C. Raphelt, B.T. Roeder, and T. A. Werke, *Nucl. Instrum. Methods Phys. Res.* **A678**, 1 (2012).

Measurement of the $^{nat}\text{Lu}(p,X)^{175}\text{Hf}$ excitation function, M.E. Bennett, D.A. Mayorov, K.D. Chapkin, M.C. Alfonso, T.A. Werke, and C.M. Folden III, *Nucl. Instrum. Methods Phys. Res.* **B276**, 62 (2012).

Theory of deuteron stripping: From surface integrals to a generalized R -matrix approach, A.M. Mukhamedzhanov, *Phys. Rev. C* **84**, 044616 (2011).

New measurement of the $^{11}\text{B}(p,\alpha_0)^8\text{Be}$ bare-nucleus $S(E)$ factor via the Trojan horse method, L. Lamia, C. Spitaleri, V. Burjan, N. Carlin, S. Cherubini, V. Crucillà, M. Gameiro Munhoz, M. Gimenez Del Santo, M. Gulino, Z. Hons, G. G. Kiss, V. Kroha, S. Kubono, M. La Cognata, C. Li, J. Mrazek, A. Mukhamedzhanov, R.G. Pizzone, S.M.R. Puglia, Q. Wen, G.G. Rapisarda, C. Rolfs, S. Romano, M.L. Sergi, E. Somorjai, F.A. Souza, A. Szanto de Toledo, G. Tabacaru, A. Tumino, Y. Wakabayashi, H. Yamaguchi, and S.-H. Zhou, *J. Phys. G* **39**, 015106 (2012).

The fluorine destruction in stars: first experimental study of the $^{19}\text{F}(p, \alpha_0)^{16}\text{O}$ reaction at astrophysical energies, M. La Cognata, A.M. Mukhamedzhanov, C. Spitaleri, I. Indelicato, M. Aliotta, V. Burjan, S. Cherubini, A. Coc, M. Gulino, Z. Hons, G.G. Kiss, V. Kroha, L. Lamia, J. Mrázek, S. Palmerini, S. Piskoř, R.G. Pizzone, S.M.R. Puglia, G.G. Rapisarda, S. Romano, M.L. Sergi, and A. Tumino, *Astrophys. J. Lett.* **739**, L54 (2011).

Reexamination of the astrophysical S factor for the $\alpha+d\rightarrow^6\text{Li}+\gamma$ reaction, A.M. Mukhamedzhanov, L.D. Blokhintsev, and B.F. Irgaziev, *Phys. Rev. C* **83**, 055805 (2011).

Low-energy d+d fusion reactions via the Trojan Horse method, A. Tumino, C. Spitaleri, A.M. Mukhamedzhanov, S. Typel, M. Aliotta, V. Burjan, M. Gimenez del Santo, G.G. Kiss, V. Kroha, Z.

Hons, M. La Cognata, L. Lamia, J. Mrazek, R.G. Pizzone, S. Piskor, G.G. Rapisarda, S. Romano, M.L. Sergi, and R. Sparta, *Phys. Lett. B* **700**, 111 (2011).

Clustered low density nuclear matter in near Fermi energy collisions, J.B. Natowitz, K. Hagel, R. Wada, L. Qin, Z. Chen, P. Sahu, G. Ropke, S. Kowalski, C. Bottosso, S. Shlomo, M. Barbui, D. Fabris, M. Lunardon, S. Moretto, G. Nebbia, S. Pesente, V. Rizzi, G. Viesti, M. Cinausero, G. Prete, T. Keutgen, Y. El Masri and Z. Majka, 2nd Workshop on State of The Art in Nuclear Cluster Physics, *Int. J. Mod. Phys. E* **20**, 987 (2011).

Equation of state of symmetric and asymmetric nuclear matter at various densities and temperatures, S. Shlomo, 24th Nuclear Physics Conference – Nuclear Physics in Astrophysics V (NPA5), *J. Phys.: Conference Series* **337**, 012014 (2012).

Virial expansion of the nuclear equation of state, Ruslan Magana, Hua Zheng, Aldo Bonasera, *Int. J. Mod. Phys. E* **21**, 1250006 (2012).

Non-Abelian behavior of alpha bosons in cold symmetric nuclear matter, Hua Zheng, Aldo Bonasera, *Phys. Rev. C* **83**, 057602 (2011).

Deuteron-induced reactions generated by intense lasers for PET isotope production, Sachie Kimura and Aldo Bonasera, *Nucl. Instrum. Methods Phys. Res. A* **637** 1 (2011).

Energy release from hadron-quark phase transition in neutron stars and the axial w mode of gravitational waves, W. Lin, B.A. Li, J. Xu, C.M. Ko, and D.H. Wen, *Phys. Rev. C* **83**, 045802 (2011).

Identifying multiquark hadrons from heavy ion collisions, S. Cho, T. Furumoto, T. Hyodo, D. Jido, C. M. Ko, S.H. Lee, M. Nielsen, A. Ohnishi, T. Sekihara, S. Yasui, and K. Yazaki, *Phys. Rev. Lett.* **106**, 212001 (2011).

Jet conversion and quark coalescence in relativistic heavy-ion collisions, C.M. Ko, *IL Nuovo Cimento*, **34**, 13 (2011).

Triangular flow in heavy ion collisions in a multiphase transport model, J. Xu and C.M. Ko, *Phys. Rev. C* **84**, 014903 (2011).

Jet conversion in quark-gluon plasma, C.M. Ko, *Int. J. Mod. Phys. E* **20**, 1641 (2011).

$D_{sJ}(2317)$ meson production at RHIC, M. Nielsen, L.W. Chen, C.M. Ko, and W. Liu, *Ind. J. Phys.* **85**, 867 (2011).

Analytical relations between nuclear symmetry energy and single-nucleon potentials in isospin asymmetric nuclear matter, C. Xu, B.A. Li, L.W. Chen, and C.M. Ko, Nucl. Phys. **A865**, 1 (2011).

Λ c Enhancement from strongly coupled QGP, S. Yasui, S.H. Lee, K. Ohnishi, I.K. Yoo, and C.M. Ko, Ind. J. Phys. **85**, 1043 (2011).

Charmonium production in relativistic heavy-ion collisions, T. Song, K. Han, and C.M. Ko, Phys. Rev. C **84**, 034907 (2011).

Higher-order anisotropic flows and dihadron Correlations in Pb-Pb collisions at $s_{NN}^{1/2} = 2.76$ TeV in a multiphase transport model, J. Xu and C.M. Ko, Phys. Rev. C **84**, 044907 (2011).

Dilepton production in nucleus-nucleus collisions at top CERN Super Proton Synchrotron energy within the parton-hadron-string-dynamics transport model, O. Linnyk, E.L. Bratkovskaya, V. Ozvenchuk, W. Cassing, and C.M. Ko, Phys. Rev. C **84**, 054917 (2011).

Exotic hadrons in heavy ion collisions, S. Cho, T. Furumoto, T. Hyodo, D. Jido, C.M. Ko, S.H. Lee, M. Nielsen, A. Ohnishi, T. Sekihara, S. Yasui, and K. Yazaki, Phys. Rev. C **84**, 064910 (2011).

Bottomonia suppression in relativistic heavy-ion collisions, T. Song, K.C. Han, and C.M. Ko, Phys. Rev. C **85**, 014902 (2012).

Analysis of dilepton production in Au+Au collisions at $s_{NN}^{1/2}=200$ GeV within the parton-hadron-string-dynamics transport Approach, O. Linnyk, W. Cassing, J. Manninen, E.L. Bratkovskaya, and C. M. Ko, Phys. Rev. C **85**, 024910 (2012).

Imprints of nuclear symmetry energy on properties of neutron stars, B.A. Li, L.W. Chen, M. Gearheart, J. Hooker, C.M. Ko, P.G. Krastev, W.K. Lin, W.G. Newton, D.H. Wen, C. Xu, and J. Xu, Proceedings of International Nuclear Physics Conference, Vancouver, Canada, July 4-9, 2010, J. Phys.: Conf. Ser. **312**, 042006 (2011).

Exotics from heavy ion collisions, A. Ohnishi, S. Cho, T. Furumoto, T. Hyodo, D. Jido, C.M. Ko, S.H. Lee, M. Nielsen, T. Sekihara, S. Yasui, and K. Yazaki, Proceedings of International Conference on Structure of Baryons, Osaka, Japan, December 7-11, 2010, AIP Conference Proceeding **1388**, 404 (2011).

Anisotropic flow and dihadron correlations in a multiphase transport model, C.M. Ko and J. Xu, Proceedings of VII Workshop on Particle Correlations and Femtoscopy, Tokyo, Japan, September 2011, edited by F. Hirano, Proceedings of Sciences **057**, 1 (2012).

Thermal relaxation of charm in hadronic matter, Min He, Rainer J. Fries, and Ralf Rapp, Phys. Lett. **701**, 445 (2011).

Quark recombination and heavy quark diffusion in hot nuclear matter, Rainer J. Fries, Min He, and Ralf Rapp, J. Phys. G **38**, 124068 (2011).

Ideal hydrodynamics for bulk and multistrange hadrons in $\sqrt{s_{NN}} = 200$ AGeV Au-Au Collisions, Min He, Rainer J. Fries, and Ralf Rapp, Phys. Rev. C **85**, 044911 (2012).

Selfconsistent evaluation of charm and charmonium in the quark-gluon plasma, F. Riek and R. Rapp, New J. Phys. **13**, 045007 (2011).

Medium modifications and production of charmonia at LHC, X. Zhao and R. Rapp, Nucl. Phys. **A859** 114 (2011).

Theory of heavy flavor in the quark-gluon plasma, R. Rapp, Nucl. Phys. **A862**,153 (2011).

Thermal Photons and Collective Flow at the Relativistic Heavy-Ion Collider, H. van Hees, C. Gale and R. Rapp, Phys. Rev. C **84**, 054906 (2011).

Theory of soft electromagnetic emission in heavy-ion collisions, R. Rapp, Acta Phys. Pol. **42**, 2823 (2011).

Bottomonia in the quark-gluon plasma and their production at RHIC and LHC, A. Emerick, X. Zhao and R. Rapp, Eur. Phys. J. A **48** 72 (2012).

Quarkonium correlators in the QGP: A T-matrix approach, D. Cabrera and R. Rapp, AIP Conference Proceedings **1343**, 616 (2011).

Heavy quark dynamics in the QGP, V. Greco, H. van Hees, and R. Rapp, AIP Conference Proceedings **1422**, 117 (2012).

Rapidity dependence of deuteron production in central Au+Au collisions at $\sqrt{s_{NN}}=200$ GeV, I.C. Arsene, I.G. Bearden, D. Beavis, S. Bekele, C. Besliu, B. Budick, H. Boggild, C. Chasman, C.H. Christensen, P. Christiansen, H.H. Dalgaard, R. Debbé, J.J. Gaardhoje, K. Hagel, H. Ito, A. Jipa, E.B. Johnson, C.E. Jorgensen, R. Karabowicz, N. Katrynska, E.J. Kim, T.M. Larsen, J.H. Lee, G. Lovhoiden, Z. Majka, M.J. Murray, J.B. Natowitz, B.S. Nielsen, C. Nygaard, D. Pal, A. Qviller, F. Rami, C. Ristea, O. Ristea, D. Rohrich, S.J. Sanders, P. Staszé, T.S. Tveter, F. Videbaek, R. Wada, H. Yang, Z. Yin, and I.S. Zgura, Phys. Rev. C **83**, 044906 (2011).

ρ^0 photoproduction in AuAu collisions at $\sqrt{s_{NN}} = 62.4$ GeV with STAR, G. Agakishiev *et al.* (STAR Collaboration), Phys. Rev. C **85**, 014910 (2012).

Identified hadron compositions in p+p and Au+Au collisions at high transverse momenta at Strangeness enhancement in Cu+Cu and Au+Au collisions at $\sqrt{s_{NN}} = 200$ GeV, G. Agakishiev *et al.* (STAR Collaboration), Phys. Rev. Lett. **108**, 072302 (2012).

System size and energy dependence of near-side di-hadron correlations, G. Agakishiev *et al.* (STAR Collaboration), Phys. Rev. C **85**, 014903 (2012).

Strangeness enhancement of Cu+Cu and Au+Au in $\sqrt{s_{NN}} = 200$ GeV collisions, G. Agakishiev *et al.* (STAR Collaboration), Phys. Rev. Lett. **108**, 072301 (2012).

Directed and elliptic flow of charged particles in Cu+Cu collisions at $\sqrt{s_{NN}} = 22.4$ GeV, G. Agakishiev *et al.* (STAR Collaboration), Phys. Rev. C **85**, 014901 (2012).

Evolution of the differential transverse momentum correlation function with centrality in Au+Au collisions at $\sqrt{s_{NN}} = 200$ GeV, G. Agakishiev *et al.* (STAR Collaboration), Phys. Lett. B **704**, 467 (2011).

Precise measurement of parity violation in polarized muon decay, J.F. Bueno, R. Bayes, Yu.I. Davydov, P. Depommier, W. Faszer, C.A. Gagliardi, A. Gaponenko, D.R. Gill, A. Grossheim, P. Gumpfinger, M.D. Hasinoff, R.S. Henderson, A. Hillairet, J. Hu, D.D. Koetke, R.P. MacDonald, G.M. Marshall, E.L. Mathie, R.E. Mischke, K. Olchanski, A. Olin, R. Openshaw, J.-M. Poutissou, R. Poutissou, V. Selivanov, G. Sheffer, B. Shin, T.D.S. Stanislaus, R. Tacik, and R.E. Tribble, Phys. Rev. D **84**, 032005 (2011).

K^{*0} production in Cu+Cu and Au+Au collisions at $\sqrt{s_{NN}} = 200$ GeV, M.M. Aggarwal *et al.* (STAR Collaboration), Phys. Rev. C **84**, 034909 (2011).

Pion femtoscopy in p+p collisions at $\sqrt{s_{NN}} = 200$ GeV, M.M. Aggarwal *et al.* (STAR Collaboration), Phys. Rev. C **83**, 064905 (2011).

Experimental studies of di-jet survival and surface emission bias in Au+Au collisions via angular correlations with respect to back-to-back leading hadrons, H. Agakishiev *et al.* (STAR Collaboration), Phys. Rev. C **83**, 061901 (R) (2011).

Observation of the anti-matter helium-4 nucleus, G. Agakishiev *et al.* (STAR Collaboration), Nature **473**, 353 (2011).

High p_T nonphotonic electron production in p + p collisions at $\sqrt{s_{NN}} = 200$ GeV, H. Agakishiev *et al.* (STAR Collaboration), Phys. Rev. D **83**, 052006 (2011).

Scaling properties at freeze-out in relativistic heavy-ion collisions, M.M. Aggarwal *et al.* (STAR Collaboration), Phys. Rev. C **83**, 034910 (2011).

Performance of a new LMRPC prototype for the STAR MTD system, Y. Wang *et al.*, Nucl. Instrum. Methods Phys. Res. **A640**, 85 (2011).

Production of Ω mesons in p+p, d+Au, Cu+Cu, and Au+Au collisions at $\sqrt{s_{NN}} = 200$ GeV, A. Adare *et al.* (PHENIX Collaboration), Phys. Rev. C **84**, 044902 (2011).

Event structure and double helicity asymmetry in jet production from polarized p+p collisions at $\sqrt{s_{NN}} = 200$ GeV, A. Adare *et al.* (PHENIX Collaboration), Phys. Rev. D **84**, 012006 (2011).

Heavy quark production in p+p and energy loss and flow of heavy quarks in Au+Au collisions $\sqrt{s_{NN}} = 200$ GeV, A. Adare *et al.* (PHENIX Collaboration), Phys. Rev. C **84**, 044905 (2011).

STAR science for the coming decade, C.A. Gagliardi (for the STAR Collaboration), J. Phys. G **38**, 124130 (2011).

Exploring gluon polarization in the proton with STAR, C.A. Gagliardi (for the STAR Collaboration), Proc. 19th Part. Nucl. Int. Conf. (PANIC11), AIP Conference Proceedings **1441**, 249 (2012).

Gluon polarization and jet production at STAR, P. Djawotho (for the STAR Collaboration), Proc. 19th Int. Spin Phys. Symp. (SPIN2010), J. Phys.: Conf. Ser. **295**, 012061 (2011).

SECTION VII

APPENDIX

TALKS PRESENTED
April 1, 2011 – March 31, 2012

Status of $0^+ \rightarrow 0^+$ superallowed beta decay: tests of CVC and CKM unitarity, J.C. Hardy and I.S. Towner, **J.C. Hardy**, **Invited talk**, International Workshop, “Isospin Symmetry and its breaking in nuclear structure,” sponsored by the Espace de Structure Nucleaire Theoretique (ESNT), Gif-sur-Yvette, France (April 2011).

Precise measurements of the decay properties of superallowed 0^+ -to- 0^+ beta emitters with $T_Z = -1$, **J.C. Hardy**, **Invited talk**, International Conference on Advances in Radioactive Isotope Science, ARIS-2011, Leuven, Belgium (May 2011).

Ernest Rutherford and the origins of nuclear physics, **J.C. Hardy**, **Invited talk**, Annual Congress of the Canadian Association of Physicists, St John’s, Newfoundland, Canada (June 2011).

Nuclear tests of the standard model: vector conservation and CKM unitarity, **J.C. Hardy**, **Invited talk**, XXXII Mazurian Lakes Conference on Physics, Piaski, Poland (September 2011).

Do radioactive half-lives vary with the earth-to-sun distance?, **J.C. Hardy**, **Invited talk**, 18th International Conference on Radionuclide Metrology and its Applications, ICRM 2011, Tsukuba, Japan (September 2011).

Superallowed $0^+ \rightarrow 0^+$ beta decay from $T_Z = -1$ sd-shell nuclei, **J.C. Hardy**, **Invited talk**, XXXV Symposium on Nuclear Physics, Cocoyoc, Mexico (January 2012).

Isospin symmetry-breaking corrections in nuclear beta decay, I.S. Towner and J.C. Hardy, **I.S. Towner**, **Invited talk**, International Workshop, “Isospin Symmetry and its breaking in nuclear structure,” sponsored by the Espace de Structure Nucleaire Theoretique (ESNT), Gif-sur-Yvette, France (April 2011).

Nuclear tests of the standard model: vector current conservation and CKM unitarity, **J.C. Hardy**, **Colloquium** at the University of Bordeaux, Bordeaux, France (May 2011).

Ernest Rutherford and the origins of nuclear physics, **J.C. Hardy**, **Colloquium**, Texas A&M University, College Station, Texas (February 2012).

How idiosyncratic is the weak force? **J.C. Hardy**, **Lecture** to REU students, Cyclotron Institute, Texas A&M University, College Station, Texas (July 2011).

ANC's and (or?) spectroscopic factors from transfer reactions, **R.E. Tribble**, **Invited PlenaryTalk**, ECT Workshop on Transfer Reactions, Trento, Italy (May 2011).

Fundamental symmetries – the standard model, **R.E. Tribble**, **Invited Lecture**, at the National Nuclear Physics Summer School, University of North Carolina, Carolina (July, 2011).

Fundamental symmetries – nuclear beta decay, **R.E. Tribble**, **Invited Lecture**, at the National Nuclear Physics Summer School, University of North Carolina, North Carolina (July, 2011).

Fundamental symmetries – muons, **R.E. Tribble**, **Invited Lecture**, at the National Nuclear Physics Summer School, University of North Carolina, North Carolina (July, 2011).

The worldwide development of rare isotope beam facilities, **R.E. Tribble**, **Invited Talk**, US-Korea Summit on Science and Engineering-UKC2011, Park City, Utah (August, 2011).

Facilities other than US user facilities for nuclear structure and nuclear astrophysics, **R.E. Tribble**, **Invited Talk**, Joint ATLAS-HRIBF-NSCL-FRIB Users Meeting, Michigan State University, East Lansing, Michigan (August, 2011).

The worldwide effort to understand the visible matter in the universe, **R.E. Tribble**, **Invited PlenaryTalk**, Texas Section APS, Commerce, Texas (October, 2011).

Radioactive ion beams for nuclear astrophysics at Texas A&M university, **R.E. Tribble**, **Invited Talk**, International Symposium on the Physics of Unstable Nuclei, Hanoi, Vietnam (November, 2011).

Development of new techniques to determine neutron induced reaction rates, **R.E. Tribble**, **Invited Talk**, 2012 Stewardship Science Academic Alliances Symposium, Washington, D. C. (February, 2012).

Exploring Gluon Polarization in the Proton with STAR, **C.A. Gagliardi**, **Invited Talk**, (for the STAR Collaboration), 19th Part. Nucl. Int. Conf. (PANIC11), Cambridge, Massachusetts (July 2011).

STAR Science for the Coming Decade, **C.A. Gagliardi**, **Invited Talk**, (for the STAR Collaboration), XXII Int. Conf. Ultra-Relativistic Nucl.-Nucl. Coll. (Quark Matter 2011), Annecy, France (May, 2011).

Exploring the Proton Spin with STAR, **C.A. Gagliardi**, **Seminar**, Physics Dept., Penn State University, State College, Pennsylvania (April 2011).

Precision measurements and significance assessment in gamma-ray spectroscopy data evaluation, **N. Nica**, **Seminar** at Horia Hulubei National Institute of Physics and Nuclear Engineering, Bucharest, Romania (April 2011).

Probing fundamental electroweak physics with superallowed beta-decay experiments, **L. Chen**, **Seminar** at Triangle Universities Nuclear Laboratory, Durham, North Carolina (November 2011).

Probing fundamental electroweak physics with superallowed beta-decay experiments, **L. Chen**, **Seminar** at Argonne National Laboratory, Argonne, Illinois (December 2011).

Probing fundamental electroweak physics with superallowed beta-decay experiments, **L. Chen**, **Seminar** at Indiana University, Bloomington, Indiana (December 2011).

High-precision measurements of the superallowed $0^+ \rightarrow 0^+$ beta decays of ^{38}Ca and ^{46}V , **H.I. Park**, **Seminar** at Argonne National Laboratory, Argonne, Illinois (June 2011).

A Study of the Superallowed β^+ Decay of ^{38}Ca , **H.I. Park**, J.C. Hardy, V.E. Iacob, L. Chen, J. Goodwin, V. Horvat, N. Nica, L. Trache and R.E. Tribble, APS Meeting, Anaheim, California (April 2011).

Application of a high speed digitizer to high-precision nuclear β -decay lifetime measurements, **Lixin Chen** and J.C. Hardy, APS Meeting, Anaheim, California (April 2011).

High-precision digital β counting for superallowed β -decay studies, **Lixin Chen** and J.C. Hardy, APS Meeting, East Lansing, Michigan (October 2011).

Superallowed branching ratio in the β decay of ^{34}Ar , **V.E. Jacob** and J.C. Hardy, APS Meeting, East Lansing, Michigan (October 2011).

The search for nuclear molecules in isobaric analog states of ^{10}B , **A. Kuchera**, G. Rogachev, V. Goldberg, E. Johnson, L. Miller, S. Cherubini, M. Gulino, J.C. Hardy, M. LaCognata, M. Lattuada, R.G. Pizzone, S. Romano, C. Spitaleri, R.E. Tribble, W. Trzaska and A. Tumino, APS Meeting, East Lansing, Michigan (October 2011).

Further test of internal conversion theory with a measurement in $^{119\text{m}}\text{Sn}$, **N. Nica**, 19th meeting of the Nuclear Structure and Decay Data (NSDD) network, IAEA, Vienna, Austria (April 2011).

How to draw a level scheme, or about the nature of gamma-ray spectroscopy data evaluation, **N. Nica**, 19th meeting of the Nuclear Structure and Decay Data (NSDD) network, IAEA, Vienna, Austria (April 2011).

Further test of internal-conversion theory with a measurement in $^{119}\text{Sn}^m$, **N. Nica**, U.S. Nuclear Data Program annual meeting, Brookhaven National Laboratory, Upton, New York (November 2011).

Systematic of giant monopole resonance and recent results, **Y.-W. Lui**, **Invited Seminar**, Heavy Ion Research Facility in Lanzhou (HIRFL), Lanzhou, China (September 2011).

Systematic of giant monopole resonance: expected and unexpected, **Y.-W. Lui**, **Invited Seminar**, Chinese Institute of Atomic Energy (CIAE), Beijing, China (September 2011).

The recent result of the giant monopole resonance measurements and their implications, **Y.-W. Lui**, **Invited Seminar**, Konan University, Kobe, Japan (November 2011).

Resonance scattering to study exotic nuclei at the limits of stability, **V.Z. Goldberg**, **Invited Talk**, Nuclear Physics in Astrophysics V (NPA5), Eilat, Israel (April 2011).

Light proton rich nuclei at the border of nuclear stability and beyond? **V.Z. Goldberg**, **Invited Talk**, 4th International Conference on Proton-emitting Nuclei (PROCON2011), Bordeaux, France (June 2011).

Resonance scattering induced by rare beams (status and future), **V.Z. Goldberg**, **Invited Seminar**, Grand Accelérateur National d'Ions Lourds (GANIL), Caen, France (June 2011).

Resonance study of the $\alpha+^{15}\text{N}$ interaction, **V.Z. Goldberg**, **Invited Seminar**, Laboratori Nazionali del Sud (LNS), Catania, Italy (June 2011).

Mysteries of extreme neutron rich light nuclei, can they be solved? **V.Z. Goldberg**, **Invited Seminar**, Joint Institute for Nuclear Research (JINR), Dubna, Russia (July 2011).

The $^{13}\text{C}+\alpha$ reaction is for nuclear physics and astrophysics, **V.Z. Goldberg**, **Invited Seminar**, Cyclotron Laboratory, EuroAsian University, Astana, Kazakstan (October 2011).

Decay spectroscopy for nuclear astrophysics: beta- and beta-delayed proton decay, **L. Trache**, **Invited Talk**, NPA5: 5th Biannual Conference on Nuclear Physics in Astrophysics, Eilat, Israel (April 2011).

Decay Spectroscopy for Nuclear Astrophysics: β -delayed Proton Decay, **L. Trache**, PROCON2011: 4th International Conference on Proton Emitting Nuclei and Related Topics, Bordeaux, France (June 2011).

Indirect methods for nuclear astrophysics: reactions with RIBs. The ANC method, **L. Trache**, **Invited Lecture**, ENAS 6 – VI European Summer School on Experimental Nuclear Astrophysics, St.Tecla Palace, Acireale, Italy (September 2011).

Decay spectroscopy for nuclear astrophysics, **L. Trache**, **Invited Lecture**, ENAS 6 - VI European Summer School on Experimental Nuclear Astrophysics, St.Tecla Palace, Acireale, Italy (September 2011).

Nuclear astrophysics at Texas A&M with indirect methods using Rare Ion Beams, **L. Trache**, **Invited Lecture**, 9th Russbach Workshop on Nuclear Astrophysics, Russbach, Austria (March 2012)..

New Results with TECSA, **B.T. Roeder**, APS Texas Sections Fall Meeting, Texas A&M University, Commerce, Commerce, Texas (October 2011).

Astrobox - a novel detector for nuclear astrophysics studies with low-energy protons, **B.T. Roeder**, APS Division of Nuclear Physics, East Lansing, Michigan (October 2011).

Radioactive Ion Beam Production, **B.T. Roeder**, XVII Escola de Verao "Jorge Andre Swieca" de Fisica Nuclear Experimental-2012, IFUSP, Sao Paulo, Brazil (January 2012).

New Results with TECSA: Study of the $d(^{26}\text{Al},p)^{27}\text{Al}$ Reaction, **B.T. Roeder**, Direct Reaction with Exotic Beams 2012, Pisa, Italy (March 2012).

The Beta-delayed Proton and Gamma Decay of ^{27}P for Nuclear Astrophysics, **Ellen Simmons**, ENAS 6 – VI European Summer School on Experimental Nuclear Astrophysics, St.Tecla Palace, Acireale, Italy (September 2011).

A New Detection System for Very Low-Energy Protons from β -Delayed p -Decay, **Alexandra Spiridon**, ENAS 6 – VI European Summer School on Experimental Nuclear Astrophysics, St.Tecla Palace, Acireale, Italy (September 2011).

Gluon polarization and jet production at STAR, **P. Djawotho**, **Invited Talk**, (for the STAR Collaboration), XIX Int. Workshop Deep-Inelastic Scat. Related Subjects (DIS 2011), Newport News, Virginia (April 2011).

Gluon polarization measurements with STAR, **P. Djawotho**, **Invited Talk**, (for the STAR Collaboration), 4th Workshop APS Topical Group on Hadronic Physics (GHP 2011), Anaheim, California (April 2011).

π^0 -Charged Particle Correlations at $2.5 < \eta < 4.0$ from $p+p$ Collisions at $\sqrt{s} = 200$ GeV, **J. Drachenberg** (for the STAR Collaboration), APS Div. Nucl. Phys. Meeting, East Lansing, Michigan (October 2011).

Learning from early research experience, **S. Mioduszewski**, **Invited Talk**, Women in Physics Conference, Texas A^M University, College Station, Texas (January 2012).

Probing high-temperature QCD matter, **S. Mioduszewski**, **Invited Colloquium**, Florida Atlantic University, Boca Raton, Florida (April 2012).

High- p_T particle productions and correlations in Au+Au Collisions, **Ahmed Hamed**, 6th International Workshop high- p_T physics at LHC 2011, Utrecht, Netherlands (April 2011).

Gamma-hadron correlations at RHIC, **Ahmed Hamed**, The 9th workshop on QCD phase transition and heavy ion collisions, Hangzhou, China (July 2011).

Exploring the quantum universe, **Ahmed Hamed**, **Invited Colloquium**, Public lecture at Ain-Shams University, Cairo Egypt (August 2011).

Quarks, gluons, and the big bang, **Ahmed Hamed**, **Invited Colloquium**, Public lecture at Ain-Shams University, Cairo Egypt (December 2011).

The early universe, **Ahmed Hamed**, **Invited Colloquium**, Public lecture at Cairo University, Cairo Egypt (December 2011).

Our universe, **Ahmed Hamed**, **Invited Colloquium**, Public lecture at American University in Cairo, Cairo Egypt (December 2011).

High- p_T phenomena at RHIC, **Ahmed Hamed**, The Egyptian Center for Theoretical Physics (ECTP) International conference in LHC era, Cairo, Egypt (December 2011).

Relativistic heavy ion collisions and relics from the early universe, **Ahmed Hamed**, Colloquium at Rice University, Houston, Texas (March 2012).

Heavy quarkonia results in the STAR experiment at RHIC, **Matthew Cervantes**, XIX International Workshop on Deep-Inelastic Scattering and Related Subjects (DIS 2011), Newport News, Virginia (April 2011).

Probing symmetries of the weak interaction via the β decay of laser-cooled, polarized ^{37}K , **D. Melconian**, **Invited Seminar**, Indiana University Cyclotron Facility, Indiana University, Bloomington, Indiana (April 2011).

Physics with stopped beams at the TRIP-TRAP facility, **P.D. Shidling**, Joint ATLAS-HRIBF-NSCL-FRIB User Workshop, East Lansing, Michigan (August 2011).

Isospin symmetry breaking in the β decay of ^{32}Cl , **D. Melconian**, **Invited Talk**, XXXII Mazurian Lakes Conference on Physics, Piaski, Poland (September 2011).

Precise lifetime measurement of ^{37}K , **P.D. Shidling**, APS April Meeting, Anaheim, California (April 2011).

Search for superheavy elements in $^{197}\text{Au} + ^{232}\text{Th}$ collisions near the Coulomb barrier, **K. Hagel**, 2011 APS DNP Meeting, East Lansing, Michigan (October 2011).

Low density matter and Bose-Einstein condensate, **Katarzyna Schmidt**, 2011 APS DNP Meeting, East Lansing, Michigan (October 2011).

Measuring cluster fusion plasma temperature and density from $^3\text{He}(d,p)^4\text{He}$ and $d(d,p)^3\text{H}$ reactions, **M. Barbui**, 2011 APS DNP Meeting, East Lansing, Michigan (October 2011).

Flow and correlations: recent experimental results on the symmetry energy and reaction dynamics, **Alan McIntosh**, **Invited Talk**, 7th ANL/INT/JINA/MSU annual FRIB Workshop on Interfaces Between Nuclear Reactions and Structure, Institute for Nuclear Theory, University of Washington, Seattle, Washington (August 2011).

Isotopic trends in dynamical breakup, **Alan McIntosh**, **Invited Talk**, Gordon Research Conference on Nuclear Chemistry, New London, New Hampshire (June 2011)

Nuclear temperatures from quadrupole fluctuations, **Alan McIntosh**, **Invited Talk**, Garvin-Olin Medal Symposium in Honor of Sherry Yennello, APS Meeting, Anaheim, California (April 2011)

Nuclear reactions: how to boil a nucleus and what do we Learn from it? **Sherry Yennello**, **Invited Talk**, International Workshop on Nuclear Physics, Stellenbosch, South Africa (May 2011).

Future perspective on symmetry energy investigations, Sherry Yennello, **Invited Talk**, 2nd International Symposium on Nuclear Symmetry Energy (NuSYM), Northhamptom, Massachusetts (June 2011).

Constraining the symmetry energy of nuclear matter using heavy-ion reactions, **Sherry Yennello**, **Invited Talk**, American Chemical Society Meeting, Denver, Colorado (August 2011).

Investigation of the symmetry energy from transverse collective flow, **Sherry Yennello**, **Invited Talk**, Third International Conference on Nuclear Fragmentation (NUFRA2011), Antalya, Turkey (October 2011).

Studies of heavy residues from peripheral collisions near the Fermi energy, **Sherry Yennello**, **Invited Talk**, APS Division of Nuclear Physics Meeting, East Lansing, Michigan (November, 2011).

Constraining the nuclear symmetry energy from fragment yields, **Paola Marini**, **Invited Talk**, Clusters in Nuclei, Nuclear Matter, HIC and Astrophysics ECT* Trento, Italy (June 2011).

SAMURAI TPC: A time projection chamber for constraining the asymmetry energy at high density, **Alan McIntosh**, APS Division of Nuclear Physics, East Lansing, Michigan (November 2011)

Nuclear caloric curves from quadrupole fluctuations, **Alan McIntosh**, APS Meeting, Anaheim, California (April 2011).

Investigation of the affect of a Coulomb force on velocity distributions in multifragmentation, **L. Heilborn**, APS Division of Nuclear Physics, East Lansing, Michigan (October 2011)

Constraining the symmetry energy from fragment yields, **Paola Marini**, International Workshop on Multifragmentation and Related Topics (IWM2011), GANIL, Caen, France (November 2011).

Approaching neutron-rich nuclei towards the r-process path in deep-inelastic collisions at 15 MeV/nucleon, **G. Souliotis**, 3rd International Conference on Nuclear Fragmentation (NUFRA-2011), Antalya, Turkey (October 2011).

Approaching r-process path nuclei in peripheral heavy-ion collisions at 15 MeV/nucleon, **G. Souliotis**, **Invited Talk**, Dynamical Aspects of Nuclear Fission (DANF-2011), Smolenice, Slovakia (October 2011).

Prospects for the Discovery of the Next New Element, **C.M. Folden III**, **Invited Talk**, 11th International Conference on Nucleus-Nucleus Collisions, San Antonio, Texas (May 2012).

Nuclear Science and Society: Radioactivity, Nuclear Power, and Modern Life, Science Café at Café Revolution, **C.M. Folden III**, Bryan, Texas (March 2012).

Introduction to the Heaviest Elements, **C.M. Folden III**, **Invited Talk**, Nuclear Solutions Institute Colloquium, Texas A&M University, College Station, Texas (November 2011).

The Role of Energy in the Formation of the Heaviest Elements, **C.M. Folden III**, **Invited Talk**, XXXII Mazurian Lakes Conference on Physics, Piaski, Poland (September 2011).

Extraction Chromatographic Studies of Rf Homologs using Crown Ether Based Resins, **M.E. Bennett**, 4th International Conference on the Chemistry and Physics of the Transactinide Elements, Sochi, Russia (September 2011).

The Role of Energy in the Formation of the Heaviest Elements, **C.M. Folden III**, 4th International Conference on the Chemistry and Physics of the Transactinides Elements, Sochi, Russia (September 2011).

Extraction Chromatographic Studies of Rf Homologs using Crown Ether Based Resins, **M.E. Bennett**, 242nd American Chemical Society National Meeting, Denver, Colorado (August 2011).

Extraction Chromatographic Studies of Rf Homologs using Crown Ether Based Resins, **M.E. Bennett**, American Nuclear Society National Meeting, Hollywood, Florida (June 2011).

Hadronization by quark coalescence, **C.M. Ko**, **Invited talk**, Jet and Electromagnetic Tomography Summer School, Duke University, Durham, North Carolina (June 2011).

Pion production in transport models, **C.M. Ko**, **Invited talk**, International Symposium on Nuclear Symmetry Energy, Smith College, Northampton, Massachusetts (June 2011).

Triangular flow in relativistic heavy ion collisions, **C.M. Ko**, **Invited talk**, Workshop on QCD Phase Transitions and Relativistic Heavy Ion Collisions, Hangzhou, China (July 2011).

Quarkonia production in HIC, **C.M. Ko**, **Invited talk**, International Symposium on Non-equilibrium Dynamics, Heraklion, Crete, Greece (August 2011).

Anisotropic flows and dihadron correlations in heavy ion collisions, **C.M. Ko**, International Workshop on Particle Correlations and Femtoscopy, Tokyo, Japan (September 2011).

Quarkonia production in heavy ion collisions, **C.M. Ko**, **Invited talk**, International Conference on Primordial QCD Matter in LHC Era, Cairo, Egypt (December 2011).

Exotic hadrons production in HIC, **C.M. Ko**, **Invited talk**, Workshop on Hyperon-Hyperon Interactions and Searches for Exotic Di-Hyperons in Nuclear Collisions, Brookhaven National Laboratory, Upton, New York (February 2012).

Resonances in AMPT, **C.M. Ko**, **Invited talk**, Workshop on Hadronic Resonance Production in Heavy Ion and Elementary Collisions, Austin, Texas (March 2012).

*Short-range correlations, nuclear reactions and spectroscopic information, **A.M. Mukhamedzhanov, Invited Talk***, ECT* Workshop on Correlations in Light Systems, Trento, Italy (June 2011).

*Advances in nuclear reaction theory, **A.M. Mukhamedzhanov, Invited Talk***, DEO Panel (June 2011).

*Equation of state of symmetric and asymmetric nuclear matter at various densities and temperatures, **S. Shlomo, Invited Talk***, European Physical Society – 24th Nuclear Physics Conference :Nuclear Physics in Astrophysics V (NPA5), Eilat, Israel (April 2011).

*Modern energy density functional and the equation of state of nuclear matter. **S. Shlomo, Invited Talk***, Department of Physics, Ohio University, Athens Ohio (February 2012).

*Quark recombination and heavy quarks, **Rainer J. Fries, Invited Talk***, 6th Workshop on High- P_T Physics at LHC, Utrecht, Netherlands (April 2011).

*Quark recombination and heavy quarks, **Rainer J. Fries, Invited Seminar***, University of Minnesota, Minneapolis Minnesota (April 2011).

*Quark recombination and heavy quark diffusion, **Rainer J. Fries***, Quark Matter 2011, Annecy, France (May 2011).

*Heavy flavor diffusion and hadronization in quark-gluon plasma, **Min He, Invited talk***, RHIC & AGS Annual Users' Meeting 2011, Brookhaven National Laboratory, Upton, New York (June 2011).

*Toward a complete description of heavy flavor transport in medium, **Min He***, 7th International Workshop on the Critical Point and Onset of Deconfinement, CCNU, Wuhan, China (November 2011).

*Quark-gluon plasma: from QCD thermodynamics to heavy ion collision phenomenology, **M. He***, Shanghai Jiaotong University, Shanghai, China (October 2011).

*Quark-gluon plasma: from QCD thermodynamics to heavy ion collision phenomenology, **M. He***, Tsinghua University, Beijing, China (October 2011).

*Quark-gluon plasma: from QCD thermodynamics to heavy ion collision phenomenology, **M. He***, National University of Defence Technology, Changsha, China (November 14, 2011).

*Quark-gluon plasma: from QCD thermodynamics to heavy ion collision phenomenology, **M. He***, Nanjing University, Nanjing, China (November 2011).

*Quark-gluon plasma: from QCD thermodynamics to heavy ion collision phenomenology, **M. He***, University of Science & Technology of China, Hefei, China (November 2011).

*Ideal hydrodynamics for bulk & multistrange hadrons at RHIC, **Min He***, Ohio State University, Columbus, Ohio (March 2012).

*Theory of thermal dilepton emission, **R. Rapp, Invited Talk***, Int. Symposium on Charm, Dileptons and Deconfinement, Helmholtz Zentrum Rossendorf, Dresden, Germany (April 2011).

*Many-body approach to heavy flavor in QGP, **R. Rapp, Invited Talk***, Brookhaven Summer Program on Quarkonium in Hot Media, Brookhaven National Laboratory, Upton, New York (June 2011).

Theory of soft electromagnetic emission in heavy-ion collisions, **R. Rapp**, **Invited Lectures**, 51th Cracow School of Theoretical Physics on Soft Side of the LHC, Zakopane, Poland (June 2011).

Overview of open and hidden heavy flavor in hot matter, **R. Rapp**, **Invited Opening Theory Lecture**, 486th Heraeus Seminar (workshop) on Characterizing the QGP with Heavy Quarks, Physikzentrum Bad Honnef, Bad Honnef, Germany (July 2011).

Thermal dileptons: a versatile meter of quark-hadron matter in heavy-ion collisions, **R. Rapp**, **Invited Talk**, STAR Analysis Meeting, University of California at Davis, Davis, California (August 2011).

T-matrix approach to quarkonia in QGP, **R. Rapp**, **Invited Talk**, Int. EMMI workshop on Quarkonia in Deconfined Matter, Acitrezza, Sicily, Italy (September 2011).

Heavy flavor in medium, **R. Rapp**, **Invited Talk**, Quarkonium Theory Workshop, TRIUMF, Vancouver, Canada (October 2011).

Theory of thermal dilepton emission, **R. Rapp**, **Invited Lecture**, Int. School for High-Energy Nuclear Collisions, Central China Normal University, Wuhan, China (October 2011).

The versatility of thermal photons and dileptons, **R. Rapp**, **Invited Talk**, Int. workshop on Thermal Photons and Dileptons, Brookhaven National Laboratory, Upton, New York (December 2011).

In-medium sum rules for vector and axialvector mesons, **P. Hohler**, **Invited Talk**, Int. Resonance Workshop at University of Texas, Austin, Texas (March 2012).

Heavy flavor in hot/dense matter, **R. Rapp**, **Invited Seminar**, RIKEN/BNL Nuclear Theory seminar, Brookhaven National Laboratory, Upton, New York (March 2012).

Mass dissolution and deconfinement, and the quark-gluon plasma, **R. Rapp**, Graduate Student Research Seminar, Texas A&M University, College Station, Texas (November 2011).

RESEARCH PERSONNEL AND ENGINEERING STAFF

April 1, 2011 - March 31, 2012

Faculty and Research Group Leaders

Aldo Bonasera, Research Scientist
Charles M. Folden III, Assist. Prof. of Nuclear
Chemistry
Rainer Fries, Assist. Professor of Physics
Carl A. Gagliardi, Professor of Physics
John C. Hardy, Professor of Physics
Che Ming Ko, Professor of Physics
Dan Melconian, Assist. Professor of Physics
Saskia Mioduszewski, Assist. Prof. of Physics
J. B. Natowitz, Professor of Chemistry, Bright Chair
Ralf Rapp Associate Professor of Physics
Shalom Shlomo, Senior Scientist
Robert E. Tribble, Professor of Physics, Director
Rand L. Watson, Professor of Chemistry - Retired
Sherry J. Yennello, Professor of Chemistry
Dave H. Youngblood, Professor of Physics
Akram M. Zhanov, Senior Scientist

Research Staff

Marina Barbui, Assist. Research Scientist
Henry Clark, Accelerator Physicist (50%)
Grigor Chubaryan, Research Scientist
Vladilen Goldberg, Research Scientist
John C. Hagel, Research Scientist (50%)
Vladimir Horvat, Research Scientist (50%)
Victor Iacob, Associate Research Scientist
Yiu-Wing Lui, Research Scientist
Ninel Nica, Assist. Research Scientist
George Souliotis, Associate Research Scientist
Livius Trache, Research Scientist
Meiko Uesaka, Research Scientist – From 2/1/12
Ryoichi Wada, Research Scientist – Retired

Visiting Scientists

Ian Towner – From 6/29/11 To 8/31/11

Accelerator Physics and Radiation Line Staff

Joseph Brinkley, Research Associate
Henry Clark, Accelerator Physicist (50%)
Vladimir Horvat, Research Scientist (50%)
Bruce Hyman, Research Associate
George Kim, Accelerator Physicist
Don May, Accelerator Physicist

Brian Roeder, Accelerator Physicist – From
2/1/12

Gabriel Tabacaru, Accelerator Physicist

Computer Systems Staff

Robert Burch, Jr., Lead Microcomputer/LAN
Administrator

John C. Hagel, Research Scientist (50%)

Engineering Staff

Greg Derrig, Senior Mechanical Engineer
Robert Olsen, Senior Mechanical Engineer

Postdoctoral Research Associates

Megan Bennett – From 5/25/11

Lixin Chen

Pibero Djawotho

Vasily Eremenko – From 3/1/12

Gianluca Giuliani – From 7/13/11

Ahmed Hamed

Min He

Paul Hohler – From 9/1/11

Krishichayan – To 9/1/11

Paola Marini – To 9/2/11

Matthew McCleskey – From 9/1/11

Alan McIntosh

Mirganka Mondal – From 11/21/11

Hyo-In Park – From 11/1/11

Gian Luca Pizzone

Marcia Rodrigues – To 6/3/11

Brian Roeder – To 1/31/12

Antti Saastamoinen – From 3/29/12

Katarzyna Schmidt

Praveen Shidling

Taesoo Song

Jun Xu – To 12/31/11

STUDENTS

April 1, 2011 - March 31, 2012

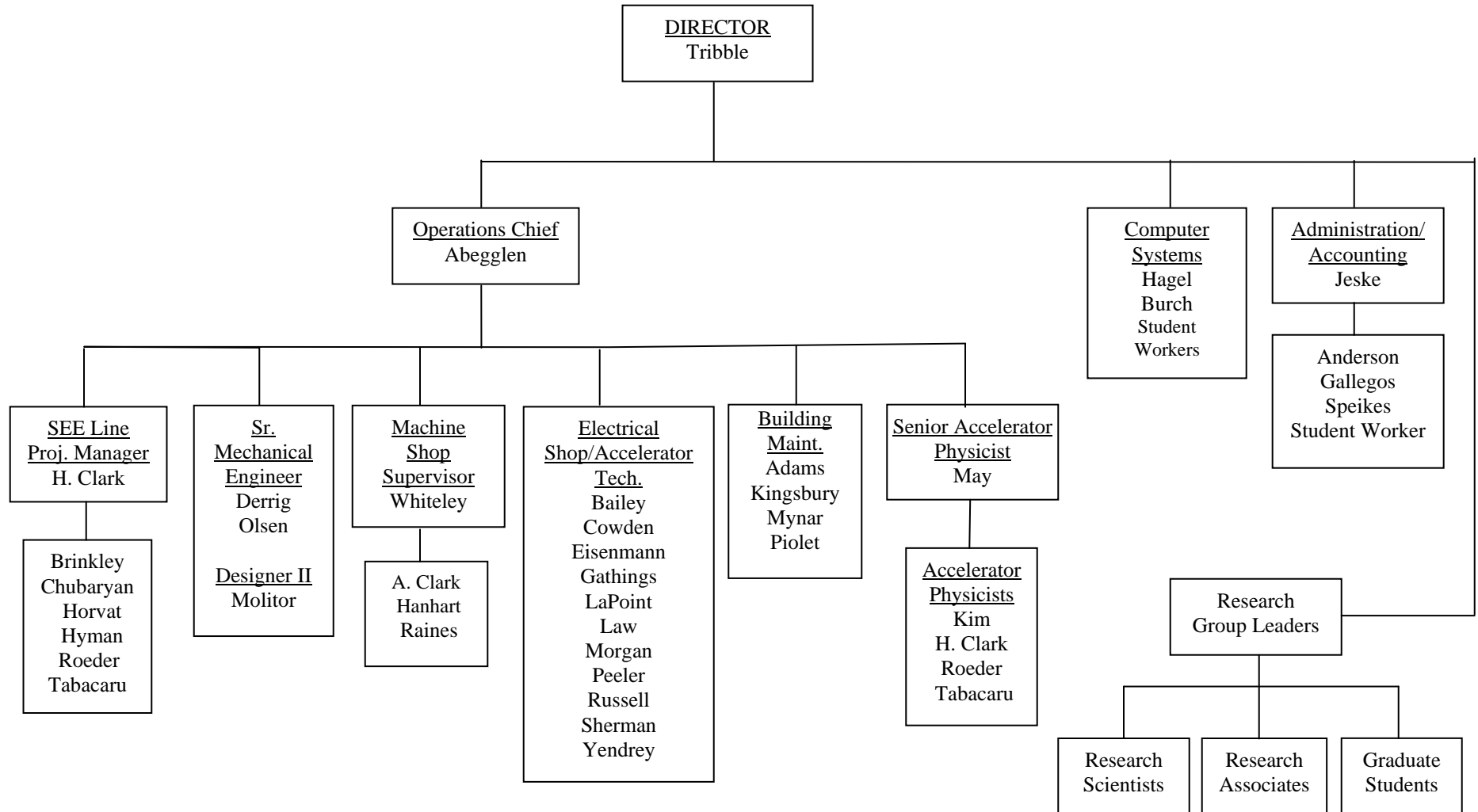
Graduate Students

Mason Anders
Marisa Alfonso
Matteo Barbarino
Richard Spence Behling
Miguel Bencomo – From 6/1/11
Jonathan Button
Paul Cammarata – From 6/1/11
Zilong Chang – From 6/1/11
Matthew Cervantes
Roman Chyzh
Guangyao Chen
Martin Codrington
James Drachenberg
Benjamin Fenker
John Goodwin
Kyong Choi Han
Lauren Heilborn
Kyle Higgins
Nathan Holt – From 6/1/11
Liaoyuan Huo
Feng Li
Larry May
Demitri Mayarov
Matthew McCleskey – To 8/31/11
Michael Mehlman
Hyo-In Park – To 8/31/11
Andrew Raphelt
Ellen Simmons
Alexandra Spiridon
Sidharth Somanathan – From 6/1/11
Brian Stein
Tyler Werke
Hua Zheng

Undergraduates and Student Technicians

Morgan Allen – From 5/18/11
Giacoma Bonasera
Kathrine Galvin – From 7/6/11
Zachary Gastony – From 2/3/12
Mathew Johnson – From 9/8/11
Kyle Molitor – To 12/21/11
Ashley Noack – To 5/15/11
Amanda Spaw – To 7/5/11

ORGANIZATIONAL CHART - CYCLOTRON INSTITUTE



VII-12

**STUDENTS WHO RECEIVED GRADUATE DEGREES
FROM THESIS WORK CONDUCTED
AT
THE CYCLOTRON INSTITUTE**

April 1, 2011 – March 31, 2012

Name	Year	Thesis Title	Advisor	Present Position
Hyo-In Park	2011	<i>High-Precision Measurements of the Superaligned $0^+ \rightarrow 0^+$ Beta Decays of ^{38}Ca and ^{46}V</i>	J. C. Hardy	Post Doc., Cyclotron Institute, Texas A&M University, College Station, Texas
Mathew McCleskey	2011	<i>$^{14}\text{C}(n,g)^{15}\text{C}$ as a Test Case in the Evaluation of a New Method to Determine Spectroscopic Factors Using Asymptotic Normalization Coefficients</i>	R. E. Tribble	Post Doc., Lawrence Livermore National Laboratory, Livermore, California and Cyclotron Institute, Texas A&M University, College Station, Texas

INSTITUTE COLLOQUIA AND SEMINARS
April 1, 2011-March 31, 2012

2011

April 21	Dr. Pibero Djawotho, Cyclotron Institute, Texas A&M University, College Station, Texas	<i>Gluon Polarization Measurements with STAR</i>
May 2	Professor G. Wolschin, University of Heidelberg, Heidelberg, Germany	<i>Heavy Ion at LHC Energies: Selected Predictions vs. First Data</i>
May 10	Professor J. Stone, Oxford University, United Kingdom and University of Tennessee, Knoxville, Tennessee	<i>Nuclear Matter and Giant Resonance Constraints on Models of Nucleon-Nucleon Interaction</i>
May 11	Professor N. Stone, Oxford University, United Kingdom and University of Tennessee, Knoxville, Tennessee	<i>Pathological Physics is Alive and Well</i>
May 12	Dr. R. K Choudhury, Nuclear Physics Division, Bhabha Atomic Research Center, Mumbai, India	<i>Near Scission Alpha-particle Emission in Fission</i>
May 19	Professor Vitaly Efimov, University of Washington, Seattle	<i>Giant Quantum Few-Body Systems</i>
May 26	Professor Igal Talmi, Weizmann Institute of Science, Rehovot, Israel	<i>The Nuclear Shell Model – Older Than 60 Years</i>
June 8	Dr. Woosuk Bang, Fusion Research Center, The University of Texas at Austin, Austin, Texas	<i>Cluster Fusion Experiment on the Texas Petawatt</i>
August 2	Dr. Marco Mazzocco, Dipartimento di Fisica and INFN – Sezione di Padova, Padova, Italy	<i>Reaction Dynamics Studies with the Facility EXOTIC at LNL</i>
August 16	Professor George A. Souliotis, Laboratory of Physical Chemistry, Department of Chemistry, National and Kapodistrian University of Athens, Athens, Greece and Cyclotron Institute, Texas A&M University, College Station, Texas	<i>Production of Neutron-rich Nuclei Towards the r-process Path in Peripheral Heavy-Ion Collisions at 15 MeV/nucleon</i>

August 23	Professor Bao-An Li, Department of Physics and Astronomy, Texas A&M University – Commerce, Commerce, Texas	<i>A Few New Issues Regarding the Density Dependence of Nuclear Symmetry Energy</i>
September 13	Dr. Kenneth Nollett, Physics Division, Argonne National Laboratory, Argonne, Illinois	<i>Ab Initio Nuclear Widths, Real and Virtual</i>
September 20	Professor Andrzej Wieloch, M. Smoluchowski Institute of Physics, Jagiellonian University, Krakow, Poland	<i>Critical-like Behavior in a Lattice Gas Model</i>
September 27	Professor Gerd Roepke, Institute of Physics, University of Rostock, Rostock, Germany	<i>Cluster Formation in Nuclear Systems</i>
October 31	Professor C. O. Dorso, GEBI - University of Buenos Aires, Buenos Aires, Argentina	<i>From Nuclei to Neutron Stars</i>
November 29	Professor C. Spitaleri, Dipartimento di Fisica ed Astronomia, University of Catania and INFN – Laboratori Nazionali del Sud, Catania, Italy	<i>Recent Results in Nuclear Astrophysics with the Trojan Horse Method</i>
December 6	Dr. Felix Liang, Physics Division, Oak Ridge National Laboratory, Oak Ridge, Tennessee	<i>Fusion Induced by Neutron-rich Radioactive Sn Nuclei</i>
<u>2012</u>		
February 21	Dr. M. La Cognata, INFN - Laboratori Nazionali del Sud, Catania, Italy	<i>The Fluorine Destruction in Stars: First Experimental Study of the $^{19}\text{F}(p,\alpha_0)^{16}\text{O}$ reaction at Astrophysical Energies</i>
February 28	Dr. Marisa Gulino, INFN LNS and Kore University of Enna, Sicily, Italy	<i>Neutron Induced Reactions and Trojan Horse Method</i>
March 6	Dr. Robert Michaels, Thomas Jefferson National Accelerator Facility, Newport News, Virginia	<i>Electron Scattering at JLab and Lead Radius Experiment PREX</i>